



# MULTI-SCALE COMPUTATIONAL CARDIOLOGY

EDITED BY: Ling Xia, Henggui Zhang and Dingchang Zheng  
PUBLISHED IN: Frontiers in Physiology



# frontiers

## Frontiers eBook Copyright Statement

The copyright in the text of individual articles in this eBook is the property of their respective authors or their respective institutions or funders. The copyright in graphics and images within each article may be subject to copyright of other parties. In both cases this is subject to a license granted to Frontiers.

The compilation of articles constituting this eBook is the property of Frontiers.

Each article within this eBook, and the eBook itself, are published under the most recent version of the Creative Commons CC-BY licence.

The version current at the date of publication of this eBook is CC-BY 4.0. If the CC-BY licence is updated, the licence granted by Frontiers is automatically updated to the new version.

When exercising any right under the CC-BY licence, Frontiers must be attributed as the original publisher of the article or eBook, as applicable.

Authors have the responsibility of ensuring that any graphics or other materials which are the property of others may be included in the CC-BY licence, but this should be checked before relying on the CC-BY licence to reproduce those materials. Any copyright notices relating to those materials must be complied with.

Copyright and source acknowledgement notices may not be removed and must be displayed in any copy, derivative work or partial copy which includes the elements in question.

All copyright, and all rights therein, are protected by national and international copyright laws. The above represents a summary only. For further information please read Frontiers' Conditions for Website Use and Copyright Statement, and the applicable CC-BY licence.

ISSN 1664-8714

ISBN 978-2-88974-594-4

DOI 10.3389/978-2-88974-594-4

## About Frontiers

Frontiers is more than just an open-access publisher of scholarly articles: it is a pioneering approach to the world of academia, radically improving the way scholarly research is managed. The grand vision of Frontiers is a world where all people have an equal opportunity to seek, share and generate knowledge. Frontiers provides immediate and permanent online open access to all its publications, but this alone is not enough to realize our grand goals.

## Frontiers Journal Series

The Frontiers Journal Series is a multi-tier and interdisciplinary set of open-access, online journals, promising a paradigm shift from the current review, selection and dissemination processes in academic publishing. All Frontiers journals are driven by researchers for researchers; therefore, they constitute a service to the scholarly community. At the same time, the Frontiers Journal Series operates on a revolutionary invention, the tiered publishing system, initially addressing specific communities of scholars, and gradually climbing up to broader public understanding, thus serving the interests of the lay society, too.

## Dedication to Quality

Each Frontiers article is a landmark of the highest quality, thanks to genuinely collaborative interactions between authors and review editors, who include some of the world's best academicians. Research must be certified by peers before entering a stream of knowledge that may eventually reach the public - and shape society; therefore, Frontiers only applies the most rigorous and unbiased reviews. Frontiers revolutionizes research publishing by freely delivering the most outstanding research, evaluated with no bias from both the academic and social point of view. By applying the most advanced information technologies, Frontiers is catapulting scholarly publishing into a new generation.

## What are Frontiers Research Topics?

Frontiers Research Topics are very popular trademarks of the Frontiers Journals Series: they are collections of at least ten articles, all centered on a particular subject. With their unique mix of varied contributions from Original Research to Review Articles, Frontiers Research Topics unify the most influential researchers, the latest key findings and historical advances in a hot research area! Find out more on how to host your own Frontiers Research Topic or contribute to one as an author by contacting the Frontiers Editorial Office: [frontiersin.org/about/contact](https://frontiersin.org/about/contact)



# MULTI-SCALE COMPUTATIONAL CARDIOLOGY

Topic Editors:

**Ling Xia**, Zhejiang University, China

**Henggui Zhang**, The University of Manchester, United Kingdom

**Dingchang Zheng**, Coventry University, United Kingdom

**Citation:** Xia, L., Zhang, H., Zheng, D., eds. (2022). Multi-Scale Computational Cardiology. Lausanne: Frontiers Media SA. doi: 10.3389/978-2-88974-594-4

# Table of Contents

- 05 Editorial: Multi-Scale Computational Cardiology**  
Ling Xia, Henggui Zhang and Dingchang Zheng
- 07 A Novel Model Based on Spatial and Morphological Domains to Predict the Origin of Premature Ventricular Contraction**  
Kaiyue He, Jian Sun, Yiwen Wang, Gaoyan Zhong and Cuiwei Yang
- 18 A New Method for Detecting Myocardial Ischemia Based on ECG T-Wave Area Curve (TWAC)**  
Ronghua Li, Xiaoye Zhao, Yinglan Gong, Jucheng Zhang, Ruiqing Dong and Ling Xia
- 26 Recurrence Plot-Based Approach for Cardiac Arrhythmia Classification Using Inception-ResNet-v2**  
Hua Zhang, Chengyu Liu, Zhimin Zhang, Yujie Xing, Xinwen Liu, Ruiqing Dong, Yu He, Ling Xia and Feng Liu
- 39 The Comparison of Different Constitutive Laws and Fiber Architectures for the Aortic Valve on Fluid–Structure Interaction Simulation**  
Li Cai, Ruihang Zhang, Yiqiang Li, Guangyu Zhu, Xingshuang Ma, Yongheng Wang, Xiaoyu Luo and Hao Gao
- 56 HADLN: Hybrid Attention-Based Deep Learning Network for Automated Arrhythmia Classification**  
Mingfeng Jiang, Jiayan Gu, Yang Li, Bo Wei, Jucheng Zhang, Zhikang Wang and Ling Xia
- 66 Development of Novel Fractal Method for Characterizing the Distribution of Blood Flow in Multi-Scale Vascular Tree**  
Peilun Li, Qing Pan, Sheng Jiang, Molei Yan, Jing Yan and Gangmin Ning
- 78 Comparison of Newtonian and Non-newtonian Fluid Models in Blood Flow Simulation in Patients With Intracranial Arterial Stenosis**  
Haipeng Liu, Linfang Lan, Jill Abrigo, Hing Lung Ip, Yannie Soo, Dingchang Zheng, Ka Sing Wong, Defeng Wang, Lin Shi, Thomas W. Leung and Xinyi Leng
- 89 Corrigendum: Comparison of Newtonian and Non-newtonian Fluid Models in Blood Flow Simulation in Patients With Intracranial Arterial Stenosis**  
Haipeng Liu, Linfang Lan, Jill Abrigo, Hing Lung Ip, Yannie Soo, Dingchang Zheng, Ka Sing Wong, Defeng Wang, Lin Shi, Thomas W. Leung and Xinyi Leng
- 90 Etiology-Specific Remodeling in Ventricular Tissue of Heart Failure Patients and Its Implications for Computational Modeling of Electrical Conduction**  
Aparna C. Sankarankutty, Joachim Greiner, Jean Bragard, Joseph R. Visker, Thirupura S. Shankar, Christos P. Kyriakopoulos, Stavros G. Drakos and Frank B. Sachse

- 107 Consistency in Geometry Among Coronary Atherosclerotic Plaques Extracted From Computed Tomography Angiography**  
Haipeng Liu, Aleksandra Wingert, Xinhong Wang, Jucheng Zhang, Jianzhong Sun, Fei Chen, Syed Ghufraan Khalid, Yinglan Gong, Ling Xia, Jun Jiang, Jian'an Wang and Dingchang Zheng
- 119 Mitochondrial Contributions in the Genesis of Delayed Afterdepolarizations in Ventricular Myocytes**  
Vikas Pandey, Lai-Hua Xie, Zhilin Qu and Zhen Song
- 128 Pacing Electrocardiogram Detection With Memory-Based Autoencoder and Metric Learning**  
Zhaoyang Ge, Huiqing Cheng, Zhuang Tong, Lihong Yang, Bing Zhou and Zongmin Wang
- 142 Preliminary Study: Learning the Impact of Simulation Time on Reentry Location and Morphology Induced by Personalized Cardiac Modeling**  
Lv Tong, Caiming Zhao, Zhenyin Fu, Ruiqing Dong, Zhenghong Wu, Zefeng Wang, Nan Zhang, Xinlu Wang, Boyang Cao, Yutong Sun, Dingchang Zheng, Ling Xia and Dongdong Deng



# Editorial: Multi-Scale Computational Cardiology

Ling Xia<sup>1\*</sup>, Henggui Zhang<sup>2</sup> and Dingchang Zheng<sup>3</sup>

<sup>1</sup> Department of Biomedical Engineering, Zhejiang University, Hangzhou, China, <sup>2</sup> Biological Physics Group, The University of Manchester, Manchester, United Kingdom, <sup>3</sup> Research Centre of Intelligent Healthcare, Coventry University, Coventry, United Kingdom

**Keywords:** computational cardiology, computational fluid dynamics - CFD, cardiac electrophysiology, modeling and simulation, ECG signal processing

## Editorial on the Research Topic

### Multi-Scale Computational Cardiology

Computational cardiology plays an increasingly important role in elucidating the physiological and pathological mechanism(s) of normal and abnormal cardiac functions, guiding the development of new diagnostic technologies and treatment strategies, and predicting treatment outcomes. Recently, we called for paper submissions on the Research Topic of *Multi-Scale Computational Cardiology*. Twelve manuscripts were finally accepted for publications, where important scientific progress has been reported, covering computational fluid dynamics of circulation system (four papers), multi-scale cardiac electrophysiology modeling and simulation (three papers), and AI-related ECG signal processing (five papers). There are briefly summarized below.

Coronary artery disease (CAD) is the leading cause of death globally, but there is a lack of studies on the three-dimensional (3D) geometric characteristics of coronary plaque. Liu, Wingert et al. investigated whether coronary plaques of different sizes were consistent in geometric properties. Nineteen cases with symptomatic stenosis caused by atherosclerotic plaques in the left coronary artery were included in their study. 3D coronary atherosclerotic plaques and calcifications were identified, reconstructed, and manually revised based on computed tomography angiography images. Multidimensional geometric parameters were measured on the 3D models of plaques and calcifications. Linear and non-linear (power function) fittings were used to investigate the relationship between multidimensional geometric parameters. Their results disclosed the geometric consistency among coronary atherosclerotic plaques of different sizes.

Newtonian fluid model has been commonly applied in simulating cerebral blood flow in intracranial atherosclerotic stenosis (ICAS) cases using computational fluid dynamics (CFD) modeling, while blood is a shear-thinning non-Newtonian fluid. Liu, Lan et al. investigated the difference of cerebral hemodynamic metrics in CFD models with both Newtonian and non-Newtonian fluid assumptions, in patients with ICAS. The results suggested that Newtonian fluid model could be applicable for pressure ratio calculation, but caution needs to be taken when using the Newtonian assumption in simulating wall shear stress especially in severe ICAS cases considering the observable differences of wall shear stress between Newtonian and non-Newtonian estimations in areas with low shear rates distal to a stenosis.

It has been reported that 250,000 heart valve surgeries are performed worldwide each year. Among these, aortic valve (AV) diseases have become the second-leading cause of cardiovascular diseases due to their high morbidity and mortality. Numerical simulations of the AV dynamics can be applied to assess the hemodynamic performance, predict the effectiveness and persistence of surgical treatments, thereby guide AV disease management. Cai et al. presented a simulation study of different constitutive laws and fiber architectures for the AV on fluid-structure interaction. The results suggested that the strain energy function with exponential terms for both the fiber and cross-fiber directions could be more suitable for describing the AV leaflet mechanical behaviors.

## OPEN ACCESS

### Edited and reviewed by:

Raimond L. Winslow,  
Johns Hopkins University,  
United States

### \*Correspondence:

Ling Xia  
xialing@zju.edu.cn

### Specialty section:

This article was submitted to  
Computational Physiology and  
Medicine,  
a section of the journal  
Frontiers in Physiology

**Received:** 01 January 2022

**Accepted:** 13 January 2022

**Published:** 07 February 2022

### Citation:

Xia L, Zhang H and Zheng D (2022)  
Editorial: Multi-Scale Computational  
Cardiology. *Front. Physiol.* 13:847118.  
doi: 10.3389/fphys.2022.847118

Blood perfusion is an important index for the function of the cardiovascular system. It can be indicated by the blood flow distribution in the vascular tree. Li et al. proposed a novel fractal method for characterizing the distribution of blood flow in multi-scale vascular tree. Their validation on real arterial trees verified the ability of the produced parameters (fractal dimension and multifractal spectrum) in distinguishing the blood flow distribution under different physiological states. The results suggested that both the vascular structure and the blood flow distribution affect the fractal parameters for blood flow.

In recent years, ventricular tachycardia ablation strategy based on personalized virtual-heart technology has been researched and gradually applied to clinical practice. Due to the high demanding of computational resource of modeling, the arrhythmias induced in the models are usually simulated only for a few seconds. In clinic, however, it is common that arrhythmias last for more than several minutes and the morphologies of reentries are not always stable. So scientific evidence is required to demonstrate how long the simulation of arrhythmias is efficient to match the arrhythmias detected in real patients. Tong et al.'s investigation suggested that 10 s simulation was sufficient to make arrhythmias simulation results stable.

Recent experimental evidence has indicated that mitochondrial depolarization promotes arrhythmogenic delays afterdepolarizations (DADs) in cardiac myocytes. However, the non-linear interactions among the  $\text{Ca}^{2+}$  signaling pathways, ROS, and oxidized  $\text{Ca}^{2+}$ /calmodulin-dependent protein kinase II (CaMKII) pathways make it difficult to reveal the mechanisms. Based on a recently developed spatiotemporal ventricular myocyte computer model, Pandey et al. concluded that the direct redox effect of ROS on ryanodine receptors (RyRs) plays a critical role in promoting  $\text{Ca}^{2+}$  waves and DADs under the acute effect of mitochondrial depolarization.

Computational modeling of the failing heart provides insights into mechanisms of arrhythmogenesis, risk stratification of patients, and clinical treatment. Sankarankutty et al. provided a microscopy-based foundation for modeling conduction in HF tissues. Their result suggested that conduction differs in the two etiologies due to the characteristics of fibrosis, highlighting the importance of the etiology-specific modeling of HF tissues and integration of medical history into electrophysiology models for personalized risk stratification and treatment planning.

Pace mapping is commonly used to locate the origin of ventricular arrhythmias, especially premature ventricular contraction (PVC). He et al. proposed a novel model based on spatial and morphological domains to predict the origin of PVC. The results showed that the proposed model was slightly superior to other models by achieving the most hits, the smallest estimated errors, and the biggest reduced distances for the PVC origin site estimation.

Remote ECG diagnosis has been gradually used in the clinical ECG workflow, especially for patients with pacemaker. An automatic detection pacing ECG method can help cardiologists reduce the workload and the rates of misdiagnosis. Ge et al. proposed a novel autoencoder framework of detecting pacing ECG. The results showed that the proposed method could

achieve a significant performance with high accuracy, sensitivity, and F1-score through a series of experiments.

Recently, various deep learning techniques have been utilized to classify arrhythmias, including the use of one-dimensional convolutional neural network (CNN) model to handle the ECG signals in the time domain. Zhang et al. developed a new solution for cardiac arrhythmia classification in two dimensions by introducing the recurrence plot combined with an Inception-residual convolutional neural network-v2 (Inception-ResNet-v2). The results with only two leads of the 12-lead ECG original data showed that their proposed method achieved the highest average F1-score of 0.844, which outperformed other works. Jiang et al. proposed a hybrid attention-based deep learning network (HADLN) method for arrhythmia classification. The HADLN makes full use of the advantages of residual network and bidirectional long-short-term memory architecture to obtain fusion features containing local and global information and improve the interpretability of the model through the attention mechanism. Their experimental results showed that the HADLN method can achieve precision of 0.866, recall of 0.859, accuracy of 0.867, and F1-score of 0.880 on 10-fold cross-validation.

The clinical manifestations of myocardial ischemia (MI) are mainly the changes of ST-T segment of ECG. Nearly one third of patients with coronary heart disease, however, has no obvious ECG changes. Li et al. proposed a new method of detecting MI based on the T-wave area curve (TWAC). The preliminary test results showed that the sensitivity, specificity, and accuracy of the proposed method for detecting MI were 84.3, 83.6, and 84%, respectively, suggesting that the TWAC based approach may be an effective method for detecting MI, especially for the patients with no obvious ECG changes.

In summary, the 12 research papers in the Research Topic summarized the challenges and some of the most recent development and ideas in *Multi-Scale Computational Cardiology* and computational analysis of multimodal cardiovascular data, which will be useful for researchers working in the related fields.

## AUTHOR CONTRIBUTIONS

LX wrote the manuscript. HZ and DZ revised the manuscript. All authors contributed to the article and approved the submitted version.

**Conflict of Interest:** The authors declare that the research was conducted in the absence of any commercial or financial relationships that could be construed as a potential conflict of interest.

**Publisher's Note:** All claims expressed in this article are solely those of the authors and do not necessarily represent those of their affiliated organizations, or those of the publisher, the editors and the reviewers. Any product that may be evaluated in this article, or claim that may be made by its manufacturer, is not guaranteed or endorsed by the publisher.

Copyright © 2022 Xia, Zhang and Zheng. This is an open-access article distributed under the terms of the Creative Commons Attribution License (CC BY). The use, distribution or reproduction in other forums is permitted, provided the original author(s) and the copyright owner(s) are credited and that the original publication in this journal is cited, in accordance with accepted academic practice. No use, distribution or reproduction is permitted which does not comply with these terms.



# A Novel Model Based on Spatial and Morphological Domains to Predict the Origin of Premature Ventricular Contraction

Kaiyue He<sup>1†</sup>, Jian Sun<sup>2†</sup>, Yiwen Wang<sup>1</sup>, Gaoyan Zhong<sup>1</sup> and Cuiwei Yang<sup>1,3,4\*</sup>

<sup>1</sup> Department of Electronic Engineering, Fudan University, Shanghai, China, <sup>2</sup> Department of Cardiology, School of Medicine, Xinhua Hospital, Shanghai Jiao Tong University, Shanghai, China, <sup>3</sup> Key Laboratory of Medical Imaging Computing and Computer Assisted Intervention of Shanghai, Shanghai Medical College of Fudan University, Shanghai, China, <sup>4</sup> Shanghai Engineering Research Center of Cardiac Electrophysiology, Shanghai, China

## OPEN ACCESS

### Edited by:

Dingchang Zheng,  
Coventry University, United Kingdom

### Reviewed by:

Peng Li,  
Harvard Medical School,  
United States  
Dongdong Deng,  
Dalian University of Technology, China

### \*Correspondence:

Cuiwei Yang  
yangcw@fudan.edu.cn

<sup>†</sup> These authors have contributed  
equally to this work

### Specialty section:

This article was submitted to  
Computational Physiology  
and Medicine,  
a section of the journal  
Frontiers in Physiology

**Received:** 14 December 2020

**Accepted:** 22 January 2021

**Published:** 24 February 2021

### Citation:

He K, Sun J, Wang Y, Zhong G  
and Yang C (2021) A Novel Model  
Based on Spatial and Morphological  
Domains to Predict the Origin  
of Premature Ventricular Contraction.  
*Front. Physiol.* 12:641358.  
doi: 10.3389/fphys.2021.641358

Pace mapping is commonly used to locate the origin of ventricular arrhythmias, especially premature ventricular contraction (PVC). However, this technique relies on clinicians' ability to rapidly interpret ECG data. To avoid time-consuming interpretation of ECG morphology, some automated algorithms or computational models have been explored to guide the ablation. Inspired by these studies, we propose a novel model based on spatial and morphological domains. The purpose of this study is to assess this model and compare it with three existing models. The data are available from the Experimental Data and Geometric Analysis Repository database in which three *in vivo* PVC patients are included. To measure the hit rate (A hit occurs when the predicted site is within 15 mm of the target) of different algorithms, 47 target sites are tested. Moreover, to evaluate the efficiency of different models in narrowing down the target range, 54 targets are verified. As a result, the proposed algorithm achieves the most hits (37/47) and fewest misses (9/47), and it narrows down the target range most, from  $27.62 \pm 3.47$  mm to  $10.72 \pm 9.58$  mm among 54 target sites. It is expected to be applied in the real-time prediction of the origin of ventricular activation to guide the clinician toward the target site.

**Keywords:** pace mapping, ventricular arrhythmias, ablation, automated algorithm, origin of PVC

## INTRODUCTION

Premature ventricular contraction (PVC) is one of the most common ventricular arrhythmias encountered in clinical practice, occurring in 1–4% of the general population (Kostis et al., 1981). Frequent and repetitive PVCs can increase the risk of arrhythmia-induced syncope, ventricular dysfunction, and sudden death (Ahn, 2013). Hitherto, catheter ablation has become an important therapy in the management of ventricular arrhythmias (Al-Khatib et al., 2018). In the last decade (from 2000 to 2012), the annual ventricular tachycardia (VT) ablation volumes have quadrupled (Hsia and Xiong, 2019). Also, multiple studies have shown that catheter ablation can be more effective in reducing arrhythmia recurrence than anti-arrhythmic drugs (Sapp et al., 2016).

It is of therapeutical importance to localize the origin of abnormal ventricular activation before catheter ablation. The localization can be done by several approaches. Activation mapping is the



most direct technique which can be applied in patients with frequent PVCs (Adams et al., 2012). Yet, it requires time-consuming intracardiac mapping by moving the catheter to different sites of the ventricles, and it can only be performed in a small number of patients who can endure a sustained VT during the whole mapping operation. Since the origin of PVC largely determines the QRS morphology of 12-lead ECG (Josephson et al., 1982), an alternative technique, known as pace mapping, can be applied in more patients by physically stimulating multiple ventricle sites until finding the site where pacing reproduces the morphology of spontaneous PVC (Kobayashi, 2018). However, this practice relies heavily on rapid and accurate manual interpretation of ECG.

In order to automatically analyze the information of pacing sites and progressively guide the clinician to the origin of PVC, several methods have been developed. One method is to train a universal model from a cohort of patients based on machine learning methods (Sapp et al., 2017; Zhou et al., 2019). However, due to anatomical and physiological variations in patients, there is a limited accuracy when a universal model is applied to a new patient. An alternative strategy is to build patient-specific prediction models. To our knowledge, some studies have used the image-based simulated ECG data to train a customized prediction model for each patient (Potse et al., 2000; Yang et al., 2018) and the domain adaptation method has newly been applied to modify the prediction model with clinical data to account for the potential errors in the simulation data (Alawad and Wang, 2019).

In addition to the image-based simulation method, some simpler but less computational models based on information of multiple pacing sites have also been investigated. Lately, the QRS integrals (QRS-Ints) of 12-lead ECG have been used to predict the 3D coordinate of the PVC origin directly (Sapp et al., 2017; Zhou et al., 2018). Besides, the relationship between distance and change in 12-lead ECG morphology has also been inspected to assist in the localization of PVC origin (Li et al., 2017, 2018; Odille et al., 2019; Dharmapranj et al., 2020).

Inspired by previous studies, in this paper, a novel model only based on the information of pacing sites is proposed and compared with three existing models [QRS-Int Model (Sapp et al., 2017), dis-E12 Model (Li et al., 2017), and dis-corr Model (Dharmapranj et al., 2020)]. We evaluated these models in three patients with PVC and found that the proposed model was slightly superior to the other three models. This method is very suitable for the location of PVC origins in non-organic heart disease.

## MATERIALS AND METHODS

### Data

The data used throughout this study is obtained from the Experimental Data and Geometric Analysis Repository (EDGAR) database (Aras et al., 2015). The data were collected during endocardial pacing from three PVC patients. The patients were consented for an add-on experimental procedure involving ventricular pacing, performed according to a protocol approved

by the ethical committee of Charles University Hospital, Prague, Czechia (Erem et al., 2014). For each patient, there is a mean of  $25 \pm 6$  distinct sites of endocardial pacing with known coordinates. For each pacing site, a mean of  $28 \pm 8$  ECG beats are available and a representative beat is calculated by averaging these beats. The equation is as follows:

$$V_i = \frac{1}{N} \sum_{n=1}^N V_i^{(n)} \quad (1)$$

where  $V_i$  and  $V_i^{(n)}$  are the  $i$ th-lead ECG signals of representative beat and beat  $n$ , respectively.

## Models

### QRS-Int Model

The QRS-Int values were proposed by Sapp et al. (2017) as predictor variables to fit the geometric coordinate system of the heart. A statistical estimate of the coordinates  $\hat{x}$ ,  $\hat{y}$ , and  $\hat{z}$  for any pacing site can be obtained by fitting the multiple linear regression equation with intercept. The equation is as follows:

$$\begin{bmatrix} \hat{x} \\ \hat{y} \\ \hat{z} \end{bmatrix} = \begin{bmatrix} \hat{\alpha}_0 & \hat{\alpha}_1 & \cdots & \hat{\alpha}_k \\ \hat{\beta}_0 & \hat{\beta}_1 & \cdots & \hat{\beta}_k \\ \hat{\gamma}_0 & \hat{\gamma}_1 & \cdots & \hat{\gamma}_k \end{bmatrix} \begin{bmatrix} 1 \\ I_1 \\ \vdots \\ I_k \end{bmatrix} \quad (2)$$

where  $\hat{\alpha}_i$ ,  $\hat{\beta}_i$ , and  $\hat{\gamma}_i$  are estimated regression coefficients, and  $I_i$  represents the QRS-Int. To minimize the training set of required pacing sites, three optimal predictors (the initial 120-ms QRS-Int of leads III, V2, and V6) were found by exhaustive search (Sapp et al., 2017). Then, the least-square method was used to solve 4 equations ( $k = 3$ ) to obtain the patient-specific QRS integral model (QIM). We used at least 5 pacing points to avoid matrix singularity. The best regression coefficients can be calculated by least-square regression (Sapp et al., 2017). Once the regression coefficients best fitted for the training-set data are found, they can be used for prediction of the unknown site. Here, the initial 120-ms QRS-Int values are extracted manually from the representative beat of each pacing site.

### dis-E12 Model

The E12 value proposed by Anthony et al. (Li et al., 2017) can be used to quantify the difference of 12-lead ECG between 2 pacing sites.

$$E_{12} = \sum_{i=1}^{12} \sqrt{\frac{1}{N} \sum_{j=1}^N (V_{i,j} - V_{i,j}^r)^2}$$

$$dis = \sqrt{(x - x^r)^2 + (y - y^r)^2 + (z - z^r)^2} \quad (3)$$

$$dis = k_1 \cdot E_{12}$$

$$\widehat{dis}^i = k_1 \cdot E_{12}(V^{ith-known}, V^{unknown})$$

where  $V$  and  $V^r$  represent 2 pacing beats being compared, which are 150-ms waveforms centered on the maximum of the 12-lead composite signal (Li et al., 2017), and  $V_{i,j}$  and  $V_{i,j}^r$  represent the



voltages of one moment of the ECG.  $N$  is the length of the ECG signal.  $i$  ranges from 1 to 12, representing the index of 12 leads.  $dis$  represents the Euclidean distance between pacing sites. Similarly, the patient-specific dis-E12 model (DEM) can be solved by origin-constrained least-square linear regression. After that, the E12 value between the unknown site and each known site is calculated and then used to estimate the corresponding distance  $\widehat{dis}^i$  for  $i = 1, 2, \dots, m$ . Finally, by minimizing the following cost function  $J$ , a statistical estimate of coordinates  $\hat{x}$ ,  $\hat{y}$ , and  $\hat{z}$  for the unknown site can be found.

$$J = \sum_{i=1}^m (\sqrt{(\hat{x} - x_i)^2 + (\hat{y} - y_i)^2 + (\hat{z} - z_i)^2} - \widehat{dis}^i)^2 \quad (4)$$

### dis-Corr Model

The correlation coefficient (Corr) proposed by Dharmapalani et al. (2020) can be used to quantify the similarity of ECG morphology between 2 pacing sites.

$$r(X, Y) = \frac{\sum_{i=1}^n (X_i - \bar{X})(Y_i - \bar{Y})}{\sqrt{\sum_{i=1}^n (X_i - \bar{X})^2} \sqrt{\sum_{i=1}^n (Y_i - \bar{Y})^2}}$$

$$Corr = \frac{1}{12} \sum_{i=1}^{12} r(V_i, V_i^r)$$

$$dis = \sqrt{(x - x^r)^2 + (y - y^r)^2 + (z - z^r)^2} \quad (5)$$

$$\widehat{dis}^i = k_2 \cdot (Corr - 1)$$

$$\widehat{dis}^i = k_2 \cdot (1 - Corr(V^{ith-known}, V^{unknown}))$$

where  $r(X, Y)$  represents the Pearson correlation coefficient between time series  $X$  and  $Y$ . Moreover, the Corr value is the average result of 12 leads. Similarly, the patient specific dis-Corr model (DCM) can be solved by constrained least-square linear regression, and the Corr value between the unknown site and each known site can also be calculated and transformed into the estimated distance  $\widehat{dis}^i$  for  $i = 1, 2, \dots, m$ . Finally, by minimizing the cost function  $J$  presented in Eq. (4), a statistical estimate of coordinates  $\hat{x}$ ,  $\hat{y}$ , and  $\hat{z}$  for the unknown site can be found.

### dp-dw Model

In this study, we observed a phenomenon that there are some connections between waveform morphology and physical position. **Figures 1, 2** show two examples based on simulation data and real data, respectively. The simulation data were generated by an isotropic ventricular simulation model with electric conduction rate of 0.7 m/s (Schulze et al., 2015). As can be observed from **Figure 1**, points 1, 2, 3, 4, and 5 are almost on the same line, while points 3, 6, and 7 are almost on another line. **Figure 1B** shows the splicing signal of 12-lead ECG in accordance with positions, and **Figure 1C** shows the waveform difference between each pair of positions. It seems that the waveform differences on the same line are more similar, while those on different lines are less similar. For example,

s31, s32, s34, and s35 are similar with each other and so are s36 and s37, but s31 and s37 are less similar. Then the real data are extracted from the first patient. As can be seen from **Figure 2**, points LVP11, LVP1, and LVP20 are almost on the same line, while LVP18 and LVP4 are almost on another line. Besides, the two lines are nearly parallel. Similarly, we observed the similarity of waveform differences on the same line. We also observed the similarity of waveform differences between parallel lines.

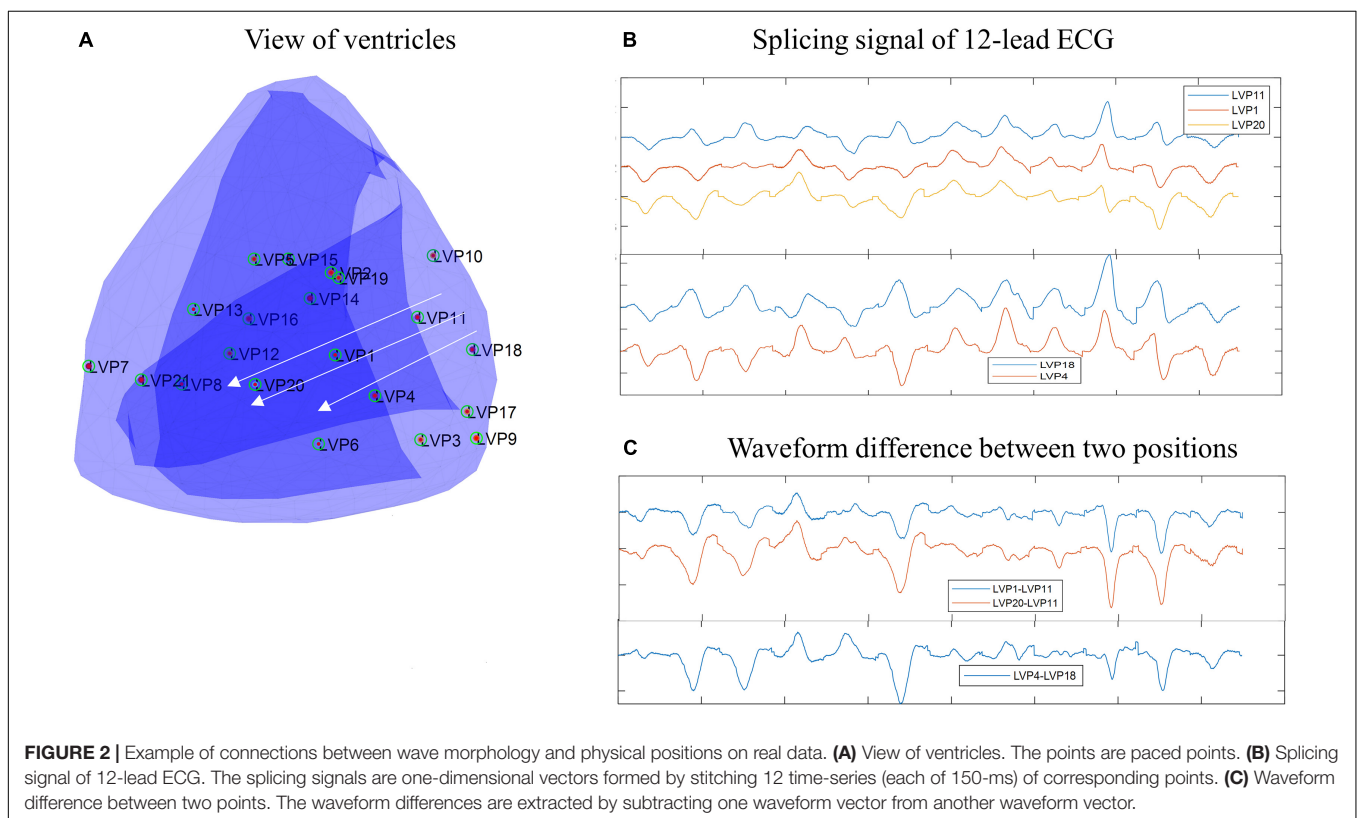
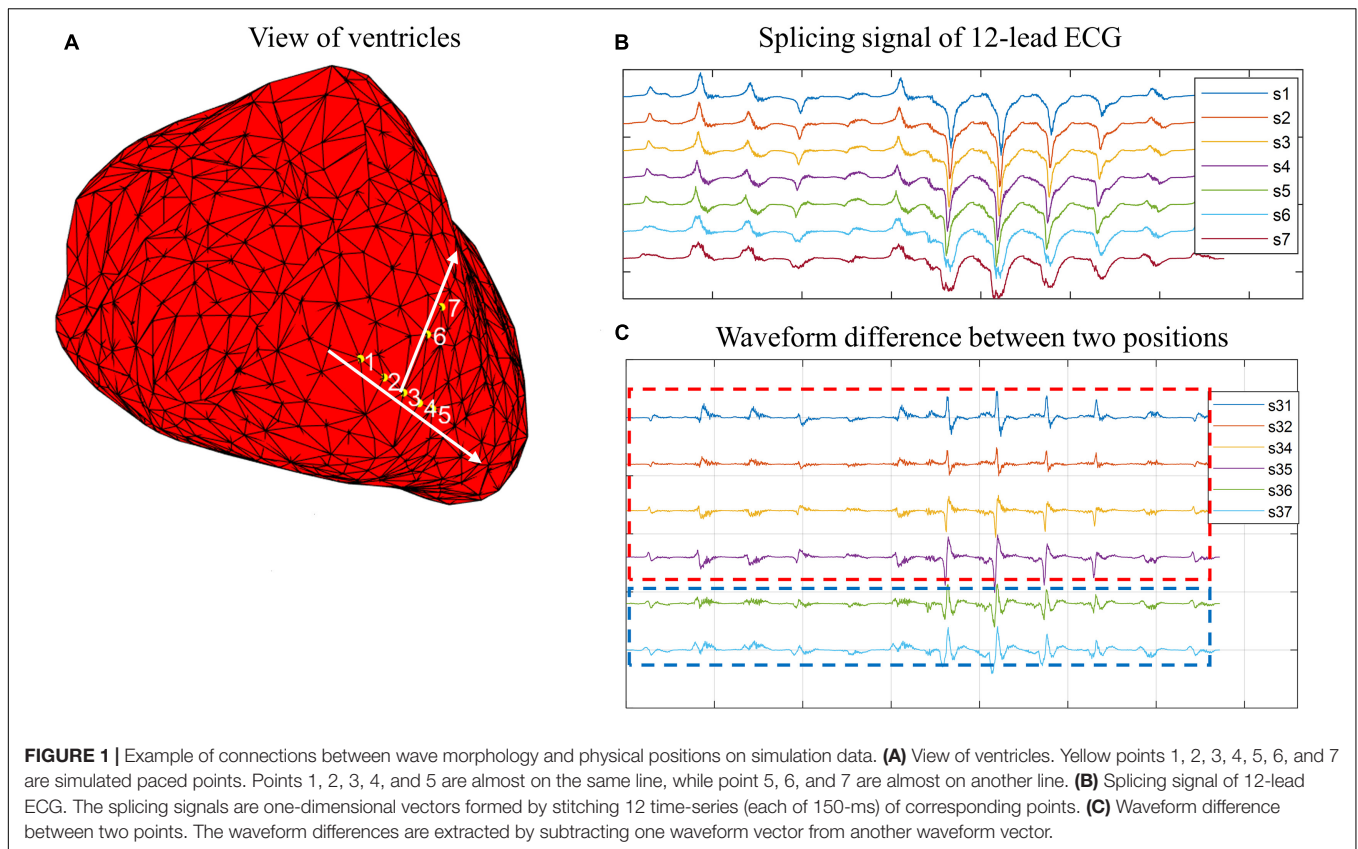
The above phenomenon may be explained by the theory of electrocardiographic dipoles. During ventricular depolarization, electric dipoles can be formed between depolarized and non-depolarized regions, and the integrated vector of all dipoles can be recorded by 12 leads from different positions and directions. The recorded voltage on each lead at one moment is related to the distances between the recording electrode and the electric dipoles, and it is also related to the cosine angles formed by the orientation of the lead axis and the directions of myocardial depolarization. When a ventricular premature occurs, the depolarization wave spreads from the earliest excitation point to all sides, and the directions of electric dipoles are the same as the directions of myocardial depolarization. When the earliest excitation point moves along a certain direction, the electric dipoles will change most in the same direction, which may lead to more obvious waveform changes in leads parallel to the direction and less obvious waveform changes in leads perpendicular to the direction. Therefore, there might be a certain relationship between the waveform changes of 12-lead ECG and the position changes of the earliest excitation point.

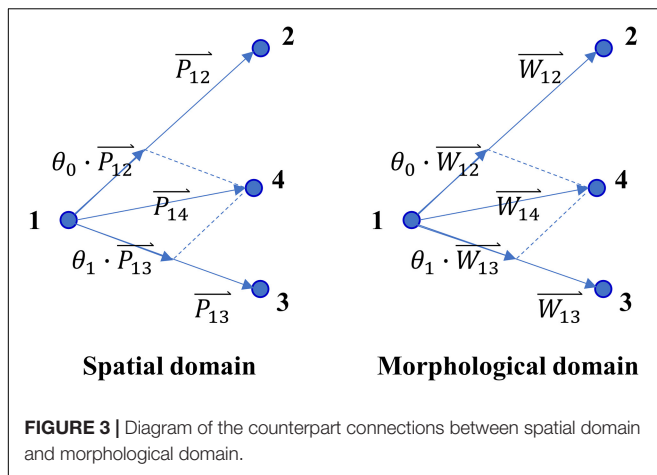
Based on these observations, we proposed a novel prediction model based on the assumption that there are some counterpart connections between the spatial domain and the morphological domain. As **Figure 3** shows,  $\vec{P}_{ij}$  and  $\vec{W}_{ij}$  represent the vector of position difference (dp) and the vector of waveform difference (dw) between point  $i$  and point  $j$ , respectively. Here,  $\vec{W}_i$  represents a one-dimensional vector formed by stitching 12 time-series (each of 150-ms) of pacing site  $i$  together, and  $\vec{W}_{ij}$  is obtained by subtracting  $\vec{W}_i$  from  $\vec{W}_j$ . Supposing Eq. (6) holds in the spatial domain, and then Eq. (7) holds in the morphological domain, and vice versa.

$$\vec{P}_{14} = \theta_0 \cdot \vec{P}_{12} + \theta_1 \cdot \vec{P}_{13} \quad (6)$$

$$\vec{W}_{14} = \theta_0 \cdot \vec{W}_{12} + \theta_1 \cdot \vec{W}_{13} \quad (7)$$

**Figure 4** illustrates the establishment and prediction process of the dp-dw model (DDM). As shown in the figure, points 1, 2, and 3 are the known sites whose 12-lead ECG signals and physical locations are known by us, while point O is the unknown site whose 12-lead ECG information is known by us, but its physical location needs to be estimated by algorithm. Of course, the actual physical location of point O is known, but we pretend not to know that. Moreover, we use the waveform difference between point





O and its adjacent points to estimate its location. The vectors of dp and dw between each pair of known sites are calculated as  $[\Delta P] \begin{bmatrix} \vec{P}_{12}, \vec{P}_{13} \end{bmatrix}$  and  $[\Delta W] \begin{bmatrix} \vec{W}_{12}, \vec{W}_{13} \end{bmatrix}$ , and the vector of dw between the unknown site and each known site is calculated as  $[\Delta W^*] \begin{bmatrix} \vec{W}_{1O}, \vec{W}_{2O}, \vec{W}_{3O} \end{bmatrix}$ . Analogously, the transfer matrix  $[\theta]$  mapping  $[\Delta W]$  to  $[\Delta W^*]$  can be found by least-square regression [Eq. (8)]. Then, by applying the same transfer matrix  $[\theta]$  to the spatial domain, the estimated vector of dp between the unknown site and each known site can be calculated as shown in Eq. (9). Finally, a statistical estimate of coordinates  $\hat{x}$ ,  $\hat{y}$ , and  $\hat{z}$  for the unknown site can be calculated as Eq. (10).

$$[\Delta W^*] = [\Delta W] \times [\theta]$$

$$[\theta] = ([\Delta W]^T \times [\Delta W])^{-1} \times [\Delta W]^T \times [\Delta W^*] \quad (8)$$

$$[\Delta P^*] = [\Delta P] \times [\theta]$$

$$[\Delta P^*] = [P_{1O}, P_{2O}, P_{3O}] \quad (9)$$

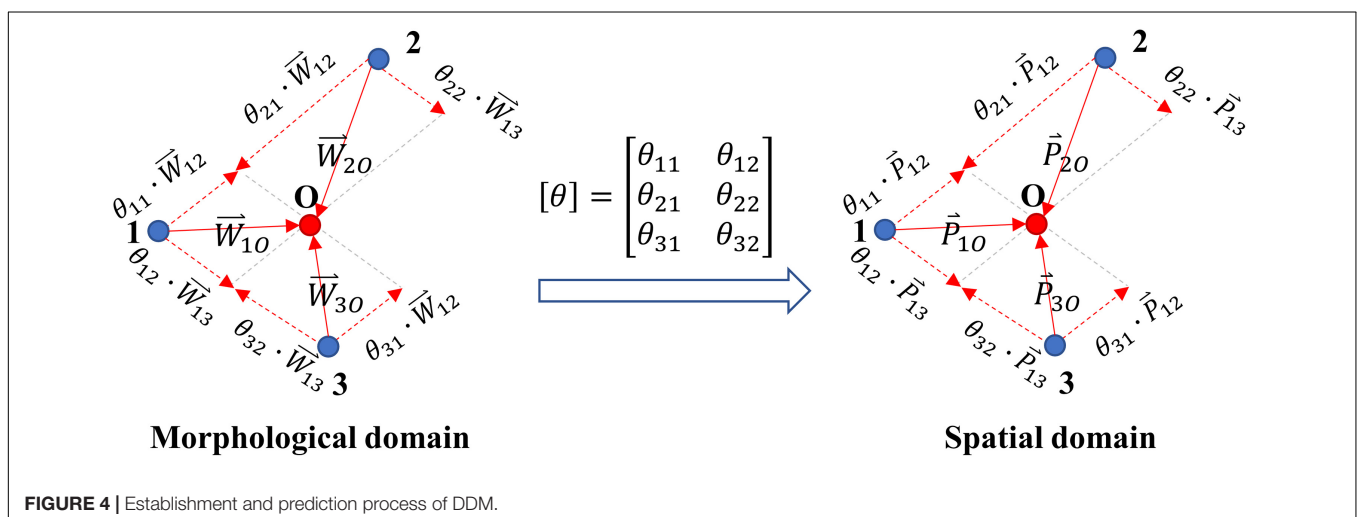
$$\begin{bmatrix} \hat{x} \\ \hat{y} \\ \hat{z} \end{bmatrix} = \frac{1}{3} \sum_{i=1}^3 \left( P_i + \hat{P}_{iO} \right) \quad (10)$$

Figure 5 shows an example of using DDM to predict the PVC origin. In Figure 5A, the red point represents the unknown site, the green points represent the known sites, and the yellow point represents the predicted position. Figure 5B shows the waveform differences (dws) between the known sites, and Figure 5D shows the dws between the known sites and the unknown site. By using least-square regression, the estimated dws between the known sites and the unknown site can be transformed from the dws between the known sites, as Figure 5C shows. Finally, by applying the same transfer matrix  $[\theta]$  in the spatial domain, the position differences (dps) between the known sites and the unknown site could be calculated. And by executing Eq.(10), the predicted position was obtained.

## Emulation of Clinical Protocols

### Target Site Selection

Two target site selection schemes were adopted for different purposes. First, in order to evaluate the hit rate (a hit occurs when the predicted site is within 15 mm of the target), the target site is defined as the site with at least 5 adjacent sites which are greater than 15 mm and less than 35 mm away from it, and a total of 47 pacing sites meet the conditions. Secondly, in order to evaluate the efficiency of different models in narrowing down the target range, the target site is defined having at least 5 adjacent sites within the range of 35 mm of it, and a total of 54 pacing sites meet the requirement. Once a target site is selected, its adjacent sites that meet the corresponding definition serve as potential modeling sites. In this study, the modeling sites are those whose physical locations and corresponding 12-lead ECG signals are known, while the target sites are those whose 12-lead ECG signals are known, but their physical locations need to be estimated by the algorithm.



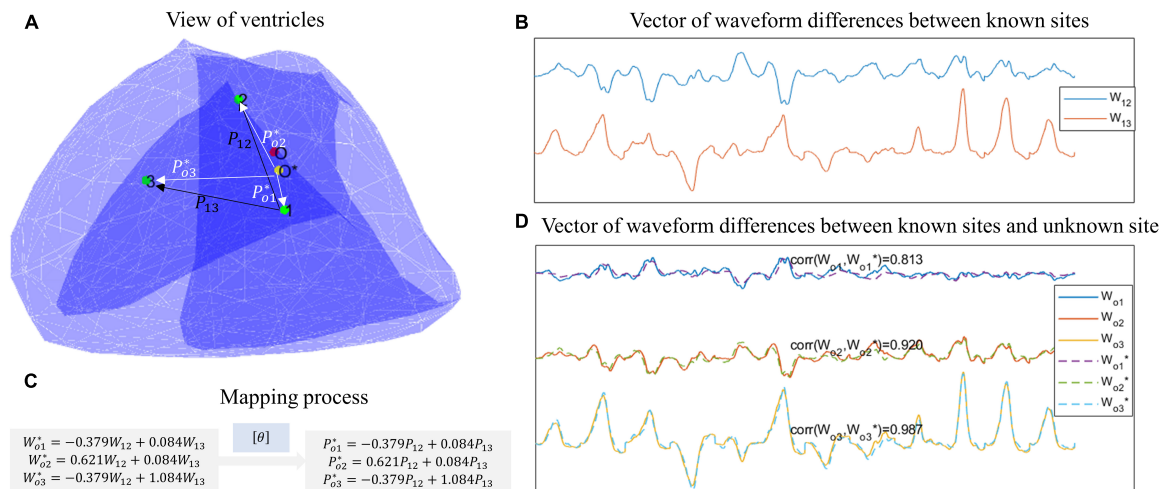


**FIGURE 5 |** An example of using DDM to predict the PVC origin. **(A)** View of ventricles. The green points represent known sites, the red point represents the unknown site, and the yellow site represents the predicted site. **(B)** Vector of waveform differences between known sites. For example,  $W_{12}$  is extracted by subtracting the waveform of point 1 from the waveform of point 2. **(C)** Mapping process. By least-square regression, the estimated waveform differences between the known sites and the unknown sites can be transformed from the waveform differences between the known sites. Then by applying the same transfer matrix in the spatial domain, the position differences between the known sites and the unknown site can be calculated. **(D)** Vector of waveform difference between known sites and unknown site. The ground-truth waveform differences are shown with solid lines, while the estimated waveform differences are shown with dotted lines.

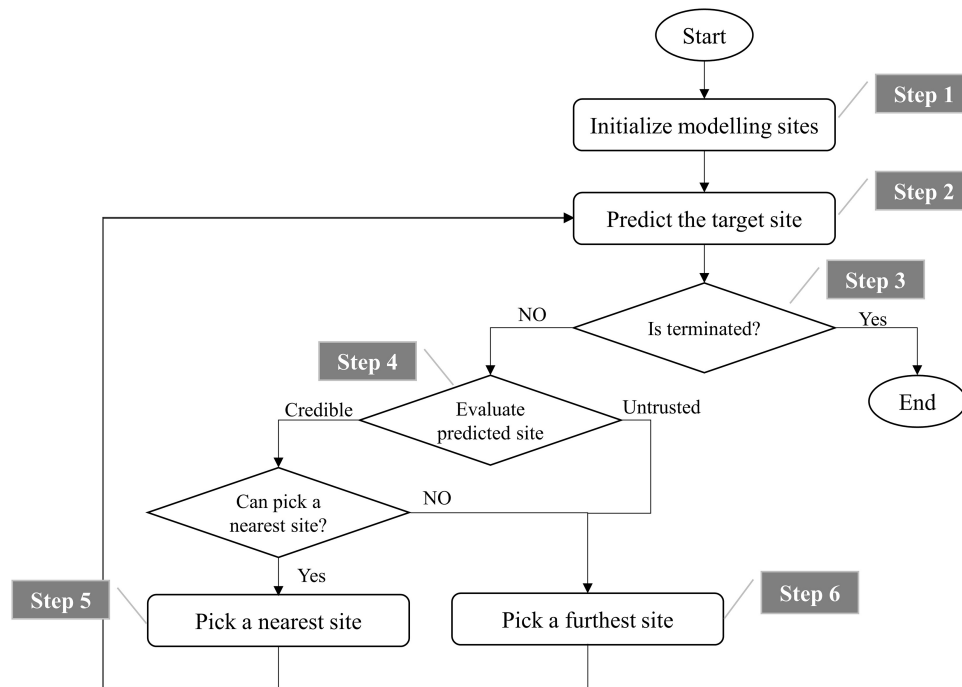


**FIGURE 6 |** Flowchart of modeling and prediction.

## Modeling and Prediction

Figure 6 shows the flowchart of the process of modeling and prediction. It can be divided into the following six steps.

Step 1: Initialize modeling sites. The 3 or 5 farthest unused potential modeling sites (3 for DEM, DCM, and DDM, and 5 for QIM) from the target site are selected as initial modeling

sites, and they will be removed from the list of unused potential modeling sites. For example, supposing point 0 is selected as the target site, and its adjacent points 1, 2, 3, 4, 5, and 6 match the definition of potential modeling sites. Therefore, the initial list of unused potential modeling sites is (Kostis et al., 1981; Adams et al., 2012; Ahn, 2013; Sapp et al., 2016; Al-Khatib et al.,



2018; Hsia and Xiong, 2019). We first pick out three farthest modeling sites to predict the coordinates of point 0. Assuming points 1, 2, and 3 are selected, then we will remove them from the list of potential modeling sites that have never been used, so as not to select the duplicate modeling sites next time. Hence, the list will be updated to Adams et al. (2012), Sapp et al. (2016), Hsia and Xiong (2019).

Step 2: Train the models mentioned above to predict the target site.

Step 3: Termination judgment. If there are no unused potential modeling sites left, terminate. If the predicted site hits the target, terminate.

Step 4: Evaluate predicted site. If the predicted site is outside 35 mm of the target site, it is not credible, skip to step 6.

Step 5: Pick out a nearest site from the unused potential modeling sites if it is within 15 mm of the predicted site, then remove it from the list of unused potential modeling sites and skip to step 2. Otherwise, there is no unused potential modeling site that can replace the predicted site, turn to the next step.

Step 6: Pick out a site that is farthest from the geometric center of current modeling sites to obtain as much spatial information as possible, and remove it from the list of unused potential modeling sites and skip to step 2.

## RESULTS

### Hits and Misses

A total of 47 target sites are used to evaluate the hit rate of four models. As **Figure 7A** shows, the proposed DDM presents with the most hits (37/47), the fewest misses (9/47), and one early termination. Here an early termination means that the reduction of estimated error is interrupted by lack of potential modeling sites. Then, slightly inferior to DDM, DEM performs with 35 hits, 11 misses, and one early termination. Finally, inferior to DDM and DEM, QIM and DCM achieve with 31 hits, 14 misses, one early termination and 29 hits, 18 misses, and no early termination, respectively. In addition, when the number of modeling sites is 5, DDM has much more hits than other models.

### Estimated Error

**Figure 7B** presents the trend of estimated errors of four models with the increase of modeling sites. It must be noted that for each target site, the estimated error remains unchanged after minimization. As can be observed from the figure, with the increase of modeling sites, the estimated errors of four models tend to decrease, especially when the number of modeling sites is less than 8 when most of the samples remained non-minimization (see **Figure 7A**). In terms of decline velocity of estimated error, DCM and DDM perform better than QIM and DEM when number of modeling sites is less than 5. Also, in terms of final estimated error, DEM and DDM perform better than QIM and DCM.

### Reduced Distance

The reduced distance is equal to the minimum distance between the modeling sites and the target site minus the estimated

error, and a positive reduced distance indicates a reduction in the unknown range of the target by modeling and prediction. **Figure 7C** shows the reduced distances of four models with the increase of modeling sites. For each number of modeling sites, samples that have reached the minimum estimated error are not counted. As the figure shows, for different numbers of modeling sites, the mid-values of reduced distances of four models are almost positive, indicating that four models tend to reduce the unknown range of the target. When the number of modeling sites is 5, QIM has the largest mid-value of reduced distances and the corresponding hit rate also rises rapidly (see **Figure 7A**). However, due to the cumulative reduction of distances in the previous two rounds, DDM still has the highest hit rate.

### Target Range

A total of 54 target sites are used to evaluate the efficiency of different models in narrowing down the target range. **Figure 8** shows two examples of the predicted sites of four models with the increase of modeling sites. The initial target range (marked in orange in **Figure 8**) is defined by the maximum radius of adjacent sites, and the final target range is defined by the minimum estimated error. As the figure shows, the first target site has an initial radius of 32.92 mm; after modeling and prediction, the radius is reduced to 8.51, 3.34, 9.86, and 5.19 mm with 4 models, respectively. Similarly, the radius of the second target is reduced from 33.13 to 8.80, 9.34, 10.98, and 7.39 mm with 4 models, respectively.

**Table 1** lists the statistical results of 54 target sites. Among the four models, DDM narrows down the target range most, from  $27.62 \pm 3.47$  mm to  $10.72 \pm 6.22$  mm, and DEM uses the fewest modeling sites ( $5.98 \pm 2.49$ ) to minimize the target range. In addition, *t* tests show that the estimation errors of DCM and DDM have a significant difference ( $P = 0.046$ ), and the numbers of modeling sites of QIM and DEM, QIM and DDM have a significant difference ( $P = 0.007$ ,  $P = 0.045$ ), indicating that DCM has the worst estimated error and QIM used the most modeling sites.

## DISCUSSION

This work proposed a novel model for the localization of PVC target sites based on the mapping between the spatial domain and the morphological domain. In our study, the pacing sites are not as adjacent as those generated by clinical pace mapping, so we selected modeling sites from a larger range to predict the target site step by step. For inexperienced doctors, the results obtained by our method may provide a reference location, so that they can simply determine the most likely ablation site as soon as possible and shorten the mapping procedure. We compared our model with three existing models and found that the proposed model was slightly superior to other models by achieving the most hits, the smallest estimated errors, and the biggest reduced distances. Especially when the number of modeling sites is small, the advantages of our model are more obvious. By observation of **Figure 7**, it can be found that the proposed DDM tends to have more hits,

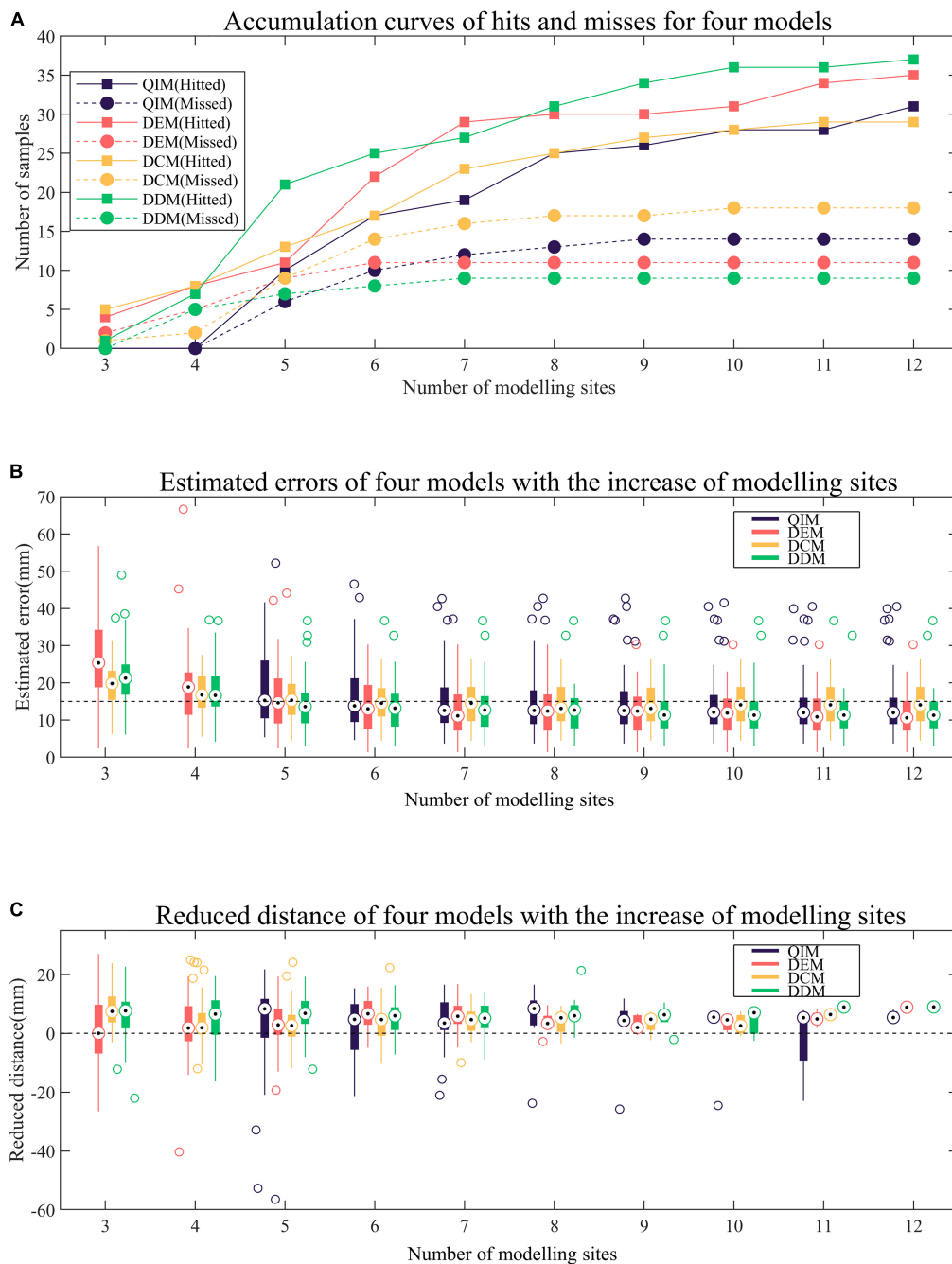
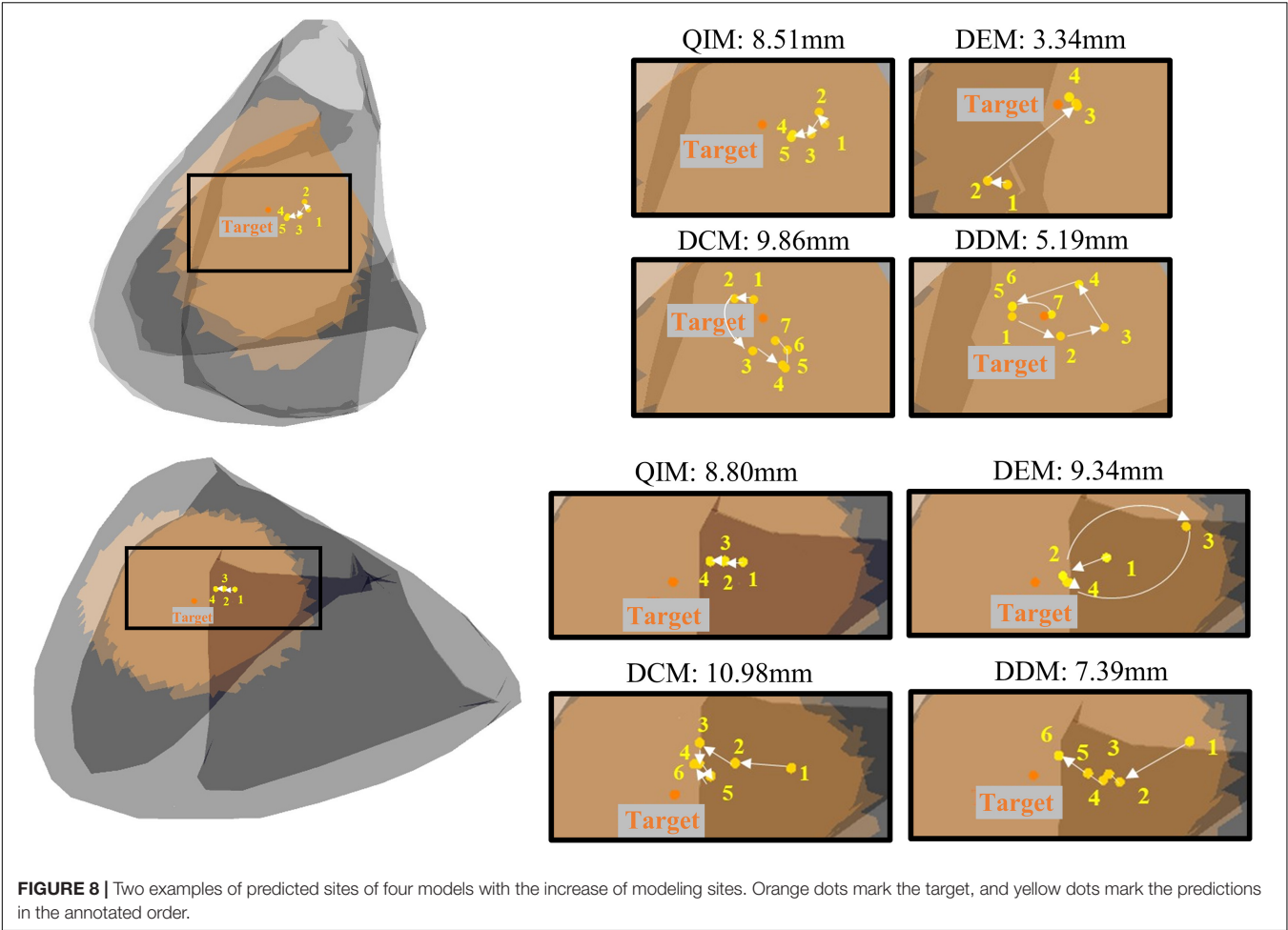


**FIGURE 7 |** Comparison of four models. **(A)** Accumulation curves of hits and misses for four models. A hit occurs when the predicted site is within 15 mm of the target. **(B)** Estimated errors of four models with the increase of modeling sites. The estimated error is the distance between the predicted site and the target. **(C)** Reduced distance of four models with the increase of modeling sites. The reduced distance is equal to the minimum distance between the modeling sites and the target minus the estimated error.

smaller estimated errors, and bigger reduced distances than the other methods when the number of modeling sites is less than 6.

Then, as can be observed from **Table 1**, considering the minimum estimated error, DDM, and DEM perform better than QIM and DCM. Compared with DDM and DEM, QIM only uses

the information of three-lead ECG, which may account for its less satisfying result. Though DCM also uses full information of 12-lead ECG, according to reference (Li et al., 2017), in contrast to Corr, E12 theoretically has no upper limit and, therefore, can provide better quantification of the morphology difference than Corr.



In addition, there is a certain relationship between DDM and DEM. In essence, DEM is to establish a scalar model through the relationship of the module length between  $dp$  and  $dw$ , while DDM directly uses the relationship between  $dp$  and  $dw$  to build a vector model. When the number of modeling sites is less than 5, the prediction effect of DEM is worse than that of DDM, which is likely due to the lack of direction information. However, when the number of modeling sites increases, the

**TABLE 1 |** Comparison of four models in narrowing down the target range.

Models	Radius of neighboring sites (mm)	Estimated error (mm)	Number of modeling sites used
QIM	Mean: 27.62	Mean: 12.41	Mean: 7.28 <sup>*2, *3</sup>
	Std: 3.47	Std: 8.05	Std: 2.43
	Mid: 27.53	Mid: 10.05	Mid: 7
DEM	Mean: 27.62	Mean: 11.08	Mean: <b>5.98<sup>*2</sup></b>
	Std: 3.47	Std: 6.03	Std: 2.49
	Mid: 27.53	Mid: 9.71	Mid: <b>5.5</b>
DCM	Mean: 27.62	Mean: 13.03 <sup>*1</sup>	Mean: 6.80
	Std: 3.47	Std: 5.67	Std: 2.47
	Mid: 27.53	Mid: 12.21	Mid: 6
DDM	Mean: 27.62	Mean: <b>10.72<sup>*1</sup></b>	Mean: 6.37 <sup>*3</sup>
	Std: 3.47	Std: 6.22	Std: 2.22
	Mid: 27.53	Mid: <b>9.58</b>	Mid: 6

<sup>\*1</sup>, <sup>\*2</sup>, and <sup>\*3</sup> represent statistically significant differences between groups.

**TABLE 2 |** Summary comparison of four models.

Model	Principles	Properties	Performance
QIM	Using QRS-Ints as predictors	Less computation, using information of 3-lead ECG and containing direction information	Second least hits and second least reduced target range
DEM	Based on the relationship between distance and morphology difference	More computation, using information of 12-lead ECG and lack of direction information	Second most hits and second most reduced target range
DCM			Least hits and least reduced target range
DDM	Based on the mapping between spatial domain and morphological domain	Moderate computation, using information of 12-lead ECG and containing direction information	Most hits and most reduced target range



lack of direction information is gradually compensated by more and more complete distance network between points, and DEM achieves a similar result to DDM.

Finally, in terms of computational complexity, QIM, and DDM are simpler since the fitted models can be used for prediction directly, while DEM and DCM are more complex due to the additional search for optimal solution that can minimize the cost function  $J$ . Table 2 lists a summary comparison of four models.

However, there still exist some limitations in this study. First, the way of picking out modeling sites is relatively random. Theoretically, the next modeling site should be the predicted result if it is reliable; otherwise, the next modeling site is selected by the doctor. Limited by the actual distribution of pacing sites, we take the second place and replace the predicted site with the nearest one among the unused potential modeling sites, which may cause the randomness in modeling site selection due to the different prediction results of four models, for example, when we design a fixed modeling site selection scheme, in which we choose a furthest site from the remaining potential sites in each round. Consequently, QIM, DEM, DCM, and DDM achieve 32, 35, 28, and 33 hits, respectively, indicating that the way of modeling site selection has a certain impact on the research results and the proposed DDM is more suitable for selecting modeling sites by referring to the predicted positions. Because collecting multiple-pace data in clinical practice will increase the risk of patients during operation, this kind of data is difficult to obtain. Therefore, we mainly used the data in the open database collected from three volunteers provided by Charles University in accordance with the strict experimental process. From the perspective of the number of individual patients, our sample is still relatively small, but the total number of test sites used in this paper is relatively large. In the future research, we can also consider the application of four methods to animal experimental data or retrospective clinical data analysis.

## CONCLUSION

To conclude, it is a desirable goal to develop an automated algorithm for the localization of PVC origins. This work provided

a novel solution based on the mapping between spatial domain and morphological domain. It performs better with fewer modeling points and is expected to be used to predict the origin of ventricular activation in real-time and guide clinicians to focus on ablation targets.

## DATA AVAILABILITY STATEMENT

The raw data supporting the conclusions of this article will be made available by the authors, without undue reservation.

## ETHICS STATEMENT

The studies involving human participants were reviewed and approved by the Ethical Committee of Charles University Hospital, Prague, Czechia. The patients/participants provided their written informed consent to participate in this study.

## AUTHOR CONTRIBUTIONS

KH and JS: conceptualization, formal analysis, and methodology. CY: resources, supervision, and project administration. KH, YW, and GZ: software and visualization. KH: writing—original draft preparation. CY and GZ: writing—review and editing. KH and YW: revising and correcting. JS, KH, and CY: clinical interpretation and discussion of findings and their relevance. All authors contributed to the article and approved the submitted version.

## FUNDING

This work was partly supported by the National Natural Science Foundation of China (61071004), Shanghai Science and Technology Support Project (18441900900), Shanghai Municipal Science and Technology Major Project (2017SHZDZX01), and the Project of Shanghai Engineering Research Center (19DZ2250800).

## REFERENCES

- Adams, J. C., Srivathsan, K., and Shen, W. K. (2012). Advances in management of premature ventricular contractions. *J. Interv. Card. Electrophysiol.* 35, 137–149. doi: 10.1007/s10840-012-9698-x
- Ahn, M. S. (2013). Current concepts of premature ventricular contractions. *J. Lifestyle Med.* 3, 26–33.
- Alawad, M., and Wang, L. (2019). Learning domain shift in simulated and clinical data: localizing the origin of ventricular activation from 12-lead electrocardiograms. *IEEE Trans. Med. Imaging* 38, 1172–1184. doi: 10.1109/tmi.2018.2880092
- Al-Khatib, S. M., Stevenson, W. G., Ackerman, M. J., Bryant, W. J., Callans, D. J., Curtis, A. B., et al. (2018). 2017 AHA/ACC/HRS guideline for management of patients with ventricular arrhythmias and the prevention of sudden cardiac death: a report of the American College of Cardiology/American Heart Association Task Force on clinical practice guidelines and the heart rhythm society. *Circulation* 138, e272–e391. doi: 10.1161/cir.0000000000000549
- Aras, K., Good, W., Tate, J., Burton, B., Brooks, D., Coll-Font, J., et al. (2015). Experimental data and geometric analysis repository-EDGAR. *J. Electrocardiol.* 48, 975–981. doi: 10.1016/j.jelectrocard.2015.08.008
- Dharmapran, D., Lahiri, A., Ganesan, A. N., Kyriacou, N., and McGavigan, A. D. (2020). Comparative spatial resolution of 12-lead electrocardiography and an automated algorithm. *Heart Rhythm* 17, 324–331. doi: 10.1016/j.hrthm.2019.08.029
- Erem, B., Coll-Font, J., Orellana, R. M., Stovicek, P., and Brooks, D. (2014). Using transmural regularization and dynamic modeling for noninvasive cardiac potential imaging of endocardial pacing with imprecise thoracic geometry. *IEEE Trans. Med. Imaging* 33, 726–738. doi: 10.1109/TMI.2013.2295220
- Hsia, H. H., and Xiong, N. (2019). Mapping and ablation of ventricular arrhythmias in cardiomyopathies. *Card. Electrophysiol. Clin.* 11, 635–655. doi: 10.1016/j.ccep.2019.08.005
- Josephson, M. E., Waxman, H. L., Cain, M. E., Gardner, M. J., and Buxton, A. E. (1982). Ventricular activation during ventricular endocardial pacing. II. Role of

- pace-mapping to localize origin of ventricular tachycardia. *Am. J. Cardiol.* 50, 11–22. doi: 10.1016/0002-9149(82)90003-0
- Kobayashi, Y. (2018). Idiopathic ventricular premature contraction and ventricular tachycardia: distribution of the origin, diagnostic algorithm, and catheter ablation. *J. Nippon Med. Sch.* 85, 87–94. doi: 10.1272/jnms.2018\_85-14
- Kostis, J. B., McCrone, K., Moreyra, A. E., Gotzoyannis, S., Aglitz, N. M., Natarajan, N., et al. (1981). Premature ventricular complexes in the absence of identifiable heart disease. *Circulation* 63, 1351–1356. doi: 10.1161/01.cir.63.6.1351
- Li, A., Davis, J. S., Grimster, A., Wierwille, J., Herold, K., Morgan, D., et al. (2018). Proof of concept study of a novel pacemapping algorithm as a basis to guide ablation of ventricular arrhythmias. *Europace* 20, 1647–1656. doi: 10.1093/europace/euy024
- Li, A., Davis, J. S., Wierwille, J., Herold, K., Morgan, D., Behr, E., et al. (2017). Relationship between distance and change in surface ECG morphology during pacemapping as a guide to ablation of ventricular arrhythmias: implications for the spatial resolution of pacemapping. *Circ. Arrhythm. Electrophysiol.* 10:e004447. doi: 10.1161/circep.116.004447
- Odille, F., Battaglia, A., Hoyland, P., Sellal, J. M., Voilliot, D., de Chillou, C., et al. (2019). Catheter treatment of ventricular tachycardia: a reference-less pace-mapping method to identify ablation targets. *IEEE Trans. Biomed. Eng.* 66, 3278–3287. doi: 10.1109/tbme.2019.2903631
- Potse, M., Linnenbank, A. C., Peeters, H. A., SippensGroenewegen, A., and Grimbergen, C. A. (2000). Continuous localization of cardiac activation sites using a database of multichannel ECG recordings. *IEEE Trans. Biomed. Eng.* 47, 682–689. doi: 10.1109/10.841340
- Sapp, J. L., Bar-Tal, M., Howes, A. J., Toma, J. E., El-Damaty, A., Warren, J. W., et al. (2017). Real-time localization of ventricular tachycardia origin from the 12-lead electrocardiogram. *JACC Clin. Electrophysiol.* 3, 687–699. doi: 10.1016/j.jacep.2017.02.024
- Sapp, J. L., Wells, G. A., Parkash, R., Stevenson, W. G., Blier, L., Sarrazin, J. F., et al. (2016). Ventricular tachycardia ablation versus escalation of antiarrhythmic drugs. *N. Engl. J. Med.* 375, 111–121. doi: 10.1056/NEJMoa1513614
- Schulze, W. H., Potyagaylo, D., Schimpf, R., Papavassiliu, T., Tülümen, E., Rudic, B., et al. (2015). “A simulation dataset for ECG imaging of paced beats with models for transmural, endo-and epicardial and pericardial source imaging,” in *Proceedings of the 1st First Meeting of the Consortium for EGI Imaging*, Bad Herrenalp.
- Yang, T., Yu, L., Jin, Q., Wu, L., and He, B. (2018). Localization of origins of premature ventricular contraction by means of convolutional neural network from 12-lead ECG. *IEEE Trans. Biomed. Eng.* 65, 1662–1671. doi: 10.1109/tbme.2017.2756869
- Zhou, S., AbdelWahab, A., Sapp, J. L., Warren, J. W., and Horáček, B. M. (2019). Localization of ventricular activation origin from the 12-lead ECG: a comparison of linear regression with non-linear methods of machine learning. *Ann. Biomed. Eng.* 47, 403–412. doi: 10.1007/s10439-018-02168-y
- Zhou, S., Sapp, J. L., AbdelWahab, A., Št'oviček, P., and Horáček, B. M. (2018). Localization of ventricular activation origin using patient-specific geometry: preliminary results. *J. Cardiovasc. Electrophysiol.* 29, 979–986. doi: 10.1111/jce.13622

**Conflict of Interest:** The authors declare that the research was conducted in the absence of any commercial or financial relationships that could be construed as a potential conflict of interest.

Copyright © 2021 He, Sun, Wang, Zhong and Yang. This is an open-access article distributed under the terms of the Creative Commons Attribution License (CC BY). The use, distribution or reproduction in other forums is permitted, provided the original author(s) and the copyright owner(s) are credited and that the original publication in this journal is cited, in accordance with accepted academic practice. No use, distribution or reproduction is permitted which does not comply with these terms.



# A New Method for Detecting Myocardial Ischemia Based on ECG T-Wave Area Curve (TWAC)

Ronghua Li<sup>1†</sup>, Xiaoye Zhao<sup>2†</sup>, Yinglan Gong<sup>1</sup>, Jucheng Zhang<sup>3</sup>, Ruiqing Dong<sup>4\*</sup> and Ling Xia<sup>1\*</sup>

<sup>1</sup> Key Laboratory for Biomedical Engineering of Ministry of Education, Institute of Biomedical Engineering, Zhejiang University, Hangzhou, China, <sup>2</sup> Department of Medical Imaging Technology, North Minzu University, Yinchuan, China, <sup>3</sup> Department of Clinical Engineering, 2nd Affiliated Hospital, School of Medicine, Zhejiang University, Hangzhou, China, <sup>4</sup> Dushu Lake Hospital Affiliated to Soochow University, Suzhou, China

## OPEN ACCESS

### Edited by:

Kuanquan Wang,  
Harbin Institute of Technology, China

### Reviewed by:

Songyun Wang,  
Renmin Hospital of Wuhan University,  
China  
Xin Li,  
University of Leicester,  
United Kingdom

### \*Correspondence:

Ruiqing Dong  
ruiqingdong@163.com  
Ling Xia  
xialing@zju.edu.cn

<sup>†</sup>These authors share first authorship

### Specialty section:

This article was submitted to  
Computational Physiology  
and Medicine,  
a section of the journal  
Frontiers in Physiology

**Received:** 29 January 2021

**Accepted:** 11 March 2021

**Published:** 31 March 2021

### Citation:

Li R, Zhao X, Gong Y, Zhang J,  
Dong R and Xia L (2021) A New  
Method for Detecting Myocardial  
Ischemia Based on ECG T-Wave Area  
Curve (TWAC).  
Front. Physiol. 12:660232.  
doi: 10.3389/fphys.2021.660232

In recent years, coronary heart disease (CHD) has become one of the main diseases that endanger human health, with a high mortality and disability rate. Myocardial ischemia (MI) is the main symptom in the development of CHD. Continuous and severe myocardial ischemia will lead to myocardial infarction. The clinical manifestations of MI are mainly the changes of ST-T segment of ECG, that is, ST segment and T wave. Nearly one third of patients with CHD, however, has no obvious ECG changes. In this paper, a new method for detecting MI based on the T-wave area curve (TWAC) was proposed. Through observation and analysis of clinical data, it was found that there exist significant correlation between the morphology of TWAC and MI. The TWAC morphology of normal subject is smooth and gentle, while the TWAC morphology of patients with coronary stenosis is mostly jagged, and the curve becomes more severe with more severe stenosis. The preliminary test results show that the sensitivity, specificity, and accuracy of the proposed method for detecting MI are 84.3, 83.6, and 84%, respectively. This study shows that the TWAC based approach may be an effective method for detecting MI, especially for the CHD patients with no obvious ECG changes.

**Keywords:** myocardial ischemia, ECG, coronary heart disease, heart, electrophysiology

## INTRODUCTION

Cardiovascular disease has long been the first cause of death. In China only, the current number of patients with cardiovascular disease is 290 million, among them 11 million are patients with coronary heart disease (CHD) (Ma et al., 2020). For patients with typical CHD, diagnosis can be made based on resting electrocardiogram (ECG), exercise ECG, cardiac ultrasound, coronary angiography, and cardiac magnetic resonance. The resting ECG is widely used in clinic due to its non-invasive, economical and simple reasons. ST-T wave change is the most commonly used ECG feature to judge myocardial ischemia (MI) (Lin and Guo, 2005). According to related research, the positive rate of resting ECG diagnosis for CHD is 71%, and the rest of 29% patients have no ECG changes and some patients with three lesions can be completely normal, indicating that patients with normal ECG cannot rule out CHD (Pijls et al., 1995).

The clinical manifestations of MI are mainly the ST-T segment changes of the electrocardiogram, that is, the ST segment and T wave. The diagnosis of MI by ECG mainly depends on the

characteristics of the ST-T segment. However, there are many factors affecting ST segment changes, such as axis shift, heart rate, electrode effects, body position changes, etc., leading to inaccurate detection of feature points, relying on ST segment shift to detect MI has a large false detection rate and missed detection rate. T wave represents the repolarization process of the ventricles. During MI, myocardial repolarization is delayed, resulting in changes in T wave morphology, such as biphasic T wave, inverted T wave, or high-tip T wave. In view of this characteristic of T wave, this paper proposes a method for diagnosing myocardial ischemia based on the T-wave area curve. By locating T-wave characteristic points, calculating T-wave area and drawing a curve with cardiac cycles, based on clinical data, the qualitative relationship between myocardial ischemia and T-wave area curve was analyzed.

## MATERIALS AND METHODS

### T-Wave Onset and Offset Detection

T wave is an important part of ECG signal. Accurate localization and morphological recognition of T wave are basic indicators for diagnosis of MI, but the shape of T wave is variable. Hayden et al. (2002) show that when ischemic cardiomyopathy occurs, the T-wave shape will change accordingly, such as inverted, biphasic, high-point, etc., and the low-frequency components near the end of the T-wave are more abundant than other bands, and more susceptible to noise and baseline drift. Accurate finding the location of the T-wave end point is with some difficulties. Therefore, T-wave detection needs to take into account the changes in T-wave morphology.

At present, T-wave ends can be detected by methods such as area method (Zhang et al., 2006; Vázquez-Seisdedos et al., 2011), wavelet transform (Martínez et al., 2004), pattern recognition (Saini et al., 2013), and artificial neural network (Maglaveras et al., 1998). Due to the noise of the T wave and the baseline drift, the wavelet transform method may contain aliasing part. Therefore, simply using the wavelet method has a higher false detection rate, and some waveforms caused by noise or baseline drift are falsely

detected as T waves. The neural network method can adapt to the change of T-wave shape when it is used for feature detection. It has good robustness, but the algorithm is more complicated. For the area-dependent methods, the algorithms can adapt to abnormal changes in T-wave shape, and have strong waveform adaptabilities. Among them, Zhang's algorithm (Zhang et al., 2006) is a good method for T-wave ends location. It was based on an indicator signal with mathematically proved consistency. It was robust to measurement noise, waveform shape changes and baseline drift, and is suitable for various forms of T waves. The computation burden of the algorithm was very low: its main computation can be implemented as a simple FIR filter. When evaluated with the PhysioNet QT database (Goldberger et al., 2000) in terms of the mean and the standard deviation of the T-wave end location errors, Zhang's algorithm outperforms the other algorithms evaluated with the same database (Zhang et al., 2006). So, in this study, Zhang's algorithm is basically used for T-wave ends location.

One key issue of the area-dependent methods is to accurately determine the search boundaries, but the search boundaries are closely related to the RR interval. If the interval of the searching window's boundaries was set too small which means that two boundary points are near the current R peak, the maximum of sliding area could not be found or the detected onset/offset of T wave are nearer to the R peak. This issue will affect detection accuracy, which results in detection error and vice versa. In order to more accurately model the relationships between RR interval and the searching boundaries, in this study, similar to Shang et al.'s work (Shang et al., 2019), we performed a k-means clustering analysis between RR intervals and  $RT_{on}$  ( $RT_{on}$  denotes the time interval between the R peak and T wave onset) as well as the relationship between the RR intervals and  $RT_{off}$  ( $RT_{off}$  the time interval between the R peak and T wave offset), which is implemented by means of the k-means function. The scatter plots with the optimal k-means clustering ( $k = 3$ ) are showed in **Figure 1**, and  $k$  is determined by combining the results of clustering and the computational complexity of parameters' settings as well as the adaptiveness of the algorithm. Then, the two relationships (between RR intervals and  $RT_{on}$ , and

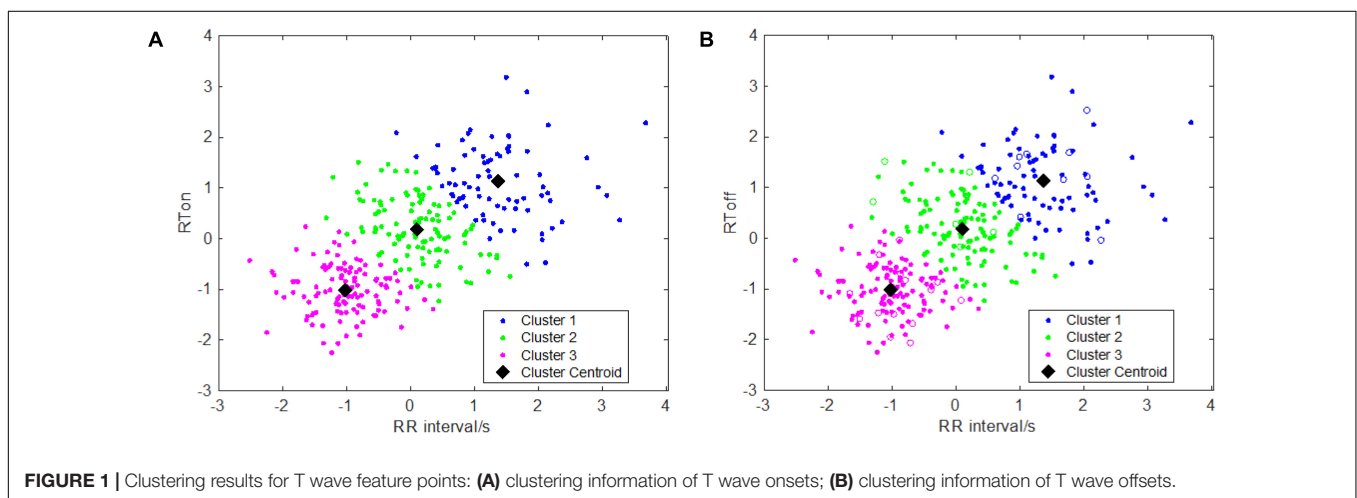


**FIGURE 1 |** Clustering results for T wave feature points: (A) clustering information of T wave onsets; (B) clustering information of T wave offsets.

between RR intervals and  $RT_{off}$ ) are obtained using the following equations:

$$\begin{aligned}
 \text{Case1: } & RR < 0.67s, \quad 0.05s < RT_{on} < 0.25s \\
 \text{Case2: } & 0.67s \leq RR < 1.23s, \quad 0.05s < RT_{on} < 0.35s \\
 \text{Case3: } & RR \geq 1.23s, \quad 0.05s < RT_{on} < 0.45s \\
 \text{Case1: } & RR < 0.71s, \quad 0.2s < RT_{off} < 0.45s \\
 \text{Case2: } & 0.71s \leq RR < 1.1s, \quad 0.2s < RT_{off} < 0.6s \\
 \text{Case3: } & RR \geq 1.1s, \quad 0.2s < RT_{off} < 0.45s
 \end{aligned} \quad (1)$$

Thus, the three piecewise functions for determining the search boundaries for T wave onset and offset detections can be obtained.

Then, the grid search was used to determine the best combination of parameters in Equations (2) and (3), which was implemented by for loop. In a loop, we changed the value of one parameter at a time, kept the other parameters unchanged, and applied the algorithm in the QT database as well as using a fivefold cross-validation. Then, we stored the sensitivity of one loop and started another loop. Through all loops, we traversed all of the combinations of parameters. After comparing the results, the combinations of parameters with the highest sensitivity were chosen. The best parameters' combinations for T wave onsets are:  $a = 0.4$ ,  $b = 0.2$ ,  $c = 0.4$ ,  $d = 0.4$ ,  $e = 0.3$ ,  $f = 0.0$ , and for T wave offsets are:  $a = 0.2$ ,  $b = 0.1$ ,  $c = 0.2$ ,  $d = 0.0$ ,  $e = 0.0$ ,  $f = 0.1$ .

$$\begin{cases}
 t_1 = ([a \times \sqrt{RR_i}] + R_i + 0.02)s \\
 t_2 = ([b \times (RR_i)] + R_i + 0.16)s \text{ if } RR_i < 0.67s \\
 t_1 = ([c \times \sqrt{RR_i}] + R_i + 0.04)s \\
 t_2 = ([d \times (RR_i)] + R_i + 0.24)s \text{ if } 0.67s \leq RR_i < 1.23s \\
 t_1 = ([e \times \sqrt{RR_i}] + R_i + 0.04)s \\
 t_2 = ([f \times (RR_i)] + R_i + 0.4)s \text{ if } RR_i \geq 1.23s
 \end{cases} \quad (2)$$

$$\begin{cases}
 t_1 = ([a \times \sqrt{RR_i}] + R_i + 0.18)s \\
 t_2 = ([b \times (RR_i)] + R_i + 0.3)s \text{ if } RR_i < 0.71s \\
 t_1 = ([c \times \sqrt{RR_i}] + R_i + 0.18)s \\
 t_2 = ([d \times (RR_i)] + R_i + 0.4)s \text{ if } 0.71s \leq RR_i < 1.1s \\
 t_1 = ([e \times \sqrt{RR_i}] + R_i + 0.18)s \\
 t_2 = ([f \times (RR_i)] + R_i + 0.48)s \text{ if } RR_i \geq 1.1s
 \end{cases} \quad (3)$$

## T-Wave Area Curve

When the T-wave onset and offset was detected, the T-wave area can be calculated as follows.

Let the T wave onset be  $T_{on}$  and the T wave offset be  $T_{off}$ . Within the fixed window  $t \in [T_{on}, T_{off}]$ , calculate the waveform area  $A_t$ :

$$A_t = \sum_{t=T_{on}}^{T_{off}} (s_t - \bar{s}_k) \quad (4)$$

where  $s_t$  is the amplitude of the t-th sample point, and  $\bar{s}_k$  is the local average amplitude (by default, a smoothing window of  $p = 0.016s$  is used), which is defined as:

$$\bar{s}_k = \frac{1}{2p+1} \sum_{j=t-p}^{t+p} S_j \quad (5)$$

Calculate the continuous T wave area of each lead, and then draw the connection line with the cardiac cycle number as the abscissa and the T wave area as the ordinate. Based on the T wave morphological variability during MI, it can be inferred that if the line is approximately straight, the ischemia test is negative. If one or more of the leads are serrated, it is positive, and if one or more of the leads are serrated, it may be related to the position of the blocked coronary artery is related.

From the T-wave area curves of 52 healthy samples in the PTB database, it was found that the curves of 43 healthy people were flat and the morphological differences were small. The difference in T-wave area per heartbeat of patients with MI, however, is obviously larger than that of healthy people. The area curve is jagged and irregular. Observing the corresponding T-wave area curve of the 15-s electrocardiogram data of 148 patients with MI in the PTB database, it was found that the curves of 115 MI patients were irregular and chaotic, which was in sharp contrast with the curves of healthy samples.

According to the characteristic that the degree of fluctuation of the T-wave area curve of patients with MI is significantly greater than that of healthy people, we used the TWAC (T-wave area curve) to detect MI. Based on the TWAC form, the gentle TWAC is defined as negative, corresponding to myocardial blood supply was normal in the subject. And the irregular jagged TWAC was defined as positive, corresponding to myocardial ischemia in the subject.

## Experimental Data

The sample number in this article is 364 in two groups: the first group contains 148 patients with MI and 52 normal persons from the PTB database (Goldberger et al., 2000); the second group contains 122 patients with suspected MI from Zhejiang Second Hospital and 42 health subjects. The detailed characteristics of the selection patients are shown in Table 1.

The clinical data of Zhejiang Second Hospital was conducted from May 2018 to December 2018. Philips TC20 ECG machine was used to record resting ECG data with a sampling rate of 1,000 Hz and 16-bit resolution. We select stable 15 s ECG data (15 s ECG data contains about 20 heart beats) to draw a 12-lead T-wave area curve. This study was approved by Zhejiang Second Hospital Review Board. After signing the informed consent, the patient was placed in the supine position, and the resting ECG was obtained after strictly following the 12-lead ECG collection procedure. Each patient was subjected to coronary angiography after ECG examination. A professional cardiology interventional doctor performed a visual assessment of the degree of coronary artery stenosis. In order to ensure the accuracy of the ECG results of this study, a professional electrocardiologist interpreted the ECG data, but he did not know the coronary angiography examination results of the patients.

Selection criteria were patients with suspected MI who had no MI characteristics on the ECG. The absence of MI characteristics means that the ST segment of any lead with R wave as the main wave is not depressed or depressed  $< 0.05$  mv, T wave is upright and  $\geq 1/10R$  wave. Suspicious MI refers to the clinical manifestations, myocardial enzymes and other tests and coronary



**TABLE 1 |** Clinical characteristics of patients.

Characteristics	Myocardial ischemia		p-value
	Yes (n = 236)	No (n = 128)	
Age	59 ± 10	55 ± 9	0.025*
Female	106/236 (45%)	49/128 (39%)	0.163
Chest pain	130/236 (55%)	51/128 (40%)	0.023 <sup>§</sup>
Dyspnea	94/236 (40%)	55/128 (43%)	0.58
Heart rate (bpm)	71 ± 8	70 ± 7	0.239
Ejection fraction (%)	65 ± 6	66 ± 2	0.012*
Left ventricular end diastolic diameter (mmHg) (mm)	47 ± 4	46 ± 2	< 0.01*
Systolic blood pressure (mmHg)	132 ± 27	122 ± 10	0.303
Diastolic blood pressure (mmHg)	76 ± 9	74 ± 6	0.03*
Smoke	113/236 (48%)	55/128 (43%)	0.5
Hypertension	144/236 (61%)	68/128 (53%)	0.197
Diabetes mellitus	73/236 (31%)	33/128 (26%)	0.354
Dyslipidemia	170/236 (72%)	78/128 (61%)	0.032 <sup>§</sup>
Family history of CAD	42/236 (18%)	18/128 (14%)	0.396

P-value are obtained using independent-samples t-test and Chi-square test.

\*Significant differences between groups using independent-samples t-test.

<sup>§</sup>Significant differences between groups using Chi-square test. Diagnostic criteria for hypertension: systolic blood pressure  $\geq 140$  mmHg in three resting days on the same day; or diastolic blood pressure  $\geq 90$  mmHg; or those with a history of hypertension who are taking antihypertensive drugs and are currently at normal blood pressure. Diabetes diagnosis criteria: fasting blood glucose  $> 7.0$  mmol/L or 2 h after meals  $> 11.1$  mmol/L; or patients with a history of diabetes who are taking drugs to treat the current normal blood sugar. Diagnostic criteria for hyperlipidemia: total blood cholesterol  $> 6.00$  mmol/L, or triglycerides  $\geq 1.69$  mmol/L during this hospitalization; or those with a history of hyperlipidemia who are currently taking hypolipidemic drugs and have normal blood lipids. Smoking history is based on past history.

CTA and other examinations suggest that the patient may have MI, which is evaluated by a professional cardiologist.

Exclusion criteria were non-sinus electrocardiograms such as atrial fibrillation and atrial flutter; premature beats; atrioventricular block or ventricular block; ventricular pre-excitation patterns; abnormal Q waves or poor R-wave increments in right chest leads; significant sinus Bradycardia (heart rate  $< 50$  beats/min); heart valve disease.

This article used the results of CAG or blood flow reserve fraction (FFR) as the gold standard for MI diagnosis, and defined coronary angiography result as a positive MI if one of the three branches of the coronary artery (anterior descending branch, circumflex branch, right coronary artery) has a stenosis degree of  $\geq 70\%$  (Tonino et al., 2009); all without stenosis or a degree of stenosis less than 70% are negative MI. Patients are considered positive MI when FFR value  $\geq 0.8$ , and negative MI if FFR value  $< 0.8$ .

## RESULTS

As mentioned above, TWAC is a curve of the T-wave area of a conventional 12-lead ECG as a function of the cardiac cycle. By analyzing the TWAC morphology of a lot of clinical data, it is found that the curve of normal people has less fluctuation, and the curve of patients with MI is mostly jagged changes in

different cardiac cycles. **Figure 2** shows an example of TWAC in two normal people, and **Figure 3** shows an example of TWAC in two patients with MI. It shows that the T-wave area curve has a significant correlation with ischemic heart disease. Therefore, in this article, TWAC of one or more leads with jagged fluctuations is identified as positive (with MI), and the fluctuations are small and gentle in TWAC is considered as negative (no MI).

Experiment results are shown in **Table 2**. The sensitivity of TWAC to the diagnosis of MI was 84.3% (199/236), the specificity was 83.6% (107/128), and the accuracy was 84.0% (306/364).

## DISCUSSION

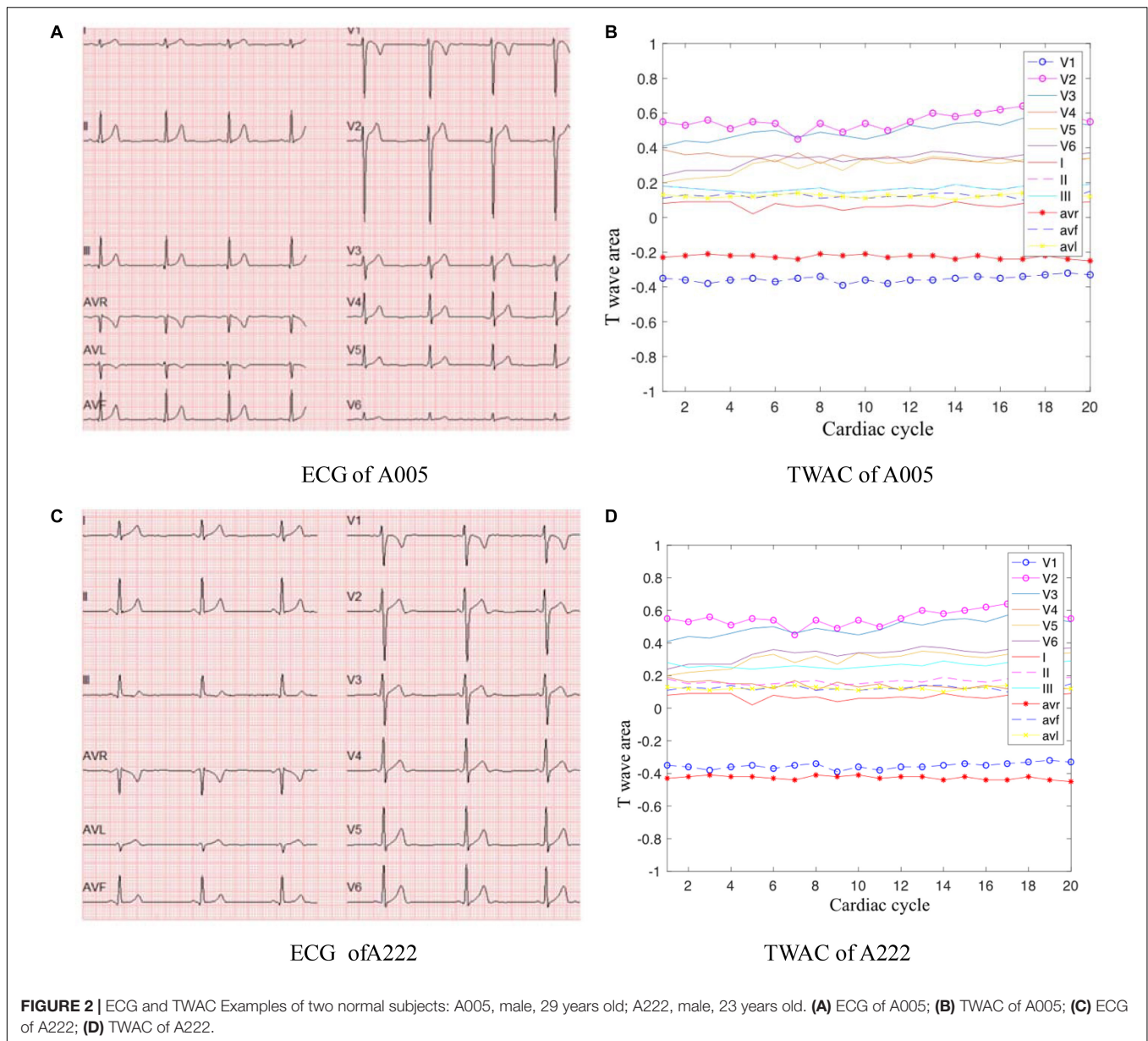
### Analysis of Misjudgment Data

The total number of patients in the false-negative group was 37, of which 13 patients had a diseased vessel stenosis of 70%. The method used in this study to interpret the degree of coronary stenosis was physician visual assessment (PVA), which is based on the personal experience of the surgeon. Judgment is relatively subjective. Studies have pointed out that the severity of stenosis of coronary lesions in PVA in China is significantly higher than quantitative coronary angiography (QCA) and there is a large difference between hospitals and doctors (Zhang et al., 2018). Therefore, the presence of false-negative patients does not rule out the possibility of overestimation of coronary artery disease caused by PVA. Single-vessel disease is more common in false-negative patients, while multiple-vessel disease is more common in true-positive patients. The range of MI caused by single vessel disease is relatively small, and negative results are easily obtained. In addition, collateral circulation is another factor of false negative results. The collateral circulation rate of patients in the false negative group is higher than that in the true positive group. Professional cardiologists have confirmed that there are 4 cases of coronary stenosis  $> 70\%$  in the false negative group. Collateral circulation can improve the heart blood supply and may make TWAC negative.

A total of 21 false-positive patients was included in this study, 15 of whom had chest tightness and chest pain. Although coronary angiography showed negative results, the possibility of MI could not be completely ruled out. In the FAME study, 35% of the lesions with a degree of coronary stenosis of 50–70% had an FFR of  $< 0.8$ , and in Park's study, 16% of the lesions with a degree of coronary stenosis of  $< 50\%$  had an FFR of  $< 0.8$ . The data indicate that MI is still possible without significant coronary stenosis (Tonino et al., 2009; Park et al., 2012; Ahmadi et al., 2015). The clinical manifestations of all these false positive patients were typical CHD and showed a higher incidence of coronary atherosclerosis than the true negative group.

### Analysis of the Relationship Between TWAC Morphology and Coronary Occlusion in Specific Leads

When the TWAC is positive, by observing the TWAC morphology on each lead, we've found that in addition to the  $V_1, V_3, V_4$  leads have obvious sharp points or inverted



phenomena, the aVL lead and aVR lead curves also fluctuate greatly, as shown in **Figure 3D**.

T wave can reflect the heterogeneity of ventricular repolarization in patients and predict cardiovascular disease to a certain extent. T wave is a potential wave formed by repolarization of ventricular cells. Repolarization is an active energy-consuming process. When MI occurs, the heart cannot normally deliver blood and nutrients. Therefore, insufficient supply of myocardial energy will cause myocardial contraction and diastolic function is impaired, which may cause T wave changes in patients with ischemic cardiomyopathy.

Studies have shown that the degree of T wave changes in aVL leads reflects the degree of ventricular muscle excitement recovery time, and reflects the heterogeneity of ventricular muscle repolarization. Compared with ST-T changes, aVL lead

T-wave changes have a higher sensitivity for the diagnosis of myocardial ischemia, which is significantly related to the number of coronary artery disease vessels and the degree of myocardial ischemic injury (Tepetam et al., 2016).

Studies have also shown that the inversion of T waves on leads  $V_3$  and  $V_4$  may indicate a middle obstruction of the left anterior descending coronary artery, which indicates that changes in T waves on specific leads can predict not only extensive myocardial ischemia, but also blockage at specific coronary arteries (De Zwaan et al., 1982). From the azimuth point, leads  $V_3$  and  $V_4$  correspond to the proximal anterior descending branch, and the coronary direction of the middle part of the left anterior descending branch is almost parallel to the aVL lead of the ECG. It can be speculated that if the adjacent area of the left anterior descending branch ischemia, the T wave of lead aVL



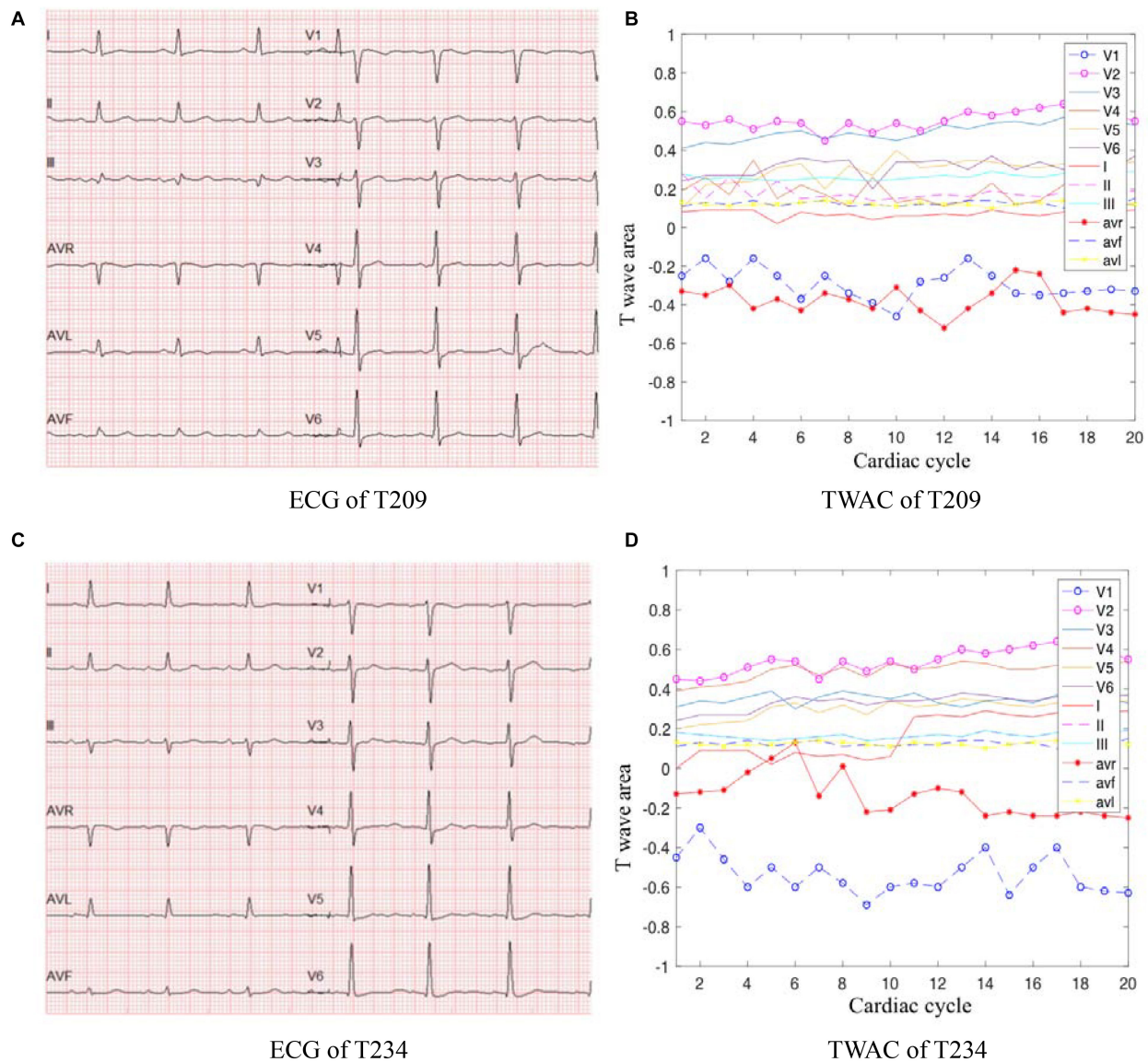


**FIGURE 3 |** ECG and TWAC examples of two MI patients: T209, female, 66 years of age, with moderate coronary stenosis; T234, male, 73 years, with severe coronary stenosis. **(A)** ECG of T209; **(B)** TWAC of T209; **(C)** ECG of T234; **(D)** TWAC of T234.

should also change. Therefore, the T wave change of lead aVL also corresponds to the anterior descending branch of the left anterior descending coronary artery.

As shown in **Figure 3B**, the aVR lead curve fluctuates in a zigzag manner, and the coordinate points in some cardiac cycles exceed the abscissa and become positive values. In a normal 12-lead ECG, the T wave on the aVR lead is inverted. This patient's CAG showed 70% stenosis of the left circumflex branch. Studies have shown that the morphological changes of the T wave in lead aVR are of great significance in predicting cardiovascular death, and its value is higher than other ECG leads, comparable to the changes in the ST segment of the aVR lead (Tan et al., 2008). If the amplitude of the inverted T wave becomes smaller, it means that the risk of cardiovascular death is gradually increased. When

the inverted T wave becomes upright, the risk of cardiovascular death is higher.

The aVR lead has been used only to judge the origin of the heart rhythm, and its role has been seriously underestimated. The aVR lead has a special position on the frontal six-axis system, that is, the aVR lead axis is between the I and II lead axes, the angle between the aVR lead axis and the ventricular depolarization vector is the smallest, and the projection is the largest, which is the most sensitive lead to the changes of the ventricular depolarization vector.

## Advantages and Limitations

Coronary atherosclerosis causes a series of electrophysiological changes that affect ventricular repolarization

**TABLE 2 |** Experimental results, where TN, TP, FN, and FP represent true negative, true positive, false negative, and false positive, respectively.

Experiment samples	TWAC		TP, TN, FP, FN				SEN (%)	SPE (%)	ACC (%)
	Positive	Negative	TN	TP	FN	FP			
PTB 148 MI	119	29	–	119	29		80.4	–	80.4
PTB 52 healthy	9	43	43	–	–	9	–	82.7	82.7
ZJU 122 MI	89	33	25	80	8	9	89.9	75.8	86.1
ZJU 42 healthy	3	39	39	–	–	3	–	92.9	92.9
Total 364	220	144	107	199	37	21	84.3	83.6	84.0

The sensitivity (SEN), specificity (SPE) and accuracy (ACC) are defined as follows:

$$\text{Sensitivity} \stackrel{\text{def}}{=} \frac{TP}{TP + FN} (\%)$$

$$\text{Specificity} \stackrel{\text{def}}{=} \frac{TN}{TN + FP} (\%)$$

$$\text{Accuracy} \stackrel{\text{def}}{=} \frac{TP + TN}{TP + TN + FP + FN} (\%)$$

(Downar et al., 1977; Janse and Wit, 1989). During cardiac ischemia, the duration of action potential and conduction velocity decrease, leading to a heterogeneous repolarization process (Janse et al., 1985). Studies have shown that ischemia increases the repolarization dispersion between normal and ischemic fibers, and between the epicardium and the endocardium (Coronel et al., 1988), which refers to the "every other heartbeat" on the ECG. The repolarization pattern has a continuous fluctuation (Arini et al., 2014). This fluctuation refers to the change in the amplitude of the T wave or the change in the ST segment between different cardiac cycles. The amplitude of these bipolar alternations (dispersions) is usually in the microvolt range and cannot be visually recognized. Computer-based signal processing and analysis technology can detect subtle ECG changes. The T wave amplitude and shape on ECG alternately change from beat to beat, which is called T wave electrical alternation (TWA) (Puletti et al., 1980). TWA represents the alternation of cardiac repolarization, is an indicator of ventricular tachycardia and ventricular fibrillation in ischemic myocardium, and can be used as an indicator of risk stratification of acute myocardial infarction. The disadvantage of TWA is that it is susceptible to breathing, electrode and skin interference, wire movement and body position changes, and further research is needed. TWAC analyzes subtle ECG signal changes and amplifies such subtle changes to detect abnormal dynamics of cardiac repolarization, and is robust to acquisition noise, baseline drift and T wave morphology.

TWAC is the T-wave area curve of 12 leads with the cardiac cycle. Different leads of the electrocardiogram record electrical signals at different positions of the heart. Therefore, the degree of fluctuation of TWAC on different leads reflects the degree of stenosis at specific blood vessels to a certain extent. This paper analyzed the TWAC and coronary angiography results of some patients, and found that the T wave changes on leads V<sub>3</sub>, V<sub>4</sub>, aVL corresponded to the obstruction of the left anterior descending branch of the coronary artery, and the T wave changes on the aVR lead predicted the stenosis at left trunk coronary arteries.

There are some limitations in this study. First, coronary angiography shows that coronary artery stenosis is not equivalent to MI (Tonino et al., 2009; Park et al., 2012;

Ahmadi et al., 2015). Clinically, it can be directly intervened when the diameter of coronary artery is narrower than 90%; if the diameter of coronary artery is not narrower than 90%, it is recommended that only FFR ≤ 0.8, or the disease with corresponding evidence of ischemia, then intervention can be taken. For moderate coronary stenosis, even the experienced cardiologist's interventional physician's visual assessment of angiography cannot accurately evaluate its physiological significance (Fischer et al., 2002). The number of patients with mismatched TWAC and CAG results in this study was 58, of which 33 (56.7%) patients had coronary stenosis with a coronary stenosis of 40–70%. It cannot be ruled out that coronary angiography could not determine the myocardial ischemia relatively accurately. The accuracy rate of FFR value ≤ 0.80 for identifying myocardial ischemia caused by coronary artery stenosis is as high as >90%. It has been confirmed by extensive randomized controlled studies that FFR is the gold standard for evaluating the physiological significance of coronary artery stenosis. Changes in hemodynamic factors such as contractile force. In future studies, FFR will be considered as the gold standard for diagnosis of MI, which can further verify the accuracy of TWAC. Secondly, the sample size is small, and more clinical research is needed to further verify the TWAC method.

## CONCLUSION

In this paper, a new method for detecting MI was proposed, unlike the conventional ST-T segment based approaches, it was based on the T-wave area curve (TWAC). Preliminary test results show that the proposed method has good sensitivity, specificity, and accuracy for MI detection, especially for the CHD patients with no obvious ECG changes.

## DATA AVAILABILITY STATEMENT

The raw data supporting the conclusions of this article will be made available by the authors, without undue reservation.

## ETHICS STATEMENT

The studies involving human participants were reviewed and approved by the Zhejiang Second Hospital Review Board. The patients/participants provided their written informed consent to participate in this study.

## AUTHOR CONTRIBUTIONS

RL and XZ contributed to the algorithm and the statistical analysis. JZ and RD contributed to the clinical data collection and interpretation. YG, RD, and LX contributed to the funding acquisition, conception, and design of the study. All authors

contributed to the writing, critical reading, and approval of the manuscript.

## FUNDING

This work was supported by the Natural Science Foundation of China (NSFC) under grant nos. 61527811 and 61701435, the Key Research and Development Program of Zhejiang Province under grant no. 2020C03016, the Zhejiang Provincial Natural Science Foundation of China under grant no. LY17H180003, and the Medical Health Science and Technology Project of Zhejiang Provincial Health Commission under grant no. 2020RC094.

## REFERENCES

- Ahmadi, A., Kini, A., and Narula, J. (2015). Discordance between ischemia and stenosis, or PINSS and NIPSS: are we ready for new vocabulary? *JACC Cardiovasc. Imaging* 8, 111–114. doi: 10.1016/j.jcmg.2014.11.010
- Arini, P. D., Baglivo, F. H., Martínez, J. P., and Laguna, P. (2014). Evaluation of ventricular repolarization dispersion during acute myocardial ischemia: spatial and temporal ECG indices. *Med. Biol. Eng. Comput.* 52, 375–391. doi: 10.1007/s11517-014-1136-z
- Coronel, R., Fiolet, J. W., Wilms-Schopman, F. J., Schaapherder, A. F., Johnson, T. A., Gettes, L. S., et al. (1988). Distribution of extracellular potassium and its relation to electrophysiologic changes during acute myocardial ischemia in the isolated perfused porcine heart. *Circulation* 77, 1125–1138.
- De Zwaan, C., Bär, F. W. H. M., and Wellens, H. J. J. (1982). Characteristic electrocardiographic pattern indicating a critical stenosis high in left anterior descending coronary artery in patients admitted because of impending myocardial infarction. *Am. Heart J.* 103, 730–736.
- Downar, E., Janse, M. J., and Durrer, D. (1977). The effect of acute coronary artery occlusion on subepicardial transmembrane potentials in the intact porcine heart. *Circulation* 56, 217–224. doi: 10.1161/01.CIR.56.2.217
- Fischer, J. J., Samady, H., McPherson, J. A., Sarembok, I. J., Powers, E. R., Gimple, L. W., et al. (2002). Comparison between visual assessment and quantitative angiography versus fractional flow reserve for native coronary narrowings of moderate severity. *Am. J. Cardiol.* 90, 210–215. doi: 10.1016/S0002-9149(02)02456-6
- Goldberger, A. L., Amaral, L. A. N., Glass, L., Hausdorff, J. M., Ivanov, P. C., Mark, R. G., et al. (2000). PhysioBank, PhysioToolkit, and PhysioNet: components of a new research resource for complex physiologic signals. *Circulation* 101, e215–e220. doi: 10.1161/01.CIR.101.23.e215
- Hayden, G. E., Brady, W. J., Perron, A. D., Somers, M. P., and Mattu, A. (2002). Electrocardiographic T-wave inversion: differential diagnosis in the chest pain patient. *Am. J. Emerg. Med.* 20, 252–262. doi: 10.1053/ajem.2002.32629
- Janse, M. J., Capucci, A., Coronel, R., and Fabius, M. A. (1985). Variability of recovery of excitability in the normal canine and the ischaemic porcine heart. *Eur. Heart J.* 6, 41–52. doi: 10.1093/eurheartj/6.suppl\_D.41
- Janse, M. J., and Wit, A. L. (1989). Electrophysiological mechanisms of ventricular arrhythmias resulting from myocardial ischemia and infarction. *Physiol. Rev.* 69, 1049–1169. doi: 10.1152/physrev.1989.69.4.1049
- Lin, R., and Guo, J. (2005). *Modern Perspective of Cardiovascular Disease*. Beijing: Peking University Medical Press.
- Ma, L., Chen, W., Gao, R., Liu, L., Zhu, M., Wang, Y., et al. (2020). China cardiovascular diseases report 2018: an updated summary. *J. Geriatr. Cardiol.* 17, 1–8. doi: 10.11909/j.issn.1671-5411.2020.01.001
- Maglaveras, N., Stamkopoulos, T., Pappas, C., and Strintzis, M. G. (1998). An adaptive backpropagation neural network for real-time ischemia episodes detection: development and performance analysis using the European ST-T database. *IEEE Trans. Biomed. Eng.* 45, 805–813. doi: 10.1109/10.686788
- Martínez, J. P., Almeida, R., Olmos, S., Rocha, A. P., and Laguna, P. (2004). A wavelet-based ECG delineator: evaluation on standard databases. *IEEE Trans. Biomed. Eng.* 51, 570–581. doi: 10.1109/TBME.2003.821031
- Park, S. J., Kang, S. J., Ahn, J. M., Shim, E. B., Kim, Y. T., Yun, S. C., et al. (2012). Visual-functional mismatch between coronary angiography and fractional flow reserve. *JACC: Cardiovasc. Interv.* 5, 1029–1036. doi: 10.1016/j.jcin.2012.07.007
- Pijls, N. H., Van Gelder, B., Van der Voort, P., Peels, K., Bracke, F. A., Bonnier, H. J., et al. (1995). Fractional flow reserve: a useful index to evaluate the influence of an epicardial coronary stenosis on myocardial blood flow. *Circulation* 92, 3183–3193. doi: 10.1161/01.CIR.92.11.3183
- Puletti, M., Curione, M., Righetti, G., and Jacobellis, G. (1980). Alternans of the ST segment and T wave in acute myocardial infarction. *J. Electrocardiol.* 13, 297–300. doi: 10.1016/s0022-0736(80)80035-5
- Saini, I., Singh, D., and Khosla, A. (2013). Delineation of ECG wave components using K-Nearest neighbor (KNN) algorithm: ECG wave delineation using KNN. In *proceedings of the 10th International Conference on Information Technology: New Generations*. Piscataway NJ: IEEE 2013, 712–717.
- Shang, H., Wei, S., Liu, F., Wei, D., Chen, L., and Liu, C. (2019). An improved sliding window area method for t wave detection. *Comput. Math. Methods Med.* 11:3130527. doi: 10.1155/2019/3130527
- Tan, S. Y., Engel, G., Myers, J., Sandri, M., and Froelicher, V. F. (2008). The prognostic value of T wave amplitude in lead aVR in males. *Ann. Noninvasive Electrocardiol.* 13, 113–119. doi: 10.1111/j.1542-474X.2008.00210.x
- Tepetam, F. M., Dağdeviren, B., Bulut, I., Karabay, C. Y., Barış, S., and Aydinler Karakoç, E. (2016). A patient with mushroom allergy; a new etiological agent of Kounis syndrome. *Tuberk. Toraks* 64, 171–174. doi: 10.5578/tt.9411
- Tonino, P. A. L., De Bruyne, B., Pijls, N. H. J., Siebert, U., Ikeno, F., van't Veer, M., et al. (2009). Fractional flow reserve versus angiography for guiding percutaneous coronary intervention. *N. Engl. J. Med.* 360, 213–224. doi: 10.1056/NEJMoa0807611
- Vázquez-Seisdedos, C. R., Neto, J. E., Marañón Reyes, E. J., Macías, F. S., Rodríguez, V. R., Chacón, L. M., et al. (2011). New approach for T-wave end detection on electrocardiogram: Performance in noisy conditions. *Biomed. Eng. Online* 10:77. doi: 10.1186/1475-925X-10-77
- Zhang, H., Mu, L., Hu, S., Nallamothu, B., Lansky, A. J., Xu, B., et al. (2018). Comparison of physician visual assessment with quantitative coronary angiography in assessment of stenosis severity in China. *JAMA Intern. Med.* 178, 239–247. doi: 10.1001/jamainternmed.2017.7821
- Zhang, Q., Manriquez, A. I., Médigue, C., Papelier, Y., and Sorine, M. (2006). An algorithm for robust and efficient location of T-wave ends in electrocardiograms. *IEEE Trans. Biomed. Eng.* 53(12 Pt 1), 2544–2552. doi: 10.1109/TBME.2006.884644

**Conflict of Interest:** The authors declare that the research was conducted in the absence of any commercial or financial relationships that could be construed as a potential conflict of interest.

Copyright © 2021 Li, Zhao, Gong, Zhang, Dong and Xia. This is an open-access article distributed under the terms of the Creative Commons Attribution License (CC BY). The use, distribution or reproduction in other forums is permitted, provided the original author(s) and the copyright owner(s) are credited and that the original publication in this journal is cited, in accordance with accepted academic practice. No use, distribution or reproduction is permitted which does not comply with these terms.





# Recurrence Plot-Based Approach for Cardiac Arrhythmia Classification Using Inception-ResNet-v2

Hua Zhang<sup>1</sup>, Chengyu Liu<sup>2</sup>, Zhimin Zhang<sup>3</sup>, Yujie Xing<sup>4</sup>, Xinwen Liu<sup>1</sup>, Ruiqing Dong<sup>5</sup>, Yu He<sup>1</sup>, Ling Xia<sup>6\*</sup> and Feng Liu<sup>1\*</sup>

<sup>1</sup> School of Information Technology and Electrical Engineering, University of Queensland, Brisbane, QLD, Australia, <sup>2</sup> School of Instrument Science and Engineering, Southeast University, Nanjing, China, <sup>3</sup> Science and Technology on Information Systems Engineering Laboratory, The 28th Research Institute of CETC, Nanjing, China, <sup>4</sup> First Department of Cardiology, People's Hospital of Shaanxi Province, Xi'an, China, <sup>5</sup> Dushuhu Public Hospital Affiliated to Soochow University, Suzhou, China, <sup>6</sup> Department of Biomedical Engineering, Zhejiang University, Hangzhou, China

## OPEN ACCESS

### Edited by:

Kuanquan Wang,  
Harbin Institute of Technology, China

### Reviewed by:

Shenda Hong,  
Peking University, China  
Xiu Ying Wang,  
The University of Sydney, Australia  
Lisheng Xu,  
Northeastern University, China

### \*Correspondence:

Ling Xia  
xialing@zju.edu.cn  
Feng Liu  
feng@itee.uq.edu.au

### Specialty section:

This article was submitted to  
Computational Physiology  
and Medicine,  
a section of the journal  
Frontiers in Physiology

**Received:** 03 January 2021

**Accepted:** 06 April 2021

**Published:** 17 May 2021

### Citation:

Zhang H, Liu C, Zhang Z, Xing Y,  
Liu X, Dong R, He Y, Xia L and  
Liu F (2021) Recurrence Plot-Based  
Approach for Cardiac Arrhythmia  
Classification Using  
Inception-ResNet-v2.  
Front. Physiol. 12:648950.  
doi: 10.3389/fphys.2021.648950

The present study addresses the cardiac arrhythmia (CA) classification problem using the deep learning (DL)-based method for electrocardiography (ECG) data analysis. Recently, various DL techniques have been utilized to classify arrhythmias, with one typical approach to developing a one-dimensional (1D) convolutional neural network (CNN) model to handle the ECG signals in the time domain. Although the CA classification in the time domain is very prevalent, current methods' performances are still not robust or satisfactory. This study aims to develop a solution for CA classification in two dimensions by introducing the recurrence plot (RP) combined with an Inception-ResNet-v2 network. The proposed method for nine types of CA classification was tested on the 1st China Physiological Signal Challenge 2018 dataset. During implementation, the optimal leads (lead II and lead aVR) were selected, and then 1D ECG segments were transformed into 2D texture images by the RP approach. These RP-based images as input signals were passed into the Inception-ResNet-v2 for CA classification. In the CPSC, Georgia, and the PTB\_XL ECG databases of the PhysioNet/Computing in Cardiology Challenge 2020, the RP-based method achieved an average F1-score of 0.8521, 0.8529, and 0.8862, respectively. The results suggested the excellent generalization ability of the proposed method. To further assess the performance of the proposed method, we compared the 2D RP-image-based solution with the published 1D ECG-based works on the same dataset. Also, it was compared with two traditional ECG transform into 2D image methods, including the time waveform of the ECG recordings and time-frequency images based on continuous wavelet transform (CWT). The proposed method achieved the highest average F1-score of 0.844, with only two leads of the 12-lead ECG original data, which outperformed other works. Therefore, the promising results indicate that the 2D RP-based method has a high clinical potential for CA classification using fewer lead ECG signals.

**Keywords:** cardiac arrhythmia classification, ECG, recurrence plot, Inception-ResNet-v2, deep learning

## INTRODUCTION

Cardiac arrhythmia (CA) is a common cardiovascular disease, and it includes various arrhythmias, such as atrial fibrillation (AF), atrioventricular block, premature atrial contraction (PAC), premature ventricular contraction (PVC), and so on. As a life-threatening risk, the CA affects more than 4.3 million people only in America at a total direct annual healthcare cost of up to \$US 67.4 billion, which is a heavy economic burden to society (Tang et al., 2014). Many arrhythmias manifest as sequences of the wave with unusual timing or morphology in electrocardiography (ECG) (De Chazal et al., 2004), and analysis of the inherent features of ECG is the most common technique for diagnosis and classification of CA.

Recently, various machine learning methods have been developed for ECG arrhythmia classification. Using the MIT-BIH arrhythmia database, a mixture-of-experts classifier structure was formed to improve the performance of ECG beat classification, which was based on three popular artificial neural networks. The self-organizing maps and the learning vector quantization algorithms were used to train the classifier, and the mixture-of-experts method was used to classify the ECG beat (Hu et al., 1997).

Based on RR-interval features, heartbeat interval features and ECG morphology features, a linear discriminants framework was proposed to allow the classification and diagnosis of CA into five groups: normal, ventricular ectopic beat (VEB), supraventricular ectopic beat (SVEB), the fusion of normal and VEBs, and unknown types (De Chazal et al., 2004). Using RR interval features and a hierarchical heartbeat classification system, another work detected the VEB based on random projection and support vector machine (SVM) ensemble and then analyzed the SVEB with a positive predictive value of 42.2% (Huang et al., 2014). For the CA prediction by traditional machine learning approaches, a set of handcrafted features was extracted from the ECG dataset and then followed by classifiers, including SVM (Ye et al., 2012), artificial neural network (Ince et al., 2009), linear discriminant framework (de Chazal and Reilly, 2006), etc. However, it requires more specific expertise in ECG, thus generally challenging to further improve the performance in complex CA classification.

Due to the improvement of computing power and the availability of a large number of datasets, deep neural networks have recently been used to perform automatic feature extraction and end-to-end classification of CA. One-dimensional (1D) deep convolutional neural networks (CNNs) have become the mainstream means to address these tasks. A 34-layer 1D CNN was applied to 1D ECG rhythm classification with a dataset recorded with a single-lead wearable monitor, which achieved an optimal performance exceeding cardiologists' performance (Rajpurkar et al., 2017). A 1D CNN was developed in another work to classify 12 rhythm classes with 91,232 single-lead ECG records. The results demonstrated that the end-to-end deep learning (DL)-based method could achieve the same performance as a cardiologist (Hannun et al., 2019). A method was proposed to classify heart diseases using a 1D CNN based on a modified ECG signal in MIT-BIH, St. Petersburg, and PTB dataset (Hasan

and Bhattacharjee, 2019). A 31-layer 1D residual CNN (ResNet) was applied to achieve an optimal accuracy in the classification of five different CA based on two-lead ECG signals (Li et al., 2020). Moreover, recurrent neural networks (RNNs) have a memory that captures information about data history and can model data of arbitrary lengths that were widely used for modeling sequential data. Xiong et al. (2018) proposed a neural network named RhythmNet, which combines the strengths of both 1D CNNs and RNNs to classify four different CAs based on the 2017 PhysioNet/Computing in the Cardiology Challenge dataset. They evaluated the algorithm on 3,658 testing data and obtained an F1 accuracy of 0.82. Long-term and short-term memory (LSTM) is one of the RNN and is widely used in time-series signal analysis, such as classification of ECG signals and speech recognition, and so on. An approach that combined 1D CNN and LSTM was developed to automatically classify six types of ECG signals from the MIT-BIH arrhythmia database (Chen et al., 2019). Besides, three works based on the 1st China Physiological Signal Challenge dataset, using 1D CNN, were combined with LSTM to classify the CA. He et al. (2019) developed a model constitutive of 1D CNN and LSTM to learn local features and global features from raw 12-lead ECG signals to realize the classification and achieved the overall F1-score 0.799. Yao et al. (2019) proposed an attention-based time-incremental CNN, using 1D CNN, LSTM, and attention module to extract both spatial and temporal fusion of information from the raw 12-lead ECG data, which reached an overall classification F1-score of 0.812. Chen et al. (2020) applied a neural network that combined 1D CNN, bidirectional RNN, and attention modules to achieve a median overall F1-score of 0.797 for nine types of CA classification based on 12-lead ECG.

In parallel to the development of DL methods for CA classification based on 1D ECG signals, alternative methods have been proposed to transform the time-series signals into 2D matrices that can be handled by those CNN networks dedicated to processing 2D or multi-dimensional signals in the fields of image processing and computer vision. An automatic algorithm was proposed to detect AF, for which the 1D ECG signals have been converted to 2D time-frequency representations and then processed by the network of 2D CNN and Densenet. The method led to an F1 of 0.82 (Parvaneh et al., 2018). In another work, a signal quality index algorithm along with dense CNNs was developed to distinguish AF based on the dataset of 2017 PhysioNet/CinC Challenge by time-frequency representations of one-lead ECG recordings which achieved an overall F1-score of 0.82 (Rubin et al., 2018). Zhao et al. (2019) proposed a method that combined the modified frequency slice wavelet transform (MFSWT) and CNN to PVC recognition. Using this method, the PVC and non-PVC ECG recordings were modeled to a set of time-frequency images, which were then fed into the CNN as the input signals to process the prediction. It achieved a high accuracy of 97.89% for the PVC recognition. Besides, using 2D grayscale images of each ECG recording as input signals, some studies developed 2D CNN to CA classification based on the MIT-BIH database (Jun et al., 2018; Izci et al., 2019).

As described above, various temporal, morphology, and time-frequency features of ECG data have been considered to study the CA classification. However, for specific complex CA

classification, these methods may still offer non-robust and unsatisfactory results, and new techniques are thus required for providing better solutions for clinical use. In this work, a 2D DL-based CA classification method using the recurrence plot (RP) technique (Eckmann et al., 1987) was developed. The RP graphically shows hidden patterns and structural changes in time signals or similarities in patterns across the time series. It has been applied to various applications, including Parkinson's disease identification (Afonso et al., 2018), heart rate variability evaluation (Marwan et al., 2002; Schlenker et al., 2015), paroxysmal AF prediction (Mohebbi and Ghassemian, 2011), and AF and VF and PAC and PVC prediction (Mathunjwa et al., 2021). Different from other time-series representations, RP may provide a visual mechanism for pattern identification, being suitable for combining with state-of-the-art DL approaches. In this work, whether the RP-based DL framework is appropriate for CA classification was studied.

The contributions of this work include the following: (i) this is a prospective study of using RP for modeling ECG signals with 2D texture images that are processed for DL-based CA classification; (ii) the optimal leads (lead II and lead aVR) were selected as an input signal to classify nine classes of CA, implemented with the 1st China Physiological Signal Challenge 2018 open database, and achieved performance with the average F1-score 0.844; (iii) the Inception-ResNet-v2 network was introduced to extract the characteristics of patterns and structural changes from the 2D RP-based images.

The rest of the paper is organized as follows: the approach and the network architecture are described in section "Methodology," the experiments are detailed in section "Experiment," and the conclusions are drawn in section "Conclusion."

## METHODOLOGY

In this work, the classification of the CA problem is modeled as a 2D image classification task using RP-based texture images and the Inception-ResNet-v2 architecture.

### Recurrence Plot

The time series such as ECG signals have typical recurrent behaviors, including periodicities and irregular cyclicities (Debayle et al., 2017), which may be difficult to visualize in the time domain. An RP was proposed to explore the m-dimensional phase space trajectory and to visualize the recurrent behaviors of the time series (Eckmann et al., 1987, 1995).

An RP can be formulated as:

$$R_{i,j} = \theta(\epsilon - \|x_i - x_j\|), \quad i, j = 1, \dots, N \quad (1)$$

where  $N$  is the number of considered states (dots at the time series)  $x_i$ ,  $\epsilon$  is a threshold distance,  $\|\cdot\|$  is a norm (e.g., Euclidean norm), and  $\theta(\cdot)$  is the Heaviside function.

$\theta(\cdot)$  is defined as:

$$\theta(Z) = \begin{cases} 0, & \text{if } z < 0 \\ 1, & \text{otherwise} \end{cases} \quad (2)$$

The original formulation Equation (1) is considered binary caused by  $\epsilon$  the threshold distance. In this paper, an unthresholded approach proposed by Faria et al. (2016) was adopted to avoid information loss by binarization of the R-matrix, with the Euclidean norm, to obtain an RGB image and to make use of the color information in RP images.

The R-matrix can be defined as:

$$R_{i,j} = \|x_i - x_j\|, \quad i, j = 1, \dots, N \quad (3)$$

In the present study, the 1D ECG signals have been converted to 2D RP images as the input signals and then fed into the 2D network for classification.

## Network Architecture

The Inception-ResNet-v2 (Szegedy et al., 2016) was used for the CA classification task. The architecture of the network is shown in **Figure 1**. It contains three parts: the stem is the deep convolutional layers and used to pre-process the original data before entering the Inception-ResNet blocks, including nine layers of convolutional and two max-pooling layers. The second part was detailed in **Figure 2**. **Figure 2A** showed the Inception-ResNet-A with two  $3 \times 3$  kernels in the inception module. The Inception-ResNet-B is detailed in **Figure 2C** with the asymmetric filter combination of one  $1 \times 7$  filter and one  $7 \times 1$  filter in the inception module. The Inception-ResNet-C can be seen in **Figure 2E** with a small and asymmetric filter combination of one  $1 \times 3$  filter and one  $3 \times 1$  filter;  $1 \times 1$  convolutions were used before the larger filters in these blocks. The network enhances the diversity of the filter patterns by asymmetric convolution splitting. The reduction of A and B in **Figures 2B,D** was made to increase the dimension, which needs to compensate for the dimensionality reduction caused by the Inception block. The last part is the prediction layer, including pooling and softmax layers.

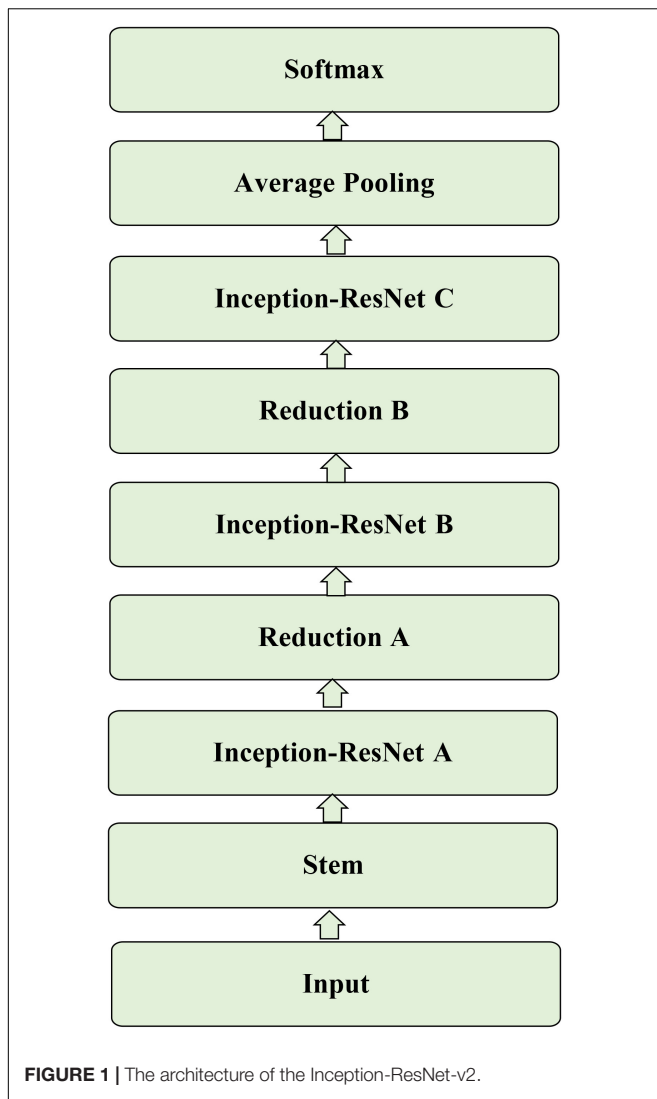
## EXPERIMENT

### ECG Database

The 1st China Physiological Signal Challenge 2018 dataset was used in this study (Liu et al., 2018). The dataset contains 6,877 12-lead ECG recordings lasting from 6 to 60 s for free download, which was labeled the most CA types according to normal sinus rhythm and eight types of arrhythmia: AF, First-degree atrioventricular block (I-AVB), Left bundle branch block (LBBB), Right bundle branch block (RBBB), PAC, PVC, ST-segment depression (STD), and ST-segment elevation (STE). These recordings were collected from 11 Chinese hospitals and sampled at 500 Hz. The dataset details are summarized in **Table 1**.

### Data Splitting and Augmentation

The investigated ECG dataset has two problems. Firstly, the range of each recording length varies from 6 to 60 s. It is not convenient for training the model with non-identical lengths of the ECG recordings. We down-sampled the raw ECG signals to 200 Hz, and then the ECG recordings were segmented into a span of 5 s. Secondly, as demonstrated in **Table 1**, the dataset is unbalanced,



which brings challenges to the classification of arrhythmias. To make it balanced, based on the number of RBBB, the other eight types of data were augmented. For instance, if the duration of the Normal, AF, and STD ECG recordings is over 10 s, the recording

were segmented into two 5 s long patches. In this way, 1,836 5 s segments of Normal, 2,195 segments of AF, and 1,651 segments of STD were obtained. For I-AVB, PAC, and PVC recordings, if the duration of the data is over 15 s, it was then divided into three segments of 5 s-long strips. In this way, there were 1,602 5 s segments of I-AVB, 1,411 segments of PAC, and 1,642 segments of PVC. For LBBB and STE recordings, the data were split into a set of 5 s segments up to eight in turn, which was repeated three times with different start points, the first time started from the first data, the 201st data for the second time, and the 401st data for the third time, respectively. Thus, 1,677 segments of LBBB and 1,896 of STE were obtained.

### Mapping ECG Signals Into Texture Images

Each data was represented by a set of 5 s ECG strips and further mapped into images through the RP operation. Then, the RP-based images were normalized to the (0–1) range. The CA classification problem was modeled as an image classification task based on RP-based images and CNN. Using a 5 s ECG signal ( $x$ ) with 1,000 data points, the 2D phase space trajectory is constructed from  $x$  by the time delay of one point. States in the phase space are shown with bold dots:  $s_1 (x_1, x_2)$ ,  $s_2 (x_2, x_3)$ , ...,  $s_{999} (x_{999}, x_{1000})$  (Debayle et al., 2017). The RP  $R$  is a  $999 \times 999$  square matrix with  $R_{i,j} = \text{dist}(s_i, s_j)$ . In **Figures 3–5**, taking each class signal in the Lead II for instance, the time waveform of ECG recordings with nine types of the classes and corresponding RP-based images were shown. In the RP, different colors can be observed, which are associated with the distance values between plots on the ECG signals. The lowest distance values are coded with a blue color, and the highest distance values are coded with a red color. Moreover, the RP contains textures that are single dots, lines including diagonal, vertical, and horizontal lines, and typography information, including those characterized as homogeneous, periodic, drift, and disrupted. Obviously, there are patterns and information in RP that are not always very easy to see in the time series visually.

### Classification

As the flow chart shown in **Figure 6**, using the RP method, a 2D representation of an ECG time-series signal was obtained and then the  $999 \times 999$  RP-based texture images of 5 s ECG strips

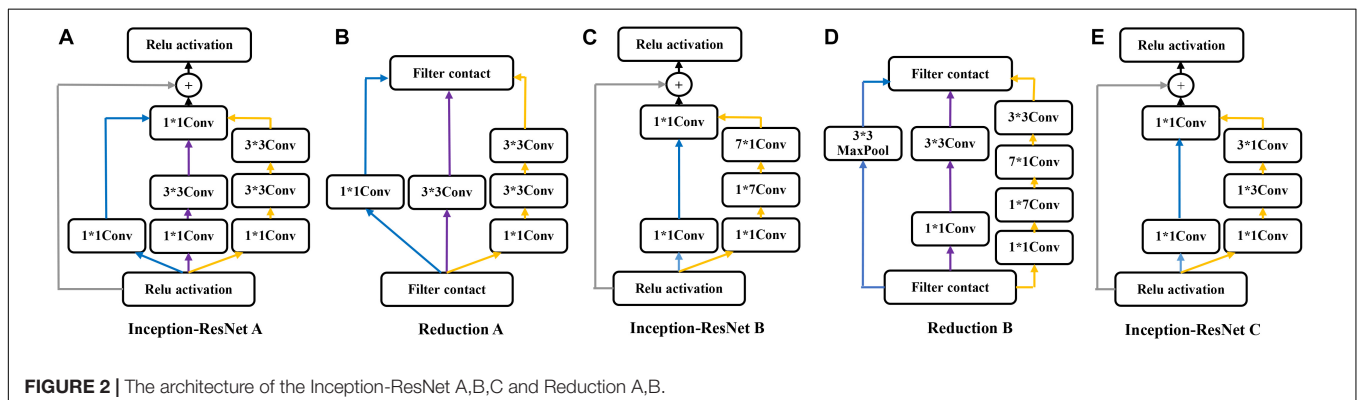




**TABLE 1** | Data profile for the ECG dataset.

Type	Recording	Time length (s)				
		Mean	SD	Min	Median	Max
Normal	918	15.43	7.61	10.00	13.00	60.00
AF	1,098	15.01	8.39	9.00	11.00	60.00
I-AVB	704	14.32	7.21	10.00	11.27	60.00
LBBB	207	14.92	8.09	9.00	12.00	60.00
RBBB	1,695	14.42	7.60	10.00	11.19	60.00
PAC	574	19.46	12.36	9.00	14.00	60.00
PVC	653	20.21	12.85	6.00	15.00	60.00
STD	826	15.13	6.82	8.00	12.78	60.00
STE	202	17.15	10.72	10.00	11.89	60.00
Total	6,877	15.79	9.04	6.00	12.00	60.00

were resized to  $299 \times 299 \times 3$  and fed into the Inceptive-ResNet-v2 model as input signals. A transfer learning approach was introduced on the generalizability of pre-trained models (Wang et al., 2019). The entire model was trained using Adam optimizer

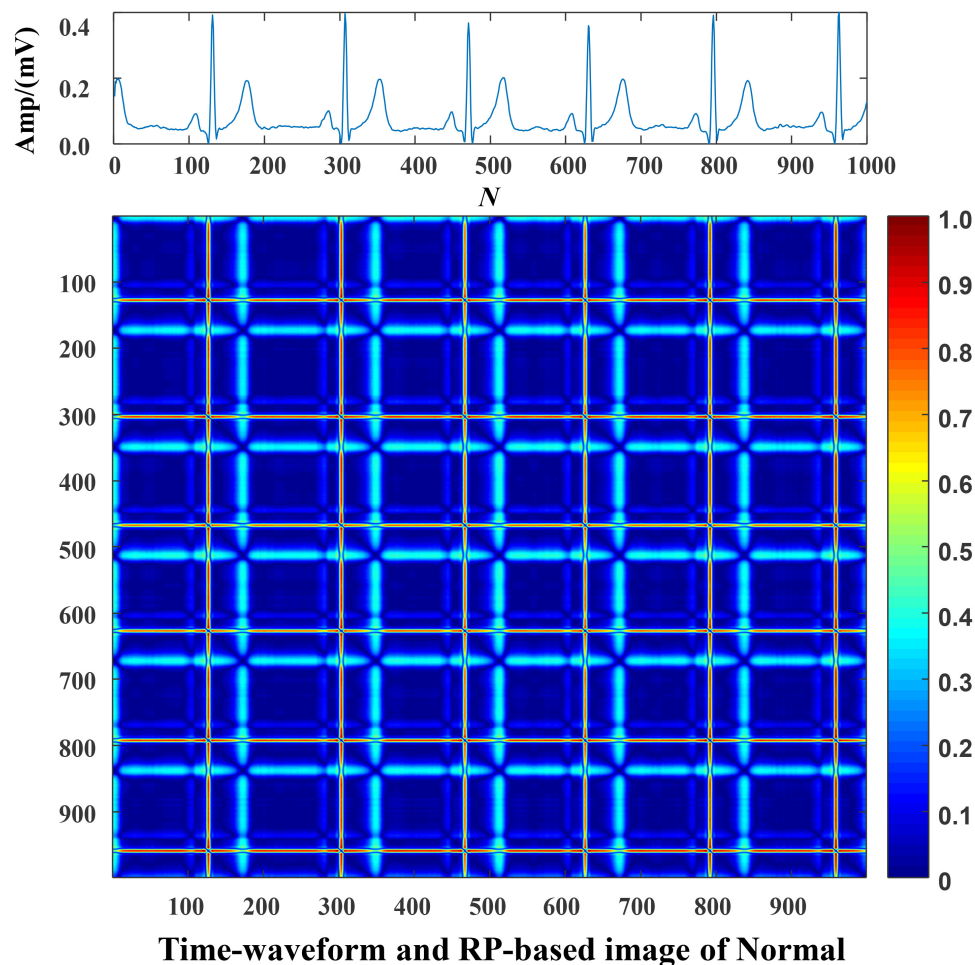
with default parameters, a learning rate of 0.001, and a batch size of 128. Cross entropy loss was calculated for the batched output and corresponding label, and the average gradient was backpropagated to all the weight in the previously mentioned layers. In the process, the training datasets were fed into the network in batches to train models. Then, the model producing the best performance on the validation dataset was selected for further classification on the test dataset. Since the fivefold cross-validation was applied, this process was repeated.

### Computing Environment

The experiments were performed on Wiener nodes of the University of Queensland computer cluster with 4\* Nvidia Volta V100 SXM2 connected GPU's per node. Each node contains 5,120 CUDA cores, 640 Tensorflow hardware cores, 32 GB of HBM2 class memory. This model was implemented using the Tensorflow 3.6 and Karas DL framework.

### Performance of Experiments

To assess whether the proposed method leads to benefits for the CA task, precision, recall, and F1-score were used to evaluate

**FIGURE 3** | The Normal ECG time waveform and its corresponding RP-based image.

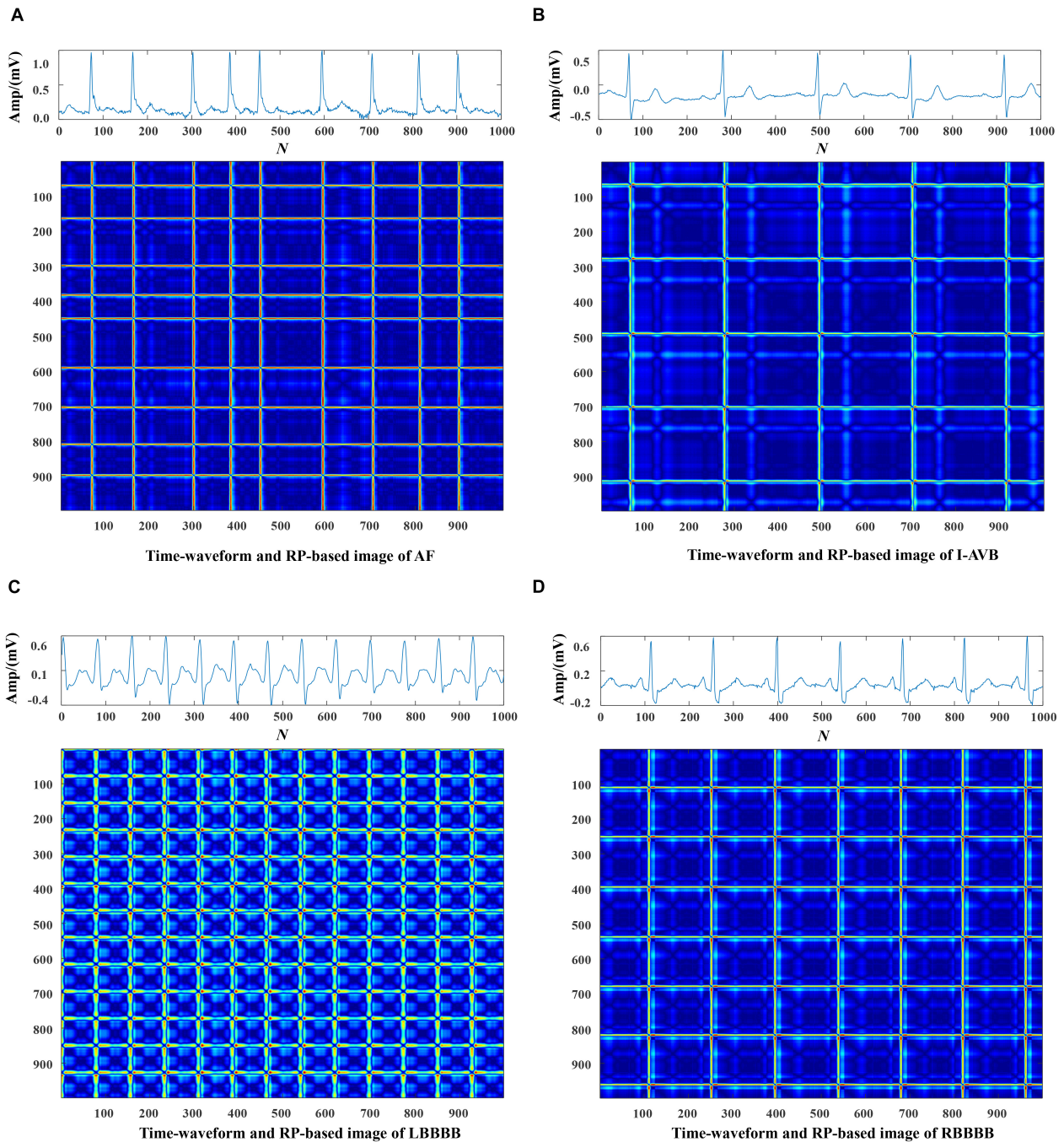


**FIGURE 4 |** The ECG time waveforms and their corresponding RP-based images of AF, I-AVB, LBBB and RBBB.

the performance of Inception-ResNet-v2 in typical classification metrics for each class. They were defined as:

$$Precision = \frac{TP}{TP + FP} \quad (4)$$

$$Recall = \frac{TP}{TP + FN} \quad (5)$$

$$F1 = \frac{2(Precision * Recall)}{Precision + Recall} \quad (6)$$

Here,  $TP$  is the number of data that are correctly classified to a specific class.  $FP$  is the number of data that are classified to a specific class, but they belonged to other classes.  $FN$  is the number of data that are misclassified to other classes, but they belonged to

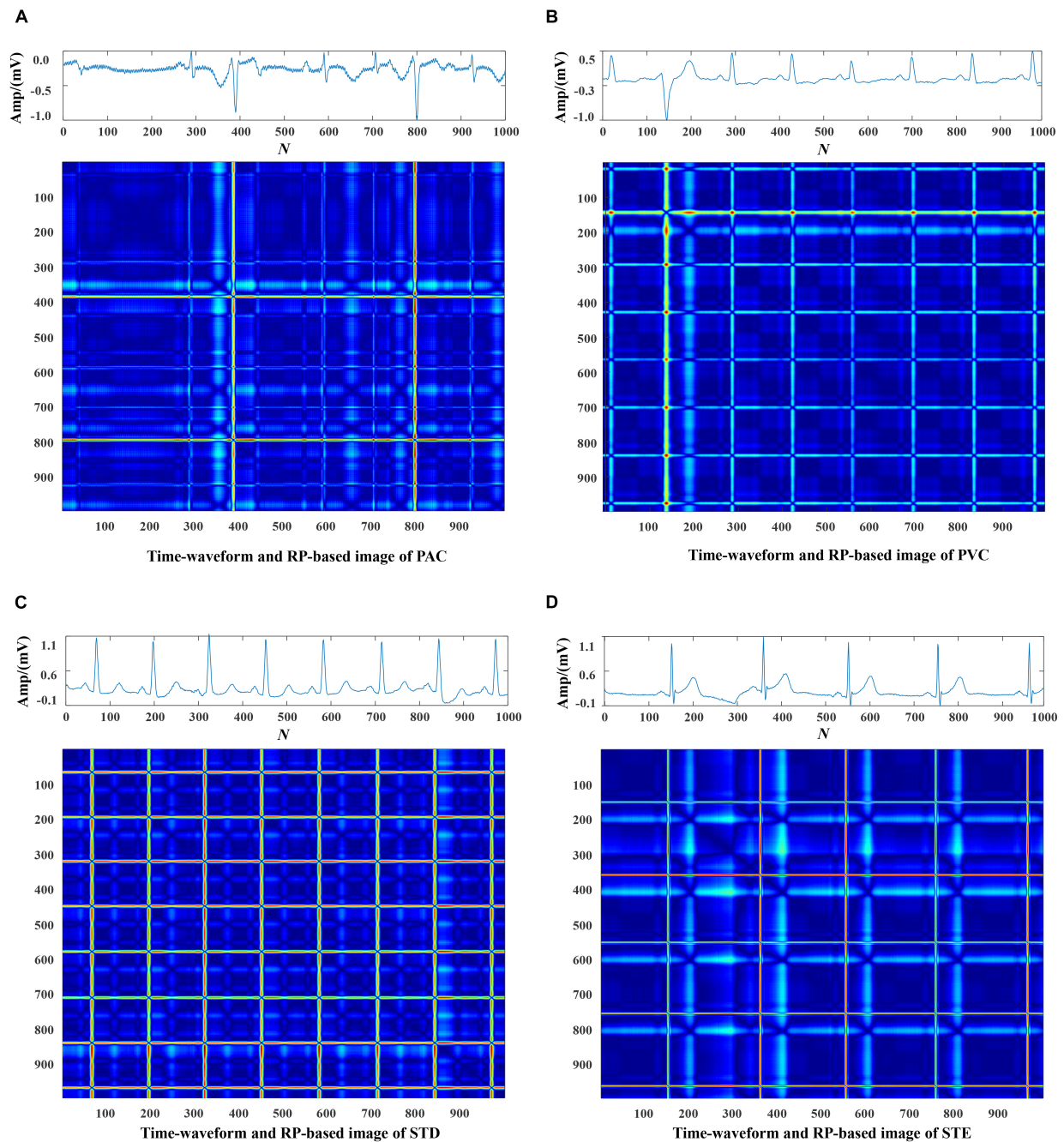


**FIGURE 5 |** The ECG time waveforms and their corresponding RP-based images of PAC, PVC, STD and STE.

a specific class. The average F1-score among classes is computed to evaluate the final performance of the model.

To introduce the RP-based Inception ResNet-v2 method for addressing the CA classification task, this section describes how to find the optimal leads of ECG as the input signal. At first, the full 12-lead RP-based ECG images were fed into the network and obtained an overall average F1-score of 0.7066. In the second step, we did the CA classification based on each single-lead RP-based images as the input signal. The results indicated that lead

II was one of the best-performing single leads, followed by the lead V4 and aVR, with the performance ranking first, second, and third in the overall nine types of classification average F1-score of 0.7337, 0.7319, and 0.7313. In the third step, using the above three leads signals, we made different random combinations as the input signals for CA classification. The optimal performance (average F1-score of 0.844) was achieved on the combination of Lead II and lead aVR. These two lead data were divided into several 5 s ECG data segments and then converted into a



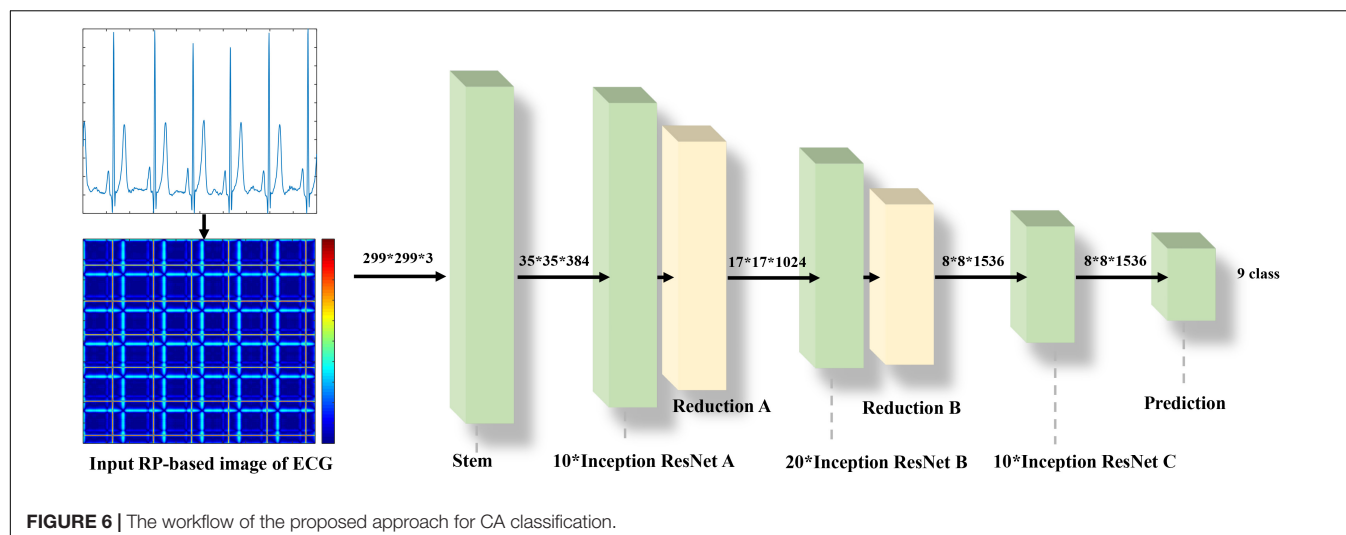


**TABLE 2 |** Classification performance of Inception-ResNet-v2 based on RP images.

CA Type	Precision	Recall	F1-score
Normal	0.797	0.827	0.812
AF	0.852	0.898	0.875
I-AVB	0.916	0.930	0.923
LBBB	0.933	0.924	0.929
RBBB	0.777	0.776	0.776
PAC	0.774	0.733	0.753
PVC	0.865	0.731	0.793
STD	0.808	0.867	0.837
STE	0.899	0.901	0.900
Avg/total	0.847	0.847	0.844

2D RP-based image separately. All these images formed into an image dataset as input signals to do the CA classification. To maintain class prevalence between data splits, 20% data of each class were randomly selected as the test set for assessing algorithm performance independently, and 80% data of each type were the training and validation sets. Then, a fivefold stratified split was applied to the training and validation sets. Data four in five were adopted to create a training set, and the other one split as the validation set.

In this section, the results concerning the Inception-ResNet-v2 with the RP-based images of Lead II and lead aVR as input data are detailed in **Table 2**. The proposed method achieved an overall F1-score of 0.844 from the fivefold cross-validation experiments. The average precision is 0.847, and the average recall is 0.847 for the nine classifications of the CA using only two leads of the recordings. Besides, the highest prediction accuracy F1-score in nine classes was obtained at LBBB (0.929) followed by I-AVB (0.923), while prediction for PAC has the lowest F1-score (0.753). In **Figure 7**, the confusion matrix of the proposed method was drawn. It outlined the data of predictions for each class. There is a relatively small error between Normal rhythm and AF, I-AVB, and LBBB, which

implies that the Inception-ResNet-v2 was effective in predicting AF, I-AVB, and LBBB based on the RP texture images, while the method had difficulties in distinguishing PAC rhythms from other rhythms.

### Comparison With Reference Models

To explore the reliability and effectiveness of the proposed method, we implemented seven state-of-the-art models, including Xception (Chollet, 2017), Resnet 50 (He et al., 2016), Resnext (Saining Xie et al., 2017), Densenet (Gao et al., 2017), Inception-ResNet-v1, Inception-v3, and Inception-v4 (Szegedy et al., 2016) as reference. The data augmentation and regularization strategies of training and testing sets are provided separately to ensure that the results of different algorithms are comparable. The same hyperparameters, including learning rate and batch size, were used for the proposed and all reference models. For comparison, the average F1-score of each class was calculated for each architecture. The results of each model can be found in **Table 3**.

The comparison highlights that for CA based on RP texture images, the Inception-ResNet-v2 achieved an average F1-score of 0.844, which was higher than other classification frameworks. It was shown that the Inception-ResNet-v2 outperformed Xception, Resnet50, Resnext, Inception V3, and Inception V4 in the F1-score of all classes and almost outperformed Densenet in all classes except for one LBBB class where two models performed comparably (F1-score 0.92). Moreover, the Inception-ResNet-v1 achieved an average F1-score of 0.81, with the optimal performance of the prediction on LBBB and STE class. In identifying the LBBB class, almost all the models achieved significantly higher F1-scores compared with other classes. However, all the models had the lowest F1-score in the prediction of the PAC class.

### Comparison of RP-Based With Other Image-Based Methods for CA Classification

In this work, for CA classification, we also compared the RP method with two other traditional methods that transform the

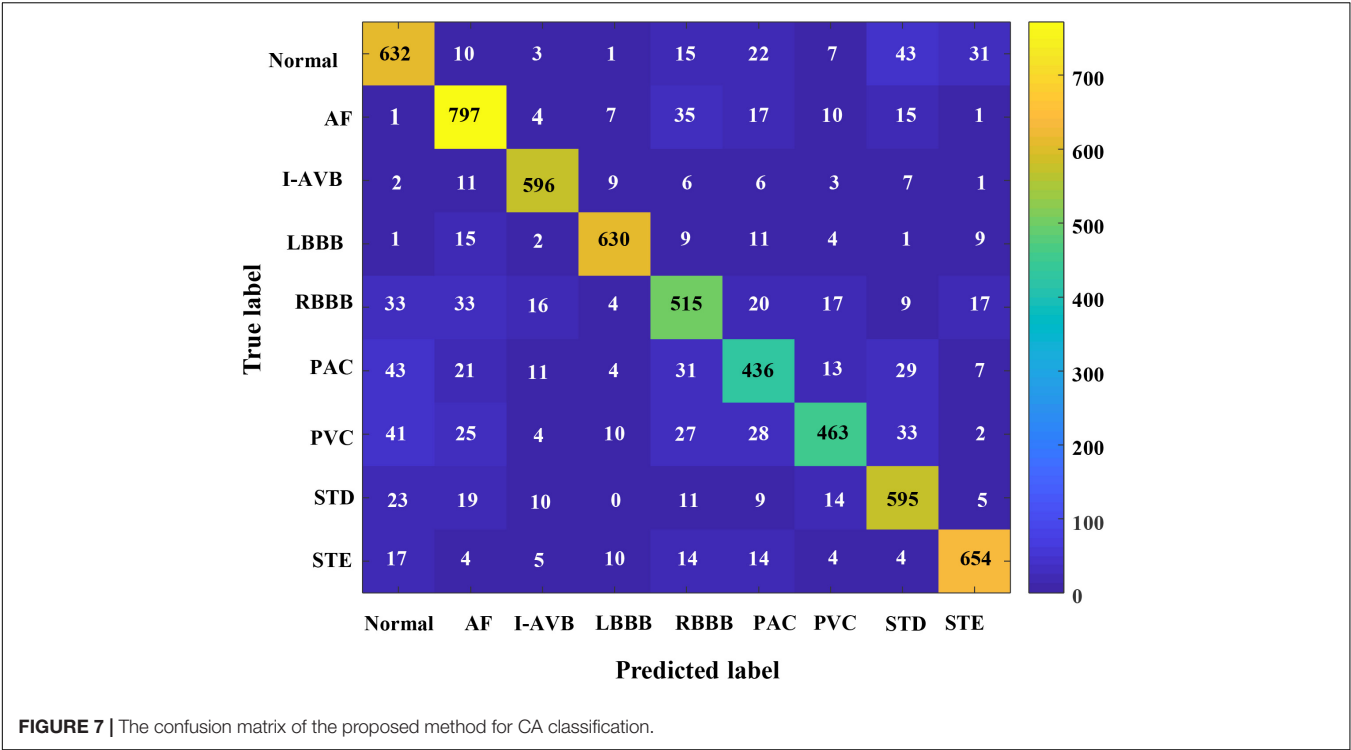


TABLE 3 | Classification performance of different reference models.

Type	F1-score							
	Xception	Resnet 50	Densenet	Resnext	Inception-ResNet-v1	Inception-v3	Inception-v4	Inception-ResNet-v2
Normal	0.77	0.76	0.75	0.75	0.78	0.72	0.73	0.812
AF	0.85	0.85	0.85	0.88	0.86	0.86	0.85	0.875
I-AVB	0.88	0.88	0.87	0.88	0.89	0.87	0.87	0.923
LBBB	0.89	0.90	0.92	0.91	0.93	0.91	0.91	0.929
RBBB	0.70	0.72	0.70	0.72	0.72	0.71	0.71	0.776
PAC	0.67	0.65	0.64	0.68	0.64	0.60	0.58	0.753
PVC	0.72	0.72	0.71	0.74	0.76	0.68	0.65	0.793
STD	0.79	0.79	0.76	0.79	0.79	0.77	0.75	0.837
STE	0.85	0.83	0.86	0.85	0.90	0.87	0.86	0.900
Avg/total	0.80	0.79	0.79	0.80	0.81	0.78	0.77	0.844

ECG signal to 2D images, including the Wavelet time-frequency images and the time waveform. In this section, the continuous wavelet transform (CWT) method (He et al., 2018) was used to transform the ECG time-domain signals, each of which has a duration of 5 s (1,000 sample points given the sampling rate of 200 Hz), into time-frequency domain signals with six continuous wavelet functions including Complex Gaussian wavelets (cgau8), Complex Morlet wavelet (cmor), Frequency B-Spline wavelets (fbps), Gaussian wavelets (gau8), Mexican hat wavelet (mexh), and Morlet wavelet, resulting in the 2D time-frequency representation of the segmented ECG recordings. The proposed Inception-ResNet-v2 was properly trained to process the CA classification. For the time waveform, the segmented 5 s ECG recordings of each class were plotted, and then the waveforms of the time series were used as input sets. These

two kinds of 2D images and the RP-based 2D images were fed into the Inception-ResNet-v2 network to process the ECG classification, respectively.

It is observed that the proposed RP method obtained the best average F1-score (0.844) far over the performance of the time waveform (0.70) and that of the Wavelet time-frequency input signals (below 0.70), as shown in **Table 4**. In identifying the LBBB class, the model achieved the highest F1-scores compared with other classes in the time waveform database and the RP-based images, while the cgau8 and fbps achieved the highest F1-score of 0.82 and 0.81 at the I-AVB class, respectively. Moreover, in the prediction of the PAC class, these three databases all obtained a poor F1-score. Additionally, the model based on the Wavelet time-frequency images performed poorly than the other two kinds of input signals.



## Comparison of the Proposed Method With Other Published Works for CA Classification Based on the 1st China Physiological Signal Challenge 2018 Dataset

In this part, we compared the proposed 2D RP-based method with 1D ECG-based works in literature based on the same public dataset (1st China Physiological Signal Challenge 2018 dataset). **Table 5** presents the F1-score on each type of CA and the average F1-score of the nine classes based on the different methods. It contains two parts, including the top three ranks in the challenge and comparison of the proposed method with methods reported. He et al. (2019) ranked first place and achieved an average F1-score for nine classes of 0.799 based on the publicly released dataset. Chen et al. (2020) ranked third place and obtained an F1-score of 0.797. Yao et al. (2019) achieved an average F1-score of 0.812. The results suggested that our proposed RP-based method reached the average nine-class F1-score of 0.844 (excellent performance), which outperformed others. Besides, on the classification of I-AVB, LBBB, STD, and STE, the proposed method achieved a better F1-score than other works. **Table 6** presents detailed information, including the input signal, ECG leads, performance, and networks used by the different approaches mentioned above. **Table 6** suggested the superiority of the proposed 2D RP approaches: the proposed method introduced the RP-based 2D images as input signals, while others all used the 1D ECG time series; in this study, we used few leads (only two of the 12-lead original ECG data); the proposed method achieved the highest average F1-score of 0.844, although with more trainable parameters than other 1D models.

## Testing the Generalization Ability of the Proposed Method Using Some Other Databases

In this section, three datasets of the PhysioNet/Computing in Cardiology Challenge 2020 (Perez Alday et al., 2021) were adopted to evaluate the generalization of the proposed method, as listed in **Table 7**.

CPSC (Liu et al., 2018). The data source is the public training dataset from the China Physiological Signal Challenge (De Chazal et al., 2004).

PTB\_XL (Wagner et al., 2020). The source is the Physikalisch Technische Bundesanstalt (PTB), Brunswick, Germany, a large, publicly available ECG dataset.

Georgia. Georgia is a 12-lead ECG Challenge Database (Emory University, Atlanta, GA, United States) representing a large population from the Southeastern United States.

The sampling rate of the signal is 500 Hz. In this experiment, the PTB\_XL includes five classes (Normal, AF, I-AVB, LBBB, and PAC), and the CPSC and Georgia contain six types (Normal, AF, I-AVB, LBBB, RBBB, and PAC). The lead II and lead aVR of each ECG data in these datasets were used as the input signal for CA classification.

Each signal was resampled at 200 Hz and then segmented into two 5 s long patches and mapped into RP-based 2D images with a normalized range (0–1). These 2D images were input signals of the network for classification. The results suggested that the proposed method achieved an average F1-score of 0.8521 on CPSC, 0.8529 on Georgia, and 0.8862 on

PTB\_XL in **Table 8**. Moreover, the performance of the proposed method on the PTB\_XL is the best, and the high prediction F1-scores were obtained at Normal (0.9417) and LBBB (0.9246); in contrast, prediction for PAC has the lowest *F*-score (0.7832). For Georgia, the proposed method can effectively classify the AF, I-AVB, LBBB, and PAC. These results highlighted that the proposed method had excellent CA classification performance and generalization ability.

## Discussion

This work intends to study whether the RP method is appropriate for the DL-based CA classification. To represent features that are not easy to be observed in the time domain, we transformed the ECG signals into 2D RP-texture images for the CNN-based CA classification. In the experiments, the results showed that different CNN models effectively learned the information based on the RP input images in the training process. Moreover, the Inception-ResNet-v2 network achieved the optimal performance with an average F1-score of 0.844, followed by the Inception-ResNet-v1 network of 0.81. It is explained that the Inception-ResNet module contains multiple filters of various sizes, capturing the RP image spatial features in different scales. Besides, larger filters may be more effective due to the increased perceptive field being able to more effectively account for the variations of the signal over time.

To analyze whether the RP-based method performs better in the CA classification than other methods, we compared the time-waveform and Wavelet time-frequency images with RP-based images as input signals, respectively. The results showed that the RP-based model achieved an optimal average F1-score of 0.844, which is better than the time-waveform and Wavelet time-frequency images. Moreover, we compared the 2D RP-based method with the published 1D ECG-based works based on the same publicly dataset (the 1st China Physiological Signal Challenge 2018 dataset). The results indicated that the proposed 2D RP-based approach outperforms 1D signal-based models in the CA classification even with only two of 12 leads. The RP method could visualize certain aspects of the 2D phase space trajectory, extracting inherent texture features between different points of an ECG recording (Ouyang et al., 2008, 2014). It highlights that the RP-based method has a high potential to improve the CA classification accuracy with the CNN framework.

Three ECG datasets of the PhysioNet/Computing in Cardiology Challenge 2020 were adopted to study the generalization ability of the proposed method. The proposed method achieved an average F1-score of 0.8529 on Georgia, 0.8521 on CPSC, and 0.8862 on PTB\_XL. The results showed that the 2D RP-based CA classification method has excellent generalization ability.

The other contribution of our work is to find the optimal ECG leads of the nine types of CA classification. Excellent classification results were obtained with lead II and lead aVR. We found that the network could successfully process the CA classification without access to the full 12 leads data. It is known that, among the 12 leads, lead II offers physician-favored signal, and lead aVR may reflect atrial and ventricular

**TABLE 4 |** Classification performance of different 2D images-based input data.

Type	F1-score						Time waveform	RP-based images
	Wavelet time-frequency images							
	Cgau8	Cmor	Fbsp	Gaus8	Mexh	Morl		
Normal	0.56	0.56	0.57	0.57	0.61	0.56	0.61	0.812
AF	0.76	0.77	0.75	0.81	0.75	0.77	0.80	0.875
I-AVB	0.82	0.80	0.81	0.77	0.80	0.78	0.81	0.923
LBBB	0.71	0.74	0.71	0.68	0.67	0.72	0.87	0.929
RBBB	0.56	0.53	0.57	0.54	0.54	0.53	0.60	0.776
PAC	0.49	0.39	0.43	0.40	0.43	0.44	0.52	0.753
PVC	0.58	0.56	0.56	0.55	0.56	0.52	0.58	0.793
STD	0.60	0.63	0.62	0.64	0.61	0.61	0.62	0.837
STE	0.53	0.41	0.51	0.44	0.47	0.56	0.81	0.900
Avg/total	0.63	0.61	0.62	0.62	0.62	0.61	0.70	0.844

**TABLE 5 |** The performance of the published 1D ECG-based works and the proposed method.

Rank	Team	Normal	AF	I-AVB	LBBB	RBBB	PAC	PVC	STD	STE	Avg/total
<b>The hidden test set of the 1st China Physiological Signal Challenge 2018 F1-score</b>											
1	He et al.	0.748	0.920	0.882	0.889	0.883	0.787	0.851	0.780	0.780	0.836
2	Cai et al.	0.765	0.927	0.887	0.886	0.880	0.812	0.800	0.784	0.753	0.833
3	Chen et al.	0.752	0.930	0.871	0.915	0.839	0.832	0.833	0.800	0.667	0.823
<b>The publicly released dataset of the 1st China Physiological Signal Challenge 2018 F1-score</b>											
	Yao et al.	0.789	0.920	0.850	0.872	0.933	0.736	0.861	0.789	0.556	0.812
	He et al.	0.755	0.846	0.870	0.869	0.780	0.751	0.829	0.790	0.704	0.799
	Chen et al.	0.795	0.897	0.865	0.821	0.911	0.734	0.852	0.788	0.509	0.797
	RP-based	0.812	0.875	0.923	0.929	0.776	0.753	0.793	0.837	0.900	0.844

**TABLE 6 |** Comparison of the published 1D ECG-based works with the proposed method.

Team	Input signal	ECG leads	Network	Parameters	Avg/total F1-score
Yao et al.	1D ECG	12 leads	ResNet+BiLSTM-GMP	4,984,640	0.812
He et al.	1D ECG	12 leads	ATI-CNN	No report	0.799
Chen et al.	1D ECG	12 leads	CNN+BRNN+Attention	28,035	0.797
RP-based	2D RP images	2 leads (lead II and aVR)	Inception-resnet-v2	46,964,673	0.844

**TABLE 7 |** Data profile for the CPSC, PTB\_XL, and Georgia ECG dataset.

Database	Sample frequency	Mean duration	Number of subjects					
			Normal	AF	I-AVB	LBBB	RBBB	PAC
CPSC	500 Hz	16.2 s	918	1,221	722	236	1,857	616
PTB_XL	500 Hz	10.0 s	18,092	1,514	797	536	0	398
Georgia	500 Hz	10.0 s	1,752	570	769	231	542	639

**TABLE 8 |** Classification performance of different ECG datasets.

Database	Avg/total F1-score	Classification of subjects F1-score					
		Normal	AF	I-AVB	LBBB	RBBB	PAC
CPSC	0.8521	0.7905	0.9269	0.8921	0.8825	0.8942	0.7266
PTB_XL	0.8862	0.9417	0.9167	0.8644	0.9246	0	0.7837
Georgia	0.8529	0.9237	0.8197	0.8706	0.8767	0.8629	0.7639

information from the right upper side of the heart (Gorgels et al., 2001). Chen et al. (2020) reported that aVR was one of the best-performance single leads in the classical CA classification experiments. In our study, it is also confirmed that the RPs of these two-lead signals are useful for the machine-learning-based CA classification. Besides, RP-based lead II and lead aVR ECG recordings performed differently in various classes. As shown in **Table 2**, the best prediction is for the LBBB (F1-score 0.929), followed by I-AVB (F1-score 0.923), while the prediction of the PAC was relatively poor. This may be due to the fact that the PAC occurs when a focus in the atrium (not the sinoatrial node) generates an action potential before the next scheduled SA node action potential, which is complex and less common. This makes it challenging to differentiate them from PVC, normal, and other arrhythmias (Surawicz et al., 2009). A similar finding has also been reported in early works (Yao et al., 2019; Chen et al., 2020).

This work studied the classification of CA based on the 1st China Physiological Signal Challenge 2018 ECG dataset. Further studies will be required to investigate those involving technical problems such as data imbalance, and the RP method will be refined to improve the prediction of PAC.

## CONCLUSION

In this paper, we proposed a DL-based method for automatic CA classification. In this method, the RP-based 2D texture images are processed as input data, which contain rich features unobservable from the standard time-domain and time-frequency domain. Based on RP-texture images, the Inception-ResNet-v2 network was used to predict and classify various CAs. In our study, the proposed method offers excellent performance with only two-lead ECG data without accessing the full 12-lead ECG recordings.

## REFERENCES

- Afonso, L. C. S., Rosa, G. H., Pereira, C. R., Weber, S. A. T., Hook, C., Albuquerque, V. H. C., et al. (2018). A recurrence plot-based approach for Parkinson's disease identification. *Future Gener. Comput. Syst.* 94, 282–292. doi: 10.1016/j.future.2018.11.054
- Chen, C., Hua, Z., Zhang, R., Liu, G., and Wen, W. (2019). Automated arrhythmia classification based on a combination network of CNN and LSTM. *Biomed. Signal Process. Control* 57, 1–10. doi: 10.1016/j.bspc.2019.101819
- Chen, T., Huang, C., Shih, E. S. C., Hu, Y., and Hwang, M. (2020). Detection and classification of cardiac arrhythmias by a challenge-best deep learning neural network model. *iScience* 23:100886. doi: 10.1016/j.isci.2020.100886
- Chollet, F. O. (2017). "Xception: deep learning with depthwise separable convolutions," in *Proceedings of the IEEE Conference on Computer Vision and Pattern Recognition (CVPR)*, (Honolulu, HI).
- Feifei, L., Liu, C., Zhao, L., Zhang, X., Wu, X., Xu, et al. "An open access database for evaluating the algorithms of electrocardiogram rhythm and morphology abnormality detection," *Journal of Medical Imaging and Health Informatics* 8, 1368–1373. doi: 10.1166/jmihi.2018.2442
- De Chazal, P., O'dwyer, M., and Reilly, R. B. (2004). Automatic classification of heartbeats using ECG morphology and heartbeat interval features. *IEEE Trans. Biomed. Eng.* 51, 1196–1206.
- de Chazal, P., and Reilly, R. B. (2006). A patient-adapting heartbeat classifier using ECG morphology and heartbeat interval features. *IEEE Trans. Biomed. Eng.* 53, 2535–2543. doi: 10.1109/TBME.2006.883802
- Debayle, J., Hatami, N., and Gavet, Y. (2017). "Classification of time-series images using deep convolutional neural networks," in *10 International Conference on Machine Vision(ICMV 2017)*, (Vienna, Austria).
- Eckmann, J.-P., Kamphors, S. O., and Ruell, D. (1987). Recurrence plots of dynamical systems. *Europhys. Lett.* 4, 973–977.
- Eckmann, J., Kamphorst, S. O., and Ruelle, D. (1995). Recurrence plots of dynamical systems. *World Sci. Ser. Nonlinear Sci. Ser. A* 16, 441–446.
- Faria, A. F., Almeida, J., Bruna, A., Morellato, L. P. C., and Ricardo, D. S. T. (2016). Fusion of time series representations for plant recognition in phenology studies. *Pattern Recognit. Lett.* 83, 205–214. doi: 10.1016/j.patrec.2016.03.005
- Gao, H., Zhuang, L., Maaten, L. V. D., and Weinberger, K. Q. (2017). "Densely connected convolutional networks," in *Proceedings of the IEEE Conference on Computer Vision and Pattern Recognition (CVPR)*, (Honolulu, HI).
- Gorgels, A. P. M., Engelen, D. J. M., and Wellens, H. J. J. (2001). Lead aVR, a mostly ignored but very valuable lead in clinical electrocardiography. *J. Am. Coll. Cardiol.* 38, 1355–1356.
- Hannun, A. Y., Rajpurkar, P., Haghpanahi, M., Tison, G. H., Bourn, C., Turakhia, M. P., et al. (2019). Cardiologist-level arrhythmia detection and classification in ambulatory electrocardiograms using a deep neural network. *Nat. Med.* 25, 65–75. doi: 10.1038/s41591-018-0268-3
- Hasan, N. I., and Bhattacharjee, A. (2019). Deep learning approach to cardiovascular disease classification employing modified ECG signal from empirical mode decomposition. *Biomed. Signal Process. Control* 52, 128–140. doi: 10.1016/j.bspc.2019.04.005
- He, K., Zhang, X., Ren, S., and Sun, J. (2016). "Deep residual learning for image recognition," in *Proceedings of the IEEE Conference on Computer Vision and Pattern Recognition (CVPR)*, (Honolulu, HI).
- He, R., Liu, Y., Wang, K., Zhao, N., Yuan, Y., Li, Q., et al. (2019). Automatic cardiac arrhythmia classification using combination of deep residual network and bidirectional LSTM. *IEEE Access* 7, 102119–102135. doi: 10.1109/ACCESS.2019.2931500

It implies that this RP-based CA classification method may have the potential to be used as a diagnostic tool in conditions/places where access to a 12-lead ECG is difficult.

## DATA AVAILABILITY STATEMENT

The publicly released dataset of the First China Physiological Signal Challenge 2018 is available at <http://2018.icbeb.org/Challenge.html>.

## AUTHOR CONTRIBUTIONS

FL conceived the study. HZ performed the design and implementation of the work. CL helped with the experiment design. ZZ helped with the implementation of the recurrent plot. YX and RD contributed to the discussion of the ECG. XL and YH helped the algorithm design of Resnet 50. HZ wrote the manuscript. FL, CL, and LX helped to review and improve the manuscript. All authors read and approved the final manuscript.

## FUNDING

This work was supported by the Natural Science Foundation of China (NSFC) under grant numbers 61527811 and 61701435, the Key Research and Development Program of Zhejiang Province under grant number 2020C03016, the Zhejiang Provincial Natural Science Foundation of China under grant number LY17H180003, the Medical Health Science and Technology Project of Zhejiang Provincial Health Commission under grant number 2020RC094, and the Science and Technology Program of Guangdong under grant number 2018B030333001.

- He, R., Wang, K., Zhao, N., Liu, Y., Yuan, Y., Li, Q., et al. (2018). Automatic detection of atrial fibrillation based on continuous wavelet transform and 2D convolutional neural networks. *Front. Physiol.* 9:1–11. doi: 10.3389/fphys.2018.01206
- Hu, Y. H., Palreddy, S., and Tompkins, W. J. (1997). "A patient-adaptable ECG beat classifier using a mixture of experts approach," in *IEEE Transactions on Biomedical Engineering*, 44, 891–900. doi: 10.1109/10.623058
- Huang, H., Liu, J., Zhu, Q., Wang, R., and Hu, G. (2014). A new hierarchical method for inter-patient heartbeat classification using random projections and RR intervals. *Biomed. Eng. Online* 13:90.
- Ince, T., Kiranyaz, S., and Gabbouj, M. (2009). A generic and robust system for automated patient-specific classification of ECG signals. *IEEE Trans. Biomed. Eng.* 56, 1415–1426. doi: 10.1109/TBME.2009.2013934
- Izci, E., Ozdemir, M. A., Degirmenci, M., and Akan, A. (2019). "Cardiac arrhythmia detection from 2D ECG images by using deep learning technique," in *Proceedings of the 2019 Medical Technologies National Congress (TIPTEKNO)*, (Izmir).
- Jun, T. J., Kang, D., Nguyen, H. M., Kim, D., Kim, D., and Kim, Y. H. (2018). ECG arrhythmia classification using a 2-D convolutional neural network. arXiv[Preprint] arXiv 1804.06812v1 [cs.CV],
- Li, Z., Zhou, D., Wan, L., Li, J., and Mou, W. (2020). Heartbeat classification using the deep residual convolutional neural network from a 2-lead electrocardiogram. *Jo. Electrocardiol.* 58, 105–112. doi: 10.1016/j.jelectrocard.2019.11.046
- Liu, F., Liu, C., Zhao, L., Zhang, X., Wu, X., Xu, X., et al. (2018). An open access database for evaluating the algorithms of electrocardiogram rhythm and morphology abnormality detection. *J. Med. Imaging Health Inform.* 8, 1368–1373. doi: 10.1166/jmihi.2018.2442
- Marwan, N., Wessel, N., Meyerfeldt, U., Schirdewan, A., and Kurths, J. (2002). Recurrence-plot-based measures of complexity and their application to heart-rate-variability data. *Phys. Rev.* 66:026702. doi: 10.1103/PhysRevE.66.026702
- Mathunjwa, B. M., Lin, Y.-T., Lin, C.-H., Abbod, M. F., and Shieh, J.-S. (2021). ECG arrhythmia classification by using a recurrence plot and convolutional neural network. *Biomed. Signal Process. Control* 64:102262. doi: 10.1016/j.bspc.2020.102262
- Mohebbi, M., and Ghassemlian, H. (2011). Prediction of paroxysmal atrial fibrillation using recurrence plot-based features of the RR-interval signal. *Physiol. Meas.* 32, 1147–1162. doi: 10.1088/0967-3334/32/8/010/meta
- Ouyang, G., Li, X., Dang, C., and Richards, D. A. (2008). Using recurrence plot for determinism analysis of EEG recordings in genetic absence epilepsy rats. *Clin. Neurophysiol.* 119, 1747–1755. doi: 10.1016/j.clinph.2008.04.005
- Ouyang, G., Zhu, X., Ju, Z., and Liu, H. (2014). Dynamical characteristics of surface EMG signals of hand grasp via recurrence plot. *IEEE J. Biomed. Health Inform.* 18, 257–265. doi: 10.1109/JBHI.2013.2261311
- Parvaneh, S., Rubin, J., Rahman, A., Conroy, B., and Babaeizadeh, S. (2018). Analyzing single-lead short ECG recordings using dense convolutional neural networks and feature-based post-processing to detect atrial fibrillation. *Physiol. Meas.* 39:084003. doi: 10.1088/1361-6579/aad5bd/meta
- Perez Alday, E. A., Gu, A., Shah, A. J., Robichaux, C., Ian Wong, A. K., Liu, C., et al. (2021). Classification of 12-lead ECGs: the PhysioNet/Computing in Cardiology Challenge 2020. *Physiol. Meas.* 41:124003. doi: 10.1088/1361-6579/abc960
- Rajpurkar, P., Hannun, A. Y., Bourn, M. H. C., and Ng, A. Y. (2017). Cardiologist-level arrhythmia detection with convolutional neural networks. arXiv[Preprint] arXiv:1707.01836v1 [cs.CV] 6,
- Rubin, J., Parvaneh, S., Rahman, A., Conroy, B., and Babaeizadeh, S. (2018). Densely connected convolutional networks for detection of atrial fibrillation from short single-lead ECG recordings. *J. Electrocardiol.* 51, S18–S21. doi: 10.1016/j.jelectrocard.2018.08.008
- Schlenker, J., Socha, V., Riedlbauchová, L., Nedělka, T., Schlenker, A., Potočková, V., et al. (2015). Recurrence plot of heart rate variability signal in patients with vasovagal syncope. *Biomed. Signal Process. Control* 25, 1–11. doi: 10.1016/j.bspc.2015.10.007
- Surawicz, B., Childers, R., Deal, B. J., Gettes, L. S., Bailey, J. J., Gorgels, A., et al. (2009). AHA/ACCF/HRS recommendations for the standardization and interpretation of the electrocardiogram: part III: intraventricular conduction disturbances: a scientific statement from the American heart association electrocardiography and arrhythmias committee, council on clinical cardiology; the American college of cardiology foundation; and the heart rhythm society: endorsed by the international society for computerized electrocardiology. *Circulation* 119, 235–240. doi: 10.1161/CIRCULATIONAHA.108.191095
- Szegedy, C., Ioffe, S., Vanhoucke, V., and Alemi, A. (2016). Inception-v4, inception-resnet and the impact of residual connections on learning. arXiv [Preprint] arXiv:1602.07261,
- Tang, D. H., Gilligan, A. M., and Romero, K. (2014). Economic burden and disparities in healthcare resource use among adult patients with cardiac arrhythmia. *Appl. Health Econ. Health Policy* 12, 59–71. doi: 10.1007/s40258-013-0070-9
- Wagner, P., Strothoff, N., Bousseljot, R. D., Kreiseler, D., Lunze, F. I., Samek, W., et al. (2020). PTB-XL, a large publicly available electrocardiography dataset. *Sci. Data* 7:154. doi: 10.1038/s41597-020-0495-6
- Wang, Y., Guan, Q., Lao, I., Wang, L., Wu, Y., Li, D., et al. (2019). Using deep convolutional neural networks for multi-classification of thyroid tumor by histopathology: a large-scale pilot study. *Ann. Transl. Med.* 7:468. doi: 10.21037/atm.2019.08.54
- Xie, S., Girshick, R., Dollar, P., Tu, Z., and He, K. (2017). "Aggregated residual transformations for deep neural networks," in *Proceedings of the IEEE Conference on Computer Vision and Pattern Recognition (CVPR)*, (Honolulu, HI).
- Xiong, Z., Nash, M. P., Cheng, E., Fedorov, V. V., Stiles, M. K., and Zhao, J. (2018). ECG signal classification for the detection of cardiac arrhythmias using a convolutional recurrent neural network. *Physiol. Meas.* 39:094006. doi: 10.1088/1361-6579/aad9ed/meta
- Yao, Q., Wang, R., Fan, X., Liu, J., and Li, Y. (2019). Multi-class arrhythmia detection from 12-lead varied-length ECG using attention-based time-incremental convolutional neural network. *Inform. Fusion* 53, 174–182. doi: 10.1016/j.inffus.2019.06.024
- Ye, C., Kumar, B. V. K. V., and Coimbra, M. T. (2012). Heartbeat classification using morphological and dynamic features of ECG signals. *IEEE Trans. Biomed. Eng.* 59, 2930–2941. doi: 10.1109/TBME.2012.2213253
- Zhao, Z., Wang, X., Cai, Z., Li, J., and Liu, C. (2019). "PVC recognition for wearable ECGs using modified frequency slice wavelet transform and convolutional neural network," in *2019 Computing in Cardiology Conference (CinC)*, (Singapore).

**Conflict of Interest:** The authors declare that the research was conducted in the absence of any commercial or financial relationships that could be construed as a potential conflict of interest.

Copyright © 2021 Zhang, Liu, Zhang, Xing, Liu, Dong, He, Xia and Liu. This is an open-access article distributed under the terms of the Creative Commons Attribution License (CC BY). The use, distribution or reproduction in other forums is permitted, provided the original author(s) and the copyright owner(s) are credited and that the original publication in this journal is cited, in accordance with accepted academic practice. No use, distribution or reproduction is permitted which does not comply with these terms.





# The Comparison of Different Constitutive Laws and Fiber Architectures for the Aortic Valve on Fluid–Structure Interaction Simulation

Li Cai<sup>1,2†</sup>, Ruihang Zhang<sup>1\*†</sup>, Yiqiang Li<sup>1\*</sup>, Guangyu Zhu<sup>3</sup>, Xingshuang Ma<sup>4</sup>, Yongheng Wang<sup>1</sup>, Xiaoyu Luo<sup>5</sup> and Hao Gao<sup>5\*</sup>

## OPEN ACCESS

### Edited by:

Ling Xia,  
Zhejiang University, China

### Reviewed by:

Haipeng Liu,  
Coventry University, United Kingdom  
Wenjun Ying,  
Shanghai Jiao Tong University, China

### \*Correspondence:

Hao Gao  
hao.gao@glasgow.ac.uk  
Ruihang Zhang  
ruihangz0313@mail.nwpu.edu.cn  
Yiqiang Li  
liyiqiang@nwpu.edu.cn

<sup>†</sup>These authors have contributed  
equally to this work

### Specialty section:

This article was submitted to  
Computational Physiology and  
Medicine,  
a section of the journal  
Frontiers in Physiology

Received: 19 March 2021

Accepted: 27 April 2021

Published: 24 June 2021

### Citation:

Cai L, Zhang R, Li Y, Zhu G, Ma X,  
Wang Y, Luo X and Gao H (2021) The  
Comparison of Different Constitutive  
Laws and Fiber Architectures for the  
Aortic Valve on Fluid–Structure  
Interaction Simulation.  
Front. Physiol. 12:682893.  
doi: 10.3389/fphys.2021.682893

<sup>1</sup> NPU-UoG International Cooperative Lab for Computation and Application in Cardiology, Northwestern Polytechnical University, Xi'an, China, <sup>2</sup> Xi'an Key Laboratory of Scientific Computation and Applied Statistics, Xi'an, China, <sup>3</sup> School of Energy and Power Engineering, Xi'an Jiaotong University, Xi'an, China, <sup>4</sup> College of Bioengineering, Chongqing University, Chongqing, China, <sup>5</sup> School of Mathematics and Statistics, University of Glasgow, Glasgow, United Kingdom

Built on the hybrid immersed boundary/finite element (IB/FE) method, fluid–structure interaction (FSI) simulations of aortic valve (AV) dynamics are performed with three different constitutive laws and two different fiber architectures for the AV leaflets. An idealized AV model is used and mounted in a straight tube, and a three-element Windkessel model is further attached to the aorta. After obtaining *ex vivo* biaxial tensile testing of porcine AV leaflets, we first determine the constitutive parameters of the selected three constitutive laws by matching the analytical stretch–stress relations derived from constitutive laws to the experimentally measured data. Both the average error and relevant R-squared value reveal that the anisotropic non-linear constitutive law with exponential terms for both the fiber and cross-fiber directions could be more suitable for characterizing the mechanical behaviors of the AV leaflets. We then thoroughly compare the simulation results from both structural mechanics and hemodynamics. Compared to the other two constitutive laws, the anisotropic non-linear constitutive law with exponential terms for both the fiber and cross-fiber directions shows the larger leaflet displacements at the opened state, the largest forward jet flow, the smaller regurgitant flow. We further analyze hemodynamic parameters of the six different cases, including the regurgitant fraction, the mean transvalvular pressure gradient, the effective orifice area, and the energy loss of the left ventricle. We find that the fiber architecture with body-fitted orientation shows better dynamic behaviors in the leaflets, especially with the constitutive law using exponential terms for both the fiber and cross-fiber directions. In conclusion, both constitutive laws and fiber architectures can affect AV dynamics. Our results further suggest that the strain energy function with exponential terms for both the fiber and cross-fiber directions could be more suitable for describing the AV leaflet mechanical behaviors. Future experimental studies are needed to identify competent constitutive laws for the AV leaflets and their associated fiber orientations with controlled



experiments. Although limitations exist in the present AV model, our results provide important information for selecting appropriate constitutive laws and fiber architectures when modeling AV dynamics.

**Keywords:** aortic valve, hybrid immersed boundary/finite element method, fluid-structure interaction, mechanical properties, dynamic behaviors, hemodynamic performance, the constitutive law

## 1. INTRODUCTION

There are up to 250,000 heart valves repaired and replaced each year worldwide (Yoganathan et al., 2004). Among these, aortic valve (AV) diseases have become the second-leading cause of cardiovascular diseases due to their high morbidity and mortality (Go et al., 2013). Major AV diseases include aortic stenosis, calcification, regurgitation, etc. (Franzone et al., 2016). Current treatments mainly focus on surgical repair and valve replacement. However, difficulties and risks exist in surgical procedures. Numerical simulations of the AV dynamics can assess the hemodynamic performance, predict the effectiveness, and persistence of surgical treatments, thereby help AV disease management (Mohammadi et al., 2016; Chen and Luo, 2018).

The AV locates at the root of the supporting aorta and provides a path of oxygenated blood to be pumped from the heart into the systemic circulation while preventing blood from flowing back from the aorta into the left ventricle (LV). The AV is composed of three relatively equal-sized semi-lunar leaflets, whose attachment forms the valve annulus and three bulges comprising the aortic sinuses. The dynamics of AV are driven by the pressure gradient between the LV and the aorta (Mohammadi et al., 2016). For example, in the systolic phase, the pressure of the LV is higher than that of the aorta, resulting in the AV opening and blood flowing from the LV into the aorta. In diastole, the AV closes as the LV pressure decreases.

Early numerical studies of the AV mainly focused on structural analysis using the finite element method (FEM). Since the mid-1970s, researchers have begun to simulate the AV based on simple geometries. In 1973, Gould et al. (1973) constructed three different geometries for the closed AV leaflets and concluded that changes in the leaflets geometry lead to great changes in the stress field. After that, Chong et al. (1978) studied the stress state of porcine AV leaflets using FEM. Since the 1990s, researchers have begun to use commercial software to analyze AV behaviors and stress distributions (Black et al., 1991). Kunzelman et al. developed the first three-dimensional FE model of the mitral valve (MV) and analyzed the deformation and stress patterns of the MV using LS-DYNA (Livermore Software Technology Corporation, Livermore, CA), followed by a series of studies, they have provided a deep understanding of normal and abnormal MV anatomy and function (Kunzelman et al., 1993, 1997, 2007). Meanwhile, their numerical MV model was the first to use patient-specific magnetic resonance imaging (MRI) data rather than idealized geometry.

Because of the strong interaction between heart valves and blood flow, fluid-structure interaction (FSI) methods were introduced. Chew et al. (1999) developed a three-dimensional (3D) model of a bioprosthetic porcine valve with non-linear

material properties, and the FSI simulation was implemented through the Arbitrary Lagrangian-Eulerian (ALE) method. De Hart et al. (2003a,b) developed a 3D model of the AV using the fictitious domain (FD) method. Van Loon et al. (2004) used a combined ALE and FD method to validate the FSI models in simulating the healthy and stenotic AV. Besides, Weinberg et al. (2010) established a multiscale FSI model of the AV to capture the mechanical behaviors of the AV. Morganti et al. (2015) utilized a patient-specific valve geometry model to simulate the closure of the AV by isogeometric analysis. Mohammadi et al. (2016) reviewed the numerical methods for studying the hemodynamics of the AV, especially the FSI method.

Due to the large deformation of the valve leaflets, severe distortion, and deterioration may exist in the fluid mesh, and the ALE method can be challenging because of the frequent mesh regeneration (Gao et al., 2017b). To overcome such difficulty, the immersed boundary (IB) method was introduced by Peskin to simulate heart valve dynamics (Peskin, 2002). The IB method greatly simplifies the mesh regeneration and facilitates the numerical simulation of large deformation in the elastic structure. Griffith et al. (2009) applied the IB method to simulate the fluid dynamics of heart valves, including a natural AV and a chorded prosthetic MV. After that, Griffith (2012) used a staggered-grid version of the IB method to simulate the AV dynamics over multiple cardiac cycles. Ma et al. (2013) utilized this IB method to perform the FSI simulation for a human anatomical MV model obtained from *in vivo* MRI data. The immersed finite element (IFE) method was an extension of the IB method, where the FE approximations were applied to the Eulerian and Lagrangian equations. Built on the classical IB method, Griffith and Luo (2017) discretized the immersed structure using the FE method and the incompressible Navier-Stokes equation using the finite difference method, which is the hybrid finite difference/finite element immersed boundary (IB/FE) method. By using the IB/FE method, Gao et al. (2014) simulated the dynamic behaviors of a human MV reconstructed from *in vivo* MRI data, then extended to a coupled MV-LV model (Gao et al., 2017a). Feng et al. (2019) achieved the FSI simulation of a coupled left atrium-MV model by the IB/FE framework. The same IB/FE framework has also been applied to AV modeling. For example, Flamini et al. (2016) studied the effects of the aortic root on the AV dynamics, and their results showed reasonable agreement with the physiological measurements. Hasan et al. (2017) constructed a realistic, three-dimensional anatomical IB/FE model of the aortic root and ascending aorta. Recently, Lee et al. (2020a) performed FSI simulations of the porcine AV and the bovine pericardial valve, with the computational results being in excellent agreement with

the experimental data. Lee et al. (2020b) further studied the experimental and IB/FE model of bioprosthetic aortic valves (BAVs).

It has been widely acknowledged that the material properties of heart valves can play an important role in valvular function. Heart valve tissue mainly consists of collagen and elastin, which is usually considered to be a material of anisotropy, hyperelasticity, non-linearity, and incompressibility (Weinberg and Kaazempur-Mofrad, 2005). To characterize the mechanical properties of the valve leaflets, the formulation of the constitutive law of heart valve tissue should be determined according to its underlying biological structure. Martin and Sun (2012) studied the biomechanical properties of the AV leaflets of the human, porcine, and ovine, and they found that the aged human AV leaflets were stiffer than the porcine and ovine AV leaflets. Pham et al. (2017) used the planar biaxial testing to characterize the mechanical and structural properties of four different heart valves, and found that great differences exist in thickness, stiffness, and anisotropy. Wang et al. (2012, 2015) adopted the anisotropic hyperelastic material model to describe the mechanical properties of the AV tissues, including the leaflets, the sinus, the ascending aorta, and the myocardium. Mao et al. (2016) compared an anisotropic and an isotropic leaflet material model in transcatheter AV simulations, and their results suggested that the isotropic model showed a stiffer leaflet behavior in the radial direction than the anisotropic model. Recent reviews of material properties of valvular tissues can be found in Sun et al. (2014).

Furthermore, the fiber architecture of the valve leaflets plays an essential role in the mechanical function of the AV. Early studies for the fiber orientation distribution of the human heart relied on the projections and the least-square fitting methods. For example, Toussaint et al. (2010) reconstructed the complete 3D human cardiac fiber architecture using a curvilinear interpolation of diffusion tensor images. At present, two different approaches are mainly used for reconstructing the fiber distribution in soft tissue. The first method is the rule-based method by assuming that collagen fibers align circumferentially based on a cylindrical coordinate system (Gao et al., 2014; Hasan et al., 2017). Rule-based methods have been widely used in soft tissue modeling, including arteries (Qi et al., 2015) and heart (Wang et al., 2013; Gao et al., 2015; Guan et al., 2020). The other approach is to map fiber distributions from *in/ex vivo* experimental measurements. For example, Aggarwal et al. (2013) used a spline-based method to obtain the fiber structure by mapping them from histological analysis of AV specimen.

There is a lack of comparative study of constitutive laws of AV in FSI simulations. Our previous studies on MV suggested that different constitutive laws can affect MV dynamics (Cai et al., 2019). Thus, in this study, we analyze the effects of three different constitutive laws and two different fiber architectures on AV dynamics and hemodynamics. We first construct an idealized AV model mounted in a straight tube coupled with a three-element Windkessel model for systemic circulation. To characterize the material properties of the leaflets,

we first measured the stiffness of porcine AV samples using biaxial tensile testing, then three different constitutive laws are considered from published studies. We then simulate the AV dynamics using the IB/FE method and finally analyze the leaflets dynamics and hemodynamic performance in six different cases.

## 2. METHODS

### 2.1. The AV Model

#### 2.1.1. The Computational Model

**Figure 1** shows the AV model mounted in a straight tube. This idealized AV model is constructed according to the porcine pericardial valve with a leaflet thickness of 0.04 cm (Zhu et al., 2017). The straight tube has a total length of 13 cm, with the inner radius 1.3 cm, and the wall thickness 0.15 cm, which is also similar to the AV model in Flamini et al. (2016). Besides, based on a novel expanded-polytetrafluoroethylene (ePTFE) stentless tri-leaflet valve, Zhu et al. (2017) experimentally assessed the dynamic and hemodynamic performance of the AV, which provides the reference values for validating this AV model.

In the previous work, Griffith (2012) used a three-element Windkessel model for providing dynamic pressure loading. Here, we follow the same approach as shown in **Figure 1**. The three-element Windkessel model consists of the characteristic resistance  $R_c$ , the peripheral resistance  $R_p$ , and the arterial compliance  $C$ . Let  $P_{LV}$  denote the left ventricular pressure (inlet pressure), and let  $P_{Ao}$  denote the aortic pressure (outlet pressure) obtained from the three-element Windkessel model.  $P_{Wk}$  is the pressure stored in the Windkessel model. Assuming  $Q_{Ao}$  is the flow rate through the outlet boundary, according to the relationship between the pressure, the flow rate, and the resistance, we have (Griffith, 2012).

$$C \frac{dP_{Wk}}{dt} + \frac{P_{Wk}}{R_p} = Q_{Ao}, \quad (1)$$

$$P_{Ao} = Q_{Ao}R_c + P_{Wk}. \quad (2)$$

The details of numerical implementation of this Windkessel model can be found in Griffith (2012). In the following simulation, we set  $R_c = 0.033 \text{ mmHg ml}^{-1} \text{ s}$ ,  $R_p = 0.79 \text{ mmHg ml}^{-1} \text{ s}$ ,  $C = 1.75 \text{ ml mmHg}^{-1}$ , and the initial pressure  $P_{Wk} = 85 \text{ mmHg}$  and  $P_{Ao} = P_{Wk}$ , which correspond to the human “Type A” beat in the work of Stergiopoulos et al. (1999).

#### 2.1.2. The Fiber Architectures of AV Leaflets

Because of lacking experimental data on collagen orientations in the leaflets, the rule-based method is used to construct two different fiber architectures in AV leaflets, which are further denoted as FD1 and FD2 as shown in **Figure 2**. Both fiber architectures are circumferentially aligned in general and constructed by solving a Poisson-type system of a scalar field  $u$  (Wong and Kuhl, 2014; Guan et al., 2020). FD1 is body-fitted,

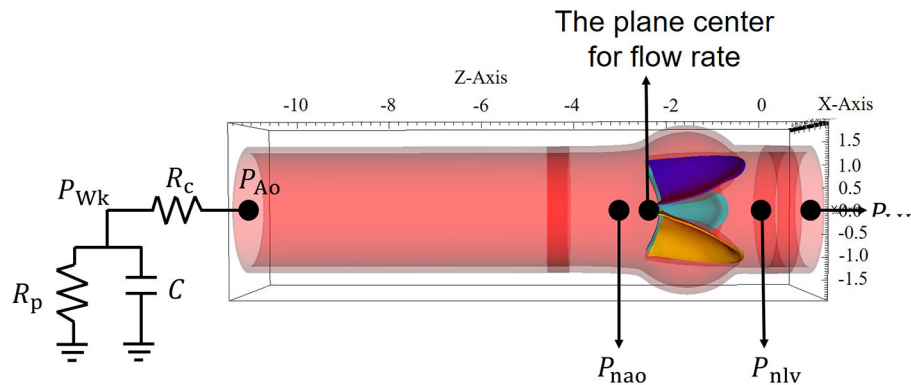


**FIGURE 1** | The geometric model of the aortic valve (AV).

and FD2 is simply the circumferential direction. In detail, the Poisson system for FD1 is defined as

$$\text{FD1:} \begin{cases} \nabla^2 u = 0, \text{ in } \mathcal{B}, \\ u|_{n_1} = 1, \\ u|_{n_2} = 0, \\ \frac{\partial u}{\partial n}|_{\Gamma^N} = 0, \end{cases} \quad (3)$$

in which  $\mathcal{B}$  represents the leaflet,  $n_1$  and  $n_2$  are the two corner points indicated in **Figure 2A**, and  $\Gamma^N$  is the surface of the leaflet. The collagen fiber direction is defined as  $\mathbf{f} = \nabla u / |\nabla u|$ .

To construct FD2, the Poisson system is defined as

$$\text{FD2:} \begin{cases} \nabla^2 u = 0, \text{ in } \mathcal{B}, \\ u|_{\tau_1} = 0, \\ u|_{\tau_2} = 1, \\ \frac{\partial u}{\partial n}|_{\Gamma^N} = 0, \end{cases} \quad (4)$$

in which  $\tau_1$  and  $\tau_2$  are the two surfaces connecting the leaflet to the aorta, and symmetric about the central line of the leaflet as shown in **Figure 2B**,  $\Gamma^N$  represents the remaining surfaces of the leaflet. The corresponding fiber direction is also given by  $\nabla u / |\nabla u|$ .

From **Figure 2**, it can be seen that the fiber architecture FD1 has a body-fitted fiber orientation, which is similar to the fiber structures in Aggarwal et al. (2013); Hasan et al. (2017). The fiber architecture FD2 is simply the circumferential direction, which has been used by Fan et al. (2013).

## 2.2. The IB/FE Method

The IB/FE method (Gao et al., 2014; Griffith and Luo, 2017) is employed here to simulate the AV dynamics, which uses the FE discretization for the immersed structure and the finite difference discretization for the viscous incompressible fluid. Let  $\mathbf{X} = (X_1, X_2, X_3) \in U$  denote Lagrangian material coordinates, and let  $\mathbf{x} = (x_1, x_2, x_3) \in \Omega$  represent physical coordinates, in which  $U \subset \mathbb{R}^3$  means the Lagrangian coordinate domain, and  $\Omega \subset \mathbb{R}^3$  denotes the fixed physical domain of the FSI system. Let

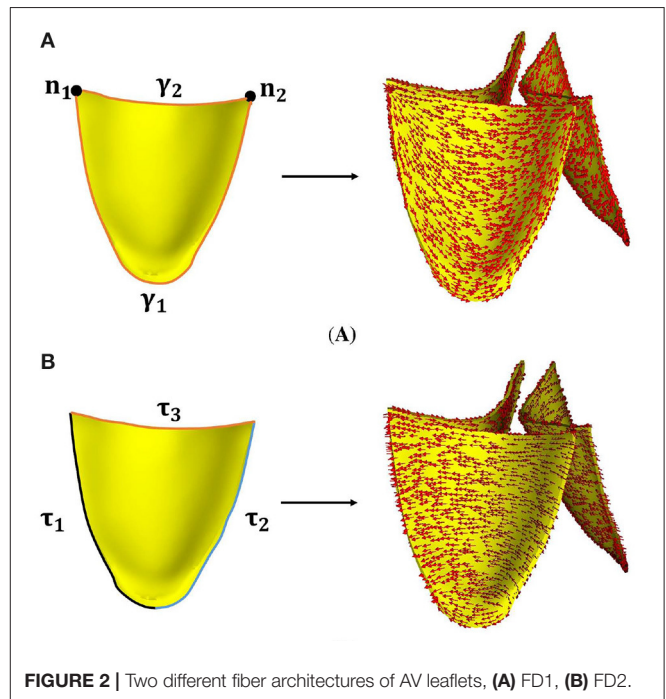


**FIGURE 2** | Two different fiber architectures of AV leaflets, (A) FD1, (B) FD2.

$\chi(\mathbf{X}, t) \in \Omega$  denote the physical position of structure point  $\mathbf{X}$  at time  $t$ , then  $\chi(U, t) \subset \Omega$  is the physical domain of the structure at time  $t$ , whereas the physical domain occupied by the fluid at time  $t$  is  $\Omega - \chi(U, t)$ . The governing equations of the FSI system are given as

$$\rho \left( \frac{\partial \mathbf{u}}{\partial t}(\mathbf{x}, t) + \mathbf{u}(\mathbf{x}, t) \cdot \nabla \mathbf{u}(\mathbf{x}, t) \right) = -\nabla p(\mathbf{x}, t) + \mu \nabla^2 \mathbf{u}(\mathbf{x}, t) + \mathbf{f}^c(\mathbf{x}, t), \quad (5)$$

$$\nabla \cdot \mathbf{u}(\mathbf{x}, t) = 0, \quad (6)$$

$$\frac{\partial \chi}{\partial t}(\mathbf{X}, t) = \int_{\Omega} \mathbf{u}(\mathbf{x}, t) \delta(\mathbf{x} - \chi(\mathbf{X}, t)) d\mathbf{x}, \quad (7)$$

$$\begin{aligned} \mathbf{f}^e(\mathbf{x}, t) = & \int_U \nabla \cdot \mathbb{P}^e(\mathbf{X}, t) \delta(\mathbf{x} - \chi(\mathbf{X}, t)) d\mathbf{X} \\ & - \int_{\partial U} \mathbb{P}^e(\mathbf{X}, t) \mathbf{N}(\mathbf{X}) \delta(\mathbf{x} - \chi(\mathbf{X}, t)) dA(\mathbf{X}), \end{aligned} \quad (8)$$

where  $\mathbf{u}(\mathbf{x}, t)$  is the Eulerian velocity field,  $p(\mathbf{x}, t)$  is the Eulerian pressure field,  $\rho = 1.0 \text{ g/ml}$  is the mass density,  $\mu = 4 \text{ cP}$  is the fluid dynamic viscosity,  $\mathbf{f}^e(\mathbf{x}, t)$  is the Eulerian elastic force density, and  $\delta(\mathbf{x}) = \delta(x_1)\delta(x_2)\delta(x_3)$  is the three-dimensional Dirac delta function.  $\mathbb{P}^e = \frac{\partial W}{\partial \mathbb{F}}$  is the first Piola–Kirchhoff stress tensor, in which  $\mathbb{F}$  is the deformation gradient related to structural deformation.  $\mathbf{N}(\mathbf{X})$  is the outer normal vector of the Lagrangian coordinate domain  $U$ , and  $dA(\mathbf{X})$  denotes the area element in the reference configuration.

The total Cauchy stress tensor of the FSI system is

$$\boldsymbol{\sigma}(\mathbf{x}, t) = \boldsymbol{\sigma}^f(\mathbf{x}, t) + \begin{cases} \boldsymbol{\sigma}^e(\mathbf{x}, t) & \text{for } \mathbf{x} \in \chi(U, t), \\ 0 & \text{otherwise,} \end{cases} \quad (9)$$

in which  $\boldsymbol{\sigma}^f = -p\mathbb{I} + \mu[\nabla\mathbf{u} + (\nabla\mathbf{u})^T]$  is the Cauchy stress tensor of the viscous incompressible fluid,  $\mathbb{I}$  is the identity matrix, and  $\boldsymbol{\sigma}^e$  is the elastic Cauchy stress tensor related to the first Piola–Kirchhoff stress tensor  $\mathbb{P}^e$ , that is  $\boldsymbol{\sigma}^e = J^{-1}\mathbb{P}^e\mathbb{F}^T$  with  $J = \det(\mathbb{F})$ .

## 2.3. The Constitutive Laws

In this study, we consider the valvular tissue to be incompressible, anisotropic, hyperelastic (Weinberg and Kaazempur-Mofrad, 2005), and use three different constitutive laws to characterize the mechanical properties of the AV leaflets, which are denoted as W1, W2, and W3. The constitutive law W1 was used to characterize the mechanical properties of the AV tissue first by Wang et al. (2012). The constitutive law W2 was first proposed by Prot et al. (2010) for modeling the mechanical behaviors of healthy MV tissue, and the constitutive law W3 was used to model human MV leaflets first by Gao et al. (2014). The corresponding strain-energy functions are

$$W1 = C_{10} \left( e^{C_{01}(I_1-3)} - 1 \right) + \frac{k_1}{2k_2} \left[ e^{k_2(I_4-1)^2} - 1 \right], \quad (10)$$

$$W2 = \mu (I_1 - 3) + c_0 \left[ e^{c_1(I_1-3)^2+c_2(I_4-1)^4} - 1 \right], \quad (11)$$

$$W3 = C_1 (I_1 - 3) + \frac{a}{2b} \left[ e^{b(I_4-1)^2} - 1 \right], \quad (12)$$

where  $C_{10}, C_{01}, k_1, k_2$  are the material parameters of Equation (10). Similarly,  $\mu, c_0, c_1, c_2$  are the material parameters of Equation (11), and  $C_1, a, b$  are the non-negative parameters in Equation (12).  $I_1 = \text{trace}(\mathbb{C})$  is the first strain invariant of the right Cauchy–Green deformation tensor  $\mathbb{C} = \mathbb{F}^T\mathbb{F}$ .  $I_4 = \mathbf{f}_0 \cdot (\mathbb{C}\mathbf{f}_0)$  is the squared stretch along the fiber direction, with  $\mathbf{f}_0$  the fiber direction in the reference state and  $\mathbf{f} = \mathbb{F}\mathbf{f}_0$  the fiber direction in the current state. The corresponding Cauchy stress tensors are

$$\boldsymbol{\sigma}^{W1} = -p\mathbb{I} + 2C_{10}C_{01}e^{C_{01}(I_1-3)}\mathbb{B} + 2k_1(I_4-1)e^{k_2(I_4-1)^2}\mathbf{f} \otimes \mathbf{f}, \quad (13)$$

$$\begin{aligned} \boldsymbol{\sigma}^{W2} = & -p\mathbb{I} + \left( 2\mu + 4c_0c_1(I_1-3)e^{c_1(I_1-3)^2+c_2(I_4-1)^4} \right) \mathbb{B} + \\ & \left( 8c_0c_2(I_4-1)^3e^{c_1(I_1-3)^2+c_2(I_4-1)^4} \right) \mathbf{f} \otimes \mathbf{f}, \end{aligned} \quad (14)$$

$$\boldsymbol{\sigma}^{W3} = -p\mathbb{I} + 2C_1\mathbb{B} + 2a(I_4-1)e^{b(I_4-1)^2}\mathbf{f} \otimes \mathbf{f}, \quad (15)$$

in which  $\mathbb{B} = \mathbb{F}\mathbb{F}^T$  is the left Cauchy–Green deformation tensor, and  $p$  is the Lagrangian multiplier to enforce the incompressibility constraint.

## 2.4. Experiments and Calibration

In this section, we performed the tensile testing experiments using postmortem porcine AV samples from a domestic butcher house in Chongqing, China. The experimental protocols were similar to our previous study of *ex vivo* biomechanical tests on mitral valvular apparatus (Chen et al., 2020). In brief, squared samples were isolated from adult porcine hearts from the domestic butcher house (1-year old,  $\geq 100 \text{ kg}$ ) and soaked in phosphate buffer saline (PBS) solution for moisture. The leaflet was cut into  $8 \times 8 \text{ mm}$  samples on the middle part from the free edge and the edge of attachment to the aortic root (see **Figure 3**). Four square markers ( $1 \times 1 \text{ mm}$ ) were glued to the surface with superglue (cyanoacrylate adhesive) for optical strain tracking as an illustration of the circumferential (X-axis) and the radial (Y-axis) directions. All samples were kept at  $37^\circ\text{C}$  PBS bath and tested using a biaxial testing machine (BioTester) from CellScale to mimic the physiological loading condition. Eight preconditioning cycles were used to release the residual stress and adjust the tissue in a zero load. AV samples were then stretched to physiological stress estimated based on Laplace's law for a spherical surface assuming the mean radius of curvature of the AV to be  $2 \text{ cm}$  and the transvalvular pressure to be  $120 \text{ mm Hg}$ . The 1:1 stress ratio in two directions was applied to measure the anisotropic behaviors of the tissue. The displacements of markers and corresponding tensile forces were then recorded and calculated for stress and strain analysis. Details of the biaxial testing protocols can be found in Chen et al. (2020).

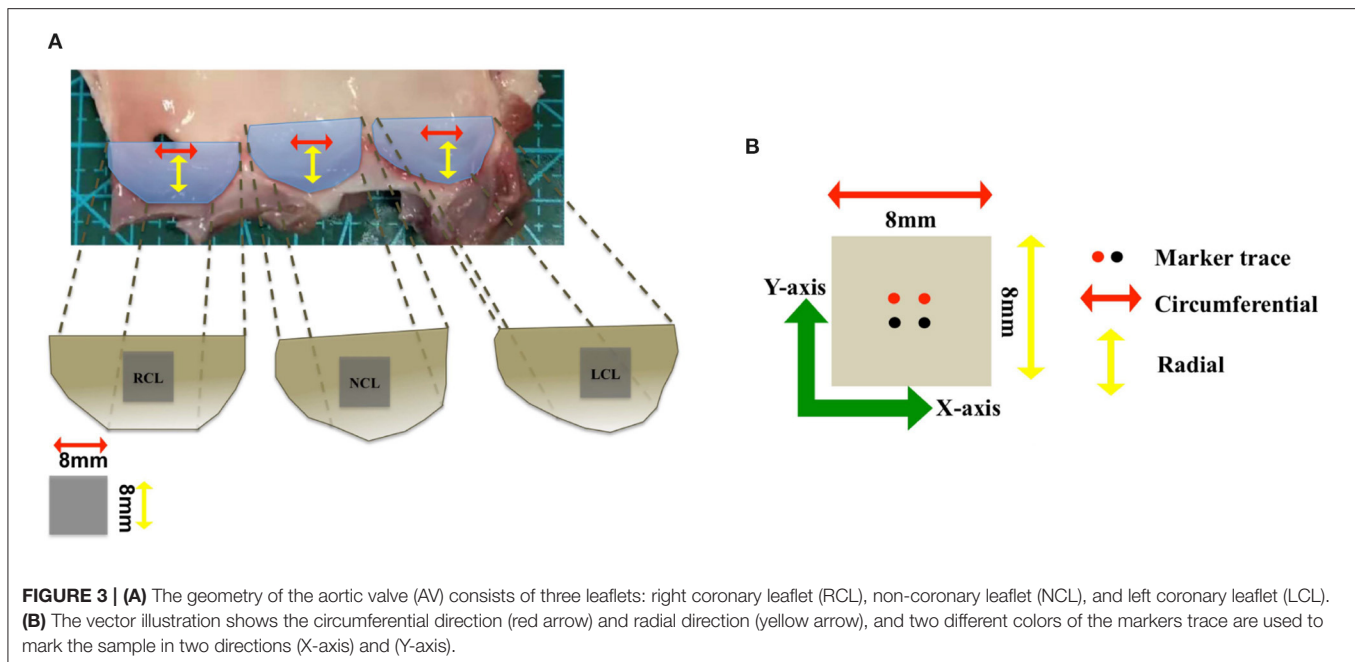
The parameters of the constitutive laws of the AV leaflets are obtained by minimizing the differences between the stretch–stress relationship derived from selected constitutive laws and corresponding experimental data. First, we obtained the experimental stretch–stress data from the biaxial testing. Second, the analytical stretch–stress relationships are obtained from Equations (13)–(15). Then, we perform the least square fitting following the same procedure in Cai et al. (2019) to determine the optimal parameters, and the *fmincon* function in Matlab is used to minimize the loss function, which is

$$f = \sum_{i=1}^n [(\sigma_{11}^W - \sigma_{11}^{\text{exp}})^2 + (\sigma_{22}^W - \sigma_{22}^{\text{exp}})^2], \quad (16)$$

where  $\sigma_{11}^{\text{exp}}$  and  $\sigma_{22}^{\text{exp}}$  are the experimental Cauchy stresses in the fiber and cross-fiber directions, and the superscript “W” indicates the stress is derived from a selected strain energy function.

In sum, we obtained nine sets of the biaxial stress tests from three porcine leaflets. Here, we further report the constitutive





parameters by taking the average of nine sets of parameters, in which each set of parameters is obtained from one experimental sample. In the least square fitting, the lowest bounds for the iterative optimization parameters are set to be zero. The average R-squared value for each constitutive law is obtained by taking the average of nine sets of R-squared values, which is defined as  $R\text{-squared} = 1 - \text{SSE}/\text{SST}$ , where SSE is the residual sum of squares and SST is the total sum of squares. The closer the R-squared value to 1, the better the goodness-of-the-fitting.

## 2.5. The Numerical Implementation and Boundary Conditions

The whole AV model is immersed in an  $8 \times 8 \times 14$  cm fluid domain, which is further discretized into a regular  $80 \times 80 \times 128$  Cartesian grid. The time step size of 5e-6 s is selected because of the explicit time-stepping scheme. The detailed spatial and temporal discretizations can be found in Griffith and Luo (2017). The numerical implementation uses the IBAMR software infrastructure (<https://github.com/IBAMR/IBAMR>), which is a distributed-memory parallel implementation of the IB method with support for Cartesian grid adaptive mesh refinement. In this study, the Cartesian computational domain is discretized with 2 nested grid levels and a refinement ratio of 4 between the two levels. Note no refinement is applied to the structural mesh.

A physiological LV pressure is used to drive blood flow through the AV, as shown in **Figure 4**. Meanwhile, a three-element Windkessel model is utilized to provide dynamic pressure loading of the aortic side for the AV model (Griffith, 2012), in which the outlet pressure of the Windkessel model is set as zero. The remaining boundaries of the FSI computational domain are with zero pressure, which is schematically illustrated in **Figure 4**. Furthermore, a large tethering force is applied at the outer surface of the aorta to keep the straight tube in place.

## 2.6. The Hemodynamic Parameters

To assess the hemodynamic performance of the AV, we introduce several hemodynamic parameters, including the regurgitant fraction, the mean transvalvular pressure gradient, the effective orifice area, and the energy loss of the LV. The regurgitant fraction reflects the regurgitant degree during valve closure and leakage. The regurgitant fraction (RF) is calculated by (Zhu et al., 2019).

$$\text{RF} = \frac{V_R + V_L}{V_F} \times 100\%, \quad (17)$$

in which  $V_F$  is the forward volume,  $V_R$  is the regurgitant volume during the valve closing, and  $V_L$  is the leakage volume after the AV closes.

The mean transvalvular pressure gradient (TPG) measures the potential energy loss when the blood flows through the AV. The smaller the TPG, the smaller the potential energy loss (Yoganathan et al., 2004). The mean transvalvular pressure gradient during the systolic phase is calculated as

$$\text{TPG} = \frac{\int_{t_{bs}}^{t_{es}} (P_{nlv} - P_{nao}) dt}{t_{es} - t_{bs}}, \quad (18)$$

in which  $P_{nlv}$  and  $P_{nao}$  are the pressures near the leaflets at the left ventricular and the aortic sides as shown in **Figure 1**, and  $t_{bs}$  and  $t_{es}$  are the beginning and end of systole as indicated in **Figure 4**.

To evaluate the impedance of the AV, the effective orifice area (EOA) is introduced as follows (Zhu et al., 2019):

$$\text{EOA} = \frac{Q_{rms}}{51.6\sqrt{\Delta P/\rho}}, \quad (19)$$

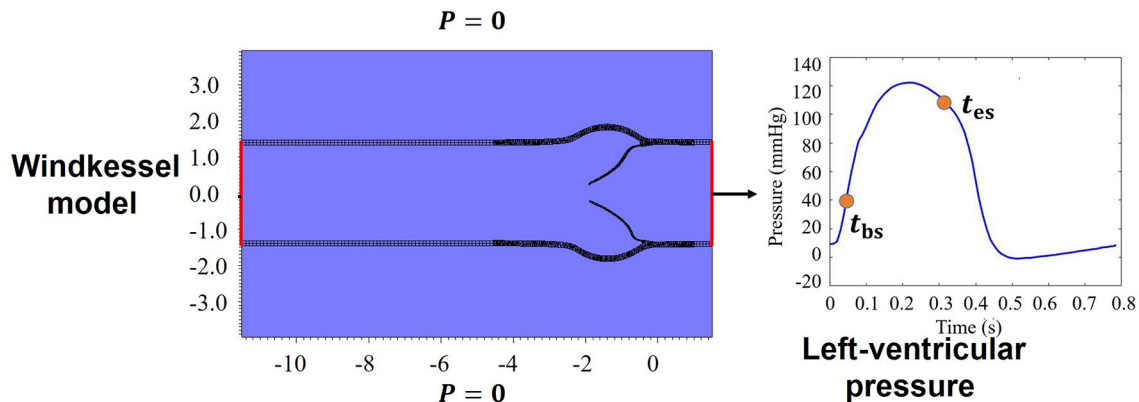


**FIGURE 4** | Boundary conditions for the aortic valve (AV) model.

$$Q_{\text{rms}} = \sqrt{\frac{\int_{t_{\text{bs}}}^{t_{\text{es}}} Q(t)^2 dt}{t_{\text{es}} - t_{\text{bs}}}}, \quad (20)$$

where  $Q(t)$  is the flow rate through the AV during the systolic phase at the center of the AV orifice as shown in **Figure 1**,  $Q_{\text{rms}}$  is the root mean square volumetric flow rate, and  $\Delta P$  is the mean systolic transvalvular pressure gradient.

The energy loss of the LV (Zhu et al., 2017) is

$$E_L = 0.1333 \int_{t_1}^{t_2} \Delta p(t) Q(t) dt, \quad (21)$$

where  $t_1$ – $t_2$  is the duration of one cardiac cycle,  $\Delta p = P_{\text{Ao}} - P_{\text{LV}}$  is the aorta-left ventricular pressure difference,  $P_{\text{LV}}$  and  $P_{\text{Ao}}$  are the pressures at the center of the inlet and the outlet as shown in **Figure 1**, and  $Q(t)$  is the corresponding flow rate through the AV.

## 2.7. Summary of Simulated Cases

We simulate the AV dynamics with three different constitutive laws (W1, W2, and W3) and two different fiber architectures (FD1 and FD2), and all cases are denoted as W1FD1, W2FD1, W3FD1, W1FD2, W2FD2, and W3FD2. Cases W1FD1, W2FD1, and W3FD1 correspond to three different constitutive laws with the fiber architecture FD1, whereas cases W1FD2, W2FD2, and W3FD2 correspond to three different constitutive laws with the fiber architecture FD2. We perform the FSI simulations over two cardiac cycles to reach periodic convergence at the second period and onward, and one period lasts 0.8 s. Results are reported from the second period.

## 3. RESULTS

### 3.1. The Experimental Fitting

The inferred constitutive parameters of three different constitutive laws (Equations 10–12) from the *ex vivo* porcine experiments are listed in **Table 1**.

From **Table 1**, we observe that the constitutive law W1 has the best agreement when fitting to the stretch–stress data from the porcine AV experiments, with the smallest error and

**TABLE 1** | Fitted parameters for the three selected constitutive laws [Equations (10)–(12)].

	Parameters				Average error (kPa)	Average R-squared
	$C_{10}$ (kPa)	$C_{01}$	$k_1$ (kPa)	$k_2$		
W1	1.21	7.99	24.23	57.62	$0.7 \pm 0.63$	0.99
	$\mu$ (kPa)	$c_0$ (kPa)	$c_1$	$c_2$		
W2	1.18	55.04	8.08	54.00	$0.75 \pm 0.92$	0.96
	$C_1$ (kPa)	$a$ (kPa)	$b$			
W3	19.59	12.94	77.79		$1.72 \pm 2.71$	0.93

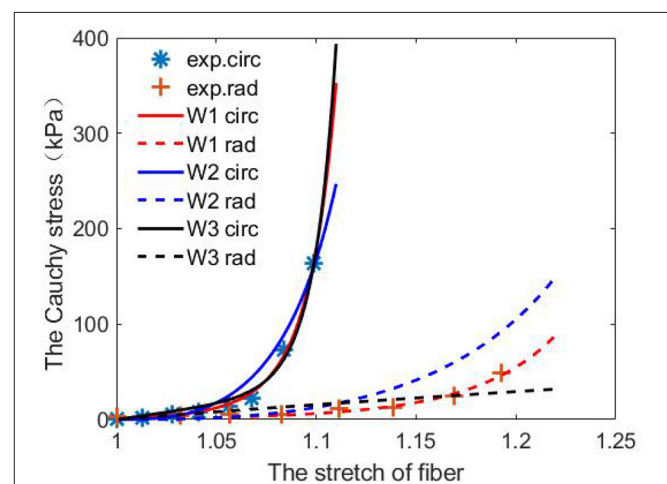


**FIGURE 5** | Predictions from the fitted three constitutive laws [Equations (10)–(12)] using one set of porcine experimental data.

highest R-squared score. While the constitutive law W3 is the poorest because of its incapability of describing the non-linear response along the cross-fiber direction. **Figure 5** shows the fitted curves from the three constitutive laws compared to the porcine experimental data.

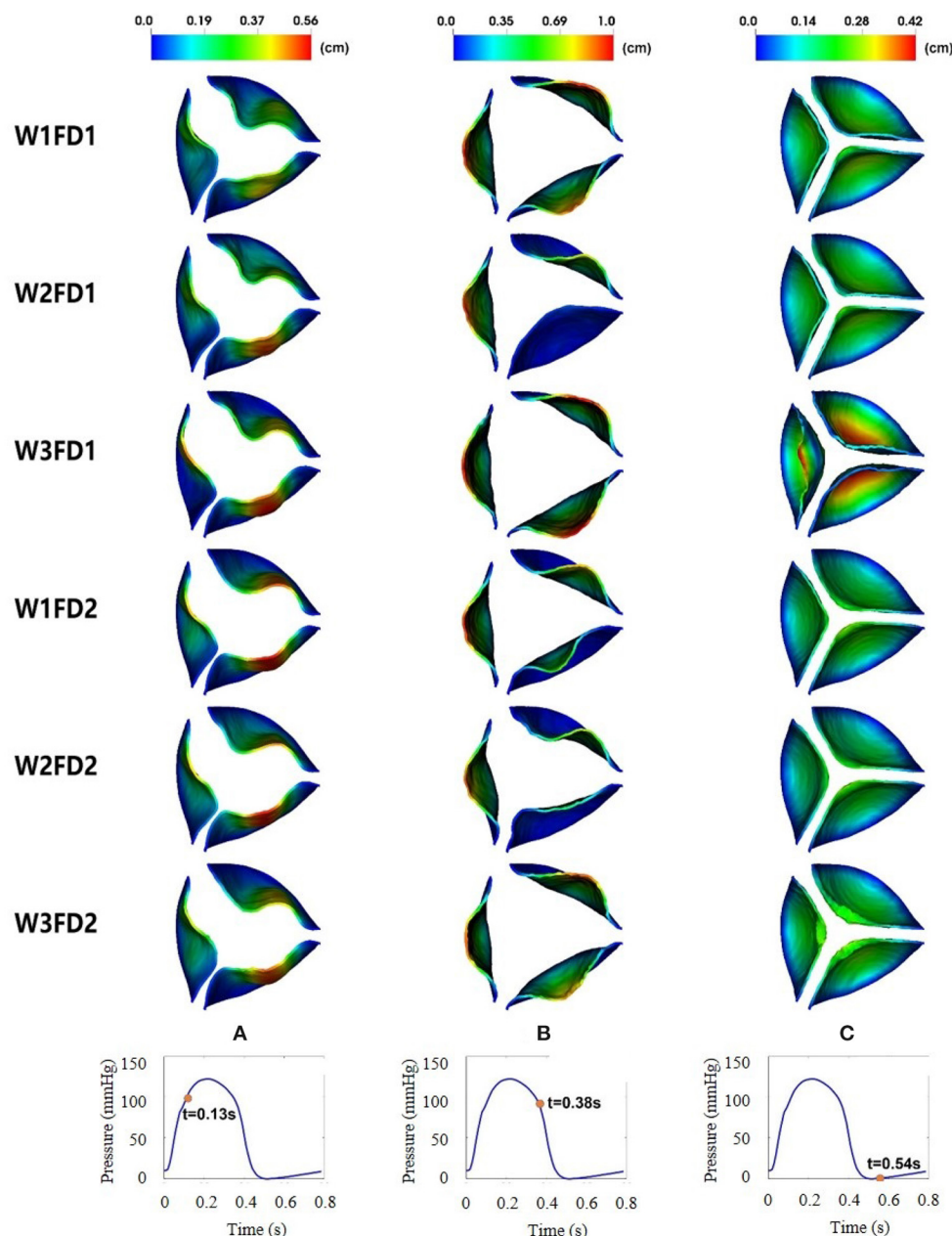


**FIGURE 6 |** Dynamic deformation of the AV leaflets for the six cases at different time. The time points from left to right are 0.13 (A), 0.38 (B), and 0.54 s (C).

### 3.2. AV Opening and Closure

**Figure 6** shows the leaflets deformation of the AV from six cases within one cardiac cycle. At  $t = 0.13$  s, the leaflet's deformation is similar for all six cases, especially the leaflet orifice area. At  $t = 0.38$  s, the AV leaflets start to close and the closure inconsistency can be seen, especially in cases W2FD1, W1FD2, and W2FD2. Compared with other cases, the AV leaflets in case W2FD1 are the first to close, which may relate to the smallest orifice area of  $1.19 \text{ cm}^2$  at  $t = 0.38$  s. At  $t = 0.54$  s, the AV leaflets are at the fully closed state, with case W3FD1 of the

largest displacements in the belly regions and the free edges of the leaflets.

**Table 2** shows the average and maximum displacements of the AV from different cases at fully opened (0.18 s), pre-close (0.38 s), and fully closed (0.54 s) states during one cardiac cycle. When the AV is at the fully opened and pre-close states, the maximum displacements from case W3FD1 are slightly larger than those from other cases, reaching around 1.05 cm. This may be because case W3FD1 has the largest orifice area of  $2.27 \text{ cm}^2$  at the fully opened state and the largest orifice area of  $2.01 \text{ cm}^2$  at

**TABLE 2 |** Average and maximum displacements of AV with six different cases.

Cases	Average displacement (cm)			Maximum displacement (cm)		
	Fully opened	Pre-close	Fully closed	Fully opened	Pre-close	Fully closed
W1FD1	0.039	0.031	0.017	0.994	0.997	0.305
W2FD1	0.036	0.022	0.017	0.939	0.982	0.269
W3FD1	0.039	0.036	0.021	0.999	1.046	0.429
W1FD2	0.038	0.024	0.016	0.990	0.991	0.291
W2FD2	0.035	0.022	0.015	0.975	0.937	0.284
W3FD2	0.038	0.028	0.017	0.960	0.946	0.312

**TABLE 3 |** The lasting time of different stages for the six cases (second).

	W1FD1	W2FD1	W3FD1	W1FD2	W2FD2	W3FD2
Opening	0.09	0.1	0.09	0.1	0.09	0.095
Fully opened	0.15	0.125	0.15	0.14	0.145	0.15
Closing	0.16	0.175	0.2	0.165	0.165	0.16

the pre-close state. Both cases W1FD1 and W1FD2 have larger maximum displacements compared with other cases when the AV is at the fully opened and pre-close states. At the pre-close state, the cases with FD1 have a larger maximum displacement than the cases with FD2 in general, which could be due to the larger orifice area of the cases with FD1. For example, the orifice area of case W1FD1 (1.92 cm<sup>2</sup>) is slightly larger than that of case W1FD2 (1.52 cm<sup>2</sup>). Compared with other constitutive laws, W2 has the smallest leaflets and displacements at the fully opened and pre-close states, which may suggest poor leaflet mobility at both opening and closing.

**Table 3** shows the duration of different stages for the six cases. Here, the opening time is the duration from pre-open to fully opened states, the fully opened time is the duration from fully opened to pre-close states, and the closing time represents the duration from pre-close to fully closed states. The opening time for the six cases is similar, which is around 0.1 s. The fully opened state of six cases lasts about 0.14 s, with case W2FD1 having the shortest duration of 0.125 s. During the closure phase, the duration of the case W3FD1 reaches the longest (0.2 s), which could indicate poor leaflet mobility during closing (Zhu et al., 2019).

### 3.3. The Flow Pattern Comparison

In this section, we compare the flow patterns of the AV from six cases. **Figure 7** plots the fluid velocity field. When the AV starts to open, the blood gradually flows from the LV to the aorta. As the AV fully opens, there is a flow jet surging into the aorta. At the fully opened state, there exists a stronger jet flow in cases W1FD1 and W2FD1. At the just-closed state, there exists some regurgitant flow to facilitate the closure action, and case W3FD1 has the largest regurgitant flow. Comparing two different fiber architectures, the forward jet flow toward the aorta in cases with FD1 seems to be stronger than that of the cases with FD2. Similar results can be found for the regurgitant flow. On the other hand,

cases with W1 and W2 have larger forward jet flow than the cases with W3, while W3 associates with the largest regurgitant flow.

**Table 4** summarizes the peak blood velocity at the fully opened and just-closed states. When the AV fully opens, the peak velocities are from 2.0 to 3.0 m/s, consistent with the simulated flow velocity in Lee's study (Lee et al., 2020a). Compared with other cases, W1FD1 and W2FD1 have a larger peak velocity at the fully opened state. At the just-closed state, the peak regurgitation velocity of case W3FD1 reaches the largest 6.7 m/s. Except for the cases with W3, the peak forward velocity in cases with FD1 is slightly larger than that cases with FD2. Compared with other constitutive laws, cases with W3 experience the largest peak regurgitation velocity, which can be explained by the much longer closure duration.

**Figure 8** shows the flow rates through the AV for the six different cases in one cardiac cycle. As the AV opens gradually, the blood flow ejects into the aorta driven by the fast increased LV pressure. Case W1FD1 experiences the largest peak flow rate of 574.05 mL/s and the largest forward volume 94.85 mL, which are slightly higher than the experimental data (Zhu et al., 2019; Lee et al., 2020a). Besides, the AV with FD1 generates a larger forward volume than that with FD2, for example, case W1FD1 can achieve 94.85 mL forward volume, higher than the value for W1FD2 (78.81 mL). During the closure, there exists a small regurgitant flow, with case W3FD1 generating the largest peak regurgitant flow rate 300.99 mL/s and the largest regurgitant volume 9.45 mL. Moreover, the regurgitant volume of the AV with FD1 is slightly larger than that with FD2, for example, the regurgitant volume of case W1FD1 (5.29 mL) is larger than case W1FD2 (3.09 mL). W1 has a slightly larger regurgitant volume than W2 in general. For example, the regurgitant volume of case W1FD1 (5.29 mL) is larger than case W2FD1 (3.07 mL). After the closure, case W3FD2 experiences the largest leakage volume 10.22 mL, which is beyond the reference value 2.81 mL. In summary, the cases with W1 have the largest peak forward flow rate and forward volume with a smaller peak regurgitant flow rate and a smaller regurgitant volume. While the cases with W3 have the largest peak flow rate of regurgitant flow and the largest regurgitant volume and the largest leakage volume. For the two different fiber architectures, the cases with FD1 have higher values in the peak forward flow rate and the forward volume than the cases with FD2. Furthermore, the oscillated flow rate after the AV closure is because of the FSI dynamics, which also appears in the MV simulations (Gao et al., 2014; Cai et al., 2019) and the



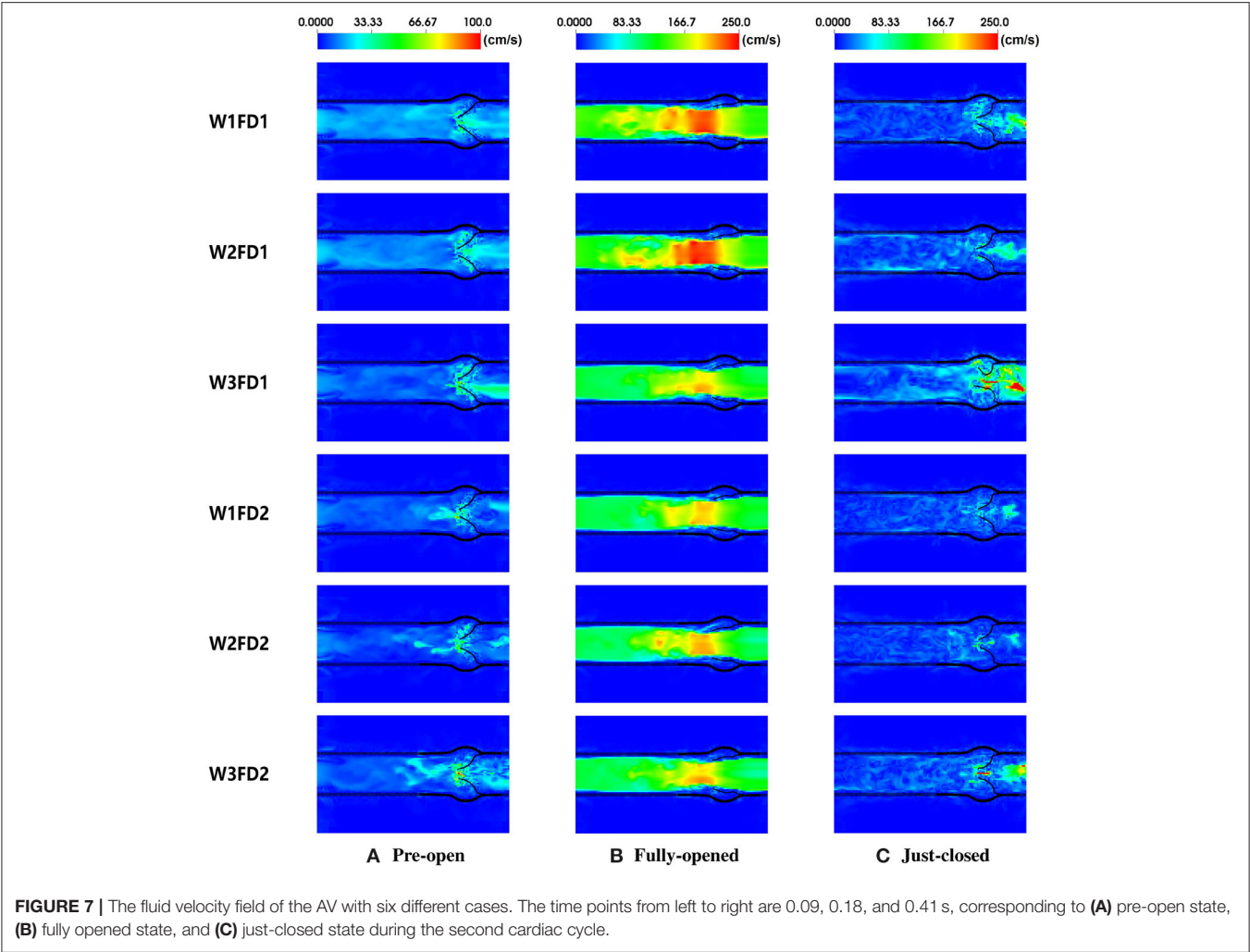


**TABLE 4 |** Peak velocity of transvalvular flow for the six cases.

Cases	Peak velocity of flow field (m/s)	
	Fully opened	Just-closed
W1FD1	2.47	2.47
W2FD1	2.57	2.00
W3FD1	2.17	6.74
W1FD2	2.14	2.20
W2FD2	2.26	3.52
W3FD2	2.21	3.65

AV simulations (Hasan et al., 2017; Lee et al., 2020a). In fact, the first peak regurgitate flow is the closure flow, which has been measured in the clinic (Hasan et al., 2017).

3.4. Strain and Stress Distributions

The fiber strain is defined as  $\mathbf{f}_0 \cdot (\mathbf{E} \cdot \mathbf{f}_0)$ , in which  $\mathbf{E} = \frac{1}{2}(\mathbb{F}^T \mathbb{F} - \mathbb{I})$  is the Green strain tensor. The fiber stress is defined as  $\mathbf{f} \cdot (\boldsymbol{\sigma} \cdot \mathbf{f})$ , in which  $\boldsymbol{\sigma}$  is the Cauchy stress tensor. The fiber

strain distributions for the six cases are shown in Figure 9. At the fully opened state, a large sporadic strain concentrates on the belly regions and the edges of the leaflets connected to the aortic wall. When the AV is at the fully closed state, the strain level of the entire leaflets reaches the largest, with case W3FD1 of the smallest strain distributional regions. Comparing two different fiber architectures, the AV with FD1 has a smaller compressed region than that with FD2 at the fully opened state. Besides, the AV with W1 shows a larger strain level of the belly region at the fully closed state. We further select two different regions of the AV leaflet, which are labeled as the belly region and the top-center region, as shown in Figure 10. Here, the belly region is defined as a circular region with the center at  $(-0.44, -0.64, -0.77)$  and a radius of 0.15 cm, and the top-center region with the center at  $(-0.19, -0.14, -1.76)$  and a radius of 0.15 cm. The average strain values of two different regions can be found in Table 5. When the leaflets are fully opened, all cases have negative strain values in the belly and top-center regions. When the leaflets are fully closed, the cases with W1 have the largest strain value in the belly and the top-center regions.

The average stresses of the two selected regions are listed in **Table 6**. At the open state, the average stresses of the two regions are negative that is because of compression, in which the cases with FD2 have the larger compressed stress level than FD1 in the top-center region, while the cases with W2 have the largest compressed stress level in the belly region. Moreover, at the closed state, the cases with FD1 have a larger stress level in the

belly region than that in the top-center region; on the contrary, the cases with FD2 experience a much larger stress level in the top-center region than that in the belly region. The previously published studies (Hasan et al., 2017; Lee et al., 2020a) have revealed that the fiber stress mainly concentrates on the belly region at the closed state, consistent with the stress distribution in the cases with FD1. Besides, the stress level of our AV is within a reasonable range compared with the reported stress levels in previous studies, for example, 150 kPa in Hasan et al. (2017) and the maximum stress level of the belly region 435 kPa in Sulejmani et al. (2019). Therefore, the stress distribution of FD1

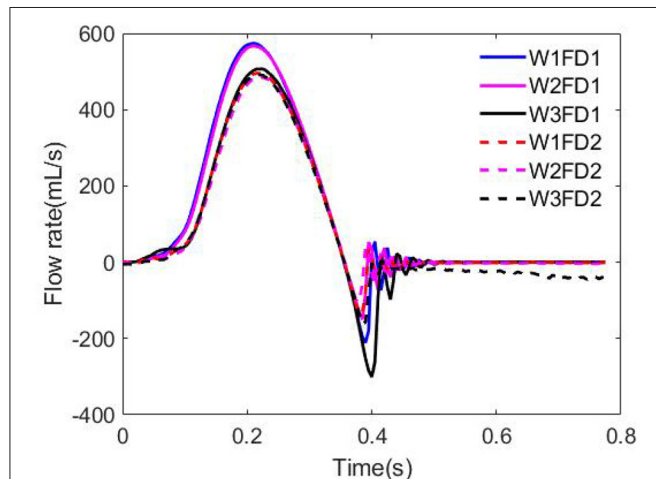


**FIGURE 8** | Flow rate comparison for the six cases.

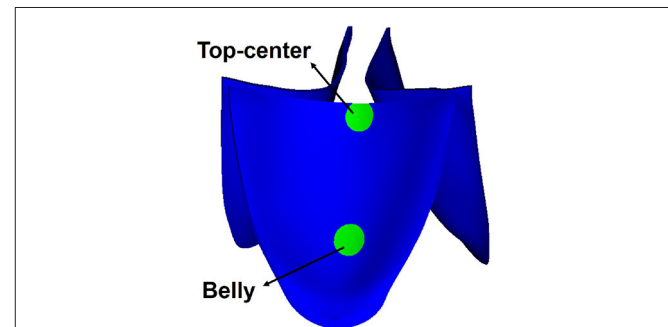


**FIGURE 10** | Two labeled regions of the aortic valve (AV) leaflet.

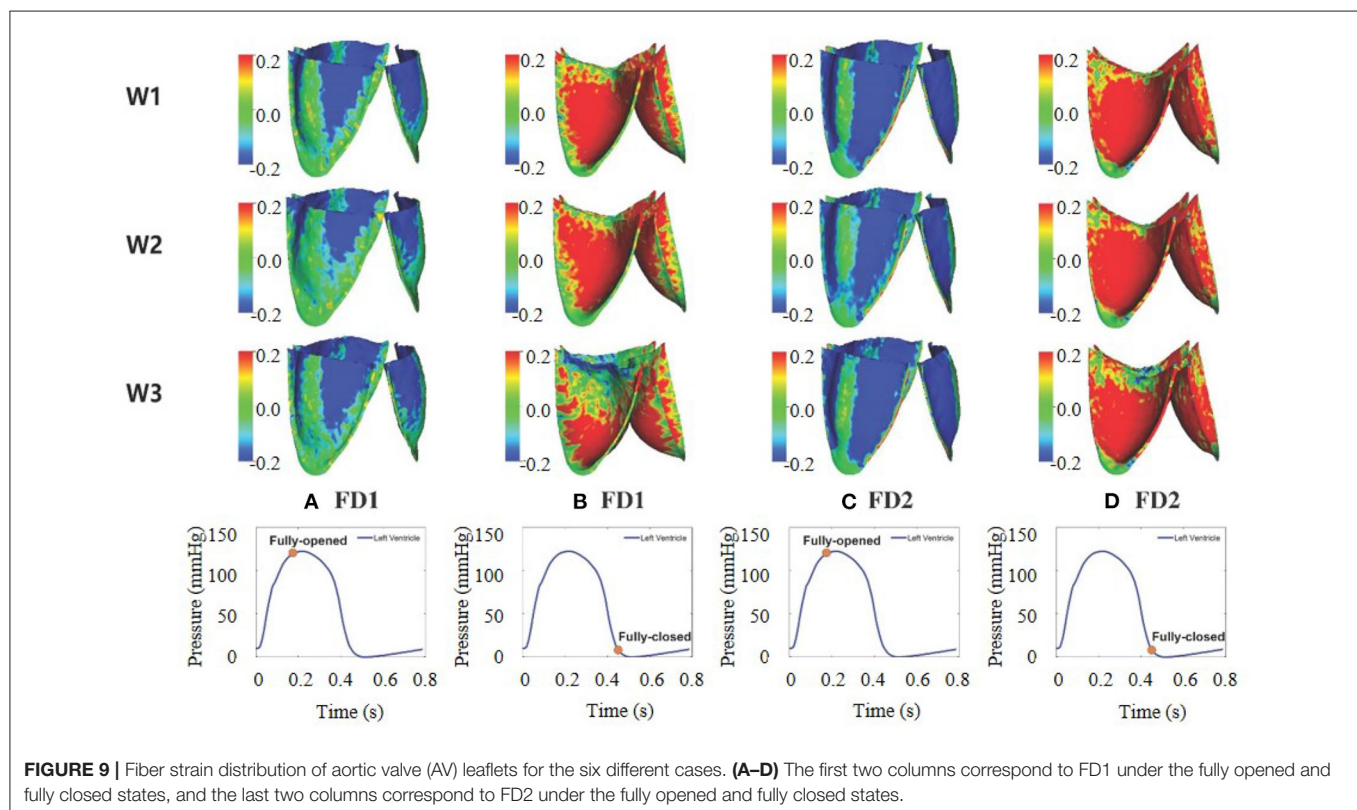


**FIGURE 9** | Fiber strain distribution of aortic valve (AV) leaflets for the six different cases. (A–D) The first two columns correspond to FD1 under the fully opened and fully closed states, and the last two columns correspond to FD2 under the fully opened and fully closed states.

**TABLE 5** | Average fiber strain of aortic valve (AV) with six different cases.

Cases	Average fiber strain			
	Fully opened		Fully closed	
	Belly	Top-center	Belly	Top-center
W1FD1	−0.03	−0.06	0.32	0.10
W2FD1	−0.06	−0.06	0.25	0.07
W3FD1	−0.05	−0.11	0.27	−0.04
W1FD2	−0.13	−0.08	0.31	0.14
W2FD2	−0.14	−0.07	0.28	0.13
W3FD2	−0.10	−0.13	0.30	−0.01

**TABLE 6** | Average fiber stress at the belly and top-center.

Cases	Average fiber stress (kPa)			
	$t = 0.32$ s (open state)		$t = 0.47$ s (closed state)	
	Belly	Top-center	Belly	Top-center
W1FD1	−36	−25	336	178
W2FD1	−41	−62	376	135
W3FD1	−22	−42	330	−4
W1FD2	−32	−48	309	480
W2FD2	−42	−92	295	555
W3FD2	−21	−43	262	54

seems to be consistent with the stress distribution of previous studies (Aggarwal et al., 2013; Hasan et al., 2017).

### 3.5. Hemodynamic Parameter Comparison

Table 7 is the comparison of the hemodynamic parameters within the six cases. Here, we further present measurements from a tri-leaflet ePTFE valve (Zhu et al., 2019), from which this computational AV model is derived.

The least RF can be found for the cases using the constitutive law W2, while the cases with W3 have significantly higher RF, but interestingly closer to the measured values (14.37) (Zhu et al., 2019). The TPG values for all cases are much lower than the reference value 9.89 mm Hg, and the highest value is found in W2FD1 (5.91 mm Hg) with the lowest in W3FD1. Except for W3, the TPG values in cases with FD2 are lower than the values with FD1. Compared with other constitutive laws, the two cases of W2 have larger TPG in systole, suggesting a higher transvalvular potential energy loss with W2. The simulated EOA values are slightly higher than the reference value  $2.86 \text{ cm}^2$  from Zhu et al. (2019), the largest EOA is found in case W3FD1, suggesting the least resistance for blood flow. As for  $E_L$ , the cases with FD1 have similar energy loss as the reported reference value (129.03 mJ), while  $E_L$  varies significantly for the cases with FD2 with the least energy loss for W1FD2 and the most energy loss for W3FD2.

### 3.6. Model Comparison and Selection

To select an appropriate constitutive law for the AV dynamics, we now propose a weighting scheme for the results from the *ex vivo* fitting, to the flow patterns, to the valvular

strain/stress, and to the hemodynamic factor as shown in Table 8. For each selected criterion, we set the best value to be 1, and the worst value to be 0, respectively. Then we project each simulated result into the interval [0, 1]. By summing all values together for each case, we can rank the six cases from the most appropriate one to the poorest one. Specifically, the selected results and the corresponding criteria are as follows

- *Ex vivo fitting*: The least error suggests the best fitting of a constitutive law to experiments, we set the least error to be 1, and the largest error to be 0.
- *Opening orifice*: The opening orifice relates to the obstruction to blood flow, and the larger the opening orifice, the less obstruction to the blood flow. Thus, we consider the largest opening orifice area to be 1 and the smallest value to be 0.
- *Duration of AV opening*: As discussed in Zhu et al. (2019), the shorter the duration of AV opening, the better the leaflet mobility. In this aspect, we set the shortest duration of AV opening (0.09 s) to be 1, and the longest duration (0.1 s) to be 0.
- *Duration of AV closing*: Similar to the duration of AV opening, the shorter the duration of AV closing, the better the leaflet mobility. Thus, we set the shortest duration of AV closing (0.16 s) to be 1, and the longest duration of AV closing (0.2 s) to be 0.
- *The forward flow*: Generally, the large forward flow means a large stroke volume (Murgu et al., 1980). Thus, we set the largest forward volume to be 1, and the smallest value to be 0.
- *Regurgitation flow*: A small regurgitation flow will suggest the AV can close swiftly. To this end, we consider the smallest value to be 1, and the largest value to be 0.
- *Strain variation*: We consider a homogeneous strain distribution with small variation will be close to the physiological homeostasis (Kassab, 2008), and a smaller strain variation represents a higher degree of strain homogeneity. In this study, the strain variation is defined as the fiber strain difference between the belly and the top-center area at the fully closed state. For example, the strain variation of case W1FD1 can be calculated by  $0.32 - 0.10 = 0.22$ . Then, we set 1 for the smallest strain variation and 0 for the largest strain variation.
- *Stress variation*: Similar to the strain variation, the stress variation is defined as the fiber stress difference between the belly and the top-center area at the closed state. Again, 1 for the smallest stress variation and 0 for the largest variation.
- *RF*: Similar to the *regurgitation volume*, we set 1 for the least value and 0 for the largest value.
- *TPG*: It relates to the flow potential energy losses when the blood flows through the AV (Yoganathan et al., 2004), thus we consider the smaller the TPG, the better performance of the AV dynamics.
- *EOA*: It is considered to be similar to the opening orifice.
- $E_L$ : The energy loss of the LV is also an important factor for assessing the AV performance (Zhu et al., 2019), in this aspect, we set the smallest  $E_L$  (82.95 mJ) to be 1.

**TABLE 7 |** The simulated hemodynamic parameters.

Parameter	W1FD1	W2FD1	W3FD1	W1FD2	W2FD2	W3FD2	Reference AV (Zhu et al., 2019)
RF (%)	6.73	4.47	13.67	5.22	4.90	18.16	14.37
TPG (mm Hg)	4.69	5.91	2.28	3.19	4.32	3.66	9.89
EOA (cm <sup>2</sup> )	3.41	3.00	4.25	3.51	2.95	3.25	2.86
E <sub>L</sub> (mJ)	107.04	106.73	110.79	82.95	92.92	200.69	129.03

**TABLE 8 |** Comparison of simulated results with scaled values.

	W1FD1	W2FD1	W3FD1	W1FD2	W2FD2	W3FD2
<i>Ex-vivo</i> fitting	1	0.95	0	1	0.95	0
Opening orifice	0.72	0	1	0.92	0.96	0.56
Duration of AV opening	1	0	1	0	1	0.5
Duration of AV closing	1	0.63	0	0.88	0.88	1
Forward flow	1	0.92	0.23	0.10	0	0.06
Regurgitation flow	0.56	0.86	0	0.86	1	0.74
Strain variation	0.56	0.81	0	0.88	1	0
Stress variation	1	0.53	0	0.93	0.42	0.72
RF	0.83	1	0.33	0.95	0.97	0
TPG	0.34	0	1	0.75	0.44	0.62
EOA	0.35	0.04	1	0.43	0	0.23
E <sub>L</sub>	0.8	0.8	0.76	1	0.92	0
Total	9.16	6.54	5.32	8.7	8.54	4.43

**Table 8** summarizes the weighting scores for the above 12 selected factors, with the total score in the last row. The rank for the six cases from the most appropriate one to the poorest one is

{W1FD1, W1FD2, W2FD2, W2FD1, W3FD1, W3FD2}.

Case W1FD1 seems to be the best choice for modeling AV dynamics within the considered six cases, with non-linear anisotropic responses in the fiber and cross-fiber direction and a fully body-fitted fiber structure. The constitutive law W3 seems to perform poorest due to its linear response along the cross-fiber direction. In summary, the constitutive law W1 could be a good choice for modeling AV mechanical behaviors, and a fully body-fitted collagen fiber architecture is marginally better than using a simplified circumferentially aligned fiber architecture.

## 4. DISCUSSION

In this study, we have used the IB/FE method to perform the FSI simulations of AV dynamics with three different constitutive laws and two different fiber architectures. The constitutive parameters of three different constitutive laws are first inferred from the experimentally measured stretch–stress data, which were from the *ex vivo* biaxial testing of three different porcine AV samples. By comparing the average errors and the average R-squared values, we observe that W1 is the most suitable constitutive law to describe the mechanical behaviors of those *ex vivo* AV

leaflet samples. The simulation results also demonstrate that the constitutive law W1 has the larger leaflets displacements at the fully opened and pre-close states, the shorter duration for opening and closing, the largest peak forward flow rate, the largest forward volume, and the smaller regurgitant volume. The combination of the anisotropic non-linear constitutive law (W1) using exponential terms for both the fiber and cross-fiber directions and the fiber architecture with body-fitted orientation (FD1) has the shortest duration for AV opening and closing, the largest forward flow, the smallest stress variation, the less RF, and the smaller energy loss of the LV. Thus, our study seems to suggest that the constitutive law W1FD1 could be the most suitable model for simulating AV dynamics.

**Figure 6** shows the dynamic deformation of the AV leaflets from six different cases. During the AV opening, the leaflet deformation is similar for the six cases, with a similar orifice shape at  $t = 0.13$  s. Besides, the duration of AV opening is around 0.1 s, which is in good agreement with the value from Zhu's study (Zhu et al., 2019). During the AV closure, the closure inconsistency exists, which may relate to the AV model itself since it was reconstructed from the porcine pericardial valve. A similar phenomenon also appears in the bovine pericardial valve reported by Lee et al. (2020a). The duration of AV closure from the six cases is around 0.16 s, which is comparable to the value (0.14 s) reported by Zhu et al. (2019).

**Figure 7** shows the fluid velocity fields of the AV. At the fully opened state, the peak velocity of the fluid field is within 2.0–3.0 m/s, which is in good agreement with the cross-sectional velocity fields reported in the previous studies (Flamini et al., 2016; Lee et al., 2020a). The peak forward flow rate is in a range from 480 to 580 mL/s, lower than the value 591.5 mL/s from Flamini's study (Flamini et al., 2016), but slightly higher than that of Lee's study (Lee et al., 2020a). The forward volume is within 75 to 95 mL, again slightly lower than the reported value 96.2 mL in Flamini's study (Flamini et al., 2016). At the just-closed state, the peak regurgitant velocity of the fluid field is slightly larger than the peak regurgitant velocity (less than 1.5 m/s) in Flamini et al. (2016); Lee et al. (2020a). The peak regurgitant flow rate is in reasonable agreement with the peak regurgitant flow rate (around 180 mL/s) compared to the value reported by Flamini et al. (2016).

Strain distributions of AV leaflets are shown in **Figure 9**. At the fully opened state, the AV leaflets experience some compression near the commissures, in which the AV with FD2 has more compressed regions than that with FD1. However, the compressed regions of the AV leaflets are much larger than those in Hasan's study (Hasan et al., 2017). While the



strain distributions under the fully closed state are similar to those in Hasan's study (Hasan et al., 2017), especially in case W1FD1 and case W2FD1. For the stress distribution, the stresses are sporadically distributed on the belly regions and the edges connected with the aortic wall, different from Lee's study (Lee et al., 2020a). When the AV is at the fully closed state, the stresses are distributed symmetrically from commissure to commissure for both FD1 and FD2. At the fully closed state, the AV with FD1 experiences higher fiber stresses in the belly region of the leaflet, whereas the AV with FD2 (case W1FD2 and W2FD2) experiences higher fiber stresses in the top-center of the leaflet, which is caused by the large deformation of the top-center region.

Valvular morphology (three-leaflets or two-leaflets), size (aortic root diameter, leaflet area), geometrical shape (curvatures, thickness), and pathological state (calcification, etc.) can vary significantly among subjects, and those variations will have a significant impact on the AV dynamics and the corresponding flow patterns (Xiong et al., 2010; Zhu et al., 2020). The current study mainly focuses on the effects of different constitutive laws and different fiber architectures on the AV dynamic characteristics and the associated flow quantities, but not aims to simulate personalized AV dynamics. Therefore, an idealized healthy AV model is constructed based on the population-average anatomical measurements. A further limitation is the idealized aortic root. Studies (Flamini et al., 2016; Hasan et al., 2017) have shown that a personalized aorta will affect the blood flow, especially the flow jet across the AV, this would further affect the AV dynamics, such as the closure. For example, Flamini et al. (2016) have found that the aortic root can ensure a more efficient AV closure when using an elastic aortic root. Built on the same IB/FE framework, Hasan et al. (2017) studied the AV dynamics within an anatomically realistic aortic root and ascending aorta, and both were reconstructed from computed tomography angiography data; they found that their AV model can support a physiological diastolic pressure load without regurgitation, and it is able to accurately capture the leaflet biomechanics. Note that the present IB/FE approach can handle personalized AV models by simply replacing the idealized AV model, while it is challenging to reconstruct a personalized AV model from *in vivo* imaging data (Hasan et al., 2017), especially the collagen fiber structure.

In this study, a simplified 3-element Windkessel model is used for providing physiologically accurate pressure boundary conditions at the outlet. Although this 3-element Windkessel model has limitations to predict spatially distributed flow quantities, it is simple and accurate to predict the ventricular after-load as discussed by Westerhof et al. (2008). There are many blood flow models ranging from the zero-dimensional models (lumped-parameter models) (Liu et al., 2020), the one-dimensional models (Olufsen et al., 2000; Chen et al., 2016; Duanmu et al., 2019), and the three-dimensional models (Lee et al., 2016). Interested reader can refer to Shi et al. (2011); Morris et al. (2016) for reviews on blood flow modeling. Because of its simplicity, the lumped parameter models are still widely used to simulate the arterial hemodynamics (Westerhof et al., 2008; Fan et al., 2020). For example, Fan et al. (2020) constructed a closed-loop lumped parameter model including the LV, the

systemic, and coronary circulations to describe the interactions between the LV and the coronary perfusion. As mentioned before, the lumped parameter model cannot assess the spatially distributed phenomena and wave propagation, being unable to capture the wave oscillations. To overcome those limitations, one-dimensional (1-D) models have been developed by taking into account geometrical measurements. For example, Chen et al. (2016) reported a coupled LV-systemic arteries model to study the effects of the arterial wall stiffness and vascular rarefaction on ventricular function. Using a similar 1-D arterial model, Duanmu et al. (2019) studied the coupling between the LV and the coronary blood flow. In this study, we do not intend to simulate patient-specific AV dynamics with detailed flow predictions in the systemic circulation, thus a 3-element Windkessel model is used. It is worth mentioning that this 3-element Windkessel model can be easily replaced by either other complex lumped parameter models or patient-specific 1-D/3-D blood flow models.

The blood flow around healthy valves is usually assumed to be laminar flow (Stijnen et al., 2004; Morbiducci et al., 2013; Wu et al., 2016; Pirola et al., 2018; Luraghi et al., 2019), while in the presence of diseased heart valves (obstructive and regurgitant valvular lesions) or prosthetic heart valves, the transition to turbulence exists (Stupak et al., 2017; Lee et al., 2020a). As suggested in Wei et al. (2018), individualized evaluations of turbulence may be needed. Turbulent models have been used in the simulations of blood flow around prosthetic AVs (Stupak et al., 2017), including direct numerical simulation (DNS), large eddy simulation (LES), and Reynolds-averaged Navier–Stokes (RANS). The turbulent model has not been employed in our AV simulations and other studies (Hasan et al., 2017; Lee et al., 2020a) using the same immersed boundary framework because explicit turbulent models have not yet been completely implemented in the present IB/FE approach. As discussed in Lee et al. (2020a), the current approach may be considered as an implicit large-eddy simulation with high-resolution slope limiters based on the piecewise parabolic method. Because of the need for fine temporal and spatial discretization, and tremendous computational cost to capture small-scale turbulent flow features in the present approach, therefore, local flow features are not reported in the present study, but more on the average flow quantities, such as flow rate, pressure, and so on. Further limitations include (1) the biaxial tests were conducted in porcine AV samples, but not from human AV leaflets; (2) personalized human AV model is not used in this study; and (3) a typical LV pressure profile is used, but not from a realistic human heart model Chen et al. (2016); Gao et al. (2017a).

## 5. CONCLUSION

In this study, we construct an idealized AV model coupled with a three-element Windkessel model. Three different anisotropic hyperelastic material models and two different symmetric fiber architectures are used for modeling the AV leaflet mechanics. By using the IB/FE method, FSI simulations of six different cases are performed in this study. Our results are in reasonable agreement with the previous

experimental and numerical studies of AV dynamics, especially the hemodynamic performance. Finally, the comparison shows that the combination of an anisotropic non-linear constitutive law using exponential terms for both the fiber and cross-fiber directions and the fiber architecture with body-fitted orientation could be suitable for characterizing the AV dynamics and its hemodynamic performance. Although there exist some limitations, our results provide references for selecting a proper material model and fiber architecture for FSI modeling of the AV dynamics.

## DATA AVAILABILITY STATEMENT

The original contributions presented in the study are included in the article/Supplementary Material, further inquiries can be directed to the corresponding author/s.

## ETHICS STATEMENT

Ethical review and approval was not required for the animal study because we performed the tensile testing experiments on post-mortem porcine AV samples from a domestic butcher house in Chongqing, thus ethical approval is not needed.

## REFERENCES

- Aggarwal, A., Aguilar, V., Lee, C.-H., Ferrari, G., Gorman, J. III, and Sacks, M. S. (2013). Patient-specific modeling of heart valves: from image to simulation. *Funct. Imaging Model. Heart.* 7945, 141–149. doi: 10.1007/978-3-642-38899-6\_17
- Black, M. M., Howard, I. C., Huang, X., and Patterson, E. A. (1991). A three-dimensional analysis of a bioprosthetic heart valve. *J. Biomech.* 24, 793–801. doi: 10.1016/0021-9290(91)90304-6
- Cai, L., Wang, Y., Gao, H., Ma, X., Zhu, G., Zhang, R., et al. (2019). Some effects of different constitutive laws on fsi simulation for the mitral valve. *Sci. Rep.* 9:12753. doi: 10.1038/s41598-019-49161-6
- Chen, S., Sari, C. R., Gao, H., Lei, Y., Segers, P., De Beule, M., et al. (2020). Mechanical and morphometric study of mitral valve chordae tendineae and related papillary muscle. *J. Mech. Behav. Biomed. Mater.* 111:104011. doi: 10.1016/j.jmbbm.2020.104011
- Chen, W., Gao, H., Luo, X., and Hill, N. (2016). Study of cardiovascular function using a coupled left ventricle and systemic circulation model. *J. Biomech.* 49, 2445–2454. doi: 10.1016/j.jbiomech.2016.03.009
- Chen, Y., and Luo, H. (2018). A computational study of the three-dimensional fluid-structure interaction of aortic valve. *J. Fluids Struct.* 80, 332–349. doi: 10.1016/j.jfluidstruct.2018.04.009
- Chew, G. G., Howard, I. C., and Patterson, E. A. (1999). Simulation of damage in a porcine prosthetic heart valve. *J. Med. Eng. Technol.* 23, 178–189. doi: 10.1080/030919099294131
- Chong, M., Eng, M., and Missirlis, Y. F. (1978). Aortic valve mechanics part II: a stress analysis of the porcine aortic valve leaflets in diastole. *Biomater. Med. Dev. Artif. Organs* 6, 225–244. doi: 10.3109/10731197809118703
- De Hart, J., Baaijens, F. P. T., Peters, G. W. M., and Schreurs, P. J. G. (2003a). A computational fluid-structure interaction analysis of a fiber-reinforced stentless aortic valve. *J. Biomech.* 36, 699–712. doi: 10.1016/S0021-9290(02)00448-7
- De Hart, J., Peters, G. W., Schreurs, P. J., and Baaijens, F. P. (2003b). A three-dimensional computational analysis of fluid-structure interaction in the aortic valve. *J. Biomech.* 36, 103–112. doi: 10.1016/S0021-9290(02)00244-0
- Duanmu, Z., Chen, W., Gao, H., Yang, X., Luo, X., and Hill, N. (2019). A one-dimensional hemodynamic model of the coronary arterial tree. *Front. Physiol.* 10:853. doi: 10.3389/fphys.2019.00853

## AUTHOR CONTRIBUTIONS

RZ and LC performed numerical modeling and wrote the manuscript. YL and GZ provided the computational AV model. XM conducted the *ex-vivo* experiments. YW assisted result analysis. HG critically reviewed the manuscript. LC, XL, and HG supervised the overall project. All authors analyzed the results, read, and edited the manuscript.

## FUNDING

This research was supported by the National Natural Science Foundation of China (Grant Nos. 11871399, 11471261, and 11571275) and the Natural Science Foundation of Shaanxi (Grant No. 2017JM1005). HG and XL are grateful for the funding provided by the UK EPSRC (EP/N014642/1, EP/S030875, EP/S020950/1, EP/S014284/1, EP/R511705/1).

## SUPPLEMENTARY MATERIAL

The Supplementary Material for this article can be found online at: <https://www.frontiersin.org/articles/10.3389/fphys.2021.682893/full#supplementary-material>

- Fan, L., Namani, R., Choy, J., Kassab, G., and Lee, L. C. (2020). Effects of mechanical dyssynchrony on coronary flow: insights from a computational model of coupled coronary perfusion with systemic circulation. *Front. Physiol.* 11:915. doi: 10.3389/fphys.2020.00915
- Fan, R., Bayoumi, A. S., Chen, P., Hobson, C. M., Wagner, W. R., Mayer, J. E., et al. (2013). Optimal elastomeric scaffold leaflet shape for pulmonary heart valve leaflet replacement. *J. Biomech.* 46, 662–669. doi: 10.1016/j.jbiomech.2012.11.046
- Feng, L., Gao, H., Griffith, B., Niederer, S., and Luo, X. (2019). Analysis of a coupled fluid-structure interaction model of the left atrium and mitral valve. *Int. J. Num. Methods Biomed. Eng.* 35:e3254. doi: 10.1002/cnm.3254
- Flamini, V., DeAnda, A., and Griffith, B. E. (2016). Immersed boundary-finite element model of fluid-structure interaction in the aortic root. *Theoret. Comput. Fluid Dyn.* 30, 139–164. doi: 10.1007/s00162-015-0374-5
- Franzone, A., Piccolo, R., Siontis George, C. M., Lanz, J., Stortecky, S., Praz, F., et al. (2016). Transcatheter aortic valve replacement for the treatment of pure native aortic valve regurgitation. *JACC Cardiovasc. Intervent.* 9, 2308–2317. doi: 10.1016/j.jcin.2016.08.049
- Gao, H., Feng, L., Qi, N., Berry, C., Griffith, B. E., and Luo, X. (2017a). A coupled mitral valve-left ventricle model with fluid-structure interaction. *Med. Eng. Phys.* 47, 128–136. doi: 10.1016/j.medengphy.2017.06.042
- Gao, H., Li, W. G., Cai, L., Berry, C., and Luo, X. Y. (2015). Parameter estimation in a Holzapfel-Ogden law for healthy myocardium. *J. Eng. Math.* 95, 231–248. doi: 10.1007/s10665-014-9740-3
- Gao, H., Ma, X., Qi, N., Berry, C., Griffith, B. E., and Luo, X. (2014). A finite strain nonlinear human mitral valve model with fluid-structure interaction. *Int. J. Num. Methods Biomed. Eng.* 30, 1597–1613. doi: 10.1002/cnm.2691
- Gao, H., Qi, N., Feng, L., Ma, X., Danton, M., Berry, C., et al. (2017b). Modelling mitral valvular dynamics-current trend and future directions. *Int. J. Num. Methods Biomed. Eng.* 33:e2858. doi: 10.1002/cnm.2858
- Go, A. S., Mozaffarian, D., Roger, V. L., Benjamin, E. J., Berry, J. D., Borden, W. B., et al. (2013). Heart disease and stroke statistics-2013 update. *Circulation* 127, e6–e245. doi: 10.1161/CIR.0b013e318282ab8f
- Gould, P. L., Cataloglu, A., Dhatt, G., Chattopadhyay, A., and Clark, R. E. (1973). Stress analysis of the human aortic valve. *Comput. Struct.* 3:377–384. doi: 10.1016/0045-7949(73)90024-2

- Griffith, B. E. (2012). Immersed boundary model of aortic heart valve dynamics with physiological driving and loading conditions. *Int. J. Num. Methods Biomed. Eng.* 28, 317–345. doi: 10.1002/cnm.1445
- Griffith, B. E., and Luo, X. (2017). Hybrid finite difference/finite element immersed boundary method. *Int. J. Num. Methods Biomed. Eng.* 33:e2888. doi: 10.1002/cnm.2888
- Griffith, B. E., Luo, X., McQueen, D. M., and Peskin, C. S. (2009). Simulating the fluid dynamics of natural and prosthetic heart valves using the immersed boundary method. *Int. J. Appl. Mech.* 01, 137–177. doi: 10.1142/S1758825109000113
- Guan, D., Yao, J., Luo, X., and Gao, H. (2020). Effect of myofibre architecture on ventricular pump function by using a neonatal porcine heart model: from dt-mri to rule-based methods. *R. Soc. Open Sci.* 7:191655. doi: 10.1098/rsos.191655
- Hasan, A., Kolahdouz, E. M., Enquobahrie, A., Caranasos, T. G., Vavalle, J. P., and Griffith, B. E. (2017). Image-based immersed boundary model of the aortic root. *Med. Eng. Phys.* 47, 72–84. doi: 10.1016/j.medengphys.2017.05.007
- Kassab, G. S. (2008). “Mechanical homeostasis of cardiovascular tissue,” in *Bioengineering in Cell and Tissue Research*, eds G. M. Artmann and S. Chien (Berlin; Heidelberg: Springer-Verlag), 371–391. doi: 10.1007/978-3-540-75409-1\_15
- Kunzelman, K. S., Cochran, R. P., Chuong, C., Ring, W. S., Verrier, E. D., and Eberhart, R. D. (1993). Finite element analysis of the mitral valve. *J. Heart Valve Dis.* 2, 326–340.
- Kunzelman, K. S., Einstein, D. R., and Cochran, R. P. (2007). Fluid-structure interaction models of the mitral valve: function in normal and pathological states. *Philos. Trans. R. Soc. Lond.* 362, 1393–1406. doi: 10.1098/rstb.2007.2123
- Kunzelman, K. S., Reimink, M. S., and Cochran, R. P. (1997). Annular dilatation increases stress in the mitral valve and delays coaptation: a finite element computer model. *Cardiovasc. Surg.* 5, 427–434. doi: 10.1016/S0967-2109(97)00045-8
- Lee, J., Nordsletten, D., Cookson, A., Rivolo, S., and Smith, N. (2016). *In silico* coronary wave intensity analysis: application of an integrated one-dimensional and poromechanical model of cardiac perfusion. *Biomech. Model. Mechanobiol.* 15, 1535–1555. doi: 10.1007/s10237-016-0782-5
- Lee, J. H., Rygg, A. D., Kolahdouz, E. M., Rossi, S., Retta, S. M., Duraiswamy, N., et al. (2020a). Fluid-structure interaction models of bioprosthetic heart valve dynamics in an experimental pulse duplicator. *Ann. Biomed. Eng.* 48, 1475–1490. doi: 10.1007/s10439-020-02466-4
- Lee, J. H., Scotten, L. N., Hunt, R., Caranasos, T. G., Vavalle, J. P., and Griffith, B. E. (2020b). Bioprosthetic aortic valve diameter and thickness are directly related to leaflet fluttering: results from a combined experimental and computational modeling study. *JTCVS Open.* 48, 1475–1490. doi: 10.1016/j.jxon.2020.09.002
- Liu, H., Wang, D., Leng, X., Zheng, D., Chen, F., Wong, L., et al. (2020). State-of-the-art computational models of circle of willis with physiological applications: a review. *IEEE Access.* 8, 156261–156273. doi: 10.1109/ACCESS.2020.3007737
- Luraghi, G., Migliavacca, F., Garcia, A., Chiastra, C., Rossi, A., Cao, D., et al. (2019). On the modeling of patient-specific transcatheter aortic valve replacement: a fluid-structure interaction approach. *Cardiovasc. Eng. Technol.* 10, 1–19. doi: 10.1007/s13239-019-00427-0
- Ma, X., Gao, H., Griffith, B. E., Berry, C., and Luo, X. (2013). Image-based fluid-structure interaction model of the human mitral valve. *Comput. Fluids* 71, 417–425. doi: 10.1016/j.compfluid.2012.10.025
- Mao, W., Li, K., and Sun, W. (2016). Fluid-structure interaction study of transcatheter aortic valve dynamics using smoothed particle hydrodynamics. *Cardiovasc. Eng. Technol.* 7, 374–388. doi: 10.1007/s13239-016-0285-7
- Martin, C., and Sun, W. (2012). Biomechanical characterization of aortic valve tissue in humans and common animal models. *J. Biomed. Mater. Res. A* 100, 1591–1599. doi: 10.1002/jbm.a.34099
- Mohammadi, H., Cartier, R., and Mongrain, R. (2016). Review of numerical methods for simulation of the aortic root: present and future directions. *Int. J. Comput. Methods Eng. Sci. Mech.* 17, 182–195. doi: 10.1080/15502287.2016.1189463
- Morbideucci, U., Ponzini, R., Gallo, D., Bignardi, C., and Rizzo, G. (2013). Inflow boundary conditions for image-based computational hemodynamics: impact of idealized versus measured velocity profiles in the human aorta. *J. Biomech.* 46, 102–109. doi: 10.1016/j.jbiomech.2012.10.012
- Morganti, S., Auricchio, F., Benson, D. J., Gambin, F. I., Hartmann, S., Hughes, T. J. R., et al. (2015). Patient-specific isogeometric structural analysis of aortic valve closure. *Comput. Methods Appl. Mech. Eng.* 284, 508–520. doi: 10.1016/j.cma.2014.10.010
- Morris, P. D., Narracott, A., von Tengg-Kobligh, H., Silva Soto, D. A., Hsiao, S., Lungu, A., et al. (2016). Computational fluid dynamics modelling in cardiovascular medicine. *Heart* 102, 18–28. doi: 10.1136/heartjnl-2015-308044
- Murgo, J. P., Westerhof, N., Giolma, J. P., and Altobelli, S. A. (1980). Aortic input impedance in normal man: relationship to pressure wave forms. *Circulation* 62, 105–116. doi: 10.1161/01.CIR.62.1.105
- Olufsen, M. S., Peskin, C. S., Kim, W. Y., Pedersen, E. M., Nadim, A., and Larsen, J. (2000). Numerical simulation and experimental validation of blood flow in arteries with structured-tree outflow conditions. *Ann. Biomed. Eng.* 28, 1281–1299. doi: 10.1114/1.1326031
- Peskin, C. S. (2002). The immersed boundary method. *Acta Num.* 11, 479–517. doi: 10.1017/S0962492902000077
- Pham, T., Sulejmani, F., Shin, E., Wang, D., and Sun, W. (2017). Quantification and comparison of the mechanical properties of four human cardiac valves. *Acta Biomater.* 54, 345–355. doi: 10.1016/j.actbio.2017.03.026
- Pirola, S., Jarral, O., O'Regan, D., Asimakopoulos, G., Anderson, J., Pepper, J., et al. (2018). Computational study of aortic hemodynamics for patients with an abnormal aortic valve: the importance of secondary flow at the ascending aorta inlet. *APL Bioeng.* 2:026101. doi: 10.1063/1.5011960
- Prot, V., Skallerud, B., Sommer, G., and Holzapfel, G. A. (2010). On modelling and analysis of healthy and pathological human mitral valves: two case studies. *J. Mech. Behav. Biomed. Mater.* 3, 167–177. doi: 10.1016/j.jmbbm.2009.05.004
- Qi, N., Gao, H., Ogden, R. W., Hill, N. A., Holzapfel, G. A., Han, H.-C., et al. (2015). Investigation of the optimal collagen fibre orientation in human iliac arteries. *J. Mech. Behav. Biomed. Mater.* 52, 108–119. doi: 10.1016/j.jmbbm.2015.06.011
- Shi, Y., Lawford, P., and Hose, R. (2011). Review of zero-D and 1-D models of blood flow in the cardiovascular system. *Biomed. Eng. Online* 10:33. doi: 10.1186/1475-925X-10-33
- Stergiopoulos, N., Westerhof, B. E., and Westerhof, N. (1999). Total arterial inductance as the fourth element of the windkessel model. *Am. J. Physiol. Heart Circ. Physiol.* 276, H81–H88. doi: 10.1152/ajpheart.1999.276.1.H81
- Stijnen, J., de Hart, J., Bovendeerd, P., and van de Vosse, F. (2004). Evaluation of a fictitious domain method for predicting dynamic response of mechanical heart valves. *J. Fluids Struct.* 19, 835–850. doi: 10.1016/j.jfluidstruct.2004.04.007
- Stupak, E., Kacianauskas, R., Kaceniauskas, A., Starikovicius, V., Maknickas, A., Pacevic, R., et al. (2017). The geometric model-based patient-specific simulations of turbulent aortic valve flows. *Arch. Mech.* 69, 317–345.
- Sulejmani, F., Caballero, A., Martin, C., Pham, T., and Sun, W. (2019). Evaluation of transcatheter heart valve biomaterials: computational modeling using bovine and porcine pericardium. *J. Mech. Behav. Biomed. Mater.* 97, 159–170. doi: 10.1016/j.jmbbm.2019.05.020
- Sun, W., Martin, C., and Pham, T. (2014). Computational modeling of cardiac valve function and intervention. *Annu. Rev. Biomed. Eng.* 16, 53–76. doi: 10.1146/annurev-bioeng-071813-104517
- Toussaint, N., Sermesant, M., Stoeck, C. T., Kozerke, S., and Batchelor, P. G. (2010). “In vivo human 3D cardiac fibre architecture: reconstruction using curvilinear interpolation of diffusion tensor images,” in *Medical Image Computing and Computer-Assisted Intervention – MICCAI 2010*, eds T. Jiang, N. Navab, J. P. W. Pluim, and M. A. Viergever (Berlin; Heidelberg: Springer), 418–425. doi: 10.1007/978-3-642-15705-9\_51
- Van Loon, R., Anderson, P., De Hart, J., and Baaijens, F. (2004). A combined fictitious domain/adaptive meshing method for fluid-structure interaction in heart valves. *Int. J. Num. Methods Fluids* 46, 533–544. doi: 10.1002/flf.775
- Wang, H. M., Gao, H., Luo, X. Y., Berry, C., Griffith, B. E., Ogden, R. W., et al. (2013). Structure-based finite strain modelling of the human left ventricle in diastole. *Int. J. Num. Methods Biomed. Eng.* 29, 83–103. doi: 10.1002/cnm.2497
- Wang, Q., Kodali, S., Primiano, C., and Sun, W. (2015). Simulations of transcatheter aortic valve implantation: implications for aortic root rupture. *Biomech. Model. Mechanobiol.* 14, 29–38. doi: 10.1007/s10237-014-0583-7
- Wang, Q., Sirois, E., and Sun, W. (2012). Patient-specific modeling of biomechanical interaction in transcatheter aortic valve deployment. *J. Biomech.* 45, 1965–1971. doi: 10.1016/j.jbiomech.2012.05.008
- Wei, Z. A., Sonntag, S., Toma, M., Singh-Gryzbom, S., and Sun, W. (2018). Computational fluid dynamics assessment associated with transcatheter heart

- valve prostheses: a position paper of the iso working group. *Cardiovasc. Eng. Technol.* 9, 289–299. doi: 10.1007/s13239-018-0349-y
- Weinberg, E. J., and Kaazempur-Mofrad, M. R. (2005). On the constitutive models for heart valve leaflet mechanics. *Cardiovasc. Eng.* 5, 37–43. doi: 10.1007/s10558-005-3072-x
- Weinberg, E. J., Shahmirzadi, D., and Mofrad, M. R. K. (2010). On the multiscale modeling of heart valve biomechanics in health and disease. *Biomech. Model. Mechanobiol.* 9, 373–387. doi: 10.1007/s10237-009-0181-2
- Westerhof, N., Lankhaar, J.-W., and Westerhof, B. (2008). The arterial windkessel. *Med. Biol. Eng. Comput.* 47, 131–141. doi: 10.1007/s11517-008-0359-2
- Wong, J., and Kuhl, E. (2014). Generating fibre orientation maps in human heart models using poisson interpolation. *Comput. Methods Biomech. Biomed. Eng.* 17, 1217–1226. doi: 10.1080/10255842.2012.739167
- Wu, W., Pott, D., Mazza, B., Sironi, T., Dordoni, E., Chiastra, C., et al. (2016). Fluid-structure interaction model of a percutaneous aortic valve: comparison with an in vitro test and feasibility study in a patient-specific case. *Ann. Biomed. Eng.* 44, 590–603. doi: 10.1007/s10439-015-1429-x
- Xiong, F. L., Goetz, W. A., Chong, C. K., Chua, Y. L., Pfeifer, S., Wintermantel, E., et al. (2010). Finite element investigation of stentless pericardial aortic valves: relevance of leaflet geometry. *Ann. Biomed. Eng.* 38, 1908–1918. doi: 10.1007/s10439-010-9940-6
- Yoganathan, A. P., He, Z., and Jones, S. C. (2004). Fluid mechanics of heart valves. *Annu. Rev. Biomed. Eng.* 6, 331–362. doi: 10.1146/annurev.bioeng.6.040803.140111
- Zhu, G., Ismail, M. B., Nakao, M., Yuan, Q., and Yeo, J. H. (2019). Numerical and *in-vitro* experimental assessment of the performance of a novel designed expanded-polytetrafluoroethylene stentless bi-leaflet valve for aortic valve replacement. *PLoS ONE* 14:e0210780. doi: 10.1371/journal.pone.0210780
- Zhu, G., Nakao, M., Yuan, Q., and Yeo, J. H. (2017). “*In-vitro* assessment of expanded-polytetrafluoroethylene stentless tri-leaflet valve prosthesis for aortic valve replacement,” in *Proceedings of the 10th International Joint Conference on Biomedical Engineering Systems and Technologies (BIOSTEC 2017)*, 186–189. doi: 10.5220/0006184401860189
- Zhu, G.-Y., Huang, H., Su, Y.-L., Yeo, J.-H., Shen, X.-Q., and Yang, C.-F. (2020). Numerical investigation of the effects of prosthetic aortic valve design on aortic hemodynamic characteristics. *Appl. Sci.* 10:1396. doi: 10.3390/app10041396

**Conflict of Interest:** The authors declare that the research was conducted in the absence of any commercial or financial relationships that could be construed as a potential conflict of interest.

Copyright © 2021 Cai, Zhang, Li, Zhu, Ma, Wang, Luo and Gao. This is an open-access article distributed under the terms of the Creative Commons Attribution License (CC BY). The use, distribution or reproduction in other forums is permitted, provided the original author(s) and the copyright owner(s) are credited and that the original publication in this journal is cited, in accordance with accepted academic practice. No use, distribution or reproduction is permitted which does not comply with these terms.





# HADLN: Hybrid Attention-Based Deep Learning Network for Automated Arrhythmia Classification

Mingfeng Jiang<sup>1\*</sup>, Jiayan Gu<sup>1</sup>, Yang Li<sup>1</sup>, Bo Wei<sup>1</sup>, Jucheng Zhang<sup>2</sup>, Zhikang Wang<sup>2\*</sup> and Ling Xia<sup>3</sup>

<sup>1</sup> School of Information Science and Technology, Zhejiang Sci-Tech University, Hangzhou, China, <sup>2</sup> Department of Clinical Engineering, The Second Affiliated Hospital, School of Medicine, Zhejiang University, Hangzhou, China, <sup>3</sup> Department of Biomedical Engineering, Zhejiang University, Hangzhou, China

## OPEN ACCESS

### Edited by:

Linwei Wang,  
Rochester Institute of Technology,  
United States

### Reviewed by:

Saman Parvaneh,  
Edwards Lifesciences, United States  
Heye Zhang,  
Sun Yat-sen University, China

### \*Correspondence:

Zhikang Wang  
2192009@zju.edu.cn  
Mingfeng Jiang  
m.jiang@zstu.edu.cn

### Specialty section:

This article was submitted to  
Computational Physiology  
and Medicine,  
a section of the journal  
Frontiers in Physiology

**Received:** 19 March 2021

**Accepted:** 27 May 2021

**Published:** 05 July 2021

### Citation:

Jiang M, Gu J, Li Y, Wei B,  
Zhang J, Wang Z and Xia L (2021)  
HADLN: Hybrid Attention-Based  
Deep Learning Network  
for Automated Arrhythmia  
Classification.  
Front. Physiol. 12:683025.  
doi: 10.3389/fphys.2021.683025

In recent years, with the development of artificial intelligence, deep learning model has achieved initial success in ECG data analysis, especially the detection of atrial fibrillation. In order to solve the problems of ignoring the correlation between contexts and gradient dispersion in traditional deep convolution neural network model, the hybrid attention-based deep learning network (HADLN) method is proposed to implement arrhythmia classification. The HADLN can make full use of the advantages of residual network (ResNet) and bidirectional long-short-term memory (Bi-LSTM) architecture to obtain fusion features containing local and global information and improve the interpretability of the model through the attention mechanism. The method is trained and verified by using the PhysioNet 2017 challenge dataset. Without loss of generality, the ECG signal is classified into four categories, including atrial fibrillation, noise, other, and normal signals. By combining the fusion features and the attention mechanism, the learned model has a great improvement in classification performance and certain interpretability. The experimental results show that the proposed HADLN method can achieve precision of 0.866, recall of 0.859, accuracy of 0.867, and F1-score of 0.880 on 10-fold cross-validation.

**Keywords:** arrhythmia classification, deep learning, bidirectional LSTM, ResNet, attention mechanism

## INTRODUCTION

Atrial fibrillation is one of the most common persistent arrhythmias. It is characterized by irregular atrial activity, increasing incidence rate, and associated complications, such as stroke and systemic thromboembolism, which pose a great threat to human health and life (Mathew et al., 2009). In addition, due to the lack of comprehensive understanding of the pathological mechanism of atrial fibrillation, the timely diagnosis of atrial fibrillation becomes a problem (Wyndham, 2000). People often miss the optimal treatment time because the early stages of atrial fibrillation are usually paroxysmal and asymptomatic (Mehall et al., 2007). Therefore, the development of a new type of automatic atrial fibrillation detection system to provide accurate and reliable diagnostic

information as early as possible is of great significance for improving the quality of treatment and reducing the further deterioration of the patient's health.

Electrocardiography (ECG) is often used for routine monitoring of physiological signals in clinical application. The effective analysis of ECG signals is helpful to detect many heart diseases such as atrial fibrillation (AF), myocardial infarction (MI), and heart failure (HF) (Turakhia, 2018). In an AF waveform, the P wave is replaced by many inconsistent fibrillatory waves, and the RR interval is irregular, which is easily mixed with other diseases (Wei et al., 2017). In the early stage, the research work of ECG classification was generally implemented by using manual feature extraction method. However, the method of manual feature extraction was not only affected by noises but also lost a lot of important information, which cause the in accuracy and low efficiency of AF classification. Moreover, its poor generalization ability cannot be used to deal with the practical application. Some signal processing methods, such as independent component analysis (Prasad et al., 2013), discrete wavelet transform (Lee et al., 2013), and entropy (Liu et al., 2018a), has been used to improve the performances of manual feature extraction. Recently, feature extraction methods based on machine learning, such as support vector machine (Liu et al., 2018b) and random forest (Kennedy et al., 2016), are proposed to classify the ECG signals.

Recently, deep neural networks (DNNs) achieved initial success in ECG data processing (Parvaneh et al., 2019), which can provide another opportunity to improve the accuracy and scalability of automatic ECG classification obviously (Hong et al., 2019). According to different network structure, DNNs can integrate different level features and classifiers to form an end-to-end multilayer model (Dang et al., 2019) without preprocessing a large amount of data by manual rules, which can overcome the limitation of traditional machine learning algorithm model with independent input and output (Schmidhuber, 2015). In addition, there have been some new attempts on DNNs, such as residual blocks (He et al., 2016), deep convolutional neural network (Wu et al., 2020), deep residual convolutional neural network (Li et al., 2020), recurrent neural network (RNN) with long-short-term memory (LSTM) (Faust et al., 2018), and deep bidirectional LSTM (Bi-LSTM) network (Yildirim, 2018). In order to effectively select feature information and enhance the interpretability of the model, the attention mechanisms had been valued in the classification of arrhythmia (Yao et al., 2020; Zhang et al., 2020). In the PhysioNet/Computing in Cardiology Challenge 2020, several classification models related to attention mechanisms have been proposed to get promising classification results. Duan et al. (2020) proposed a multiscale attention deep neural network (MADNN) method to boost capability of extracting the ECG features on different scales, combining kernel- and branch-wise attention modules, which can achieve an overall score of 0.446 on the hidden testing-set. Liu et al. (2020) proposed a novel multilabel classifier of 12-lead ECG recordings by using residual CNN and class-wise attention mechanism, which can get resulting scores of  $0.5501 \pm 0.0223$  according to the challenge metric, demonstrating a promising method for the classification of ECGs. He et al. (2020) used the mechanism of

attention to learn an attention distribution on the list of extracted features, and then, the attention weightings were integrated into a single feature vector and used for the final classification. The overall score with five cross-validation of training set is 0.543 by using the Deep Heart model, demonstrating that it may have potential practical applications. However, there still a long way to improve classification accuracy in clinical application.

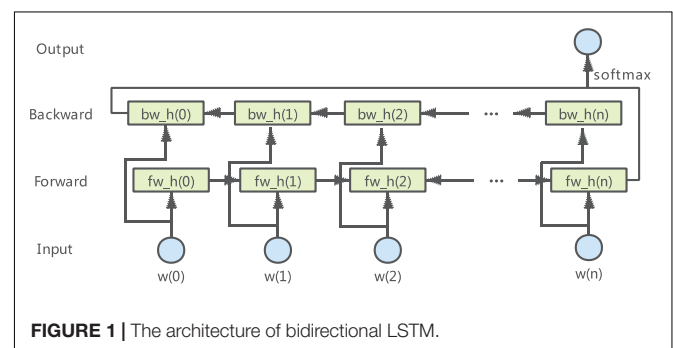
This paper proposed a hybrid attention-based deep learning network (HADLN) method to automatically implement ECG classification. The PhysioNet 2017 challenge data were used to validate the performance of HADLN method. The main contributions of this paper can be concluded as follows: (1) the ResNet part uses the superposition of 16 residual blocks to extract local features, and the bidirectional long-short-term memory network was used to extract the global features in parallel. Moreover, the global feature from Bi-LSTM and the local feature from ResNet were the fused features, which can extract multiple features of the original ECG data; (2) in this paper, a modification of the standard attention mechanism was proposed to strengthen local feature information from ResNet according to the weight parameters calculated from fused features; and (3) the features of these weighting parameters based on fused features can proved a interpretability for ECG classification results.

## BASIC THEORY

In this paper, three deep-learning approaches are utilized to form the classification model. Residual network (ResNet) and Bi-LSTM network are applied in the classification model. Besides, attention mechanism is introduced to improve the performance of classification.

### Bi-LSTM

LSTM is a typical RNN proposed by Hochreiter and Schmidhuber (1997). Due to the advantages of its gate mechanism, it is easier to learn the long-term dependencies between sequences (Tan et al., 2018). The bidirectional layer is actually composed of two LSTM layers in opposite directions: the forward LSTM layer and the backward LSTM layer. The Bi-LSTM architecture is shown in **Figure 1**, which will be able to fully consider the global features in the input data. Graves and Schmidhuber showed that such bidirectional networks



can be significantly more effective than unidirectional LSTM architectures (Graves and Schmidhuber, 2005).

## ResNet

The deep CNN network with residual blocks can solve the problem of the convergence difficulty of the deep network and overcome the problem of network degradation caused by the increase in network layers (Zagoruyko and Komodakis, 2016). As shown in **Figure 2**, the learning process is to let multiple nonlinear computing layers of continuous stack fit the residual  $F(x) = H(x) - X$  between the input data and the output data. Residual learning adds a shortcut on the basis of the traditional linear network structure, which is integrating a shortcut with the main path by the method of additive fusion.

## Attention Mechanism

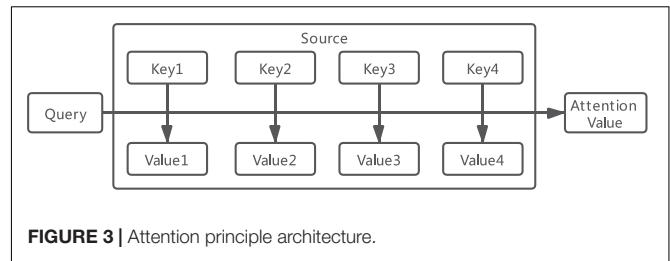
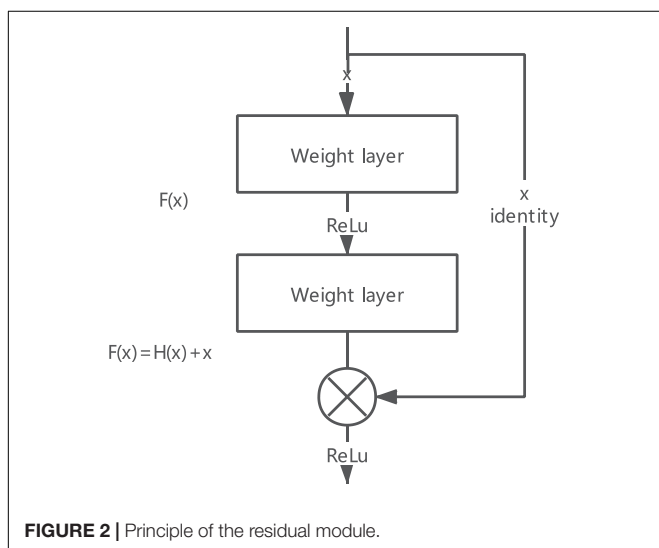
The core concept of attention mechanism is to simulate human attention mechanism to improve the performance of deep learning (Mnih et al., 2014). By using the probability distribution of attention, we can control the weighting parameters of the elements in the input sequence to generate the output sequence. As shown in **Figure 3**, the essence of the attention function can be described as a mapping from a query to a series of key-value pairs. The common similarity functions are implemented by multiplication in Equation 1, concatenation in Equation 2, and perceptron in Equation 3.

$$f(Q, K_i) = Q^T W_a K_i \quad (1)$$

$$f(Q, K_i) = W_a [Q : K_i] \quad (2)$$

$$f(Q, K_i) = v_a^T \tanh(W_a Q + U_a K_i) \quad (3)$$

where  $W_a$ ,  $U_a$ , and  $v_a$  are all learnable parameters.  $Q$  means Query, and  $K_i$  means keys.



## MATERIALS AND METHODS

### Dataset

To demonstrate the generalizability of the proposed HADLN architecture, the open dataset of the PhysioNet 2017 challenge was applied in the model (Clifford et al., 2017), which contained four rhythm categories: normal (N), atrial fibrillation (A), other (O), and noise (~). The dataset consisted of 8,528 single lead ECG data recordings, and each of them is sampled at 300 Hz with a length of 9–61 s. The dataset was divided into a training set (90%) and a testing set (10%) for training and evaluation in all tasks. Data profile of PhysioNet Challenge 2017 dataset is shown in **Table 1**.

### Proposed HADLN Architecture

As shown in **Figure 4**, the HADLN architecture was proposed to automatically detect atrial fibrillation based on the fusion of attention mechanism and deep learning model, which combines ResNet, Bi-LSTM, and attention mechanism module. The ResNet part uses the superposition of 16 residual blocks to extract local features, which can effectively solve the problem of gradient dispersion while increasing the number of network layers. At the same time, the bidirectional long-short-term memory network was used to extract the global features in parallel, and the number of units in the layer is set to 128. The global feature from Bi-LSTM and the local feature from ResNet are used to fuse the hybrid feature. Then, the weighting parameter in attention mechanism is calculated according to hybrid features by using Softmax. Finally, the weighted features are proposed to implement ECG classification.

The original ECG signal is input into several initial layers, and the output feature map is subsequently processed by 16 residual blocks sequentially including 33 convolution layers and 16

**TABLE 1 |** Data profile of PhysioNet challenge 2017 dataset.

Type	# recording	Time length (s)				
		Mean	StDev	Max	Median	Min
Normal	5,154	31.9	10.0	61.0	30	9.0
AF	771	31.6	12.5	60	30	10.0
Other rhythm	2,557	34.1	11.8	60.9	30	9.1
Noisy	46	27.1	9.0	60	30	10.2
Total	8,528	32.5	10.9	61.0	30	9.0

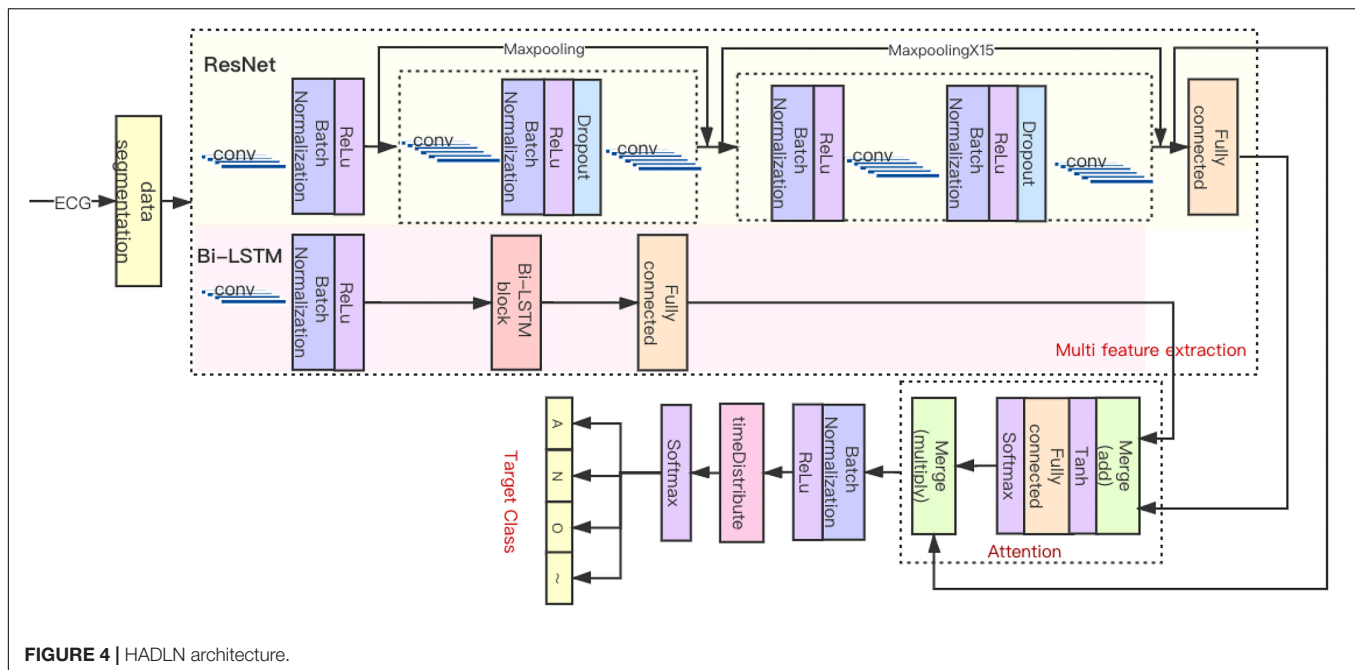


FIGURE 4 | HADLN architecture.

maximum pool layers. There are two types of residual modules, including two 1D convolutional layers, batch normalization layer, ReLU activation layer, dropout layer, and a maxpooling layer. As shown in **Table 2**, each convolutional layer has  $32 \times 2^k$  convolution kernels (where  $k$  starts out as 0 and is incremented every fourth). The difference is that the 2nd to 16th residual blocks have more batch normalization layers, ReLU activation layer, and dropout layers than the first residual block. The residual module combines the output of the quick connection and the output of the second convolutional layer by summation. When the feature map passes through the maxpooling layer with a pool

size of 2, the length of that will be halved. When the pool size is 1, there is no effect on the feature map, so only eight layers play a role in this part of ResNet. Therefore, the original input is finally subsampled by a factor of  $2^8$ , and after the local feature extraction part, the output length is  $1/256$  of the input length.

For long sequences, Bi-LSTM can be used to process input along the time sequence in a parameters-sharing manner and utilizes their internal state to memorize the context. The original signal is input to Bi-LSTM to extract global features, where the number of LSTM units in each of the forward and backward layers was set to 128. The global feature  $h_i$  from Bi-LSTM and the local feature  $v_i$  from ResNet are used to fuse the hybrid feature  $e_i$ , as shown in Equation 4. The weighting parameter  $\alpha_i$  in attention mechanism is calculated by using Equation 5, and the weighted features  $S_{HADLN}$  are proposed to implement ECG classification; specific implementation is shown in Equation 6.

$$e_i = W_a^T * \tanh(W_Q * v_i + W_k * h_i) \quad (4)$$

$$\alpha_i = \text{softmax}(e_i) = \frac{\exp(e_i)}{\sum_{i=1}^T \exp(e_i)} \quad (5)$$

$$S_{HADLN} = \sum_{i=1}^T \alpha_i * v_i \quad (6)$$

where  $e_i$  the is merged feature from  $h_i$  and  $v_i$ , with fully connected layer parameters  $W_Q$ ,  $W_k$ ,  $W_a^T$ , and  $\alpha_i$  referring to weight parameters from Softmax function, and  $S_{HADLN}$  refers to weighted features.

The classification part consists of batch normalization layer, timeDistributed layer, and two activation layers. The ReLU layer enables the classification part to accelerate the back propagation of gradients. The timeDistributed layer is fully connected in the time dimension. The second activation layer is a Softmax

**TABLE 2** | The length/number of convolution kernels and pool size of max-pooling layers in each residual module.

ResNet module	Kernel length	Kernel number	Pool size
1	16	32	1
2	16	32	2
3	16	32	1
4	16	32	2
5	16	64	1
6	16	64	2
7	16	64	1
8	16	64	2
9	16	128	1
10	16	128	2
11	16	128	1
12	16	128	2
13	16	256	1
14	16	256	2
15	16	256	1
16	16	256	2



layer, which outputs the predicted probability distribution of four classes, including atrial fibrillation, noise, other, and normal.

As a comparison, the ResNet model with attention mechanism, termed as ResNet\_A method, is proposed for ECG classification. The output of ResNet  $v_i$  is directly used to calculate the weighting parameters  $\alpha'_i$  by Softmax function in Equation 7, and then the weighting parameters are used to calculate the weighted features in Equation 8.

$$\alpha'_i = \text{softmax}(v_i) = \frac{\exp(v_i)}{\sum_{i=1}^T \exp(v_i)} \quad (7)$$

$$S_{\text{ResNet\_A}} = \sum_{i=1}^T \alpha'_i * v_i \quad (8)$$

## Model Training

Batch normalization is used to ensure the smooth convergence of the network before each convolution layer. Meanwhile, using the ReLU activation function can effectively improve the learning efficiency of the network and significantly reduce the number of iterations required for convergence in the deep learning network. The initial learning rate of the Adam optimizer was set to  $10^{-2}$  and the probability of dropout is set as 0.3. The cross-entropy function was used to evaluate the difference between the output and reference labels, as in Equation 9. The smaller the value of cross-entropy is, the closer the distribution of actual output and expected output is. According to the cross entropy, the stop mechanism in the model training can be made. When the cross-entropy value does not change in eight epochs, then the model training will stop automatically.

$$\text{loss}(X, r) = -\log \frac{\exp(P(X, r))}{\sum_{i=0}^N \exp(P(X, i))} \quad (9)$$

where  $r$  refers to label, and  $P(X, i)$  is the probability the model assigns the label  $i$  to the input  $X$ .

Moreover, the HADLN and several comparative experiments were trained and tested in a server with Tesla v100-sxm2 GPU. The deep learning model was programmed by using Python 3.6 and Keras 2.1.6 framework. Matplotlib tools are used for data visualization, and numpy1.18.1 is used for a large number of dimensional arrays and matrix operations. In addition, we used scikit-learn 0.22.1 for data mining and data analysis tools.

## RESULTS

### Performance Metric

In order to evaluate the performance of the proposed model, the precision, recall, and accuracy are listed as the following equations, respectively. The counting rules for the numbers of the variables are listed as shown in **Table 3**. In addition, the performance metric F1-score proposed by 2017 Physionet challenge was used to evaluate the performance of the proposed

**TABLE 3** | Counting rules for the numbers of the variables.

	Normal	AF	Other	Noisy	Total
Normal	Nn	Na	No	Np	$\Sigma N$
AF	An	Aa	Ao	Ap	$\Sigma A$
Other	On	Oa	Oo	Op	$\Sigma O$
Noisy	Pn	Pa	Po	Pp	$\Sigma P$
Total	$\Sigma n$	$\Sigma a$	$\Sigma o$	$\Sigma p$	

HADLN network architecture, as shown in the Equation 17.

$$\text{precision} = \frac{TP}{TP + FP} \quad (10)$$

$$\text{recall} = \frac{TP}{TP + FN} \quad (11)$$

$$\text{accuracy} = \frac{TP + TN}{TP + TN + FP + FN} \quad (12)$$

$$F_{1n} = \frac{2N_n}{(\Sigma n + \Sigma N)} \quad (13)$$

$$F_{1a} = \frac{2A_a}{(\Sigma a + \Sigma A)} \quad (14)$$

$$F_{1o} = \frac{2O_o}{(\Sigma o + \Sigma O)} \quad (15)$$

$$F_{1p} = \frac{2P_p}{(\Sigma p + \Sigma P)} \quad (16)$$

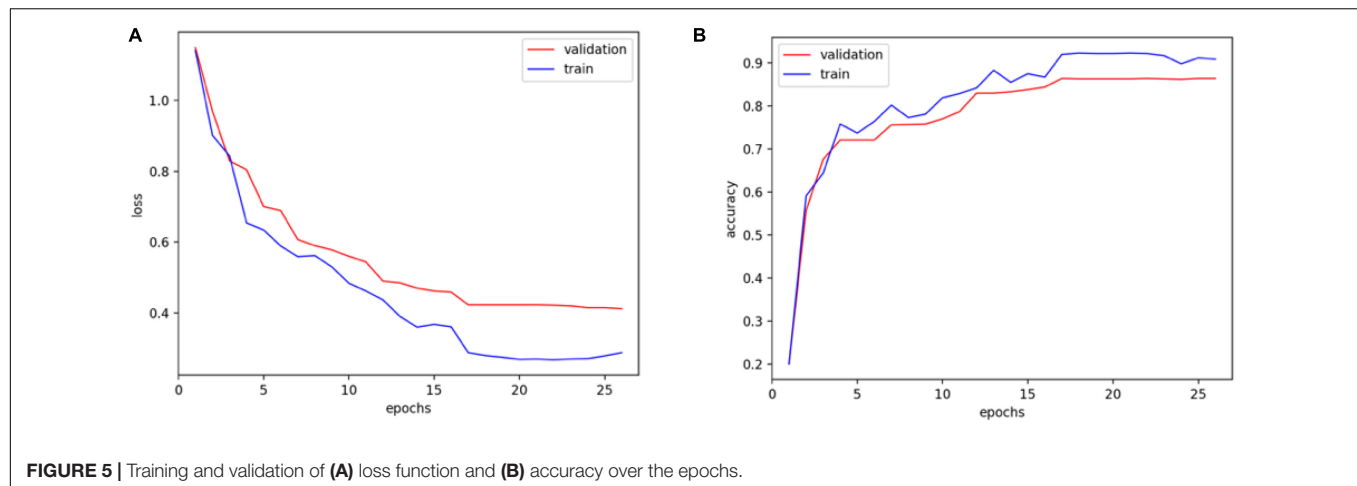
$$\text{F1-score} = \frac{(F_{1n} + F_{1a} + F_{1o} + F_{1p})}{4} \quad (17)$$

where TP means true positive, the number of AF signals classified correctly; FP means false positive, the number of AF signals classified wrongly; TN means true negative, the number of signals without AF classified correctly; and FN means false negative, the number of signals without AF classified wrongly.

## Experimental Results

As shown in **Figure 5**, the performance of the training set is slightly better than that of the validation set, and the model converges to a stable value, indicating that the parameters are not excessive when training the model. In the validation model, the proposed method works well, which can achieve the stable classification results with good accuracy.

In order to validate the performances of the proposed HADLN method, several state-of-the-art methods, such as ResNet (Hannun et al., 2019), CL3 (Warrick and Homsy, 2017), QRS-LSTM (Maknickas, 2017), and Dense-net (Rubin et al., 2017), are also provided as a comparison. In addition, self-attention based ResNet method, ResNet\_A, is also investigated for arrhythmia classification. As shown in **Table 4**, the precision, recall, F1-score, and accuracy of different DNNs architecture are presented for classifying normal (N), atrial fibrillation (A), other (O), and noise (~). It can be found that the proposed HADLN method can achieve the best classification performances with the highest metric indexes among these methods. In addition, in order to validate the robustness of the proposed HADLN method, the classification performances (F1 score,



precision, recall, accuracy) have been reported in the Table 5, which indicates that the proposed HADLN method has stable classification in different cross cases.

As shown in Figure 6, the confusion matrices were used to illustrate the discordance between the predicted labels and the real labels by using different DNNs models. The results show that compared with the baseline model ResNet, the classification effect of normal (N) and atrial fibrillation (A) in HADLN is significantly improved by 5% and 6%. The classification effect of HADLN in atrial fibrillation (A) is generally higher than that of other contrast models.

**TABLE 4 |** Classification results of weight average.

	F1-score	Precision	Recall	Accuracy
CL3	0.856	0.856	0.850	0.867
QRS-LSTM	0.666	0.770	0.714	0.770
Dense-net	0.843	0.867	0.860	0.860
ResNet	0.837	0.865	0.853	0.857
ResNet_A	0.844	0.854	0.853	0.853
HADLN	0.880	0.866	0.859	0.867

**TABLE 5 |** The classification performances of the proposed HADLN method using 10-fold cross.

No.	F1-score	Precision	Recall	Accuracy
1	0.857	0.862	0.857	0.865
2	0.850	0.865	0.856	0.860
3	0.880	0.873	0.872	0.872
4	0.887	0.890	0.879	0.890
5	0.905	0.884	0.885	0.891
6	0.887	0.877	0.876	0.888
7	0.879	0.840	0.827	0.836
8	0.911	0.839	0.833	0.837
9	0.900	0.870	0.859	0.861
10	0.848	0.858	0.850	0.867
Average	0.880	0.866	0.859	0.867
Standard deviation	0.021	0.016	0.018	0.019

## DISCUSSION

Due to the limited size, each convolution operation can only cover a small neighborhood around the sequence, so that it cannot be easily captured the global features. Although after multilayer convolution stacking, compared with the single-layer CNN, more comprehensive features can be obtained. However, it still cannot make full use of the context information, resulting in a degradation in generalization ability. The advantage of the Bi-LSTM architecture is that it can learn long-term dependencies between sequences. Therefore, the Bi-LSTM network can be used to select the global feature from the original ECG signal. As shown in Table 4, the performance of HADLN is much higher than that of the model using only LSTM to classify QRS data, higher than the model of using only deep residual network. The above experimental results prove that the proposed HADLN method can adaptively discover hidden structures of different ECG signals and automatically learn relevant information, improving the accuracy of ECG data classification.

In this paper, attention mechanism is proposed to enhance the important information in the local feature information through different weightings and to weaken the interference information that may affect the classification performance. Therefore, the proposed HADLN method can improve the generalization ability, so as to extract comprehensive information and improve the classification accuracy obviously. The HADLN model proposed in this paper can adaptively discover hidden structures of different ECG signals and automatically learn relevant information, thereby improving the accuracy of ECG data classification. Through the attention mechanism, this deep learning model has better interpretability.

As shown in the output mapping of the HADLN model represented by the blue line in Figure 7 (the weight of HADLN's attention mechanism is similar to the output mapping), the normal category ECG signal reaches peak in the PR interval, and there is consistency between adjacent beats. The characteristic components of the ECG signal of atrial fibrillation category are concentrated on the abnormal P wave, and the RR interval is irregular. The ECG signal features of other category and noise

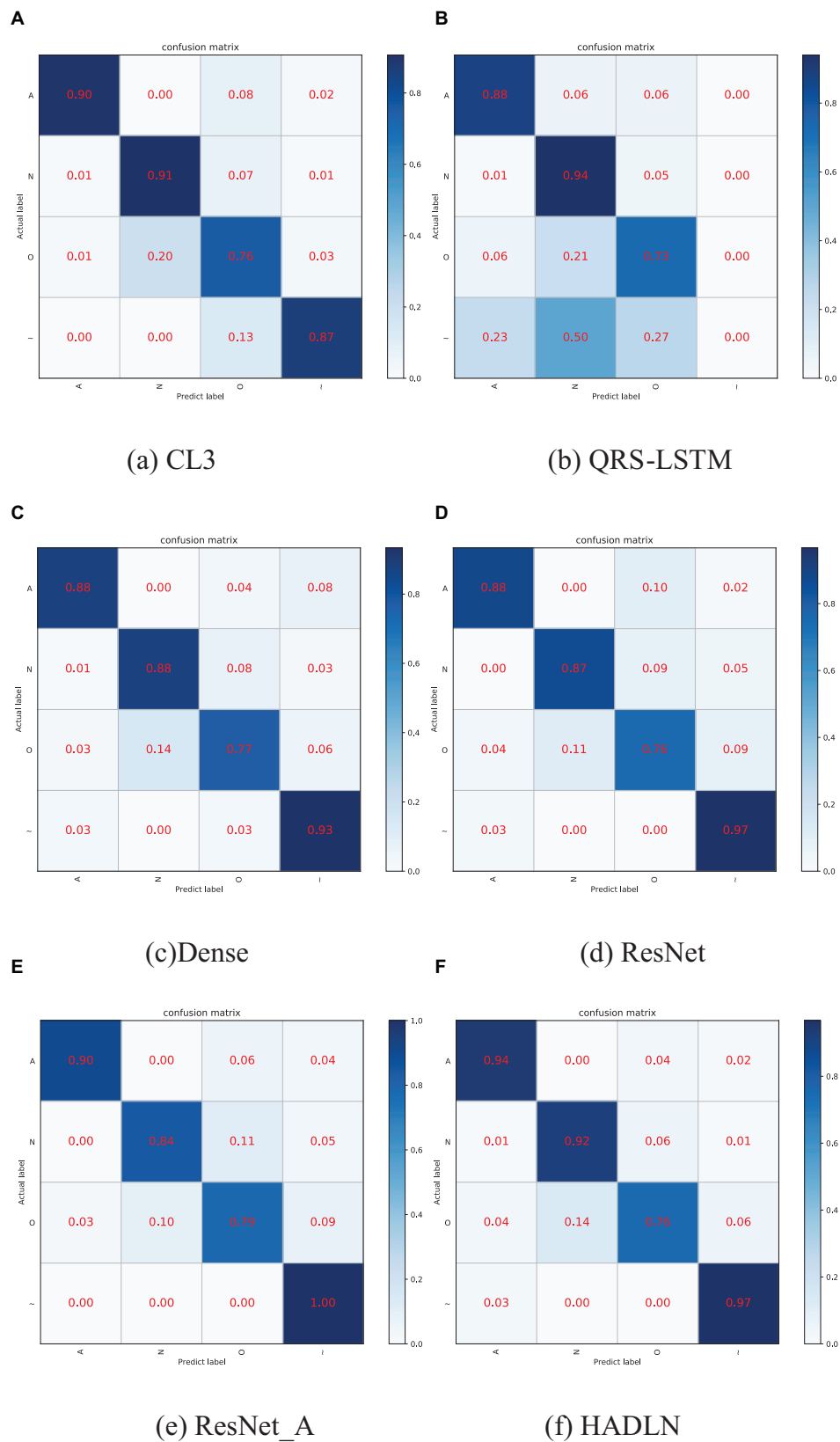


**FIGURE 6 |** Confusion matrices by using different classification methods. **(A)** CL3 method, **(B)** QRS-LSTM method, **(C)** Dense method, **(D)** ResNet method, **(E)** ResNet\_A method, and **(F)** HADLN method. The percentage of all records in each category is displayed on a color gradient scale.

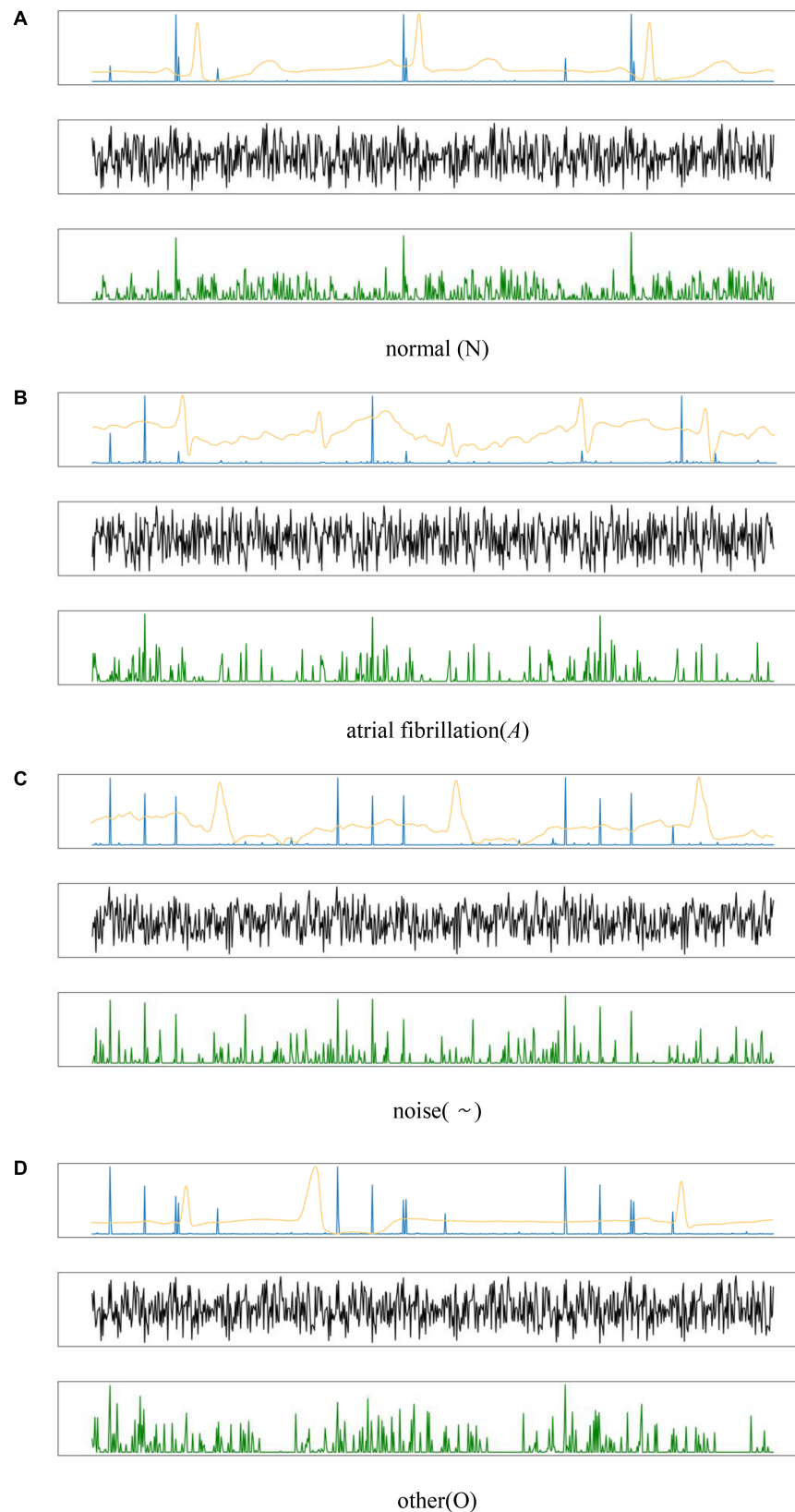


**FIGURE 7 |** The output of feature mapping by using the different types for four kinds ECG signals: **(A)** normal, **(B)** atrial fibrillation, **(C)** noise, and **(D)** other. The yellow line is the ECG signal, the green line is mapping of the ResNet model, the black line is the mapping of ResNet\_A model, and the blue line is the mapping of HADLN model.



category peaks are concentrated in multiple locations, which is far from the feature performance of normal category, and in the noise category, there are many dense and small peaks. Due to the normalization of the data, it is not very obvious in the visual display. At the same time, since some of the bands in the other category are approximately the same as the normal category, this is why the other category in the confusion matrix in **Figure 7** have poor discriminating performance.

The black line in **Figure 7** represents the output mapping of ResNet\_A model whose weight is obtained from the ResNet output and weighted by itself. It can be found that the waveforms of various ECG signals are more complicated and fuzzier than the output mapping of ResNet, and the peaks are not prominent. This is very unfavorable for the final classification of the model. As shown in the experimental results of the above table, the accuracy of the ResNet\_A model is far lower than that of ResNet and HADLN.

At the same time, by comparing the output mapping of ResNet represented by the green line in **Figure 7** and the output mapping of attention mechanism of HADLN represented by the blue line, it can be found that the model proposed in this paper is finally achieved with different weights by adding the attention mechanism module. Enhancing important information in local feature information weakens the purpose of interference information that may affect classification performance. At the same time, through the attention mechanism, this deep learning model has a better explanation. It can be seen from the correct output mapping of the attention mechanism that the features extracted by this model are consistent with clinical judgments, indicating that HADLN has potential effectiveness in the recognition of most atrial fibrillation.

In recent years, many researchers were studying the problem of automatic ECG arrhythmia classification. He et al. (2019) proposed a new method for automatic classification of arrhythmias based on deep residual convolutional module and bidirectional LSTM module. Chu et al. (2019) used multilead CNN, LSTM network, and hand-crafted method to extract features. Yildirim et al. (2019) used convolutional auto-encoder LSTM to obtain 99.23%. Yao et al. (2020) combined CNN and LSTM to detect arrhythmia using varying lengths of ECG signals. Oh et al. (2018) combined CNN and LSTM to detect arrhythmia using varying lengths of ECG signals. The proposed HADLN method in this paper can classify ECGs signals with good performance. Although the optimized model provides an effective method for the automatic classification of ECG signals, it has not been tested by actual clinical diagnosis and application of actual patients. In addition, the model proposed in this paper are limited to the four major categories of cardiovascular disease,

namely, atrial fibrillation (A), noise (~), normal (N), and other (O), which make the model's generalization in other fields have certain limitations.

## CONCLUSION

This paper proposed an HADLN method to classify four rhythm categories: normal (N), atrial fibrillation (A), other (O), and noise (~). The proposed HADLN method makes full use of the advantages of ResNet and Bi-LSTM architecture to obtain fusion features containing local and global information and improve the interpretability of the model through the attention mechanism. Compared with the most advanced classification methods, it has great advantages. This method provides a promising way to improve the accuracy and interpretability of clinical applications. In future works, the proposed HADLN method will be used for arrhythmia classification to assist in clinical diagnosis.

## DATA AVAILABILITY STATEMENT

The original contributions presented in the study are included in the article/supplementary material, further inquiries can be directed to the corresponding author/s.

## AUTHOR CONTRIBUTIONS

JG and MJ: conceptualization, formal analysis, and methodology. MJ: resources, supervision, and project administration. JG, YL, and BW: software and visualization. JG: writing—original draft preparation. MJ and YL: writing—review and editing. LX and ZW: revising and correcting. JZ, ZW, and JG: clinical interpretation and discussion of findings and their relevance. All authors contributed to the article and approved the submitted version.

## FUNDING

This work was supported in part by the Key Research and Development Program of Zhejiang Province (2020C03060 and 2020C03016), the National Natural Science Foundation of China (61672466, 62011530130, and 61671405), Joint Fund of Zhejiang Provincial Natural Science Foundation (LSZ19F010001), and this work was also supported by the 521 Talents project of Zhejiang Sci-Tech University.

## REFERENCES

- Chu, J., Wang, H., and Lu, W. (2019). A novel two-lead arrhythmia classification system based on CNN and LSTM. *J. Mech. Med. Biol.* 19:1950004. doi: 10.1142/s0219519419500040
- Clifford, G. D., Liu, C., Moody, B., Lehman, L. H., Silva, I., Li, Q., et al. (2017). "AF classification from a short single lead ECG recording: the physionet/computing in cardiology challenge 2017," in *Proceedings of the Computing in cardiology* (Rennes: IEEE).
- Dang, H., Sun, M., Zhang, G., Qi, X., Zhou, X., and Chang, Q. (2019). A novel deep arrhythmia-diagnosis network for atrial fibrillation classification using electrocardiogram signals. *IEEE Access* 7, 75577–75590. doi: 10.1109/access.2019.2918792
- Duan, R., He, X., and Ouyang, Z. (2020). "MADNN: a multi-scale attention deep neural network for arrhythmia classification," in *Proceedings of the 2020 Computing in Cardiology* (Rimini: IEEE).
- Faust, O., Shenfield, A., Kareem, M., San, T. R., Fujita, H., and Acharya, U. R. (2018). Automated detection of atrial fibrillation using long short-term memory

- network with RR interval signals. *Comput. Biol. Med.* 102, 327–335. doi: 10.1016/j.combiomed.2018.07.001
- Graves, A., and Schmidhuber, J. (2005). Framework phoneme classification with bidirectional LSTM and other neural network architectures. *Neural Netw.* 18, 602–610. doi: 10.1016/j.neunet.2005.06.042
- Hannun, A. Y., Rajpurkar, P., Haghpanahi, M., Tison, G. H., Bourn, C., Turakhia, M. P., et al. (2019). Cardiologist-level arrhythmia detection and classification in ambulatory electrocardiograms using a deep neural network. *Nat. Med.* 25, 65–69. doi: 10.1038/s41591-018-0268-3
- He, K., Zhang, X., Ren, S., and Sun, J. (2016). “Deep residual learning for image recognition,” in *Proceedings of the IEEE Conference on Computer Vision and Pattern Recognition* (Las Vegas, NV: IEEE), 770–778.
- He, R., Liu, Y., Wang, K., Zhao, N., Yuan, Y., Li, Q., et al. (2019). Automatic cardiac arrhythmia classification using combination of deep residual network and bidirectional LSTM. *IEEE Access* 7, 102119–102135. doi: 10.1109/access.2019.2931500
- He, R., Wang, K., Zhao, N., Sun, Q., Li, Y., Li, Q., et al. (2020). “Automatic classification of arrhythmias by residual network and bigru with attention mechanism,” in *Proceedings of the 2020 Computing in Cardiology* (Rimini: IEEE).
- Hochreiter, S., and Schmidhuber, J. (1997). Long short-term memory. *Neural Comput.* 9, 1735–1780. doi: 10.1162/neco.1997.9.8.1735
- Hong, S., Xiao, C., Ma, T., Li, H., and Sun, J. (2019). “Multilevel knowledge-guided attention for modeling electrocardiography signals,” in *Proceeding of 28th International Joint Conference on Artificial Intelligence*, (Macao, IJCAI), 5888–5894.
- Kennedy, A., Finlay, D. D., Guldenring, D., Bond, R. R., Moran, K., and McLaughlin, J. (2016). Automated detection of atrial fibrillation using R-R intervals and multivariate-based classification. *J. electrocardiol.* 49, 871–876. doi: 10.1016/j.jelectrocard.2016.07.033
- Lee, J., Reyes, B. A., McManus, D. D., Maitas, O., and Chon, K. H. (2013). Atrial fibrillation detection using an iPhone 4S. *IEEE Trans. Bio-med. Eng.* 60, 203–206. doi: 10.1109/TBME.2012.2208112
- Li, Z., Zhou, D., Wan, L., Li, J., and Mou, W. (2020). Heartbeat classification using deep residual convolutional neural network from 2-lead electrocardiogram. *J. electrocardiol.* 58, 105–112. doi: 10.1016/j.jelectrocard.2019.11.046
- Liu, L., Li, Q., Zhao, L., Nemati, S., and Clifford, G. D. (2018a). A comparison of entropy approaches for AF discrimination. *Physiol. Meas.* 39:074002. doi: 10.1088/1361-6579/aacc48
- Liu, N., Sun, M., Wang, L., Zhou, W., Dang, H., and Zhou, X. (2018b). A support vector machine approach for AF classification from a short single-lead ECG recording. *Physiol. Meas.* 39:064004. doi: 10.1088/1361-6579/aac7aa
- Liu, Y., Wang, K., Yuan, Y., Li, Q., Li, Y., Xu, Y., et al. (2020). “Multi-Label classification of 12-lead ECGs by using residual CNN and class-wise attention,” in *Proceedings of the 2020 Computing in Cardiology* (Rimini: IEEE).
- Maknickas, V. (2017). “Atrial fibrillation classification using qrs complex features and lstm,” in *Proceedings of the 2017 Computing in Cardiology (CinC)* (Rennes: IEEE), 1–4.
- Mathew, S. T., Patel, J., and Joseph, S. (2009). Atrial fibrillation: mechanistic insights and treatment options. *Eur. J. Intern. Med.* 20, 672–681. doi: 10.1016/j.ejim.2009.07.011
- Mehall, J. R., Kohut, R. M. Jr., Schneeberger, E. W., Merrill, W. H., and Wolf, R. K. (2007). Absence of correlation between symptoms and rhythm in “symptomatic” atrial fibrillation. *Ann. Thorac. Surg.* 83, 2118–2121. doi: 10.1016/j.athoracsur.2007.02.084
- Mnih, V., Heess, N., and Graves, A. (2014). “Recurrent models of visual attention,” in *Proceedings of the Advances in Neural Information Processing Systems*, (Montréal: ACM), 2204–2212.
- Oh, S. L., Ng, E., Tan, R. S., and Acharya, U. R. (2018). Automated diagnosis of arrhythmia using combination of CNN and LSTM techniques with variable length heart beats. *Comput. Biol. Med.* 102, 278–287. doi: 10.1016/j.combiomed.2018.06.002
- Parvaneh, S., Rubin, J., Babaeizadeh, S., and Xu-Wilson, M. (2019). Cardiac arrhythmia detection using deep learning: a review. *J. electrocardiol.* 57S, S70–S74. doi: 10.1016/j.jelectrocard.2019.08.004
- Prasad, H., Martis, R. J., Acharya, U. R., Min, L. C., and Suri, J. S. (2013). Application of higher order spectra for accurate delineation of atrial arrhythmia. *Annu. Int. Conf. IEEE Eng. Med. Biol. Soc.* 2013, 57–60. doi: 10.1109/EMBC.2013.6609436
- Rubin, J., Parvaneh, S., Rahman, A., Conroy, B., Babaeizadeh, S. (2017). “Densely connected convolutional networks and signal quality analysis to detect atrial fibrillation using short single-lead ECG recordings,” in *Proceedings of the 2017 Computing in Cardiology (CinC)* (Rennes: IEEE), 1–4.
- Schmidhuber, J. (2015). Deep learning in neural networks: an overview. *Neural Netw.* 61, 85–117. doi: 10.1016/j.neunet.2014.09.003
- Tan, J. H., Hagiwara, Y., Pang, W., Lim, I., Oh, S. L., Adam, M., et al. (2018). Application of stacked convolutional and long short-term memory network for accurate identification of CAD ECG signals. *Comput. Biol. Med.* 94, 19–26. doi: 10.1016/j.combiomed.2017.12.023
- Turakhia, M. P. (2018). Moving from big data to deep learning-the case of atrial fibrillation. *JAMA Cardiol.* 3, 371–372. doi: 10.1001/jamacardio.2018.0207
- Warrick, P., and Homsy, M. N. (2017). “Cardiac arrhythmia detection from ECG combining convolutional and long short-term memory networks,” in *Proceedings of the 2017 Computing in Cardiology (CinC)* (France: IEEE), 1–4.
- Wei, X. L., Liu, M., Yuan, X., and Li, Y. F. (2017). Atrial fibrillation detection based on multi-feature fusion and convolution neural network. *Laser J.* 5, 42–46.
- Wu, Q., Sun, Y., Yan, H., and Wu, X. (2020). ECG signal classification with binarized convolutional neural network. *Comput. Biol. Med.* 121:103800. doi: 10.1016/j.combiomed.2020.103800
- Wyndham, C. R. (2000). Atrial fibrillation: the most common arrhythmia. *Tex. Heart Inst. J.* 27, 257–267.
- Yao, Q., Wang, R., Fan, X., Liu, J., and Li, Y. (2020). Multi-class arrhythmia detection from 12-lead varied-length ECG using attention-based time-incremental convolutional neural network. *Inf. Fusion* 53, 174–182. doi: 10.1016/j.inffus.2019.06.024
- Yildirim, O., Baloglu, U. B., Tan, R. S., Ciaccio, E. J., and Acharya, U. R. (2019). A new approach for arrhythmia classification using deep coded features and LSTM networks. *Comput. Methods Programs Biomed.* 176, 121–133. doi: 10.1016/j.cmpb.2019.05.004
- Yildirim, Ö (2018). A novel wavelet sequence based on deep bidirectional LSTM network model for ECG signal classification. *Comput. Biol. Med.* 96, 189–202. doi: 10.1016/j.combiomed.2018.03.016
- Zagoruyko, S., and Komodakis, N. (2016). “Wide residual networks,” in *Proceeding of British Machine Vision Conference 2016*, York, France.
- Zhang, J., Liu, A., Gao, M., Chen, X., Zhang, X., and Chen, X. (2020). ECG-based multi-class arrhythmia detection using spatiotemporal attention-based convolutional recurrent neural network. *Artif. Intell. Med.* 106:101856. doi: 10.1016/j.artmed.2020.101856

**Conflict of Interest:** The authors declare that the research was conducted in the absence of any commercial or financial relationships that could be construed as a potential conflict of interest.

Copyright © 2021 Jiang, Gu, Li, Wei, Zhang, Wang and Xia. This is an open-access article distributed under the terms of the Creative Commons Attribution License (CC BY). The use, distribution or reproduction in other forums is permitted, provided the original author(s) and the copyright owner(s) are credited and that the original publication in this journal is cited, in accordance with accepted academic practice. No use, distribution or reproduction is permitted which does not comply with these terms.



# Development of Novel Fractal Method for Characterizing the Distribution of Blood Flow in Multi-Scale Vascular Tree

Peilun Li<sup>1</sup>, Qing Pan<sup>2</sup>, Sheng Jiang<sup>1</sup>, Molei Yan<sup>3</sup>, Jing Yan<sup>3\*</sup> and Gangmin Ning<sup>1\*</sup>

<sup>1</sup> Department of Biomedical Engineering, Zhejiang University, Hangzhou, China, <sup>2</sup> College of Information Engineering, Zhejiang University of Technology, Hangzhou, China, <sup>3</sup> Department of Intensive Care Medicine, Zhejiang Hospital, Hangzhou, China

## OPEN ACCESS

### Edited by:

Dingchang Zheng,  
Coventry University, United Kingdom

### Reviewed by:

Haipeng Liu,  
Coventry University, United Kingdom  
Lisheng Xu,  
Northeastern University, China  
Michal Strzelecki,  
Lodz University of Technology, Poland

### \*Correspondence:

Jing Yan  
zjicu@vip.163.com  
Gangmin Ning  
gmning@zju.edu.cn

### Specialty section:

This article was submitted to  
Computational Physiology  
and Medicine,  
a section of the journal  
Frontiers in Physiology

**Received:** 18 May 2021

**Accepted:** 09 July 2021

**Published:** 29 July 2021

### Citation:

Li P, Pan Q, Jiang S, Yan M, Yan J  
and Ning G (2021) Development  
of Novel Fractal Method  
for Characterizing the Distribution  
of Blood Flow in Multi-Scale Vascular  
Tree. *Front. Physiol.* 12:711247.  
doi: 10.3389/fphys.2021.711247

Blood perfusion is an important index for the function of the cardiovascular system and it can be indicated by the blood flow distribution in the vascular tree. As the blood flow in a vascular tree varies in a large range of scales and fractal analysis owns the ability to describe multi-scale properties, it is reasonable to apply fractal analysis to depict the blood flow distribution. The objective of this study is to establish fractal methods for analyzing the blood flow distribution which can be applied to real vascular trees. For this purpose, the modified methods in fractal geometry were applied and a special strategy was raised to make sure that these methods are applicable to an arbitrary vascular tree. The validation of the proposed methods on real arterial trees verified the ability of the produced parameters (fractal dimension and multifractal spectrum) in distinguishing the blood flow distribution under different physiological states. Furthermore, the physiological significance of the fractal parameters was investigated in two situations. For the first situation, the vascular tree was set as a perfect binary tree and the blood flow distribution was adjusted by the split ratio. As the split ratio of the vascular tree decreases, the fractal dimension decreases and the multifractal spectrum expands. The results indicate that both fractal parameters can quantify the degree of blood flow heterogeneity. While for the second situation, artificial vascular trees with different structures were constructed and the hemodynamics in these vascular trees was simulated. The results suggest that both the vascular structure and the blood flow distribution affect the fractal parameters for blood flow. The fractal dimension declares the integrated information about the heterogeneity of vascular structure and blood flow distribution. In contrast, the multifractal spectrum identifies the heterogeneity features in blood flow distribution or vascular structure by its width and height. The results verified that the proposed methods are capable of depicting the multi-scale features of the blood flow distribution in the vascular tree and further are potential for investigating vascular physiology.

**Keywords:** multi-scale, vascular tree, fractal, vascular modeling, blood flow heterogeneity

## INTRODUCTION

The microcirculation is the end destination of the cardiovascular system and the patency of microvascular perfusion is essential for the maintenance of tissue metabolism (Ince, 2005; Guven et al., 2020). Various cardiovascular diseases influence the blood perfusion and thus impair the physiological function of organs (Efimova et al., 2008; Kitagawa et al., 2009; Alosco et al., 2013, 2014). These findings imply that the blood perfusion may act as an important index for the physiological states of living bodies. The blood perfusion can be indicated by the blood flow distribution in the vascular tree. The blood flow in a vascular tree is distributed at different generations, varying in a large range of scales, and the blood flow distribution at a certain generation is directly affected by the superior generation. In the meantime, there is a huge difference between the magnitude of the blood flow at different generations. However, the conventional statistical parameters for characterizing the blood flow distribution, like the coefficient of variation (CV) (Bassingthwaite et al., 2001; Pries and Secomb, 2009), ignored the connection of the blood flow among multiple scales. To develop a unified description of the blood flow distribution covering all scales remains a big challenge.

To depict the scale-independent characteristic of objects, the fractal theory provides an efficient approach for multi-scale analysis (Mandelbrot, 1982). Presently, a few studies have made an effort on investigating the fractal characteristics of blood flow distribution in the vascular tree directly or indirectly. Van Beek et al. (1989) uncovered the fractality of the relative dispersion of blood flow distribution. Zamir (2001) defined the fractal dimension based on the relationship between the vessel diameter and blood flow according to Murray's law. Grasman et al. (2003) described that the distribution of blood flow at the same generation is multifractal. In all these studies, the unified description for a vascular tree by the fractal parameter all demands that the vascular tree should be a perfect binary tree, in which all interior branch nodes have two daughter branches and all terminals have the same depth or generation. However, the structures of real vascular trees are diverse which limits the physiological application of the methods above.

The fractal analysis has been widely used to investigate the geometrical characteristics of the vasculatures (Cheng and Huang, 2003; Stosic and Stosic, 2006; Lorthois and Cassot, 2010; Gould et al., 2011; Nadal et al., 2020). It inspires us to introduce the established fractal methods for geometrical architecture analysis into the hemodynamic study, and further develop a universal fractal depiction for blood flow distribution. The conservation law is common during the emergence of fractal and multifractal (Hassan, 2019). In fractal geometry, this law presents as the conservation of the number of signal pixels in an image. On the other hand, the total volume of blood flow in the vascular tree also obeys the conservation law. This consistency makes it possible to apply the principle of the fractal method for geometry to the analysis of blood flow by appropriate modification.

In this study, the primary aim is to establish fractal methods for analyzing the blood flow distribution which is potential

to be applied to real vascular trees. To achieve this goal, we firstly modified the fractal methods in geometry to accommodate the situation of blood flow and then applied the established methods on experimental data to test the validity. Further, to explore the physiological significance of the yielded fractal parameters, the blood flow distribution in vascular trees with fixed structure or with varying structures were examined in which the hemodynamics was simulated based on a hemodynamic model (Yang and Wang, 2013) and a rheological model (Pries and Secomb, 2005).

## MATERIALS AND METHODS

### Establishment of Fractal Methods for Blood Flow

The fractal dimension is the most important parameter to quantify the fractality of objects. And measuring the information dimension is an efficient way to estimate the fractal dimension in geometry (Pitsianis et al., 1989; Liu et al., 2018). For the calculation of information dimension, non-overlapping boxes are adopted to cover the image of the object and the mass probability of each box, which is defined as the ratio of the number of signal pixels in the box to that of the whole image, is obtained. And the information dimension  $D_I$  (Pitsianis et al., 1989) is estimated as:

$$D_I = \lim_{L \rightarrow 0} \frac{\sum_{i=1}^{N(L)} -P_i \log P_i}{\log(1/L)} \quad (1)$$

where  $\sum_{i=1}^{N(L)} -P_i \log P_i$  is the total entropy of mass according to the information theory,  $P_i$  is the mass probability of the  $i$ th box and  $N(L)$  is the number of boxes needed to cover the image with size  $L$ .

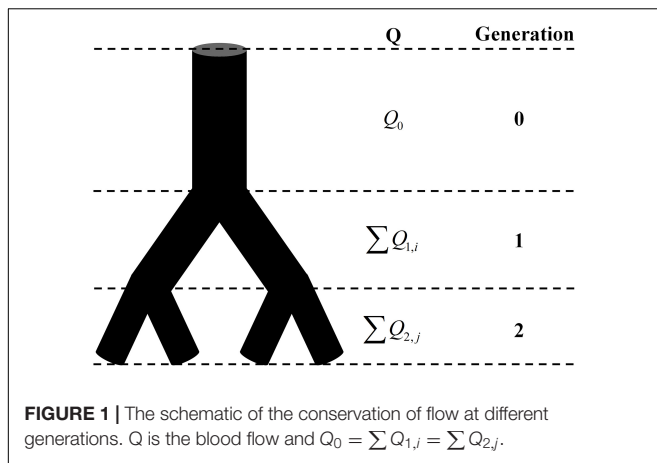
The total mass, which is the number of signal pixels in the whole image, obeys the law of conservation regardless of the box size. And so does the blood flow. As shown in **Figure 1**, the total volume of blood flow at the same generation also follows the law of conservation no matter how many times the vascular tree bifurcates. Thus, with appropriate modification, the fractal methods in fractal geometry can be introduced to investigate the fractality of blood flow. By replacing the mass probability  $P_i$  in Eq. 1 with the flow probability  $p_i$  and  $1/L$  with the number of vessel segments  $N(g)$  at generation  $g$ , the expression of the fractal dimension for the blood flow  $D_Q$  is derived as:

$$D_Q = \lim_{N(g) \rightarrow \infty} \frac{\sum -p_i \log p_i}{\log N(g)} \quad (2)$$

Practically,  $D_Q$  is estimated as the slope of the linear fitting curve of the discrete data pair  $(\log N(g), \sum -p_i \log p_i)$  (Wang et al., 2019). The precondition of the fractal analysis is scale invariance. And the strong linearity over three orders of magnitude of the fitting curve can be taken as the criteria of the existence of scale invariance (Halley et al., 2004).

For the fractal analysis in geometry, the box-counting dimension (So et al., 2017; Nayak et al., 2019), also known as capacity dimension, is the most popular. This method also





requires the image to be covered by non-overlapping boxes. However, the box-counting dimension method only considers the existence of signal pixels in the box but ignores the number of pixels. When applied to blood flow analysis, it produces fractal dimension about the vascular structure other than the distribution of blood flow. In contrast, the information dimension method takes the quantity of blood flow into account and thus can reflect the blood flow distribution.

Very few objects possess perfect mono-fractality exhibiting a single fractal dimension (Gould et al., 2011). In reality, objects with the subsets having different scaling properties are much more common and the estimation of multifractality is more desirable. For the multifractal measure of blood flow, the multifractal spectrum  $f(\alpha) \sim \alpha$  of the blood flow is adopted (Chhabra and Jensen, 1989) and modified as:

$$f(q) = \lim_{N(g) \rightarrow \infty} \frac{\sum \mu_i(q) \log [\mu_i(q)]}{\log N(g)} \quad (3)$$

$$\alpha(q) = \lim_{N(g) \rightarrow \infty} \frac{\sum \mu_i(q) \log p_i}{\log N(g)} \quad (4)$$

in which

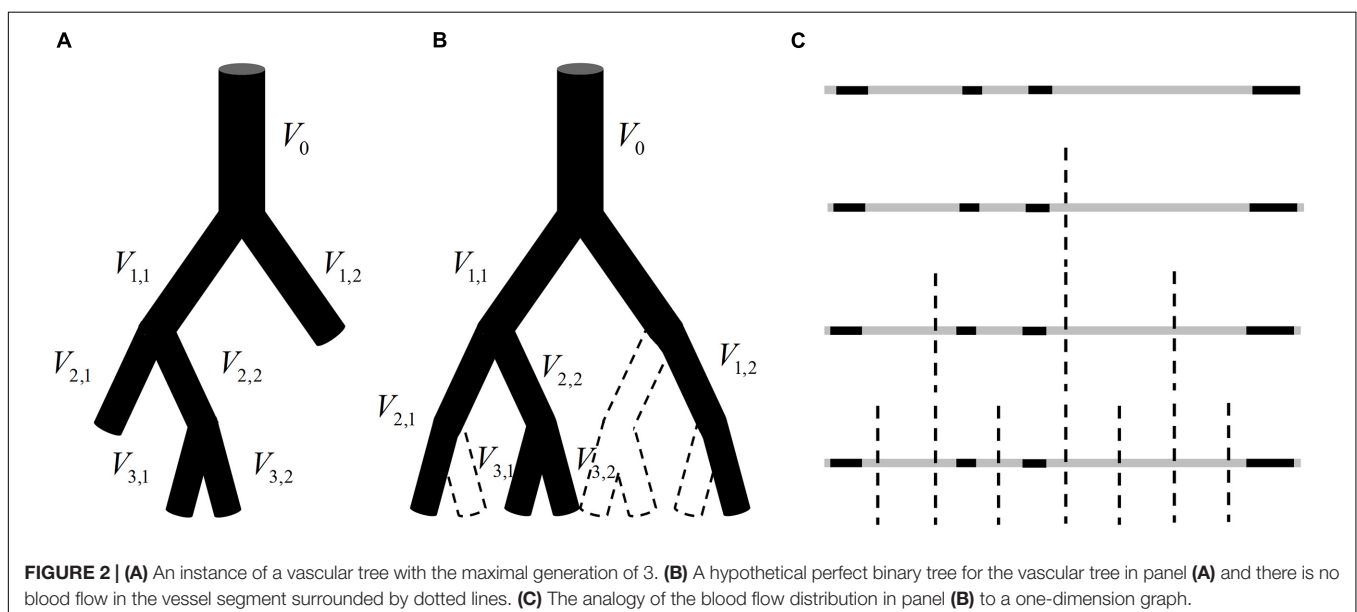
$$\mu_i(q) = \frac{p_i^q}{\sum p_i^q} \quad (5)$$

where  $q$  is the moment order. And the range of the spectrum  $\Delta\alpha = \alpha_{max} - \alpha_{min}$  can be used to measure the degree of multifractality (Halsey et al., 1986).

## Generalization of the Established Methods

The methods given in Section “Establishment of Fractal Methods for Blood Flow” are based on the premise that the total blood flow at the same generation in a vascular tree obeys the law of conservation. This premise is valid for a perfect binary tree, as shown in **Figure 1**, but not for real vascular trees as shown in **Figure 2A**. If the branch which stops bifurcating before reaching the maximal generation is regarded as a branch covering multiple generations, the vascular tree in **Figure 2A** can be thought of as the perfect binary tree as shown in **Figure 2B**. In this case, the proposed methods can be applied and a strategy for the calculation is raised: *If a vessel segment stops bifurcating at generation  $n$  ( $n$  is smaller than the maximal generation of vascular tree), it will be involved in the calculation at all the generations greater than  $n$ .*

That is to say, for the vascular tree in **Figure 2A**,  $V_{2,1}$  will be included in the calculation of total entropy at generation 3 and  $V_{1,2}$  will be included in the calculation at both generation 2 and generation 3. It should be noted that the number of vessel segments  $N$  in Eq. 2 should be  $2^n$  at generation  $n$  but not the number of vessel segments at this generation. The reason is explained below.



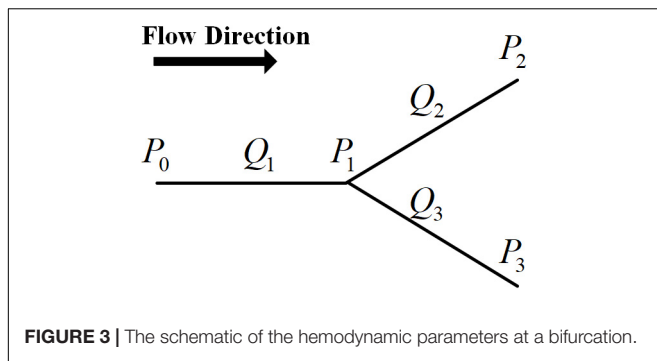


**FIGURE 3** | The schematic of the hemodynamic parameters at a bifurcation.

The blood flow distribution in the vascular tree in **Figure 2B** can be analogous to a one-dimension graph as shown in **Figure 2C**. The gray segments indicate the range of the graph and the black segments reflect the blood flow in vessel segments. Each bisection corresponds to a bifurcation of the vascular tree and divides this geometrical structure into smaller subsections. When adopting Eq. 1 for the estimation of fractal dimension for this one-dimension graph,  $L$  is corresponding to the length of the smallest subsection. And each bisection of the graph halves  $L$  no matter whether there is always a black segment in each subsection. The number of subsections should be  $2^n$  after  $n$  bisections. Similarly, the number of vessel segments  $N(g)$  in Eq. 2 should be  $2^n$  at generation  $n$ .

## Vascular Tree Construction and Hemodynamic Simulation

By now, the methods established in “Establishment of Fractal Methods for Blood Flow” and “Generalization of the Established Methods” can be used to characterize the blood flow distribution in arbitrary vascular trees. For validation, the established fractal methods were tested in a real arterial tree (Reglin et al., 2009, 2017; Wang et al., 2019) under normal and ischemic state. Besides, the capability of the derived fractal parameters was examined in two situations.

For the first situation, the vascular tree was fixed to be a perfect binary tree and the blood flow distribution was adjusted by the split ratio. For a bifurcation with a parent vessel segment and two daughter branches, the split ratio  $r$  is defined as the ratio of the smaller blood flow to the larger one in the two daughter branches, ranging from 0 to 1. Assuming that  $r$  is constant throughout the perfect binary tree, the fractal dimension for blood flow can be obtained as shown in Eq. 6. The detailed derivation of the equation is given in the **Appendix**.

$$D_Q(r) = \frac{(1+r) \log(1+r) - r \log r}{\log 2 \cdot (1+r)} \quad (6)$$

For the second situation, a series of vascular trees were constructed. The structures of these vascular trees were diverse while the blood flow distribution was estimated under the same boundary condition.

The successive dichotomous division is the most common branching pattern of the vascular tree, in which a parent vessel segment is divided into two daughter branches (Zamir, 2001).

Based on this pattern, the construction of a vascular tree calls for the determination of the vessel diameter and length. For a bifurcation with the diameter of the parent vessel being  $d_0$  and those of the two daughter branches being  $d_1$  and  $d_2$ , a power-law relationship between the diameters is given as shown in Eq. 7 according to Murray's law.

$$\begin{cases} d_0^k = d_1^k + d_2^k \\ \lambda = \frac{d_2}{d_1} \end{cases} \quad (7)$$

where  $d_0 > d_1 \geq d_2$ ,  $k$  is bifurcation exponent and  $\lambda$  is asymmetry ratio. It is reported that the  $k$  value varies from 2.33 to 3.0 (Gabrys et al., 2005). And a value above 0.6 is most commonly observed for  $\lambda$  (Schmidt et al., 2004; Cheung et al., 2011; Takahashi, 2014). Based on the power-law relationship, the diameters of all vessel segments in a vascular tree can be estimated with the given root diameter and cut-off diameter. In this study, the root diameters of all constructed vascular trees are set as 300  $\mu\text{m}$  and all the terminal diameters are 10  $\mu\text{m}$ , the size of capillaries. An empirical formula (Takahashi et al., 2009) is adopted to obtain the length  $l$  ( $\mu\text{m}$ ) from the diameter  $d$  ( $\mu\text{m}$ ):

$$l = 7.4 \cdot \left(\frac{d}{2}\right)^{1.15} \quad (8)$$

With the estimated vessel diameters and lengths, a vascular tree can be constructed, and serves for the hemodynamic simulation. According to Hagen-Poiseuille's law as shown in Eq. 9, the blood flow  $Q$  ( $\mu\text{m}^3/\text{s}$ ) in a vessel segment is proportional to the pressure drop  $\Delta P$  (Pa) between the inlet and outlet. And the flow resistance  $R$  is determined by vessel diameter  $d$  ( $\mu\text{m}$ ), vessel length  $l$  ( $\mu\text{m}$ ), and blood viscosity  $\mu$  ( $\text{Pa} \cdot \text{s}$ ).

$$\begin{cases} Q = \frac{\Delta P}{R} \\ R = \frac{128\mu l}{\pi d^4} \end{cases} \quad (9)$$

Fahraeus and Lindqvist (1931) reported a decline in apparent blood viscosity with decreasing tube diameter, the so-called Fahraeus-Lindqvist effect. Among the models to describe the relationship between the blood viscosity  $\mu$  ( $\text{mPa} \cdot \text{s}$ ) and the diameter of the vessel segment  $d$  ( $\mu\text{m}$ ), the model proposed by Pries and Secomb (2005) matches well with the *in vivo* experimental data. In this model, the *in vitro* viscosity is firstly estimated as:

$$\mu_{\text{vitro}} = 1 + (\mu_{0.45} - 1) \cdot \frac{(1 - H_d)^C - 1}{(1 - 0.45)^C - 1} \quad (10)$$

in which  $H_d$  (%) is the hematocrit and:

$$\mu_{0.45} = 220e^{-1.3d} + 3.2 - 2.44e^{-0.06d^{0.645}} \quad (11)$$

$$C = \left(0.8 + e^{-0.075d}\right) \cdot \left(\frac{1}{1 + 10^{-11} \cdot d^{12}} - 1\right) + \frac{1}{1 + 10^{-11} \cdot d^{12}} \quad (12)$$

The estimation of the *in vivo* viscosity should take account of the effect of the endothelial surface layer. This will involve two parameters, the effective diameter  $d_{eff} = d - 2W_{eff}$  and the physical diameter  $d_{ph} = d - 2W_{ph}$ . The effective thickness of the layer  $W_{eff}$  and physical thickness of the layer  $W_{ph}$  are estimated as:

$$W_{eff} = W_{as} + W_{peak} (1 + H_d \cdot E_{HD}) \quad (13)$$

$$W_{ph} = W_{as} + W_{peak} \cdot E_{peak} \quad (14)$$

$$W_{as} = \begin{cases} 0 & d \leq d_{off} \\ \frac{d - d_{off}}{d + d_{50} - 2d_{off}} \cdot W_{max} & d \geq d_{off} \end{cases} \quad (15)$$

$$W_{as} = \begin{cases} 0 & d \leq d_{off} \\ E_{amp} \cdot \frac{d - d_{off}}{d_{crit} - d_{off}} & d_{off} < d \leq d_{crit} \\ E_{amp} \cdot e^{-E_{width} \cdot (d - d_{crit})} & d > d_{crit} \end{cases} \quad (16)$$

Based on the experimental data,  $E_{HD} = 1.18$ ,  $E_{peak} = 0.6$ ,  $E_{amp} = 1.1$ ,  $E_{width} = 0.03$ ,  $D_{off} = 2.4 \mu\text{m}$ ,  $D_{crit} = 10.5 \mu\text{m}$ ,  $D_{50} = 100 \mu\text{m}$ , and  $W_{max} = 2.6 \mu\text{m}$ . By replacing the  $d$  in Eqs 11 and 12 with  $d_{ph}$ , we can get the *in vitro* viscosity  $\mu_{vitro}$ . And the *in vivo* viscosity  $\mu_{vivo}$  can be obtained as below.

$$\mu_{vivo} = \mu_{vitro} \cdot \left( \frac{d}{d_{eff}} \right)^4 \quad (17)$$

For the bifurcation as shown in **Figure 3**, the relationship between the hemodynamic parameters can be given by Eq. 18 based on Hagen-Poiseuille's law and the conservation law of flow.

$$\frac{P_0 - P_1}{R_1} + \frac{P_2 - P_1}{R_2} + \frac{P_3 - P_1}{R_3} = 0 \quad (18)$$

Without losing generality, in the hemodynamic simulation we prescribed the inlet pressure as 1 mmHg and the outlet pressure at all terminal branches as 0 mmHg (Yang and Wang, 2013). With each bifurcation of the vascular tree assigned an equation like Eq. 18, the blood pressure at each branch node can be obtained by solving these equations. Further, the blood flow in each vessel segment is estimated by Eq. 9 and finally the blood flow distribution in a tree can be acquired.

## Numerical Solution

In this study, all the calculations and simulations were programmed by MATLAB R2019a (MathWorks Co., MA, United States). Firstly, the node information for each constructed vascular tree was obtained. Then, the blood flow in each vessel segment of the constructed vascular tree was captured by solving the equations set. Ultimately, the fractal dimension and multifractal spectrum were calculated. All the results about the fractal parameters were presented as Mean  $\pm$  SD.

## RESULTS

### The Validation of the Proposed Methods

To test the validity of the proposed methods, the fractal, and multifractal analysis were conducted on a real arterial tree under normal and ischemic state. The blood flow distribution in these two states is as shown in **Figures 4A,B**. The fractal dimension for the normal and ischemic state are 0.53 and 0.40, respectively. As for the multifractal spectrum for the blood flow, the results are shown in **Figures 4C,D**. We can observe that the multifractal spectrums for both states appear as curves indicating the existence of multifractality. While the maximal values of the multifractal spectrum for the two states are the same, the range of the multifractal spectrum  $\Delta\alpha$  for the ischemic state is wider than that for the normal state which indicates a higher degree of multifractality for the ischemic state. The results verified the ability of the proposed methods in distinguishing different blood flow distribution in a real vascular tree.

### The Fractality of Blood Flow in the Perfect Binary Vascular Tree

The blood flow distribution in the perfect binary vascular tree was evaluated by both the fractal parameters and the CV, which is defined as the standard deviation divided by the mean value. For a perfect binary vascular tree with the identical split ratio for each bifurcation, the fractal dimension for blood flow was obtained based on Eq. 6. **Figure 5A** shows the trends of fractal dimension and the coefficient of variation with the change of split ratio. It is noticed that the fractal dimension increases monotonically from 0 to 1 with the increment of the split ratio. In the case  $r = 1$ , the distribution of blood flow has the highest value of fractal dimension. And the CV decreases from 10.1 to 4.4 with the increment of the split ratio.

As for the multifractal characteristic, the multifractal spectrums of the blood flow are shown in **Figure 5B**. With the decrement of the split ratio, the range of the multifractal spectrum  $\Delta\alpha$  expands while the maximal value remains unchanged. It is worth noting that the multifractal spectrum is presented as a point when  $r = 1$ , implying the absence of multifractality.

We also examined the fractal dimension and the CV of the blood flow in perfect binary vascular trees with different maximal generations. As shown in **Figure 6**, the fractal dimension holds steady with the change of maximal generation while the CV varies greatly.

### The Fractality of Blood Flow in Constructed Vascular Trees

Vascular trees with diverse structures were constructed. To reflect the heterogeneity in the real vascular tree, the bifurcation exponent  $k$ , and asymmetry ratio  $\lambda$  of the bifurcations in each constructed vascular tree were set following the normal distribution. And ten vascular trees were constructed for each pair of  $k$  and  $\lambda$ . The statistical characteristics of these vascular trees are shown in **Table 1**. In these constructed vascular trees, the hemodynamics was simulated and the results are shown

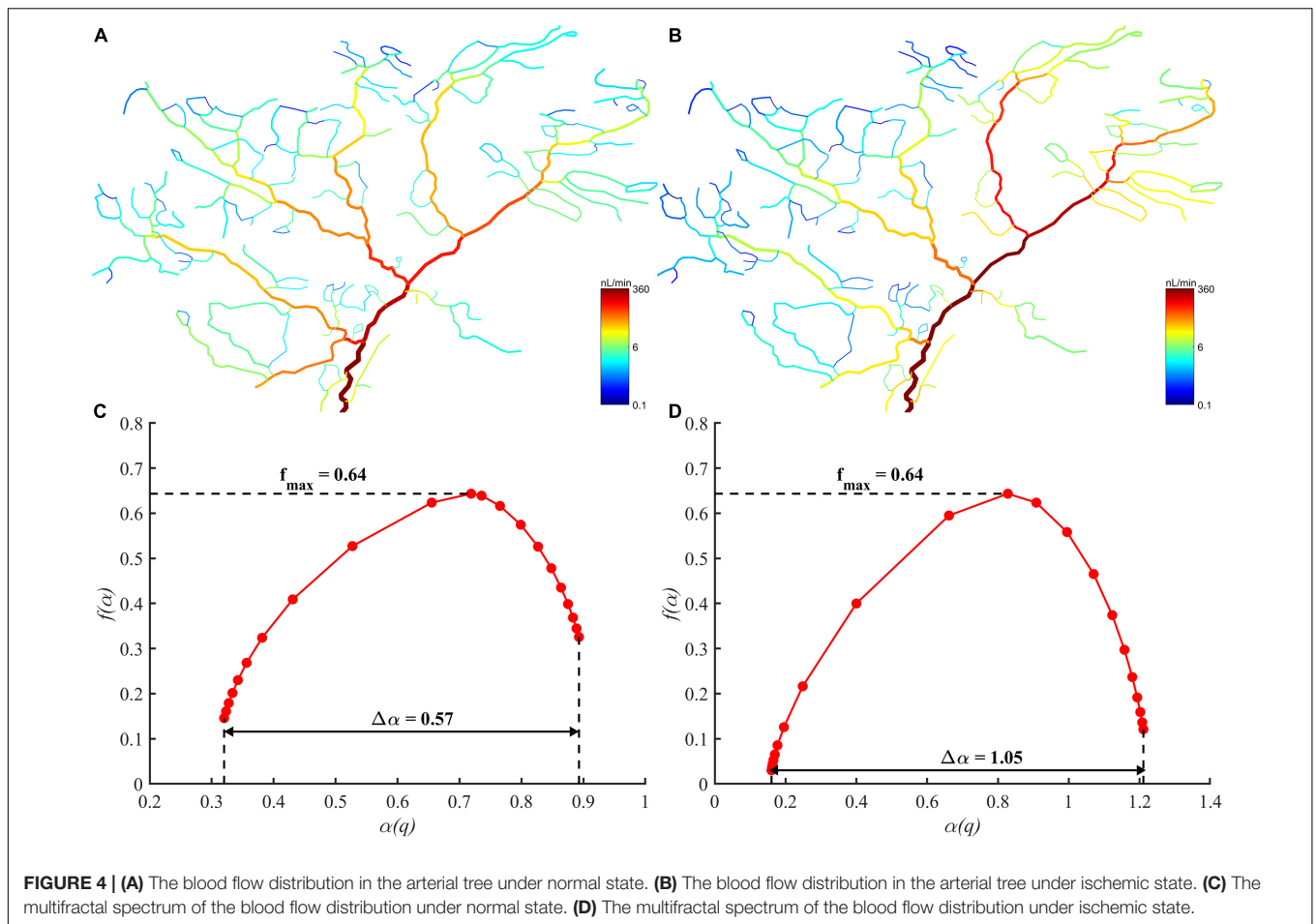


**FIGURE 4 | (A)** The blood flow distribution in the arterial tree under normal state. **(B)** The blood flow distribution in the arterial tree under ischemic state. **(C)** The multifractal spectrum of the blood flow distribution under normal state. **(D)** The multifractal spectrum of the blood flow distribution under ischemic state.

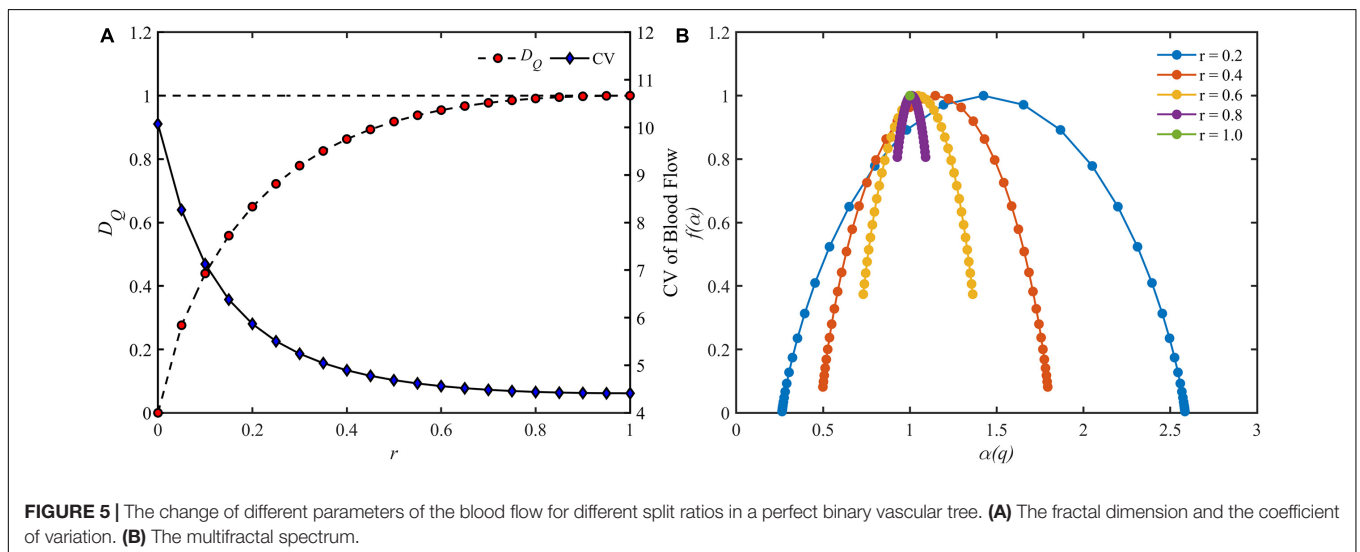


**FIGURE 5 |** The change of different parameters of the blood flow for different split ratios in a perfect binary vascular tree. **(A)** The fractal dimension and the coefficient of variation. **(B)** The multifractal spectrum.

in Figure 7. We can see that there exists a strong linear relationship between the logarithmic values of the diameter and the blood flow rate.

The fractal dimensions for blood flow in the constructed vascular trees are shown in Figure 8. For the vascular trees

with the mean  $k$  value of 2.7, the fractal dimension increases monotonically from  $0.74 \pm 0.01$  to  $1.00 \pm 0.00$  with  $\lambda$  rising from 0.60 to 1. While for the vascular trees with the mean  $\lambda$  value of 0.8, the fractal dimension fluctuates between 0.91 and 0.95 with the increment of  $k$ .



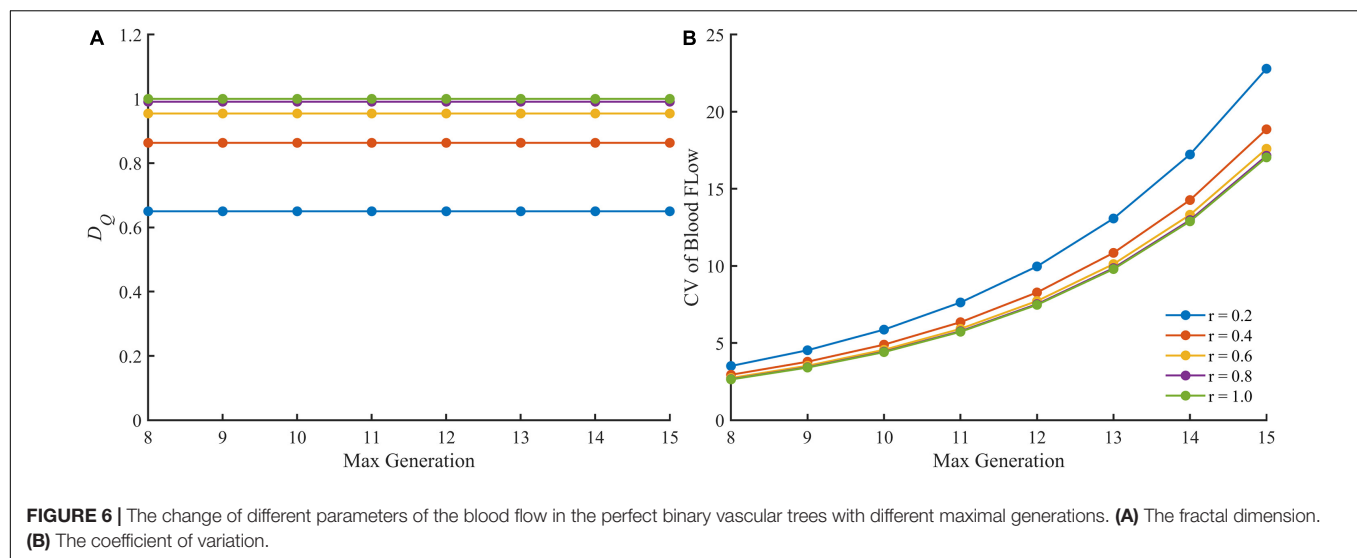


**TABLE 1 |** The characteristics of the constructed vascular trees.

$k$	$\lambda$	Vessel number	Max generation	$k$	$\lambda$	Vessel number	Max generation
2.7	0.60	7471 $\pm$ 97	33.8 $\pm$ 1.7	2.3	0.80	2822 $\pm$ 334	15.3 $\pm$ 0.6
	0.65	8261 $\pm$ 130	28.2 $\pm$ 1.2	2.4		3525 $\pm$ 281	15.8 $\pm$ 0.6
	0.70	9012 $\pm$ 83	24.9 $\pm$ 0.8	2.5		5102 $\pm$ 469	16.7 $\pm$ 0.5
	0.75	9777 $\pm$ 73	21.5 $\pm$ 0.7	2.6		6987 $\pm$ 887	17.4 $\pm$ 0.7
	0.80	10692 $\pm$ 99	19.5 $\pm$ 0.7	2.7		10210 $\pm$ 1389	18.8 $\pm$ 0.9
	0.85	11387 $\pm$ 112	17.8 $\pm$ 0.4	2.8		14672 $\pm$ 1038	20.2 $\pm$ 0.7
	0.90	12189 $\pm$ 93	16.4 $\pm$ 0.5	2.9		19149 $\pm$ 2544	21.2 $\pm$ 0.4
	0.95	12818 $\pm$ 110	15.3 $\pm$ 0.5	3.0		27222 $\pm$ 1774	22.2 $\pm$ 0.9
	1.00	16234 $\pm$ 102	13.0 $\pm$ 0.0				

The multifractal spectrums of the blood flow for these vascular trees are presented in **Figures 9A,C**. It is observed that the multifractality of blood flow exists in all vascular trees but the multifractal spectrums fluctuate. With the increment of  $\lambda$ , the range of the multifractal spectrum  $\Delta\alpha$  narrows from  $0.89 \pm 0.04$  to  $0.04 \pm 0.01$  and the maximal value grows from  $0.93 \pm 0.01$  to  $1.00 \pm 0.00$ . And with the increment of  $k$ ,  $\Delta\alpha$  expands from  $0.32 \pm 0.04$  to  $0.65 \pm 0.03$  and the maximal value grows from  $0.95 \pm 0.01$  to  $0.99 \pm 0.00$ . The features of the multifractal spectrums are shown in **Figures 9B,D**. Compared with the fractal dimensions, the difference of multifractal spectrums among these vascular trees is more striking.

## DISCUSSION

### Validity of the Hemodynamic Simulation

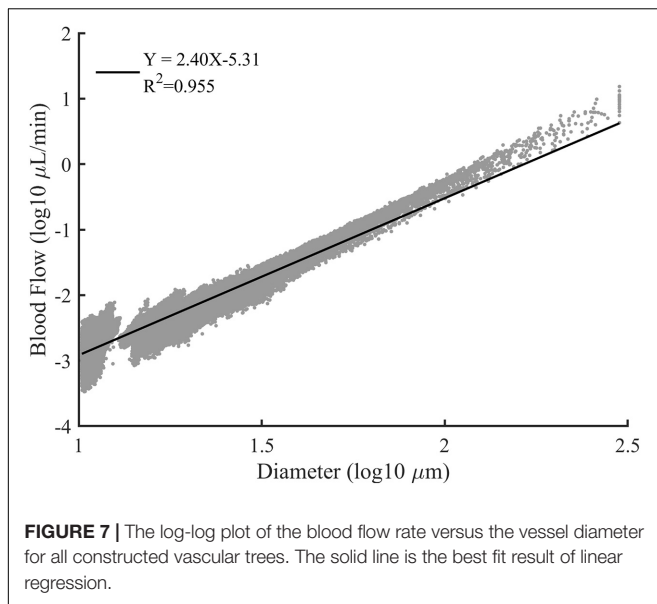
The hemodynamic simulation was conducted to investigate the variation of fractal parameters with varying blood flow distribution. To make sure that the obtained blood flow distribution is reasonable, a quantitative comparison of the hemodynamic simulation with the existing physiological studies is necessary. For avoiding losing the generality, the boundary condition in the present work was prescribed with an inlet

pressure of 1 mmHg and an outlet pressure of 0 mmHg. However, the pressure drop between the inlet and outlet may vary in different studies. Thus, for quantitative comparison, it is more appropriate to examine the relative indices.

As shown in **Figure 7**, a strong linear relationship exists between the logarithmic values of the diameter and the blood flow rate. This is consistent with the assertion in Huo and Kassab (2016) that there is a scaling law between the blood flow rate and diameter. The slope of the fitting line indicates the relation between the blood flow rate and vascular diameter thus can be an indicator for quantitative comparison. Within a similar diameter range, the slope with a value of 2.40 produced in our work is comparable with the reported work of 1.97 (Wang et al., 2009),  $2.0 \pm 0.2$  (Pijewska et al., 2020), 2.33 (Huo and Kassab, 2012), and  $2.49 \pm 0.09$  (Haindl et al., 2016). Thus, it can be concluded that the simulation results of our work are reasonable.

### Physiological Significance of the Fractal Parameters

Two fractal parameters, i.e., fractal dimension and multifractal spectrum, were obtained in this study to investigate the fractality and multifractality of blood flow.



By definition, the fractal dimension is determined by the total entropy of blood flow. And the total entropy is calculated by considering the existence as well as the quantity of blood flow in the vessel segment. The existence and the quantity of blood flow are corresponding to the vascular structure and the blood flow distribution, respectively. Thus, the fractal dimension characterizes the combination of the features of vascular structure and blood flow distribution. When the vascular structure is fixed, the lower entropy is obtained from the more heterogeneous distribution according to the information theory. That is to say, the fractal dimension reflects the degree of the blood flow heterogeneity for a specific vascular tree and the lower fractal dimension comes from the blood flow distribution with a higher degree of heterogeneity. The results in **Figure 5A** that the lower fractal dimension is corresponding to the lower split ratio also support this conclusion.

For a fractal object, the multifractal spectrum describes the scaling properties in different subsets. And when multifractality presents, the subsets of this object will be scaled by different multiples at the same  $q$  order moment during the calculation of the multifractal spectrum. Therefore, the degree of multifractality, which is measured by the width of the multifractal spectrum, essentially describes the degree of heterogeneity within the fractal object and it rises with the increment of the blood flow heterogeneity. This judgment is consistent with the results as shown in **Figure 5B**. The multifractal spectrum  $f(\alpha(q))$  reaches its maximal value when  $q = 0$ . In this case, the quantity of the blood flow volume no longer has an effect on the value of  $f(\alpha(0))$ . In other words, the height of the multifractal spectrum reflects the heterogeneity or asymmetry of the vascular structure. The higher the multifractal spectrum the closer the vascular tree is to the perfect binary tree. And this makes clear why the height of the multifractal spectrums in **Figures 4C,D** or **Figure 5B** is the same. By means of the width and height, the multifractal spectrum separates the information

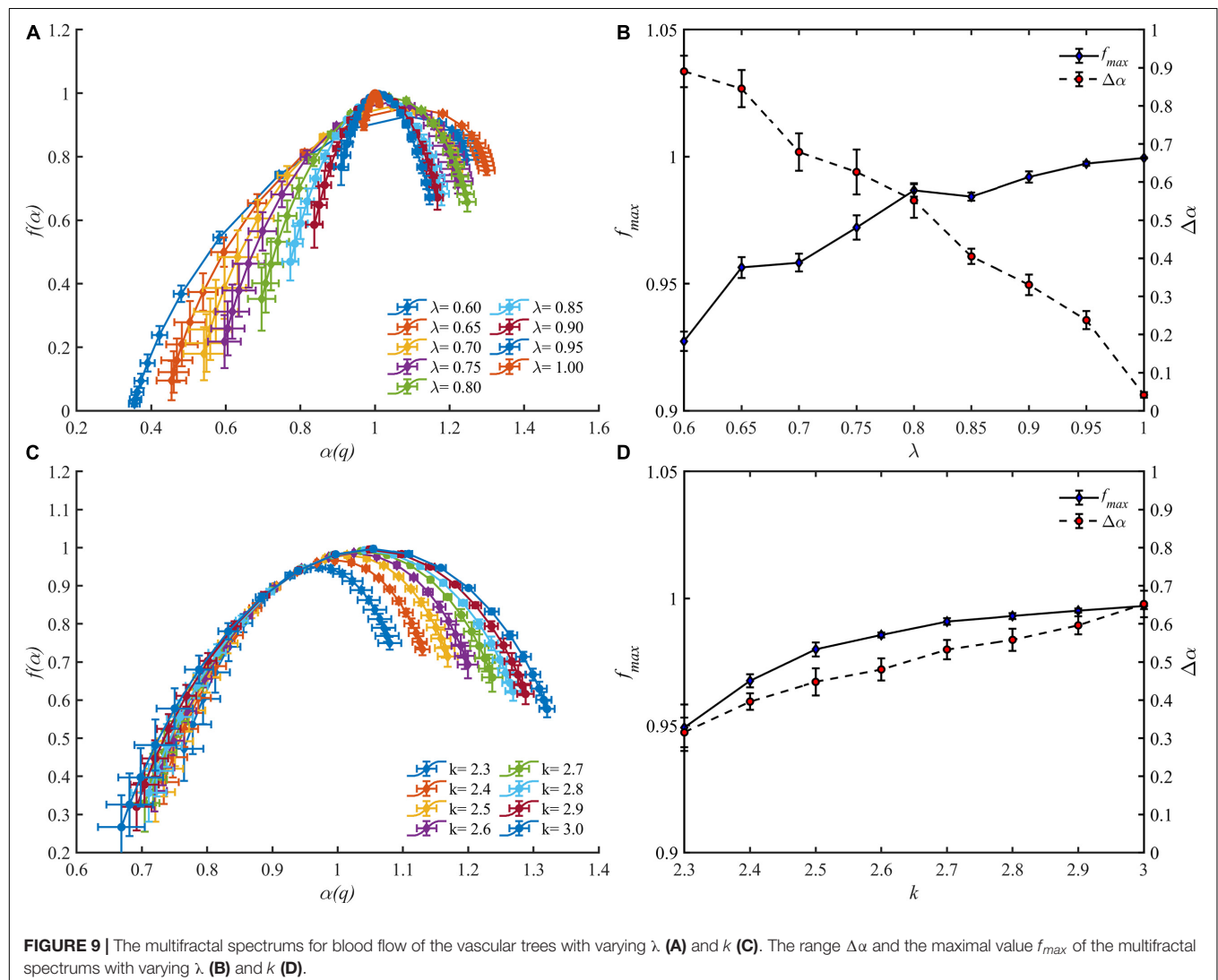
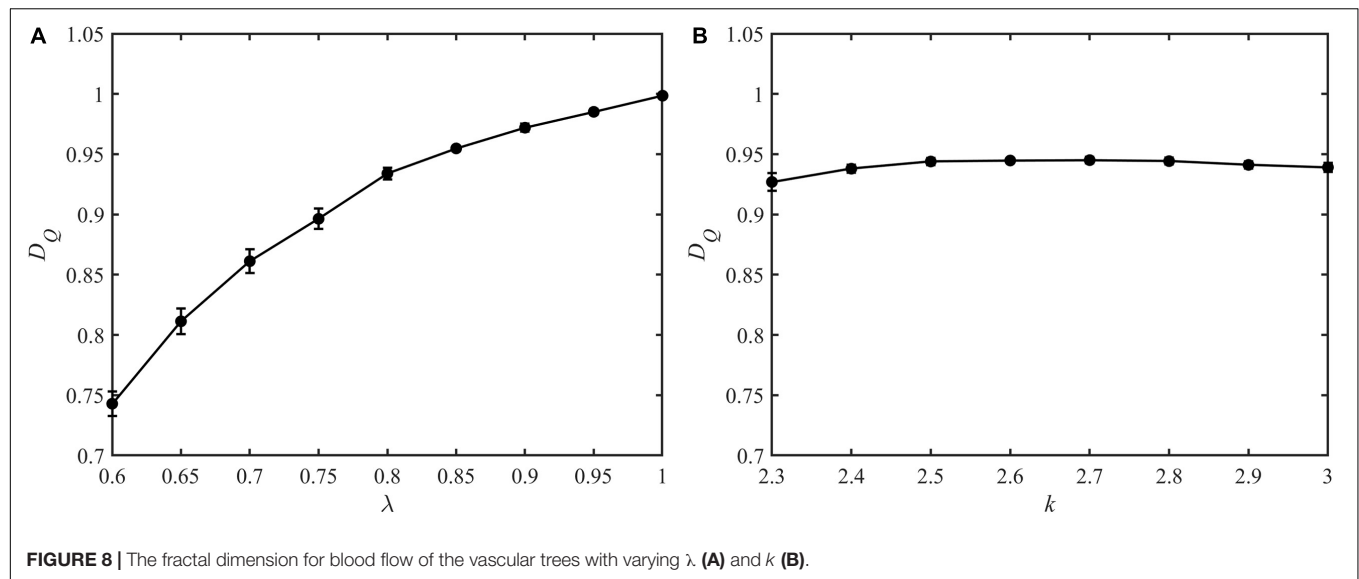
about the vascular structure and blood flow distribution. In this sense, the multifractal spectrum makes the evaluation of the blood flow distribution in different vascular trees possible. As shown in **Figure 9D**, the heterogeneity of the vascular structure decreases with the increment of the bifurcation exponent while the heterogeneity of the blood flow distribution increases. The interaction of these two opposite trends may explain why the fractal dimension changes slightly with the bifurcation exponent as shown in **Figure 8B**.

Both the fractal dimension and the multifractal spectrum reflect the blood flow heterogeneity. Physiologically speaking, the change of blood flow heterogeneity is usually associated with pathological conditions. For microcirculation, the increment of blood flow heterogeneity can be an early indicator of diseases, such as sepsis and shock (Ince, 2005; Dubin et al., 2018; Ince et al., 2018) as well as peripheral vascular disease (Butcher et al., 2013). And the increase of blood flow heterogeneity can be depicted by the decrease of fractal dimension and the broadening of the multifractal spectrum. The multifractal spectrum can separate the information about the vascular structure and blood flow distribution. Thus, the multifractal spectrum is also able to distinguish the causes responsible for the change in blood flow heterogeneity, either by hemodynamic problems or by structural alteration due to the diseases such as large vessel stenosis (Kharche et al., 2018).

There are also some other quantitative or semi-quantitative methods for characterizing the blood flow heterogeneity (Bassingthwaite et al., 1989; Pries and Secomb, 2009; Ince et al., 2018). In this study, the blood flow heterogeneity is also evaluated by CV. The results in **Figure 5A** confirm the availability of this statistical parameter. However, the CV treats different vessel segments in a vascular tree as independent components ignoring the connection of blood flow along the whole tree. This would make this parameter less accurate in some cases as discussed below. When the split ratio for each bifurcation in the perfect binary vascular tree is 1, the blood flow is evenly distributed for each generation in the vascular tree. The degree of blood flow heterogeneity should remain unchanged no matter what the maximal generation of the vascular tree is. And this property holds for the other values of the split ratio. As shown in **Figure 6A**, the fractal dimension stays the same with the change of the maximal generation. However, the values of CV for the vascular trees with different maximal generations are quite different. Considering both the connection and difference of blood flow in different vessel segments, the fractal parameters can provide a more accurate description of the blood flow heterogeneity for the tree-like vasculature.

## Limitations

It should be pointed out the hemodynamic simulation in this study was simplified. Nowadays, the RCL model has been developed for hemodynamic simulation in which the resistance (R), capacitance (C), and inductance (L) elements were used to mimic the effects of vessel resistance, vessel compliance, and blood inertia, respectively (Muller and Toro, 2014; Zhang et al., 2014). And models from 0D to 3D were established (Arciero et al., 2017; Liu et al., 2020). In the present hemodynamic model of



microcirculation, only the resistance element for a vessel segment was considered. Although in the microcirculation the resistance element plays a dominant role in hemodynamics (Katanov et al., 2015; Nichols et al., 2015; Secomb, 2017) and the results show that the model is sufficient for produce varying blood flow distribution in a tree, a comprehensive model is worth being introduced in the future study.

## CONCLUSION

In this study, the fractal methods were introduced, with appropriate modification, to characterize the multi-scale properties of blood flow. The application of the methods to the real physiological data verified its ability in distinguishing the variety of blood flow distribution. The yielded parameters, as the fractal dimension and the multifractal spectrum for blood flow, can quantify the degree of blood flow heterogeneity. With the increase of blood flow heterogeneity, the fractal dimension decreases and the multifractal spectrum expands. And the investigation on various constructed vascular trees suggests that both the vascular structure and the blood flow distribution influence the fractal parameters. With the aid of the fractal dimension, it is possible to look into the change of blood flow heterogeneity in a specific vascular tree. While the multifractal spectrum can be utilized to assess the blood flow heterogeneity for different vascular trees by considering the blood

flow distribution and the structure of vascular trees separately. It can be concluded that the proposed methods provide efficient tools to describe the multi-scale properties of the blood flow distribution and has the potential to assist the study of multi-scale vascular physiology.

## DATA AVAILABILITY STATEMENT

The original contributions presented in the study are included in the article/supplementary material, further inquiries can be directed to the corresponding authors.

## AUTHOR CONTRIBUTIONS

PL and QP: conceptualization and methodology. PL: algorithm and writing (original draft). SJ and GN: writing (review and editing). MY and JY: discussion of the results and their relevance. GN and JY: supervision and project administration. All authors approved the manuscript.

## FUNDING

This study was supported by the National Natural Science Foundation of China (Grant Numbers 81871454 and 31870938).

## REFERENCES

- Alosco, M. L., Gunstad, J., Jerskey, B. A., Xu, X., Clark, U. S., Hassenstab, J., et al. (2013). The adverse effects of reduced cerebral perfusion on cognition and brain structure in older adults with cardiovascular disease. *Brain Behav.* 3, 626–636. doi: 10.1002/brb3.171
- Alosco, M. L., Spitznagel, M. B., Cohen, R., Raz, N., Sweet, L. H., Josephson, R., et al. (2014). Reduced cerebral perfusion predicts greater depressive symptoms and cognitive dysfunction at a 1-year follow-up in patients with heart failure. *Int. J. Geriatr. Psychiatry* 29, 428–436. doi: 10.1002/gps.4023
- Arciero, J. C., Causin, P., and Malgaroli, F. (2017). Mathematical methods for modeling the microcirculation. *AIMS Biophys.* 4, 362–399. doi: 10.3934/biophys.2017.3.362
- Bassingthwaight, J. B., Beard, D. A., and Li, Z. (2001). The mechanical and metabolic basis of myocardial blood flow heterogeneity. *Basic Res. Cardiol.* 96, 582–594. doi: 10.1007/s003950170010
- Bassingthwaight, J. B., King, R. B., and Roger, S. A. (1989). Fractal nature of regional myocardial blood flow heterogeneity. *Circ. Res.* 65, 578–590. doi: 10.1161/01.res.65.3.578
- Butcher, J. T., Goodwill, A. G., Stanley, S. C., and Frisbee, J. C. (2013). Blunted temporal activity of microvascular perfusion heterogeneity in metabolic syndrome: a new attractor for peripheral vascular disease? *Am. J. Physiol. Heart Circ. Physiol.* 304, H547–H558. doi: 10.1152/ajpheart.00805.2012
- Cheng, S. C., and Huang, Y. M. (2003). A novel approach to diagnose diabetes based on the fractal characteristics of retinal images. *IEEE Trans. Inf. Technol. Biomed.* 7, 163–170. doi: 10.1109/titb.2003.813792
- Cheung, C. Y., Tay, W. T., Mitchell, P., Wang, J. J., Hsu, W., Lee, M. L., et al. (2011). Quantitative and qualitative retinal microvascular characteristics and blood pressure. *J. Hypertens.* 29, 1380–1391. doi: 10.1097/HJH.0b013e328347266c
- Chhabra, A., and Jensen, R. V. (1989). Direct determination of the  $f(\alpha)$  singularity spectrum. *Phys. Rev. Lett.* 62, 1327–1330. doi: 10.1103/PhysRevLett.62.1327
- Dubin, A., Henriquez, E., and Hernandez, G. (2018). Monitoring peripheral perfusion and microcirculation. *Curr. Opin. Crit. Care* 24, 173–180. doi: 10.1097/MCC.0000000000000495
- Efimova, I. Y., Efimova, N. Y., Triss, S. V., and Lishmanov, Y. B. (2008). Brain perfusion and cognitive function changes in hypertensive patients. *Hypertens. Res.* 31, 673–678. doi: 10.1291/hypres.31.673
- Fahraeus, R., and Lindqvist, T. (1931). The viscosity of the blood in narrow capillary tubes. *Am. J. Physiol.* 96, 562–568.
- Gabrys, E., Rybaczuk, M., and Kedzia, A. (2005). Fractal models of circulatory system. Symmetrical and asymmetrical approach comparison. *Chaos Solitons Fractals* 24, 707–715. doi: 10.1016/j.chaos.2004.09.087
- Gould, D. J., Vadakkan, T. J., Poche, R. A., and Dickinson, M. E. (2011). Multifractal and lacunarity analysis of microvascular morphology and remodeling. *Microcirculation* 18, 136–151. doi: 10.1111/j.1549-8719.2010.00075.x
- Grasman, J., Brascamp, J. W., Van Leeuwen, J. L., and Van Putten, B. (2003). The multifractal structure of arterial trees. *J. Theor. Biol.* 220, 75–82. doi: 10.1006/jtbi.2003.3151
- Guven, G., Hilty, M. P., and Ince, C. (2020). Microcirculation: physiology, pathophysiology, and clinical application. *Blood Purif.* 49, 143–150. doi: 10.1159/000503775
- Haindl, R., Trasischker, W., Wartak, A., Baumann, B., Pircher, M., and Hitzenberger, C. (2016). Total retinal blood flow measurement by three beam Doppler optical coherence tomography. *Biomed. Opt. Express* 7, 287–301. doi: 10.1364/BOE.7.000287
- Halley, J. M., Hartley, S., Kallimanis, A. S., Kunin, W. E., Lennon, J. J., and Sgardelis, S. P. (2004). Uses and abuses of fractal methodology in ecology. *Ecol. Lett.* 7, 254–271. doi: 10.1111/j.1461-0248.2004.00568.x
- Halsey, T. C., Jensen, M. H., Kadanoff, L. P., Procaccia, I. I., and Shraiman, B. I. (1986). Fractal measures and their singularities: the characterization of strange sets. *Phys. Rev. A Gen. Phys.* 33, 1141–1151. doi: 10.1103/physreva.33.1141
- Hassan, M. K. (2019). Is there always a conservation law behind the emergence of fractal and multifractal? *Eur. Phys. J. Spec. Top.* 228, 209–232. doi: 10.1140/epjst/e2019-800110-x



- Huo, Y., and Kassab, G. S. (2012). Intraspecific scaling laws of vascular trees. *J. R. Soc. Interface* 9, 190–200. doi: 10.1098/rsif.2011.0270
- Huo, Y., and Kassab, G. S. (2016). Scaling laws of coronary circulation in health and disease. *J. Biomech.* 49, 2531–2539. doi: 10.1016/j.jbiomech.2016.01.044
- Ince, C. (2005). The microcirculation is the motor of sepsis. *Crit. Care* 9(Suppl. 4), S13–S19. doi: 10.1186/cc3753
- Ince, C., Boerma, E. C., Cecconi, M., De Backer, D., Shapiro, N. I., Duranseau, J., et al. (2018). Second consensus on the assessment of sublingual microcirculation in critically ill patients: results from a task force of the European Society of Intensive Care Medicine. *Intensive Care Med.* 44, 281–299. doi: 10.1007/s00134-018-5070-7
- Katanov, D., Gommer, G., and Fedosov, D. A. (2015). Microvascular blood flow resistance: role of red blood cell migration and dispersion. *Microvasc. Res.* 99, 57–66. doi: 10.1016/j.mvr.2015.02.006
- Khariche, S. R., So, A., Salerno, F., Lee, T. Y., Ellis, C., Goldman, D., et al. (2018). Computational assessment of blood flow heterogeneity in peritoneal dialysis patients' cardiac ventricles. *Front. Physiol.* 9:511. doi: 10.3389/fphys.2018.00511
- Kitagawa, K., Oku, N., Kimura, Y., Yagita, Y., Sakaguchi, M., Hatazawa, J., et al. (2009). Relationship between cerebral blood flow and later cognitive decline in hypertensive patients with cerebral small vessel disease. *Hypertens. Res.* 32, 816–820. doi: 10.1038/hr.2009.100
- Liu, H., Wang, D., Leng, X., Zheng, D., Chen, F., Wong, L. K. S., et al. (2020). State-of-the-art computational models of circle of willis with physiological applications: a review. *IEEE Access* 8, 156261–156273. doi: 10.1109/access.2020.3007737
- Liu, J. S., Ding, W. L., Dai, J. S., Zhao, G., Sun, Y. X., and Yang, H. M. (2018). Unreliable determination of fractal characteristics using the capacity dimension and a new method for computing the information dimension. *Chaos Solitons Fractals* 113, 16–24. doi: 10.1016/j.chaos.2018.05.008
- Lorthois, S., and Cassot, F. (2010). Fractal analysis of vascular networks: insights from morphogenesis. *J. Theor. Biol.* 262, 614–633. doi: 10.1016/j.jtbi.2009.10.037
- Mandelbrot, B. B. (1982). *The Fractal Geometry of Nature*. New York, NY: W.H. Freeman.
- Muller, L. O., and Toro, E. F. (2014). A global multiscale mathematical model for the human circulation with emphasis on the venous system. *Int. J. Numer. Method. Biomed. Eng.* 30, 681–725. doi: 10.1002/cnm.2622
- Nadal, J., Deverduin, J., de Champfleure, N. M., Carriere, I., Creuzot-Garcher, C., Delcourt, C., et al. (2020). Retinal vascular fractal dimension and cerebral blood flow, a pilot study. *Acta Ophthalmol. (Copenh.)* 98, E63–E71. doi: 10.1111/aos.14232
- Nayak, S. R., Mishra, J., and Palai, G. (2019). Analysing roughness of surface through fractal dimension: a review. *Image Vis. Comput.* 89, 21–34. doi: 10.1016/j.imavis.2019.06.015
- Nichols, W. W., Heffernan, K. S., and Chirinos, J. A. (2015). "Overview of the normal structure and function of the macrocirculation and microcirculation," in *Arterial Disorders: Definition, Clinical Manifestations, Mechanisms and Therapeutic Approaches*, eds A. Berbari and G. Mancina (Cham: Springer International Publishing), 13–46.
- Pijewska, E., Sylwestrzak, M., Gorczynska, I., Tamborski, S., Pawlak, M. A., and Szkulmowski, M. (2020). Blood flow rate estimation in optic disc capillaries and vessels using doppler optical coherence tomography with 3D fast phase unwrapping. *Biomed. Opt. Express* 11, 1336–1353. doi: 10.1364/boe.382155
- Pitsianis, N., Bleris, G. L., and Argyrakakis, P. (1989). Information dimension in fractal structures. *Phys. Rev. B Condens. Matter* 39, 7097–7100. doi: 10.1103/physrevb.39.7097
- Pries, A. R., and Secomb, T. W. (2005). Microvascular blood viscosity in vivo and the endothelial surface layer. *Am. J. Physiol. Heart Circ. Physiol.* 289, H2657–H2664. doi: 10.1152/ajpheart.00297.2005
- Pries, A. R., and Secomb, T. W. (2009). Origins of heterogeneity in tissue perfusion and metabolism. *Cardiovasc. Res.* 81, 328–335. doi: 10.1093/cvr/cvn318
- Reglin, B., Secomb, T. W., and Pries, A. R. (2009). Structural adaptation of microvessel diameters in response to metabolic stimuli: where are the oxygen sensors? *Am. J. Physiol. Heart Circ. Physiol.* 297, H2206–H2219. doi: 10.1152/ajpheart.00348.2009
- Reglin, B., Secomb, T. W., and Pries, A. R. (2017). Structural control of microvessel diameters: origins of metabolic signals. *Front. Physiol.* 8:813. doi: 10.3389/fphys.2017.00813
- Schmidt, A., Zidowitz, S., Kriete, A., Denhard, T., Krass, S., and Peitgen, H. O. (2004). A digital reference model of the human bronchial tree. *Comput. Med. Imaging Graph.* 28, 203–211. doi: 10.1016/j.compmedimag.2004.01.001
- Secomb, T. W. (2017). Blood flow in the microcirculation. *Annu. Rev. Fluid Mech.* 49, 443–461. doi: 10.1146/annurev-fluid-010816-060302
- So, G. B., So, H. R., and Jin, G. G. (2017). Enhancement of the box-counting algorithm for fractal dimension estimation. *Pattern Recognit. Lett.* 98, 53–58. doi: 10.1016/j.patrec.2017.08.022
- Stosis, T., and Stosis, B. D. (2006). Multifractal analysis of human retinal vessels. *IEEE Trans. Med. Imaging* 25, 1101–1107. doi: 10.1109/tmi.2006.879316
- Takahashi, T. (2014). *Microcirculation in Fractal Branching Networks*. Tokyo: Springer.
- Takahashi, T., Nagaoka, T., Yanagida, H., Saitoh, T., Kamiya, A., Hein, T., et al. (2009). A mathematical model for the distribution of hemodynamic parameters in the human retinal microvascular network. *Biorheology* 23, 77–86.
- Van Beek, J. H., Roger, S. A., and Bassingthwaite, J. B. (1989). Regional myocardial flow heterogeneity explained with fractal networks. *Am. J. Physiol.* 257(5 Pt 2), H1670–H1680. doi: 10.1152/ajpheart.1989.257.5.H1670
- Wang, R. F., Li, P. L., Pan, Q., Li, J. K. J., Kuebler, W. M., Pries, A. R., et al. (2019). Investigation into the diversity in the fractal dimensions of arterioles and venules in a microvascular network—a quantitative analysis. *Microvasc. Res.* 125:10. doi: 10.1016/j.mvr.2019.103882
- Wang, Y., Lu, A., Gil-Flamer, J., Tan, O., Izatt, J. A., and Huang, D. (2009). Measurement of total blood flow in the normal human retina using doppler fourier-domain optical coherence tomography. *Br. J. Ophthalmol.* 93, 634–637. doi: 10.1136/bjo.2008.150276
- Yang, J., and Wang, Y. (2013). Design of vascular networks: a mathematical model approach. *Int. J. Numer. Method. Biomed. Eng.* 29, 515–529. doi: 10.1002/cnm.2534
- Zamir, M. (2001). Fractal dimensions and multifractality in vascular branching. *J. Theor. Biol.* 212, 183–190. doi: 10.1006/jtbi.2001.2367
- Zhang, C., Wang, L., Li, X. Y., Li, S. Y., Pu, F., Fan, Y. B., et al. (2014). Modeling the circle of Willis to assess the effect of anatomical variations on the development of unilateral internal carotid artery stenosis. *Biomed. Mater. Eng.* 24, 491–499. doi: 10.3233/bme-130835

**Conflict of Interest:** The authors declare that the research was conducted in the absence of any commercial or financial relationships that could be construed as a potential conflict of interest.

**Publisher's Note:** All claims expressed in this article are solely those of the authors and do not necessarily represent those of their affiliated organizations, or those of the publisher, the editors and the reviewers. Any product that may be evaluated in this article, or claim that may be made by its manufacturer, is not guaranteed or endorsed by the publisher.

Copyright © 2021 Li, Pan, Jiang, Yan, Yan and Ning. This is an open-access article distributed under the terms of the Creative Commons Attribution License (CC BY). The use, distribution or reproduction in other forums is permitted, provided the original author(s) and the copyright owner(s) are credited and that the original publication in this journal is cited, in accordance with accepted academic practice. No use, distribution or reproduction is permitted which does not comply with these terms.

## APPENDIX

For the perfect binary vascular tree where the split ratio of each bifurcation is identical, if we normalize the blood flow in the main vessel at generation 0 as 1 and denote the split ratio by  $r$ , there will be  $C_n^k$  vessels with blood flow  $\left(\frac{r}{1+r}\right)^k \left(\frac{1}{1+r}\right)^{n-k}$  at generation  $n$ . And the summed entropy of the blood flow at generation  $n$  is as below:

$$\begin{aligned} & \sum_{k=0}^n C_n^k \left[ -\frac{r^k}{(1+r)^k} \frac{1}{(1+r)^{n-k}} \log \left( \frac{r^k}{(1+r)^k} \frac{1}{(1+r)^{n-k}} \right) \right] \\ &= -\sum_{k=0}^n C_n^k \left[ \frac{r^k}{(1+r)^k} \frac{1}{(1+r)^{n-k}} \log \left( \frac{r^k}{(1+r)^k} \right) \right] - \sum_{k=0}^n C_n^k \left[ \frac{r^k}{(1+r)^k} \frac{1}{(1+r)^{n-k}} \log \left( \frac{1}{(1+r)^{n-k}} \right) \right] \\ &= -\log \left( \frac{r}{1+r} \right) \cdot \sum_{k=0}^n C_n^k \left[ k \cdot \frac{r^k}{(1+r)^k} \frac{1}{(1+r)^{n-k}} \right] - \log \left( \frac{1}{1+r} \right) \cdot \sum_{k=0}^n C_n^k \left[ k \cdot \frac{1}{(1+r)^k} \frac{r^{n-k}}{(1+r)^{n-k}} \right] \end{aligned}$$

Assuming  $p = \frac{r}{1+r}$ , there is

$$\sum_{k=0}^n C_n^k \cdot k \cdot \frac{r^k}{(1+r)^k} \frac{1}{(1+r)^{n-k}} = \sum_{k=0}^n C_n^k \cdot k \cdot p^k (1-p)^{n-k}$$

which is the expression of the expectation of a binomial distribution  $B(n, p)$  and it equals to  $np$ . Thus,

$$\begin{aligned} & -\log \left( \frac{r}{1+r} \right) \cdot \sum_{k=0}^n C_n^k \left[ k \cdot \frac{r^k}{(1+r)^k} \frac{1}{(1+r)^{n-k}} \right] - \log \left( \frac{1}{1+r} \right) \cdot \sum_{k=0}^n C_n^k \left[ k \cdot \frac{1}{(1+r)^k} \frac{r^{n-k}}{(1+r)^{n-k}} \right] \\ &= -\log \left( \frac{r}{1+r} \right) \cdot n \cdot \frac{r}{1+r} - \log \left( \frac{1}{1+r} \right) \cdot n \cdot \frac{1}{1+r} \\ &= -n \left( \frac{r \log r - (1+r) \log (1+r)}{(1+r)} \right) \end{aligned}$$

And the fractal dimension of blood flow for the perfect binary vascular tree with split ratio  $r$  is obtained as:

$$D_Q(r) = \frac{-n \left( \frac{r \log r - (1+r) \log (1+r)}{(1+r)} \right)}{\log 2^n} = \frac{(1+r) \log (1+r) - r \log r}{\log 2 \cdot (1+r)}$$



# Comparison of Newtonian and Non-newtonian Fluid Models in Blood Flow Simulation in Patients With Intracranial Arterial Stenosis

Haipeng Liu<sup>1,2,3</sup>, Linfang Lan<sup>1</sup>, Jill Abrigo<sup>2</sup>, Hing Lung Ip<sup>1</sup>, Yannie Soo<sup>1</sup>, Dingchang Zheng<sup>3</sup>, Ka Sing Wong<sup>1</sup>, Defeng Wang<sup>2</sup>, Lin Shi<sup>2\*</sup>, Thomas W. Leung<sup>1</sup> and Xinyi Leng<sup>1,4\*</sup>

<sup>1</sup> Department of Medicine and Therapeutics, The Chinese University of Hong Kong, Hong Kong, China, <sup>2</sup> Department of Imaging and Interventional Radiology, The Chinese University of Hong Kong, Hong Kong, China, <sup>3</sup> Research Centre for Intelligent Healthcare, Coventry University, Coventry, United Kingdom, <sup>4</sup> Shenzhen Research Institute, The Chinese University of Hong Kong, Shenzhen, China

## OPEN ACCESS

### Edited by:

Eun Bo Shim,  
Kangwon National University,  
South Korea

### Reviewed by:

Zhiliang Xu,  
University of Notre Dame,  
United States  
Kranthi Kolli,  
Abbott, United States

### \*Correspondence:

Xinyi Leng  
xinyi\_leng@cuhk.edu.hk  
Lin Shi  
shilin@cuhk.edu.hk

### Specialty section:

This article was submitted to  
Computational Physiology  
and Medicine,  
a section of the journal  
Frontiers in Physiology

**Received:** 01 June 2021

**Accepted:** 16 August 2021

**Published:** 06 September 2021

### Citation:

Liu H, Lan L, Abrigo J, Ip HL,  
Soo Y, Zheng D, Wong KS, Wang D,  
Shi L, Leung TW and Leng X (2021)  
Comparison of Newtonian  
and Non-newtonian Fluid Models  
in Blood Flow Simulation in Patients  
With Intracranial Arterial Stenosis.  
Front. Physiol. 12:718540.  
doi: 10.3389/fphys.2021.718540

**Background:** Newtonian fluid model has been commonly applied in simulating cerebral blood flow in intracranial atherosclerotic stenosis (ICAS) cases using computational fluid dynamics (CFD) modeling, while blood is a shear-thinning non-Newtonian fluid. We aimed to investigate the differences of cerebral hemodynamic metrics quantified in CFD models built with Newtonian and non-Newtonian fluid assumptions, in patients with ICAS.

**Methods:** We built a virtual artery model with an eccentric 75% stenosis and performed static CFD simulation. We also constructed CFD models in three patients with ICAS of different severities in the luminal stenosis. We performed static simulations on these models with Newtonian and two non-Newtonian (Casson and Carreau-Yasuda) fluid models. We also performed transient simulations on another patient-specific model. We measured translesional pressure ratio (PR) and wall shear stress (WSS) values in all CFD models, to reflect the changes in pressure and WSS across a stenotic lesion. In all the simulations, we compared the PR and WSS values in CFD models derived with Newtonian, Casson, and Carreau-Yasuda fluid assumptions.

**Results:** In all the static and transient simulations, the Newtonian/non-Newtonian difference on PR value was negligible. As to WSS, in static models (virtual and patient-specific), the rheological difference was not obvious in areas with high WSS, but observable in low WSS areas. In the transient model, the rheological difference of WSS areas with low WSS was enhanced, especially during diastolic period.

**Conclusion:** Newtonian fluid model could be applicable for PR calculation, but caution needs to be taken when using the Newtonian assumption in simulating WSS especially in severe ICAS cases.

**Keywords:** non-Newtonian fluid, intracranial atherosclerotic stenosis, computational fluid dynamics, translesional pressure ratio, wall shear stress

## INTRODUCTION

Intracranial atherosclerotic stenosis (ICAS) is a major cause for ischemic stroke and transient ischemic attack (TIA) in Asian populations (Wong, 2006). In recent years, computational fluid dynamics (CFD) modeling based on conventional neurovascular imaging has been applied to simulate *in vivo* cerebral blood flow and quantify cerebral hemodynamic metrics in the presence of ICAS, which cannot be achieved with conventional neurovascular imaging alone (Liebeskind et al., 2016; Linfang Lan, 2017; Liu et al., 2018; Chen et al., 2020).

Computational fluid dynamics modeling studies have indicated that global and focal cerebral hemodynamics may play an important role in governing the risk of stroke recurrence in patients with symptomatic ICAS (Leng et al., 2014, 2019). For instance, translesional pressure ratio (PR), calculated as the ratio of the pressures distal and proximal to an ICAS lesion obtained in a CFD model, has been put forward to reflect the hemodynamic significance of ICAS (Liebeskind and Feldmann, 2013). On the other hand, the relative change of wall shear stress (WSS) at the stenotic throat as compared to WSS at proximal “normal” vessel segment, has also been proposed to reflect the hemodynamic impact of an ICAS lesion on plaque growth and rupture (Lan et al., 2020). Both indices have been associated with the risk of stroke relapse in patients with symptomatic ICAS: those with a lower PR (i.e., larger translesional pressure gradient) and excessively elevated focal WSS at the ICAS lesion had significantly higher risk of recurrent stroke despite optimal medical treatment (Leng et al., 2019).

In most of the previous CFD studies on ICAS, blood was simulated as a Newtonian fluid for simplicity (Leng et al., 2014, 2019; Nam et al., 2016; Liu et al., 2018; Chen et al., 2020), despite the fact that blood is a non-Newtonian fluid with a shear-thinning nature (Nader et al., 2019). With increasing flow velocity and shear strain rate, blood flows more smoothly (Moon et al., 2014) and its viscosity decreases toward a constant, which has been commonly used as the viscosity of blood in a Newtonian model (Jahangiri et al., 2017). However, in the low-velocity areas, the true viscosity is much higher than this constant, when non-Newtonian rheological models could simulate the blood viscosity variations in different shear strain rates (Gijssen et al., 1999; Jahangiri et al., 2017). Previous studies simulating blood flow in intracranial aneurysms, in normal aorta, and in virtual arterial stenosis models have indicated differences in the estimations of pressure and WSS based on Newtonian and non-Newtonian models (Hippelheuser et al., 2014; Rabby et al., 2014).

In this study, we therefore aimed to investigate the differences, if any, of CFD simulation results in pressure (e.g., PR) and WSS between Newtonian and non-Newtonian fluid models, in a virtual arterial stenosis model and patient-specific ICAS models; we performed static simulations on the virtual model, and both static and transient simulations on patients-specific models.

## MATERIALS AND METHODS

This was a substudy of the SOPHIA study (Stroke Risk and Hemodynamics in Intracranial Atherosclerotic Disease), a cohort

study conducted at three teaching hospitals to investigate cerebral hemodynamics in patients with symptomatic ICAS, using routine CT angiography (CTA)-based CFD models (Leng et al., 2019). The study was approved by local institutional review board and all patients provided informed consent. We performed static CFD simulations, separately with Newtonian and non-Newtonian (Casson and Carreau-Yasuda) fluid models, in a virtual arterial stenosis model and three patient-specific ICAS models constructed based on clinically routine CTA images. We also performed transient CFD simulations in another patient-specific ICAS model, with Newtonian and non-Newtonian fluid models. We compared hemodynamic metrics (pressure and WSS) obtained by Newtonian and non-Newtonian fluid models in each case.

## Rheological Assumptions

The viscosity of blood in the Newtonian model was a constant:  $\eta = 0.0035 \text{ Pa} \cdot \text{s}$  (Bernabeu et al., 2013). The Casson and Carreau-Yasuda models are two common non-Newtonian blood models. As a function of shear strain rate  $\dot{\gamma}$ , the blood viscosity  $\eta$  in Casson model can be expressed as that in Eq. 1 (Morales et al., 2013) and Carreau-Yasuda model in Eq. 2 (Bernabeu et al., 2013). The difference in blood viscosity among the three assumptions was more significant with lower shear strain rate (Figure 1A).

$$\eta(\dot{\gamma}) = \left( \sqrt{\eta_c} + \sqrt{\tau_c / \dot{\gamma}} \right)^2 \quad (1)$$

where  $\eta_c = 0.0035 \text{ Pa} \cdot \text{s}$ ,  $\tau_c = 0.004 \text{ Pa}$ .

$$\eta(\dot{\gamma}) = \eta_\infty + (\eta_0 - \eta_\infty) (1 + (\lambda \dot{\gamma})^a)^{(n-1)/a} \quad (2)$$

where  $\eta_0 = 0.16 \text{ Pa} \cdot \text{s}$ ,  $\eta_\infty = 0.0035 \text{ Pa} \cdot \text{s}$ ,  $\lambda = 8.2 \text{ s}$ ,  $a = 0.64$ , and  $n = 0.2128$ .

## Geometry Reconstruction

### Virtual Arterial Stenosis Model

Intracranial arteries are tortuous and the geometry varies between individuals. To investigate the differences in cerebral blood flow solely due to Newtonian or non-Newtonian fluid assumptions (without considering the effects of individualized arterial geometry) in CFD simulations, we first performed static simulations in a cylinder tube with 75% area stenosis (25% area remained at the stenotic throat), eccentric from the axis (Figure 1B). The radius was 1.5 mm, similar with middle cerebral artery (MCA) *in vivo*. The model was built in Solidworks 2020 (SolidWorks Co., Concord, MA, United States).

### Static MCA Stenosis Models

Four patients with stenosed MCA recruited in the SOPHIA study (Leng et al., 2019) were analyzed in the current study. We performed static cerebral blood flow simulation in three cases and transient simulation in the remaining case.

In the SOPHIA study, cerebral CTA was performed in all patients at baseline after an acute ischemic stroke or TIA, with a 64-slice CT scanner (Lightspeed VCT, GE Healthcare) with the following protocol: intravenous contrast (Omnipaque 300) was injected via the antecubital vein at a rate of 3–3.5 mL/s with a total volume of 70 mL, and images were obtained with



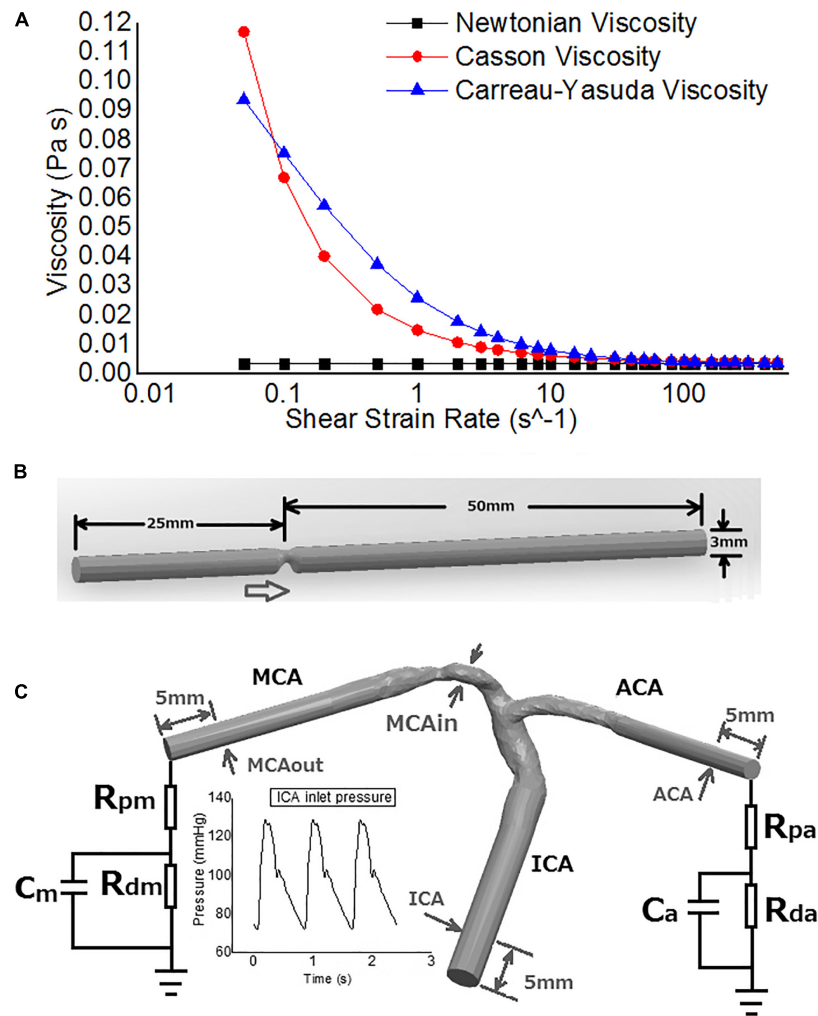


**FIGURE 1 |** The rheological and geometrical models. **(A)** Different rheologic models. Viscosity values are derived in varied shear strain rates. The shear strain rate axis is logarithmic. **(B)** Geometry of the virtual arterial stenosis model with an eccentric 75% stenosis in area (upper). **(C)** The transient MCA stenosis (about 55% in diameter and 74% in area at the throat) model with internal carotid artery (ICA)-middle cerebral artery (MCA)-anterior cerebral artery (ACA) branches (lower). Boundary conditions: pressure on ICA inlet, Windkessel models on ACA and MCA outlets. The arrows point to the positions of pressure measurement.

120 kVp, 550 mAs, 0.625 mm slice thickness and 0.4 s rotation (Lan et al., 2020).

The 3-dimensional vessel geometry of distal internal carotid artery (ICA) bifurcation with proximal MCA and anterior cerebral artery (ACA) was reconstructed based on the CTA source images, using MIMICS 18.0 (Materialise NV, Belgium). The geometry was then smoothed with errors (self-intersections, spikes, small holes, etc.) amended in Geomagic Studio 12.0 (3D Systems, Rock Hill, SC, United States). A neurologist (Dr. Lan) compared the reconstructed 3D geometry and the CTA images to confirm the correctness of the reconstructed 3D vessel geometry. These vessel geometries were patient-specific, which possessed different tortuosity and degrees of luminal stenosis.

### Transient MCA Stenosis Model

We simulated transient blood flow in another patient-specific model with MCA stenosis (55% diameter stenosis and 74%

area stenosis; **Figure 1C**). The geometry of ICA-MCA-ACA bifurcation was extracted from CTA source images similarly as the patient-specific models for static simulation. To eliminate spatial fluctuations of hemodynamic parameters adjacent to the stenotic lesion, we elongated the inlet and outlets to cylinders with identical cross-section areas in Solidworks software. The smoothing was performed in Geomagic Studio software, as for patient-specific static models.

### Mesh Generation

The geometric models were input into the ANSYS software package 2019 R1 (ANSYS, Inc., Canonsburg, PA, United States) on a DELL Precision T7610 Workstation for meshing and CFD simulation. Tetrahedral elements were used for meshing.

Currently, there is no standard on the maximal element size (maximal length of the edges of a tetrahedral element in the mesh) in meshing of the intracranial artery wall, which was

set as 0.25 mm in some previous studies (Ren et al., 2016; Vali et al., 2017; Lan et al., 2020). To preclude the possible effects of maximal element size on the simulation results, we conducted mesh independence study before determining the maximal element size to be adopted in the current study. On the three patient-specific models for static simulation, the pressure and WSS calculated using the meshes with the maximal element size of 0.5, 0.35, and 0.25 mm on intracranial artery wall were compared with the values derived from the mesh with maximal element size of 0.2 mm. The relative differences of area-averaged pressure and WSS were, respectively less than 1 and 3% in the simulations with maximal element sizes of 0.25 mm in each of the three cases. We therefore set the maximum element size as 0.25 mm globally and 0.1 mm at inlet and outlets as in the SOPHIA study (Leng et al., 2019; Lan et al., 2020). In the idealized virtual model, there were 372,567 nodes and 1,899,831 tetrahedral elements in the mesh. The number of element was larger than 410,000 in the meshes of all the three patient-specific models for static simulation. In the transient model, there were 608,462 nodes and 3,409,255 elements.

## Boundary Conditions and Computational Simulation

The meshes were input in ANSYS CFX software for CFD simulation and post-processing. With the arterial diameter of 3 mm and flow velocity of 140 cm/s at the stenotic throat, the Reynolds number is  $Re = \frac{\rho VD}{\mu} \approx 1484$ , within the range of laminar flow ( $Re < 2000$ ). Therefore, the Navier–Stokes equations were solved using finite volume method with the following settings and assumptions: (1) The fluid domain was simulated with incompressible, steady, and laminar flow assumption; (2) The density of blood was 1060 kg/m<sup>3</sup>; (3) The solid wall assumption was adopted on the artery wall; (4) The convergence criteria was 1.0e-4. The boundary conditions were set separately in different models.

On the virtual model, we simulated the average blood flow in a cardiac cycle. The inlet pressure was set as 110 mmHg while the mean velocity at the outlet was set as 35 cm/s (Liu et al., 2018). For each state, we performed the simulations with Newtonian, Casson and Carreau-Yasuda models.

In the patient-specific models for static simulation, the inlet pressure was set as 110 mmHg. Based on modified *in vivo* measurements, the mean velocities at MCA and ACA outlets were set as 35 and 31 cm/s, respectively to estimate the mass flow rates, which were in accordance with the Murray's law (Moore et al., 2006; Liu et al., 2018).

In the patient-specific model for transient simulation, we imposed physiological pressure waveform (range: 72–129 mmHg, **Figure 1C**) at the ICA inlet (Sarrami-Foroushani et al., 2015). Due to the lack of *in vivo* measurements of flow velocity at MCA/ACA outlets, we adopted 3-element Windkessel models, to avoid possible errors caused by possibly inaccurate assumptions in blood pressure or flow rate (**Figure 1C**). Parameters of the Windkessel models were based on physiological measurements that had been used in previous studies on cerebral arteries (Alastruey et al., 2007). Three transient simulations were

conducted over three cardiac cycles (with a time step length of 0.005 s) with Newtonian, Casson, and Carreau-Yasuda rheological assumptions separately.

## Measurement of Hemodynamic Metrics

Translesional PR was calculated as the ratio of post-stenotic pressure and pre-stenotic pressure (Feng et al., 2020). In the virtual model, to avoid any effect of unstable flow around the stenosis, the locations of pressure measurement were 5 mm from the inlet and the outlet. In the patient-specific models, the measurement were performed at the arterial segments away from the stenotic lesion where blood flow was possibly stable.

Wall shear stress is highly dependent on the local flow field. Considering the effect of arterial geometry (tortuosity, change of diameter, etc.) on the local flow field, WSS values were only measured in patient-specific models.

We compared the translesional PR values and WSS measures obtained with the Newtonian and non-Newtonian models, and calculated the relative between-model difference in each metric: (value from Newtonian model–value from non-Newtonian model)/value from non-Newtonian model. For each metric of interest, we also calculated the ratio of the area with high relative difference between the models (using >10% and >20% as the threshold for dichotomization) and the area of the entire model. To investigate the cyclic changes of WSS, we chose two points from the areas of high and low WSS values, respectively, and observed the waveform of WSS in a cardiac cycle.

## RESULTS

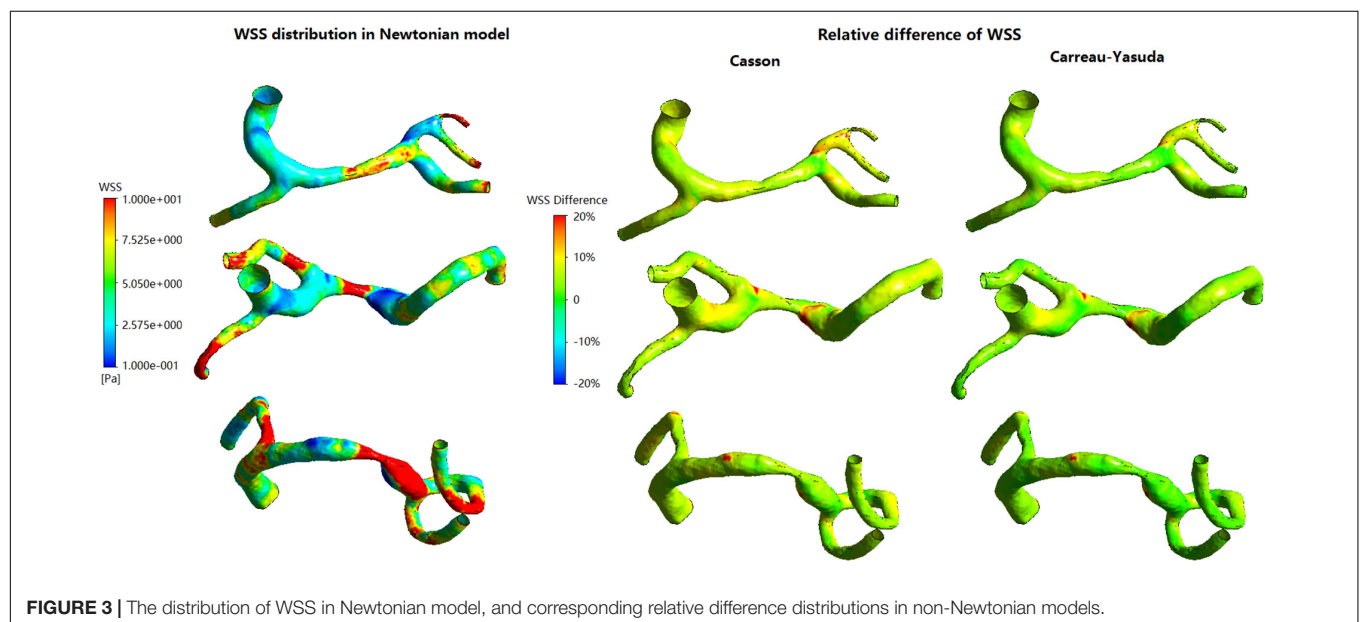
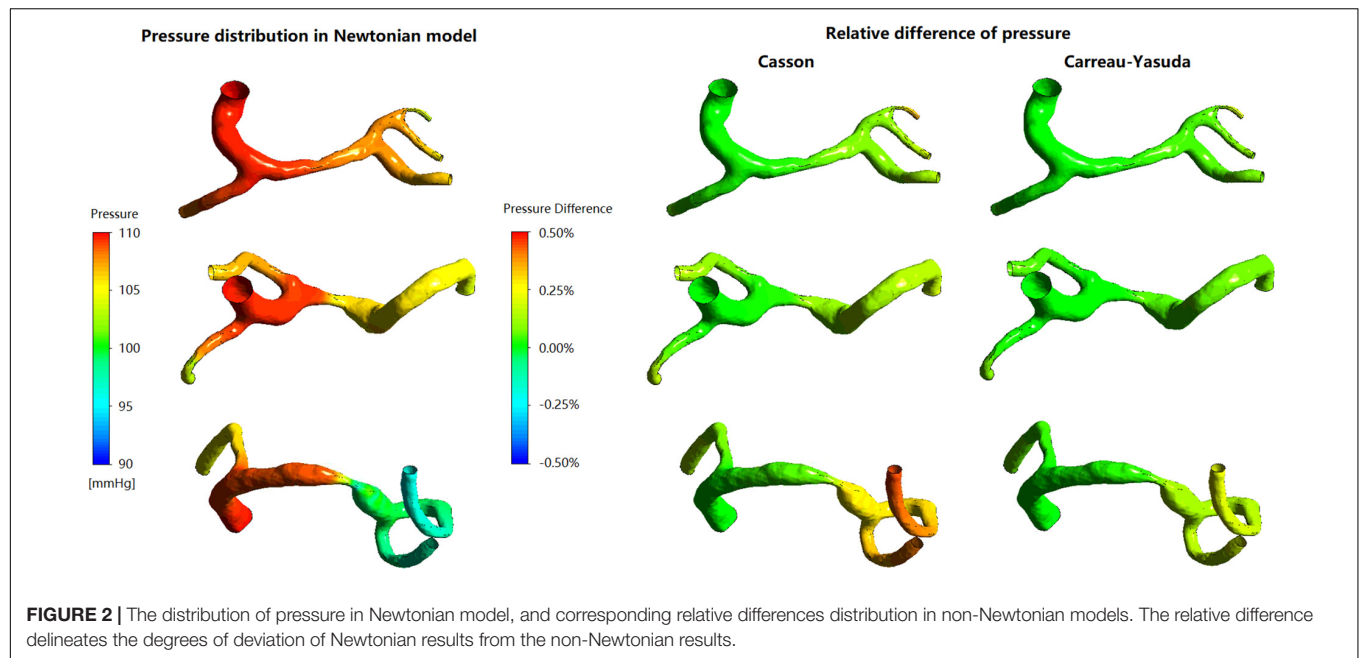
### Virtual Model of Arterial Stenosis: Static Simulation

The PR values derived by Newtonian, Casson, and Carreau-Yasuda assumptions, were 0.914, 0.913, and 0.914. Between three rheological assumptions, the differences of PR value were within 1%. The difference in PR caused by different rheological assumptions was negligible in this virtual model.

### Patient-Specific ICAS Models: Static Simulation

In the three patient-specific models of ICAS cases, the relative difference in pressure was less than 1% throughout the arterial wall (**Figure 2**). The difference between Newtonian and non-Newtonian rheological assumptions in pressure distribution (therefore PR) was negligible.

In **Figure 3**, in some areas with low WSS, large differences (>10%) between Newtonian and non-Newtonian assumptions in WSS were observed in some low-WSS areas. However, in all the three cases, the areas with the difference in WSS between Newtonian and non-Newtonian assumptions larger than 10 and 20%, were less than 7 and 1.5% of the whole surface, respectively (**Table 1**). Therefore, the difference between Newtonian and non-Newtonian rheological assumptions in WSS distribution was limited in static simulations on patient-specific models with ICAS.



## Patient-Specific ICAS Model: Transient Simulation

### Pressure and PR Values

Figure 4A showed transient pressure curves during a cardiac cycle at ICA inlet, MCA inlet (MCAin), MCA outlet (MCAout), and ACA outlet. The pressure of MCAout was the lowest due to the translesional pressure drop. There is no observable difference between the pressure curves of Newtonian and non-Newtonian assumptions.

In diastole, the maximum relative difference in pressure on the artery wall between Newtonian and non-Newtonian assumptions on the vessel wall were 0.26 and 0.14% for Casson

and Carreau-Yasuda assumptions, respectively. In systole, the corresponding values were 0.20 and 0.09% for Casson and Carreau-Yasuda assumptions.

Newtonian, Casson, and Carreau-Yasuda PR curves were comparable in systole, with minor differences in late diastole (Figure 4B). The difference between Newtonian and non-Newtonian rheological assumptions in PR value was negligible in the transient simulation on the patient-specific model with ICAS.

### WSS Distribution

In all simulations the highest WSS areas existed at the throat of MCA stenosis (Figure 5A). WSS distribution fluctuated

**TABLE 1** | The areas (in percentage) in each case with the relative difference between Newtonian and non-Newtonian models larger than 10 and 20%.

Cases	Stenosis ratio in area	Area (in percentage) with WSS relative difference >10%		Area (in percentage) with WSS relative difference >20%	
		Casson	Carreau-Yasuda	Casson	Carreau-Yasuda
Case 1	37.4%	6.88%	3.02%	1.12%	0.73%
Case 2	67.1%	5.77%	2.37%	0.78%	0.47%
Case 3	84.2%	5.47%	2.05%	0.67%	0.22%

obviously during a cardiac cycle (**Figures 5B,C**). Between Newtonian and non-Newtonian assumptions, large differences (higher than 20%) in WSS appeared in less than 6% area of vessel wall in systole, but quadrupled in diastole (**Figures 5B,D**). In diastole, compared with Newtonian results, the percentage of vessel wall area with difference in WSS higher than 10 and 20% were 37.56 and 1.32% for Casson assumption,

while 8.29 and 0.69% for Carreau-Yasuda assumption. In systole, the corresponding results were 5.40 and 1.09% for Casson assumption, while 2.03 and 0.59% for Carreau-Yasuda assumption. Higher differences in WSS appeared in the areas with low WSS values.

The rheological influence on minimum WSS was observable (**Table 2**). Between Newtonian and non-Newtonian models, the difference in maximum WSS was within 8%, while the difference in minimum WSS exceeded 40%. The difference between Newtonian and non-Newtonian rheological assumptions was obvious in low-WSS (lower than 0.1 Pa) areas (**Figure 5D**).

The fluctuations of the WSS in a cardiac cycle was observed at two points from the areas with high and low WSS (**Figure 6A**). There was no significant between-model difference in the WSS waveforms for the high-WSS point (**Figure 6B**). For the low-WSS point, the differences between Newtonian and non-Newtonian models were more significant in late diastole, with a relative difference larger than 10%, where the WSS fluctuated between consecutive time steps (**Figure 6C**).

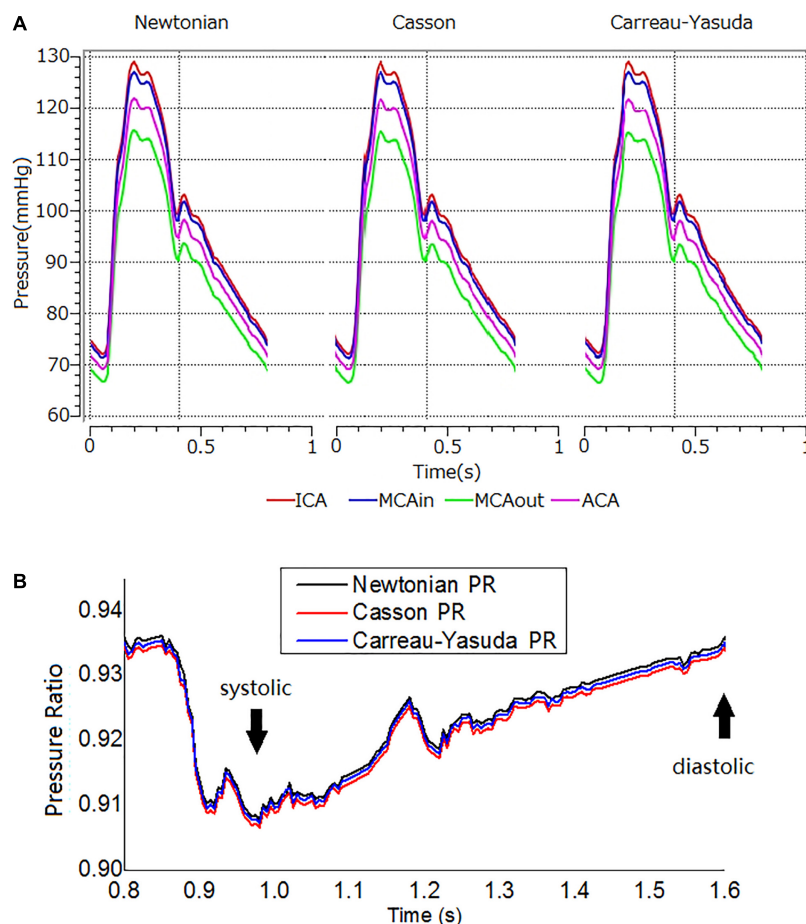


**FIGURE 4** | The transient pressure and PR distribution. **(A)** Transient pressure curves in the ICA-MCA-ACA branching model with Newtonian, and Casson, and Carreau-Yasuda rheological models in a cardiac cycle. The simulations lasted for three cardiac cycles. The results are from the second cardiac cycle. The positions of measurement are shown in **Figure 1C**. **(B)** The transient PR curves in Newtonian, Casson, and Carreau-Yasuda models during the second cardiac cycle. PR was calculated as the area-averaged pressure at MCAout divided by the area-averaged pressure at MCAin (locations of MCAout and MCAin are shown in **Figure 1C**).



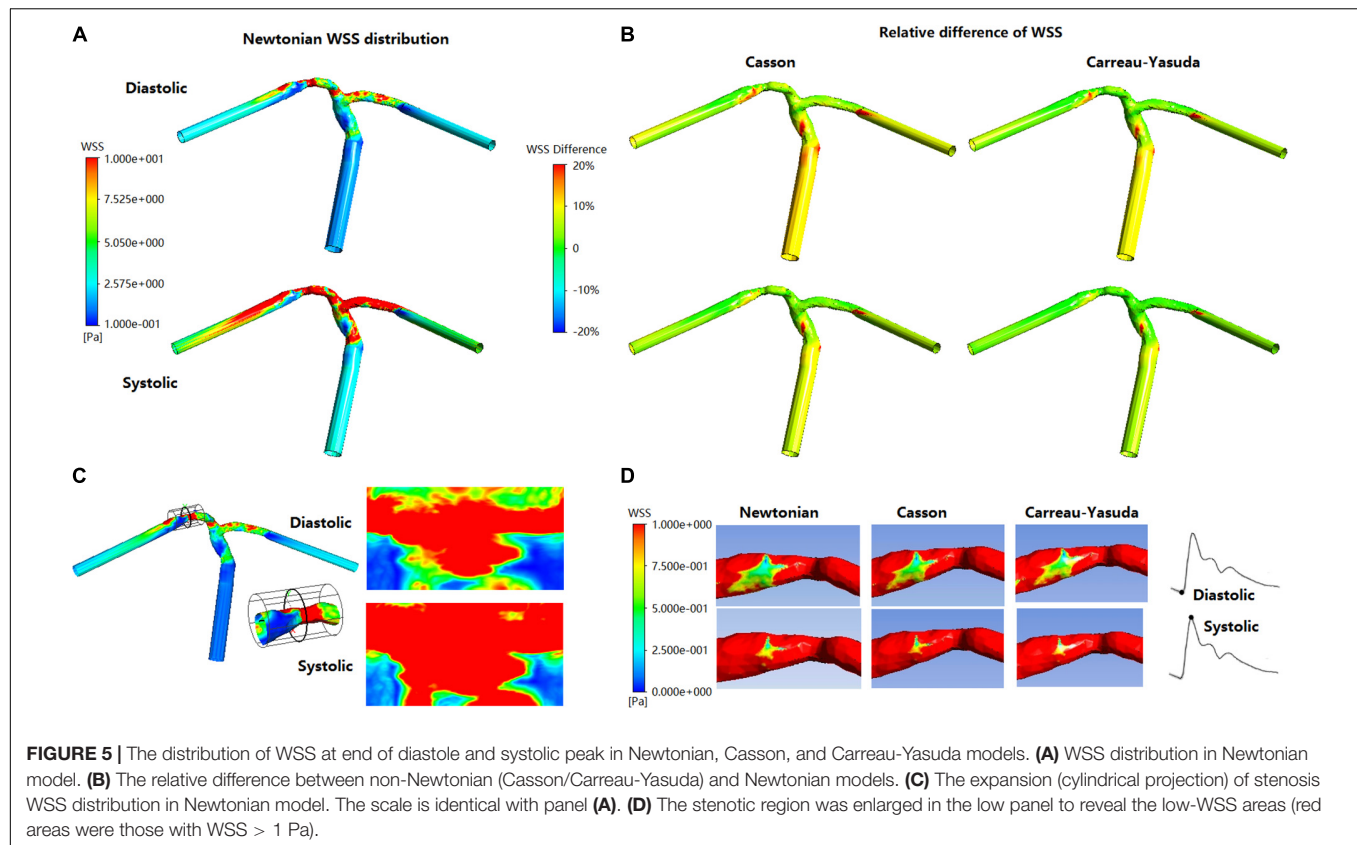


**TABLE 2 |** Maximum and minimum WSS values in a MCA stenosis model with Newtonian and non-Newtonian assumptions in transient CFD simulation.

	Systolic			Diastolic		
	Newtonian	Casson	Carreau-Yasuda	Newtonian	Casson	Carreau-Yasuda
Max WSS	6.368	6.836 (7.3%)	6.718 (5.4%)	1.31	1.335 (1.9%)	1.318 (0.6%)
Min WSS	1.263e-2	1.698e-2 (34.4%)	9.416e-3 (25.1%)	2.279e-2	6.7e-3 (70.6%)	3.29e-2 (44.3%)

In non-Newtonian results, the relative differences compared with Newtonian model were in brackets.

## DISCUSSION

In this study, using virtual and patient-specific models, we investigated the effects of Newtonian and non-Newtonian (Casson and Carreau-Yasuda) fluid assumptions on computational simulation results of cerebral hemodynamics in the presence of ICAS. We found no significant difference in pressure distribution or translesional PR obtained by the different assumptions in virtual or static/transient patient-specific models. The difference in WSS distribution was limited in static patient-specific ICAS models, which, however, was considerable in the low-WSS regions of the transient patient-specific models especially during late diastole.

Despite the shear-thinning effect of blood, currently there is no consensus on non-Newtonian fluid model for blood flow simulation (Hippelheuser et al., 2014). There are many non-Newtonian blood models such as Casson, Carreau-Yasuda, Cross, Power-law, and Quemada models (Sochi, 2013). The Quemada model is mainly used for the simulation of microcirculation in

arterioles and capillaries, while the Cross model could derive far different results with other non-Newtonian models (Karimi et al., 2014; Sriram et al., 2014). In contrast, the Casson and Carreau-Yasuda models have been widely applied in the simulation of arterial blood flow (Bernabeu et al., 2013; Morales et al., 2013), which therefore were used in this study. We did not observe any significant difference between Newtonian and non-Newtonian assumptions in estimating translesional pressure drops or PR values (representing the relative translesional pressure drop). Our results were in accordance with theoretical analysis and previous CFD studies. Theoretically, the translesional pressure drop ( $\Delta P$ ) caused by the stenosis can be expressed as a quadratic function of flow rate ( $Q$ ):  $\Delta P = AQ^2 + BQ$ , where  $A$  and  $B$  are parameters associated with the stenosis geometry and blood viscosity. The quadratic item shows the effects of turbulence on energy dissipation caused by stenosis (Young and Tsai, 1973). At the stenotic throat where the velocity and shear strain rate are high, the Newtonian and non-Newtonian assumptions have similar viscosity values (Figure 1A). Thus, the effect of different

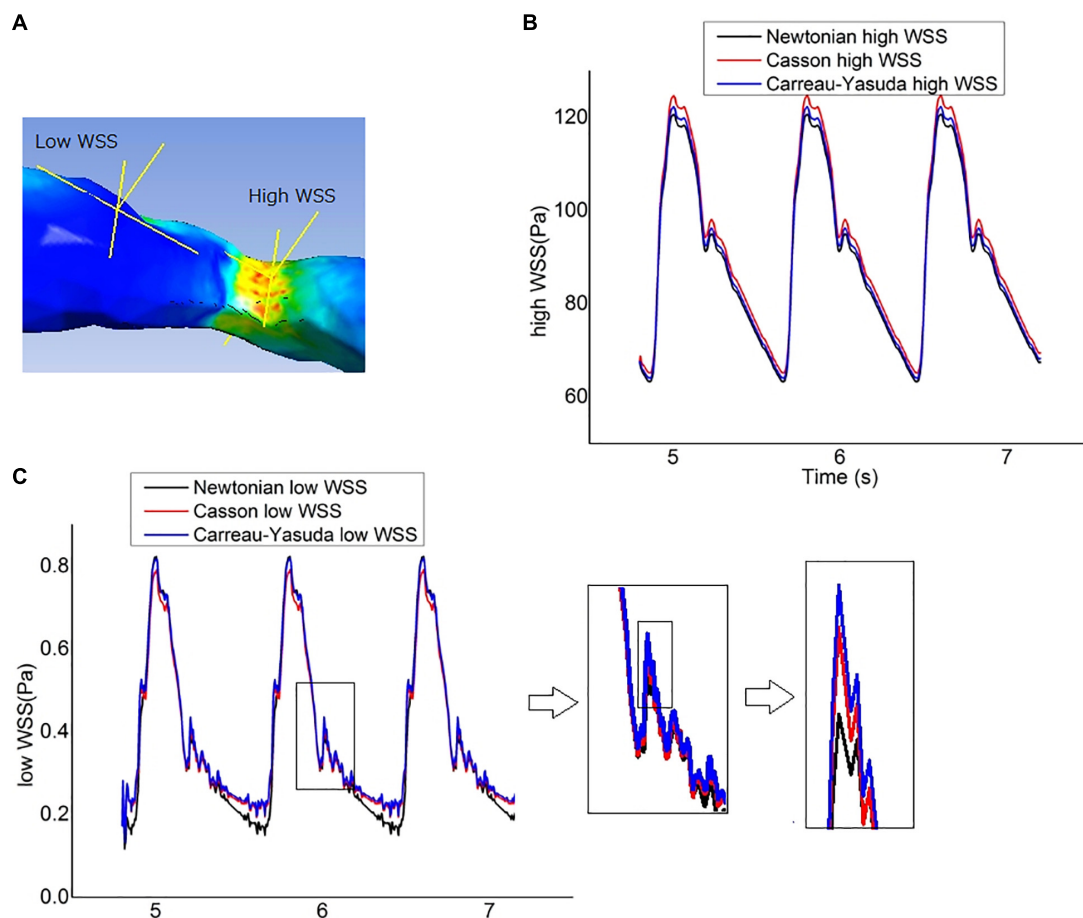


**FIGURE 6 |** Wall shear stress (WSS) measurement. **(A)** The locations of two points chosen to represent the high-WSS and low-WSS areas. **(B)** Curves of transient WSS during three cardiac cycles in Newtonian and non-Newtonian models, as measured at the representative high-WSS location. **(C)** Curves of transient WSS during three cardiac cycles as measured at the representative low-WSS location, which diverged in late diastole in Newtonian and non-Newtonian models.

rheological assumptions on PR estimation is limited. Some previous CFD studies on the blood flow of other arteries had also concluded that Newtonian and non-Newtonian assumptions can derive similar results in pressure distributions (Amornsamankul et al., 2006; Mamun et al., 2016). However, the high tortuosity and varying diameter of intracranial arteries may influence the pressure drop. To our best knowledge, this study was among the first to investigate the rheological effect of Newtonian and non-Newtonian assumptions on pressure and PR estimations in the presence of ICAS.

Wall shear stress is an important hemodynamic factor in the development and progression of ICAS. Low and oscillatory WSS is related with initiation and early development of atherosclerosis, while high WSS upon an atherosclerotic plaque might increase the risk of plaque instability (Peiffer et al., 2013). Previous studies had conflicting results on the effects of Newtonian and non-Newtonian assumptions on WSS distributions in simulating arterial blood flow; some found similar between-model results (Johnston et al., 2006; Bernabeu et al., 2013), while others studies derived opposite conclusions (Karimi et al., 2014; Sriram et al., 2014). Furthermore, the geometry of intracranial

arteries especially in ICAS cases would also have complex influence on the distribution of WSS in different rheological assumptions. Therefore, we investigated the effects of Newtonian and non-Newtonian assumptions on WSS distributions in ICAS cases in this study.

The Newtonian and non-Newtonian rheological assumption had been compared in the CFD simulation of intracranial and extracranial (e.g., carotid) arteries (Xiang et al., 2012; Gambaruto et al., 2013; Morales et al., 2013; Frolov et al., 2016; Guerciotti and Vergara, 2018; Valen-Sendstad et al., 2018; Saqr et al., 2019). Morales et al. (2013) simulated the area-averaged WSS on three patient-specific models with intracranial aneurysms in a steady state based on a time-averaged inlet flow rate, and found that the maximal difference in area-averaged WSS between non-Newtonian (Casson) and Newtonian rheological assumptions was 12%. Frolov et al. (2016) simulated the WSS on intracranial aneurysm at the end of systole, where the WSS varied from 3.52 mPa to 10.21 Pa for the Newtonian rheological model, and 2.94 mPa to 9.14 Pa for the non-Newtonian model. As a result, the relative difference in minimum WSS (16.4%) was much higher than that in maximal WSS (10.5%).

Xiang et al. (2012) reported that the Casson and Newtonian rheological assumptions derived similar time-averaged WSS on most areas of an intracranial aneurysm, but the difference reached 55% on dome area where the WSS was low. In carotid artery studies, Guerciotti and Vergara (2018) found that the difference in area-averaged WSS between non-Newtonian (Carreau-Yasuda) and Newtonian rheological assumptions was within 10% during systole but increased to 18.4% during diastole. These previous findings in general agreed with our findings. In our results, the difference between Newtonian and non-Newtonian assumptions in WSS was not significant in static simulations. In the transient simulation, the WSS values derived by the three rheological assumptions were also comparable in high-WSS areas, whereas the differences were noteworthy in low-WSS areas, especially during late diastole when WSS was low (Figure 6). Moreover, the difference in WSS between Carreau-Yasuda and Newtonian assumptions was smaller than that between Casson and Newtonian assumptions, which was in accordance with the rheological properties of the three assumptions as shown in Figure 1A.

According to this and previous relevant studies, the Newtonian assumption would be applicable for WSS estimation in normal intracranial arteries as long as the Reynolds number is within the range of laminar flow ( $Re < 2000$ ), which appears in most intracranial arteries with ICAS (Lee and Steinman, 2007; Samady et al., 2011). However, caution needs to be taken when the Newtonian assumption is applied in some extreme cases ( $Re > 2000$ , which may appear locally due to a stenosis), particularly in estimating the WSS values in low-WSS regions. This is in accordance with existing studies on CFD simulation of arteries with stenosis or aneurysm when the abnormal geometry altered focal hemodynamics, e.g., the formation of vortices and recirculation zone, with significant rheological effect on WSS distribution (Cho and Kensey, 1991; Hippelheuser et al., 2014; Liu et al., 2017). Overall, the current study on intracranial stenosis and previous studies on intracranial aneurysms suggest that the choice of rheological assumption impacts the results in simulating cerebral hemodynamics in low-WSS areas (Gambaruto et al., 2013). To achieve reliable WSS estimation in such scenarios, non-Newtonian assumptions should be considered.

Another factor that may have impact on the simulation results is the velocity conditions used. The Womersley velocity profile has been widely applied in the CFD simulation of blood flow in proximal major arteries. However, intracranial arteries are highly curved, which significantly influences the velocity profile. It was found that the variations of Womersley number only slightly affects the normalized WSS (maximum of 14%) in simulating hemodynamics in intracranial aneurysms (Asgharzadeh and Borazjani, 2016). A recent study also found that Womersley number has minimal effect on time-averaged aneurysm circulation compared with Dean and Reynolds numbers (Barbour et al., 2021). Furthermore, it was suggested that the difference between the Poiseuille and Womersley solutions is less significant in the arteries far from the heart such as cerebral arteries, where parabolic velocity distribution is a permissible approximation (Ugron and Paál, 2014). Therefore, in

the current study, we extended the inlet segment of the model to have fully developed flow in the models, rather than adopt the Womersley velocity profile in the simulation.

This study had limitations. Firstly, we adopted the solid wall assumption while *in vivo* arterial walls are elastic; but the compliance of intracranial arteries is less than that of aorta and common carotid artery by 1–2 orders of magnitude (Zhang et al., 2014), and we adopted the pressure waveform of ICA in the transient simulations in which the compliance of aorta and large arteries had been incorporated. Secondly, the rheological properties of blood vary between individuals, but in this study the boundary conditions and rheological properties of blood and the parameters in the Casson and Carreau-Yasuda assumptions were not patient-specific, due to the lack of *in vivo* measurements. Additionally, in this pilot study we used unstructured mesh, whilst enhancing the mesh in the near wall zone with boundary layers could better capture the near wall behavior of the flow and may provide more accurate estimation of the WSS measures in future studies. Finally, only three cases were analyzed in this pilot study. More cases are needed for further validation of the findings and for correlation with the clinical outcomes. In future studies, compliance of arterial walls, mesh enhancement, patients-specific boundary conditions (e.g., velocity profile derived from dynamic clinical imaging) and rheological properties, and a larger-scale validation, could be considered to achieve more reliable estimations of the cerebral hemodynamic parameters, and to reveal the differences between Newtonian and non-Newtonian assumptions in cerebral blood flow simulation results in ICAS cases.

## CONCLUSION

The study indicated negligible difference in pressure distribution in ICAS cases between CFD models with Newtonian and non-Newtonian fluid assumptions. Regarding the WSS simulation results, the difference between Newtonian and non-Newtonian models was trivial in high-WSS area but considerable in low-WSS area and in late diastole in a cardiac cycle. Therefore, in cerebral blood flow simulation in ICAS patients, the Newtonian fluid assumption could be applied in pressure estimation, and WSS estimation in high- or normal-WSS regions, but caution needs to be taken when using the Newtonian assumption in estimating WSS in low-WSS regions in such cases.

## DATA AVAILABILITY STATEMENT

The original contributions presented in the study are included in the article/supplementary material, further inquiries can be directed to the corresponding author/s.

## ETHICS STATEMENT

The studies involving human participants were reviewed and approved by The Joint Chinese University of Hong Kong–New Territories East Cluster Clinical Research Ethics Committee. The

patients/participants provided their written informed consent to participate in this study.

## AUTHOR CONTRIBUTIONS

HL performed design the details of this study and performed the simulations, and drafted the manuscript. LL, HI, TL, and XL analyzed the clinical data and selected the cases for study. DZ and XL critically reviewed and edited the manuscript. XL and LS supervised the project that led to production of the results shown

here. All authors contributed to the discussion and manuscript revision and concur with the current submitted version.

## FUNDING

The work described in this paper was partially supported by: General Research Fund (Reference No. 14106019), Research Grants Council of Hong Kong; the Lee Hysan Postdoctoral Fellowship in Clinical Neurosciences, the Chinese University of Hong Kong; and the Young Scientists Fund (Reference No. 81601000), National Natural Science Foundation of China.

## REFERENCES

- Alastruey, J., Parker, K., Peiró, J., Byrd, S., and Sherwin, S. (2007). Modelling the circle of Willis to assess the effects of anatomical variations and occlusions on cerebral flows. *J. Biomech.* 40, 1794–1805.
- Amornsamankul, S., Wiwatanapatapee, B., Wu, Y. H., and Lenbury, Y. (2006). Effect of non-newtonian behaviour of blood on pulsatile flows in stenotic arteries. *Int. J. Biol. Med. Sci.* 1, 42–46.
- Asgharzadeh, H., and Borazjani, I. (2016). Effects of reynolds and womersley numbers on the hemodynamics of intracranial aneurysms. *Comp. Mathem. Methods Med.* 2016:7412926. doi: 10.1155/2016/7412926
- Barbour, M. C., Chassagne, F., Chivukula, V. K., Machicoane, N., Kim, L. J., Levitt, M. R., et al. (2021). The effect of dean, reynolds and womersley numbers on the flow in a spherical cavity on a curved round pipe. Part 2. the haemodynamics of intracranial aneurysms treated with flow-diverting stents. *J. Fluid Mechan.* 915:A124. doi: 10.1017/jfm.2020.1115
- Bernabeu, M. O., Nash, R. W., Groen, D., Carver, H. B., Hetherington, J., Krüger, T., et al. (2013). Impact of blood rheology on wall shear stress in a model of the middle cerebral artery. *Interface Focus* 3:20120094. doi: 10.1098/rsfs.2012.0094
- Chen, Z., Qin, H., Liu, J., Wu, B., Cheng, Z., Jiang, Y., et al. (2020). Characteristics of wall shear stress and pressure of intracranial atherosclerosis analyzed by a computational fluid dynamics model: a pilot study. *Front. Neurol.* 10:1372. doi: 10.3389/fneur.2019.01372
- Cho, Y. I., and Kenney, K. R. (1991). Effects of the non-Newtonian viscosity of blood on flows in a diseased arterial vessel. Part 1: steady flows. *Biorheology* 28, 241–262. doi: 10.3233/BIR-1991-283-415
- Feng, X., Chan, K. L., Lan, L., Abrigo, J., Ip, V. H. L., Soo, Y. O. Y., et al. (2020). Translesional pressure gradient alters relationship between blood pressure and recurrent stroke in intracranial stenosis. *Stroke* 51, 1862–1864. doi: 10.1161/STROKEAHA.119.028616
- Frolov, S. V., Sindeev, S. V., Liepsch, D., and Balasso, A. (2016). Experimental and CFD flow studies in an intracranial aneurysm model with Newtonian and non-Newtonian fluids. *Technol. Health Care* 24, 317–333. doi: 10.3233/THC-161132
- Gambaruto, A., Janela, J., Moura, A., and Sequeira, A. (2013). Shear-thinning effects of hemodynamics in patient-specific cerebral aneurysms. *Mathem. Biosci. Eng.* 10:649. doi: 10.3934/mbe.2013.10.649
- Gijzen, F. J. H., van de Vosse, F. N., and Janssen, J. D. (1999). The influence of the non-Newtonian properties of blood on the flow in large arteries: steady flow in a carotid bifurcation model. *J. Biomech.* 32, 601–608. doi: 10.1016/S0021-9290(99)00015-19
- Guercioti, B., and Vergara, C. (2018). “Computational comparison between newtonian and non-newtonian blood rheologies in stenotic vessels,” in *Biomedical Technology: Modeling, Experiments and Simulation*, eds P. Wriggers and T. Lenarz (Cham: Springer International Publishing), 169–183. doi: 10.1007/978-3-319-59548-1\_10
- Hippelheuser, J. E., Lauric, A., Cohen, A. D., and Malek, A. M. (2014). Realistic non-Newtonian viscosity modelling highlights hemodynamic differences between intracranial aneurysms with and without surface blebs. *J. Biomech.* 47, 3695–3703. doi: 10.1016/j.jbiomech.2014.09.027
- Jahangiri, M., Saghaian, M., and Sadeghi, M. R. (2017). Numerical simulation of non-Newtonian models effect on hemodynamic factors of pulsatile blood flow in elastic stenosed artery. *J. Mechan. Sci. Technol.* 31, 1003–1013. doi: 10.1007/s12206-017-0153-x
- Johnston, B. M., Johnston, P. R., Corney, S., and Kilpatrick, D. (2006). Non-Newtonian blood flow in human right coronary arteries: transient simulations. *J. Biomech.* 39, 1116–1128. doi: 10.1016/j.jbiomech.2005.01.034
- Karimi, S., Dabagh, M., Vasava, P., Dadvar, M., Dabir, B., and Jalali, P. (2014). Effect of rheological models on the hemodynamics within human aorta: CFD study on CT image-based geometry. *J. Non-Newtonian Fluid Mechan.* 207, 42–52. doi: 10.1016/j.jnnfm.2014.03.007
- Lan, L., Liu, H., Ip, V., Soo, Y., Abrigo, J., Fan, F., et al. (2020). Regional high wall shear stress associated with stenosis regression in symptomatic intracranial atherosclerotic disease. *Stroke* 51, 3064–3073. doi: 10.1161/STROKEAHA.120.030615
- Lee, S.-W., and Steinman, D. A. (2007). On the relative importance of rheology for image-based CFD models of the carotid bifurcation. *J. Biomech. Eng.* 129, 273–278. doi: 10.1115/1.2540836
- Leng, X., Lan, L., Ip, H. L., Abrigo, J., Scalzo, F., Liu, H., et al. (2019). Hemodynamics and stroke risk in intracranial atherosclerotic disease. *Ann. Neurol.* 85, 752–764. doi: 10.1002/ana.25456
- Leng, X., Scalzo, F., Ip, H. L., Johnson, M., Fong, A. K., Fan, F. S., et al. (2014). Computational fluid dynamics modeling of symptomatic intracranial atherosclerosis may predict risk of stroke recurrence. *PLoS One* 9:e97531. doi: 10.1371/journal.pone.0097531
- Liebeskind, D. S., and Feldmann, E. (2013). Fractional flow in cerebrovascular disorders. *Interventional Neurol.* 1, 87–99. doi: 10.1159/000346803
- Liebeskind, D. S., Scalzo, F., Woolf, G. W., Zubak, J. M., Cotsolis, G. A., Lynn, M. J., et al. (2016). Computational fluid dynamics of CT angiography in SAMMPRIS reveal blood flow and vessel interactions in middle cerebral artery stenoses. *Stroke* 47(Suppl. 1):A99.
- Linfang Lan, X. L. (2017). Computational fluid dynamics modeling in intracranial atherosclerotic disease. *J. Trans. Neurosci.* 2, 7–15. doi: 10.3868/j.issn.2096-0689.2017.02.002
- Liu, H., Gong, Y., Leng, X., Xia, L., Wong, K. S., Ou, S., et al. (2017). Estimating current and long-term risks of coronary artery in silico by fractional flow reserve, wall shear stress and low-density lipoprotein filtration rate. *Biomed. Phys. Eng. Exp.* 4:025006. doi: 10.1088/2057-1976/aa9a09
- Liu, H., Lan, L., Leng, X., Ip, H. L., Leung, T. W. H., Wang, D., et al. (2018). Impact of side branches on the computation of fractional flow in intracranial arterial stenosis using the computational fluid dynamics method. *J. Stroke Cerebrov. Dis.* 27, 44–52. doi: 10.1016/j.jstrokecerebrovasdis.2017.02.032
- Mamun, K., Akhter, M., and Ali, M. (2016). Physiological non-Newtonian blood flow through single stenosed artery. *Theoretical Appl. Mechan.* 43, 99–115. doi: 10.1063/1.4958361
- Moon, J. Y., Suh, D. C., Lee, Y. S., Kim, Y. W., and Lee, J. S. (2014). Considerations of blood properties, outlet boundary conditions and energy loss approaches in computational fluid dynamics modeling. *Neurointervention* 9, 1–8. doi: 10.5469/neuroint.2014.9.1.1



- Moore, S., David, T., Chase, J. G., Arnold, J., and Fink, J. (2006). 3D models of blood flow in the cerebral vasculature. *J. Biomech.* 39, 1454–1463. doi: 10.1016/j.jbiomech.2005.04.005
- Morales, H. G., Larrabide, I., Geers, A. J., Aguilar, M. L., and Frangi, A. F. (2013). Newtonian and non-Newtonian blood flow in coiled cerebral aneurysms. *J. Biomech.* 46, 2158–2164. doi: 10.1016/j.jbiomech.2013.06.034
- Nader, E., Skinner, S., Romana, M., Fort, R., Lemonne, N., Guillot, N., et al. (2019). Blood Rheology: key parameters, impact on blood flow, role in sickle cell disease and effects of exercise. *Front. Physiol.* 10:1329. doi: 10.3389/fphys.2019.01329
- Nam, H. S., Scalzo, F., Leng, X., Ip, H. L., Lee, H. S., Fan, F., et al. (2016). Hemodynamic impact of systolic blood pressure and hematocrit calculated by computational fluid dynamics in patients with intracranial atherosclerosis. *J. Neuroimaging* 26, 331–338. doi: 10.1111/jon.12314
- Peiffer, V., Sherwin, S. J., and Weinberg, P. D. (2013). Does low and oscillatory wall shear stress correlate spatially with early atherosclerosis? a systematic review. *Cardiovas. Res.* 99, 242–250. doi: 10.1093/cvr/cvt044
- Rabby, M. G., Shupiti, S. P., and Molla, M. M. (2014). Pulsatile non-Newtonian laminar blood flows through arterial double stenoses. *J. Fluids* 2014, 1–13. doi: 10.1155/2014/757902
- Ren, Y., Chen, G.-Z., Liu, Z., Cai, Y., Lu, G.-M., and Li, Z.-Y. (2016). Reproducibility of image-based computational models of intracranial aneurysm: a comparison between 3D rotational angiography, CT angiography and MR angiography. *BioMed. Eng. Online* 15:50. doi: 10.1186/s12938-016-0163-164
- Samady, H., Eshtehardi, P., McDaniel, M. C., Suo, J., Dhawan, S. S., Maynard, C., et al. (2011). Coronary artery wall shear stress is associated with progression and transformation of atherosclerotic plaque and arterial remodeling in patients with coronary artery disease. *Circulation* 124, 779–788. doi: 10.1161/CIRCULATIONAHA.111.021824
- Saqr, K. M., Mansour, O., Tupin, S., Hassan, T., and Ohta, M. (2019). Evidence for non-Newtonian behavior of intracranial blood flow from Doppler ultrasonography measurements. *Med. Biol. Eng. Comp.* 57, 1029–1036. doi: 10.1007/s11517-018-1926-1929
- Sarrami-Foroushani, A., Esfahany, M. N., Moghaddam, A. N., Rad, H. S., Firouznia, K., Shakiba, M., et al. (2015). Velocity measurement in carotid artery: quantitative comparison of time-resolved 3D phase-contrast MRI and image-based computational fluid dynamics. *Iranian J. Radiol.* 12:e18286. doi: 10.5812/iranjradiol.18286
- Sochi, T. (2013). Non-Newtonian rheology in blood circulation. *arXiv [preprint]*. Available online at: <https://arxiv.org/abs/1306.2067>. (accessed June 09, 2014).
- Sriram, K., Intaglietta, M., and Tartakovsky, D. M. (2014). Non-Newtonian flow of blood in arterioles: consequences for wall shear stress measurements. *Microcirculation* 21, 628–639. doi: 10.1111/micc.12141
- Ugron, Á., and Paál, G. (2014). On the boundary conditions of cerebral aneurysm simulations. *Periodica Polytechnica Mechan. Eng.* 58, 37–45. doi: 10.3311/PPme.7392
- Valen-Sendstad, K., Bergersen, A. W., Shimogonya, Y., Goubergrits, L., Bruening, J., Pallares, J., et al. (2018). Real-World variability in the prediction of intracranial aneurysm wall shear stress: the 2015 international aneurysm CFD challenge. *Cardiovas. Eng. Technol.* 9, 544–564. doi: 10.1007/s13239-018-00374-372
- Vali, A., Abba, A. A., Lawton, M. T., Saloner, D., and Rayz, V. L. (2017). Computational fluid dynamics modeling of contrast transport in basilar aneurysms following flow-altering surgeries. *J. Biomech.* 50, 195–201. doi: 10.1016/j.jbiomech.2016.11.028
- Wong, L. K. S. (2006). Global burden of intracranial atherosclerosis. *Int. J. Stroke* 1, 158–159. doi: 10.1111/j.1747-4949.2006.00045.x
- Xiang, J., Tremmel, M., Kolega, J., Levy, E. I., Natarajan, S. K., and Meng, H. (2012). Newtonian viscosity model could overestimate wall shear stress in intracranial aneurysm domes and underestimate rupture risk. *J. NeuroInt. Surg.* 4:351. doi: 10.1136/neurintsurg-2011-010089
- Young, D. F., and Tsai, F. Y. (1973). Flow characteristics in models of arterial stenoses—II. unsteady flow. *J. Biomechan.* 6, 547–559. doi: 10.1016/0021-9290(73)90012-90012
- Zhang, C., Li, S., Pu, F., Fan, Y., and Li, D. (2014). The effect of anatomic variations of circle of Willis on cerebral blood distribution during posture change from supination to standing: a model study. *Biomed. Mater. Eng.* 24, 2371–2380. doi: 10.3233/BME-141050

**Conflict of Interest:** The authors declare that the research was conducted in the absence of any commercial or financial relationships that could be construed as a potential conflict of interest.

**Publisher's Note:** All claims expressed in this article are solely those of the authors and do not necessarily represent those of their affiliated organizations, or those of the publisher, the editors and the reviewers. Any product that may be evaluated in this article, or claim that may be made by its manufacturer, is not guaranteed or endorsed by the publisher.

Copyright © 2021 Liu, Lan, Abrigo, Ip, Soo, Zheng, Wong, Wang, Shi, Leung and Leng. This is an open-access article distributed under the terms of the Creative Commons Attribution License (CC BY). The use, distribution or reproduction in other forums is permitted, provided the original author(s) and the copyright owner(s) are credited and that the original publication in this journal is cited, in accordance with accepted academic practice. No use, distribution or reproduction is permitted which does not comply with these terms.



# Corrigendum: Comparison of Newtonian and Non-newtonian Fluid Models in Blood Flow Simulation in Patients With Intracranial Arterial Stenosis

Haipeng Liu<sup>1,2,3</sup>, Linfang Lan<sup>1</sup>, Jill Abrigo<sup>2</sup>, Hing Lung Ip<sup>1</sup>, Yannie Soo<sup>1</sup>, Dingchang Zheng<sup>3</sup>, Ka Sing Wong<sup>1</sup>, Defeng Wang<sup>2</sup>, Lin Shi<sup>2\*</sup>, Thomas W. Leung<sup>1</sup> and Xinyi Leng<sup>1,4\*</sup>

<sup>1</sup> Department of Medicine and Therapeutics, The Chinese University of Hong Kong, Hong Kong, China, <sup>2</sup> Department of Imaging and Interventional Radiology, The Chinese University of Hong Kong, Hong Kong, China, <sup>3</sup> Research Centre for Intelligent Healthcare, Coventry University, Coventry, United Kingdom, <sup>4</sup> Shenzhen Research Institute, The Chinese University of Hong Kong, Shenzhen, China

## OPEN ACCESS

### Approved by:

Frontiers Editorial Office,  
Frontiers Media SA, Switzerland

### \*Correspondence:

Xinyi Leng  
xinyi\_leng@cuhk.edu.hk  
Lin Shi  
shilin@cuhk.edu.hk

### Specialty section:

This article was submitted to  
Computational Physiology and  
Medicine,  
a section of the journal  
Frontiers in Physiology

**Received:** 24 September 2021

**Accepted:** 28 September 2021

**Published:** 19 October 2021

### Citation:

Liu H, Lan L, Abrigo J, Ip HL, Soo Y, Zheng D, Wong KS, Wang D, Shi L, Leung TW and Leng X (2021) Corrigendum: Comparison of Newtonian and Non-newtonian Fluid Models in Blood Flow Simulation in Patients With Intracranial Arterial Stenosis. *Front. Physiol.* 12:782647. doi: 10.3389/fphys.2021.782647

**Keywords:** non-Newtonian fluid, intracranial atherosclerotic stenosis, computational fluid dynamics, translesional pressure ratio, wall shear stress

## A Corrigendum on

### Comparison of Newtonian and Non-newtonian Fluid Models in Blood Flow Simulation in Patients With Intracranial Arterial Stenosis

by Liu, H., Lan, L., Abrigo, J., Ip, H. L., Soo, Y., Zheng, D., Wong, K. S., Wang, D., Shi, L., Leung, T. W., and Leng, X. (2021). *Front. Physiol.* 12:718540. doi: 10.3389/fphys.2021.718540

In the published article, there was an error regarding the affiliations for Dr. Xinyi Leng. As well as having affiliation 1, Dr. Leng should also have “4. Shenzhen Research Institute, The Chinese University of Hong Kong, Shenzhen, China”.

The authors apologize for this error and state that this does not change the scientific conclusions of the article in any way. The original article has been updated.

**Publisher's Note:** All claims expressed in this article are solely those of the authors and do not necessarily represent those of their affiliated organizations, or those of the publisher, the editors and the reviewers. Any product that may be evaluated in this article, or claim that may be made by its manufacturer, is not guaranteed or endorsed by the publisher.

Copyright © 2021 Liu, Lan, Abrigo, Ip, Soo, Zheng, Wong, Wang, Shi, Leung and Leng. This is an open-access article distributed under the terms of the Creative Commons Attribution License (CC BY). The use, distribution or reproduction in other forums is permitted, provided the original author(s) and the copyright owner(s) are credited and that the original publication in this journal is cited, in accordance with accepted academic practice. No use, distribution or reproduction is permitted which does not comply with these terms.



# Etiology-Specific Remodeling in Ventricular Tissue of Heart Failure Patients and Its Implications for Computational Modeling of Electrical Conduction

Aparna C. Sankarankutty<sup>1,2</sup>, Joachim Greiner<sup>3,4</sup>, Jean Bragard<sup>5</sup>, Joseph R. Visker<sup>1,6</sup>, Thirupura S. Shankar<sup>1,2</sup>, Christos P. Kyriakopoulos<sup>1,6</sup>, Stavros G. Drakos<sup>1,2,6</sup> and Frank B. Sachse<sup>1,2\*</sup>

<sup>1</sup> Nora Eccles Harrison Cardiovascular Research and Training Institute, University of Utah, Salt Lake City, UT, United States,

<sup>2</sup> Department of Biomedical Engineering, University of Utah, Salt Lake City, UT, United States, <sup>3</sup> Institute for Experimental Cardiovascular Medicine, University Heart Center Freiburg-Bad Krozingen, Freiburg, Germany, <sup>4</sup> Faculty of Medicine, University of Freiburg, Freiburg, Germany, <sup>5</sup> Department of Physics and Applied Mathematics, School of Sciences, University of Navarra, Pamplona, Spain, <sup>6</sup> Division of Cardiovascular Medicine, University of Utah School of Medicine, Salt Lake City, UT, United States

## OPEN ACCESS

### Edited by:

Henggui Zhang,  
The University of Manchester,  
United Kingdom

### Reviewed by:

Al Benson,  
University of Leeds, United Kingdom  
Gernot Plank,  
Medical University of Graz, Austria

### \*Correspondence:

Frank B. Sachse  
frank.sachse@utah.edu

### Specialty section:

This article was submitted to  
Computational Physiology  
and Medicine,  
a section of the journal  
Frontiers in Physiology

**Received:** 25 June 2021

**Accepted:** 07 September 2021

**Published:** 05 October 2021

### Citation:

Sankarankutty AC, Greiner J, Bragard J, Visker JR, Shankar TS, Kyriakopoulos CP, Drakos SG and Sachse FB (2021) Etiology-Specific Remodeling in Ventricular Tissue of Heart Failure Patients and Its Implications for Computational Modeling of Electrical Conduction. *Front. Physiol.* 12:730933. doi: 10.3389/fphys.2021.730933

With an estimated 64.3 million cases worldwide, heart failure (HF) imposes an enormous burden on healthcare systems. Sudden death from arrhythmia is the major cause of mortality in HF patients. Computational modeling of the failing heart provides insights into mechanisms of arrhythmogenesis, risk stratification of patients, and clinical treatment. However, the lack of a clinically informed approach to model cardiac tissues in HF hinders progress in developing patient-specific strategies. Here, we provide a microscopy-based foundation for modeling conduction in HF tissues. We acquired 2D images of left ventricular tissues from HF patients ( $n = 16$ ) and donors ( $n = 5$ ). The composition and heterogeneity of fibrosis were quantified at a sub-micrometer resolution over an area of  $1 \text{ mm}^2$ . From the images, we constructed computational bidomain models of tissue electrophysiology. We computed local upstroke velocities of the membrane voltage and anisotropic conduction velocities (CV). The non-myocyte volume fraction was higher in HF than donors ( $39.68 \pm 14.23$  vs.  $22.09 \pm 2.72\%$ ,  $p < 0.01$ ), and higher in ischemic (IC) than nonischemic (NIC) cardiomyopathy ( $47.2 \pm 16.18$  vs.  $32.16 \pm 6.55\%$ ,  $p < 0.05$ ). The heterogeneity of fibrosis within each subject was highest for IC ( $27.1 \pm 6.03\%$ ) and lowest for donors ( $7.47 \pm 1.37\%$ ) with NIC ( $15.69 \pm 5.76\%$ ) in between.  $K$ -means clustering of this heterogeneity discriminated IC and NIC with an accuracy of 81.25%. The heterogeneity in CV increased from donor to NIC to IC tissues. CV decreased with increasing fibrosis for longitudinal ( $R^2 = 0.28$ ,  $p < 0.05$ ) and transverse conduction ( $R^2 = 0.46$ ,  $p < 0.01$ ). The tilt angle of the CV vectors increased  $2.1^\circ$  for longitudinal and  $0.91^\circ$  for transverse conduction per 1% increase in fibrosis. Our study suggests that conduction fundamentally differs in the two etiologies due to the characteristics of fibrosis. Our study highlights the importance of the etiology-specific modeling of HF tissues and integration of medical history into electrophysiology models for personalized risk stratification and treatment planning.

**Keywords:** heart failure, cardiac fibrosis, cardiac modeling, electrical conduction, conduction velocity

## INTRODUCTION

An estimated 64.3 million people are diagnosed with heart failure (HF) worldwide, incurring an enormous burden on healthcare systems and economies (Bragazzi et al., 2021). The prevalence of HF continues to rise with an aging population in the developed world, and HF incidence is rapidly climbing in developing countries. A broad range of structural or functional cardiac abnormalities is causing or associated with HF. Ischemic heart disease is a major cause, accounting for 26.5% of the HF cases (Bragazzi et al., 2021).

Heart failure and many other heart diseases can be accompanied by fibrosis, which is caused by the increased production of extracellular matrix (ECM) proteins due to the proliferation and differentiation of fibroblasts. ECM deposition as an acute response strengthens the tissue scaffold and replaces cells in the myocardium post-injury. However, chronic fibrotic remodeling adversely affects the ability of the myocardium to propagate electrical signals and circulate blood efficiently.

Cardiac fibrosis is traditionally classified based on the cause that triggered remodeling of the myocardium. Other classifications characterize fibrosis in terms of its location and the nature of remodeling. The condition that led to the remodeling of the myocardium can drive fibrosis to be either reparative or reactive (Silver et al., 1990). Reparative fibrosis, also known as replacement fibrosis, occurs from ischemia and other causes of myocardial injury. Here, the ECM replaces myocytes following necrosis or apoptosis, thereby repairing the scaffold. On the other hand, reactive fibrosis formed in response to various stimuli including pressure overload intersperses with myofibers and is called interstitial fibrosis (González et al., 2018). While reparative fibrosis might result in stable scars, reactive fibrosis can be progressive. Perivascular fibrosis, defined as the increased accumulation of connective tissue around vessels, results from reactive fibrosis and, many times, progresses to interstitial fibrosis (Swynghedauw, 1999).

More recently, fibrosis was characterized by its spatial distribution in the myocardium. A classification of fibrosis in terms of architecture used histological assessment of human cardiac tissue samples, including both ischemic (IC) and nonischemic cardiomyopathies (NIC) (Kawara et al., 2001). Here, fibrosis was categorized as patchy, diffuse, and stringy. Analysis of fibrosis in transmural biopsies from NIC at sub-millimeter scale led to further classification of the architecture as interstitial, diffuse, patchy, and compact (Glashan et al., 2020). Patchy refers to a tightly knit group of fibrotic strands that can be several millimeters long. Diffuse fibrosis consists of less than 1 mm long strands spread over a large area. These strands can form a mesh interspersed with the myocardium or separated with a network of myocardium in between. Stringy fibrosis is composed of thin, long, and well-separated strands homogeneously distributed in the tissue. Finally, fibrosis is defined in this classification as compact when the entire transmural section is fibrotic without any viable myocardium.

Fibrosis is commonly quantified by the fractional space occupied by the collagen-specific stain in histology or intensity thresholding in late gadolinium-enhanced magnetic resonance

imaging (MRI). The degree of fibrosis estimated by different methods has been clinically correlated with progression, type, and outcome of heart diseases (González et al., 2018; Hinderer and Schenke-Layland, 2019). The increased extracellular volume fraction calculated from cardiac MRI was associated with an increased risk of hospitalization due to HF and death among varied stages of HF and a spectrum of left ventricular ejection fractions (Schelbert et al., 2015). However, a high amount of fibrosis evaluated histologically was associated with death and adverse events only in HF patients with reduced ejection fraction (Aoki et al., 2011). While initially fibrosis was only associated with IC diseases with scars, varied architectures of fibrosis are increasingly associated with NIC diseases (Jellis et al., 2010). Compact fibrosis was found to be rare in NIC, with patchy being the most common. A combination of 2 or 3 types was found in 90% of NIC biopsies (Glashan et al., 2020). Though these observations show the need to assess the heterogeneity of fibrosis for risk stratification, our quantitative understanding of fibrosis and its heterogeneity in human HF is sparse.

65% of HF patients do not survive past 5 years from their initial diagnosis (Bleumink et al., 2021). They are twice as likely to develop arrhythmias compared to the rest of the population, and 50% of mortality is attributed to sudden death primarily resulting from ventricular tachyarrhythmias (Tomaselli and Zipes, 2004; Khurshid et al., 2018). It is well established that fibrosis and structural remodeling in cardiac tissue lead to abnormal conduction patterns (Spach and Boineau, 1997; Nguyen et al., 2014). However, different types of fibrosis can affect conduction differently. For instance, patchy fibrosis contributed to conduction slowing more than stringy and diffuse fibrosis (Kawara et al., 2001).

Computational models of electrical conduction in fibrotic cardiac tissues are extensively used in predicting arrhythmia, especially in determining its origin and features (Trayanova et al., 2018). Personalized models of fibrotic substrates were developed to identify the location for catheter ablation to prevent recurring atrial fibrillations and ventricular tachycardia (Prakosa et al., 2018; Boyle et al., 2019). Commonly, monodomain models of heart tissue are applied, where the myocardium is described as a single continuous domain. Since the extracellular space (ES) is not explicitly described, fibrosis is treated as non-excitable regions with either reduced or no conductivity. Interstitial fibrosis was introduced in such models by decoupling the transverse cellular connections to reflect the distribution of non-conductive collagenous interstitium (Spach et al., 2007). Also, the spatial distribution of fibrosis was modeled by spatially varying the diffusion coefficient of the myocyte domain based on Gaussian random fields (Clayton, 2018). Another model of diffuse fibrosis was introduced as non-conductive collagen randomly distributed in the myocyte layer or myocardial blobs sprinkled in the collagen layer and a fibroblast model coupled with the monodomain model (Chen et al., 2018). Interstitial and patchy fibrosis were modeled based on histological images by only including regions corresponding to myocardium in the simulation of conduction (Campos et al., 2013). In this work, a monodomain model was used and extracellular potentials calculated assuming infinite uniform conductor.



**TABLE 1** | Baseline demographic and clinical characteristics of donor and heart failure (HF) population.

	Donor ( <i>n</i> = 5)	HF ( <i>n</i> = 16)		
		All HF	IC ( <i>n</i> = 8)	NIC ( <i>n</i> = 8)
Age (years)	51.2 ± 13.48	53.44 ± 10.28	58.50 ± 6.74 <sup>§</sup>	48.38 ± 11.07
Male, <i>n</i> (%)	2 (40)	13 (81.25)	7 (87.50)	6 (75)
Height (cm)	161.03 ± 8.90	176.67 ± 8.27	178.77 ± 5.95	174.56 ± 10.06
Weight (kg)	68.12 ± 13.23	93.55 ± 22.8	101.82 ± 19.53	85.28 ± 24
BMI (kg/m <sup>2</sup> )	26.01 ± 2.91	29.94 ± 7.11	31.98 ± 6.33	27.89 ± 7.67
LVEF (%)	71.40 ± 7.02	21.56 ± 11.25	24.38 ± 10.5	18.75 ± 11.96
NYHA class III, <i>n</i> (%)		5 (31.25)	3 (37.50)	2 (25)
NYHA class IV, <i>n</i> (%)		11 (68.75)*	5 (62.50)	6 (75)
Duration of HF (months)		62.81 ± 53.04	61.75 ± 53.69	63.88 ± 56.05
LVAD, <i>n</i> (%)		11 (68.75)	5 (62.50)	6 (75)
Direct transplant, <i>n</i> (%)		5 (31.25)	3 (37.50)	2 (25)

Values are shown in *n* (%) or mean ± SD when appropriate.

<sup>§</sup>*p* < 0.05 between IC and NIC.

\*NYHA class for an IC patient was III or IV and is considered IV here.

BMI, body mass index; LVEF, left ventricular ejection fraction; NYHA, New York Heart Association.

A computationally more demanding alternative to monodomain modeling is bidomain modeling, which comprises a description of the ES (Sepulveda et al., 1989). Here, the ES has an electrical conductivity separate from the myocyte domain. The primary constituent of the ES is conductive interstitial fluid, and ECM proteins contribute only a marginal volume fraction. It is commonly assumed that the interstitial fluid determines the conductivity in the extracellular domain. An expansion of interstitial space is also well documented in different cardiomyopathies (Halliday and Prasad, 2019). In addition to fibrosis and changes in interstitial space, the clefts that separate myocyte sheets modulates the conductivity of ES. The anisotropy of the ES conductivity is well-established and less pronounced than the anisotropy of the myocyte domain (Johnston and Johnston, 2020). Hence the bidomain model is more appropriate to describe features of fibrotic remodeling in cardiac tissues. Fibrosis was modeled as selected nodes in the extracellular domain duplicated and decoupled from the myocyte domain at locations based on collagen in MRI images (Costa et al., 2014). This method was used to simulate interstitial fibrosis (Balaban et al., 2018) and scars (Balaban et al., 2020). Still, image-based microscopic detail of fibrosis is not yet captured in computational models of ventricular tissue in human HF.

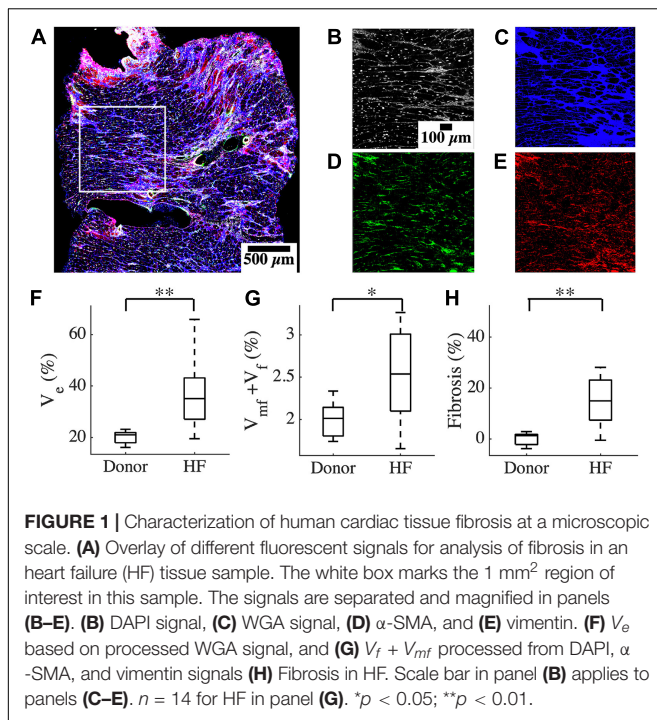
We hypothesized that heterogeneity in fibrosis varies in HF patients and the heterogeneity will alter the conduction patterns depending on the etiology of disease. To test this hypothesis, we introduced an approach to quantify the microscopic distribution of fibrosis and its variation within subjects to characterize the heterogeneity of fibrosis. We investigated the relationship between fibrotic remodeling and conduction abnormalities using electrophysiological simulations on image-based meshes of cardiac tissue. For this, we applied confocal microscopic tile scanning of tissue sections from donors and HF patients. Fibrosis was characterized in terms of composition as well as its heterogeneity within each subject. Further, this quantification was used to build electrophysiological models of cardiac tissue

to explore the microscopic disturbances in electrical conduction. Finally, we analyzed the influence of different types of fibrosis and the associated HF etiology on electrical conduction velocity (CV) and its dispersion at the microscopic scale.

## RESULTS

### Microstructural Remodeling Distinguishes Heart Failure From Donor Tissues

We characterized the composition of left ventricular mid-myocardial apical tissue from HF patients (*n* = 16) and donors (*n* = 5) through immunohistochemistry and tile scanning confocal microscopy. Baseline demographic and clinical characteristics of the donor and HF population are presented in **Table 1**. A tile scan of an HF tissue section with an overlay of the fluorescent signals is illustrated in **Figure 1A**. The individual signals in a region of 1 mm<sup>2</sup> area within this overlay are magnified in **Figures 1B–E**. The nuclei are densely present with varying sizes, reflecting the diversity of cells in cardiac tissue (**Figure 1B**). The ES labeled by wheat germ agglutinin (WGA) comprises interstitial clefts and larger patches with fibrotic remodeling (**Figure 1C**). The  $\alpha$ -smooth muscle actin ( $\alpha$ -SMA) (**Figure 1D**) and vimentin signals (**Figure 1E**) correspond to the presence of myofibroblasts (MF) and fibroblasts (F), respectively. We calculated the fractional space occupied by ES ( $V_e$ ), fibroblasts ( $V_f$ ), and myofibroblasts ( $V_{mf}$ ) by processing the signals.  $V_e$  in HF was higher than that of donors ( $37.49 \pm 13.98$  vs.  $20.1 \pm 2.75\%$ , *p* <  $5 \times 10^{-4}$ ; **Figure 1F**). The summed  $V_f$  and  $V_{mf}$  was higher in HF compared to donors ( $2.5 \pm 0.5$  vs.  $2.0 \pm 0.23\%$ , *p* < 0.05; **Figure 1G**). Individually  $V_f$  and  $V_{mf}$  were not different in HF and donors (**Supplementary Figure 1**). The total non-myocyte volume fraction ( $V_{nm}$ ), i.e., the sum of  $V_e$ ,  $V_f$ , and  $V_{mf}$ , was



higher in HF than donors ( $39.68 \pm 14.23$  vs.  $22.09 \pm 2.72\%$ ,  $p < 5e-4$ ). The fibrosis in HF, calculated as the difference between  $V_{nm}$  in HF and the mean  $V_{nm}$  of donors, was  $17.59 \pm 14.23\%$  (Figure 1H).

## Heterogeneity of Fibrosis Differentiates Heart Failure Etiologies

The large spread of fibrosis in HF motivated further investigation of variability in intra-subject non-myocyte fractions (*intra*  $V_{nm}$ ). We calculated  $V_{nm}$  of each  $50 \times 50 \mu\text{m}^2$  sub-image within the overall region of analysis in each subject and obtained their probability distribution. Subregions within a donor sample were similar to each other (Figures 2A–C). The two representative sub-images indicate normal myocyte dimensions (Figures 2B,C). *Intra*  $V_{nm}$  was  $23.54 \pm 7.54\%$  with its distribution concentrated near the mean (Figure 2D). A subject with NIC whose *intra*  $V_{nm}$  of  $40.25 \pm 12.85\%$  is close to the mean  $V_{nm} = 39.68\%$  of all HF revealed sub-images with enlarged ES (Figures 2E–G). The interstitial space varied but was expanded and distinct from that of the donor. Though the  $V_{nm}$  distribution spread wider than the donor, its peak was near the mean (Figure 2H). Images from an HF subject with IC etiology and an *intra*  $V_{nm} = 50.01 \pm 34.61\%$  revealed patches of fibrosis covering the entire area in many sub-images that were devoid of any myocytes (Figures 2I–L). While some sub-images displayed the myocytes and ES similar to the donor sample and some others reflected the average fibrosis with thickened collagen deposits and hypertrophic myocytes, many sub-images with 100%  $V_{nm}$  shifted the distribution. The distribution covered almost the entire range, peaking between 20 and 40% and again, at 100%, all distinct from the mean  $V_{nm}$  (Figure 2L).

## Characteristics of Fibrosis Distinguished Between Ischemic and Nonischemic Etiologies

The clinical characterization of two distinct groups of HF prompted us to investigate the relationship between the etiology of the disease and the characteristics of fibrosis based on *intra*  $V_{nm}$ . Splitting HF into IC ( $n = 8$ ) and NIC ( $n = 8$ ) revealed that the large spread of  $V_{nm}$  of HF is primarily due to the IC (Figure 3A).  $V_{nm}$  was higher for IC vs. NIC ( $47.2 \pm 16.18$  vs.  $32.16 \pm 6.55\%$ ,  $p < 0.05$ ). However, it did not differ between NIC and donor groups. We further analyzed the standard deviation (SD) of *intra*  $V_{nm}$  ( $\sigma_{intra, V_{nm}}$ ) between these groups (Figure 3B). As expected,  $\sigma_{intra, V_{nm}}$  was higher in HF vs. donor ( $21.4 \pm 8.2$  vs.  $7.47 \pm 1.37\%$ ,  $p < 5e-6$ ). Additionally, this measure was not only different between IC and NIC ( $27.1 \pm 6.03$  vs.  $15.69 \pm 5.76\%$ ,  $p < 0.05$ ), but also between NIC and donor ( $15.69 \pm 5.76$  vs.  $7.47 \pm 1.37\%$ ,  $p < 0.05$ ). Regression analysis revealed a strong relationship between  $\sigma_{intra, V_{nm}}$  and  $V_{nm}$  ( $R^2 = 0.74$ ,  $p < 1e-6$ ; Figure 3C). Separately, IC samples corresponded to a 3% increase in  $\sigma_{intra, V_{nm}}$  for every 10% increase in  $V_{nm}$ . Comparatively, the increase in  $\sigma_{intra, V_{nm}}$  for the NIC samples was 5.4% for every 10% increase in  $V_{nm}$ . The donors, in contrast, formed a cluster with low  $V_{nm}$  and low  $\sigma_{intra, V_{nm}}$ . Overlap of IC and NIC samples was present in a region for  $V_{nm}$  between 30 and 40% and  $\sigma_{intra, V_{nm}}$  between 15 and 25%.

Since  $\sigma_{intra, V_{nm}}$  was markedly different between IC and NIC, we used it as a feature to cluster HF using a *k*-means algorithm. The centroids of clusters calculated from the *k*-means algorithm was used to assign the true labels. 7 out of 8 IC and 6 out of 8 NIC were correctly classified (Figure 3D). A  $\sigma_{intra, V_{nm}}$  of 20.58%, which is the mean of the centroids of the two clusters separated IC and NIC (Figure 3C). Further, we explored the geometrical features of the fibrotic patches extracted from the binary image of  $V_{nm}$  for each subject that can distinguish between IC and NIC. By analyzing the properties of connected components of the images that have areas larger than  $150 \mu\text{m}^2$ , we assessed the area of the largest component (Figure 3E) and the mean area of all the components in an image (Figure 3F). By fitting the individual components to ellipses, we also calculated the mean length of the major axis (Figure 3G), minor axis (Figure 3H), and mean eccentricity of the components (Figure 3I). The connected components in each image were counted as well (Figure 3J). The largest fibrotic patch area was higher in IC than NIC ( $23.96e4 \pm 24.46e4$  vs.  $4.39e4 \pm 4.09e4 \mu\text{m}^2$ ,  $p < 0.05$ ). The other features were not different between both groups. Both, IC and NIC images exhibited many distinct elongated fibrotic patches.

We compared the ability of  $\sigma_{intra, V_{nm}}$  to discriminate between IC and NIC samples with that of  $V_{nm}$  and the area of the largest fibrotic patch. The comparison was based on accuracy, sensitivity, specificity, positive, and negative predictive value (Table 2). The accuracy was highest (81.25%) when  $\sigma_{intra, V_{nm}}$  alone was used as the clustering feature. While the specificity and positive predictive value was 100% for the other two classifiers, the low values for sensitivity and negative predictive values make them less effective. Applying the algorithm on a combination of these features did not yield higher accuracy than  $\sigma_{intra, V_{nm}}$  alone.

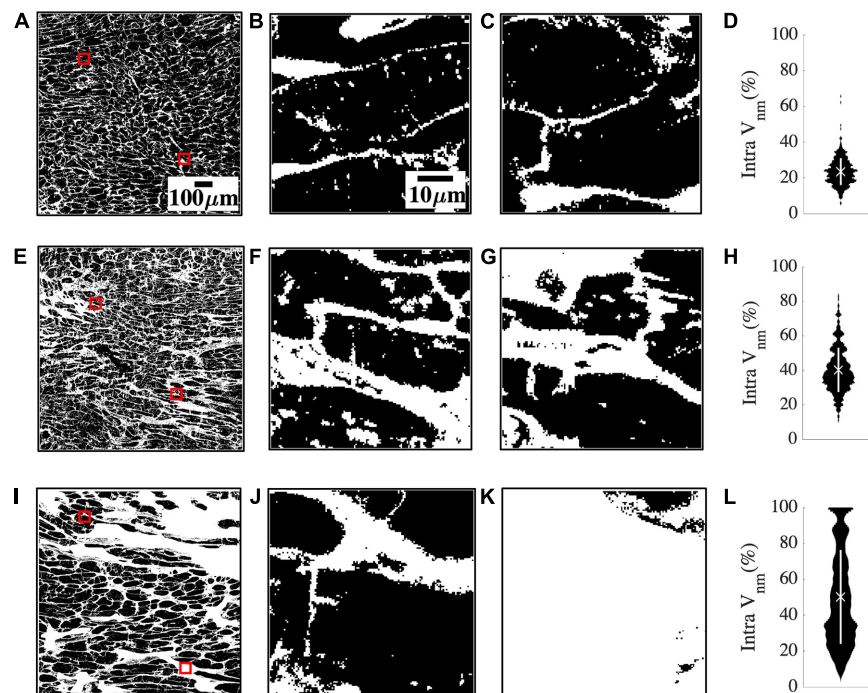


**FIGURE 2 |** Quantification of heterogeneity of  $V_{nm}$  in a representative donor (A–D), mean fibrosis HF (E–H), and high fibrosis HF (I–L). (A) 1 mm<sup>2</sup> region of segmented non-myocyte space in white in a donor tissue section with two of the 400 sub-images of size 50 × 50 μm<sup>2</sup> highlighted with red boxes. (B,C) Zoom-ins of regions within red boxes in panel (A) revealed normal myocyte membranes and capillaries. (D) The probability distribution of  $V_{nm}$  in all the sub-images of panel (A) was narrowly spread. The mean marked with “X” aligned with the distribution peak, and SD marked with the white line segment was small. (E) Region of interest in HF tissue with fibrosis similar to the mean of all HF. (F,G) Magnified sub-images within red boxes in panel (E) indicated enlarged ES. (H) Though the probability distribution was spread wider than panel (D), the mean  $V_{nm}$  was close to the peak. (I) Region of interest in a high fibrosis HF tissue. (J,K) Magnified sub-images within red boxes in panel (I) were very different from each other. (J) Had enlarged interstitial ES while panel (K) was highly fibrotic and devoid of any myocytes. (L) The distribution was more uniformly spread out than panel (H) with the peaks away from the mean. Scale bar in panel (A) applies to panels (E,I). Scale bar in panel (B) applies to panels (C,F,G,J,K).

**TABLE 2 |** Comparison of the binary clustering of HF as ischemic (IC) and nonischemic (NIC) cardiomyopathy by *k*-means algorithm applied to different features from image analysis.

Clustering features	Accuracy (%)	Sensitivity (%)	Specificity (%)	Positive predictive value	Negative predictive value
$\sigma_{intra,V_{nm}}$	81.25	87.5	75	0.78	0.86
$V_{nm}$	75	50	100	1.00	0.67
Area of largest fibrotic patch	62.5	25	100	1.00	0.57

## Patterns of Conduction Have Pronounced Variation in Different Heart Failure Etiologies

We evaluated the characteristics of action potential conduction using a bidomain model based on 2D images of donor and HF tissues. By applying a line stimulus based on voltage clamping for 2 ms, the local activation and CV were assessed over the domain. Example simulations in **Figure 4** revealed the relationship between the conduction and the underlying microstructure. We overlaid the activation time contours on representative segmented binary WGA images. We also overlaid CV vectors on the WGA images at the locations where they were calculated in the mesh. The longitudinal and transverse

conduction was evaluated separately by placing the stimulus corresponding to the myocyte orientation in the images.

For the mesh generated from a donor tissue sample image, a line stimulus at the left edge of the domain initiated longitudinal conduction aligned with the orientation of the long axis of myocytes (**Figure 4A**). The activation wavefronts through the domain at different timepoints were primarily smooth and parallel to the stimulus. The complete domain was activated at ~4.4 ms (**Supplementary Movie 1**). A line stimulus at the top edge of the same mesh generated transverse conduction (**Figure 4B**). The transverse wavefronts were again smooth and parallel to the stimulus, and the activation was completed at ~7.4 ms. The simulation of longitudinal conduction was also performed by placing the stimulus at the right edge of the

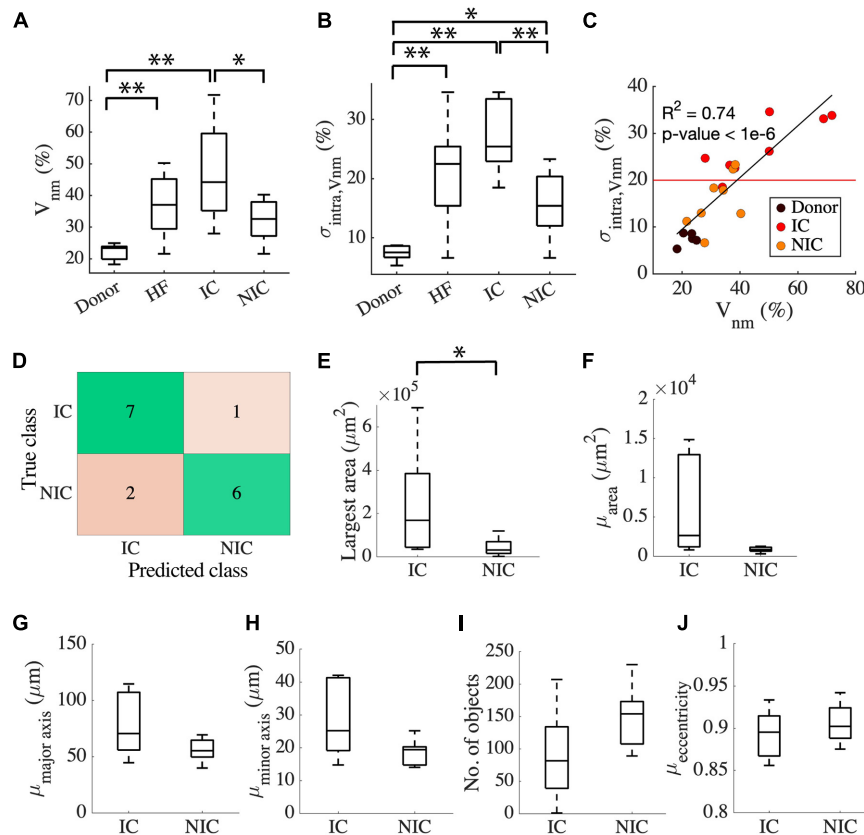


**FIGURE 3 |** Classification of HF by fibrosis characteristics relates to disease etiology. **(A)**  $V_{nm}$  of the donor has an interquartile range (IQR) of ~5% compared to HF with an IQR of ~30%. HF split to IC ( $n = 8$ ), and NIC ( $n = 8$ ) revealed an IQR of ~10% for NIC and ~35% for IC. **(B)**  $\sigma_{intra,Vnm}$  has a median <10% for donors, >20% for IC, and ~15% for NIC. **(C)** Strong relationship between  $\sigma_{intra,Vnm}$  vs.  $V_{nm}$  displayed by the linear regression represented by the black line segment. The red line segment shows that  $\sigma_{intra,Vnm} = 20.58\%$  discriminated most IC from NIC. **(D)** Classification of HF by  $k$ -means algorithm applied to  $\sigma_{intra,Vnm}$  was 81.25% accurate. Connected component analysis of fibrotic objects in images showed that **(E)** area of the largest object was larger in IC than NIC. **(F)** The mean area and the mean lengths of **(G)** major and **(H)** minor axes of the patches were not different for IC and NIC. IC and NIC were not differentiated by **(I)** the number of isolated fibrotic objects with area > 150  $\mu m^2$  or **(J)** the eccentricity of the patches. \* $p < 0.05$ ; \*\* $p < 0.01$ . Outliers in HF are not indicated in panel **(A)**.

domain. Similarly, transverse conduction was repeated by placing the stimulus at the bottom edge.

We evaluated the CV vectors in the four simulations for each mesh at four uniformly distributed points by calculating its magnitude ( $|CV|$ ) and tilt ( $\angle CV$ ) from the direction normal to the line stimulus. An example is shown in **Figure 4C**. The four CV vectors at each location correspond to the four directions of conduction, i.e., two longitudinal CVs (CVLs) and two transverse CVs (CVTs). The four CV vectors in the donor mesh were similar to each other, except for a vector for the right to left longitudinal conduction. The magnitudes of CVL ( $|CVL|$ ) ranged between 0.26 and 0.54 m/s, and the tilt angles of CVL ( $\angle CVL$ ) varied from  $-15^\circ$  to  $2^\circ$ .  $|CVT|$  were 0.16–0.18 m/s and  $\angle CVT$  ranged from  $-0.2^\circ$  to  $2.9^\circ$ . The direction of vectors corresponding to the conduction from left to right and right to left was mostly, but not always, mirrored.

In simulations with an example mesh from NIC tissue, the wavefronts of longitudinal conduction were distinct from the donor because of their complex geometry (**Figure 4D**). The wavefront lost its smoothness, especially in regions with

prominent fibrotic patches. The conduction was faster than the donor, with the activation completed at 3.9 ms (**Supplementary Movie 2**). The transverse conduction, in this case, completed activation slightly faster than the donor sample at 7 ms (**Figure 4E**). The wavefronts were mainly parallel to the stimulus. In this HF sample with low fibrosis and restricted chiefly to interstitial fibrosis,  $|CVL|$  from 0.23 to 0.68 m/s spanned a more extensive range than that of the donor (**Figure 4F**).  $\angle CVL$  of  $-61.2^\circ$  to  $11^\circ$  presented remarkably more tilt than that of the donor, and the differences between conduction in opposite directions were more pronounced. The bottom right location surrounded by fibrotic patches illustrates this variation in CVL (**Figure 4G**).  $|CVT|$  of 0.16–0.2 m/s and  $\angle CVT$  of  $-0.38^\circ$  to  $2.3^\circ$  in this example of NIC was similar to that of the donor.

In high fibrosis HF with IC etiology, the longitudinal wavefronts were heavily distorted with conduction blocked at the top right corner. The conduction was delayed, with activation completed for the rest of the domain at 4.7 ms. The wavefront for transverse conduction was heavily distorted in



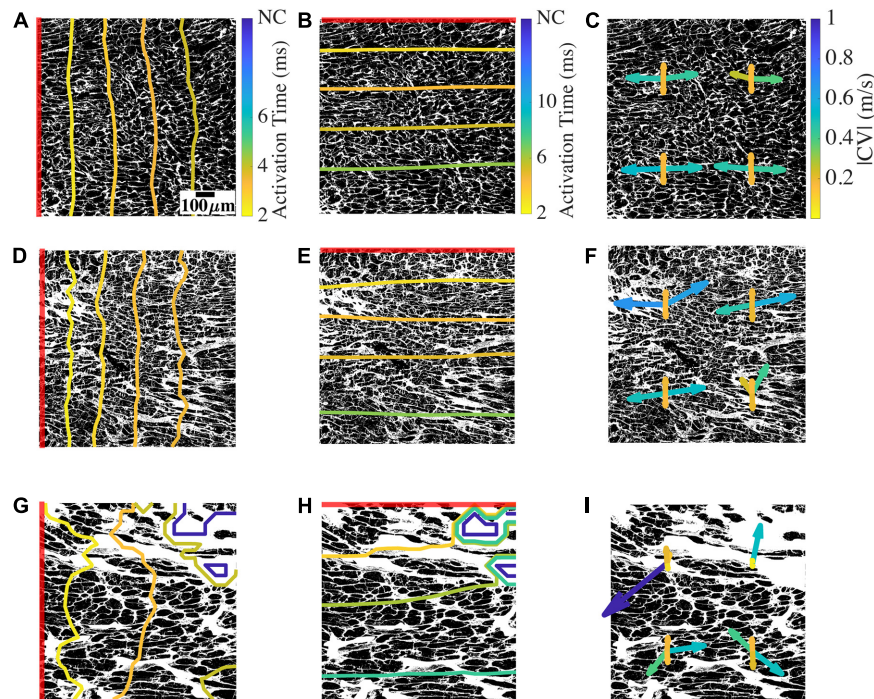


**FIGURE 4 |** Conduction and CV in bidomain model based on a representative donor, low fibrosis HF, and high fibrosis HF tissue. **(A)** Longitudinal conduction in an example donor tissue shown by activation times as contour plot overlaid on the non-myocyte fraction from which the mesh was generated. **(B)** Transverse conduction in the donor. **(C)** CV vectors at four positions in the mesh. At each position, two CV vectors correspond to longitudinal conduction from left to right and right to left, and two CV vectors correspond to transverse conduction from top to bottom and bottom to top. **(D–F)** Conduction and CV vectors for low fibrosis HF. **(G–I)** Longitudinal and transverse conduction and CV vectors for high fibrosis HF. The red line segment in each image shows the location of the applied stimulus. NC indicates no conduction. Scale bar in panel **(A)** applies to all figures. Color bar in panel **(A)** applies to panels **(D,G)**, **(B)** applies to panels **(E,H)**, and **(C)** applies to panels **(F,I)**.

the beginning due to the block. The wavefront regained the smoothness and became parallel to the stimulus as conduction reached near the end of the mesh (**Figure 4H**). The activation was completed for conductive regions of the domain at 8.5 ms, slower than the donor and NIC samples (**Supplementary Movie 3**).  $|CVL|$  of 0.01–1.11 m/s in this example of IC displayed even larger variations in longitudinal conduction than NIC (**Figure 4I**).  $\angle CVL$  of  $-90.29^\circ$  to  $89.59^\circ$  illustrated some CV almost perpendicular to the original direction of conduction. The difference in the direction of CV vectors between the opposing conduction was particularly evident. The CVL at the top left corresponding to conduction beginning at the left end was very small and almost parallel to the stimulus. In contrast, the local instantaneous CVL for the opposite conduction was larger than 1 m/s but less deviated. Similarly, the two CVL vectors of opposing direction of conduction at the top right differed since they were at the edge of the conductive region. Though both their directions are  $90^\circ$  from the expected conduction direction, one had a magnitude  $\sim 0.5$  m/s, and the other was close to 0 m/s. The two lower sets of CV vectors are comparable to those observed in **Figure 4F**.  $|CVT|$  of 0.04–0.52 m/s and  $\angle CVT$  of  $-3.26^\circ$  to  $167.99^\circ$  indicated magnitudes at the top two locations much smaller than the bottom two locations as well as the donor and NIC cases. The vector for conduction

from left to right near the block was large and opposite to the conduction direction.

By analyzing activation times in all the samples, we found that 9 out of the 16 HF models had at least one non-conductive region. In two HF models, longitudinal conduction in either direction was fully blocked and did not reach the opposite end. In addition, transverse conduction in one direction of an HF mesh was blocked before reaching the opposite end.

To evaluate boundary effects on our simulation and calculation of CV, we expanded the computational domain for a donor tissue sample (**Supplementary Figure 4A**). The domain was extended by incorporating meshes with homogenous volume fractions to the left and right of the donor mesh (**Supplementary Figure 4B**). Similar as described above, we performed simulations by applying the voltage clamp on the left and right end of this domain to calculate longitudinal conductivities at the same four locations as the original donor mesh. However, because of the increased length of the domain, the measurement of CV was more than 2 mm away from the boundary. We obtained a mean error of 0.00125 m/s for  $|CVL|$  and  $-1.5^\circ$  for  $\angle CVL$  between the original and extended meshes. The root mean square error was 2.04 and 2.79% for  $|CVL|$  and  $\angle CVL$ , respectively. This example indicates that boundary effects are marginal.

## Etiology-Dependent Heterogeneity of Conduction Velocity Vectors

We calculated the four CV vectors at four locations from all the HF and donor samples to evaluate the distribution of CV vectors and their relationship with fibrosis. While the mean  $|CVL|$  of donors, IC, and NIC were 0.4 m/s, the probability distribution of CV vectors exhibited a large spread in HF vs. donors (**Figure 5A**).  $|CVL|$  was more widely spread in IC compared to NIC ( $0.4 \pm 0.49$  vs.  $0.4 \pm 0.14$  m/s) whereas it was more compact in donors than NIC ( $0.4 \pm 0.09$  vs.  $0.4 \pm 0.14$  m/s). Donors had a distinct peak in the distribution that is close to its mean. SD in  $|CVL|$  was three times larger in IC than NIC and less than NIC in donors.  $|CVL|$  for conduction from left to right and right to left for donors was similar, but less symmetric for NIC (**Supplementary Figure 2A**).

Tilt angles of CVL was most pronounced for IC, much smaller for NIC, and negligible in donors ( $-16.85^\circ \pm 62.85^\circ$  vs.  $0.66^\circ \pm 32.03^\circ$  vs.  $0.03^\circ \pm 7.94^\circ$ ) (**Figure 5B**). In IC, the direction of the CV vector reversed with respect to the conduction in a few cases. SD in  $\angle CVL$  of IC was nearly twice that of NIC, and that in donors was a quarter of NIC. The symmetry of conduction in the two opposite directions in donor was also reflected in low  $\angle CVL$  (**Supplementary Figure 2B**). This symmetry was lost in IC and NIC. The heterogeneity in CVL is corroborated by the spread of maximal upstroke velocities in longitudinal conduction for the three groups (**Supplementary Figure 3A**). While maximal upstroke velocity in donors clustered at  $\sim 200$  V/s, the maximal upstroke velocity in IC and NIC was more widely spread. The absence of activation was present only in IC.

$|CVT|$  was marginally larger in IC than NIC ( $0.23 \pm 0.42$  vs.  $0.18 \pm 0.07$  m/s) and the mean coincided with the peak of their distribution for NIC and donors (**Figure 5C**). The mean  $|CVT|$  for donors at  $0.17 \pm 0.01$  m/s was similar to NIC. The wide spread of  $|CVT|$  in IC and the distinct lump at 0 m/s, indicating no conduction, was similar to that of  $|CVL|$ . The SD of  $|CVT|$  was seven times larger for IC vs. NIC and six times larger for NIC vs. donors. The symmetry between the two directions of transverse conduction was similar to longitudinal conduction in donors. The  $|CVT|$  symmetries were higher for IC and NIC than  $|CVL|$  symmetries (**Supplementary Figure 2C**).  $\angle CVT$  was much smaller than  $\angle CVL$  for all groups, with the tilt angles limited between  $-45^\circ$  to  $+45^\circ$  (**Figure 5D**).  $\angle CVT$  was most prominent for IC, smallest for NIC, and negligible for donors ( $-12.37^\circ \pm 53.76^\circ$  vs.  $-0.09^\circ \pm 5.04^\circ$  vs.  $0.22^\circ \pm 3^\circ$ ). The spread was smallest in donors, largest in IC, and in the middle for NIC. The SD of  $\angle CVT$  in IC was ten times larger than in NIC. The asymmetry in  $\angle CVT$  was pronounced in IC (**Supplementary Figure 2D**). The maximal upstroke velocity in transverse conduction peaked at  $\sim 250$  V/s for both donor and NIC groups, though NIC had a greater spread of values similar to longitudinal conduction (**Supplementary Figure 3B**). We performed *t*-tests between donors, IC and NIC groups for  $|CVL|$ ,  $|CVT|$ ,  $\angle CVL$ , and  $\angle CVT$  and found that variances were different in all comparisons ( $p < 0.01$ ).

Results of linear regression analysis between variables of CV and our fibrosis measures are summarized in **Table 3**. Median  $|CVL|$  for each subject decreased with increasing  $V_{nm}$

of the subjects (**Figure 5E**). Median absolute value of  $\angle CVL$  ( $|\angle CVL|$ ) exhibited a strong positive linear relationship with  $V_{nm}$  (**Figure 5F**). Median  $|CVT|$  decreased (**Figure 5G**) and median absolute value of  $\angle CVT$  ( $|\angle CVT|$ ) increased (**Figure 5H**) as  $V_{nm}$  increased.  $|\angle CVL|$  increased by  $2.1^\circ$  and  $|\angle CVT|$  increased by  $0.91^\circ$  per 1% increase in fibrosis. While the median  $|CVL|$  and  $|CVT|$  displayed negative relationships with  $\sigma_{intra,Vnm}$  similar to that with  $V_{nm}$  (**Figures 5I,K**), median  $|\angle CVL|$  and  $|\angle CVT|$  displayed weaker relationship with  $\sigma_{intra,Vnm}$  than  $V_{nm}$  (**Figures 5J,L**).

$\sigma_{|CVL|}$  and  $\sigma_{|CVT|}$  did not have any relationship with  $\sigma_{intra,Vnm}$  (**Supplementary Figures 3C,D**). In contrast,  $\sigma_{|\angle CVL|}$  and  $\sigma_{|\angle CVT|}$  displayed strong positive relationship with  $\sigma_{intra,Vnm}$  (**Supplementary Figures 3E,F**). The anisotropy  $|CVL| / |CVT|$  in all the cases and the three groups ranged between 1 and 3. The anisotropies were not affected by  $V_{nm}$  or  $\sigma_{intra,Vnm}$  (**Supplementary Figures 3G,H**).

## DISCUSSION

This study revealed fundamental differences in microscopic electrical conduction in ventricular tissues in normal human hearts and hearts from end-stage HF patients of different etiologies. These differences in conduction were caused by fibrotic remodeling that varied with HF etiology. The heterogeneity of fibrosis in HF discriminated the etiology with a high accuracy of 81.25%. We quantified fibrosis considering the cellular constituents, i.e., fibroblasts and myofibroblasts, in addition to the ES, and also analyzed intra-subject heterogeneity of fibrosis at a microscopic scale. Commonly, this microscopic heterogeneity is not assessed in fibrosis quantifications, but it strongly affected outcomes of computational modeling of conduction in HF tissues.

### Heterogeneity of Fibrosis in Heart Failure

Current histological methods for quantifying myocardial fibrosis rely exclusively on the collagen content, and clinical imaging methods cannot provide information on fibrosis at the microscopic scale. Most measures of fibrosis used to parameterize conduction models do not account for fibroblasts and myofibroblasts that are major cellular constituents of the remodeling. Our past work on the analysis of fibrosis in healed myocardial infarction in an animal model showed a significant increase in fibroblasts and myofibroblasts in the scar border zone (Greiner et al., 2018). While the  $V_f + V_{mf}$  was 9% proximal to the scar, it dropped to  $\sim 5\%$  at a distance  $\sim 1$  mm from the scar. Here, our analysis indicates that  $V_f + V_{mf}$  increased in the end-stage HF vs. donors, but to a smaller extent than in the infarction model. A potential explanation is that the tissue is not undergoing active remodeling since most samples are from chronic HF patients (**Table 1**).

The increase in  $\sigma_{intra,Vnm}$  was related to the increase in  $V_{nm}$  across all samples. Separately the samples of NIC showed a stronger effect of  $V_{nm}$  on  $\sigma_{intra,Vnm}$ , while the samples of IC revealed smaller increases in  $\sigma_{intra,Vnm}$  with increase in  $V_{nm}$ .

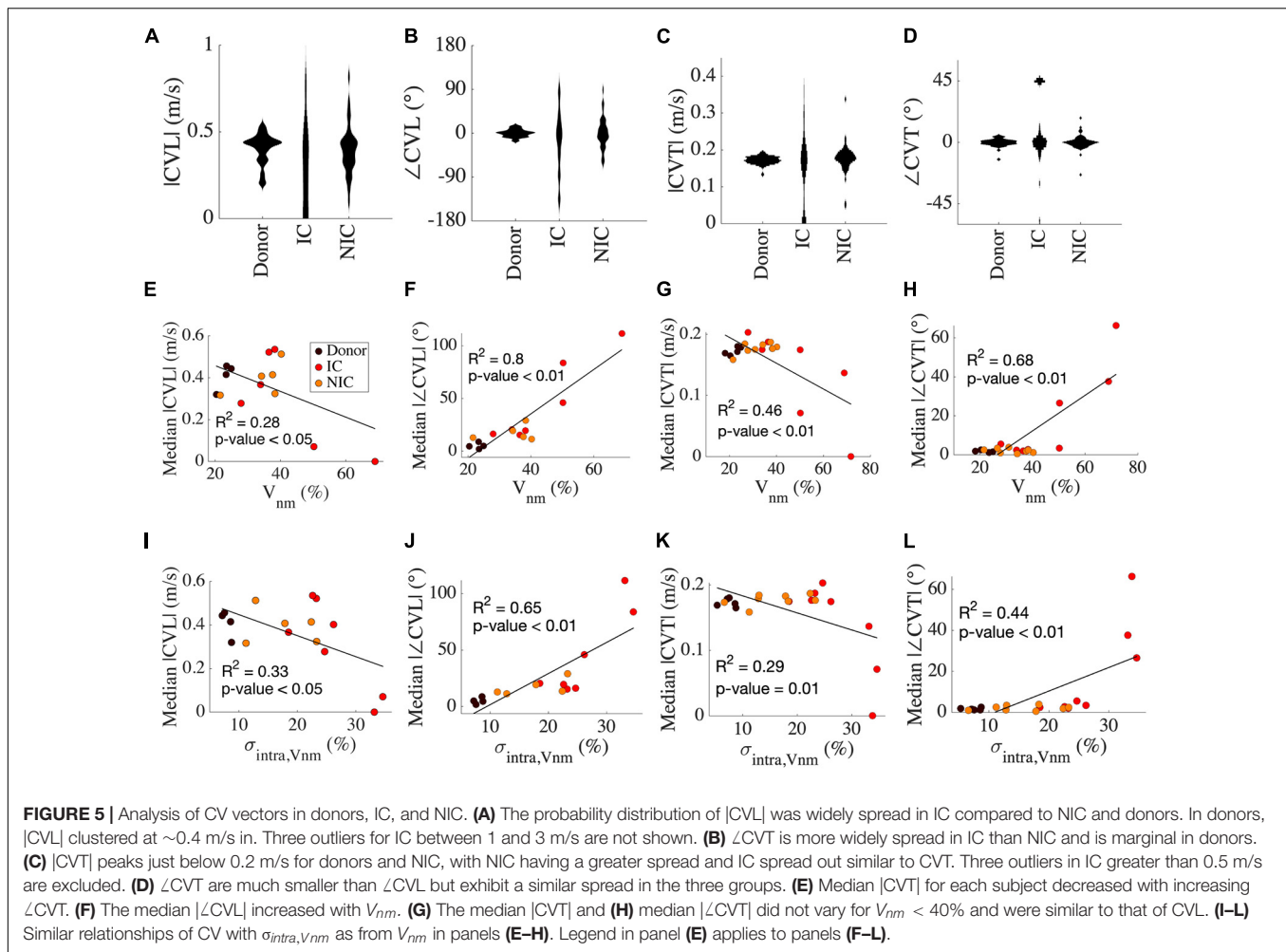


**TABLE 3 |** Results of linear regression analysis between conduction velocities (CV) and fibrosis.

x variable	y variable	Model for linear regression	Coefficient of determination ( $R^2$ )	Significance vs. constant model ( $p$ )
$V_{non-my0}$	Median  CVL	$y = -0.01x + 0.58$	0.28	0.03
$V_{non-my0}$	Median  ∠CVL	$y = 2.10x - 48.69$	0.80	3.1e-6
$V_{non-my0}$	Median  CVT	$y = -0.002x + 0.24$	0.46	7.3e-4
$V_{non-my0}$	Median  ∠CVT	$y = 0.91x - 24.27$	0.68	4.8e-6
$\sigma_{intra-subject,Vnon-my0}$	Median  CVL	$y = -0.01x + 0.54$	0.33	0.02
$\sigma_{intra-subject,Vnon-my0}$	Median  ∠CVL	$y = 2.75x - 25.84$	0.65	1.7e-4
$\sigma_{intra-subject,Vnon-my0}$	Median  CVT	$y = -0.003x + 0.21$	0.29	0.01
$\sigma_{intra-subject,Vnon-my0}$	Median  ∠CVT	$y = 1.15x - 12.69$	0.44	9.6e-4
$\sigma_{intra-subject,Vnon-my0}$	$\sigma_{ CVL }$	$y = 1.40x - 4.49$	0.78	6.6e-6
$\sigma_{intra-subject,Vnon-my0}$	$\sigma_{ \angle CVT }$	$y = 1.79x - 18.77$	0.59	4.3e-5
$\sigma_{intra-subject,Vnon-my0}$	$\sigma_{ CVL }$	$y = 0.01x + 0.001$	0.18	0.1
$\sigma_{intra-subject,Vnon-my0}$	$\sigma_{ CVT }$	$y = 0.01x - 0.04$	0.11	0.13
$V_{non-my0}$	CVL  /  CVT	$y = 0.01x + 1.89$	0.07	0.35
$\sigma_{intra-subject,Vnon-my0}$	CVL  /  CVT	$y = -0.01x + 2.41$	0.06	0.41

Hence, the increase in heterogeneity not only corresponded to the amount of fibrosis but also the HF etiology. A study on fibrosis in tetralogy of Fallot showed that intra-subject variability was similar to the inter-subject variability in single

2D histological thereby limiting the quantification of fibrosis in a truly representative manner (Wuelfers et al., 2021). In our results, the intra-subject variability was higher than inter subject variability of all HF. The recovery of cardiac function in HF



patients caused by mechanical unloading using left ventricular assist devices (LVADs) has been previously associated with an increase in fibrosis (Drakos et al., 2010). However, specific changes in composition and distribution of fibrosis underlying this change remain unknown. We suggest that quantifying the heterogeneity of fibrosis will increase understanding of the role of fibrosis in recovery for different HF etiologies.

Our study showed that heterogeneity of fibrosis is a valuable measure to predict the etiology of HF patients. We also evaluated many geometric features of fibrotic patches in the images of IC and NIC samples for their ability to predict etiology. Comparing these features revealed the compact grouping of NIC. The largest and mean area, as well as the length of the major and minor axis of the ellipse fitted to fibrotic patches were small in NIC. However, in IC these geometric features were widely spread, resulting in the inability to cluster all IC. This reflects not only the heterogeneity in HF but also the heterogeneity of fibrosis patterns, particularly in IC. Previously, a combination of different patterns of fibrosis was observed in a majority of NIC samples (Glashan et al., 2020). In contrast, our analysis of geometric features showed that IC has an even more pronounced variety of fibrosis patterns.

## Alteration of Propagation and Conduction Velocities Due to Fibrosis

In this study, we applied a novel characterization of CV vectors and their tilt from the expected direction of conduction. We found that though mean values of  $|CV|$  did not change between donor, IC, and NIC samples, their distribution differed. IC displayed the largest SD, followed by NIC, and donors displayed the smallest SD. The median  $|CV|$  decreased with increasing fibrosis and its heterogeneity (Table 3). Various studies on human hearts revealed the diversity of changes in the CV in different heart diseases, including fibrosis (Table 4). For example, CV decreased in both sub-endocardial and sub-epicardial LV in end-stage HF patients with NIC (Glukhov et al., 2012). In contrast, CV increased in DCM with fibrosis (Anderson et al., 1993). Though the primary factor for decreased CV in NIC was found to be the remodeling of connexin 43, the abnormal features in conduction, including discontinuities and CV alternans, were attributed to the interstitial fibrosis in HF vs. normal hearts.

Conduction velocities in the ischemic LV free wall was found to decrease in all three directions vs. normal tissue (Taggart et al., 2000–2004). Increased transmural CV was observed in the ventricular septum in hypertrophic hearts, compared to decreased transmural CV in HF vs. normal hearts (Toyoshima et al., 1982). Conduction patterns and spatial heterogeneity of activation were correlated with fibrosis in DCM patients (Anderson et al., 1993). This study revealed three sub-groups of DCM patients with group 1 similar to the donor, group 2 with moderately disturbed conduction, and group 3 with severely distorted conduction patterns. The fibrosis in groups 1–3 were  $4.6 \pm 5.6$ ,  $9.5 \pm 7.8$ , and  $28.3 \pm 21\%$ . However, the specific patterns of fibrosis were not characterized. The only published data on associations between fibrosis patterns and CV suggested that CVL did not change with different amounts of fibrosis in NIC patients (Kawara et al., 2001). However, CVT decreased with

higher fibrosis. Notably, anisotropy in stringy fibrosis was lowest, followed by patchy fibrosis and the highest anisotropy was for diffuse fibrosis (1.35 vs. 2.04 vs. 2.42, respectively).

Prior simulations of fibrotic human cardiac tissues generally showed a decrease in CV with increasing fibrosis. Several approaches were introduced to model the effects of fibrosis. Modeling diffuse fibrosis as non-excitable obstacles that randomly replaced myocytes in the computational mesh and by altering the myocyte model yielded a decrease in CV to 0.3 m/s at 40% fibrosis and 0.1 m/s at 65% fibrosis vs. normal CV of 0.7 m/s (Ten Tusscher and Panfilov, 2007). This approach was modified for stringy fibrosis by introducing unexcitable obstacles as parallel segments of varying lengths (Nezlobinsky et al., 2020). CVL was reduced more with shorter segments, while the CVT was more reduced with longer segments. Simulation with a myocyte model coupled with a fibroblast model and fibrosis determined by the fraction of random sites defined as fibroblasts showed decreasing CV with increasing fibrosis (Majumder et al., 2012). With stronger coupling between fibroblasts and myocytes, the decrease in CV occurred at lower fibrosis. In several simulations of IC samples, we observed high local CV in the vicinity of high local fibrosis levels. This local increase is explained by a source-sink mismatch. Regions with high fibrosis ahead in the direction of conduction reduce the intracellular sink considerably while the source is large.

We showed that  $\angle CV$  is strongly affected by  $V_{nm}$  and  $\sigma_{intra,Vnm}$ .  $\angle CV$  provides a local measure of the wavefront curvature. With increasing fibrosis,  $|\angle CV|$  increased and also  $|CV|$  decreased. CV decreases in a convex wavefront due to a larger sink, and at a concave wavefront CV increases due to a smaller sink compared to the source (Fast and Kléber, 2021). An increased curvature of the wavefront is reflected in more spread in  $|CV|$ . We showed that  $\angle CV$  increased from donors to NIC to IC corresponding to increasing SD in  $|CV|$ . Our results also indicate that curvature of the wavefront increased with increasing fibrosis, especially for longitudinal conduction. Local distortions in the wavefront arose due to underlying fibrotic patterns, which depended on the etiological origins of HF. Similar zig-zag patterns of conduction are well documented as precursors for reentry and slowed conduction fundamental to arrhythmogenesis (Bakker et al., 1993).

Linear regression analysis revealed that median  $|CVT|$  decreased (Figures 5G,K) and median  $|\angle CVT|$  increased (Figures 5H,L) as  $V_{nm}$  and  $\sigma_{intra,Vnm}$  increased (Table 3). However, visual inspection of the sample distribution showed that this relationship was caused by deviations from an otherwise constant distribution for  $V_{nm} > 40\%$  and  $\sigma_{intra,Vnm} > 25\%$ . The changes in median  $|CVT|$  and median  $|\angle CVT|$  were negligible for  $V_{nm} < 40\%$  and  $\sigma_{intra,Vnm} < 25\%$ . The deviations were for IC samples, which stresses the importance of etiology-specific modeling.

We found that CV anisotropy was not affected by fibrosis. Median anisotropy was around  $\sim 2$  for donors and HF. The anisotropy is consistent with the observations in the normal myocardium (Spach et al., 1981). Prior measurements of CVL and CVT in various diseased LV in humans show anisotropy in the range of 1.5–3.4 (Table 4). A similar variation is observed in



**TABLE 4 |** Clinical and experimental measures of CV in human cardiac ventricles.

Normal			Disease			Disease type	Tissue type	References
L (cm/s)	T (cm/s)	N (cm/s)	L (cm/s)	T (cm/s)	N (cm/s)			
56.1	14.6		51.3 ± 4.6			Hypertrophy	LV epi	Doshi et al., 2015
		40 ± 2			28 ± 3	NIC end-stage HF	Basal LV	Dhillon et al., 2013
		49 ± 2			39 ± 3	NIC end-stage HF	LV epi	Glukhov et al., 2012
					41–87	CM	LV endo	Glukhov et al., 2012
							RV free wall	Nanthakumar et al., 2007
60, 85			58 ± 15	24 ± 4		Post VT ablation	LV free wall	Yue et al., 2005
			57 ± 13	28 ± 7		Diffuse fibrosis (20.7 ± 13.7%)	LV/RV epi	Kawara et al., 2001
			53 ± 19	39 ± 13		Patchy fibrosis (21.8 ± 13.8%)	LV/RV epi	Kawara et al., 2001
						Stringy fibrosis (11.8 ± 2.7%)	LV/RV epi	Kawara et al., 2001
65	48	51	56	32	26	Ischemia	LV free wall	Taggart et al., 2000–2004
			66 ± 9	<20		DCM, congestive HF	LV /RV	Wu et al., 1998
			70	20		DCM	Papillary muscle	Bakker et al., 1996
80 ± 8	23 ± 3		84 ± 9	23 ± 3		DCM (fibrosis 4.6 ± 5.6%)	LV epi	Anderson et al., 1993
			90 ± 9			DCM (fibrosis 9.5 ± 7.8%)	LV epi	Anderson et al., 1993
			79	7		Infarction	Papillary muscle	Bakker et al., 1993
		19.86 ± 5.44			30.55 ± 7.58	Hypertrophy	Septum	Toyoshima et al., 1982
					45	Hypertrophy	LV free wall	Dam et al., 1972
		46.4 ± 2.7					LV free wall	Durrer et al., 1970
		43.4, 44.9					Septum	Durrer et al., 1970

L: Longitudinal, T: Transverse, N: Transmural, CM: Cardiomyopathy, DCM: Dilated Cardiomyopathy, LV: Left ventricle, RV: Right ventricle, epi: sub-epicardial, endo: sub-endocardial.

very limited measurements available from normal human hearts. Anisotropy was found to increase with increasing fibrosis at different rates depending on the dimensions of fibrotic patterns in the domain (Nezlobinsky et al., 2020). However, the combination of different patterns and dimensions of fibrosis within each patient introduces more complexity.

In our simulations, we observed that maximum upstroke velocity was lower during fast longitudinal conduction and higher during slow transverse conduction (**Supplementary Figures 3A,B**). The higher upstroke velocity along the transverse direction is due to less charge dissipation to sink. This is consistent with the current understanding of anisotropic conduction based on seminal experiments on normal canine cardiac tissue (Spach et al., 1981). The smaller sink provides a higher safety factor for transverse relative to longitudinal conduction providing a path for conduction to proceed even when longitudinal conduction is blocked (Valderrabano, 2007).

The pronounced etiology-dependent differences in  $|CV|$  and  $\angle CV$  indicate a need to adjust modeling parameters based on the clinical background of patients. Our study suggests that conduction fundamentally differs in two major etiologies of HF due to the characteristics of fibrosis. We showed that the etiology is reflected on the heterogeneity of fibrosis. We

propose that including heterogeneity in the modeling of tissue of HF patients based on their clinical data is essential to uncover abnormalities of microscopic conduction. Our study stresses the clinical need to identify disease-specific fibrotic patterns in HF patients and stratify them based on the risk of arrhythmogenesis.

## Limitations

This study has several limitations. The tissue samples from patients undergoing LVAD implantation were procured close to the apex and had mixed orientation of myocytes. We minimized this effect by choosing a region of analysis from the image where the myocyte orientation is uniform. The samples were also distal from any scar and hence not confounded by scar fibrosis. We imaged a single slice for characterizing the fibrosis for each subject, which only coarsely represents the overall fibrosis and its heterogeneity in left ventricles. Analysis of larger areas would more comprehensively represent the heterogeneity in tissue remodeling as suggested in Wuelfers et al. (2021). The 2D imaging and modeling does not completely represent the transmural heterogeneity and anisotropy of the myocardium. Further sampling of ventricular tissue could reveal if the analysis of a small sample from any region can

distinguish the etiology and also if the apical tissue is a good representative for the ventricular tissue. Due to limitations of tissue procurement from HF patients, a more extensive sampling was not feasible.

The bidomain electrophysiological simulations utilized the concept of homogenized media of myocyte and ES that coexist at every mesh element. However, a more microscopically realistic modeling approach could consider volumes of ES and myocytes as distinct spaces separated by a membrane (Roberts et al., 2008). Our detailed microscopic images form a basis for such modeling.

In this work, an explicit time-stepping scheme was utilized for simulations requiring a time resolution of 1e-8s for such a fine mesh grid. The computation time was ~650 s for a mesh with 400 elements simulated for a duration of 15 ms. Using an implicit scheme might allow a coarser time resolution and shorter run time with similar accuracy. Due to the time required for simulations, we characterized conduction for a single wave through the domain. Investigations on the effect of basic cycle length on CV were not performed but might provide insights into arrhythmogenesis in heterogeneous domains. A second order polynomial model to interpret the relationship between CV and fibrosis values gives an increased  $R^2$ . However, we do not have a good biophysical model describing the relationships between fibrosis measures and conduction. Hence, we applied a simple linear regression model to make coarse statements about the relationships. We lack functional measurements from this tissue to compare the results from simulations. However, we discussed our results in the context of published experimental data to arrive at conclusions.

## MATERIALS AND METHODS

### Tissue Collection

The tissue collection and clinical characterization for this study were approved by the Institutional Review Board of the University of Utah Health, Intermountain Medical Center, Salt Lake City VA Medical Center, which are members of the Utah Transplantation Affiliated Hospitals Cardiac Transplant Program. Transmural tissue biopsies from the left ventricular apical region of HF with reduced ejection fraction ( $n = 16$ ) and non-failing donor hearts ( $n = 5$ ) were fixed immediately in 10% formalin. The biopsies were from the apical core of patients undergoing LVAD implantation or from matching locations in the failed heart during transplant and the donor hearts. The donor hearts were not suitable for transplantation due to non-cardiac reasons. The demographics and clinical data for donors and HF patients are summarized in Table 1.

### Tissue Processing

The fixed tissue samples were rinsed in phosphate buffered saline (PBS) within a day of fixation. The samples were then embedded in 3% agarose gel and sectioned using a vibratome Leica VT1200S (Leica Biosystems, Wetzlar, Germany) to obtain

slices of 100  $\mu\text{m}$  thickness. The midmyocardial slices were detached from agarose and washed in PBS before performing immunohistochemistry. We applied primary antibodies A5228 and V6630 (Sigma-Aldrich, St. Louis, MO, United States) at a concentration of 1:200 in a blocking solution with normal goat serum to bind to the proteins  $\alpha$ -SMA and vimentin, respectively. Vimentin marked fibroblasts and endothelial cells in blood vessels. Smooth muscle cells, including myofibroblasts, were marked with  $\alpha$ -SMA. Slices were incubated overnight on a rocker at room temperature. After washing with PBS three times, goat anti-mouse secondary antibodies A21137 and A21240 (Thermo Fisher Scientific, Waltham, MA, United States), conjugated to AF 555 and AF 647, respectively, were applied at 1:200 in the blocking solution to attach to the corresponding primary antibodies. We incubated these slices for 6 h at room temperature on the rocker together with 4',6-diamidino-2-phenylindole (DAPI, D3571, Thermo Fisher Scientific) at 3  $\mu\text{g}/\text{ml}$  to label the nuclei. After another set of three rinses of the slices in PBS, we applied WGA conjugated to a green fluorescent dye (CF488A, Biotium Inc., Fremont, CA, United States) at a concentration of 40  $\mu\text{g}/\text{mL}$  in PBS to the slices for at least 4 h to label the glycocalyx and ECM proteins. Post incubation, the slices were washed with PBS and mounted on coverslips of 0.16–0.19 mm thickness with Fluoromount-G (#17984-25, Electron Microscopy Science, Hatfield, PA, United States) using a compression-free mounting method (Seidel et al., 2016). After curing for 24 h at a relative humidity between 30 and 35%, the samples were coated with a nail hardener before imaging. The humidity was controlled by placing the samples in a chamber with a bath of saturated NaI solution.

### Imaging and Image Processing

We imaged the coverslips with human cardiac tissue slices using a laser scanning confocal microscope Leica TCS SP8 (Leica Microsystems, Wetzlar, Germany) with a 40x oil immersion objective at a resolution of 378 nm per pixel. The imaging regions were chosen where the long-axis of myocytes were parallel to the X-axis of the coordinate axis. To cover areas of 1 mm<sup>2</sup> and larger, several images of the size 1,024  $\times$  1,024 pixels were stitched together using the merge tool in the post-processing software of the microscope (Leica Application Suite X 3.5.5). For this merging, imaging was performed with an overlap of 10% between adjacent images. The depth of imaging within the 100  $\mu\text{m}$  slice was chosen to obtain uniform intensity throughout the area covered. We analyzed the signals in a region of interest of approximately 1 mm<sup>2</sup> area chosen by avoiding edges of the section as well as blood vessels within the image (Figure 1A). The raw images of DAPI (Figure 1B), WGA (Figure 1C), vimentin (Figure 1D), and  $\alpha$ -SMA (Figure 1E) were initially segmented using histogram-based thresholding as described in Seidel et al. (2016). WGA labeled collagen as well as extracellular membrane. To avoid the exclusion of regions from ES due to variation in intensities of collagen labeling, masks covering non-myocyte spaces were manually drawn and added to the thresholded WGA signal to obtain the

segmented ES using Fiji (Schindelin et al., 2012). The  $\alpha$ -SMA and vimentin signals were processed to avoid the labeling of endothelial and smooth muscle cells through a one-pixel opening followed by removing objects larger than 1,000 pixels from the thresholded images. The nuclei within one pixel of  $\alpha$ -SMA or vimentin signal were incorporated as myofibroblasts or fibroblasts, respectively.

## Analysis of Fibrosis

We calculated  $V_{nm}$  as the fraction of the segmented non-myocyte space within the selected area in the image of each sample. We also calculated  $V_f$  and  $V_{mf}$  as the fraction occupied by fibroblasts and myofibroblasts, respectively.  $V_e$  was defined as the fraction of ES. The non-myocyte space was defined as the sum of  $V_e$ ,  $V_f$ , and  $V_{mf}$ .

$$V_{nm} = V_e + V_f + V_{mf} \quad (1)$$

Fibrosis in each HF sample was defined as the increase of the non-myocyte space from the average  $V_{nm}$  in donors.

$$Fibrosis = V_{nm,HF} - \text{mean}(V_{nm,Donors}) \quad (2)$$

We determined the group-wise  $V_{nm}$  from the images for donors and HF. The calculation of  $V_{nm}$  was repeated by dividing the image into  $50 \mu\text{m} \times 50 \mu\text{m}$  sub-images to find the intra-subject heterogeneity. The variability of intra-subject fibrosis  $\sigma_{intra,Vnm}$  was calculated based on SD of  $V_{nm}$  of sub-sampled regions within each subject. We performed linear regression analyses of  $\sigma_{intra,Vnm}$  with respect to  $V_{nm}$ . We further separated HF into IC and NIC samples to assess  $V_{nm}$  and  $\sigma_{intra,Vnm}$ .

## Classification of Heart Failure and Association to Etiology

The HF samples were clustered based on different measures of fibrosis. The clusters were evaluated in their ability to differentiate their clinical etiology as IC and NIC. In addition to  $V_{nm}$  and  $\sigma_{intra,Vnm}$ , features from images that capture the pattern and arrangement of fibrotic patches were used for classification. We processed the images to extract the connected components that are larger than  $150 \mu\text{m}^2$  from the binary images of non-myocyte fractions. Among these objects, the object with the largest area and the mean area of objects were calculated. We calculated the eccentricity, major, and minor axes of an ellipse that has the same second central moment as the object for all the objects in each image. Eccentricity was defined as the ratio of the major to the minor axis. We compared these image features in IC vs. NIC, and features with significant differences were noted. Next, we performed binary clustering of subjects using the  $k$ -means algorithm with these image features,  $V_{nm}$  and  $\sigma_{intra,Vnm}$  individually and in different combinations as the input. The algorithm was repeated 50 times for each clustering, and the clusters with the lowest sum of Euclidean distances of points to the cluster centroid were chosen as the result. To evaluate the clustering, the cluster with the lower centroid was assigned the label of NIC and that with the higher centroid was assigned IC.

For clustering by  $\sigma_{intra,Vnm}$  only, the mean of the two centroids was calculated as the value of  $\sigma_{intra,Vnm}$  that can discriminate between IC and NIC. After assigning labels to the clusters, we calculated the positive and negative predictive value, accuracy, specificity, and sensitivity for the classification.

## Modeling of Fibrotic Tissue and Simulation

We utilized the bidomain model of cardiac tissue electrophysiology to characterize the electrical conduction in fibrotic tissue (Tung, 1978). In this model, the cardiac tissue is described with a myocyte and an extracellular domain. These two domains coexist at every point of space and are subject to principles of current conservation. Any current flowing out of one domain has to enter the second domain, and the net current is zero. Two Poisson equations describe the relationship between current and potential for each domain and the interaction between the two domains:

$$\nabla \cdot (\sigma_{myo} \nabla \phi_{myo}) = -f_{s,myo} + \beta_{myo} I_{myo,e} \quad (3)$$

$$\nabla \cdot (\sigma_e \nabla \phi_e) = -f_{s,e} - \beta_{myo} I_{myo,e} \quad (4)$$

where  $\sigma_{myo}$  and  $\sigma_e$  are the electrical conductivity tensors (S/m) of the myocyte and extracellular domain, respectively, and  $\phi_{myo}$  and  $\phi_e$  are the electrical potentials (V) of the myocyte and extracellular domain, respectively.  $f_{s,myo}$ , and  $f_{s,e}$  are the current source densities (A/m<sup>3</sup>) for the myocyte and extracellular domain, respectively. Current flowing between the myocyte and extracellular domain,  $I_{myo,e}$  (A) was calculated using the electrophysiological model of a normal human ventricular myocyte (Tusscher et al., 2004).

$$I_{myo,e} = I_{ion} + C_m \frac{\partial V_{m,myo}}{\partial t} \quad (5)$$

where  $I_{ion}$  (A) is the total ion channel current flowing through the membrane of a myocyte and  $C_m = 2\text{e}7\text{nF}$  is the membrane capacitance per myocyte. Membrane voltage of myocytes  $V_{m,myo}$  (V) was defined as the difference between  $\phi_{myo}$  and  $\phi_e$ .  $I_{ion}$  defined by the biophysical model of human ventricular myocyte includes fast  $\text{Na}^+$  current ( $I_{Na}$ ), L-type  $\text{Ca}^{2+}$  current ( $I_{CaL}$ ), transient outward current ( $I_{to}$ ), rapid delayed rectifier current ( $I_{Kr}$ ), slow delayed rectifier current ( $I_{Ks}$ ), inward rectifier K current ( $I_{K1}$ ),  $\text{Na}^+/\text{Ca}^{2+}$  exchanger current ( $I_{NaCa}$ ),  $\text{Na}^+/\text{K}^+$  pump current ( $I_{NaK}$ ), plateau  $\text{Ca}^{2+}$  and  $\text{K}^+$  currents ( $I_{pK}$  and  $I_{pCa}$ ), and background  $\text{Ca}^{2+}$  and  $\text{K}^+$  currents ( $I_{bCa}$  and  $I_{bK}$ ). These individual membrane currents are defined based on the specific channel conductances and transmembrane voltage.

$$I_{ion} = I_{Na} + I_{K1} + I_{to} + I_{Kr} + I_{Ks} + I_{CaL} + I_{NaCa} + I_{NaK} + I_{pCa} + I_{pK} + I_{bCa} + I_{bNa} \quad (6)$$

The conductivity tensors for myocyte and extracellular domains were defined by a linear relationship with their respective volume fractions,  $V_{myo}$  and  $V_e$  (dimensionless):

$$\sigma_{myo} = V_{myo} \bar{\sigma}_{myo} \quad (7)$$

$$\sigma_e = V_e \bar{\sigma}_e \quad (8)$$

where the tensors  $\sigma_{myo} = 0.5$  S/m and  $\sigma_e = 1$  S/m described longitudinal conductivity for the volume fraction of 100% for the respective domains. The longitudinal to transverse anisotropy of the conductivity with respect to the myocyte orientation was 10 and 2 for intra- and extracellular domains, respectively. We defined the relationship between the volume fractions of bidomain domains as:

$$V_{myo} = 1 - V_e - V_f - V_{mf} \quad (9)$$

where  $V_e$ ,  $V_f$ , and  $V_{mf}$  are the volumes equivalent to the fractional areas of ES, fibroblasts, and myofibroblasts, respectively, calculated for each mesh element. Since the total area occupied by fibroblasts and myofibroblasts combined was within 5% and intercellular coupling through gap junctions was neglected, they were not considered to form a separate domain. Their fractional space in the images translated to a non-conductive fraction in the mesh. Hence the conductivities associated with  $V_f$  and  $V_{mf}$  are zero. The number of myocytes per unit volume  $\beta_{myo}$  ( $1/\text{m}^3$ ) was defined as:

$$\beta_{myo} = \frac{V_{myo}}{V_{myo, single}} \quad (10)$$

where  $V_{myo, single}$  is the individual volume for a myocyte.  $V_{myo, single} = 41,073 \mu\text{m}^3$  was set to reflect the volume of a human myocyte (Gerdes et al., 1992).

2D meshes for bidomain cardiac electrophysiological simulation of fibrotic tissue were generated by selecting rectangular regions from the segmented binary WGA labeling of tissue images. The volume-based quantities in the domain are defined for 2D by treating the third dimension as having a unit length. The variation of fibrosis calculated for each image was incorporated by varying  $V_e$ ,  $V_f$ , and  $V_{mf}$ , at each element of the mesh according to the underlying image intensities. We downsampled each image such that the area covered by each mesh element is  $2,500 \mu\text{m}^2$  of the image. The simulations were run for 15 ms with a time step resolution of  $1\text{e-}8\text{s}$ . The rectangular domains of around  $1 \text{ mm}^2$  with a regular grid and an element edge length of  $50 \mu\text{m}$  were activated using Dirichlet boundary conditions that held the transmembrane voltage of one edge of the domain at 1 mV for 2 ms after allowing the system to equilibrate for 2 ms. The extracellular and intracellular source currents were zero. The domain was subjected to no flux Neumann boundary condition.

We applied an implementation of the bidomain model (Seemann et al., 2010) that uses the Portable, Extensible Toolkit for Scientific Computation (Balay et al., 1997) to solve the Poisson equations. The Eqs 3, 4 are recast as an elliptic PDE (Eq. 11) and a parabolic PDE (Eq. 12):

$$\nabla \cdot ((\sigma_{myo} + \sigma_e) \nabla \Phi_e) = -\nabla \cdot (\sigma_{myo} \nabla V_{m, myo}) \quad (11)$$

$$\begin{aligned} \nabla \cdot (\sigma_{myo} \nabla V_{m, myo}) + \nabla \cdot (\sigma_{myo} \nabla \Phi_e) \\ = \beta_{myo} \left( C_m \frac{dV_{m, myo}}{dt} + I_{ion} \right) \end{aligned} \quad (12)$$

This implementation utilizes an operator splitting method with a forward Euler scheme for time-stepping. This modeling framework was benchmarked against other frameworks through monodomain simulations [acCELLerate indexed I in Niederer et al. (2011)]. We performed the calculations at each time step with the Generalized Minimal Residual method and additive Schwarz preconditioner to solve the linear system of equations limiting the relative and absolute tolerance to  $1\text{e-}12$ .

The orientation of the myocytes combined with the placement of stimulus was used to determine the direction of conduction as longitudinal or transverse. All the images in which the long axes of myocytes were visualized were simulated with the activation on all four edges of the domain ( $n = 16$ ). These images were rotated to align the long axis of myocytes along the X-axis. The two simulations with stimulus normal to the long axis were used to evaluate the longitudinal conduction. The other two simulations where the activation edge was parallel to the long axis were analyzed as transverse conduction. Only transverse conduction was evaluated when the image captured the axial cross-section of myocytes ( $n = 5$ ).

## Evaluation of Conduction

The activation times at every element of the domains were determined to identify cases with regions of conduction block. The activation time was defined as the time of maximum upstroke velocity of the membrane potential within the range of -60 and 0 mV. We recorded the maximum upstroke velocities at four sets of three adjacent grid points spread uniformly over the mesh. Each set of three grid points are placed so that two of them lie along the X-axis and two of them lie along the Y-axis, with one point common to both pairs. The activation times at these points were also used to calculate the CV as described below applicable for regular rectangular grids. The magnitude and direction of the CV vectors, CVL and CVT, were measured for transverse and longitudinal conduction, respectively, according to

$$|CV| = \frac{l}{\sqrt{tx^2 + ty^2}} \quad (13)$$

and

$$\angle CV = \begin{cases} +x : \tan^{-1} \frac{ty}{tx} \\ -x : 180^\circ - \tan^{-1} \frac{ty}{tx} \\ +y : 90^\circ - \tan^{-1} \frac{tx}{ty} \\ -y : 90^\circ + \tan^{-1} \frac{tx}{ty} \end{cases} \quad (14)$$

where  $tx$  and  $ty$  are the activation time differences between the two adjacent grid points along the X- and Y-axis, respectively. The distance between two adjacent grid points,  $l$ , was  $50 \mu\text{m}$ .  $x$  and  $y$  correspond to longitudinal and transverse conduction.  $+$  corresponds to the left to right or top to bottom while  $-$  corresponds to the conduction in opposite directions. The



simulations in two opposing directions of longitudinal and transverse conduction were separately analyzed to quantify the effect of direction in the image-based mesh. They were pooled together to analyze the conduction with respect to different groups and the relationship between the conduction and fibrosis.  $|\angle CV|$  was calculated to measure the tilt of CV vectors.

To evaluate the effect of the boundary on CV, we performed the simulation of a donor sample mesh embedded in a homogenous mesh (**Supplementary Figure 4**). We calculated the space constants of the domain,  $\lambda_l$  and  $\lambda_t$  for the longitudinal and transverse directions, respectively, according to Roth (1997).

$$\lambda_l = \sqrt{\frac{R}{\beta} \frac{(\sigma_{myot} \sigma_{el})}{(\sigma_{myot} + \sigma_{el})}} \quad (15)$$

$$\lambda_t = \sqrt{\frac{R}{\beta} \frac{(\sigma_{myot} \sigma_{el})}{(\sigma_{myot} + \sigma_{el})}} \quad (16)$$

where  $R = 0.2 \Omega m^2$  is the membrane resistance and  $\beta = 2e5 m^{-1}$  is the myocyte surface-to-volume ratio (Tusscher et al., 2004). In our simulations, we have set the conductivities for 100% volume fractions,  $\sigma_{myot} = 0.1 S/m$ ,  $\sigma_{el} = 1 S/m$ ,  $\sigma_{myot} = 0.01 S/m$ , and  $\sigma_{el} = 0.5 S/m$ . Thus,  $\lambda_l = 0.30 mm$  and  $\lambda_t = 0.09 mm$ .

Each element of the homogenous mesh was composed of volume fractions that are the mean value of the volume fractions of elements in the donor mesh. The dimensions of this domain were 5 mm in X direction and 1 mm in Y direction, with the donor mesh (**Supplementary Figure 4A**) forming the middle part of the new domain from 2 to 3 mm (**Supplementary Figure 4B**).  $|CV|$  and  $\angle CV$  calculated from longitudinal propagation with voltage clamping at the left end or right end of the domain were compared with those from the original donor mesh. The evaluation of CV at the same positions as the original mesh was now  $> 2 mm$  from the boundary which is more than five times  $\lambda_l$ . We evaluated mean error and root mean square error percent to determine the effect.

## Statistical Analysis

All statistical analyses were performed in MATLAB 2020a or later (Mathworks, Natick, MA, United States). Student's *t*-test for unequal variances was performed to compare the composition of fibrosis in donors and HF, and  $p < 0.05$  was considered significant. The ratio of variance in HF to that in donor for all the variables considered for *t*-test with unequal variances was larger than 5. Violin plots were generated using external code developed for MATLAB (Jonas, 2008). Inter-subject and intra-subject heterogeneity in fibrosis between IC, NIC, and donors were compared using one-way ANOVA, and  $p < 0.05$  was considered significant. Boxes in the boxplots represented interquartile range, and whiskers extend to median  $\pm 2.7 SD$ . Values beyond whiskers were considered outliers. All values for fibrosis characterization and CV were reported as mean  $\pm SD$ . The variances between magnitude and tilt angles of CV were compared between different groups using a two-sample *f*-test. Regression analysis was performed using a linear model of the form  $y = Ax + B$ . The model was compared to a constant model and evaluated using the coefficient of determination ( $R^2$ ).  $p < 0.05$  was considered significant.

## DATA AVAILABILITY STATEMENT

The datasets presented in this study can be found in online repositories. The names of the repository/repositories and accession number(s) can be found below: Hive, University of Utah, <https://doi.org/10.7278/S50D-BPS8-R06S>.

## ETHICS STATEMENT

The studies involving human participants were reviewed and approved by IRB, University of Utah. The patients/participants provided their written informed consent to participate in this study.

## AUTHOR CONTRIBUTIONS

ACS: sample preparation, imaging, analyses, manuscript draft, and revision. JG and JB: analyses and manuscript revision. JRV: sample acquisition, preparation, and manuscript revision. TSS: sample acquisition and preparation. CPK: sample, acquisition, preparation, and clinical data preparation. SGD: donor identification and manuscript revision. FBS: study design, manuscript draft, and revision. All authors contributed to the article and approved the submitted version.

## FUNDING

This work was supported by the National Institutes of Health R01HL132067 (SGD and FBS) and the Nora Eccles Treadwell Foundation (SGD and FBS). SGD was also supported by AHA Heart Failure Strategically Focused Research Network 6SFRN29020000, NHLBI R01 HL135121-01 and Merit Review Award I01 CX002291 United States Department of Veterans Affairs. JB has financial support from MICINN (Spain) through Grant No. SAF-2017-88019-C3-2-R.

## ACKNOWLEDGMENTS

The authors are grateful to the donor families for their generosity, and DonorConnect (<https://www.donorconnect.life/>), Salt Lake City, Utah, for facilitating the work of our research team members acquiring myocardial tissue in the operating rooms of several hospitals of the Intermountain West. ACS acknowledges the financial support and discussion for the work presented at the workshop on Uncertainty Quantification for Cardiac Models, 2019 at Cambridge, United Kingdom. JG acknowledges membership in Collaborative Research Centre SFB1425 of the German Research Foundation (DFG #422681845).

## SUPPLEMENTARY MATERIAL

The Supplementary Material for this article can be found online at: <https://www.frontiersin.org/articles/10.3389/fphys.2021.730933/full#supplementary-material>

## REFERENCES

- Anderson, K. P., Walker, R., Urie, P., Ershler, P. R., Lux, R. L., and Karwande, S. V. (1993). Myocardial electrical propagation in patients with idiopathic dilated cardiomyopathy. *J. Clin. Invest.* 92, 122–140. doi: 10.1172/JCI116540
- Aoki, T., Fukumoto, Y., Sugimura, K., Oikawa, M., Satoh, K., Nakano, M., et al. (2011). Prognostic impact of myocardial interstitial fibrosis in non-ischemic heart failure –comparison between preserved and reduced ejection fraction heart failure. *Circ. J.* 75, 2605–2613. doi: 10.1253/circj.11-0568
- Bakker, J. M. T., Capelle, F. J. L., Janse, M. J., Tasseron, S., Vermeulen, J. T., Jonge, N., et al. (1996). Fractionated electrograms in dilated cardiomyopathy: origin and relation to abnormal conduction. *J. Am. Coll. Cardiol.* 27, 1071–1078. doi: 10.1016/0735-1097(95)00612-5
- Bakker, J. M., Capelle, F. J., Janse, M. J., Tasseron, S., Vermeulen, J. T., Jonge, N., et al. (1993). Slow conduction in the infarcted human heart. ‘Zigzag’ course of activation. *Circulation* 88, 915–926. doi: 10.1161/01.cir.88.3.915
- Balaban, G., Costa, C. M., Porter, B., Halliday, B., Rinaldi, C. A., Prasad, S., et al. (2020). 3D electrophysiological modeling of interstitial fibrosis networks and their role in ventricular arrhythmias in non-ischemic cardiomyopathy. *IEEE Trans. Biomed. Eng.* 67, 3125–3133. doi: 10.1109/TBME.2020.2976924
- Balaban, G., Halliday, B. P., Mendonca Costa, C., Bai, W., Porter, B., Rinaldi, C. A., et al. (2018). Fibrosis microstructure modulates reentry in non-ischemic dilated cardiomyopathy: insights from imaged guided 2D computational modeling. *Front. Physiol.* 9:1832. doi: 10.3389/fphys.2018.01832
- Balay, S., Gropp, W. D., McInnes, L. C., and Smith, B. F. (1997). “Efficient management of parallelism in object-oriented numerical software libraries,” in *Modern Software Tools for Scientific Computing*, eds E. Arge, A. M. Bruaset, and H. P. Langtangen (Boston, MA: Birkhäuser Boston), 163–202.
- Bleumink, G. S., Knetisch, A. M., Sturkenboom, M. C. J. M., Straus, S. M. J. M., Hofman, A., Deckers, J. W., et al. (2021). Quantifying the heart failure epidemic: prevalence, incidence rate, lifetime risk and prognosis of heart failure. The Rotterdam Study. *Eur. Heart J.* 25, 1614–1619. doi: 10.1016/j.ehj.2004.06.038
- Boyle, P. M., Zghaib, T., Zahid, S., Ali, R. L., Deng, D., Franceschi, W. H., et al. (2019). Computationally guided personalized targeted ablation of persistent atrial fibrillation. *Nat. Biomed. Eng.* 3, 870–879. doi: 10.1038/s41551-019-0437-9
- Bragazzi, N. L., Zhong, W., Shu, J., Abu Much, A., Lotan, D., Grupper, A., et al. (2021). Burden of heart failure and underlying causes in 195 countries and territories from 1990 to 2017. *Eur. J. Prevent. Cardiol.* zwaa147. doi: 10.1093/eurjpc/zwaa147 [Epub ahead of print].
- Campos, F. O., Wiener, T., Prassl, A. J., dos Santos, R. W., Sanchez-Quintana, D., Ahammer, H., et al. (2013). Electroanatomical characterization of atrial microfibrosis in a histologically detailed computer model. *IEEE Trans. Biomed. Eng.* 60, 2339–2349. doi: 10.1109/TBME.2013.2256359
- Chen, R., Wen, C., Fu, R., Li, J., and Wu, J. (2018). The effect of complex intramural microstructure caused by structural remodeling on the stability of atrial fibrillation: insights from a three-dimensional multi-layer modeling study. *PLoS One* 13:e0208029. doi: 10.1371/journal.pone.0208029
- Clayton, R. H. (2018). Dispersion of recovery and vulnerability to re-entry in a model of human atrial tissue with simulated diffuse and focal patterns of fibrosis. *Front. Physiol.* 9:1052. doi: 10.3389/fphys.2018.01052
- Costa, C. M., Campos, F. O., Prassl, A. J., Santos, R. W., Sánchez-Quintana, D., Ahammer, H., et al. (2014). An efficient finite element approach for modeling fibrotic clefts in the heart. *IEEE Trans. Biomed. Eng.* 61, 900–910. doi: 10.1109/TBME.2013.2292320
- Dam, R. T. V., Roos, J. P., and Durrer, D. (1972). Electrical activation of ventricles and interventricular septum in hypertrophic obstructive cardiomyopathy. *Heart* 34, 100–112. doi: 10.1136/hrt.34.1.100
- Dhillon, P. S., Gray, R., Kojodjojo, P., Jabr, R., Chowdhury, R., Fry, C. H., et al. (2013). Relationship between gap-junctional conductance and conduction velocity in mammalian myocardium. *Circ. Arrhythm. Electrophysiol.* 6, 1208–1214. doi: 10.1161/CIRCEP.113.000848
- Doshi, A., Walton, R., Krul, S., Groot, J., Bernus, O., Efimov, I., et al. (2015). Feasibility of a semi-automated method for cardiac conduction velocity analysis of high-resolution activation maps. *Comput. Biol. Med.* 65, 177–183. doi: 10.1016/j.combiomed.2015.05.008
- Drakos, S. G., Kfoury, A. G., Hammond, E. H., Reid, B. B., Revelo, M. P., Rasmusson, B. Y., et al. (2010). Impact of mechanical unloading on microvasculature and associated central remodeling features of the failing human heart. *J. Am. Coll. Cardiol.* 56, 382–391. doi: 10.1016/j.jacc.2010.04.019
- Durrer, D., Dam, R. T., Freud, G. E., Janse, M. J., Meijler, F. L., and Arzbaecher, R. C. (1970). Total excitation of the isolated human heart. *Circulation* 41, 899–912. doi: 10.1161/01.cir.41.6.899
- Fast, V. G., and Kléber, A. G. (2021). Role of wavefront curvature in propagation of cardiac impulse. *Cardiovasc. Res.* 33, 258–271. doi: 10.1016/S0008-6363(96)00216-7
- Gerdes, A. M., Kellerman, S. E., Moore, J. A., Muffly, K. E., Clark, L. C., Reaves, P. Y., et al. (1992). Structural remodeling of cardiac myocytes in patients with ischemic cardiomyopathy. *Circulation* 86, 426–430.
- Glashan, C. A., Androulakis, A. F. A., Tao, Q., Glashan, R. N., Wisse, L. J., Ebert, M., et al. (2020). Whole human heart histology to validate electroanatomical voltage mapping in patients with non-ischaemic cardiomyopathy and ventricular tachycardia. *Eur. Heart J.* 39, 2867–2875. doi: 10.1093/eurheartj/ehy168
- Glukhov, A. V., Fedorov, V. V., Kalish, P. W., Ravikumar, V. K., Lou, Q., Janks, D., et al. (2012). Conduction remodeling in human end-stage nonischemic left ventricular cardiomyopathy. *Circulation* 125, 1835–1847. doi: 10.1161/CIRCULATIONAHA.111.047274
- González, A., Schelbert, E. B., Díez, J., and Butler, J. (2018). Myocardial interstitial fibrosis in heart failure: biological and translational perspectives. *J. Am. Coll. Cardiol.* 71, 1696–1706. doi: 10.1016/j.jacc.2018.02.021
- Greiner, J., Sankarankutty, A. C., Seemann, G., Seidel, T., and Sachse, F. B. (2018). Confocal microscopy-based estimation of parameters for computational modeling of electrical conduction in the normal and infarcted heart. *Front. Physiol.* 9:239. doi: 10.3389/fphys.2018.00239
- Halliday, B. P., and Prasad, S. K. (2019). The interstitium in the hypertrophied heart. *JACC Cardiovasc. Imag.* 12(11 Pt 2), 2357–2368. doi: 10.1016/j.jcmg.2019.05.033
- Hinderer, S., and Schenke-Layland, K. (2019). Cardiac fibrosis – A short review of causes and therapeutic strategies. *Adv. Drug Deliv. Rev.* 146, 77–82. doi: 10.1016/j.addr.2019.05.011
- Jellis, C., Martin, J., Narula, J., and Marwick, T. H. (2010). Assessment of nonischemic myocardial fibrosis. *J. Am. Coll. Cardiol.* 56, 89–97. doi: 10.1016/j.jacc.2010.02.047
- Johnston, B. M., and Johnston, P. R. (2020). Approaches for determining cardiac bidomain conductivity values: progress and challenges. *Med. Biol. Eng. Comput.* 58, 2919–2935. doi: 10.1007/s11517-020-02272-z
- Jonas, D. (2008). “Violin Plots for Plotting Multiple Distributions (distributionplot.m)”. 7.6.0.324 ed.: MATLAB Central File Exchange.
- Kawara, T., Derksen, R., Groot, J. R., Coronel, R., Tasseron, S., Linnenbank, A. C., et al. (2001). Activation delay after premature stimulation in chronically diseased human myocardium relates to the architecture of interstitial fibrosis. *Circulation* 104, 3069–3075.
- Khurshid, S., Choi, S. H., Weng, L.-C., Wang, E. Y., Trinquart, L., Benjamin, E. J., et al. (2018). Frequency of cardiac rhythm abnormalities in a half million adults. *Circ. Arrhythm. Electrophysiol.* 11:e006273. doi: 10.1161/CIRCEP.118.006273
- Majumder, R., Nayak, A., and Pandit, R. (2012). Nonequilibrium arrhythmic states and transitions in a mathematical model for diffuse fibrosis in human cardiac tissue. *PLoS One* 7:e45040. doi: 10.1371/journal.pone.0045040
- Nanthakumar, K., Jalife, J., Massé, S., Downar, E., Pop, M., Asta, J., et al. (2007). Optical mapping of Langendorff-perfused human hearts: establishing a model for the study of ventricular fibrillation in humans. *Am. J. Physiol. Heart Circ. Physiol.* 293, H875–H880. doi: 10.1152/ajpheart.01415.2006
- Nezlobinsky, T., Solovyova, O., and Panfilov, A. V. (2020). Anisotropic conduction in the myocardium due to fibrosis: the effect of texture on wave propagation. *Sci. Rep.* 10:764. doi: 10.1038/s41598-020-57449-1
- Nguyen, T. P., Qu, Z., and Weiss, J. N. (2014). Cardiac fibrosis and arrhythmogenesis: the road to repair is paved with perils. *J. Mol. Cell. Cardiol.* 70, 83–91. doi: 10.1016/j.yjmcc.2013.10.018
- Niederer, S. A., Kerfoot, E., Benson, A. P., Bernabeu, M. O., Bernus, O., Bradley, C., et al. (2011). Verification of cardiac tissue electrophysiology simulators using an N-version benchmark. *Philos. Trans. A Math. Phys. Eng. Sci.* 369, 4331–4351. doi: 10.1098/rsta.2011.0139
- Prakosa, A., Arevalo, H. J., Deng, D., Boyle, P. M., Nikolov, P. P., Ashikaga, H., et al. (2018). Personalized virtual-heart technology for guiding the ablation of infarct-related ventricular tachycardia. *Nat. Biomed. Eng.* 2, 732–740. doi: 10.1038/s41551-018-0282-2

- Roberts, S. F., Stinstra, J. G., and Henriquez, C. S. (2008). Effect of nonuniform interstitial space properties on impulse propagation: a discrete multidomain model. *Biophys. J.* 95, 3724–3737. doi: 10.1529/biophysj.108.137349
- Roth, B. J. (1997). Electrical conductivity values used with the bidomain model of cardiac tissue. *IEEE Trans. Biomed. Eng.* 44, 326–328. doi: 10.1109/10.563303
- Schelbert, E. B., Piehler, K. M., Zareba, K. M., Moon, J. C., Ugander, M., Messroghli, D. R., et al. (2015). Myocardial fibrosis quantified by extracellular volume is associated with subsequent hospitalization for heart failure, death, or both across the spectrum of ejection fraction and heart failure stage. *J. Am. Heart Assoc.* 4:e002613. doi: 10.1161/JAHA.115.002613
- Schindelin, J., Arganda-Carreras, I., Frise, E., Kaynig, V., Longair, M., Pietzsch, T., et al. (2012). Fiji: an open-source platform for biological-image analysis. *Nat. Methods* 9, 676–682. doi: 10.1038/nmeth.2019
- Seemann, G., Sachse, F. B., Karl, M., Weiss, D. L., Heuveline, V., and Dössel, O. (2010). “Framework for modular, flexible and efficient solving the cardiac bidomain equations using PETSc,” in *Progress in Industrial Mathematics at ECMI 2008*, eds A. D. Fitt, J. Norbury, H. Ockendon, and E. Wilson (Berlin: Springer), 363–369.
- Seidel, T., Edelmann, J.-C., and Sachse, F. B. (2016). Analyzing remodeling of cardiac tissue: a comprehensive approach based on confocal microscopy and 3D reconstructions. *Ann. Biomed. Eng.* 44, 1436–1448. doi: 10.1007/s10439-015-1465-6
- Sepulveda, N., Roth, B., and Jr, J. W. (1989). Current injection into a two-dimensional anisotropic bidomain. *Biophys. J.* 55, 987–999. doi: 10.1016/S0006-3495(89)82897-8
- Silver, M. A., Pick, R., Brilla, C. G., Jalil, J. E., Janicki, J. S., and Weber, K. T. (1990). Reactive and reparative fibrillar collagen remodelling in the hypertrophied rat left ventricle: two experimental models of myocardial fibrosis. *Cardiovasc. Res.* 24, 741–747. doi: 10.1093/cvr/24.9.741
- Spach, M. S., Heidlage, J. F., Dolber, P. C., and Barr, R. C. (2007). Mechanism of origin of conduction disturbances in aging human atrial bundles: experimental and model study. *Heart Rhythm* 4, 175–185. doi: 10.1016/j.hrthm.2006.10.023
- Spach, M. S., Miller, W. T. III, Geselowitz, D. B., Barr, R. C., Kootsey, J. M., and Johnson, E. A. (1981). The discontinuous nature of propagation in normal canine cardiac muscle. Evidence for recurrent discontinuities of intracellular resistance that affect the membrane currents. *Circ. Res.* 48, 39–54. doi: 10.1161/01.res.48.1.39
- Spach, M., and Boineau, J. (1997). Microfibrosis produces electrical load variations due to loss of side-to-side cell connections: a major mechanism of structural heart disease arrhythmias. *Pacing Clin. Electrophysiol.* 20(2 Pt 2), 397–413. doi: 10.1111/j.1540-8159.1997.tb06199.x
- Swynghedauw, B. (1999). Molecular mechanisms of myocardial remodeling. *Physiol. Rev.* 79, 215–262. doi: 10.1152/physrev.1999.79.1.215
- Taggart, P. S., Sutton, P. M., Opthof, T., Coronel, R., Trimlett, R., Pugsley, W., et al. (2000–2004). Inhomogeneous transmural conduction during early ischaemia in patients with coronary artery disease. *J. Mol. Cell. Cardiol.* 32, 621–630.
- Ten Tusscher and Panfilov, K. H. W. J., and Panfilov, A. V. (2007). Influence of diffuse fibrosis on wave propagation in human ventricular tissue. *EP Europace* 9(suppl\_6), vi38–vi45. doi: 10.1093/europace/eum206
- Tomaselli, G. F., and Zipes, D. P. (2004). What causes sudden death in heart failure? *Circ. Res.* 95, 754–763. doi: 10.1161/01.RES.0000145047.14691.db
- Toyoshima, H., Park, Y.-D., Ishikawa, Y., Nagata, S., Hirata, Y., Sakakibara, H., et al. (1982). Effect of ventricular hypertrophy on conduction velocity of activation front in the ventricular myocardium. *Am. J. Cardiol.* 49, 1938–1945. doi: 10.1016/0002-9149(82)90213-2
- Trayanova, N., Boyle, P., and Nikolov, P. (2018). Personalized imaging and modeling strategies for arrhythmia prevention and therapy. *Curr. Opin. Biomed. Eng.* 5, 21–28. doi: 10.1016/j.cobme.2017.11.007
- Tung, L. (1978). *A Bi-Domain Model for Describing Ischemic Myocardial D-C Potentials*. Ph D. thesis. Cambridge, MA: MIT.
- Tusscher, K. H. W. J., Noble, D., Noble, P. J., and Panfilov, A. V. (2004). A model for human ventricular tissue. *AJP Heart* 286, H1573–H1589. doi: 10.1152/ajpheart.00794.2003
- Valderrabano, M. (2007). Influence of anisotropic conduction properties in the propagation of the cardiac action potential. *Prog. Biophys. Mol. Biol.* 94, 144–168. doi: 10.1016/j.pbiomolbio.2007.03.014
- Wu, T. J., Ong, J. J., Hwang, C., Lee, J. J., Fishbein, M. C., Czer, L., et al. (1998). Characteristics of wave fronts during ventricular fibrillation in human hearts with dilated cardiomyopathy: role of increased fibrosis in the generation of reentry. *J. Am. Coll. Cardiol.* 32, 187–196. doi: 10.1016/S0735-1097(98)00184-3
- Wuelfers, E. M., Greiner, J., Giese, M., Madl, J., Kroll, J., Stiller, B., et al. (2021). Quantitative collagen assessment in right ventricular myectomies from patients with tetralogy of Fallot. *Europace* 23(Suppl. 1), i38–i47. doi: 10.1093/europace/eaab389
- Yue, A. M., Franz, M. R., Roberts, P. R., and Morgan, J. M. (2005). Global endocardial electrical restitution in human right and left ventricles determined by noncontact mapping. *J. Am. Coll. Cardiol.* 46, 1067–1075. doi: 10.1016/j.jacc.2005.05.074

**Conflict of Interest:** The authors declare that the research was conducted in the absence of any commercial or financial relationships that could be construed as a potential conflict of interest.

**Publisher's Note:** All claims expressed in this article are solely those of the authors and do not necessarily represent those of their affiliated organizations, or those of the publisher, the editors and the reviewers. Any product that may be evaluated in this article, or claim that may be made by its manufacturer, is not guaranteed or endorsed by the publisher.

Copyright © 2021 Sankarankutty, Greiner, Bragard, Visker, Shankar, Kyriakopoulos, Drakos and Sachse. This is an open-access article distributed under the terms of the Creative Commons Attribution License (CC BY). The use, distribution or reproduction in other forums is permitted, provided the original author(s) and the copyright owner(s) are credited and that the original publication in this journal is cited, in accordance with accepted academic practice. No use, distribution or reproduction is permitted which does not comply with these terms.



# Consistency in Geometry Among Coronary Atherosclerotic Plaques Extracted From Computed Tomography Angiography

Haipeng Liu<sup>1,2†</sup>, Aleksandra Wingert<sup>2†</sup>, Xinhong Wang<sup>3</sup>, Jucheng Zhang<sup>4</sup>, Jianzhong Sun<sup>3</sup>, Fei Chen<sup>5</sup>, Syed Ghufuran Khalid<sup>1,6</sup>, Yinglan Gong<sup>7</sup>, Ling Xia<sup>7</sup>, Jun Jiang<sup>8\*</sup>, Jian'an Wang<sup>8</sup> and Dingchang Zheng<sup>1\*</sup>

<sup>1</sup> Research Centre for Intelligent Healthcare, Coventry University, Coventry, United Kingdom, <sup>2</sup> Faculty of Health, Education, Medicine, and Social Care, Anglia Ruskin University, Chelmsford, United Kingdom, <sup>3</sup> Department of Radiology, The Second Affiliated Hospital, School of Medicine, Zhejiang University, Hangzhou, China, <sup>4</sup> Department of Clinical Engineering, School of Medicine, The Second Affiliated Hospital, Zhejiang University, Hangzhou, China, <sup>5</sup> Department of Electrical and Electronic Engineering, Southern University of Science and Technology, Shenzhen, China, <sup>6</sup> Department of Medical Physics, Guy's and St Thomas' NHS Foundation Trust, London, United Kingdom, <sup>7</sup> Key Laboratory for Biomedical Engineering of Ministry of Education, Institute of Biomedical Engineering, Zhejiang University, Hangzhou, China, <sup>8</sup> Department of Cardiology, School of Medicine, The Second Affiliated Hospital, Zhejiang University, Hangzhou, China

## OPEN ACCESS

### Edited by:

Carlos D. Maciel,  
University of São Paulo, Brazil

### Reviewed by:

Hao Gao,  
University of Glasgow,  
United Kingdom  
Luiz Otavio Murta Jr,  
University of São Paulo, Brazil

### \*Correspondence:

Jun Jiang  
jiang-jun@zju.edu.cn  
Dingchang Zheng  
dingchang.zheng@coventry.ac.uk

†These authors share first authorship

### Specialty section:

This article was submitted to  
Computational Physiology and  
Medicine,  
a section of the journal  
Frontiers in Physiology

Received: 26 May 2021

Accepted: 03 September 2021

Published: 12 October 2021

### Citation:

Liu H, Wingert A, Wang X, Zhang J, Sun J, Chen F, Khalid SG, Gong Y, Xia L, Jiang J, Wang J and Zheng D (2021) Consistency in Geometry Among Coronary Atherosclerotic Plaques Extracted From Computed Tomography Angiography. *Front. Physiol.* 12:715265. doi: 10.3389/fphys.2021.715265

**Background:** The three-dimensional (3D) geometry of coronary atherosclerotic plaques is associated with plaque growth and the occurrence of coronary artery disease. However, there is a lack of studies on the 3D geometric properties of coronary plaques. We aim to investigate if coronary plaques of different sizes are consistent in geometric properties.

**Methods:** Nineteen cases with symptomatic stenosis caused by atherosclerotic plaques in the left coronary artery were included. Based on attenuation values on computed tomography angiography images, coronary atherosclerotic plaques and calcifications were identified, 3D reconstructed, and manually revised. Multidimensional geometric parameters were measured on the 3D models of plaques and calcifications. Linear and non-linear (i.e., power function) fittings were used to investigate the relationship between multidimensional geometric parameters (length, surface area, volume, etc.). Pearson correlation coefficient ( $r$ ),  $R$ -squared, and  $p$ -values were used to evaluate the significance of the relationship. The analysis was performed based on cases and plaques, respectively. Significant linear relationship was defined as  $R$ -squared  $> 0.25$  and  $p < 0.05$ .

**Results:** In total, 49 atherosclerotic plaques and 56 calcifications were extracted. In the case-based analysis, significant linear relationships were found between number of plaques and number of calcifications ( $r = 0.650$ ,  $p = 0.003$ ) as well as total volume of plaques ( $r = 0.538$ ,  $p = 0.018$ ), between number of calcifications and total volume of plaques ( $r = 0.703$ ,  $p = 0.001$ ) as well as total volume of calcification ( $r = 0.646$ ,  $p = 0.003$ ), and between the total volumes of plaques and calcifications ( $r = 0.872$ ,  $p < 0.001$ ). In plaque-based analysis, the power function showed higher  $R$ -squared values than the linear function in fitting the relationships of multidimensional geometric



parameters. Two presumptions of plaque geometry in different growth stages were proposed with simplified geometric models developed. In the proposed models, the exponents in the power functions of geometric parameters were in accordance with the fitted values.

**Conclusion:** In patients with coronary artery disease, coronary plaques and calcifications are positively related in number and volume. Different coronary plaques are consistent in the relationship between geometry parameters in different dimensions.

**Keywords:** coronary artery disease, atherosclerotic plaques, computed tomography (CT), three-dimensional reconstruction, plaque morphology

## INTRODUCTION

Coronary artery disease is a cardiovascular disease that has been the leading cause of death globally (Malakar et al., 2019). The formation of atherosclerotic plaques in the coronary arteries plays a key role in the development of coronary artery disease (CAD). With the growth of an atherosclerotic plaque, the stenosis in the affected coronary artery reduces the myocardial blood flow and oxygen supply. Evidence has shown that the geometry of a plaque, which determines the severity of arterial stenosis, is related to the risks of clinical events, including myocardial infarction in patients with CAD (Choi et al., 2015; Lee et al., 2019a). Further investigation of coronary plaque geometry is, therefore, recognised as an important pathway toward understanding the pathophysiology and improving the diagnosis and treatment of CAD (Ratiu et al., 2018).

Currently, computerised tomography (CT) scan is the most commonly used medical imaging technique in the diagnosis of CAD (Gaur et al., 2016). The coronary computed tomography angiography (CCTA) images have a high spatial resolution to reflect the geometry and morphology of coronary plaques (Stefanini Giulio and Windecker, 2015). CCTA can achieve a higher resolution than cardiac magnetic resonance imaging (MRI) (Liu et al., 2021). The severity of luminal stenosis evaluated by CCTA was in similar accuracy as that obtained from intravascular ultrasound (IVUS) (Lee et al., 2019b). The coronary angiography (CAG) is also widely used in the diagnosis of CAD. Compared with MRI, IVUS, and CAG, CCTA is low-cost, non-invasive, and safe to use on patients with implants (Wang et al., 2018). CCTA can visualise different types of plaque composition. Non-calcified, partially calcified, and calcified plaques could be extracted separately based on their attenuation values (Daghem et al., 2020). Therefore, CCTA has been widely applied in the analysis of coronary plaque geometry (Rinehart et al., 2011; Ratiu et al., 2019).

Using the three-dimensional reconstruction of plaque geometry from CCTA images, many geometric parameters can be accurately estimated, including the burden (i.e., the severity of stenosis), size, diameter, and composition of coronary artery plaques (Liu et al., 2021). The geometry of a plaque can influence the hemodynamic parameters, such as wall shear stress, which, in turn, influence the evolution of plaque geometry (Yamamoto et al., 2017; Arzani, 2020; Pleouras et al., 2020a). For

example, the clinical observation and computational simulation have disclosed that plaques grow faster in the downstream areas than the upstream areas (Arzani, 2020). Considering the haemodynamics-driven plaque growth, in this study, we hypothesize that different coronary plaques may be consistent in geometry.

The geometric consistency among different objects can be investigated using the relationships between multidimensional geometric parameters (i.e., parameters defined in different geometric dimensions). For example, sphericity has been proposed to evaluate the geometric consistency between different objects. It was defined as the ratio of the surface area of a sphere, which has the same volume as the given particle to the surface area of that particle (Li et al., 2012). The surface-area-volume ratio has been applied in investigating the taxonomic groups of insects (Kühnel et al., 2017), as well as the relationship between human brain size and cortex folding (Toro et al., 2008). However, despite the fact the many geometric parameters have been applied in the evaluation of coronary plaques (Liu et al., 2021), as far as we know, the geometric consistency of coronary plaques has not been comprehensively investigated using multidimensional geometric parameters based on patient-specific CCTA imaging data.

In order to comprehensively understand coronary plaque geometry and its evolution, we aim to investigate the relationship between different multidimensional geometric parameters of coronary plaques reconstructed from CCTA images. Considering the geometric and hemodynamic differences between left and right coronary arteries, we focus on the plaques in left coronary arteries in this pilot study.

## METHODS

### Patients and CCTA Imaging Protocol

In this retrospective study, the CCTA imaging data were collected from 25 patients with CAD in the Second Affiliated Hospital of Zhejiang University in China from 2015 to 2016 with approval from the local ethics committee for sharing and analysing retrospective anonymised patient data with informed consent form waived. Details of the CCTA scan protocol are listed in **Table 1**. Each scan was visually examined for visible coronary stenosis, culprit lesions, and calcifications. The resultant datasets

**TABLE 1** | CCTA data acquisition.

Parameter name	Name/qty
Scanner type	Somatom definition flash
Number of slices	128
Patient's position	Supine
Patient's heart rate (beats per minute, mean $\pm$ SD)	70.125 $\pm$ 14.047
Contrast type	Ultravist 370
Any beta-blockers?	No
Any nitro-glycerine?	Yes- one subject, the rest- no
Time of the scan (minutes, mean $\pm$ SD)	2.805 $\pm$ 2.464

**TABLE 2** | Characteristics of patients.

Patients, <i>n</i>	19
Female, <i>n</i>	6
Age (years, mean $\pm$ SD)	63.421 $\pm$ 9.532
Total number of plaques, <i>n</i>	49
Number of plaques per case (mean $\pm$ SD)	2.579 $\pm$ 1.387
Total number of calcifications, <i>n</i>	56
Number of calcifications per case (mean $\pm$ SD)	3.158 $\pm$ 1.803
Mean calcified plaque volume (per case, $mm^3$ , mean $\pm$ SD)	24.137 $\pm$ 24.156
Mean whole plaque volume (per case, $mm^3$ , mean $\pm$ SD)	151.084 $\pm$ 115.431
Mean plaque surface area (per case, $mm^2$ , mean $\pm$ SD)	313.995 $\pm$ 186.056

of systolic and diastolic scans were compared regarding the quality of images, with the better one selected for analysis.

In six patients, there was no observable plaque or significant stenosis ( $>50\%$  in diameter) in left coronary artery. In total, 19 patients (13 males, 6 females, mean  $\pm$  SD of age: 63.4  $\pm$  9.5 years) were finally included for analysis, as listed in **Table 2**. The observer was blinded for the case diagnosis. The quantity, location, and type of atherosclerotic plaques have been confirmed by a radiologist and a cardiologist.

### 3D Reconstruction of Coronary Arteries

The 3D geometry of coronary arteries and plaques was reconstructed from the CCTA images using the software MIMICS 20.0 (Materialise N.V., Belgium). The reconstruction method was semiautomatic, using the Coronary Segmentation Tool of Mimics Medical Suite. Firstly, the position of the aorta was marked. Then, with start and end points marked on the CCTA image dataset, an arterial segment can be automatically reconstructed with the result saved in an independent set (a "mask" in MIMICS). For the left coronary artery tree, artery segments were extracted from the left main coronary artery (LM) to major branches, including the left anterior descending artery (LAD) and left circumflex artery (LCX), and, finally, the distal branches. The small branches (diameter  $< 1$  mm, or blurred structure) were trimmed off. The left coronary artery tree was

derived by connecting artery segments using the union operation of different sets.

### Extraction of Coronary Atherosclerotic Plaques: A Two-Step Approach

The 3D reconstruction of coronary plaques was based on a semiautomatic two-step approach. It is difficult to distinguish between fibrotic, fibro-fatty, and fatty atherosclerotic lesions. Therefore, in this study, the plaque components were categorised as calcified (calcification) and non-calcified. Firstly, based on the position of plaque on the two-dimensional (2D) CCTA images, the spatial ranges of plaque were set in three directions (sagittal, coronal, and transverse). In the 3D space defined by the ranges, the plaque was automatically extracted using thresholds of CT attenuation value (in Hounsfield units, or HU). Due to the difference in plaque composition, the CT attenuation value varies among different scans. Therefore, the thresholds were set patient specifically. Low attenuation values (0–150 HU) were used to identify non-calcified plaques, whereas high attenuation values ( $>150$ –1,334 HU) were used for calcified components. Firstly, the calcifications were automatically extracted (**Figure 1**). The demarcation between non-calcified plaque components, vessel lumen, and other tissues was inaccurate due to the varying local attenuation. Therefore, a mask was developed by using a wide HU range for all the non-calcified components, including the vessel wall. By using union Boolean operation, an outer boundary was derived that wraps the vessel lumen and the whole plaque (the cyan part in **Figure 2**).

In the second step, the plaque geometry was further modified. Considering the blooming artefact caused by calcification, the surrounding non-calcified components have higher HU values. The boundaries between non-calcified components and calcification or artery lumen were checked and adjusted manually. The areas opposite to the calcification were also reviewed to add the non-calcified plaque components that were not detected by the threshold used in the first step due to the effect of surrounding tissues (the magenta part in **Figure 2**).

### Measurement of Multidimensional Geometric Parameters

The measurement of multidimensional geometric parameters in different dimensions was performed using the Materialise 3-Matic software (Materialise N.V., Belgium) on the whole plaques and calcifications, respectively.

For each plaque and calcification, firstly, the volume and the surface area were measured automatically. Secondly, the length, surface distance, cross-sectional area, and diameter were measured manually. The length of a plaque or calcification was defined as the longest straight-line distance between its proximal and distal ends. The surface distance was defined as the length of the shortest path on the surface between the proximal and distal ends. For the whole plaque, the cross-section area was measured on the cross-section perpendicular to the local centerline of the arterial segment with the maximal area (**Figure 3**). The cross-section diameter was measured as the longest distance on the cross-section area. Compared with the plaques, calcifications had

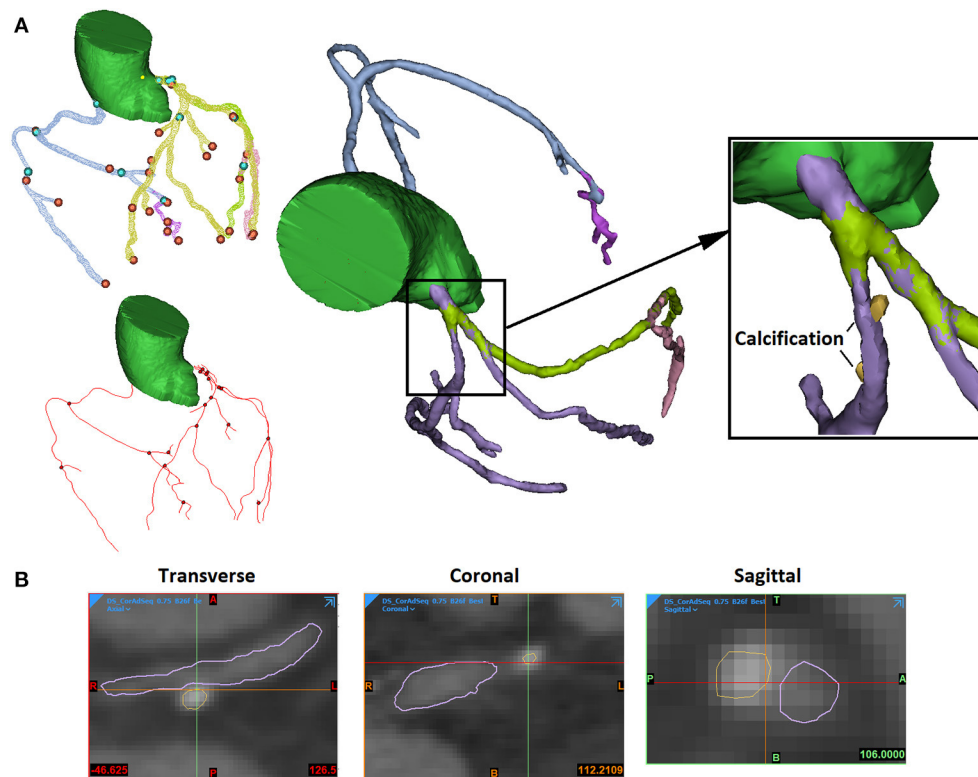


**FIGURE 1 |** The extraction of arterial lumen and calcification. **(A)** The 3D view. The blue and orange points present the start and the end points of extracted artery segments. The red lines and black points present the centerlines of artery segments and connecting points (left). The arterial segments were extracted in different masks (in different colours) and connected (middle). The calcifications were extracted independently (right). **(B)** The 2D views of stenosed artery in three directions (sagittal, coronal, and transverse).

much smaller size, rounder shape, and were positioned in variable directions in spatial distribution. Therefore, the cross-section area and the diameter were not measured on calcifications.

## Statistical Analysis

The statistical analysis was performed using SPSS 24.0 software (IBM SPSS Inc., Chicago, IL, USA) based on each case, plaque, and calcification, respectively.

In the case-based analysis, the sum of volumes of different plaques or calcifications was calculated for each subject. The relationships among the numbers and volumes of plaques and calcifications were investigated using simple linear regression with Pearson correlation coefficient ( $r$ ), coefficient of determination ( $R$ -squared), and  $p$ -value calculated. A significant linear relationship was defined as  $r > 0.5$  ( $R$ -squared  $> 0.25$ ) and  $p < 0.05$ . A strong linear relationship was defined as  $r > 0.8$  ( $R$ -squared  $> 0.64$ ) and  $p < 0.05$ .

We investigated the multidimensional geometric parameters in the plaque- and calcification-based analyses. Each pair of parameters was in different dimensions except for length and surface distance which can reflect the smoothness of the plaque surface. In the plaque-based analysis, simple linear regression analysis was performed between different geometric parameters (i.e., volume, surface area, length, surface distance, cross-section

area, and cross-section diameter) of plaques. Similarly, in the calcification-based analysis, simple linear regression analysis was performed on the geometric parameters measured from each calcification (i.e., volume, surface area, length, and surface distance). If any significant linear relationship was found between two parameters of different dimensions (e.g., surface area and volume), the non-linear regression analysis based on power function was performed. The results of linear and non-linear regressions were compared using their  $R$ -squared values. Finally, to further investigate the relationship between plaques and calcifications in volume, simple linear regression analysis was performed in the plaque-based analysis between the plaque volume and the total volume of calcifications in the plaque.

## Geometric Modelling

Based on the analysis of multidimensional parameters (see Results), we proposed two models to describe the geometry of small (patchy) and big (circular) coronary plaques. All the plaques were simplified as a part of a cylindrical shell with uniform thickness (**Figure 6**). To evaluate if the models can accurately reflect the plaque geometry, the ratio between plaque length, surface area, and volume was calculated and compared with the obtained measurement results.

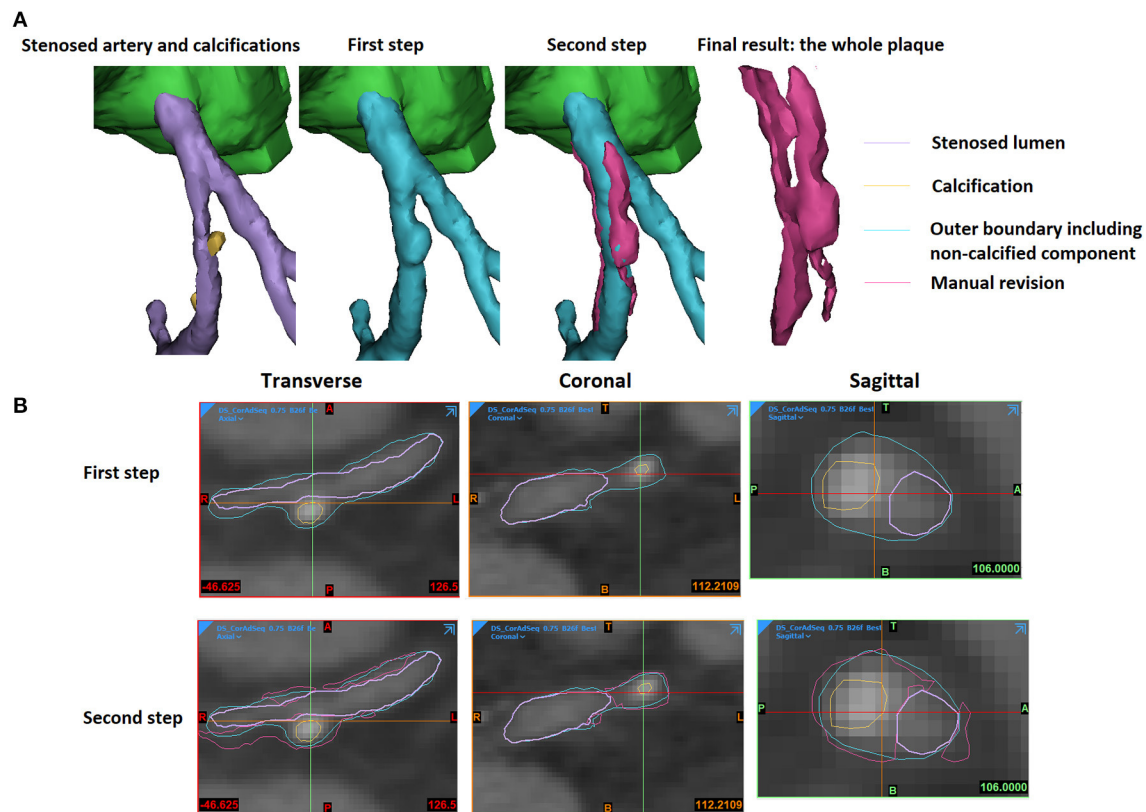


**FIGURE 2 |** The extraction of an atherosclerotic plaque. **(A)** The 3D view. **(B)** The 2D views. The stenosed artery lumen, calcification, outer boundary that wraps vessel lumen and non-calcified components, as well as the manually revised results were shown in purple, yellow, cyan, and magenta colours in the 3D and 2D views.

## RESULTS

### Summary

In the 19 subjects, in total, 49 atherosclerotic plaques and 56 calcifications were extracted from the left coronary arteries. In each case, the numbers of plaques and calcifications were (mean  $\pm$  SD)  $2.579 \pm 1.387$  and  $3.158 \pm 1.803$ ; the mean calcification volume and mean whole plaque volume were  $24.137 \pm 24.156 \text{ mm}^3$  and  $151.084 \pm 115.431 \text{ mm}^3$ , respectively. The plaques located in all the major branches of left coronary artery tree: LAD (in 18 subjects), LCX (in 7 subjects), LM (in 5 subjects), as well as the diagonal (in 4 subjects), and marginal (in 3 subjects) branches. The CA scores ranged from 1.2 to 856.4. Therefore, the plaques in this study were diverse in location and composition.

### Case-Based Analysis

The results of case-based analysis showed a strong relationship between the plaques and calcifications in number and volume. Significant linear relationships were observed between the number of plaques and the number of calcifications ( $r = 0.650$ ,  $p = 0.003$ ), between the number of plaques and the volume of plaques ( $r = 0.538$ ,  $p = 0.018$ ), between the number of calcifications and the volume of plaques ( $r = 0.703$ ,  $p = 0.001$ ), and between the number of calcifications and the volume of calcifications ( $r = 0.646$ ,  $p = 0.003$ ). The volume of plaques and

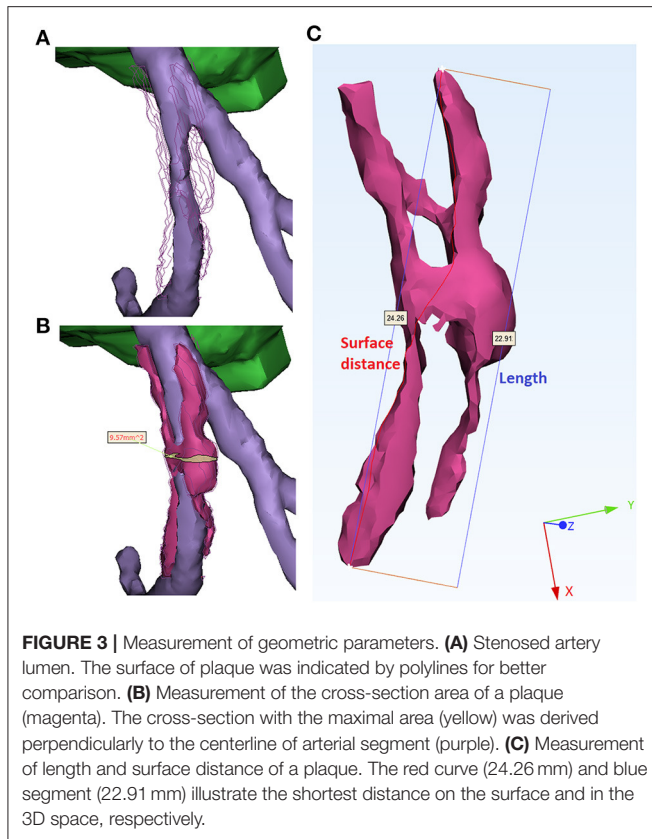
volume of calcifications showed a strong linear relationship ( $r = 0.872$ ,  $r < 0.001$ ) (Table 3).

### Plaque-Based and Calcification-Based Analysis: Linear and Non-linear Regressions

For the plaques, a significant linear relationship was found between the volume and the cross-section area ( $r = 0.506$ ,  $p < 0.001$ ). Strong linear relationships were found between the volume and the surface area ( $r = 0.944$ ,  $p < 0.001$ ), volume and length ( $r = 0.861$ ,  $p < 0.001$ ), volume and surface distance ( $r = 0.843$ ,  $p < 0.001$ ), surface area and length ( $r = 0.925$ ,  $p < 0.001$ ), surface area and surface distance ( $r = 0.908$ ,  $p < 0.001$ ), length and surface distance ( $r = 0.997$ ,  $p < 0.001$ ), as well as cross-section diameter and cross-section area ( $r = 0.866$ ,  $p < 0.001$ ). There was a significant linear relationship between the plaque volume and the total volume of calcifications in each plaque ( $r = 0.754$ ,  $p < 0.001$ ).

In Figure 4, the non-linear regression shows a higher R-squared value than linear regression in most relationships except between the volume and the cross-section area where the relationship is just above the significant threshold (R-squared: 0.256 and 0.236 for linear and non-linear regressions), as well as between the length and the surface distance where the values





are very approximate ( $R$ -squared: 0.993 and 0.990 for linear and nonlinear regressions).

In the calcification-based analysis, strong linear relationships were found between volume and length ( $r = 0.895$ ,  $p < 0.001$ ), volume and surface distance ( $r = 0.850$ ,  $p < 0.001$ ), as well as length and surface distance ( $r = 0.888$ ,  $p < 0.001$ ). In **Figure 5**, the linear regression always shows a higher  $R$ -squared value than the non-linear regression. All the relationships in **Figure 5** are weaker than the corresponding ones in **Figure 4**.

## Geometric Modelling of Coronary Plaques: Two Presumptions

### Presumption 1: Cylindrical Ring Shape of Fully Developed Plaques

It can be observed in **Figure 6** that the fully developed plaques are nearly symmetric circumferentially but asymmetric along the artery wall. In a large-scale study of coronary plaque geometry using intravascular ultrasound, 50.2% were concentric in 1,441 cross-sections (Komiya et al., 2016). Longitudinally, atherosclerotic plaques often grow faster along one side of the artery wall due to the difference in hemodynamic effect (Gnasso et al., 1997; Samady et al., 2011). Therefore, we presume that a fully developed plaque has a nearly cylindrical ring shape in the middle segment and extends slantly toward the proximal and distal arterial segments. Accordingly, we developed a model of cylindrical ring shape with slanted cross-sections at both ends (Model 1 in **Figure 6**). The ratio between the surface area ( $S$ ) and

**TABLE 3 |** Linear regression results of case-based analysis.

	Number of plaques	Number of calcifications	Total volume of plaques	Total volume of calcification
Number of plaques		$r = 0.650$ , $p = 0.003^*$	$r = 0.538$ , $p = 0.018^*$	$r = 0.411$ , $p = 0.080$
Number of calcifications			$r = 0.703$ , $p = 0.001^*$	$r = 0.646$ , $p = 0.003^*$
Total volume of plaques				$r = 0.872$ , $p < 0.001^{**}$

\*marks significant linear relationship ( $R$ -squared  $> 0.25$  (i.e.,  $r > 0.5$ ) and  $p < 0.05$ ).

\*\*marks strong linear relationship ( $R$ -squared  $> 0.64$  (i.e.,  $r > 0.8$ ) and  $p < 0.05$ ).

the volume ( $V$ ) can be derived as

$$\frac{S}{V} = \frac{2}{R-r} + \frac{1}{h} \left( \frac{1}{\cos \theta_1} + \frac{1}{\cos \theta_2} \right) \quad (1)$$

where  $R$ ,  $r$ , and  $h$  are the external radius, internal radius, and height on the centerline.  $\theta_1$  and  $\theta_2$  describe the dihedral angles between the surface planes and the perpendicular cross-section plane at both ends. When the size of plaque increases, the value of  $\frac{S}{V}$  decreases:  $\frac{S}{V} = 0$ , which is in accordance with the observation in **Figure 4A**. The exponent in the power function relationship between  $S$  and  $V$  can be derived as

$$\frac{\ln S}{\ln V} = \frac{\ln \pi + \ln(R+r) + \ln \left[ 2h + (R-r) \left( \frac{1}{\cos \theta_1} + \frac{1}{\cos \theta_2} \right) \right]}{\ln \pi + \ln h + \ln(R+r) + \ln(R-r)} \quad (2)$$

which can be estimated based on the following two hypotheses on plaque geometry evolution:

**Hypothesis 1.1:** during the growth of a plaque, the values of  $R$ ,  $r$ , and  $h$  are linearly related while  $\theta_1$  and  $\theta_2$  are independent. Under this hypothesis, it can be derived that

$$\lim_{V \rightarrow \infty} \frac{\ln S}{\ln V} = \frac{2}{3} \quad (3)$$

**Hypothesis 1.2:** with the growth of plaque, the atherosclerosis extends asymmetrically on the artery wall toward the proximal and distal arterial segments, where the values of  $R$ ,  $r$ ,  $\frac{1}{\cos \theta_1}$ ,  $\frac{1}{\cos \theta_2}$ , and  $h$  are linearly related. It can be derived that

$$\lim_{V \rightarrow \infty} \frac{\ln S}{\ln V} = 1 \quad (4)$$

In **Figure 4A**, the exponent in the power function fitting is 0.741, which is between  $\frac{2}{3}$  and 1. Therefore, this geometric model reflects the relationship between the surface area and the volume in real coronary plaques.

To investigate the relationship between plaque length and volume, the length was calculated under two hypotheses:

**Hypothesis 1.3:** the plaque length ( $L$ ) locates along the external wall

$$L = h + R(\tan \theta_1 + \tan \theta_2) \quad (5)$$

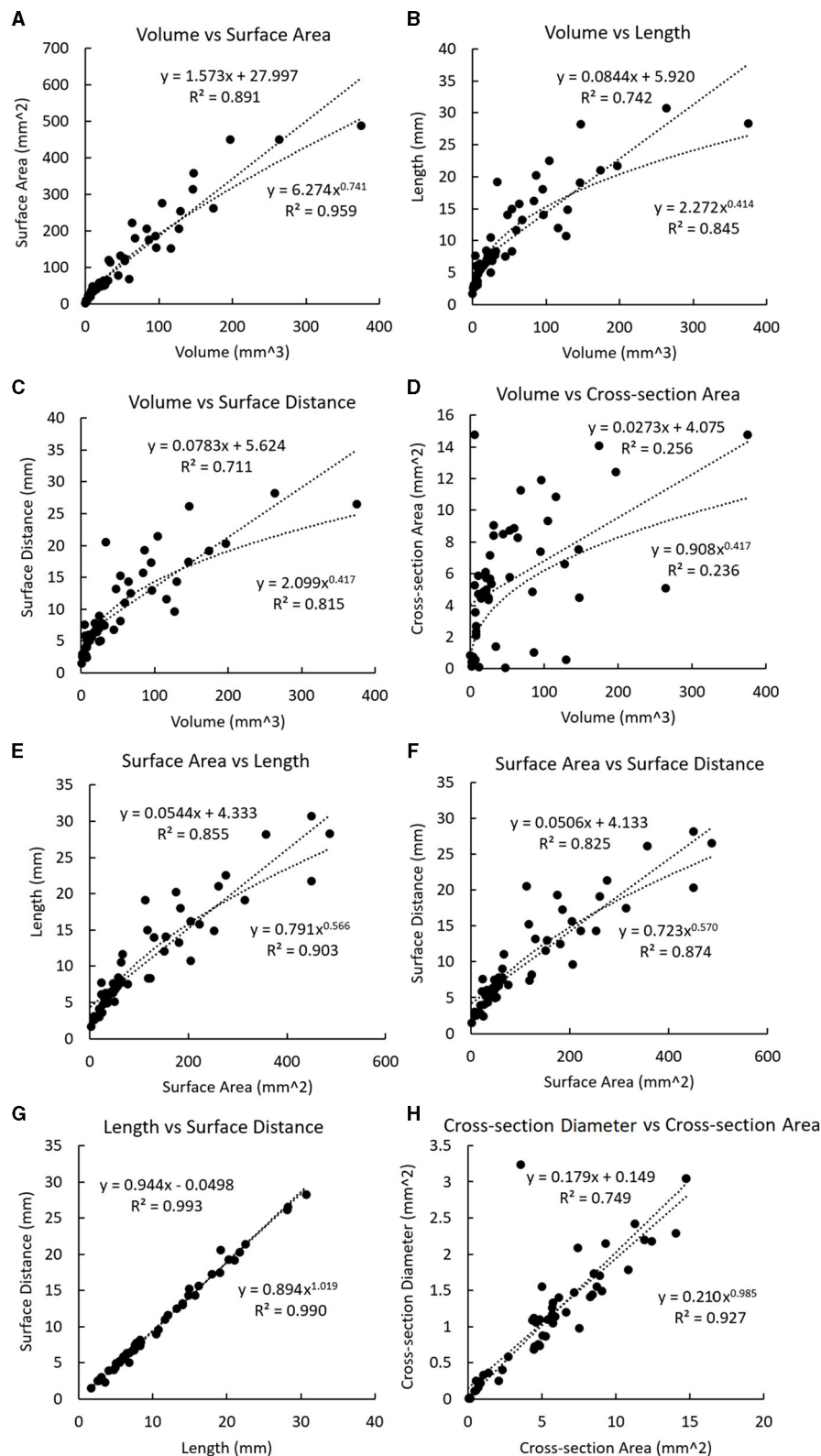


**FIGURE 4 |** Linear and non-linear regression fittings on the geometric parameters of plaques. The regression line and curve are shown in dotted lines. **(A)** The volume and the surface area. **(B)** Volume and length. **(C)** Volume and surface distance. **(D)** Volume and the cross-section area. **(E)** The surface area and length. **(F)** The surface area and surface distance. **(G)** Length and surface distance. **(H)** Cross-section diameter and the cross-section area.

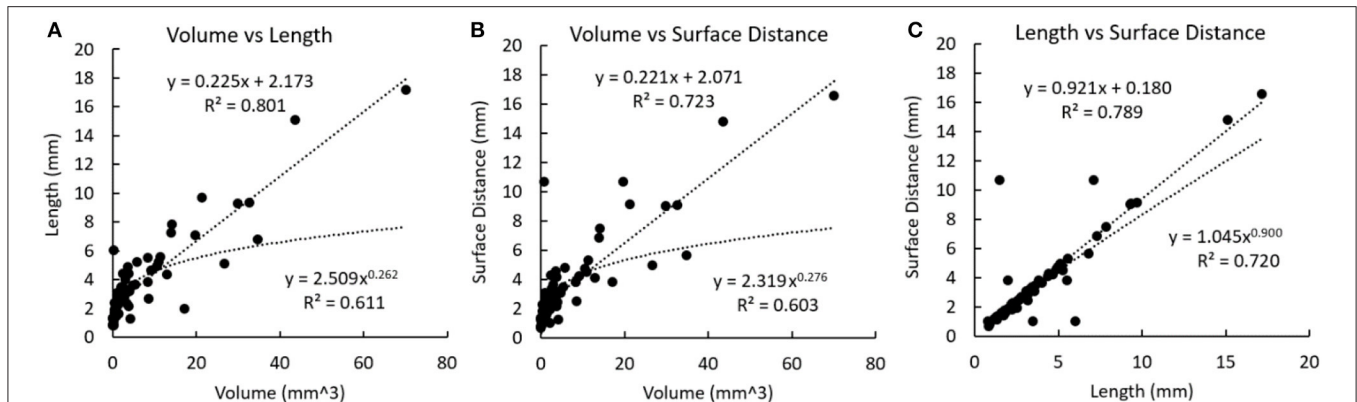


**FIGURE 5** | Linear and non-linear regression fittings on the geometric parameters of calcifications. The regression line and curve are shown in dotted lines. **(A)** Volume and length. **(B)** Volume and surface distance. **(C)** Length and surface distance.

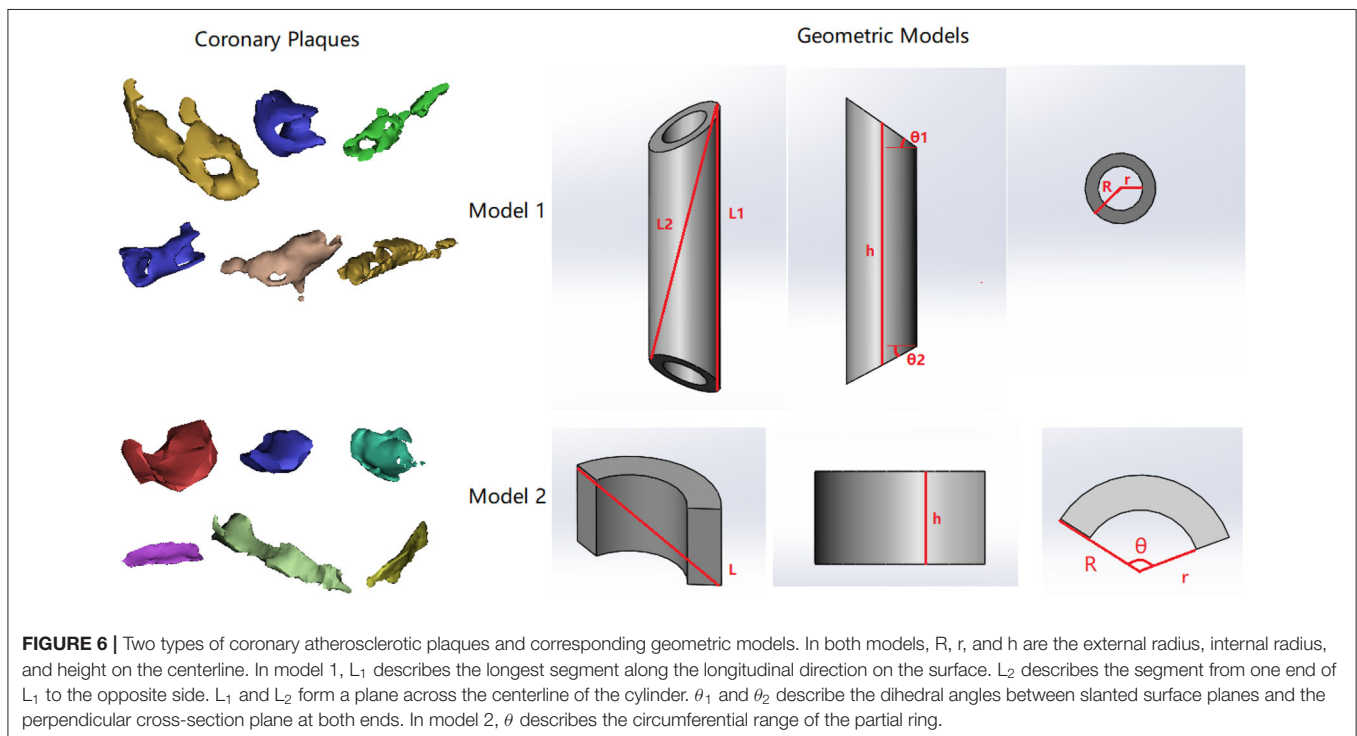


**FIGURE 6** | Two types of coronary atherosclerotic plaques and corresponding geometric models. In both models,  $R$ ,  $r$ , and  $h$  are the external radius, internal radius, and height on the centerline. In model 1,  $L_1$  describes the longest segment along the longitudinal direction on the surface.  $L_2$  describes the segment from one end of  $L_1$  to the opposite side.  $L_1$  and  $L_2$  form a plane across the centerline of the cylinder.  $\theta_1$  and  $\theta_2$  describe the dihedral angles between slanted surface planes and the perpendicular cross-section plane at both ends. In model 2,  $\theta$  describes the circumferential range of the partial ring.

**Hypothesis 1.4:** the plaque length ( $L$ ) goes across the geometry

$$L = \sqrt{(2R)^2 + (h + R \tan \theta_1 - R \tan \theta_2)^2} \quad (6)$$

In both cases, it can be derived that  $\frac{\ln L}{\ln V} \approx \frac{1}{3}$  under hypothesis 1.1, and  $\frac{\ln L}{\ln V} \approx \frac{2}{3}$  under hypothesis 1.2. In **Figure 4B**, the exponent in the power function fitting is 0.414, which is between  $\frac{1}{3}$  and  $\frac{2}{3}$ . Therefore, this model is in accordance with the geometric properties of real coronary plaques.

### Presumption 2: Partial Cylindrical Ring Shape of Early-Stage Plaques

In the early stage of plaque formation, the vessel wall thickening often emerges from one side of coronary artery and extends both longitudinally and circumferentially. Therefore, we proposed a model that describes the geometry of an early-stage plaque that covers circumstantially a part of the artery wall (Model 2 in **Figure 6**, in which  $\theta$  describes the circular range of the plaque and  $\theta < \pi$ ). The ratio between the surface area and the volume can be derived as:

$$\frac{S}{V} = 2 \left[ \frac{2}{\theta(R+r)} + \frac{1}{h} + \frac{1}{R-r} \right] \quad (7)$$

When the size of a plaque increases, the value of  $\frac{S}{V}$  decreases:  $\lim_{V \rightarrow \infty} \frac{S}{V} = 0$ , which is in accordance with the observation in **Figure 4A**. The exponent in the power function relationship between  $S$  and  $V$  can be calculated as

$$\frac{\ln S}{\ln V} = \frac{\ln [2h(R-r) + \theta(R+h)(R-r+h)]}{\ln \theta + \ln h + \ln(R+r) + \ln(R-r) - \ln 2} \quad (8)$$

We investigated the plaque geometry under the following hypothesis:

**Hypothesis 2.1:** The growth of atherosclerotic plaque extends in axial and circumferential directions, where  $h$ ,  $R$ , and  $r$  are linearly related, while  $\theta$  increases toward  $2\pi$ .

Thus, the following relationships could be derived:

$$\lim_{V \rightarrow \infty} \frac{\ln S}{\ln V} = \frac{2}{3} \quad (9)$$

$$L = \sqrt{h^2 + \left(2R \sin \frac{\theta}{2}\right)^2} \quad (10)$$

$$\frac{L}{V} = \frac{2\sqrt{h^2 + \left(2R \sin \frac{\theta}{2}\right)^2}}{\theta h (R^2 - r^2)} \quad (11)$$

$$\frac{\ln L}{\ln V} = \frac{\ln 2 + 0.5 \ln \left(h^2 + \left(2R \sin \frac{\theta}{2}\right)^2\right)}{\ln \theta + \ln h + \ln(R+r) + \ln(R-r)} \quad (12)$$

$$\lim_{V \rightarrow \infty} \frac{\ln L}{\ln V} = \frac{1}{3} \quad (13)$$

In **Figure 4**, the values of exponents for  $\lim_{V \rightarrow \infty} \frac{\ln S}{\ln V}$  and  $\lim_{V \rightarrow \infty} \frac{\ln L}{\ln V}$  are 0.741 and 0.414, which are in accordance with the values derived from the model (difference  $< 0.08$  and  $< 0.09$  for  $\frac{S}{V}$  and  $\frac{L}{V}$ , respectively). Therefore, this model is also in accordance with the geometric properties of real coronary plaques.

## DISCUSSION

The results disclosed the geometric consistency among coronary atherosclerotic plaques of different sizes. Based on the results, we proposed two simplified geometric models of coronary plaques whose geometric properties were in accordance with the measurement results. As far as we know, this is the first study on the geometry properties of coronary plaques in different dimensions.

In this pilot study, the coronary plaques were extracted from CCTA images and manually revised. As aforementioned, some invasive imaging methods, such as IVUS and optical coherence tomography, can achieve a high accuracy in detecting the geometry and morphology of atherosclerotic plaques while CCTA is non-invasive and widely used in the diagnosis of CAD. Additionally, CCTA has high reproducibility (Symons et al., 2016) and reliability in evaluating coronary plaques (Dweck et al., 2016). However, automatic extraction of coronary plaques from CCTA images could cause under- or over-estimation of plaque size, especially for calcified plaques where blooming artefact

could increase the attenuation value of adjacent tissues, leading to the inaccurate estimation of plaque volume (Liu et al., 2021). Additionally, the automatic separation of a non-calcified (lipid or fibrotic) plaque from surrounding tissues could be difficult due to the similarity in attenuation value (Liu et al., 2019). Therefore, for CCTA images, the manual revision could reduce the inaccuracy in plaque geometry. These results were also assessed and corrected by experienced radiologists to provide a basis for reliable geometric analysis.

In some studies on the computational simulation of CAD, simplified 2D models of different atherosclerotic plaques have been developed, including carotid plaque models (Yuan et al., 2015; Shahidian and Hassankiadeh, 2017) and idealised plaque models (Shimizu and Ohta, 2015). On the cross-section plane perpendicular to the centerline of a local arterial segment, the circular, elliptical, crescent, and irregular shapes have been used to describe the plaque geometry where the internal and external boundaries of the arterial wall were modelled using a circle and an ellipse, respectively (Shahidian and Hassankiadeh, 2017). By changing the size of the crescent shape, Kumar and Balakrishnan investigated the stress on coronary plaques with different sizes (Krishna Kumar and Balakrishnan, 2005). On the cross-section plane along the artery centerline, Konala et al. used a simplified trapezoid model to describe the longitudinal coronary plaque geometry along the local artery segment (Konala et al., 2011). As a result, the 3D geometry of the plaque had adjustable slopes of the proximal and distal segments (Karimi et al., 2012, 2014c). Some smoother shapes were also developed to describe the longitudinal plaque geometry. Yasutomoa and Makotoa used a semicircle model to investigate the recirculation area distal to the plaque (Shimizu and Ohta, 2015). To describe the longitudinal change of radius along the stenotic artery segment in a more accurate way, Moreno and Bhaganagar used a cosine function to describe the boundary between coronary plaque and the lumen in the longitudinal direction (Moreno and Bhaganagar, 2013). With these smoother functions, saddle-shaped 3D plaque geometry could be derived to describe the geometry of eccentric plaques (Karimi et al., 2014a,b; Yuan et al., 2015). However, the geometric models in existing studies were highly simplified without validation using patient-specific imaging data. Based on the patient-specific CCTA imaging data, we found the consistency in geometry among different coronary plaques and developed two geometric models whose geometry properties were in accordance with the measured results. These results provide an important reference for the pathophysiological and computational studies on coronary plaques.

The power function relationship between multidimensional geometric parameters (volume, surface area, and length) of coronary plaques is a novel finding. As we observed, coronary plaques often grow along the artery wall, forming curved shells, rings, or more complicated shapes, which are quite different from a sphere (**Figure 6**). Therefore, instead of using sphericity to evaluate geometric consistency of coronary plaques, we directly investigated the relationship between geometric parameters in different dimensions. The consistency of plaque geometry is related to plaque growth. With a certain degree of stenosis, the plaque geometry has a direct effect on the turbulence flow characteristics in the surrounding areas (Bhaganagar, 2009). As



a result, an area with low values of wall shear stress (WSS), which is a hemodynamic parameter directly related to endothelial function and atherosclerosis, will appear in the distal segment of the plaque, accelerating the plaque growth (Liu et al., 2018; Arzani, 2020). In a study on 900 artery segments extracted from 94 patient-specific coronary arteries, Pleouras et al. found that the plaque growth and degree of stenosis predicted using the baseline WSS values derived from computational simulation were in accordance with the follow-up clinical observation (Pleouras et al., 2020b). Therefore, the plaque geometry can influence the plaque growth by hemodynamic effects in pathological mechanisms, which contributes to the geometric consistency of different coronary plaques.

On the other hand, geometrical parameters of coronary plaques can provide information about many CAD-related clinical risks: the severity of ischemia, the risky areas of plaque growth, and the stability of arteriosclerotic plaques (Choi et al., 2015; Driessen Roel et al., 2018). Therefore, the accurate evaluation of plaque geometry in different dimensions can help to determine the pathological and morphological properties of coronary plaques which will improve the diagnosis, treatment, and management of CAD.

The calcifications and plaques showed different geometric properties. Firstly, the case-based analysis disclosed that plaques and calcifications were significantly correlated in number and total volume (Table 3). This is in accordance with the fact that calcification occurs in the mature plaques. The plaque-based analysis showed a significant relationship between plaque volume and total calcification volume in the plaque. In carotid and coronary arteries, the volume of calcification is closely related to the intima-media thickness (IMT) (Araki et al., 2015). Pathologically, calcification often appears in the later stages of the atherosclerotic lesion (Shioi and Ikari, 2017). Thus, in the case-based analysis, the total calcification volume was not significantly related to the total number of plaques (Table 3). Secondly, compared with the plaques, the calcifications had less significant relationships between multidimensional geometric parameters (Figures 4, 5), which suggested that the geometry of calcification is more irregular. In atherosclerotic plaques, the formation of calcification is influenced by different pathophysiological mechanisms, including the death of inflammatory cells, releasing of matrix vesicles, reduced local expression of mineralisation inhibitors, and induction of bone formation resulting from differentiation of pericytes and/or vascular smooth muscle cells (Nakahara et al., 2017). Therefore, the distribution of calcifications is discontinuous with irregular geometry. It was observed that calcification itself exists in a diverse range of morphologies from spherical microcalcifications to large irregular-shaped macrocalcifications (Cahalane and Walsh, 2021). Additionally, the calcification geometry extracted from CCTA images is influenced by the image quality and the blooming artefact (Liu et al., 2021). Due to the limited resolution of imaging techniques, detailed shape features of calcifications have not been analysed (Shi et al., 2020a). The shape of calcification was found to be significantly related to the rupture of carotid plaques where the calcifications in the ruptured plaques displayed a remarkably lower ratio between the long axis and

the short axis (Shi et al., 2020b). Therefore, the 3D geometry of coronary calcification may provide valuable information to improve the diagnosis and prognosis of CAD, which deserves further investigation.

This study has some limitations. Firstly, only 19 subjects were included in this pilot study, in which there was no plaque rupture. All the plaques were from the left coronary arteries. The size and composition of plaques vary across different epicardial coronary arteries (Bax et al., 2021) and are influenced by some physiological factors, such as age and gender (Khosa et al., 2013). The plaque diversity deserves further consideration. Secondly, the plaques were manually extracted, which is time-consuming, unstandardized, and difficult for large-scale clinical application. Finally, we focused on the geometry of the plaques. The relationship between plaque geometry and other pathophysiological factors, including local coronary artery geometry and medical history of CAD, deserves further investigation. In future studies, the large-scale study based on automatic extraction algorithms of plaque and calcification could be considered to cover different types of coronary plaques and subjects. The geometry of calcification could be further investigated using more accurate imaging technologies (e.g., IVUS). Based on the large-scale data, the relationship between the plaque geometry and the pathophysiological factors of CAD could be investigated.

## CONCLUSION

The coronary plaques with different sizes showed consistency in geometry with power function relationships between geometric parameters of different dimensions. The calcifications and plaques are significantly related in terms of number and total volume.

## DATA AVAILABILITY STATEMENT

The original contributions presented in the study are included in the article/supplementary material, further inquiries can be directed to the corresponding author/s.

## ETHICS STATEMENT

The studies involving human participants were reviewed and approved by Ethics Committee of the Second Affiliated Hospital of Zhejiang University School of Medicine. Written informed consent for participation was not required for this study in accordance with the national legislation and the institutional requirements.

## AUTHOR CONTRIBUTIONS

HL conceived and planned the study and proposed the geometry models. AW reconstructed the models of coronary artery and plaques and measured the geometric parameters. HL, AW, and XW checked the original images and manually revised the models. HL and AW performed the statistical analysis. DZ

supervised the project that led to production of the results. All authors contributed to the discussion and revision of the manuscript and concur with the current submitted version.

## FUNDING

This study was supported by the National Natural Science Foundation of China (Grant No. 61828104), the Zhejiang

Provincial Department of Science and Technology (Grant No. 2020C03016), and the Basic Research Foundation of Shenzhen (Grant No. GJHZ20180928155002157).

## ACKNOWLEDGMENTS

We acknowledge the Medical Technology Research Centre of Anglia Ruskin University for their kind support.

## REFERENCES

- Araki, T., Ikeda, N., Dey, N., Acharjee, S., Molinari, F., Saba, L., et al. (2015). Shape-based approach for coronary calcium lesion volume measurement on intravascular ultrasound imaging and its association with carotid intima-media thickness. *J. Ultrasound Med.* 34, 469–482. doi: 10.7863/ultra.34.3.469
- Arzani, A. (2020). Coronary artery plaque growth: A two-way coupled shear stress-driven model. *Int. J. Numer. Method. Biomed. Eng.* 36:e3293. doi: 10.1002/cnm.3293
- Bax, A. M., Van Rosendaal, A. R., Ma, X., Van Den Hoogen, I. J., Gianni, U., Tantawy, S. W., et al. (2021). Comparative differences in the atherosclerotic disease burden between the epicardial coronary arteries: quantitative plaque analysis on coronary computed tomography angiography. *Europ. Heart J.* 22, 322–330. doi: 10.1093/ehjci/jeaa275
- Bhaganagar, K. (2009). Direct numerical simulation of flow in stenotic channel to understand the effect of stenotic morphology on turbulence. *J. Turbulence* 10:N41. doi: 10.1080/14685240903468796
- Cahalane, R. M., and Walsh, M. T. (2021). Nanoindentation of calcified and non-calcified components of atherosclerotic tissues. *Exp. Mech.* 61, 67–80. doi: 10.1007/s11340-020-00635-z
- Choi, G., Lee, J. M., Kim, H.-J., Park, J.-B., Sankaran, S., Otake, H., et al. (2015). Coronary artery axial plaque stress and its relationship with lesion geometry: application of computational fluid dynamics to coronary CT angiography. *JACC Cardiovasc. Imaging* 8, 1156–1166. doi: 10.1016/j.jcmg.2015.04.024
- Daghem, M., Bing, R., Fayad Zahi, A., and Dweck Marc, R. (2020). Noninvasive imaging to assess atherosclerotic plaque composition and disease activity. *JACC Cardiovasc. Imaging* 13, 1055–1068. doi: 10.1016/j.jcmg.2019.03.033
- Driessen Roel, S., Stuijzand Wijnand, J., Rajmakers Pieter, G., Danad, I., Min James, K., Leipsic Jonathon, A., et al. (2018). Effect of plaque burden and morphology on myocardial blood flow and fractional flow reserve. *J. Am. Coll. Cardiol.* 71, 499–509. doi: 10.1016/j.jacc.2017.11.054
- Dweck, M. R., Doris, M. K., Motwani, M., Adamson, P. D., Slomka, P., Dey, D., et al. (2016). Imaging of coronary atherosclerosis — evolution towards new treatment strategies. *Nat. Rev. Cardiol.* 13, 533–548. doi: 10.1038/nrcardio.2016.79
- Gaur, S., Øvrehus, K. A., Dey, D., Leipsic, J., Bøtcher, H. E., Jensen, J. M., et al. (2016). Coronary plaque quantification and fractional flow reserve by coronary computed tomography angiography identify ischaemia-causing lesions. *Eur. Heart J.* 37, 1220–1227. doi: 10.1093/eurheartj/ehv690
- Gnasso, A., Irace, C., Carallo, C., De Franceschi, M. S., Motti, C., Mattioli, P. L., et al. (1997). *In vivo* association between low wall shear stress and plaque in subjects with asymmetrical carotid atherosclerosis. *Stroke* 28, 993–998. doi: 10.1161/01.STR.28.5.993
- Karimi, A., Navidbakhsh, M., Faghihi, S., Shojaei, A., and Hassani, K. (2012). A finite element investigation on plaque vulnerability in realistic healthy and atherosclerotic human coronary arteries. *Proc. Inst. Mech. Eng. H* 227, 148–161. doi: 10.1177/0954411912461239
- Karimi, A., Navidbakhsh, M., and Razaghi, R. (2014a). A finite element study of balloon expandable stent for plaque and arterial wall vulnerability assessment. *J. Appl. Phys.* 116:044701. doi: 10.1063/1.4891019
- Karimi, A., Navidbakhsh, M., Razaghi, R., and Haghpahan, M. (2014b). A computational fluid-structure interaction model for plaque vulnerability assessment in atherosclerotic human coronary arteries. *J. Appl. Phys.* 115:144702. doi: 10.1063/1.4870945
- Karimi, A., Navidbakhsh, M., Shojaei, A., Hassani, K., and Faghihi, S. (2014c). Study of plaque vulnerability in coronary artery using mooney–rivlin model: a combination of finite element and experimental method. *Biomed. Eng.* 26:1450013. doi: 10.4015/S1016237214500136
- Khosha, F., Khan, A. N., Nasir, K., Bedayat, A., Malik, Z., Jon, A. F., et al. (2013). Comparison of coronary plaque subtypes in male and female patients using 320-row MDCTA. *Atherosclerosis* 226, 428–432. doi: 10.1016/j.atherosclerosis.2012.11.033
- Komiyama, H., Takano, H., Nakamura, S., Takano, M., Hata, N., Yasushi, M., et al. (2016). Geographical predisposition influences on the distribution and tissue characterisation of eccentric coronary plaques in non-branching coronary arteries: cross-sectional study of coronary plaques analysed by intravascular ultrasound. *Cardiovasc. Ultrasound* 14:47. doi: 10.1186/s12947-016-0090-3
- Konala, B. C., Das, A., and Banerjee, R. K. (2011). Influence of arterial wall-stenosis compliance on the coronary diagnostic parameters. *J. Biomech.* 44, 842–847. doi: 10.1016/j.jbiomech.2010.12.011
- Krishna Kumar, R., and Balakrishnan, K. R. (2005). Influence of lumen shape and vessel geometry on plaque stresses: possible role in the increased vulnerability of a remodelled vessel and the “shoulder” of a plaque. *Heart* 91:1459. doi: 10.1136/hrt.2004.049072
- Kühnel, S., Brückner, A., Schmelzle, S., Heethoff, M., and Blüthgen, N. (2017). Surface area–volume ratios in insects. *Insect Sci.* 24, 829–841. doi: 10.1111/1744-7917.12362
- Lee, J. M., Choi, K. H., Koo, B.-K., Park, J., Kim, J., Hwang, D., et al. (2019a). Prognostic implications of plaque characteristics and stenosis severity in patients with coronary artery disease. *J. Am. Coll. Cardiol.* 73, 2413–2424. doi: 10.1016/j.jacc.2019.02.060
- Lee, S.-E., Villines, T. C., and Chang, H.-J. (2019b). Should CT replace IVUS for evaluation of CAD in large-scale clinical trials: effects of medical therapy on atherosclerotic plaque. *J. Cardiovasc. Comput. Tomogr.* 13, 248–253. doi: 10.1016/j.jcct.2019.06.017
- Li, T., Li, S., Zhao, J., Lu, P., and Meng, L. (2012). Sphericities of non-spherical objects. *Particuology* 10, 97–104. doi: 10.1016/j.partic.2011.07.005
- Liu, H., Gong, Y., Leng, X., Xia, L., Wong, K. S., Ou, S., et al. (2018). Estimating current and long-term risks of coronary artery *in silico* by fractional flow reserve, wall shear stress and low-density lipoprotein filtration rate. *Biomed. Phys. Eng. Express* 4:025006. doi: 10.1088/2057-1976/aa9a09
- Liu, H., Wingert, A., Jian'an Wang, J. Z., Wang, X., Sun, J., Chen, F., et al. (2021). Extraction of coronary atherosclerotic plaques from computed tomography imaging: a review of recent methods. *Front. Cardiovasc. Med.* 8:597568. doi: 10.3389/fcvm.2021.597568
- Liu, J., Jin, C., Feng, J., Du, Y., Lu, J., and Zhou, J. (2019). “A vessel-focused 3D convolutional network for automatic segmentation and classification of coronary artery plaques in cardiac CTA,” in *Statistical Atlases and Computational Models of the Heart. Atrial Segmentation and LV Quantification Challenges*, eds. M. Pop, M. Sermesant, J. Zhao, S. Li, K. McLeod, A. Young, et al. (Granada: Springer International Publishing), 131–141. doi: 10.1007/978-3-030-12029-0\_15
- Malakar, A. K., Choudhury, D., Halder, B., Paul, P., Uddin, A., and Chakraborty, S. (2019). A review on coronary artery disease, its risk factors, and therapeutics. *J. Cell. Physiol.* 234, 16812–16823. doi: 10.1002/jcp.28350
- Moreno, C., and Bhaganagar, K. (2013). Modeling of stenotic coronary artery and implications of plaque morphology on blood flow. *Model. Simulat. Eng.* 2013:390213. doi: 10.1155/2013/390213

- Nakahara, T., Dweck Marc, R., Narula, N., Pisapia, D., Narula, J., and Strauss, H. W. (2017). Coronary artery calcification: from mechanism to molecular imaging. *JACC Cardiovasc. Imaging* 10, 582–593. doi: 10.1016/j.jcmg.2017.03.005
- Pleouras, D. S., Sakellarios, A. I., Loukas, V. S., Kyriakidis, S., and Fotiadis, D. I. (2020a). “Prediction of the development of coronary atherosclerotic plaques using computational modeling in 3D reconstructed coronary arteries,” in *2020 42nd Annual International Conference of the IEEE Engineering in Medicine & Biology Society (EMBC)* (Montreal, QC: IEEE), 2808–2811. doi: 10.1109/EMBC44109.2020.9176219
- Pleouras, D. S., Sakellarios, A. I., Tsompou, P., Kigka, V., Kyriakidis, S., Rocchiccioli, S., et al. (2020b). Simulation of atherosclerotic plaque growth using computational biomechanics and patient-specific data. *Sci. Rep.* 10:17409. doi: 10.1038/s41598-020-74583-y
- Ratiu, M., Chitu, M., Benedek, I., Benedek, T., Kovacs, I., Rat, N., et al. (2018). Impact of coronary plaque geometry on plaque vulnerability and its association with the risk of future cardiovascular events in patients with chest pain undergoing coronary computed tomographic angiography—the GEOMETRY study: Protocol for a prospective clinical trial. *Medicine* 97:e13498. doi: 10.1097/MD.00000000000013498
- Ratiu, M., Rat, N., Nyulas, T., Moldovan, G., Rus, V., Benedek, T., et al. (2019). Coronary plaque geometry and thoracic fat distribution in patients with acute chest pain—a CT angiography study. *J. Cardiovasc. Emerg.* 5, 18–24. doi: 10.2478/jce-2019-0001
- Rinehart, S., Vazquez, G., Qian, Z., Murrieta, L., Christian, K., and Voros, S. (2011). Quantitative measurements of coronary arterial stenosis, plaque geometry, and composition are highly reproducible with a standardized coronary arterial computed tomographic approach in high-quality CT datasets. *J. Cardiovasc. Comput. Tomogr.* 5, 35–43. doi: 10.1016/j.jcct.2010.09.006
- Samady, H., Eshthardi, P., Mcdaniel, M. C., Suo, J., Dhawan, S. S., Maynard, C., et al. (2011). Coronary artery wall shear stress is associated with progression and transformation of atherosclerotic plaque and arterial remodeling in patients with coronary artery disease. *Circulation* 124, 779–788. doi: 10.1161/CIRCULATIONAHA.111.021824
- Shahidian, A., and Hassankiadeh, A. G. (2017). Stress analysis of internal carotid artery with low stenosis level: the effect of material model and plaque geometry. *J. Mech. Med. Biol.* 17:1750098. doi: 10.1142/S0219519417500981
- Shi, X., Gao, J., Lv, Q., Cai, H., Wang, F., Ye, R., et al. (2020a). Calcification in Atherosclerotic Plaque Vulnerability: Friend or Foe? *Front. Physiol.* 11:56. doi: 10.3389/fphys.2020.00056
- Shi, X., Han, Y., Li, M., Yin, Q., Liu, R., Wang, F., et al. (2020b). Superficial calcification with rotund shape is associated with carotid plaque rupture: an optical coherence tomography study. *Front. Neurol.* 11:563334. doi: 10.3389/fneur.2020.563334
- Shimizu, Y., and Ohta, M. (2015). Influence of plaque stiffness on deformation and blood flow patterns in models of stenosis. *Biorheology* 52, 171–182. doi: 10.3233/BIR-14016
- Shioi, A., and Ikari, Y. (2017). Plaque calcification during atherosclerosis progression and regression. *J. Atheroscler. Thromb.* 25, 294–303. doi: 10.5551/jat.RV17020
- Stefanini Giulio, G., and Windecker, S. (2015). Can coronary computed tomography angiography replace invasive angiography? *Circulation* 131, 418–426. doi: 10.1161/CIRCULATIONAHA.114.008148
- Symons, R., Morris, J. Z., Wu, C. O., Pourmorteza, A., Ahlman, M. A., Lima, J., et al. (2016). Coronary CT angiography: variability of ct scanners and readers in measurement of plaque volume. *Radiology* 281, 737–748. doi: 10.1148/radiol.2016161670
- Toro, R., Perron, M., Pike, B., Richer, L., Veillette, S., Pausova, Z., et al. (2008). Brain size and folding of the human cerebral cortex. *Cerebral Cortex* 18, 2352–2357. doi: 10.1093/cercor/bhm261
- Wang, Y., Osborne, M. T., Tung, B., Li, M., and Li, Y. (2018). Imaging cardiovascular Calcification 7:e008564. doi: 10.1161/JAHA.118.008564
- Yamamoto, E., Siasos, G., Zaromytidou, M., Coskun Ahmet, U., Xing, L., Bryniarski, K., et al. (2017). Low endothelial shear stress predicts evolution to high-risk coronary plaque phenotype in the future. *Circulation* 10:e005455. doi: 10.1161/CIRCINTERVENTIONS.117.005455
- Yuan, J., Teng, Z., Feng, J., Zhang, Y., Brown, A. J., Gillard, J. H., et al. (2015). Influence of material property variability on the mechanical behaviour of carotid atherosclerotic plaques: a 3D fluid-structure interaction analysis. *Int. J. Numer. Method. Biomed. Eng.* 31:e02722. doi: 10.1002/cnm.2722

**Conflict of Interest:** The authors declare that the research was conducted in the absence of any commercial or financial relationships that could be construed as a potential conflict of interest.

**Publisher’s Note:** All claims expressed in this article are solely those of the authors and do not necessarily represent those of their affiliated organizations, or those of the publisher, the editors and the reviewers. Any product that may be evaluated in this article, or claim that may be made by its manufacturer, is not guaranteed or endorsed by the publisher.

Copyright © 2021 Liu, Wingert, Wang, Zhang, Sun, Chen, Khalid, Gong, Xia, Jiang, Wang and Zheng. This is an open-access article distributed under the terms of the Creative Commons Attribution License (CC BY). The use, distribution or reproduction in other forums is permitted, provided the original author(s) and the copyright owner(s) are credited and that the original publication in this journal is cited, in accordance with accepted academic practice. No use, distribution or reproduction is permitted which does not comply with these terms.



# Mitochondrial Contributions in the Genesis of Delayed Afterdepolarizations in Ventricular Myocytes

Vikas Pandey<sup>1</sup>, Lai-Hua Xie<sup>2</sup>, Zhilin Qu<sup>1,3</sup> and Zhen Song<sup>1,4\*</sup>

<sup>1</sup> Department of Medicine, David Geffen School of Medicine, University of California, Los Angeles, Los Angeles, CA, United States, <sup>2</sup> Department of Cell Biology and Molecular Medicine, Rutgers New Jersey Medical School, Newark, NJ, United States, <sup>3</sup> Department of Computational Medicine, David Geffen School of Medicine, University of California, Los Angeles, Los Angeles, CA, United States, <sup>4</sup> Peng Cheng Laboratory, Shenzhen, China

## OPEN ACCESS

### Edited by:

Ling Xia,  
Zhejiang University, China

### Reviewed by:

Dongdong Deng,  
Dalian University of Technology, China  
Michael Alan Colman,  
University of Leeds, United Kingdom

### \*Correspondence:

Zhen Song  
songzh01@pcl.ac.cn

### Specialty section:

This article was submitted to  
Computational Physiology  
and Medicine,  
a section of the journal  
Frontiers in Physiology

**Received:** 19 July 2021

**Accepted:** 02 September 2021

**Published:** 14 October 2021

### Citation:

Pandey V, Xie L-H, Qu Z and  
Song Z (2021) Mitochondrial  
Contributions in the Genesis  
of Delayed Afterdepolarizations  
in Ventricular Myocytes.  
Front. Physiol. 12:744023.  
doi: 10.3389/fphys.2021.744023

Mitochondria fulfill the cell's energy demand and affect the intracellular calcium ( $\text{Ca}^{2+}$ ) dynamics via direct  $\text{Ca}^{2+}$  exchange, the redox effect of reactive oxygen species (ROS) on  $\text{Ca}^{2+}$  handling proteins, and other signaling pathways. Recent experimental evidence indicates that mitochondrial depolarization promotes arrhythmogenic delayed afterdepolarizations (DADs) in cardiac myocytes. However, the nonlinear interactions among the  $\text{Ca}^{2+}$  signaling pathways, ROS, and oxidized  $\text{Ca}^{2+}$ /calmodulin-dependent protein kinase II (CaMKII) pathways make it difficult to reveal the mechanisms. Here, we use a recently developed spatiotemporal ventricular myocyte computer model, which consists of a 3-dimensional network of  $\text{Ca}^{2+}$  release units (CRUs) intertwined with mitochondria and integrates mitochondrial  $\text{Ca}^{2+}$  signaling and other complex signaling pathways, to study the mitochondrial regulation of DADs. With a systematic investigation of the synergistic or competing factors that affect the occurrence of  $\text{Ca}^{2+}$  waves and DADs during mitochondrial depolarization, we find that the direct redox effect of ROS on ryanodine receptors (RyRs) plays a critical role in promoting  $\text{Ca}^{2+}$  waves and DADs under the acute effect of mitochondrial depolarization. Furthermore, the upregulation of mitochondrial  $\text{Ca}^{2+}$  uniporter can promote DADs through  $\text{Ca}^{2+}$ -dependent opening of mitochondrial permeability transition pores (mPTPs). Also, due to much slower dynamics than  $\text{Ca}^{2+}$  cycling and ROS, oxidized CaMKII activation and the cytosolic ATP do not appear to significantly impact the genesis of DADs during the acute phase of mitochondrial depolarization. However, under chronic conditions, ATP depletion suppresses and enhanced CaMKII activation promotes  $\text{Ca}^{2+}$  waves and DADs.

**Keywords:** delayed afterdepolarization,  $\text{Ca}^{2+}$  wave, mitochondrion, cardiac cell,  $\text{Ca}^{2+}$  signaling

## INTRODUCTION

Delayed afterdepolarizations (DADs) are abnormal depolarizations during the diastolic phase following an action potential (AP) and could trigger cardiac arrhythmias (Rosen et al., 1984; January and Fozzard, 1988; Katta and Laurita, 2005; Qu et al., 2014; Song et al., 2017). DADs are known to be caused by spontaneous calcium ( $\text{Ca}^{2+}$ ) waves (Rosen et al., 1984; Marban et al., 1986; January and Fozzard, 1988), occurring due to spontaneous  $\text{Ca}^{2+}$  release from the intracellular  $\text{Ca}^{2+}$  store,



sarcoplasmic reticulum (SR), *via* the ryanodine receptors (RyRs).  $\text{Ca}^{2+}$  waves are known to be promoted by  $\text{Ca}^{2+}$  overload under normal (Cheng et al., 1996) and pathological conditions, such as heart failure (Pogwizd and Bers, 2003; Hoeker et al., 2009), long QT syndrome (Mohler et al., 2003), ischemia (Ross and Howlett, 2009), and catecholaminergic polymorphic ventricular tachycardia (CPVT) (Watanabe et al., 2009). During a cardiac cycle,  $\text{Ca}^{2+}$  enters into the cytosol from the extracellular space mainly *via* L-type  $\text{Ca}^{2+}$  channels (LCCs) during membrane depolarization, which causes  $\text{Ca}^{2+}$  release from the SR, a process called  $\text{Ca}^{2+}$ -induced  $\text{Ca}^{2+}$  release (CICR; Bers, 2002).  $\text{Ca}^{2+}$  is extruded from the cell mainly through the  $\text{Na}^{+}$ - $\text{Ca}^{2+}$  exchanger (NCX) and taken back to the SR through sarcoplasmic reticulum  $\text{Ca}^{2+}$ -ATPase (SERCA). Meanwhile, mitochondria, as another  $\text{Ca}^{2+}$  store, are involved in intracellular  $\text{Ca}^{2+}$  cycling *via* mitochondrial  $\text{Ca}^{2+}$  uniporter (MCU; Baughman et al., 2011; De Stefani et al., 2011), mitochondrial  $\text{Na}^{+}$ - $\text{Ca}^{2+}$  exchangers (mNCX; Palty et al., 2010), and the mitochondrial permeability transition pore (mPTP; Hunter et al., 1976). Besides the direct  $\text{Ca}^{2+}$  exchange, mitochondria may indirectly alter the cytosolic  $\text{Ca}^{2+}$  dynamics through many different ways under abnormal conditions (Yan et al., 2008; Florea and Blatter, 2010; Zhao et al., 2013; Xie et al., 2018), thus impacting  $\text{Ca}^{2+}$  waves and DADs. Under normal conditions, the occurrence of mitochondrial depolarizations through the mPTP opening is rare (Lu et al., 2016). However, the mPTP open probability increases in abnormal conditions, resulting in a higher degree of mitochondrial depolarization in the cell. The critical consequences that affect intracellular  $\text{Ca}^{2+}$  dynamics include an increased cytosolic reactive oxygen species (ROS) level, enhanced  $\text{Ca}^{2+}$ /calmodulin-dependent protein kinase II (CaMKII) activation *via* oxidative stress,  $\text{Ca}^{2+}$  influx into the cytosol from the mitochondria, and a decrease in the cytosolic ATP level, etc.

Reactive oxygen species can directly affect the RyRs hyperactivity and SERCA pump strength *via* its redox effect (Zima and Blatter, 2006; Wagner et al., 2013) or indirectly *via* oxidized CaMKII signaling (Xie et al., 2009; Foteinou et al., 2015). CaMKII activation is known to increase SERCA pump through phosphorylation of phospholamban (Hund and Rudy, 2004; Mattiazzi and Kranias, 2014), make RyRs leakier (Ai et al., 2005), and modulate LCCs and other membrane ionic currents (Anderson et al., 1994; Xiao et al., 1994; Yuan and Bers, 1994; Hund and Rudy, 2004; Hund et al., 2008). Furthermore, ATP depletion impairs the SERCA pump function (Sakamoto and Tonomura, 1980). Due to their highly complex interactions, it is difficult to dissect out the individual roles of mitochondrial  $\text{Ca}^{2+}$  exchange, ROS, ATP, and CaMKII activation in the genesis of DADs during mitochondrial depolarization by experiments. We have recently developed a whole-cell ventricular myocyte model consisting of a network of intermingled  $\text{Ca}^{2+}$  release units (CRUs) and mitochondria, which contains physiological details of mitochondrial membrane potential, mitochondrial  $\text{Ca}^{2+}$  cycling, mPTP stochastic opening and closing, intracellular ROS, and oxidized CaMKII signaling. Using this model, we have investigated the underlying

mechanisms of  $\text{Ca}^{2+}$  alternans and early afterdepolarizations caused by mitochondrial depolarization and dissected each of the components (Xie et al., 2018; Song et al., 2019; Pandey et al., 2021).

We used this model to investigate the underlying mechanisms of spontaneous  $\text{Ca}^{2+}$  release mediated DADs under mitochondrial depolarization due to mPTP openings in the present work. Specifically, we performed computer simulations to reveal individual contributions of the components mentioned earlier to the genesis of  $\text{Ca}^{2+}$  waves and DADs. Our previous work provided mechanistic insights of generation of  $\text{Ca}^{2+}$  alternans under mitochondrial depolarization, and we have reported that the redox effect of ROS on RyRs and SERCA pump synergistically promote alternans (Pandey et al., 2021). Here, we show that the ROS redox regulation of RyRs plays a significant role in the genesis of  $\text{Ca}^{2+}$  waves and DADs during the acute phase of mitochondrial depolarization. Also, upregulation of MCU can promote DADs through  $\text{Ca}^{2+}$ -dependent openings of mPTPs. However, the changes of oxidized CaMKII activation and the cytosolic ATP level are at much slower time scales than the redox effects of ROS, and thereby, they do not significantly impact the genesis of DADs in a relatively short duration after mitochondrial depolarization. Whereas, under chronic conditions, ATP depletion suppresses and enhanced CaMKII activation promotes the  $\text{Ca}^{2+}$  waves and DADs.

## MATERIALS AND METHODS

The details of the model, including the mathematical formulations and control values of the parameters, can be found in Song et al. (2019) and Pandey et al. (2021). Here, we describe some of the essential aspects of the model for the sake of this study.

### The Overall Ventricular Myocyte Model Structure

Our rabbit ventricular myocyte model consists of a 3-dimensional coupled network of CRUs and mitochondria. This network contains 21504 (64 28 12) CRUs and 5376 (64 14 6) mitochondria. The membrane potential ( $V$ ) of the cell is described by

$$C_m \frac{dV}{dt} = I_{Na} + I_{Na,L} + I_{Ca,L} + I_{NCX} + I_{K1} + I_{Kr} + I_{Ks} + I_{to,f} + I_{to,s} + I_{NaK} + I_{K,ATP} + I_{Ca,b} - I_{sti} \quad (1)$$

where  $C_m = 1 \text{ mF/cm}^2$  is the cell membrane capacitance, and  $I_{sti}$  is the stimulus pulse with the current density being  $-80 \text{ mA/cm}^2$  and the duration being 0.5 ms.

### Regulations of Reactive Oxygen Species and CaMKII on Ryanodine Receptors

The oxidized CaMKII activation and the redox effect of ROS both increase the open probability of RyRs (Wehrens et al., 2004; Ai et al., 2005; Guo et al., 2006; Zima and Blatter, 2006;

Wagner et al., 2013). To incorporate these effects, the close-to-open rate ( $k_{12}$ ) of RyRs was modeled as follows:

$$k_{12} = k_{base}k_u (1 + \Delta k_{CaMKII} + \Delta k_{ROS}) ([Ca^{2+}]_p)^2 \quad (2)$$

$$\Delta k_{CaMKII} = \frac{\Delta k_{CaMK,max}}{1 + \left( \frac{\Delta k_{CaMKRyR}}{[CaMKII]_{act}} \right)^{h_{CaMKIIyR}}} \quad (3)$$

$$\Delta k_{ROS} = \frac{\Delta k_{ROS,max}}{1 + \left( \frac{\Delta k_{mROSyR}}{[ROS]_{cyt}} \right)^{h_{ROSyR}}} \quad (4)$$

where  $\Delta k_{CaMKII}$  and  $\Delta k_{ROS}$  are the CaMKII-dependent (Eq. 3) and ROS-dependent components (Eq. 4), respectively.  $k_{base}$  and  $k_u$  are the rate constants.  $[Ca^{2+}]_p$  is the  $Ca^{2+}$  concentration in the dyadic space of a CRU.  $[CaMKII]_{act}$  and  $[ROS]_{cyt}$  are the CaMKII activation level and the cytosolic ROS concentration in each CRU, respectively. The increase in CaMKII activation and ROS level increase  $k_{12}$ , which in turn increases the open probability of RyRs.

## Regulations of Reactive Oxygen Species and CaMKII on Sarcoplasmic Reticulum $Ca^{2+}$ -ATPase Pump

The formulation of SERCA is

$$J_{up} = v_{up}f_{up,ATP}f_{up,ROS} \frac{[Ca^{2+}]_i^2}{[Ca^{2+}]_i^2 + (K_i - PLB([CaMKII]_{act}))^2} \quad (5)$$

where  $f_{up,ATP}$  and  $f_{up,ROS}$  are ATP and ROS-dependent functions (Song et al., 2019):

$$f_{up,ATP} = \frac{1}{1 + \frac{[ADP]_f}{k_{i,up}} + \left( 1 + \frac{[ADP]_f}{k_{i,up}} \right) \frac{k_{mup,ATP}}{[ATP]}} \quad (6)$$

$$f_{up,ROS} = \frac{1}{1 + \left( \frac{[ROS]_{cyt}}{k_{d,ros}} \right)^{h_{ros,SERCA}}} + \frac{0.75}{1 + \left( \frac{k_{d,ros}}{[ROS]_{cyt}} \right)^{h_{ros,SERCA}}} \quad (7)$$

$v_{up}$  is the maximum SERCA strength and  $K_i$  the half-maximum value.  $PLB([CaMKII]_{act})$  is a CaMKII dependent function.  $[CaMKII]_{act}$  is CaMKII activation level in the cytosolic space of a CRU.

## The Mitochondrial Permeability Transition Pore Model

We used a 3-state (two close states  $C_0$  and  $C_1$ , and an open state O) Markov model to simulate the stochastic opening and closing of the mPTP. The transition rate from the  $C_0$  state to the  $C_1$  state,  $k_{c0c1}$ , is set as:

$$k_{c0c1} = \alpha_0 \left( 1 + 199 * \frac{[Ca^{2+}]_m^{h_{mPTP}}}{[Ca^{2+}]_m^{h_{mPTP}} + [Ca^{2+}]_0^{h_{mPTP}}} \right) \quad (8)$$

where  $h_{mPTP}$  is the Hill coefficient,  $[Ca^{2+}]_m$  is the mitochondrial free  $Ca^{2+}$  in the corresponding mitochondrion, and  $[Ca^{2+}]_0$  is the half-maximum value. We assume that other transition rates are constants. To simulate different levels of mPTP open probability, we multiplied a factor,  $\alpha_{mPTP}$ , to the transition rate from  $C_1$  to O,  $k_{c1o}^0$ , i.e.,

$$k_{c1o} = \alpha_{mPTP}k_{c1o}^0 \quad (9)$$

## RESULTS

### Mitochondrial Depolarization Due to Openings of Mitochondrial Permeability Transition Pore Promotes Spontaneous $Ca^{2+}$ Release and Delayed Afterdepolarizations

We investigated the impact of mitochondrial depolarizations on the occurrence of  $Ca^{2+}$  waves and DADs via mPTP opening. We performed simulations over a wide range of  $\alpha_{mPTP}$  values at the PCL of 300 ms (Figure 1A).  $\alpha_{mPTP}$  is a factor multiplied to transition rate of mPTP opening, and increasing its value results in higher mPTP opening. For each simulation, the cell was paced for 140 beats (42 s), following 3 s without pacing in order to observe  $Ca^{2+}$  waves and DADs. As shown in Figure 1A, the amplitude of DAD increases with  $\alpha_{mPTP}$ , suggesting that mitochondrial depolarization due to openings of mPTP promotes spontaneous  $Ca^{2+}$  release and DADs. Also, when  $\alpha_{mPTP}$  is greater than ~50, the proarrhythmic effect appears to saturate. Under the control condition ( $\alpha_{mPTP} = 1$ ), there is no occurrence of DADs (Figures 1A,B). The cytosolic ROS is ~2  $\mu$ M, CaMKII activation is ~0.2%, the cytosolic ATP is ~5 mM, and most of the mitochondria remain repolarized ( $-\Delta\psi = \sim 180$  mV, and the mPTP open probability ~0.8%, mitochondrial  $Ca^{2+}$  amplitude is ~0.8  $\mu$ M) (Figure 1B). However, with the higher open probability of mPTP (~42%, for  $\alpha_{mPTP} = 60$ ), we observed DADs. The corresponding line-scan image clearly shows enhanced spontaneous  $Ca^{2+}$  release as compared to a few scattered  $Ca^{2+}$  sparks under the control condition (Figure 1C). In this case, we should note that the mitochondrial  $Ca^{2+}$  amplitude increased to ~1.2 M, and the cytosolic ROS drastically increased to ~86  $\mu$ M. Still, the CaMKII activation and the cytosolic ATP level insignificantly changed (~0.6% and ~4.8 mM, respectively).

### Role of Reactive Oxygen Species in the Genesis of Delayed Afterdepolarizations

The concentration of the cytosolic ROS depends on the level of mitochondrial depolarization, and thus, increasing  $\alpha_{mPTP}$  increases the open probability of mPTP, which, in turn, elevates the level of cytosolic ROS. To further identify the role of cytosolic ROS in the genesis of DADs, we performed simulations for a clamped ROS level at the PCL 300 ms. In the free-running ROS case as shown in Figure 1, the ROS dynamics in the model remains intact, while in the clamped ROS condition, the cytosolic ROS is clamped to a constant regardless the level of

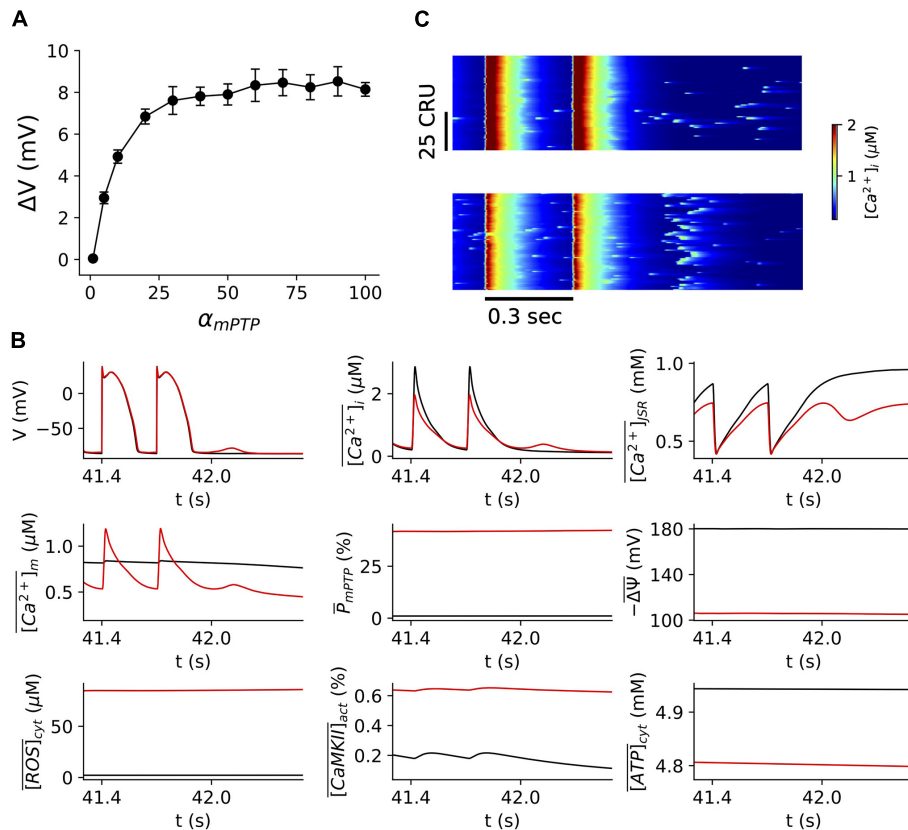


**FIGURE 1 |** Mitochondrial depolarization via mPTP opening promotes DADs. **(A)** The amplitude of DADs vs.  $\alpha_{mPTP}$ . The resting potential is  $-86.0$  mV. Note that for the range of  $\alpha_{mPTP}$  in these simulations, we observed only one DAD after stopping pacing. **(B)** Time traces of  $V$ ,  $[Ca^{2+}]_i$ ,  $[Ca^{2+}]_{SR}$ ,  $[Ca^{2+}]_m$ ,  $\bar{P}_{mPTP}$ ,  $-\Delta\psi$ ,  $[ROS]_{cyt}$ ,  $[CaMKII]_{lact}$ ,  $[ATP]_{cyt}$  for normal control ( $\alpha_{mPTP} = 1$ ) in black and mitochondrial depolarization conditions ( $\alpha_{mPTP} = 60$ ) in red, respectively. The pacing cycle length is 300 ms, and we stopped pacing after 140 beats (i.e., 42 s). This pacing protocol was used throughout the whole study. **(C)** Linescan images of the cytosolic  $Ca^{2+}$  for normal (top) and mitochondrial depolarization (bottom) conditions as in panel **(B)**.

mitochondrial depolarization is. Here we clamped ROS to be  $1.0 \mu M$ , which is close to the level under the normal control condition. We then measured the amplitude of DAD with different  $\alpha_{mPTP}$  values for the clamped ROS (Figure 2, red) condition. We observed that when the ROS was clamped at the control level ( $1.0 \mu M$ ), no DADs occurred, suggesting that the cytosolic ROS plays a critical role in inducing DADs during mitochondrial depolarization.

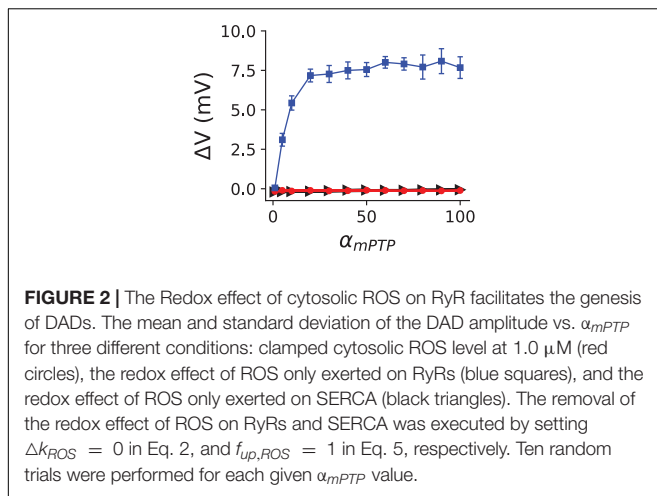
Furthermore, the cytosolic ROS is known to alter the characteristics of both SERCA and RyRs (Zima and Blatter, 2006; Wagner et al., 2013). Therefore, we investigated the redox effect of ROS on the RyRs and SERCA pump separately to dissect out its individual role. We observed that DADs disappeared when we removed the redox effect of ROS on the RyRs (Figure 2, green). However, removing the redox effect on SERCA did not significantly impact the amplitude of DADs (Figure 2, blue), suggesting that the redox effect on SERCA may not play a critical role in the genesis of DADs. In fact, the direct redox effect of ROS inhibits the SERCA pump activity. Thus, removing the redox effect on SERCA increased the SR  $Ca^{2+}$  load instead, causing higher amplitudes of DADs. For instance, at  $\alpha_{mPTP} = 20$ , the

amplitude of DAD is  $7.17$  mV when the redox effect of ROS is only exerted on RyRs (Figure 2, blue), but  $6.84$  mV under control as shown in Figure 1A.

## Role of the Mitochondrial $Ca^{2+}$ in the Genesis of the Delayed Afterdepolarizations

Several studies have shown that under certain pathological conditions, MCU activity is enhanced (Santulli et al., 2015; Xie et al., 2018), which may elevate the mitochondrial free  $Ca^{2+}$ . Our previous study (Song et al., 2019) showed that the increase of MCU up to 20-fold does not alter cytosolic  $Ca^{2+}$  markedly at the steady-state. However, we hypothesize that the higher mitochondrial  $Ca^{2+}$  due to MCU overexpression could increase the mPTP open probability and cause higher ROS production in the cytosol (Korge et al., 2011). To test this hypothesis, we performed simulations to examine the effect of MCU overexpression on the genesis of DADs.

We multiplied a factor, denoted as  $\alpha_{MCU}$ , to the maximal MCU conductance.  $\alpha_{MCU} = 1$  represents the control case and



higher  $\alpha_{MCU}$  values are used to represent the different levels of MCU activity. We plotted in **Figure 3A** the amplitude of DADs for different  $\alpha_{MCU}$  and  $\alpha_{mPTP}$ . We observed that at  $\alpha_{mPTP} = 1$ , increasing the MCU activity did not result in DADs even for  $\alpha_{MCU} = 50$ . When  $\alpha_{mPTP}$  becomes greater, the effect of MCU on promoting DADs appears to be more significant. Time traces of membrane voltage, the whole-cell averaged cytosolic  $\text{Ca}^{2+}$  and the mitochondrial free  $\text{Ca}^{2+}$  for the three marked locations in the phase map (**Figure 3A**) are shown in **Figure 3B**. These results indicate that increasing MCU activity could promote spontaneous  $\text{Ca}^{2+}$  release and DADs. The mechanism revealed in the model is that increasing MCU activity elevates the mitochondrial free  $\text{Ca}^{2+}$ , which increases the open probability of mPTP, resulting in the elevation of the cytosolic ROS, which in turn promotes the spontaneous  $\text{Ca}^{2+}$  release and DADs.

## Role of Oxidized CaMKII Activation and ATP in the Genesis of Delayed Afterdepolarizations

As seen in **Figure 1B**, the CaMKII activation and ATP appeared to change slowly during the simulations due to the slow

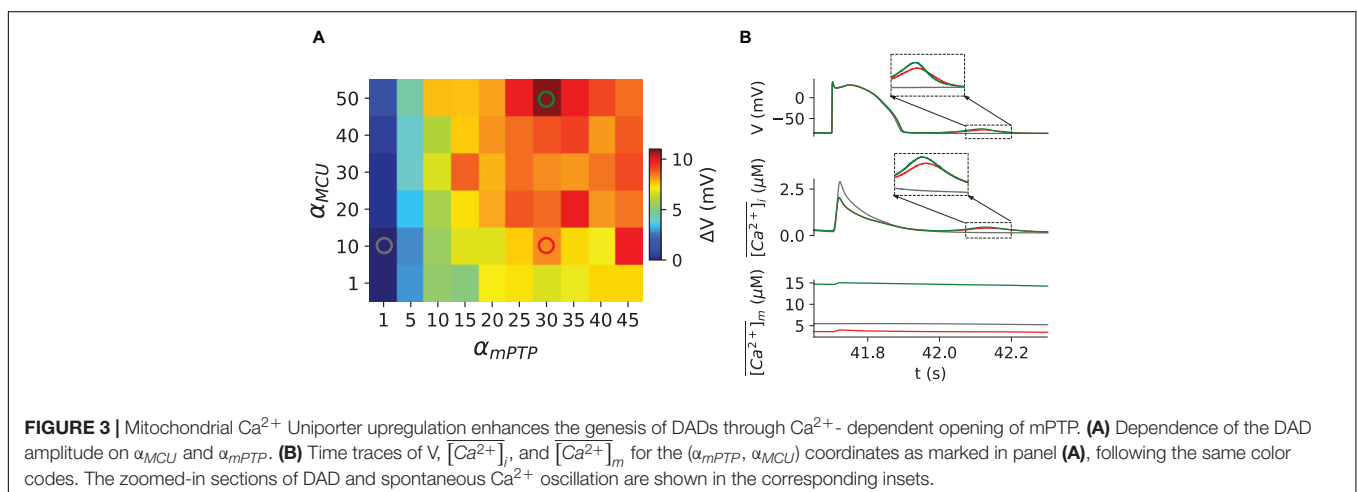
kinetics in the governing equations of their dynamics. It is computationally cumbersome to run long simulations (up to several thousand beats) for these variables to reach their steady states. Therefore, to evaluate the individual role of CaMKII activation and ATP in the genesis of DADs, we clamped them to different constant values, respectively.

**Figure 4A** shows the relationship between the amplitude of DADs and the CaMKII activation level. Our results clearly show that increasing CaMKII activation promotes DADs. However, due to its slow kinetics, CaMKII activation insignificantly changes during the acute phase of mitochondrial depolarization (**Figure 1B**), suggesting that CaMKII activation may not play a primary role in the genesis of DADs during the short period immediately after mitochondrial depolarization. Still, it may promote DADs chronically due to its regulation on SERCA, LCC, and RyRs (Wang et al., 2020).

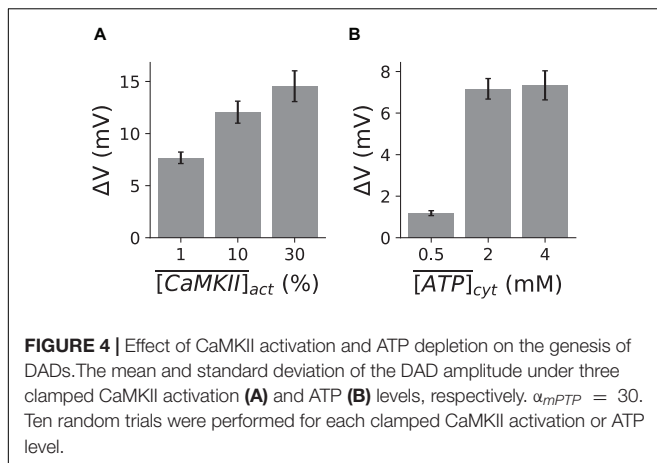
Since the SERCA pump requires ATP for its normal function, a lower level of ATP directly impairs the SERCA pump activity (Eq. 5). However, ATP depletion is a slow process, which is evident from **Figure 1B**. Hence, we clamped ATP at different levels for  $\alpha_{mPTP} = 30$  from the beginning of the simulations. **Figure 4B** plots the relationship between the amplitude of DADs and the cytosolic ATP concentration, and it shows that ATP depletion suppresses DADs during mitochondrial depolarization ( $\alpha_{mPTP} = 30$ ). Our results demonstrate that the cytosolic ATP level has a significant impact on the genesis of DADs. However, the depletion of the cytosolic ATP concentration during mitochondrial depolarization is a relatively slow process. Therefore, ATP depletion should not play a central role in the genesis of DADs during the acute phase of mitochondrial depolarization. Thus, similar to CaMKII activation, ATP depletion may only suppress DADs in a much longer time scale.

## DISCUSSION

We used a physiological detailed ventricular myocyte model consisting of a 3D network of coupled CRUs and mitochondria







to investigate the roles of mitochondrial depolarization *via* mPTP opening in the genesis of DADs. The systematic investigation of individual roles, including the cytosolic ROS, mitochondrial  $\text{Ca}^{2+}$ , CaMKII activation, and the cytosolic ATP, reveals that the redox effect of ROS on RyRs may play an essential role in the occurrence of DADs during the acute phase of mitochondrial depolarization. Furthermore, increasing the MCU activity could promote DADs by increasing the mPTP open probability through mitochondrial  $\text{Ca}^{2+}$  dependent kinetics of mPTP. In addition, oxidized CaMKII activation promotes, and ATP depletion suppresses DADs chronically in the condition of mitochondrial depolarization.

## Role of Reactive Oxygen Species, CaMKII Activation and ATP Depletion on the Genesis of Delayed Afterdepolarizations

Experimental findings reported that the mitochondria depolarization through the application of FCCP promotes  $\text{Ca}^{2+}$  waves (Zhao et al., 2013). Furthermore, the effects of FCCP were counteracted by the application of mPTP blocker cyclosporine A (Zhao et al., 2013). Also, our previous experimental observations using cyclophilin D knockout mouse model showed attenuation of  $\text{Ca}^{2+}$  waves (Gordan et al., 2016). Elevation of cytosolic ROS during mPTP opening could be a significant factor, and experimental evidence showed that oxidative stress during mitochondrial depolarization slightly alters SR  $\text{Ca}^{2+}$  leaks ( $\text{Ca}^{2+}$  spark) amplitude but drastically increases its frequency (Yan et al., 2008; Zhou et al., 2011; Williams et al., 2013). Furthermore, ROS can oxidize CaMKII and enhance its activation. It has been shown that ROS and CaMKII activation act on the major  $\text{Ca}^{2+}$  handling proteins, such as RyRs and SERCA (Hund and Rudy, 2004; Wehrens et al., 2004; Ai et al., 2005; Guo et al., 2006; Zima and Blatter, 2006; Wagner et al., 2013). The direct redox effect of ROS increases the leakiness of RyRs and decreases the strength of SERCA (Zima and Blatter, 2006; Wagner et al., 2013), whereas CaMKII activation increases both the leakiness of RyRs and the strength of SERCA (Hund and Rudy, 2004; Ai et al., 2005; Mattiazzi and Kranias, 2014). Thus, the observed  $\text{Ca}^{2+}$

waves in experiments during mitochondrial depolarization are the consequences of the combined effects of the above factors. However, what is the primary player remains unclear. Here, by using our previously established physiologically detailed computer model, we show that our simulation results agree with the experimental observations that mitochondrial depolarization could induce spontaneous  $\text{Ca}^{2+}$  release and DADs. Furthermore, we found that it is the redox effect on RyRs that causes the DADs under the acute effect of mitochondrial depolarization, and the redox effect of ROS on reducing SERCA strength may not be sufficient to suppress DADs (Figure 2).

In addition, we indeed observed an increase in CaMKII activation due to the mPTP opening (Figure 1B), but the dynamics of CaMKII activation appeared much slower than that of the ROS. The CaMKII activation was increased from  $\sim 0.2\%$  under control to  $\sim 0.6\%$  during the mitochondrial depolarization for a 45-sec long simulation (Figure 1B). A further simulation showed that CaMKII activation could reach up to  $\sim 40\%$  for a much more extended duration (1200 s). These results suggest that CaMKII activation may be too slow to play an essential role in inducing DADs under the acute effect of mitochondrial depolarization. However, simulations with different clamped CaMKII activation levels reveal that CaMKII activation may play a vital role in causing spontaneous  $\text{Ca}^{2+}$  release and DADs chronically, since a higher CaMKII activation level caused a greater DAD amplitude (Figure 4A).

Similarly, we have observed a slight change in cytosolic ATP under the acute effect of mitochondrial depolarizations in our simulations (Figure 1B). Therefore, within a relatively short duration after mitochondrial depolarization, ATP may not be involved in the genesis of spontaneous  $\text{Ca}^{2+}$  release and DADs. Clamped ATP simulations showed that a lower cytosolic ATP level is linked to a smaller amplitude of DADs (Figure 4B). This is because the reduction of ATP impaired SERCA activity and suppress the DADs, which agree well with experimental evidence that ATP synthase inhibitor, oligomycin, does not promote DADs (Zhao et al., 2013). Although ATP reduction seems to suppress  $\text{Ca}^{2+}$  waves and DADs, our simulations and other's experimental work suggest that ATP reduction could promote  $\text{Ca}^{2+}$  alternans, which is still arrhythmogenic (Hüser et al., 2000; Kocksämper et al., 2005; Zima and Blatter, 2006; Pandey et al., 2021).

## Mitochondrial $\text{Ca}^{2+}$ Uniporter Overexpression and Delayed Afterdepolarizations

Mitochondrial  $\text{Ca}^{2+}$  uptake has been reported to rise in heart failure (Santulli et al., 2015; Xie et al., 2018) and can promote EADs (Xie et al., 2018) and  $\text{Ca}^{2+}$  alternans (Pandey et al., 2021). Our previous work demonstrated MCU upregulation could promote EADs in heart failure conditions without mPTP openings (Xie et al., 2018). And MCU upregulation promotes  $\text{Ca}^{2+}$  alternans through the  $\text{Ca}^{2+}$  dependent opening of mPTPs (Pandey et al., 2021). The previous experiment by Zhao et al. (2013) reported that the mitochondrial  $\text{Ca}^{2+}$  efflux in the proximity of the junctional SR played an essential role in the regulation of  $\text{Ca}^{2+}$  waves. Furthermore, our previous study has

shown that MCU overexpression can lead to  $\text{Ca}^{2+}$  overload in mitochondria (Song et al., 2019). Also, there is evidence that mitochondrial  $\text{Ca}^{2+}$  overload can cause the  $\text{Ca}^{2+}$ -dependent opening of mPTP (Kwong and Molkentin, 2015), resulting in mitochondrial depolarization (Santulli et al., 2015). Here, our simulation study shows that increasing MCU activity promotes spontaneous  $\text{Ca}^{2+}$  release and DADs (Figure 3). The underlying mechanism revealed in our simulations is that increasing MCU activity enhanced mitochondrial depolarization through the  $\text{Ca}^{2+}$ -dependent openings of mPTP, which resulted in spontaneous  $\text{Ca}^{2+}$  release primarily due to the direct redox effect of ROS on RyRs.

## Pathophysiological and Clinical Relevance

Mitochondrial dysfunction has been associated with increased arrhythmic risk (Santulli et al., 2015; Shimizu et al., 2015; Xie et al., 2015, 2018; Gordan et al., 2016), which could account for mortality in many cardiac diseases such as cardiomyopathy, heart failure, and ischemia/reperfusion injury (IRI). We have demonstrated that the direct redox effect of ROS on RyRs plays a critical role in promoting  $\text{Ca}^{2+}$  waves and DADs under the acute effect of mitochondrial depolarization. Furthermore, the upregulation of MCU can promote DADs through  $\text{Ca}^{2+}$ -dependent opening of mPTPs. These findings suggest that pharmacological interventions targeted at avoiding ROS buildup and MCU upregulation may provide novel therapeutics to prevent or treat cardiac arrhythmias.

## Limitations

This detailed model coupled AP, CRUs, and mitochondria to capture excitation-contraction-metabolism coupling in ventricular myocytes. However, it has some limitations. For instance, heterogeneities in T-tubule networks and distributions of ion channels and  $\text{Ca}^{2+}$  handling proteins are a few examples (Soeller and Cannell, 1999; Baddeley et al., 2009) that should be considered in the future analysis. These

heterogeneities in T-tubule networks may alter the genesis of DADs (Song et al., 2018).

We note that in Figure 3A, for  $\alpha_{mPTP} = 1$ , there was virtually no DAD occurring even with  $\alpha_{MCU} = 50$ , suggesting that the proposed mechanism of increasing MCU activity inducing DADs in this study requires a certain basal level of mPTP opening. In this model, we consider the mPTP gating kinetics only mitochondrial  $\text{Ca}^{2+}$  dependent. However, the ROS-induced ROS release mechanism also impacts the mPTP open probability (Zorov et al., 2000, 2006), which is essential for modeling mitochondrial depolarization waves (Yang et al., 2010; Zhou et al., 2010; Nivala et al., 2011). Thus, this ROS-induced ROS release mechanism may provide another critical positive feedback loop between mitochondrial and cytosolic  $\text{Ca}^{2+}$  instability. In the future, the ROS-induced ROS release will be added to our model to study the role of mitochondrial depolarization waves in the genesis of arrhythmias in diseased conditions, such as heart failure.

## DATA AVAILABILITY STATEMENT

The original contributions presented in the study are included in the article/supplementary material, further inquiries can be directed to the corresponding author/s.

## AUTHOR CONTRIBUTIONS

VP performed the simulations, analyzed simulation results, and drafted the manuscript. ZS prepared the figures. All the authors conceived and designed the study, interpreted the results, and edited and revised the manuscript.

## FUNDING

This study is supported by the National Institutes of Health grant R01 HL139829.

## REFERENCES

- Ai, X., Curran, J. W., Shannon, T. R., Bers, D. M., and Pogwizd, S. M. (2005).  $\text{Ca}^{2+}$ /calmodulin-dependent protein kinase modulates cardiac ryanodine receptor phosphorylation and sarcoplasmic reticulum  $\text{Ca}^{2+}$  leak in heart failure. *Circ. Res.* 97, 1314–1322. doi: 10.1161/01.RES.0000194329.41863.89
- Anderson, M. E., Braun, A. P., Schulman, H., and Premack, B. A. (1994). Multifunctional  $\text{Ca}^{2+}$  / Calmodulin-dependent protein kinase mediates  $\text{Ca}^{2+}$ -induced enhancement of the L-type  $\text{Ca}^{2+}$  current in Rabbit ventricular myocytes. *Circ. Res.* 75, 854–861.
- Baddeley, D., Jayasinghe, I. D., Lam, L., Rossberger, S., Cannell, M. B., and Soeller, C. (2009). Optical single-channel resolution imaging of the ryanodine receptor distribution in rat cardiac myocytes. *Proc. Natl. Acad. Sci. U.S.A.* 106, 22275–22280. doi: 10.1073/pnas.0908971106
- Baughman, J. M., Perocchi, F., Girgis, H. S., Plovanich, M., Belcher-Timme, C. A., Sancak, Y., et al. (2011). Integrative genomics identifies MCU as an essential component of the mitochondrial calcium uniporter. *Nature* 476, 341–345. doi: 10.1038/nature10234
- Bers, D. M. (2002). Cardiac excitation-contraction coupling. *Nature* 415, 379–383. doi: 10.1016/B978-0-12-378630-2.00221-8
- Cheng, H., Lederer, M. R., Lederer, W. J., and Cannell, M. B. (1996). Calcium sparks and  $[\text{Ca}^{2+}]_i$  waves in cardiac myocytes. *Am. J. Physiol. Cell Physiol.* 270(1 Pt 1), C148–C159. doi: 10.1152/ajpcell.1996.270.1.c148
- De Stefani, D., Raffaello, A., Teardo, E., Szabó, I., and Rizzuto, R. (2011). A forty-kilodalton protein of the inner membrane is the mitochondrial calcium uniporter. *Nature* 476, 336–340. doi: 10.1038/nature10230
- Florea, S. M., and Blatter, L. A. (2010). The role of mitochondria for the regulation of cardiac alternans. *Front. Physiol.* 1:141. doi: 10.3389/fphys.2010.00141
- Foteinou, P. T., Greenstein, J. L., and Winslow, R. L. (2015). Mechanistic Investigation of the Arrhythmogenic Role of Oxidized CaMKII in the Heart. *Biophys. J.* 109, 838–849. doi: 10.1016/j.bpj.2015.06.064
- Gordan, R., Fefelova, N., Jk, G., and Xie, L. H. (2016). Involvement of mitochondrial permeability transition pore (mPTP) in cardiac arrhythmias: evidence from Cyclophilin D knockout mice. *Cell Calcium* 60, 363–372. doi: 10.1016/j.ceca.2016.09.001
- Involvement

- Guo, T., Zhang, T., Mestril, R., and Bers, D. M. (2006). Ca<sup>2+</sup>/calmodulin-dependent protein kinase II phosphorylation of ryanodine receptor does affect calcium sparks in mouse ventricular myocytes. *Circ. Res.* 99, 398–406. doi: 10.1161/01.RES.0000236756.06252.13
- Hoeker, G. S., Katra, R. P., Wilson, L. D., Plummer, B. N., and Laurita, K. R. (2009). Spontaneous calcium release in tissue from the failing canine heart. *Am. J. Physiol. Hear. Circ. Physiol.* 297, 10–15. doi: 10.1152/ajpheart.01320.2008
- Hund, T. J., Decker, K. F., Kanter, E., Mohler, P. J., Boyden, P. A., Schuessler, R. B., et al. (2008). Role of activated CaMKII in abnormal calcium homeostasis and INa remodeling after myocardial infarction: insights from mathematical modeling. *J. Mol. Cell. Cardiol.* 45, 420–428. doi: 10.1016/j.jmcc.2008.06.007
- Hund, T. J., and Rudy, Y. (2004). Rate dependence and regulation of action potential and calcium transient in a canine cardiac ventricular cell model. *Circulation* 110, 3168–3174. doi: 10.1161/01.CIR.0000147231.69595.D3
- Hunter, D. R., Haworth, R. A., and Southard, J. H. (1976). Relationship between configuration, function, and permeability in calcium treated mitochondria. *J. Biol. Chem.* 251, 5069–5077. doi: 10.1016/s0021-9258(17)33220-9
- Hüser, J., Wang, Y. G., Sheehan, K. A., Cifuentes, F., Lipsius, S. L., and Blatter, L. A. (2000). Functional coupling between glycolysis and excitation-contraction coupling underlies alternans in cat heart cells. *J. Physiol.* 524, 795–806. doi: 10.1111/j.1469-7793.2000.00795.x
- January, C. T., and Fozzard, H. (1988). Delayed afterdepolarizations in Heart muscle: mechanisms and relevance. *Pharmacol. Rev.* 40, 219–224.
- Katra, R. P., and Laurita, K. R. (2005). Cellular mechanism of calcium-mediated triggered activity in the heart. *Circ. Res.* 96, 535–542. doi: 10.1161/01.RES.0000159387.00749.3c
- Kocksämper, J., Zima, A. V., and Blatter, L. A. (2005). Modulation of sarcoplasmic reticulum Ca<sup>2+</sup> release by glycolysis in cat atrial myocytes. *J. Physiol.* 564, 697–714. doi: 10.1113/jphysiol.2004.078782
- Korge, P., Yang, L., Yang, J. H., Wang, Y., Qu, Z., and Weiss, J. N. (2011). Protective role of transient pore openings in calcium handling by cardiac mitochondria. *J. Biol. Chem.* 286, 34851–34857. doi: 10.1074/jbc.M111.239921
- Kwong, J. Q., and Molkentin, J. D. (2015). Physiological and pathological roles of the mitochondrial permeability transition pore in the Heart. *Cell Metab.* 21, 206–214. doi: 10.1016/j.cmet.2014.12.001
- Lu, X., Kwong, J. Q., Molkentin, J. D., and Bers, D. M. (2016). Individual cardiac mitochondria undergo rare transient permeability transition pore openings. *Circ. Res.* 118, 834–841. doi: 10.1161/CIRCRESAHA.115.308093
- Marban, E., Robinson, S. W., and Wier, W. G. (1986). Mechanisms of arrhythmogenic delayed and early afterdepolarizations in ferret ventricular muscle. *J. Clin. Invest.* 78, 1185–1192. doi: 10.1172/JCI112701
- Mattiazzi, A., and Kranias, E. G. (2014). The role of CaMKII regulation of phospholamban activity in heart disease. *Front. Pharmacol.* 5:5. doi: 10.3389/fphar.2014.00005
- Mohler, P. J., Schott, J. J., Gramolini, A. O., Dilly, K. W., Guatimosim, S., DuBell, W. H., et al. (2003). Ankyrin-B mutation causes type 4 long-QT cardiac arrhythmia and sudden cardiac death. *Nature* 421, 634–639. doi: 10.1038/nature01335
- Nivala, M., Korge, P., Nivala, M., Weiss, J. N., and Qu, Z. (2011). Linking flickering to waves and whole-cell oscillations in a mitochondrial network model. *Biophys. J.* 101, 2102–2111. doi: 10.1016/j.bpj.2011.09.038
- Palty, R., Silverman, W. F., Hershfinkel, M., Caporale, T., Sensi, S. L., Parnis, J., et al. (2010). NCLX is an essential component of mitochondrial Na<sup>+</sup>/Ca<sup>2+</sup> exchange. *Proc. Natl. Acad. Sci. U.S.A.* 107, 436–441. doi: 10.1073/pnas.0908091107
- Pandey, V., Xie, L., Id, Z. Q., and Id, Z. S. (2021). Mitochondrial depolarization promotes calcium alternans: mechanistic insights from a ventricular myocyte model. *PLoS Comput. Biol.* 17:e1008624. doi: 10.1371/journal.pcbi.1008624
- Pogwizd, S. M., and Bers, D. M. (2003). Calcium cycling in heart failure. *Respir. Circ.* 51, 67–76.
- Qu, Z., Gang, H., Garfinkel, A., and Weiss, J. N. (2014). Nonlinear and stochastic dynamics in the Heart. *Phys. Rep.* 543, 61–162. doi: 10.1038/jid.2014.371
- Rosen, M. R., Moak, J. P., and Damiano, B. (1984). The clinical relevance of afterdepolarizations. *Ann. N. Y. Acad. Sci.* 427, 84–93.
- Ross, J. L., and Howlett, S. E. (2009).  $\beta$ -Adrenoceptor stimulation exacerbates detrimental effects of ischemia and reperfusion in isolated guinea pig ventricular myocytes. *Eur. J. Pharmacol.* 602, 364–372. doi: 10.1016/j.ejphar.2008.11.034
- Sakamoto, J., and Tonomura, Y. (1980). Order of release of ADP and Pi from phosphoenzyme with bound ADP of Ca<sup>2+</sup>-dependent ATPase from sarcoplasmic reticulum and of Na<sup>+</sup>, K<sup>+</sup>-dependent ATPase studied by ADP-inhibition patterns. *J. Biochem.* 87, 1721–1727. doi: 10.1093/oxfordjournals.jbchem.a132916
- Santulli, G., Xie, W., Reiken, S. R., and Marks, A. R. (2015). Mitochondrial calcium overload is a key determinant in heart failure. *Proc. Natl. Acad. Sci. U.S.A.* 112, 11389–11394. doi: 10.1073/pnas.1513047112
- Shimizu, H., Schredelseker, J., Huang, J., Lu, K., Naghdi, S., Lu, F., et al. (2015). Mitochondrial Ca<sup>2+</sup> uptake by the voltage-dependent anion channel 2 regulates cardiac rhythmicity. *eLife* 4, 1–20. doi: 10.7554/eLife.04801
- Soeller, C., and Cannell, M. B. (1999). Examination of the transverse tubular system in living cardiac rat myocytes by 2-photon microscopy and digital image-processing techniques. *Circ. Res.* 84, 266–275. doi: 10.1161/01.RES.84.3.266
- Song, Z., Liu, M. B., and Qu, Z. (2018). Transverse tubular network structures in the genesis of intracellular calcium alternans and triggered activity in cardiac cells. *J. Mol. Cell. Cardiol.* 114, 288–299. doi: 10.1016/j.jmcc.2017.12.003
- Song, Z., Qu, Z., and Karma, A. (2017). Stochastic initiation and termination of calcium-mediated triggered activity in cardiac myocytes. *Proc. Natl. Acad. Sci. U.S.A.* 114, E270–E279. doi: 10.1073/pnas.1614051114
- Song, Z., Xie, L. H., Weiss, J. N., and Qu, Z. (2019). A spatiotemporal ventricular myocyte model incorporating mitochondrial calcium cycling. *Biophys. J.* 117, 2349–2360. doi: 10.1016/j.bpj.2019.09.005
- Wagner, S., Rokita, A. G., Anderson, M. E., and Maier, L. S. (2013). Redox regulation of sodium and calcium handling. *Antioxidants Redox Signal.* 18, 1063–1077. doi: 10.1089/ars.2012.4818
- Wang, W., Shen, W., Zhang, S., Luo, G., Wang, K., Xu, Y., et al. (2020). The Role of CaMKII overexpression and oxidation in atrial fibrillation—A simulation study. *Front. Physiol.* 11:607809. doi: 10.3389/fphys.2020.607809
- Watanabe, H., Chopra, N., Laver, D., Hwang, H. S., Davies, S. S., Roach, D. E., et al. (2009). Flecainide prevents catecholaminergic polymorphic ventricular tachycardia in mice and humans. *Nat. Med.* 15, 380–383. doi: 10.1038/nm.1942
- Wehrens, X. H. T., Lehnart, S. E., Reiken, S. R., and Marks, A. R. (2004). Ca<sup>2+</sup>/calmodulin-dependent protein kinase II phosphorylation regulates the cardiac ryanodine receptor. *Circ. Res.* 94, e61–e70. doi: 10.1161/01.res.0000125626.33738.e2
- Williams, G. S. B., Boyman, L., Chikando, A. C., Khairallah, R. J., and Lederer, W. J. (2013). Mitochondrial calcium uptake. *Proc. Natl. Acad. Sci. U.S.A.* 110, 10479–10486. doi: 10.1073/pnas.1300410110
- Xiao, R. P., Cheng, H., Lederer, W. J., Suzuki, T., and Lakatta, E. G. (1994). Dual regulation of Ca<sup>2+</sup>/calmodulin-dependent kinase II activity by membrane voltage and by calcium influx. *Proc. Natl. Acad. Sci. U.S.A.* 91, 9659–9663. doi: 10.1073/pnas.91.20.9659
- Xie, A., Song, Z., Liu, H., Zhou, A., Shi, G., Wang, Q., et al. (2018). Mitochondrial Ca<sup>2+</sup> influx contributes to arrhythmic risk in nonischemic cardiomyopathy. *J. Am. Heart Assoc.* 7, 1–20. doi: 10.1161/JAHA.117.007805
- Xie, L. H., Fuhua, C., Karagueuzian, H. S., and Weiss, J. N. (2009). Oxidative stress-induced afterdepolarizations and calmodulin kinase II signaling. *Circ. Res.* 104, 79–86. doi: 10.1161/CIRCRESAHA.108.183475.Oxidative
- Xie, W., Santulli, G., Reiken, S. R., Yuan, Q., Osborne, B. W., Chen, B. X., et al. (2015). Mitochondrial oxidative stress promotes atrial fibrillation. *Sci. Rep.* 5, 1–11. doi: 10.1038/srep11427
- Yan, Y., Liu, J., Wei, C., Li, K., Xie, W., Wang, Y., et al. (2008). Bidirectional regulation of Ca<sup>2+</sup> sparks by mitochondria-derived reactive oxygen species in cardiac myocytes. *Cardiovasc. Res.* 77, 432–441. doi: 10.1093/cvr/cvm047
- Yang, L., Korge, P., Weiss, J. N., and Qu, Z. (2010). Mitochondrial oscillations and waves in cardiac myocytes: insights from computational models. *Biophys. J.* 98, 1428–1438. doi: 10.1016/j.bpj.2009.12.4300
- Yuan, W., and Bers, D. M. (1994). Ca-dependent facilitation of cardiac Ca current is due to Ca-calmodulin-dependent protein kinase. *Am. J. Physiol.* 267(3 Pt 2), 982–993.
- Zhao, Z., Gordan, R., Wen, H., Fefelova, N., Zang, W. J., and Xie, L. H. (2013). Modulation of intracellular calcium waves and triggered activities by

- mitochondrial Ca flux in mouse cardiomyocytes. *PLoS One* 8:e0080574. doi: 10.1371/journal.pone.0080574
- Zhou, L., Aon, M. A., Almas, T., Cortassa, S., Winslow, R. L., and O'Rourke, B. (2010). A reaction-diffusion model of ROS-induced ROS release in a mitochondrial network. *PLoS Comput. Biol.* 6:e1000657. doi: 10.1371/journal.pcbi.1000657
- Zhou, L., Aon, M. A., Liu, T., and O'Rourke, B. (2011). Dynamic modulation of Ca<sup>2+</sup> sparks by mitochondrial oscillations in isolated guinea pig cardiomyocytes under oxidative stress. *J. Mol. Cell. Cardiol.* 51, 632–639. doi: 10.1016/j.yjmcc.2011.05.007
- Zima, A. V., and Blatter, L. A. (2006). Redox regulation of cardiac calcium channels and transporters. *Cardiovasc. Res.* 71, 310–321. doi: 10.1016/j.cardiores.2006.02.019
- Zorov, D. B., Filburn, C. R., Klotz, L. O., Zweier, J. L., and Sollott, S. J. (2000). Reactive oxygen species (ROS)-induced ROS release: a new phenomenon accompanying induction of the mitochondrial permeability transition in cardiac myocytes. *J. Exp. Med.* 192, 1001–1014. doi: 10.1084/jem.192.7.1001
- Zorov, D. B., Juhaszova, M., and Sollott, S. J. (2006). Mitochondrial ROS-induced ROS release: an update and review. *Biochim. Biophys. Acta Bioenerg.* 1757, 509–517. doi: 10.1016/j.bbabo.2006.04.029
- Conflict of Interest:** The authors declare that the research was conducted in the absence of any commercial or financial relationships that could be construed as a potential conflict of interest.
- Publisher's Note:** All claims expressed in this article are solely those of the authors and do not necessarily represent those of their affiliated organizations, or those of the publisher, the editors and the reviewers. Any product that may be evaluated in this article, or claim that may be made by its manufacturer, is not guaranteed or endorsed by the publisher.
- Copyright © 2021 Pandey, Xie, Qu and Song. This is an open-access article distributed under the terms of the Creative Commons Attribution License (CC BY). The use, distribution or reproduction in other forums is permitted, provided the original author(s) and the copyright owner(s) are credited and that the original publication in this journal is cited, in accordance with accepted academic practice. No use, distribution or reproduction is permitted which does not comply with these terms.





# Pacing Electrocardiogram Detection With Memory-Based Autoencoder and Metric Learning

Zhaoyang Ge<sup>1,2</sup>, Huiqing Cheng<sup>1,2</sup>, Zhuang Tong<sup>3</sup>, Lihong Yang<sup>4\*</sup>, Bing Zhou<sup>1,2</sup> and Zongmin Wang<sup>1,2</sup>

<sup>1</sup> School of Information Engineering, Zhengzhou University, Zhengzhou, China, <sup>2</sup> Cooperative Innovation Center of Internet Healthcare, Zhengzhou University, Zhengzhou, China, <sup>3</sup> Big Data Center of Clinical Medicine, The First Affiliated Hospital of Zhengzhou University, Zhengzhou, China, <sup>4</sup> Department of Cardio-Pulmonary Function, Henan Provincial People's Hospital, Zhengzhou, China

## OPEN ACCESS

### Edited by:

Henggui Zhang,  
The University of Manchester,  
United Kingdom

### Reviewed by:

M. Sabarimalai Manikandan,  
Indian Institute of Technology  
Bhubaneswar, India  
Honghua Dai,  
Deakin University, Australia

### \*Correspondence:

Lihong Yang  
ylhzyq@126.com

### Specialty section:

This article was submitted to  
Computational Physiology and  
Medicine,  
a section of the journal  
Frontiers in Physiology

**Received:** 18 June 2021

**Accepted:** 16 November 2021

**Published:** 17 December 2021

### Citation:

Ge Z, Cheng H, Tong Z, Yang L,  
Zhou B and Wang Z (2021) Pacing  
Electrocardiogram Detection With  
Memory-Based Autoencoder and  
Metric Learning.  
Front. Physiol. 12:727210.  
doi: 10.3389/fphys.2021.727210

Remote ECG diagnosis has been widely used in the clinical ECG workflow. Especially for patients with pacemaker, in the limited information of patient's medical history, doctors need to determine whether the patient is wearing a pacemaker and also diagnose other abnormalities. An automatic detection pacing ECG method can help cardiologists reduce the workload and the rates of misdiagnosis. In this paper, we propose a novel autoencoder framework that can detect the pacing ECG from the remote ECG. First, we design a memory module in the traditional autoencoder. The memory module is to record and query the typical features of the training pacing ECG type. The framework does not directly feed features of the encoder into the decoder but uses the features to retrieve the most relevant items in the memory module. In the training process, the memory items are updated to represent the latent features of the input pacing ECG. In the detection process, the reconstruction data of the decoder is obtained by the fusion features in the memory module. Therefore, the reconstructed data of the decoder tends to be close to the pacing ECG. Meanwhile, we introduce an objective function based on the idea of metric learning. In the context of pacing ECG detection, comparing the error of objective function of the input data and reconstructed data can be used as an indicator of detection. According to the objective function, if the input data does not belong to pacing ECG, the objective function may get a large error. Furthermore, we introduce a new database named the pacing ECG database including 800 patients with a total of 8,000 heartbeats. Experimental results demonstrate that our method achieves an average F1-score of 0.918. To further validate the generalization of the proposed method, we also experiment on a widely used MIT-BIH arrhythmia database.

**Keywords:** electrocardiogram signals, autoencoder, heartbeat arrhythmias detection, metric learning, attention mechanism

## 1. INTRODUCTION

The electrocardiogram (ECG) is an important tool in the everyday practice of clinical medicine (Hannun et al., 2019), especially for patients who are fitted with a pacemaker. The application of a pacemaker effectively alleviates the condition of patients with heart disease and extends the survival period of patients. But these patients require regular in-hospital checks of the pacemaker

and cardiac abnormalities. Therefore, remote cardiac monitoring for pacemaker patients becomes increasingly important. To find cardiac abnormalities in time, computer-aided diagnosis provides real-time ECG analysis without any manual intervention by physicians.

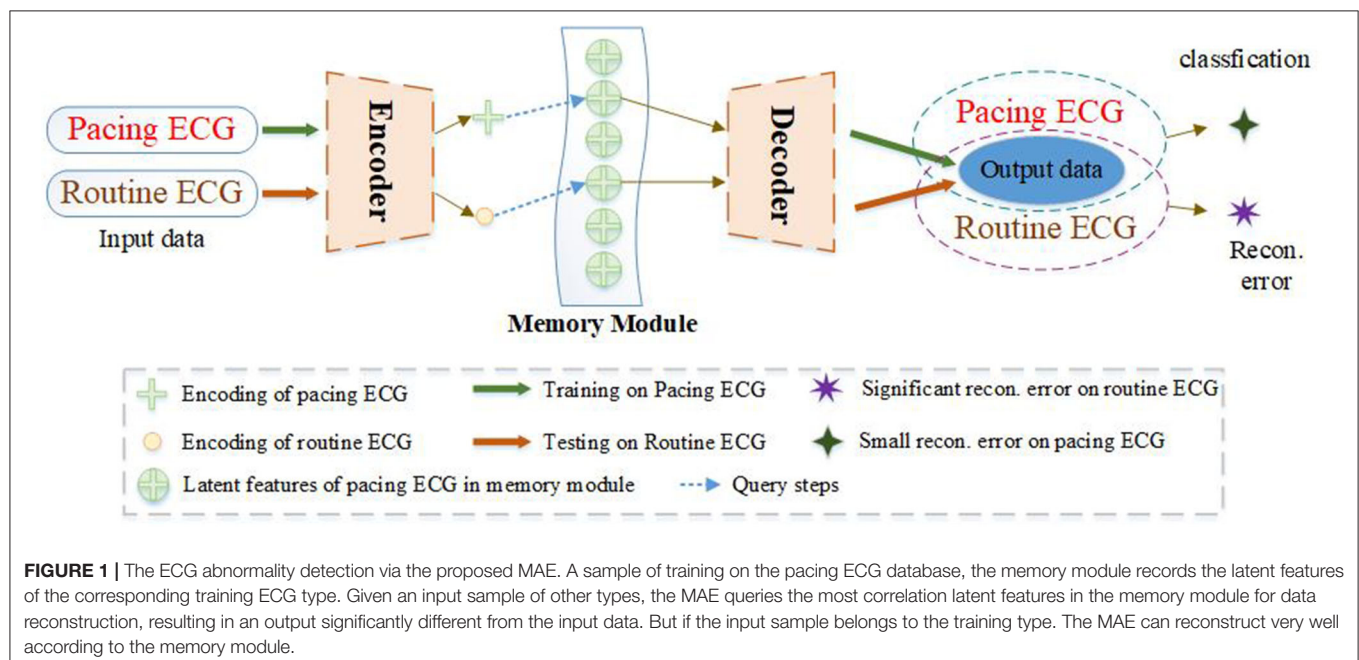
The pacing ECG detection still confronts many challenges. First, the procedure of remote ECG diagnosis only contains ECG signals from the patients, and doctors cannot check the patient's medical history in advance. Second, there are different performances in morphological features between pacing ECG and routine ECG for the same disease. And in clinical ECG data, the ECG morphology of the pacemaker patient is interfered with by the pacemaker, which brings disturbance to the ECG abnormality diagnosis. For example, ventricular pacing is often confused with the left bundle branch block of routine ECG. Suppose we do not inform the doctor that the remote ECG data comes from a pacemaker patient. In that case, the doctor may diagnose certain pacing heart rhythms as other abnormalities of the routine ECG. To solve the above problems, we constructed an extensive, novel ECG database named Pacing ECG Database, which includes 800 samples of ECG data annotated by the clinician. To the best of our knowledge, this is the first ECG signals database faced with pacing ECG. The automatic recognition of the pacemaker provides a solid guide to distinguish abnormal ECG accurately, which can improve the performance of abnormal ECG classification.

Motivated by the recent success of autoencoder as a time series detection tool, several promising autoencoder for ECG abnormality detection have been proposed. Specifically, it is generally assumed that the reconstruction error trained by the traditional autoencoder will be lower for the training data

of the input type. In contrast, reconstruction error becomes significant for other abnormalities. Therefore, the autoencoder (AE) is trained by minimizing the reconstruction error in each class and then utilizes an objective function based on reconstruction error to classify ECG abnormalities. However, many works have proved that autoencoder's generalization ability can sometimes well express other abnormal samples that the inputs do not belong to the training type (Zong et al., 2018; Gong et al., 2019). This is because the decoder is powerful for decoding some abnormal encodings well, so the AE sometimes also gets a lower reconstruction error for other ECG abnormalities.

To improve the drawback of traditional AEs, we propose a new model of memory-based autoencoder (MAE) for pacing ECG detection, as illustrated in **Figure 1**. In the MAE model, we first utilize a deep autoencoder to extract the typical features of high-dimensional ECG data. But the decoder of MAE does not directly reconstruct the data from the encoding. We added a memory module between the encoder and decoder. The memory module is to record and query the typical features of the training pacing ECG type. MAE does not directly feed features of encoder into the decoder but uses the features to retrieve the most relevant items in memory module. Those features are aggregated and delivered to the decoder. Meanwhile, we further utilize a sparse coding strategy to induce sparsity for the memory module, which can easily match the memory items to the query of the feature space.

We are also inspired by metric learning. The goal of metric learning is to learn a distance metric that puts the same positive types close together and negative types far away. In this paper, the MAE is trained by minimizing the error of objective function on the pacing ECG and then uses the error of objective function as



an indicator of pacing ECG detection. In the training process, the features of the pacing ECG are learned and stored by the MAE model. The purpose is to obtain a lower reconstruction error for pacing ECG. In the detection process, the reconstruction data of the decoder is fused with the features in the memory module. Because the reconstruction data is obtained from the feature of the pacing ECG in the memory module, the output of the decoder tends to be close to the pacing ECG. In the results, if the input data does not belong to pacing ECG, the objective function may get a significant error. The proposed MAE is not only for detecting the pacing ECG but also can be applied to solve other ECG abnormality detection. We also apply the proposed MAE on the MIT-BIH Arrhythmia Database. The experiments prove the excellent generalization and effectiveness of the model.

To summarize, the contributions of this paper are as follows.

- (1) A novel autoencoder framework named MAE is proposed to detect the pacing ECG. The memory module is added between the encoder and decoder. The memory module is used to record the features of the training data.
- (2) We introduce a new objective function that is based on metric learning, which can better represent the error among the different types. Because of the memory module, the reconstruction tends to be close to the training types. When the input types are not similar to the training types, the objective function has a significant score.
- (3) We collect a new database named Pacing ECG Database for evaluation of the MAE framework. The database includes 800 annotated samples and each ECG data is de-identified according to the privacy policy.
- (4) The experiments conducted on Pacing ECG Database, demonstrate that the proposed MAE reliably improves the performance of pacing ECG. To further validate the generalization, the MAE framework is also applied on MIT-BIH Arrhythmia Database and is superior to the state-of-the-art detectors.

This reminder of the paper is organized as follows. Section 2 presents the related works. Section 3 introduces the proposed memory-based autoencoder method. The experimental results and analysis are given in section 4. Finally, section 5 concludes this paper.

## 2. RELATED WORK

In recent years, many approaches have been proposed to automatically process physiological signals in the field of artificial intelligence (Gao et al., 2018; Wang et al., 2020; Yao et al., 2020; Zhou and Tan, 2020). For abnormal ECG detection, the performance is consistently improved in terms of accuracy on major challenges and benchmarks, such as MIT-BIH (Moody and Mark, 2001), CPSC\_2018 (Liu et al., 2018a). Nevertheless, there are few solutions for pacing ECG, which pacing ECG is only regarded as a kind of ECG abnormality in the classification task. In this paper, we focus on improving the accuracy detection of pacing ECG.

### 2.1. ECG Abnormality Classification

Cardiovascular diseases can be divided into cardiomyopathy, ischemic heart disease, myocardial infarction and so on (Hao et al., 2021). Many clinicians focused on using computer-aided diagnosis to detect one of the heart diseases (Baloglu et al., 2019). For example, Adam et al. (2018) focused on classifying hypertrophic heart disease, dilated cardiomyopathy, hypertrophic cardiomyopathy. Many researchers are interested in studying ECG bundle branch block, which is heart disease with high mortality. It can be divided into the left bundle branch block (LBBB) and the right bundle branch block (RBBB) (Zhang et al., 2012). There is also a part of clinical research that focused on the use of electrocardiograms to detect specific abnormalities such as myocardial infarction (Liu et al., 2018b; Baloglu et al., 2019).

Some approaches have been devoted to improving the performance of ECG abnormality diagnosis in recent years (Mondéjar-Guerra et al., 2019; Hao et al., 2021; Wang et al., 2021). The signal processing is essential for clinical monitoring. Typically, one kind of methods (Mondéjar-Guerra et al., 2019; Wang et al., 2021) is to diagnose ECG on features of high-dimensional space with rich fine features of ECG abnormalities. In previous studies on ECG abnormality classification, which focused on preprocessing to segment the raw ECG sequence to heartbeats (Sodmann and Vollmer, 2020). And then, feature descriptions of abnormal ECG are calculated from the heartbeats (Sangaiah et al., 2020), for example, RR interval features extraction (Chen et al., 2017), wavelets (Mar et al., 2011; He et al., 2018), higher-order statistics (HOS) (Osowski and Tran, 2001). Other methods based on deep learning can learn useful features from raw ECG data without requiring signal preprocessing (Fan et al., 2018; Ma et al., 2020). A series of typical strategies focus on designing network architecture to extract multiple features to improve ECG abnormality classification accuracy. However, in practice, these methods need a sufficient amount of handcraft labels or features.

Recent studies of ECG abnormality classification have concentrated on deep learning (Hannun et al., 2019; Saadatnejad et al., 2020; Zhang et al., 2020). A convolutional neural network (CNN) is an effective method for extracting features due to its local connectivity and parameter sharing. Hannun et al. (2019) developed a 34-layer CNN that classifies 12 types of ECG signals and achieves cardiologist-level performance. The RNN-based (Wang et al., 2018; Chen et al., 2020) method, such as the Gated Recurrent Unit (Zhang et al., 2019), the Long Short Term Memory (Tan et al., 2018; Saadatnejad et al., 2020), is a type of neural network used for processing ECG signal. The RNN is used to extract global features and then classified the ECG abnormalities. Saadatnejad et al. (2020) proposed a continuous and real-time patient-specific ECG classification algorithm based on wavelet transform and multiple LSTM. Other effective methods (Chen et al., 2020; Wang et al., 2020; Yao et al., 2020) to develop the architectures combining CNN with RNN for detecting multi-class ECG abnormalities. But in these works of ECG diagnosis, the pacing rhythm is only detected as a kind of ECG abnormality.

## 2.2. Autoencoder

The autoencoder belongs to unsupervised tasks of deep learning and does not need data annotation for training samples. The autoencoder is composed of three layers, in which the number of neurons in the input layer is the same as the number of neurons in the output layer, and the number of neurons in the middle layer is less than that of the input and output layer. During the training phase, for each training sample, a new signal will be generated in the output layer through the network. The purpose of training is to make the output signal and the input signal as similar as possible. In the testing phase of autoencoder, it can be composed of two parts. The first part is the input layer and the middle layer, which can use to compress the signal. The second part is the middle layer and the output layer, which can restore the compression signal.

With the development of artificial intelligence, it is already widely applied to many areas such as bioinformatics (Oyetunde et al., 2018), engineering technology (Samaniego et al., 2020) and clinical medicine (Chen et al., 2018). Thinsungnoen et al. (2018) proposed the deep autoencoder (AE) which is a powerful tool to deal with the high-dimensional data in the unsupervised task of processing ECG signals. They have great success in some application domains as well, such as denoising autoencoders (DAEs) (Dasan and Panneerselvam, 2021), ECG data dimension reduction (Wang et al., 2013). And a series of work has been conducted in ECG data classification using an autoencoder model. However, in practice, the pacemaker can interfere with the ECG signal. It often leads to the morphological difference between cases with pacemaker and cases without pacemaker in the same ECG abnormality. Lack of pacing ECG data has limited many models design for abnormal ECG classification. Meanwhile, the existing autoencoder for ECG classification algorithms still has a misdiagnosis rate. Therefore, we collect a large pacing ECG database and design a novel autoencoder model to detect the pacing ECG.

Traditional autoencoders are mainly used for ECG signal reconstruction. For example, Majumdar et al. (2016) design a stacked autoencoder (SAE) model which mainly uses semi-supervised deep learning approach for ECG signal reconstruction. In the research of industrial anomaly detection, Hasan et al. (2016) use the reconstruction error of a convolutional AE to detect the anomalies in video sequences. However, these methods neglect the generalization capability of the autoencoder model and lack a mechanism to encourage the autoencoders to produce larger reconstruction errors for abnormalities.

Recently, existing a novel method introduces the memory-augmented networks to solve the anomaly detection by reconstructing the input data (Kim et al., 2018). Gong et al. (2019) detect the anomalies according to the reconstruction error of a memory-augmented AE. The memory module can record features stably. Santoro et al. (2016) use the idea to handle the one-shot learning problem. These methods show significant performance gain, especially for anomaly detection. However, these algorithms only detect one class, which makes them infeasible for ECG diagnosis.

The previous work focused on the autoencoder conduct to deal with the issue of data imbalanced or noise reduction. Inspired by these methods, we propose the MAE model using an attention-based memory module to record latent features of corresponding ECG abnormalities. We also propose a quantitative assessment criterion to cluster each ECG abnormality type. Then, we verify the performance of our model on different databases. The proposed MAE model shows drastic improvements for ECG abnormality diagnosis.

## 3. METHOD

Previous AE architectures for ECG signal processing focused on data denoising and data dimensionality reduction. In this paper, we propose a novel autoencoder architecture containing a memory module that can record the latent features of the training type, as shown in **Figure 2**. And we also introduce a new objective function that can calculate a similarity score between the output of the decoder and the input data. As a result, we define the estimated score of the data as the clustering criteria. This makes the proposed MAE model especially suitable for ECG abnormality classification.

### 3.1. Encoder and Decoder

The encoder of MAE model can obtain the features from input data, which is beneficial for data dimension reduction. The features can be used as a key to match the relevant features in the memory module. In our method, the output of the encoder can be seen as a generator of a feature dictionary. The decoder is trained to reconstruct the samples by taking the retrieved memories as input.

In this paper, we consider multi-channel time-series recordings of ECG. We first define  $X$  to represent the domain of the ECG data samples. Each ECG is a multivariate time-series where the rows define the channel dimension, and the columns capture the time dimension. One ECG sample is represented by the following matrix  $x_i = \{x_i^1, x_i^2, \dots, x_i^C\} \in \mathbb{X}^{C \times T}$  where  $C$  denotes the channels of ECG sequence and  $T$  is the number of sample points per channel. Our MAE architecture is first composed of an encoder, where  $Z$  represents the domain of the encodings. Let  $f_e(X) \rightarrow Z$  denote the encoder. The encoder aims to provide a low dimensional latent representation domain  $Z$  from the input data domain  $X$ . Given a sample  $x_i \in X$ , the encoder converts it to an encoded representation as  $z_i \in Z$ , as follows:

$$z_i = f_e(x_i; \theta_e), \quad (1)$$

where  $\theta_e$  denotes the parameters of the encoder  $f_e$ .

The second half of the MAE model architecture contains a decoder, which aims to reconstruct the samples. Let  $f_d(Z) \rightarrow X$  denote the decoder. And the decoder is trained to reversely mapping a latent representation  $\hat{z}_i \in Z$  to the domain  $X$ . It should be specially explained that the proposed MAE model is different from the standard AE model. For tradition AE model, the  $\hat{z}_i$  should be  $z_i$ . But in this paper, the latent features  $z_i$  in the training phase are stored in the feature dictionary, and in the testing phase



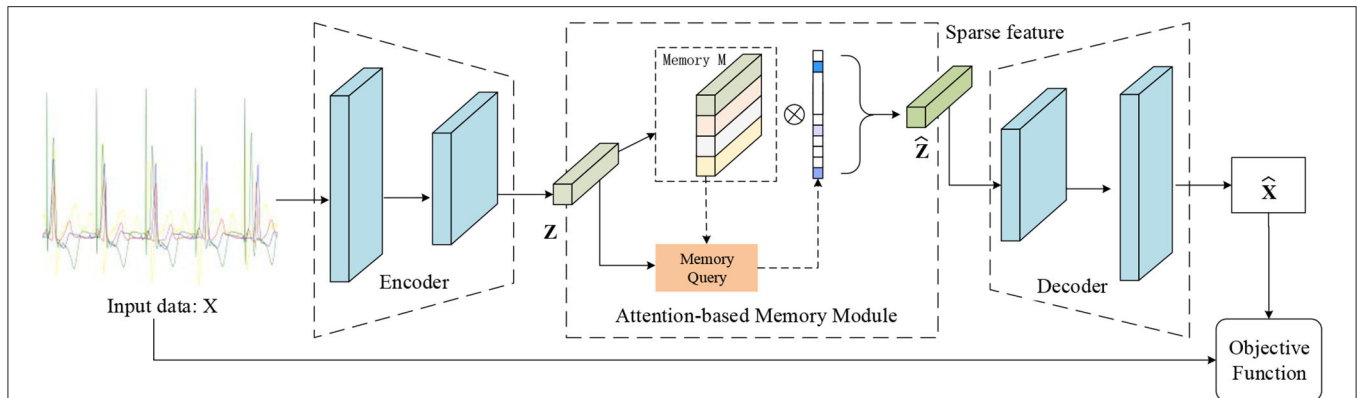


**FIGURE 2 |** Illustration of the proposed MAE model. The memory module records latent features and the memory query can obtain the weight of the degree of similarity between the features of input data and the record features. Note that the output of the memory module is the input of the decoder.

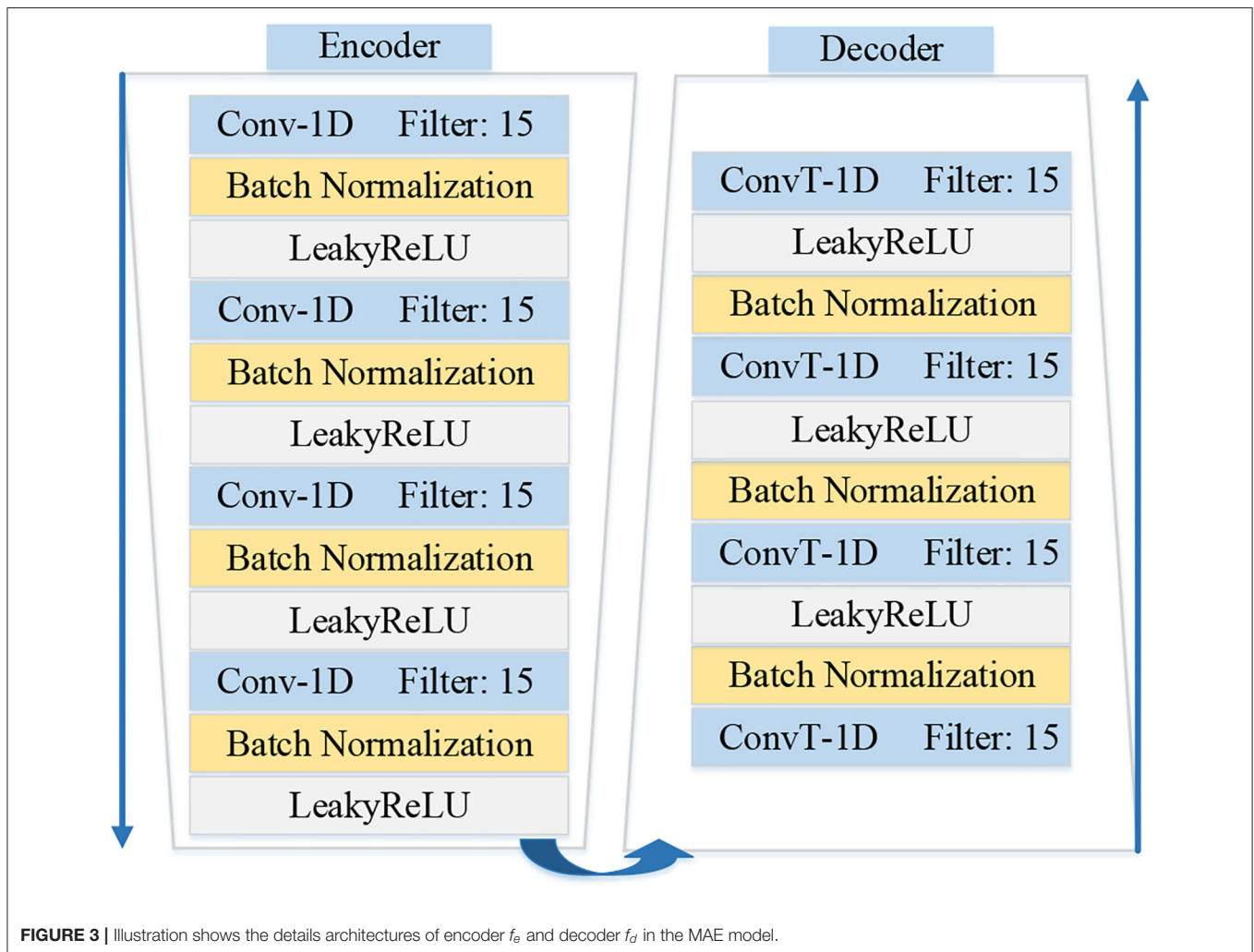


**FIGURE 3 |** Illustration shows the details architectures of encoder  $f_e$  and decoder  $f_d$  in the MAE model.

are regarded as a keyword to query, and  $\hat{z}_i$  is obtained from the memory unit, as follows:

$$\hat{x}_i = f_d(\hat{z}_i; \theta_d), \quad (2)$$

where  $\theta_d$  denotes the parameters of the decoder  $f_d$ .

The architectures of encoder  $f_e$  and decoder  $f_d$  are shown in **Figure 3**. The architecture of the encoder contains four one-dimensional convolutional layers. And each convolutional

layer is followed by a normalization layer and an activation layer. The convolution layers with the kernel size of  $1 \times 15$  are applied to capture the latent features. The fractionally-strided convolution is used in the decoder, which is often used to enlarge the size of the image in image processing. The operation of the fractionally-strided convolution and the normal convolution is exactly the opposite. In this paper, we use the fractionally-strided convolution to restore the input ECG signal type from the low-dimensional latent features.

### 3.2. Attention-Based Memory Module

The purpose of the memory module is to record the most representative features in the input pacing data during training. The above section encoder converts the input data to the internal feature representation. The memory module can be regarded as a dictionary  $D$  with a querying scheme and is designed as a matrix  $D \in R^{N \times C}$  containing  $N$  real-valued vectors of fixed dimension and to record the prototypical correlation internal feature of pacing ECG during training. The output feature map  $\hat{z}$  of memory unit combines the new input  $z$  with the entry in current memory state  $k$ , where  $k \in R^{1 \times N}$  is a row vector with non-negative entries that sum to one. The weight vector  $k$  is computed according to  $z$ . The output of latent features  $\hat{z}$  will be obtained via  $\hat{z} = k \cdot D$ .

Let the row vector  $m_i, \forall i \in \{1, 2, \dots, N\}$  denote the  $i$ -th row of  $D$ , where  $\{N\}$  denotes the set of integers from 1 to  $N$ . Each  $m_i$  denotes the item in the dictionary  $D$ . The parameter  $N$  defines the maximum capacity of the memory unit. The typical memory module is developed to query prototypical pacing ECG features, as illustrated in **Figure 2**.

To be specific, we first introduce a query strategy that computes attention weights  $k_i$  based on the similarity of the items of the dictionary and the input feature  $z$ . Each weight  $k_i$  is computed via a softmax operation:

$$k_i = \frac{\exp(d(z, m_i))}{\sum_{j=1}^N \exp(d(z, m_j))}, \quad (3)$$

where  $d(z, m_i)$  denotes a correlation measurement between  $z$  and  $m_i$ . Following the work, we define function of  $d(z, m_i)$  as cosine similarity:

$$d(z, m_i) = \frac{z \cdot m_i^T}{\|z\| \cdot \|m_i\|}, \quad (4)$$

Then, considering that the low-level features are more cluttered, some other group of ECG abnormalities may still have the chance to be reconstructed into the pacing ECG. To alleviate this issue, we apply a sparse coding strategy to promote the sparsity of  $k_i$ . Sparse coding strategy encourages the model to represent a sample of pacing ECG using fewer but more relevant memory items, leading to learning more features from the memory unit. We define the sparse coding following the work Gong et al. (2019). Considering that all entries in  $k$  are non-negative, the sparse coding strategy is redefined via the continuous ReLU activation function as

$$\hat{k}_i = \frac{\max(k_i - \alpha, 0) \cdot k_i}{|k_i - \alpha| + \epsilon}, \quad (5)$$

where  $\hat{k}_i$  represents the  $i$ -th entry in current memory state  $k$ , the  $\max(k_i - \alpha, 0)$  is also obtained as Relu activation. The  $\alpha$  is a sparse threshold which is set the value in the interval  $[1/N, 3/N]$ . And  $\epsilon$  is a very small positive scalar.

Finally, we normalize the weight vector  $\hat{k}$  by letting  $\hat{k}_i = k_i / \|\hat{k}\|$ . Therefore, the output  $\hat{z}_i$  of memory unit is defined as.

$$\hat{z} = \hat{k} \cdot D = \sum_{i=1}^N \hat{k}_i \cdot m_i, \quad (6)$$

### 3.3. Training and Testing

Given a database  $X$  containing  $N$  samples, let  $\hat{x}_i$  denote the reconstructed sample corresponding each input sample  $x_i$ . In the training phase, the  $L(x, \hat{x})$  is used to measure the reconstruction error:

$$L(x, \hat{x}) = \frac{1}{n} \sum \|x_i - \hat{x}_i\|^p, \quad (7)$$

where  $p$  is set to 1 or 2 in our paper. When  $p = 1$ , formula 7 is the mean absolute error, which can also be regarded as the L1-loss. When  $p = 2$ , formula 7 can be regarded as the mean square error, which is L2-loss. Due to the ECG abnormality diagnosis application scenario, we design ablation experiments to find the optimum value of  $p$ .

Due to the memory module of the testing phase, the learned memory content is fixed. Only the feature in the dictionary of the training type in the memory module can be retrieved for reconstruction. Thus the samples of one type can be reconstructed well. Conversely, the encoding of another ECG abnormality input will be replaced by the retrieved trained features, resulting in significant reconstruction error on this input data.

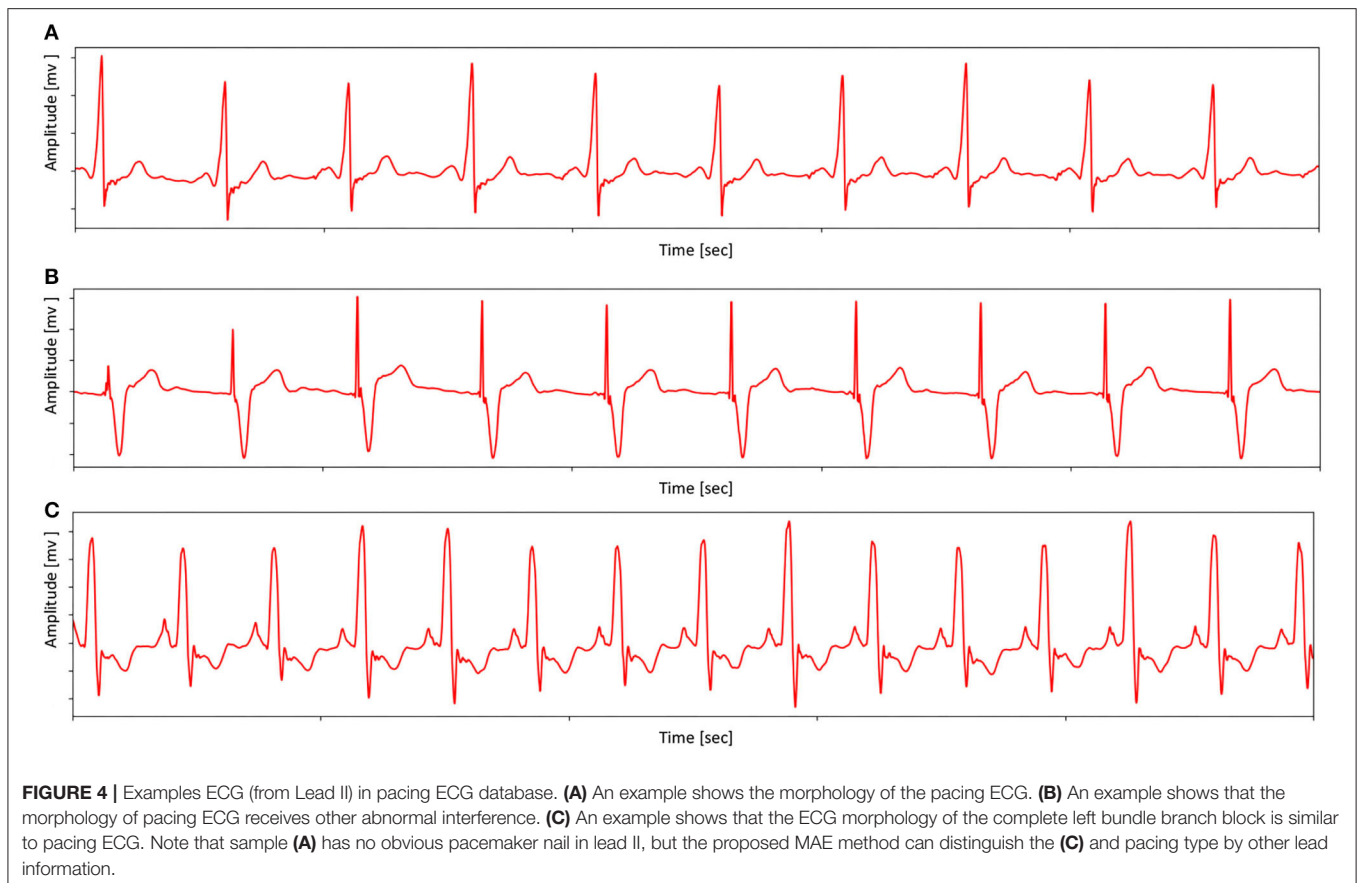
In the testing phase, we also need to define the rule to classify ECG abnormalities according to the MAE model. For example, given an input ECG data  $x_i$  and the reconstruction error are used to determine the classification.  $P_n$  denoted that the samples are the class of target domain  $n$ . Therefore, we define the set of samples in the target domain as:

$$T(x_i) = \left\{ x_i \in P_n, \text{ with } \|x_i - f_{d_n}(f_{e_n}(x_i; \theta_e); \theta_d)\|^p \leq \|x_i - f_{d_q}(f_{e_q}(x_i; \theta_e); \theta_d)\|^p \right\}, \quad (8)$$

where, the  $f_{e_n}$  and  $f_{d_n}$  represent the operation of encoder and decoder which the training phase records the latent features of target class  $n$  in the memory module. The  $f_{e_q}$  and the  $f_{d_q}$  represent the operation of encoder and decoder in which the training phase records the latent features of target class  $q$  in the memory module. This equation essentially defines the distance relationship between samples of the same classes and samples of different classes.

## 4. EXPERIMENTS

In this section, we validate the proposed MAE framework for pacing ECG detection. Meanwhile, to show the applicability



of the method, we also conduct experiments on the MIT-BIH Arrhythmia Database. First, the evaluation metric used in the experiments will be introduced. The quality and performance of the proposed MAE framework are evaluated by utilizing standard metrics: precision, recall, and f1-score. And then, the experimental database will be described. Finally, we present the experimental results and analysis. Additionally, the results are compared with other methods of ECG abnormality detection.

## 4.1. Evaluation Metric

In this paper, typical classification metrics, including precision, recall, and F1-score were used for each class. Precision is the ratio of the number of correct positive predictions to the total number of positive predictions. Recall is the ratio of the number of correct positive predictions to the total number of true positive and false negatives. F1-score is the weighted average of precision and recall. They are defined as:

$$\text{Precision}(+p) = \frac{TP}{TP + FP}, \quad (9)$$

$$\text{Recall}(Rec) = \frac{TP}{TP + FN}, \quad (10)$$

$$F1 - score = \frac{2 \times \text{Precision} \times \text{Recall}}{\text{Precision} + \text{Recall}}, \quad (11)$$

where  $TP$ ,  $TN$ ,  $FP$ , and  $FN$  represent the numbers of true positives, true negatives, false positives, and false negatives, respectively.

## 4.2. Experiments on Pacing-ECG Detection

### 4.2.1. The Pacing-ECG Database

The professional database plays a more important role in automatic ECG diagnosis than the algorithm and employed techniques. One of the obstacles in the research on fully automatic analysis in ECG is the insufficient quantity of available databases (Shen et al., 2020).

In this paper, we collect an extensive, novel ECG database named Pacing ECG Database. The pacing ECG database can be used to evaluate the proposed MAE framework. It should be noted that all extracted data were de-identified according to the privacy policy. Fully de-identified patient data can be used for research purposes. The main goal is to detect the morphology of pacing ECG from various interferences. And some of the samples may contain other abnormalities in the pacing ECG database. We aim to distinguish between the sample with a pacemaker and the sample without a pacemaker under the interference of these abnormalities.

The pacing ECG database contains 800 recordings of data annotated by the clinician lasting for 10 s, sampled at 500 Hz. Each sample acquired by the device is all 12-lead (channel) ECGs, digitized at 500 samples per second per channel and lasting for 10

**TABLE 1** | The specific data distribution in each database.

Database	Number of patients	Record	Objective
MIT-BIH (Moody and Mark, 2001)	48	N:90595, S:2781, V:7235, F:802, Q:8041.	Heartbeat arrhythmia analysis.
CPSC_2018 (Liu et al., 2018a)	6877	Normal:918, AF:1098, RBBB:1695, STD:825, PAC:556, PVC:672, LBBB:207, 1-VAB:704, STE:202.	Automatic identification of the rhythm abnormalities.
Pacing ECG	800	Pacing ECG:400, Routine ECG:400.	Pacing ECG detection.

s. The sample ECG sequences in the pacing ECG database are illustrated in **Figure 4**. The specific data distribution is shown in **Table 1**. We also evaluated the quality of ECG sequences. According to the standard of work (Shen et al., 2020), as shown in **Table 2**, each sample can be divided into good signal quality, medium signal quality, and poor signal quality. Our pacing ECG database only retains good quality signals.

#### 4.2.2. Evaluation and Analysis

We carry out experiments on the pacing ECG database to further evaluate the proposed method for pacing ECG detection. The samples are split into training and test set with a rate of 3:1. Following the experimental setting used in these works (Gong et al., 2019; Hannun et al., 2019), the training set only consists of samples of the target class. There is no overlap between the training set and the testing set.

In this experiment, we mainly verify the effectiveness of our memory module and the encoder and decoder based on convolutional neural networks. First, we implement the encoder using 1-D convolution and the decoder using 1-D fractionally-strided convolution. Each convolutional layer is followed by batch normalization and a ReLU activation function. The details of the encoder and decoder are shown in **Figure 3**. We set the size of the memory module at 300. We also conduct the comparisons with some baseline variants of MAE to show the importance of the significant components, including the autoencoder without memory module (AE) and different reconstruction errors.

As shown in **Table 3**, we conduct several ablation studies to investigate the effectiveness of the major components of the proposed method, such as MAE and its backbone AE. And

the MAE model with  $P = 2$  gets better diagnosis results. As observed in **Table 3**, MAE with  $P = 2$  achieve 91.8% F1-score, outperforming AE with  $P = 1$  (4.0% F1-score), AE with  $P = 2$  (3.4% F1-score), MAE with  $P = 1$  (1.7% F1-score). It is also seen that the proposed MAE achieves competitive results compared to other state-of-the-art methods. These methods like the Resnet backbone network architecture of Hannun et al. (2019) and a combination of RNN+CNN architecture of Yao et al. (2020). The MAE model outperforms the methods of the Hannun et al. (2019) by a margin, with a gain of 1.0% improvements in F1-score.

In **Figure 5**, we visualize the ECG data reconstruction process under the memory module. Since the trained memory only records the latent features of training type, given a routine ECG sample as input, the MAE trained on pacing ECG type, resulting in significant reconstruction error in the kind of input data. Note that the reconstructed pacing ECG of MAE has a similar feature to the input routine ECG type because the memory module retrieves the most identical memory features. The ECG data has periodicity, and the AE model without memory module records some features that are more similar. Thus other types of samples sometimes may also be reconstructed well. **Figure 6** shows that the objective function score obtained by MAE immediately changes when different types of ECG abnormalities samples appear in the dataset.

### 4.3. Experiments on MIT-BIH Arrhythmia Database

The proposed MAE model also can be generally applied to diagnose other ECG abnormalities. We carry out the

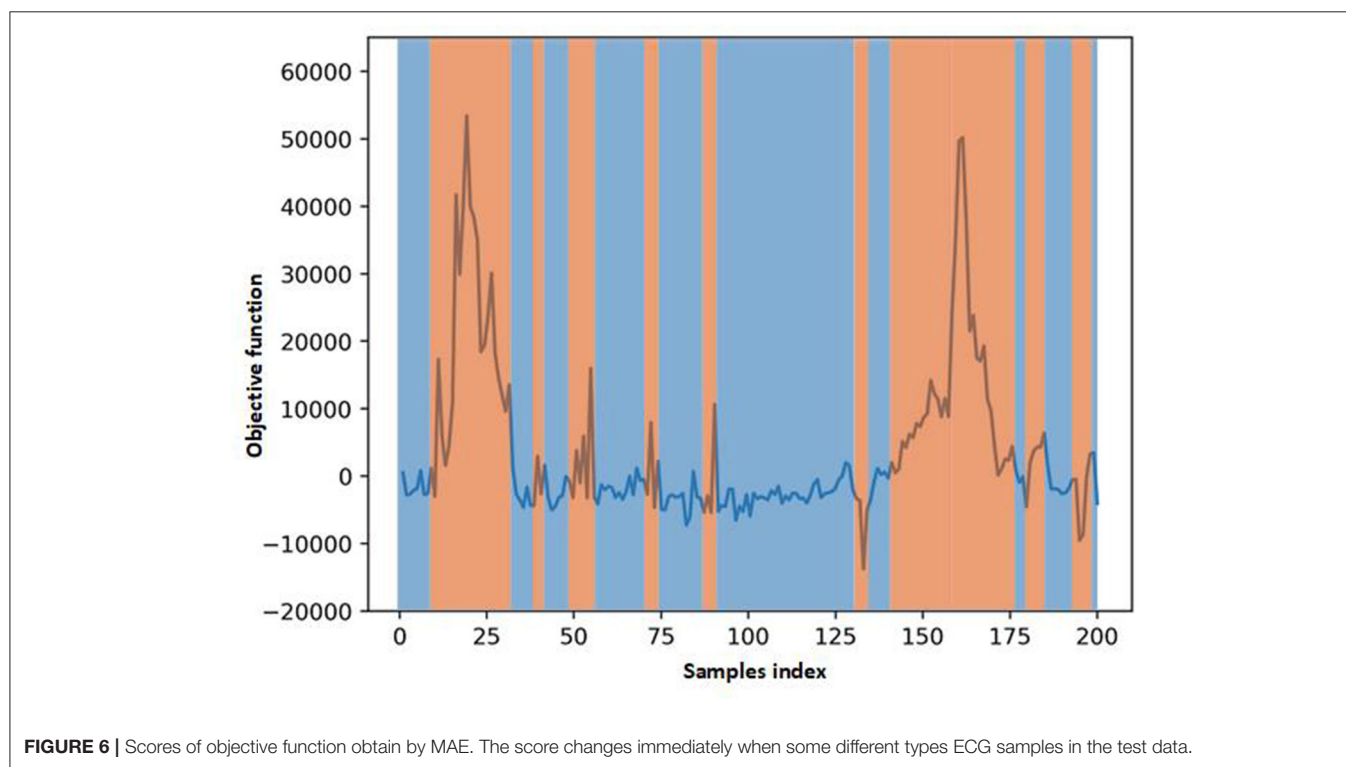
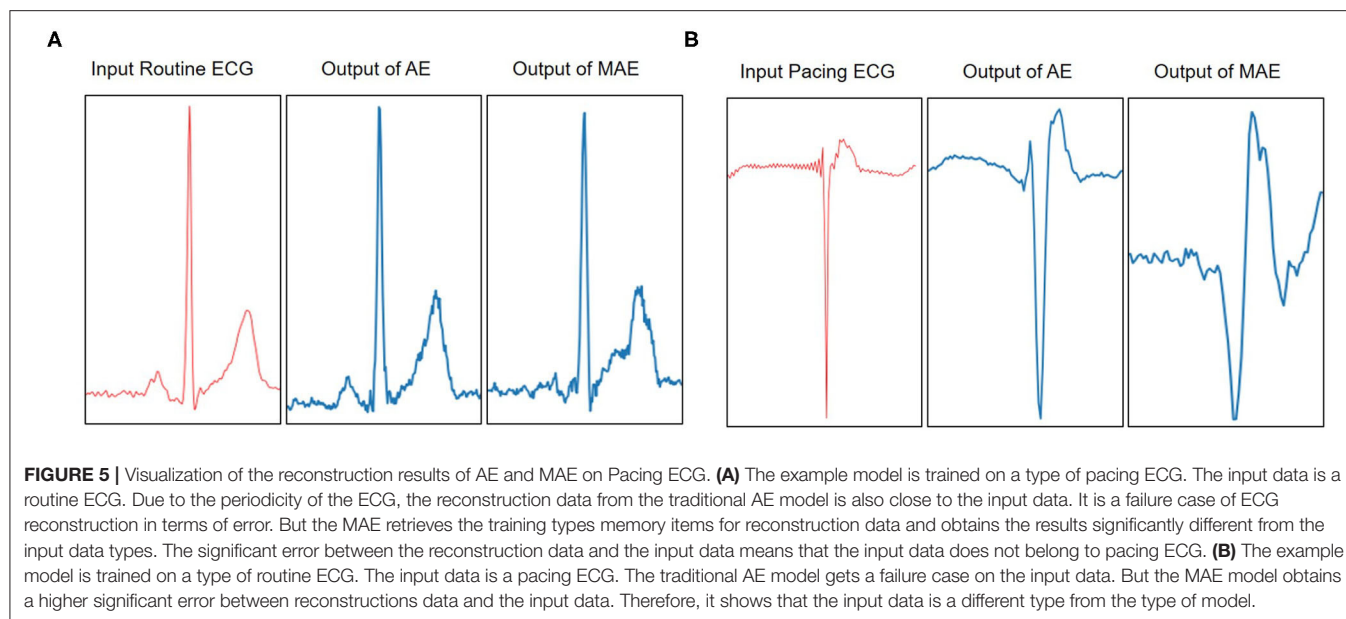
**TABLE 2** | Specification for signal quality division (Shen et al., 2020).

Category	Symbol	Definition
Good	A	Signal with apparent P-QRS-T morphologies Signal with slightly baseline drift or transient artifacts
Medium	B	A good recording contaminated severely in a narrow window A good recording with one or a few missing signals A poor recording that may be interpretable with difficulty
Poor	C	Signal usefulness in clinical applications (maybe caused by misplaced electrodes, poor skin-electrode contact)

**TABLE 3** | The performance of  $+P$ ,  $Rec$ ,  $F1$  – score of different methods on the pacing ECG database.

Method	Pacing ECG database		
	$+P$	$Rec$	$F1$ – score
Hannun et al., 2019	0.913	0.905	0.908
Oh et al., 2018	0.881	0.921	0.899
AE <sub>J1</sub>	0.882	0.874	0.878
AE <sub>J2</sub>	0.889	0.880	0.884
MAE <sub>J1</sub>	0.906	0.897	0.901
MAE <sub>J2</sub>	0.912	0.925	0.918





experiments on the MIT-BIH Arrhythmia database to evaluate the proposed method.

#### 4.3.1. MIT-BIH Arrhythmia Database

The MIT-BIH Arrhythmia database (Moody and Mark, 2001) contains 48 half-hour excerpts of two-channel ambulatory ECG recordings. The recordings are digitized at 360 samples per second per channel. Each record comprises two signals. For all the records, the first one is the modified-lead II

(MLII), whereas the second one corresponds to V1, V2, V4, or V5, depending on the records. Therefore, only the MLII is provided by all the records. The database contains two or more expert cardiologists independently annotated approximately 110,000 beats, all of them, and the disagreements were resolved. The MIT-BIH heartbeat types are grouped into five heartbeat classes which are recommended by the Association for the Advancement of Medical Instruments (AAMI), as shown in **Table 4**. Example

signals for the MIT-BIH Arrhythmia database are shown in **Figure 7**.

### 4.3.2. Evaluation and Analysis

It should be noted that the MIT-BIH Arrhythmia database has unbalanced distribution. Therefore, we abandon some samples, which doesn't affect the final performance. Following the works (Kachuee et al., 2018; Wang et al., 2021), we balanced the number of beats in each type before splitting the testing phase. This paper selects and tests on 600 heartbeat samples. In this paper, only lead II is considered to detect the ECG abnormalities. This decision is motivated by the following works (Mondéjar-Guerra et al., 2019), which proved that using only one lead is sufficient for the arrhythmia classification task. And the 235 points are extracted as single heartbeat morphology features. For experiment settings, the total number of iterations is 200, and the batch size is set to 16. We apply an initial learning rate of  $10^{-5}$ . The **Figure 8** shows the classification results of the MAE model with data splitting. In addition, among those works shown in **Table 5**, these methods are designed for improving the accuracy of ECG heartbeat abnormality detection. Nevertheless, the MAE model can still exceed them with a large margin, which can further demonstrate the effectiveness of the proposed

approach for ECG heartbeat abnormality detection. Meanwhile, MAE produces the highest F1-score for most heartbeat types, such as type of F performance has significant improvement. The improvements are mainly attributed to the memory module.

Specifically, **Table 5** shows the  $+p$  and  $Rec$  and F1 of the proposed MAE model and other popular methods on the database testing set. The experimental results show that the F1-score of N category is 97.2%, the F1-score of S category is 90.0%, the F1-score of V category is 88.3%, the F1-score of F category is 92.6%, and the F1-score of Q category is 98.3%. **Table 6** shows the overall results of the MAE model and compares it with the state-of-the-art methods in other literature. Some method results show that the classification performances for type F and type Q are not satisfactory. It may be that these beats are harder to classify. On the whole, our MAE model achieves better performance for type N, S, V, F, and Q. Moreover, the MAE model can also outperform these typical classifiers based on CNN, for example, the 9-layer CNN proposed by Acharya et al. (2017) (92.5%, 2.4% higher F1-score), the combination of CNN with LSTM proposed by Shi et al. (2019) (93.6%, 1.3% higher F1-score).

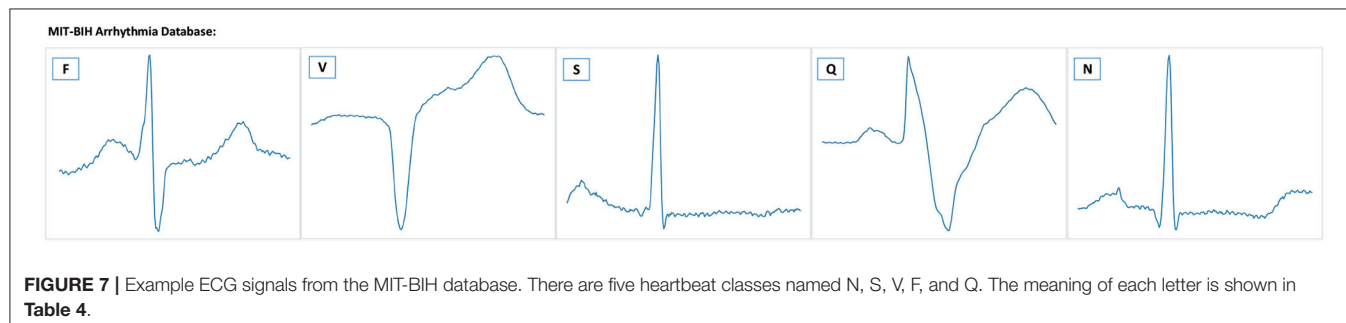
We also visualize data reconstruction in the MIT-BIH Arrhythmia database, shown as **Figure 9**. The trained memory module records the latent features of the input type. Given a testing data ECG of "N" type, the memory module trained on "N" type reconstructs the "N" type, resulting in a low error on the input data. But the memory items trained on the "F" type reconstruct the "N" type, given a testing data ECG "N" type, resulting in a significant error on the input data "N" type. Note that the reconstructed "F" type of MAE has a similar shape to the input "N" since the memory module retrieves the most similar latent features. By comparing the errors, we can easily get the type of input test data. Despite some data having noise, the MAE model can still detect the type of heartbeat, which benefits from the memory module designed in MAE. Meanwhile, the compelling performance also demonstrates the generalization ability of the MAE model.

## 5. CONCLUSION AND FUTURE WORK

In this paper, a memory-based autoencoder was proposed to construct the intelligent diagnosis model for ECG abnormality detection. We designed a novel autoencoder using a memory module to record the latent features from the training data of corresponding types. The key features of MAE are to preserve the latent features to obtain low average reconstruction error

**TABLE 4** | Mapping the heartbeat types to the AAMI heartbeat categories and data distribution statistics (Moody and Mark, 2001).

AAMI	MIT-BIH	Heartbeat types	Total
N	N	Normal beat	90,462
	L	Left bundle branch block beat	
	R	Right bundle branch block beat	
	e	Atrial escape beat	
S	j	Nodal(Junctional) escape beat	2,777
	A	Atrial premature beat	
	a	Aberrated atrial premature beat	
	J	Nodal(Junctional) premature beat	
V	S	Supraventricular premature or ectopic beat	7,223
	V	Premature ventricular contraction	
F	E	Ventricular escape beat	802
	F	Fusion of ventricular and normal beat	
Q	/	Paced beat	8,027
	f	Fusion of paced and normal beat	
	Q	Unclassifiable beat	



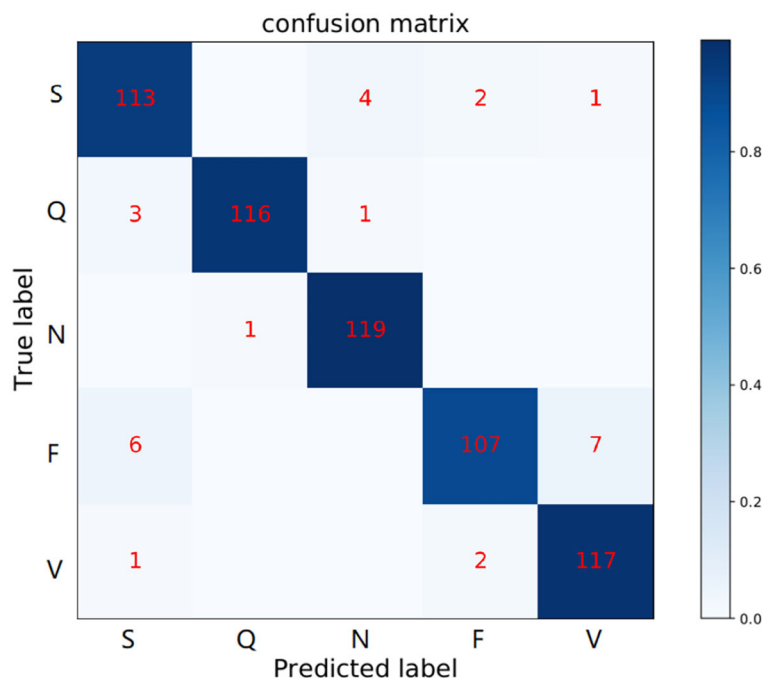


**FIGURE 8 |** Confusion matrix of MAE model in the MIT-BIH Arrhythmia database. The row labels represent the true class records in each row and the column labels represent the class records predicted by our method. Numbers in each grid show the number of records classified as column labels when its true class is indicated by row label.

**TABLE 5 |** Comparisons of +P, Rec, and F1 – score for each type on the MIT-BIH Arrhythmia database.

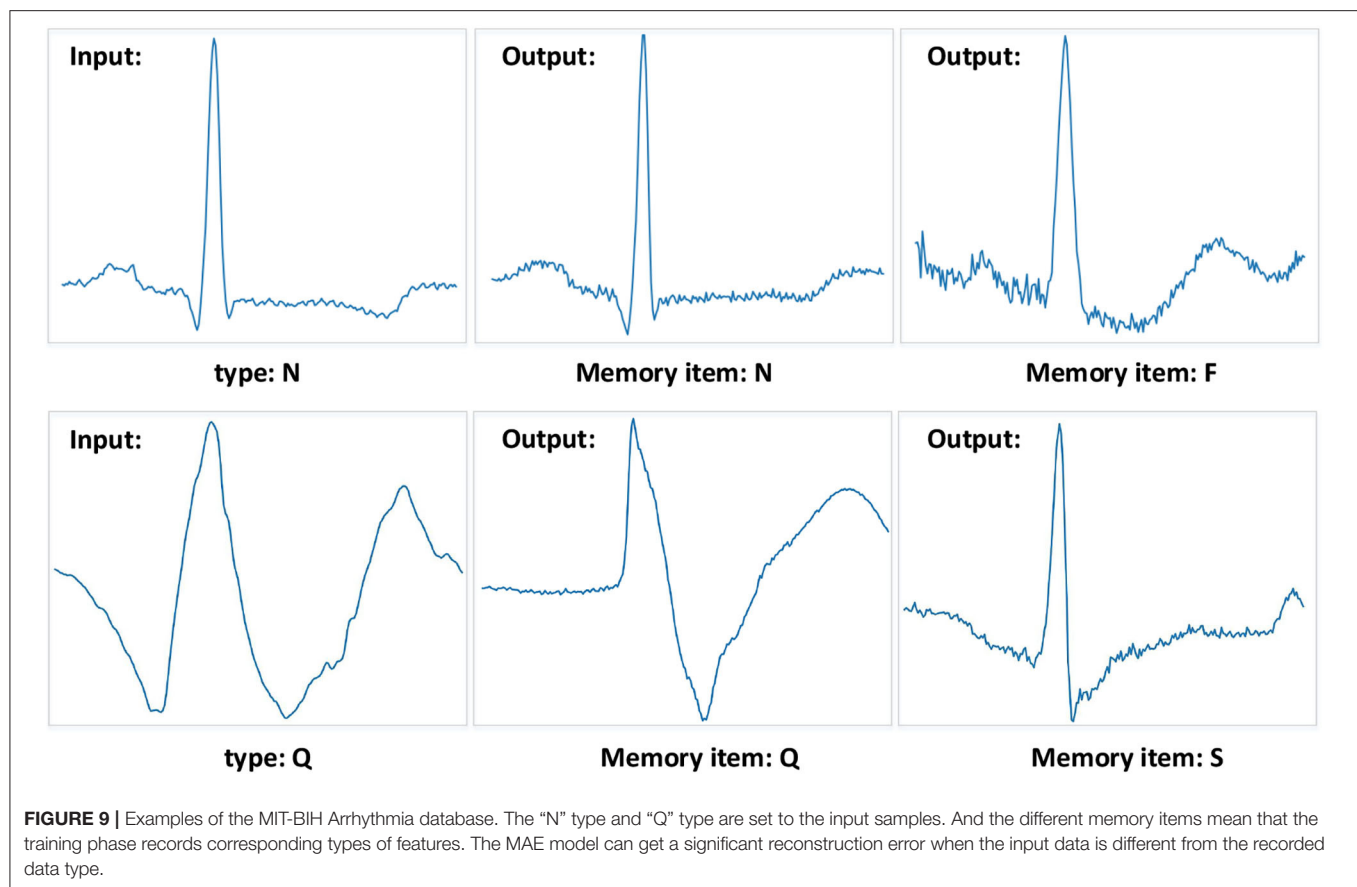
Methods	N			S			V			F			Q		
	+P	Rec	F1	+P	Rec	F1	+P	Rec	F1	+P	Rec	F1	+P	Rec	F1
Zhang et al., 2014	0.990	0.889	0.937	0.359	0.791	0.494	0.927	0.855	0.842	0.137	0.938	0.220	–	–	–
Ming et al., 2020	0.984	0.953	0.968	0.938	0.785	0.832	0.938	0.957	0.947	0.088	0.438	0.146	–	–	–
Li et al., 2019	0.975	0.910	0.941	0.780	0.638	0.702	0.865	0.884	0.874	0.907	0.873	0.890	0.994	0.966	0.994
Hannun et al., 2019	0.948	0.950	0.948	0.826	0.720	0.769	0.872	0.890	0.880	0.942	0.786	0.856	0.990	0.990	0.990
Mondéjar-Guerra et al., 2019	0.982	0.959	0.970	0.497	0.781	0.607	0.939	0.947	0.994	0.236	0.124	0.162	–	–	–
Memory-AE	0.960	0.992	0.972	0.936	0.867	0.900	0.807	0.975	0.883	0.964	0.892	0.926	0.991	0.975	0.983

**TABLE 6 |** Comparisons with the popular methods for overall types on the MIT-BIH Arrhythmia database.

Typical methods	ECG beat types	Classifier	Performance		
			+P	Rec	F1-score
Acharya et al., 2017	N S V F Q	CNN	89.5%	95.9%	92.5%
Niu et al., 2020	N S V F Q	Multi-Perspective CNN	96.4%	–	–
Shi et al., 2019	N S V F	CNN-LSTM	94.2%	93.1%	93.6%
Mondéjar-Guerra et al., 2019	N S V F	Ensemble SVMs	94.5%	70.3%	80.6%
Proposed MAE	N S V F Q	Memory-based Autoencoder	95.8%	94.0%	94.9%

in the training phase. And in the testing phase, the output data of reconstruction will reference the memory items which were selected as similar items of the encoding of the input data. Furthermore, we also defined an objective function that can compute the distance relationship between samples of the

same types and samples of different types. In brief, the proposed MAE can well reconstruct the input data consistent with the training types to get a low objective function error and enlarge the objective function error of other abnormal ECG types, which the objective function is the better criterion of abnormal ECG



detection. The results demonstrate that the proposed model achieves a significant performance gain with accuracy, sensitivity, and F1-score through a series of experiments.

In future work, since the same types of ECG abnormality has differences between different patients, we aim to record the latent features in the same types of ECG abnormality of other individuals. By analyzing these individual differences, we further explore to improve the accuracy, sensitivity, and F1 score of the model. Additionally, the diagnostic efficiency of the model is also an important indicator of clinical ECG diagnosis. We also aim to design a more lightweight and efficient diagnostic model which can be better applied in clinical ECG diagnosis.

## DATA AVAILABILITY STATEMENT

The raw data supporting the conclusions of this article will be made available by the authors, without undue reservation. The publicly released dataset of the MIT-BIH Arrhythmia Database is available at: <https://www.physionet.org/content/mitdb>.

## REFERENCES

Acharya, U. R., Oh, S. L., Hagiwara, Y., Tan, J. H., Adam, M., Gertych, A., et al. (2017). A deep convolutional neural network model to classify heartbeats. *Comput. Biol. Med.* 89, 389–396. doi: 10.1016/j.compbiomed.2017.08.022

## ETHICS STATEMENT

The studies involving human participants were reviewed and approved by Life Science Ethics Review Committee Zhengzhou University. Written informed consent for participation was not required for this study in accordance with the national legislation and the institutional requirements.

## AUTHOR CONTRIBUTIONS

ZT and ZG conceived the study. ZG performed the design and implementation of the work and wrote the manuscript. HC and ZT helped with the experiment design and implementation. LY provided the experimental data and annotated the data. BZ and ZW helped to review and improved the manuscript. All authors read and approved the final manuscript.

Adam, M., Lih, O. S., Sudarshan, V. K., Koh, J. E., Hagiwara, Y., Hong, T. J., et al. (2018). Automated characterization of cardiovascular diseases using relative wavelet nonlinear features extracted from ECG signals. *Comput. Methods Prog. Biomed.* 161, 133–143. doi: 10.1016/j.cmpb.2018.04.018



- Baloglu, U., Talo, M., yildirim, O., Tan, R. S., and Acharya, U. R. (2019). Classification of myocardial infarction with multi-lead ECG signals and deep CNN. *Pattern Recogn. Lett.* 122, 23–30. doi: 10.1016/j.patrec.2019.02.016
- Chen, C., Hua, Z., Zhang, R., Liu, G., and Wen, W. (2020). Automated arrhythmia classification based on a combination network of CNN and LSTM. *Biomed. Signal Process. Control* 57:101819. doi: 10.1016/j.bspc.2019.101819
- Chen, P. J., Lin, M. C., Lai, M. J., Lin, J. C., Lu, H. S., and Tseng, V. S. (2018). Accurate classification of diminutive colorectal polyps using computer-aided analysis. *Gastroenterology* 154, 568–575. doi: 10.1053/j.gastro.2017.10.010
- Chen, S., Hua, W., Li, Z., Li, J., and Gao, X. (2017). Heartbeat classification using projected and dynamic features of ECG signal. *Biomed. Signal Process. Control* 31, 165–173. doi: 10.1016/j.bspc.2016.07.010
- Dasan, E., and Pannierselvar, I. (2021). A novel dimensionality reduction approach for ECG signal via convolutional denoising autoencoder with LSTM. *Biomed. Signal Process. Control* 63:102225. doi: 10.1016/j.bspc.2020.102225
- Fan, X., Yao, Q., Cai, Y., Miao, F., Sun, F., and Li, Y. (2018). Multiscaled fusion of deep convolutional neural networks for screening atrial fibrillation from single lead short ECG recordings. *IEEE J. Biomed. Health Inform.* 22, 1744–1753. doi: 10.1109/JBHI.2018.2858789
- Gao, Y., Zhou, B., Zhou, Y., Shi, L., Tao, Y., and Zhang, J. (2018). “Transfer learning-based behavioural task decoding from brain activity,” in *The International Conference on Healthcare Science and Engineering* (Guilin: Springer), 71–81. doi: 10.1007/978-981-13-6837-0\_6
- Gong, D., Liu, L., Le, V., Saha, B., Mansour, M. R., Venkatesh, S., et al. (2019). “Memorizing normality to detect anomaly: memory-augmented deep autoencoder for unsupervised anomaly detection,” in *Proceedings of the IEEE/CVF International Conference on Computer Vision* (Seoul), 1705–1714. doi: 10.1109/ICCV.2019.00179
- Hannun, A. Y., Rajpurkar, P., Haghighpanahi, M., Tison, G. H., Bourn, C., Turakhia, M. P., et al. (2019). Cardiologist-level arrhythmia detection and classification in ambulatory electrocardiograms using a deep neural network. *Nat. Med.* 25, 65–69. doi: 10.1038/s41591-018-0268-3
- Hao, D., Hsin-Ginn, H., and Vincent, S. T. (2021). Convolutional neural network based automatic screening tool for cardiovascular diseases using different intervals of ECG signals. *Comput. Methods Prog. Biomed.* 203:106035. doi: 10.1016/j.cmpb.2021.106035
- Hasan, M., Choi, J., Neumann, J., Roy-Chowdhury, A., and Davis, L. (2016). “Learning temporal regularity in video sequences,” in *The IEEE Conference on Computer Vision and Pattern Recognition (CVPR)* (Las Vegas, NV), 733–742. doi: 10.1109/CVPR.2016.86
- He, R., Wang, K., Zhao, N., Liu, Y., Yuan, Y., Li, Q., et al. (2018). Automatic detection of atrial fibrillation based on continuous wavelet transform and 2D convolutional neural networks. *Front. Physiol.* 9:1206. doi: 10.3389/fphys.2018.01206
- Kachuee, M., Fazeli, S., and Sarrafzadeh, M. (2018). “ECG heartbeat classification: a deep transferable representation,” in *2018 IEEE International Conference on Healthcare Informatics (ICHI)* (New York, NY), 443–444. doi: 10.1109/ICHI.2018.00092
- Kim, Y., Kim, M., and Kim, G. (2018). “Memorization precedes generation: learning unsupervised GANS with memory networks,” in *International Conference on Learning Representations (ICLR)* (Vancouver, BC).
- Li, R., Zhang, X., Dai, H., Zhou, B., and Wang, Z. (2019). Interpretability analysis of heartbeat classification based on heartbeat activity’s global sequence features and BiLSTM-attention neural network. *IEEE Access* 7, 109870–109883. doi: 10.1109/ACCESS.2019.2933473
- Liu, F., Liu, C., Zhao, L., Zhang, X., Wu, X., Xu, X., et al. (2018a). An open access database for evaluating the algorithms of electrocardiogram rhythm and morphology abnormality detection. *J. Med. Imaging Health Inform.* 8, 1368–1373. doi: 10.1166/jmihi.2018.2442
- Liu, N., Wang, L., Chang, Q., Xing, Y., and Zhou, X. (2018b). A simple and effective method for detecting myocardial infarction based on deep convolutional neural network. *J. Med. Imaging Health Inform.* 8, 1508–1512. doi: 10.1166/jmihi.2018.2463
- Ma, C., Wei, S., Chen, T., Zhong, J., Liu, Z., and Liu, C. (2020). Integration of results from convolutional neural network in a support vector machine for the detection of atrial fibrillation. *IEEE Trans. Instrument. Measure.* 70, 1–10. doi: 10.1109/TIM.2020.3044718
- Majumdar, A., Gogna, A., and Ward, R. (2016). Semi-supervised stacked label consistent autoencoder for reconstruction and analysis of biomedical signals. *IEEE Trans. Biomed. Eng.* 64, 2196–2205. doi: 10.1109/TBME.2016.2631620
- Mar, T., Zaunseder, S., Martinez, J. P., Llamedo, M., and Poll, R. (2011). Optimization of ECG classification by means of feature selection. *IEEE Trans. Biomed. Eng.* 58, 2168–2177. doi: 10.1109/TBME.2011.2113395
- Ming, C., Wang, G., Ding, Z., Li, J., and Yang, H. (2020). “Unsupervised domain adaptation for ECG arrhythmia classification,” in *Annual International Conference of the IEEE Engineering in Medicine and Biology Society (EMBC)* (Montreal, QC), 304–307.
- Mondéjar-Guerra, V., Novo, J., Rouco, J., Penedo, M. G., and Ortega, M. (2019). Heartbeat classification fusing temporal and morphological information of ECGs via ensemble of classifiers. *Biomed. Signal Process. Control* 47, 41–48. doi: 10.1016/j.bspc.2018.08.007
- Moody, G., and Mark, R. (2001). The impact of the mit-bih arrhythmia database. *IEEE Eng. Med. Biol. Mag.* 20, 45–50. doi: 10.1109/51.932724
- Niu, J., Tang, Y., Sun, Z., and Zhang, W. (2020). Inter-patient ECG classification with symbolic representations and multi-perspective convolutional neural networks. *IEEE J. Biomed. Health Inform.* 24, 1321–1332. doi: 10.1109/JBHI.2019.2942938
- Oh, S. L., Ng, E., Tan, R. S., and Acharya, U. R. (2018). Automated diagnosis of arrhythmia using combination of CNN and LSTM techniques with variable length heart beats. *Comput. Biol. Med.* 102, 278–287. doi: 10.1016/j.compbiomed.2018.06.002
- Osowski, S., and Tran, L. (2001). ECG beat recognition using fuzzy hybrid neural network. *IEEE Trans. Biomed. Eng.* 48, 1265–1271. doi: 10.1109/10.959322
- Oyetunde, T., Bao, F. S., Chen, J. W., Martin, H. G., and Tang, Y. J. (2018). Leveraging knowledge engineering and machine learning for microbial bio-manufacturing. *Biotechnol. Adv.* 36, 1308–1315. doi: 10.1016/j.biotechadv.2018.04.008
- Saadatnejad, S., Oveisi, M., and Hashemi, M. (2020). LSTM-based ECG classification for continuous monitoring on personal wearable devices. *IEEE J. Biomed. Health Inform.* 24, 515–523. doi: 10.1109/JBHI.2019.2911367
- Samaniego, E., Anitescu, C., Goswami, S., Nguyen-Thanh, V. M., Guo, H., Hamdia, K., et al. (2020). An energy approach to the solution of partial differential equations in computational mechanics via machine learning: concepts, implementation and applications. *Comput. Methods Appl. Mech. Eng.* 362:112790. doi: 10.1016/j.cma.2019.112790
- Sangaiah, A. K., Arumugam, M., and Bian, G.-B. (2020). An intelligent learning approach for improving ECG signal classification and arrhythmia analysis. *Artif. Intell. Med.* 103:101788. doi: 10.1016/j.artmed.2019.101788
- Santoro, A., Bartunov, S., Botvinick, M., Wierstra, D., and Lillicrap, T. (2016). One-shot learning with memory-augmented neural networks. *arXiv preprint arXiv:1605.06065*.
- Shen, Q., Gao, H., Li, Y., Sun, Q., Chen, M., Li, J., et al. (2020). An open-access arrhythmia database of wearable electrocardiogram. *J. Med. Biol. Eng.* 40, 564–574. doi: 10.1007/s40846-020-00554-3
- Shi, H., Qin, C., Xiao, D., Zhao, L., and Liu, C. (2019). Automated heartbeat classification based on deep neural network with multiple input layers. *Knowledge Based Syst.* 188:105036. doi: 10.1016/j.knsys.2019.105036
- Sodmann, P., and Vollmer, M. (2020). “ECG segmentation using a neural network as the basis for detection of cardiac pathologies,” in *Computing in Cardiology Conference (CINIC)* (Rimini), 1–4. doi: 10.22489/CinC.2020.356
- Tan, J. H., Hagiwara, Y., Pang, W., Lim, I., Oh, S. L., Adam, M., et al. (2018). Application of stacked convolutional and long short-term memory network for accurate identification of cad ECG signals. *Comput. Biol. Med.* 94, 19–26. doi: 10.1016/j.compbiomed.2017.12.023
- Thinsungnoen, T., Kerdprasop, K., and Kerdprasop, N. (2018). Deep autoencoder networks optimized with genetic algorithms for efficient ECG clustering. *Int. J. Mach. Learn. Comput.* 8, 112–116. doi: 10.18178/ijmlc.2018.8.2.672
- Wang, G., Zhang, C., Liu, Y., Yang, H., Fu, D., Wang, H., et al. (2018). A global and updatable ECG beat classification system based on recurrent neural networks and active learning. *Inform. Sci.* 501, 23–42. doi: 10.1016/j.ins.2018.06.062
- Wang, J., Qiao, X., Liu, C., Wang, X., Liu, Y., Yao, L., et al. (2021). Automated ECG classification using a non-local convolutional block attention module. *Comput. Methods Prog. Biomed.* 203:106006. doi: 10.1016/j.cmpb.2021.106006

- Wang, J.-S., Chiang, W.-C., Hsu, Y.-L., and Yang, Y.-T. C. (2013). ECG arrhythmia classification using a probabilistic neural network with a feature reduction method. *Neurocomputing* 116, 38–45. doi: 10.1016/j.neucom.2011.10.045
- Wang, R., Fan, J., and Li, Y. (2020). Deep multi-scale fusion neural network for multi-class arrhythmia detection. *IEEE J. Biomed. Health Inform.* 24, 2461–2472. doi: 10.1109/JBHI.2020.2981526
- Yao, Q., Wang, R., Fan, X., Liu, J., and Li, Y. (2020). Multi-class arrhythmia detection from 12-lead varied-length ECG using attention-based time-incremental convolutional neural network. *Inform. Fusion* 53, 174–182. doi: 10.1016/j.inffus.2019.06.024
- Zhang, J., Chen, X., Liu, A., Xiang, C., Zhang, X., and Gao, M. (2020). ECG-based multi-class arrhythmia detection using spatio-temporal attention-based convolutional recurrent neural network. *Artif. Intell. Med.* 106:101856. doi: 10.1016/j.artmed.2020.101856
- Zhang, X., Li, R., Dai, H., Liu, Y., Zhou, B., and Wang, Z. (2019). Localization of myocardial infarction with multi-lead bidirectional gated recurrent unit neural network. *IEEE Access* 7, 161152–161166. doi: 10.1109/ACCESS.2019.2946932
- Zhang, Z., Dong, J., Luo, X., Choi, K. S., and Wu, X. (2014). Heartbeat classification using disease-specific feature selection. *Comput. Biol. Med.* 46, 79–89. doi: 10.1016/j.combiomed.2013.11.019
- Zhang, Z. M., Rautaharju, P. M., Soliman, E. Z., Manson, J., Cain, M. E., Martin, L. W., et al. (2012). Mortality risk associated with bundle branch blocks and related repolarization abnormalities (from the Women's Health Initiative [WHI]). *Am. J. Cardiol.* 110, 1489–1495. doi: 10.1016/j.amjcard.2012.06.060
- Zhou, S., and Tan, B. (2020). Electrocardiogram soft computing using hybrid deep learning CNN-elm. *Appl. Soft Comput.* 86:105778. doi: 10.1016/j.asoc.2019.105778
- Zong, B., Song, Q., Min, M. R., Cheng, W., Lumezanu, C., Cho, D., et al. (2018). "Deep autoencoding Gaussian mixture model for unsupervised anomaly detection," in *International Conference on Learning Representations (ICLR)* (Vancouver, BC).

**Conflict of Interest:** The authors declare that the research was conducted in the absence of any commercial or financial relationships that could be construed as a potential conflict of interest.

**Publisher's Note:** All claims expressed in this article are solely those of the authors and do not necessarily represent those of their affiliated organizations, or those of the publisher, the editors and the reviewers. Any product that may be evaluated in this article, or claim that may be made by its manufacturer, is not guaranteed or endorsed by the publisher.

Copyright © 2021 Ge, Cheng, Tong, Yang, Zhou and Wang. This is an open-access article distributed under the terms of the Creative Commons Attribution License (CC BY). The use, distribution or reproduction in other forums is permitted, provided the original author(s) and the copyright owner(s) are credited and that the original publication in this journal is cited, in accordance with accepted academic practice. No use, distribution or reproduction is permitted which does not comply with these terms.



# Preliminary Study: Learning the Impact of Simulation Time on Reentry Location and Morphology Induced by Personalized Cardiac Modeling

## OPEN ACCESS

### Edited by:

Kuanquan Wang,  
Harbin Institute of Technology, China

### Reviewed by:

Xin Gao,  
Nanjing University of Aeronautics and  
Astronautics, China  
Shijie Zhou,  
Miami University, United States

### \*Correspondence:

Ling Xia  
xialing@zju.edu.cn  
Dongdong Deng  
dengdongdong@dlut.edu.cn

<sup>†</sup> These authors have contributed  
equally to this work

### Specialty section:

This article was submitted to  
Computational Physiology  
and Medicine,  
a section of the journal  
Frontiers in Physiology

**Received:** 30 June 2021

**Accepted:** 30 November 2021

**Published:** 24 December 2021

### Citation:

Tong L, Zhao C, Fu Z, Dong R,  
Wu Z, Wang Z, Zhang N, Wang X,  
Cao B, Sun Y, Zheng D, Xia L and  
Deng D (2021) Preliminary Study:  
Learning the Impact of Simulation  
Time on Reentry Location  
and Morphology Induced by  
Personalized Cardiac Modeling.  
*Front. Physiol.* 12:733500.  
doi: 10.3389/fphys.2021.733500

Lv Tong<sup>1†</sup>, Caiming Zhao<sup>2†</sup>, Zhenyin Fu<sup>3†</sup>, Ruiqing Dong<sup>4</sup>, Zhenghong Wu<sup>3</sup>,  
Zefeng Wang<sup>5</sup>, Nan Zhang<sup>6</sup>, Xinlu Wang<sup>5</sup>, Boyang Cao<sup>1</sup>, Yutong Sun<sup>1</sup>,  
Dingchang Zheng<sup>7</sup>, Ling Xia<sup>3\*</sup> and Dongdong Deng<sup>1\*</sup>

<sup>1</sup> School of Biomedical Engineering, Dalian University of Technology, Dalian, China, <sup>2</sup> Department of Cardiology, The First Affiliated Hospital of Soochow University, Suzhou, China, <sup>3</sup> College of Biomedical Engineering and Instrument Science, Zhejiang University, Hangzhou, China, <sup>4</sup> Department of Cardiology, Dushu Lake Hospital Affiliated to Soochow University, Suzhou, China, <sup>5</sup> Department of Cardiology, Beijing Anzhen Hospital Affiliated to Capital Medical University, Beijing, China, <sup>6</sup> Department of Radiology, Beijing Anzhen Hospital Affiliated to Capital Medical University, Beijing, China, <sup>7</sup> Research Centre for Intelligent Healthcare, Faculty of Health and Life Science, Coventry University, Coventry, United Kingdom

Personalized cardiac modeling is widely used for studying the mechanisms of cardiac arrhythmias. Due to the high demanding of computational resource of modeling, the arrhythmias induced in the models are usually simulated for just a few seconds. In clinic, it is common that arrhythmias last for more than several minutes and the morphologies of reentries are not always stable, so it is not clear that whether the simulation of arrhythmias for just a few seconds is long enough to match the arrhythmias detected in patients. This study aimed to observe how long simulation of the induced arrhythmias in the personalized cardiac models is sufficient to match the arrhythmias detected in patients. A total of 5 contrast enhanced MRI datasets of patient hearts with myocardial infarction were used in this study. Then, a classification method based on Gaussian mixture model was used to detect the infarct tissue. For each reentry, 3 s and 10 s were simulated. The characteristics of each reentry simulated for different duration were studied. Reentries were induced in all 5 ventricular models and sustained reentries were induced at 39 stimulation sites in the model. By analyzing the simulation results, we found that 41% of the sustained reentries in the 3 s simulation group terminated in the longer simulation groups (10 s). The second finding in our simulation was that only 23.1% of the sustained reentries in the 3 s simulation did not change location and morphology in the extended 10 s simulation. The third finding was that 35.9% reentries were stable in the 3 s simulation and should be extended for the simulation time. The fourth finding was that the simulation results in 10 s simulation matched better with the clinical measurements than the 3 s simulation. It was shown that 10 s simulation was

sufficient to make simulation results stable. The findings of this study not only improve the simulation accuracy, but also reduce the unnecessary simulation time to achieve the optimal use of computer resources to improve the simulation efficiency and shorten the simulation time to meet the time node requirements of clinical operation on patients.

**Keywords:** reentry, arrhythmias, computational modeling, simulation time, Gaussian mixture model method

## INTRODUCTION

Ventricular tachycardia (VT) is a life-threatening heart disease that occurs frequently in patients with myocardial infarction (MI), and one of the most prominent causes of sudden cardiac death (SCD) (Kusumoto et al., 2018). After acute MI, the myocardium in the center of infarct area is replaced by electric insulated fibrotic tissue, while some active myocardial cells extend into the dense fibrosis to form a slow conduction area which usually is called as gray zone (GZ). Thus, the heart tissue in patients with MI can be divided into three categories: non-infarct tissue, core scar, and GZ (Wu, 2017). The heterogeneity in the GZ slows down the electrical conduction in this part of the tissue, which in turn causes unidirectional conduction block and predisposes to reentry, leading to arrhythmias and increasing the risk of infarction in patients.

Clinical and experimental studies have shown that reentries in patients with VT can be sustained by anatomic reentry or functional reentry (Aguilar and Nattel, 2015; Martin et al., 2018). The anatomical reentry is very stable and always rotates around a fixed area (Fernández-Armenta et al., 2013; Josephson et al., 2014; Soto-Iglesias et al., 2020). For the functional reentry, the electric impulse proceeds as a single wavefront through a constrained region known as the central common pathway or isthmus of the reentrant circuit (Ciaccio et al., 2016; Martin et al., 2018; Crinion et al., 2020). In clinic, the critical isthmuses which sustain that the anatomical reentry can be measured by the high-density electroanatomic multipolar mapping system, but it is not easy to directly measure the critical isthmuses which sustain functional reentry (Martin et al., 2018; Crinion et al., 2020), especially for those unstable or non-sustained reentries (Nishimura et al., 2020).

Computational modeling has been widely used for the non-invasive investigation of lethal heart rhythm disorders and their treatment, including not only risk stratification of patients with MI (Behradfar et al., 2014; Deng et al., 2016; Lopez-Perez et al., 2019), the prediction of reentry location (Deng et al., 2015), but also guiding for VT ablation in clinic (Prakosa et al., 2018). Due to the high demand of computational resource of modeling, the reentries (both anatomic and functional) induced in the models are usually simulated for just a few seconds which is usually less than 5 s (Deng et al., 2015, 2016, 2019a,b; Arevalo et al., 2016; Prakosa et al., 2018; Ukwatta et al., 2018). In our previous work, we found that some reentries induced in the model were not stable, and become non-sustained before the end of simulation. In clinic, it is common that reentries last for more than several minutes and the morphologies of reentries are not always stable (Katritsis et al., 2012; Martin et al., 2018; Nishimura et al., 2020), so it is not clear that whether the simulation of reentries for just

a few seconds is long enough to match the arrhythmias measured in clinic. Furthermore, as far as we know, still no work has been done to study whether the personalized cardiac modeling can reproduce most of the VT categories which include sustained stable reentry, sustained non-stable reentry, and non-sustained reentry measured in clinic.

In this study, we used personalized virtual heart models to: (1) find out an optimal dynamic stimulation protocol to save computational resources and make the simulation results more robust; and (2) study whether the personalized cardiac modeling can reproduce most of the VT categories measured in clinic.

## MATERIALS AND METHODS

### Clinical Data

For this retrospective study, we used data from five patients who suffered from ischemic cardiomyopathy between 2018 and 2019 at Beijing Anzhen Hospital, and this study was approved by the Institutional Review Board of Beijing Anzhen Hospital. Cardiovascular magnetic resonance-late gadolinium enhancement (CMR-LGE) images of the five patients were collected and used to build the heart models. Cardiac MRI were acquired by 3.0 T scanner (Sonata, Siemens, Erlangen, Germany) or GE scanner (DISCOVERY MR 750w; GE, Boston, MA, United States). The detailed image acquisition protocol can be found in the previous published literature (Woodard et al., 2007; Klinke et al., 2013; Kramer et al., 2020). The scanning layer thickness was 8–10 mm with image resolution between 1.36 and 1.64 mm (detailed information is listed in **Table 1**).

### Image Processing Pipeline

All analyses and measurements were manipulated on custom software developed in MATLAB (MathWorks Inc., MA, United States). The epicardial and endocardial boundaries, for each two-dimensional slice in the LGE images, were manually segmented by two experienced specialists and excluded papillary

**TABLE 1** | Detailed cardiovascular magnetic resonance-late gadolinium enhancement (CMR-LGE) images information of each patient.

	Size	In-plane resolution (mm)	Slice thickness (mm)	Layer count
PAT01	256 × 208	1.52344 × 1.52344	9	14
PAT02	208 × 256	1.5625 × 1.5625	8	13
PAT03	256 × 192	1.36719 × 1.36719	8.4	10
PAT04	240 × 256	1.52344 × 1.52344	10	10
PAT05	208 × 256	1.48438 × 1.48438	8	11



muscles from the endocardium. The part of pixels between the boundaries were considered as the myocardium. Then, the modified Gaussian mixture model (MGMM) method was used for the subsequent processing of the segmented myocardium, summarized as follows (Hennemuth et al., 2013; Pop et al., 2013).

### Modified Gaussian Mixture Model Method

A classification method based on Gaussian mixture model (GMM) was used to segment the tissue inside the epi- and endocardium boundaries. GMM assumes that the image intensity of each class of tissues obeys a Gaussian distribution, where each class has its own mean intensity and variance, and classifies the tissues into different classes by best fitting the image histogram based on the expectation maximization method (Figure 1A). One slice of the original CMR-LGE images was shown in Figure 1B. Then, two different categories that included non-infarct and infarct tissue were obtained (Figure 1C). Next, the maximal component in each layer and the components with pixels more than 50% of the maximal components were kept. Finally, the regions in each image layer with more than 15 pixels were retained to remove small clusters of pixels affected by noise or blood vessels. The detailed process of the MGMM method can be found in our previously published paper (Wu et al., 2021).

To further segment the infarct tissue detected by the MGMM-based classification method and Threshold method into GZ and core scar, the maximal ( $\text{intensity}_{\max}$ ) and minimal ( $\text{intensity}_{\min}$ ) values of the pixels in the infarct tissue were calculated, then the pixels  $> (\text{intensity}_{\max} - \text{intensity}_{\min}) \times 50\%$  were assigned as core scar, and the rest pixels in the infarct area were assigned as GZ (Figure 1D).

### Model Construction and Simulation Protocol

After image segmentation, CardioViz3D (Toussaint et al., 2008) (INRIA, Sophia Antipolis, France) was used to interpolate the segmented low-resolution images to high-resolution images (about 0.4 mm). The 3D geometry of the infarct tissue which includes core scar and GZ was reconstructed using log odds method (Ukwatta et al., 2015), and merged with the corresponding ventricular high-resolution images. For each patient-specific bi-ventricular geometry, the commercial software Mimics Innovation Suite (Materialise NV, Leuven, Belgium) was used to generate the finite-element mesh (Figure 2A). The target average edge lengths were about 400  $\mu\text{m}$ . Fiber orientations in the mesh were assigned using a previously validated rule-based method (Bayer et al., 2012). It uses the Laplace–Dirichlet method to define transmural and apicobasal directions at every point in the ventricles, and then employs the bi-directional spherical linear interpolation to assign fiber orientations based on experimental measured angles (Eggen et al., 2012; Lombaert et al., 2012) ( $-40$  to  $+65^\circ$  from epi- to endocardium) (Figure 2B).

Electrophysiology properties were assigned in the model as previously described (Prakosa et al., 2018; Deng et al., 2019a). Briefly, non-infarcted tissue was assigned with the human ventricular myocyte action potential cell model of ten Tusscher et al. (2004; Figure 2C). Action potential remodeling in the GZ based on experimental recordings was implemented as follows

(Arevalo et al., 2013; Deng et al., 2016): peak sodium current, peak L-type calcium current, peak potassium currents  $\text{IKr}$ , and  $\text{IKs}$  were decreased to 38, 31, 30, and 20% of the original values in the Ten Tusscher model, respectively. Core scar was modeled as passive tissue. Conductivity values were assigned such that resultant conduction velocities (0.60 m/s in non-infarct tissue and 0.30 m/s in the GZ) were approximate to that measured clinically in the model, as illustrated in Anter et al. (2016).

The propagation of electrical activity in the heart model was simulated by solving a reaction-diffusion partial differential equation with finite-element method (Plank et al., 2008). Simulations of electrical activity in the patient-specific heart models with Neumann boundary conditions were executed in a monodomain representation of the myocardium using the openCARP simulation environment (Plank et al., 2021)<sup>1</sup> on high performance computers at Dalian University of Technology, China. Programmed electrical stimulation used in the previously published articles (Prakosa et al., 2018; Deng et al., 2019a) was used to induce VTs in the models of five patients. In brief, the protocol was consisted with 6 beats of 600 mm cycle length (S1), followed by premature stimulus (S2) at 90% of the S1 cycle length. The time between S1 and S2 was gradually shortened until VT was induced. If VT was not induced, a second premature stimulus was performed after S2. If VT was still not induced, a third premature stimulus was performed after S3. Furthermore, all models were paced from 19 ventricular sites, such as 17 sites on the LV (left ventricular), 1 near the right ventricular outflow tract, and 1 at the right ventricle apex, according to American Heart Association Classification Standards (Cerqueira et al., 2002; Figure 2D). After reentry was induced, 10 s of VT were simulated to detect the presence of arrhythmia. The VT morphology and location at the end of 3 and 10 s were analyzed and compared.

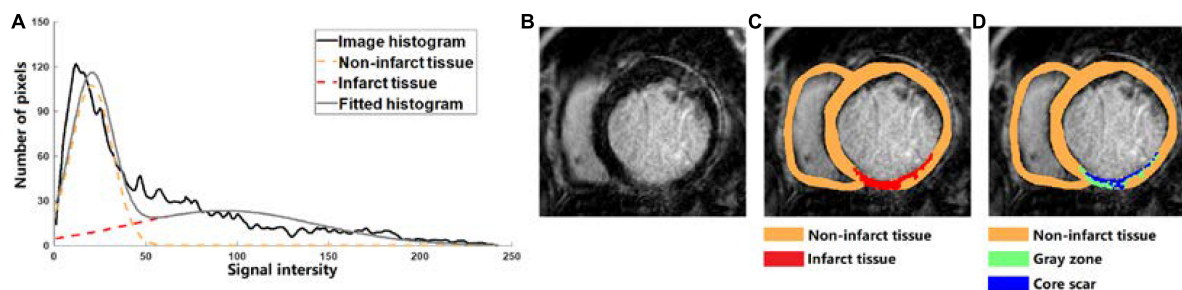
## RESULTS

Table 2 summarized the volumes of normal myocardium, GZ, and core scar in the reconstructed heart models from the MRI images of 5 patients. The mean ventricular volume was 176.4  $\text{cm}^3$ . The percentage of volume in the non-infarcted ventricular myocardium had a range from 86.4%~96.4%, while the percentage of GZ volume and core scar ranged from 2.8%~7.6% and 0.8%~7.1%, respectively.

Our simulation results showed that 59.0% (23/39) of VTs induced in the 3 s simulation continued propagating to the end of 10 s simulation, but some of the induced VT morphologies had great difference before and after 3 s simulation. We divide the VTs into four different types based on the stable time of the final VT morphology (Tables 3, 4).

For type 1 VT, the VT location and morphology was not stable, it changed location in 1–3 cycles, but in the last 2–3 cycles, the VT location and morphology became stable. And in the extended 10 s simulation, the VT location and morphology was the same as the VT at the end of 3 s simulation. About 25.6% (10/39)

<sup>1</sup><https://opencarp.org/>



**FIGURE 1 | (A)** Tissue classification example of cardiovascular magnetic resonance-late gadolinium enhancement (LGE-MRI) scanned from one human heart into two categories which are non-infarct tissue (orange dotted line) and infarct tissue (red dotted line) by using the Gaussian mixture model (GMM) method. **(B–D)** Based on the LGE-MRI of patient, the myocardial tissue was divided into non-infarct region (orange) and infarcted region (red) by GMM method, and the infarcted region was further divided into gray zone (GZ) (green) and core scar (blue).

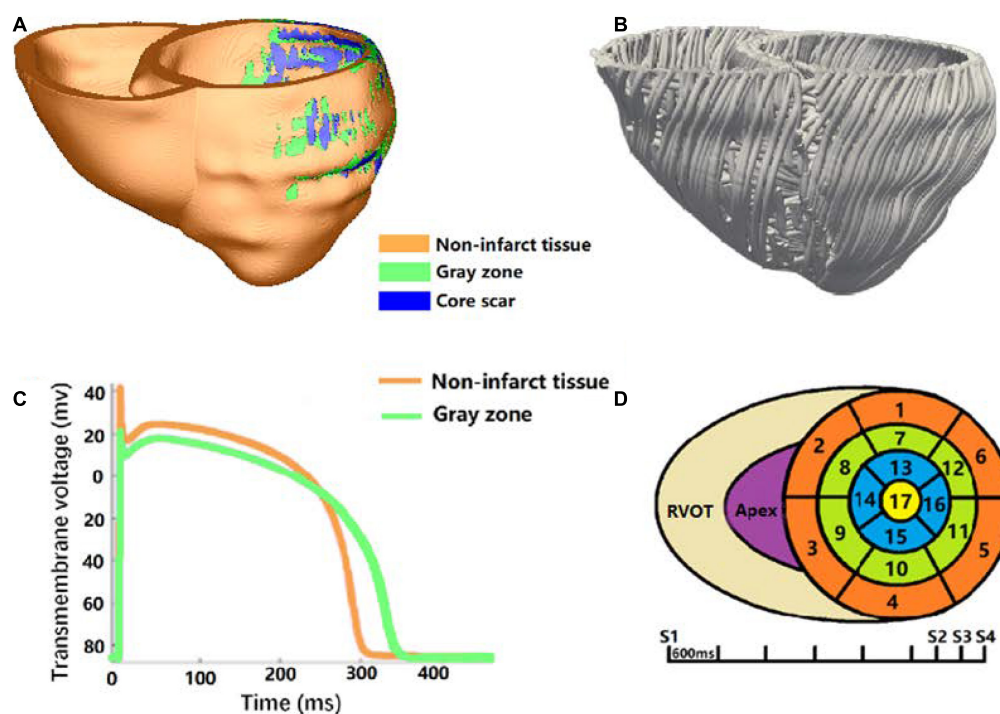


**FIGURE 2 |** Virtual-heart arrhythmia risk predictor methodology. **(A)** High-resolution ventricular structure model segmented into normal tissue, GZ, and core scar; **(B)** visualization of myocardial fiber orientations; **(C)** action potential for non-infarcted tissue (orange) and GZ (green); **(D)** virtual-heart arrhythmia risk predictor pacing sites.

**TABLE 2 |** Summary volume database of five patients.

Model	Normal tissue (cm <sup>3</sup> )	% of total volume	GZ (cm <sup>3</sup> )	% of total volume	Core scar (cm <sup>3</sup> )	% of total volume	Total volume of heart
PAT01	208.1	94.8	6.7	3.0	4.9	2.2	219.7
PAT02	175.2	86.4	13.2	6.5	14.3	7.1	202.7
PAT03	164.1	93.8	6.6	3.8	4.3	2.4	175.0
PAT04	230.6	96.4	6.6	2.8	1.9	0.8	239.1
PAT05	104.2	87.3	9.0	7.6	6.1	5.1	119.3
Mean $\pm$ SD	176.4 $\pm$ 48.2	91.7 $\pm$ 4.6	8.4 $\pm$ 2.9	4.7 $\pm$ 2.2	6.3 $\pm$ 4.7	3.5 $\pm$ 2.5	191.2 $\pm$ 46.6

**TABLE 3 |** Ventricular tachycardias (VTs) induced in all 5 models with simulation time of 3 and 10 s.

	3 s simulation	Reentry morphology	10 s simulation	Reentry morphology	Total VTs	Percentage
Type 1	Sustained reentry	Not stable reentry	Sustained reentry	Stable reentry	10	25.6%
Type 2	Sustained reentry	Not stable reentry	Sustained reentry	New stable reentry	4	10.3%
Type 3	Sustained reentry	Stable reentry	Sustained reentry	Same stable reentry	9	23.1%
Type 4	Sustained reentry	Stable reentry	Non-sustained reentry	No reentry	16	41.0%

**TABLE 4 |** Simulation time statistics when 39 stimulus sites induced reentry reached stability.

Patient number	Type 1		Type 2		Type 3		Type 4	
	Number of VTs	Time of VTs to be stable	Number of VTs	Time of VTs to be stable	Number of VTs	Time of VTs to be stable	Number of VTs	Time of VTs to be disappeared
PAT01	1	2.35 s	\	\	\	\	1	3.9 s
PAT02	3	2.6–2.9 s	3	4.1–7.3 s	5	1.46–2.3 s	\	\
PAT03	1	2.5 s	1	3.3 s	4	1.4–2.3 s	6	3.09–8.9 s
PAT04	\	\	\	\	\	\	4	3.06–5.3 s
PAT05	\	\	\	\	\	\	5	3.02–8.31 s
Total	10	2.35–2.9 s	4	3.3–7.3 s	9	1.4–2.3 s	16	3.02–8.9 s

"\" indicates that no corresponding type of VT was induced in the model, and thus the "Time of VTs to be stable" was not applicable.

VTs were type 1 reentry, and the time of VTs to be stable varied from 2.35 to 2.9 s.

**Figure 3** showed one example of type 1 VT. The initial reentry took place in the front of mid anterior cavity of endocardium isthmus, and the breakthrough (**Figure 3A**) presented here was transmitted from epicardium, where the reentrant loop was large and lasted for 5 cycles. While the simulation reached the end of 3 s, a stable "figure of eight" reentry propagated two cycles at the middle part of anterior wall (**Figure 3B**). As shown in **Figure 3C**, with the extended 10 s simulation, the reentry kept rotating without any changes.

For type 2 VT, the VT location and morphology was not stable, it changed locations during the entire 3 s simulation. But in the extended 10 s simulation, the VT location stabilized to a fixed location and the morphology did not change. About 10.3% (4/39) VTs were type 2 reentry, and the time of VTs to be stable varied from 3.3 to 7.3 s.

**Figure 4** showed one example of type 2 VT. During the 3 s simulation, several reentries were observed between myocardium and epicardium. The electrical propagation progress began with 3 cycles of one reentry with breakthrough at the epicardial surface. Then, the reentry changed to the anterior basal part of LV, and followed by changing to a new location with 2 cycles (**Figure 4A**). In the extended 10 s simulation, the chaotic reentry disappeared, and a new stable reentry formed at the anterior wall which lasted to the end of 10 s simulation (**Figure 4B**).

For type 3 VT, the VT location and morphology was stable in the 3 s simulation, and it did not change location and morphology in the extended 10 s simulation. Approximately, 23.1% (9/39) VTs were type 3 reentry, and the time of VTs to be stable varied from 1.4 to 2.3 s.

**Figure 5** showed one example of type 3 VT. **Figure 5A** showed one reentry induced in a model in the 3 s simulation. The reentry

located at the middle part of anterior wall, and it was a circulator. When the simulation was extended, there were little changes of morphology and position over time.

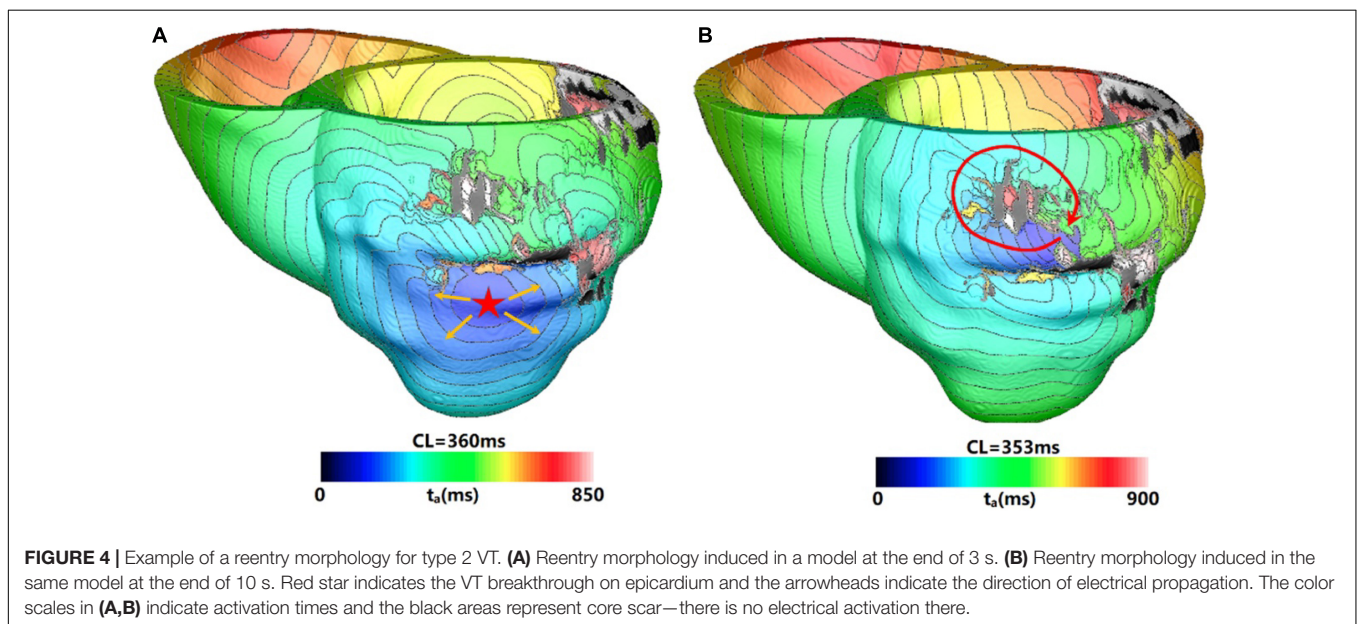
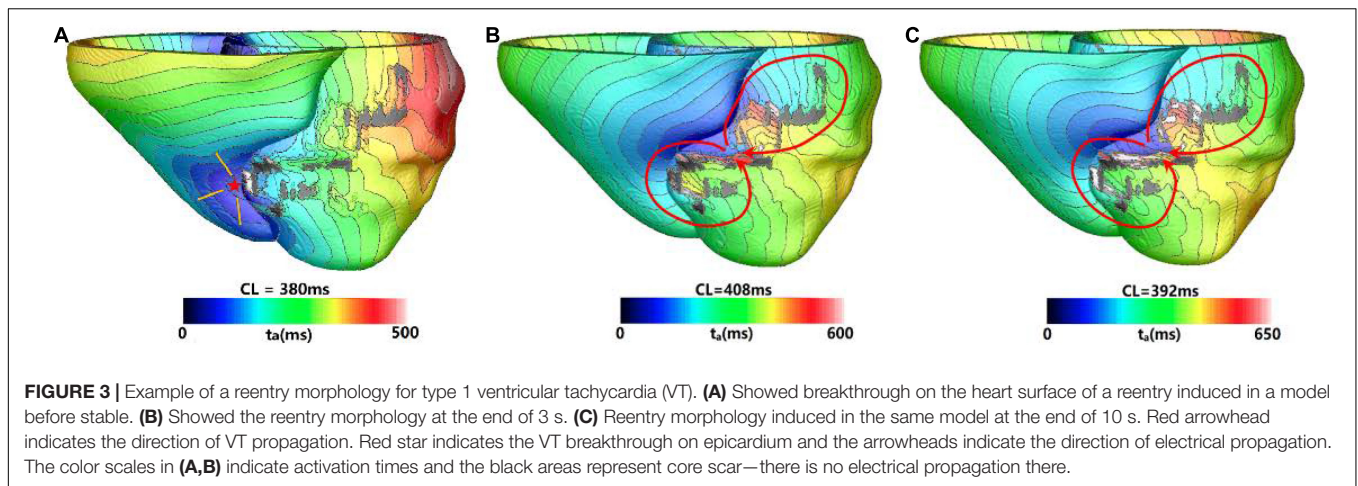
For type 4 VT, the VT location and morphology may change or be stable at the end of 3 s simulation, but they disappeared in the extended 10 s simulation. About 41.0% (9/39) VTs were type 4 reentry, and the time of VTs to be disappeared varied from 3.02 to 8.9 s.

**Figure 6** showed one example of type 4 VT. The reentry induced in the 3 s simulation disappeared in the extending 10 s simulation. In the 3 s simulation, the reentry propagated from epicardial surface into the interior wall and backed to the surface. A total of six reentry cycles occurred, as shown in **Figures 6A,B**. When the simulation time was extended, the reentry at middle part of LV lateral wall in the 3 s simulation disappeared. A new reentry emerged at the posterior basal wall, and it lasted for six cycles and then disappeared (**Figure 6C**).

**Table 5** summarized the clinical measurements and the 3 and 5 s simulation results of all five patients. For patient 1, the clinical diagnosis showed that there was no VT event when the patient was in hospital. Two sustained VTs were induced in the corresponding model of patient 1 in the 3 s simulation. In the 10 s simulation, 1 VT was terminated and the other survived to 10 s. Although 1 VT was induced in the 10 s simulation, the VT inducing ratio (5.3%) was very low, suggesting that the patient had a low probability to induce VT. Therefore, the result of 10 s simulation matched better than the 3 s simulation with the clinical diagnosis.

For patient 2, VT events were monitored four times and the location of VT was at the middle lateral wall of the LV. There were three different VTs induced in the 3 s simulation, one VT was related to the clinical measured location. The rest 2 VTs were not related to the clinical location. Two different VTs were induced in





the 10 s simulation, one VT induced by 10 of 19 pacing sites was related to the clinical measured location. The rest one induced in only 1 pacing site was in another location.

For patient 3, VT events were monitored and the VT was epicardial reentry close to apex. Three sustained VTs were induced in the corresponding model of patient 3 in the 3 s simulation. One was related to the clinical measurement, and the other two VTs induced in 6 pacing sites were not related to the clinical location and terminated in the 10 s simulation. There was only one sustained VT induced in 6 pacing sites in the 10 s simulation which was related to the clinical measurement.

For patient 4, the clinical diagnosis showed that there was no infarct related VT event when the patient was in hospital, and this patient only had ventricular premature beat. There was one sustained VT induced in 4 pacing sites in the 3 s simulation, but the VT only lasted to maximum 5 s in the 10 s simulation. There was no sustained reentry induced in the 10 s simulation, it was corresponded to the clinical diagnosis.

For patient 5, the clinical diagnosis showed that there was non-sustained VT event when the patient was in hospital, and VT was not inducible in this patient during implantable cardioverter defibrillator (ICD) implantation procedure. There were 2 sustained VTs induced in 5 pacing sites in the 3 s simulation, but all these VTs terminated in the 10 s simulation. One VT lasted to 8.3 s in the 10 s simulation, this was corresponding to the clinical diagnosis of non-sustained VT.

Based on the comparison of results in 3 and 10 s simulation with clinical measurements (as shown in **Table 5**), the results showed that sustained VTs induced in 16 pacing sites in 3 s simulation were terminated in the 10 s simulation, this meant that 41% (16/39) of the sustained VTs in the 3 s simulation became non-sustained in the 10 s simulation. The clinical measurements of patient 4 and 5 showed that the simulation results in 10 s simulation were more accurate than the 3 s simulation. In the 3 s simulation, more VTs were induced than the 10 s simulation, and some of VTs were not corresponding to clinical measurements.



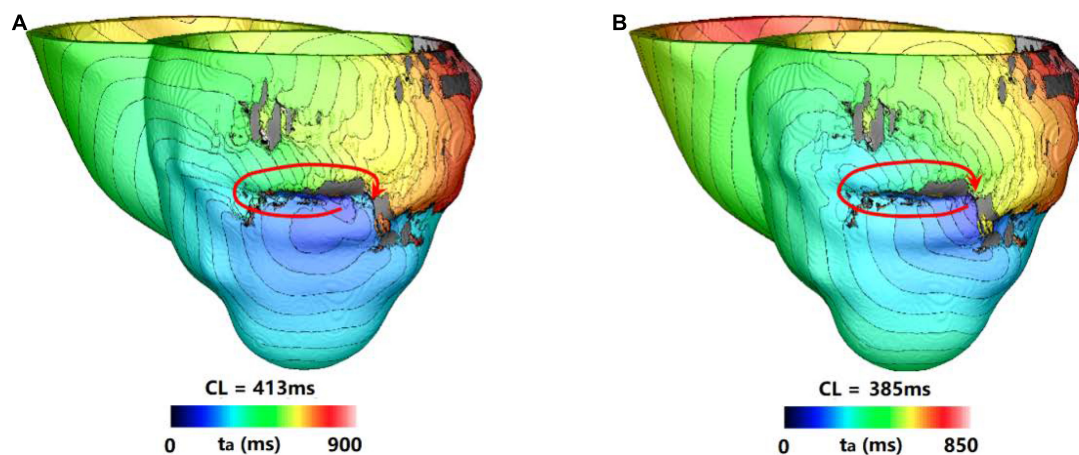


**FIGURE 5 |** Example of a reentry morphology for type 3 VT. **(A)** Reentry morphology induced in a model at the end of 3 s. **(B)** Reentry morphology induced in the same model at the end of 10 s. Red arrowhead indicates the direction of VT propagation.

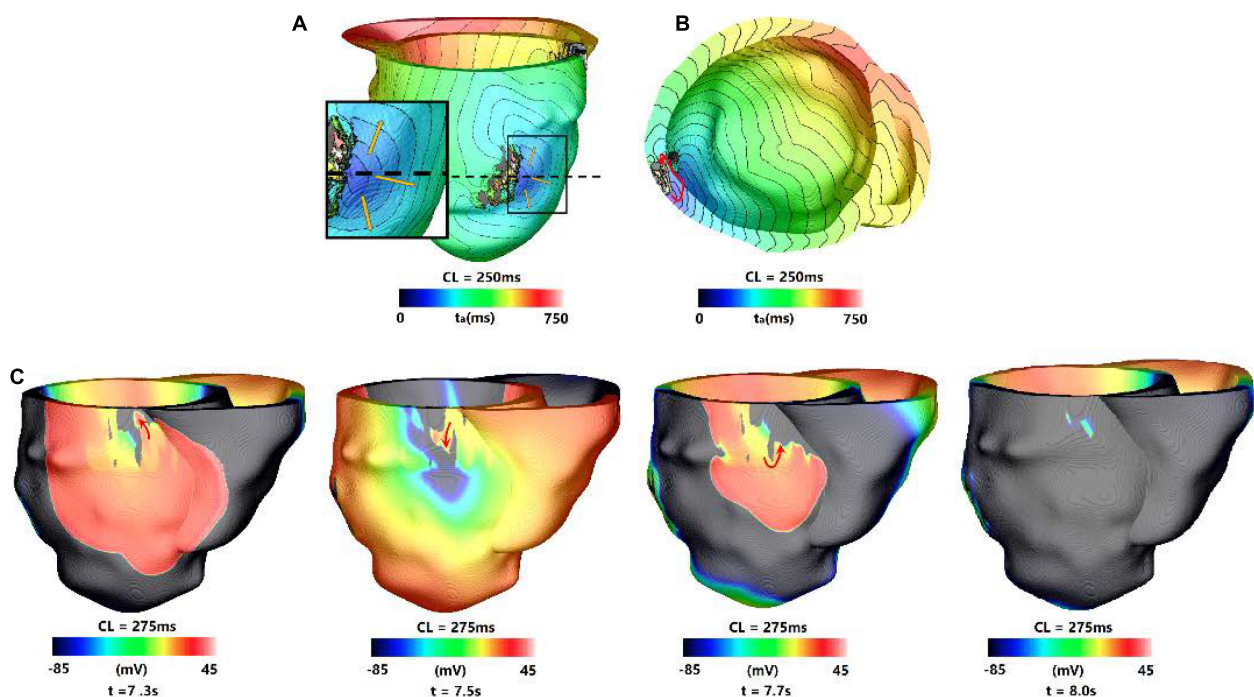


**FIGURE 6 |** Example of a reentry morphology for type 4 VT. **(A)** Reentry morphology induced in a model at the end of 3 s, yellow arrow indicates the direction of propagation. **(B)** The entire reentry conduction pathway as shown in the **(A)**. **(C)** Electrical propagation of the reentry in 10 s simulation. Red arrows show direction of propagation. The color bar shows the transmembrane potentials, and the instant time (t) of each map is shown below.

## DISCUSSION

In this study, we used personalized computational MI models which were reconstructed from LGE-MRI images to observe how long simulation of the induced arrhythmias in the personalized cardiac models is sufficient to get a stable location and morphology, and whether these characteristics have difference with varied simulation time. Based on the simulation results, we found that 41% of the sustained reentries in the 3 s

simulation group terminated in the longer simulation groups (10 s). The second finding in our simulation was that only 23.1% of the sustained reentries in the 3 s simulation did not change location and morphology in the extended 10 s simulation. The third finding is that 35.9% reentries were not stable when using 3 s simulation, which means that an extended simulation time is necessary.

For type 1 and 2 VT, because it is not stable when the simulation time is over, we should extend the simulation to a

**TABLE 5 |** Comparison of 3 and 10 s simulation results of modified Gaussian mixture model (MGMM) model with clinical data.

Clinical measurements			Simulation results of MGMM method					
PAT	VT in clinic	VT location	Results in 3 s simulation			Results in 10 s simulation		
			Number of VTs	Number of VTs related to clinic	Induction ratio	Number of VTs	Number of VTs related to clinic	Induction ratio
PAT01	N	–	2	–	10.5% (2/19)	1	–	5.3% (1/19)
PAT02	Y	Middle lateral wall of LV	3	1	57.9% (11/19)	2	1	57.9% (11/19)
PAT03	Y	Close to apex	3	1	63.2% (12/19)	1	1	31.6% (6/19)
PAT04	N	–	1	–	21.1% (4/19)	0	–	0% (0/19)
PAT05	N	–	2	–	26.3% (5/19)	0	–	0% (0/19)

Number of VTs indicates the number of sustained VT morphology induced in the model. Induction ratio refers to the proportion of pacing sites induced sustained reentry in the 19 pacing sites.

longer time to make sure the reentry become stable. But it is hard to give a consistent value for the simulation time based on the large variation of VT termination time. It should be possible to use a dynamic simulation time for each induced reentry, that is, 3, or 5, or 7, until 10 s. This will not only save the simulation resources, and make the simulation results more robust. These two types of VT may be related to the clinical hemodynamically unstable tachycardia (Nishimura et al., 2020). These kind of VTs are more likely sustained by functional reentry, this means that the involved VT is sustained by reentries through conduction channels around an area of functional block (Aguilar and Nattel, 2015; Deng et al., 2019a). The morphology and location of this kind of reentry were complex. The unstable characteristics of functional reentry was due to the intrinsic nature of the cardiac single cells (action potential duration adaptation, conductivity adaptation, etc.) (Chang et al., 2009; Lawson et al., 2020).

For type 3 VT, because the reentry gets stable at very early stage, and it does not change location and morphology in the extended simulation, thus for these reentries 3 s simulation is sufficient to get a robust result. This will save a lot of simulation resources and analysis time. This kind of VT is more likely sustained by anatomical reentry (Aguilar and Nattel, 2015), this means that the VT is sustained by reentries through conduction channels surrounded by scar on all sides. This kind of reentry was reported in other personalized heart modeling (Deng et al., 2019a; Kruithof et al., 2021) and clinical measurements (Anter et al., 2016; Nishimura et al., 2020). Our simulation results showed that type 3 VT was very stable, its morphology and location did not change during the entire 10 s simulation after reentry was initiated.

For type 4 VT, because the reentry gets disappeared in the extended simulation, this will not only spend more simulation resources to get robust results, but also make the results analysis more complex. It is very hard to recognize this kind of reentry as sustained reentry or non-sustained reentry as compared with the clinical definition (Katrakis et al., 2012). Besides, here rises a question that should this reentry be treated as an ablation target? These questions will be studied in the future when the clinical data of these patients become available.

For type 1, 2, and 4 VTs, the simulation results showed that simulation time must be extended to get the final stable reentry. Furthermore, the sustained reentry in 3 s simulation may become non-sustained reentry (or disappear in other word), this is consistent with clinical measurements that some reentries were unstable and may disappear in a few seconds (Ukwatta et al., 2015). In addition, the simulation results showed similar findings that no big morphological differences in circuit dimensions between stable and unstable VTs with the clinical measurements (Nishimura et al., 2020). We found that the CL of non-sustained reentry (type 4 VT) is shorter than other type of reentry, and the CL of type 1, 2, and 4 VTs did not have significant differences.

## CONCLUSION

In the current work, we not only quantitatively analyzed the commonly clinical measured phenomena which were some arrhythmias lasted for more than several minutes but others lasted only a couple of cycles or seconds, and some arrhythmias had no stable morphology or location, and the morphologies of reentries were not always stable, but also proposed a dynamic stimulation protocol to save computational resources and make simulation results more robust. We believe that the findings of this study not only improve the simulation accuracy, but also reduce unnecessary simulation time to achieve the optimal use of computer resources, thus improve the simulation efficiency and shorten the simulation time to meet the time node requirements of clinical operation on patients.

## LIMITATIONS

One limitation of the current study is the small sample size of five patients, but it could demonstrate the findings in the conclusion section. Another limitation is that we did not compare the non-sustained reentry with the clinical definition, but we have compared the simulation results with clinical diagnosis. We define the sustained and non-sustained reentry only based on the lasting time of reentry within 10 s. We will improve the

comparison when we get available clinical data in the future. The third limitation is that we have not done the quantitative comparison of VT characteristics in the model with clinical data, this is because that we do not have the corresponding patient data. But our simulation results can reproduce a lot of clinical measured phenomenon, this demonstrate that the personalized virtual heart simulation approach may provide a useful tool to help in understanding the underling mechanism of VT and assist in clinical decisions to identify and ablate the reentrant circuit(s).

## DATA AVAILABILITY STATEMENT

The original contributions presented in the study are included in the article/supplementary material, further inquiries can be directed to the corresponding author/s.

## ETHICS STATEMENT

The studies involving human participants were reviewed and approved by the Beijing Anzhen Hospital. Written

informed consent for participation was not required for this study in accordance with the National Legislation and the Institutional Requirements.

## AUTHOR CONTRIBUTIONS

CZ, RD, ZFW, NZ, and XW provided the human MRI and clinical data. DD, CZ, and LX designed the idea of the manuscript. ZF, ZHW, LT, NZ, BC, and YS did the manual segmentation. ZF, LT, ZHW, BC, and YS generated the figures. ZF, LT, DD, DZ, and LX wrote and revised the manuscript. All authors discussed the results and commented on the manuscript.

## FUNDING

This work was supported by grants from the National Natural Science Foundation of China (81901841 to DD), Fundamental Research Funds for the Central Universities (DUT21YG102 to DD), and Key Research and Development Program of Zhejiang Province (2020C03016 to LX).

## REFERENCES

- Aguilar, M., and Nattel, S. (2015). The pioneering work of George Mines on cardiac arrhythmias: groundbreaking ideas that remain influential in contemporary cardiac electrophysiology. *J. Physiol.* 594, 2377–2386. doi: 10.1113/JP270506
- Anter, E., Tschabrunn, C. M., Buxton, A. E., and Josephson, M. E. (2016). High-Resolution Mapping of Postinfarction Reentrant Ventricular Tachycardia: Electrophysiological Characterization of the Circuit. *Circulation* 134, 314–327. doi: 10.1161/CIRCULATIONAHA.116.021955
- Arevalo, H. J., Vadakkumpadan, F., Guallar, E., Jebb, A., Malamas, P., Wu, K. C., et al. (2016). Arrhythmia risk stratification of patients after myocardial infarction using personalized heart models. *Nat. Commun.* 7:11437. doi: 10.1038/ncomms11437
- Arevalo, H., Plank, G., Helm, P., Halperin, H., and Trayanova, N. (2013). Tachycardia in Post-Infarction Hearts: Insights from 3D Image-Based Ventricular Models. *PLoS One* 8:0068872. doi: 10.1371/journal.pone.0068872
- Bayer, J. D., Blake, R. C., Plank, G., and Trayanova, N. A. (2012). A Novel Rule-Based Algorithm for Assigning Myocardial Fiber Orientation to Computational Heart Models. *Ann. Biomed. Eng.* 40, 2243–2254. doi: 10.1007/s10439-012-0593-5
- Behradfar, E., Nygren, A., and Vigmond, E. J. (2014). The Role of Purkinje-Myocardial Coupling during Ventricular Arrhythmia: A Modeling Study. *PLoS One* 9:e88000. doi: 10.1371/journal.pone.0088000
- Cerqueira, M. D., Weissman, N. J., Dilsizian, V., Jacobs, A. K., Kaul, S., Laskey, W. K., et al. (2002). Standardized Myocardial Segmentation and Nomenclature for Tomographic Imaging of the Heart. *J. Cardiovasc. Magnet. Reson.* 4, 203–210. doi: 10.1081/jcmr-120003946
- Chang, M. G., Zhang, Y., Chang, C. Y., Xu, L., Emokpae, R., Tung, L., et al. (2009). Spiral Waves and Reentry Dynamics in an In Vitro Model of the Healed Infarct Border Zone. *Circulat. Res.* 105, 1062–1071. doi: 10.1161/CIRCRESAHA.108.176248
- Ciaccio, E. J., Coromilas, J., Wit, A. L., Peters, N. S., and Garan, H. (2016). Formation of Functional Conduction Block During the Onset of Reentrant Ventricular Tachycardia. *Circulat. Arrhythm. Electrophysiol.* 9:e004462. doi: 10.1161/CIRCEP.116.004462
- Crinion, D., Neira, V., Al Hamad, N., de Leon, A., Bakker, D., Korogyi, A., et al. (2020). Close-coupled Pacing to Identify the 'Functional' Substrate of Ventricular Tachycardia: Long-term Outcomes of the Paced Electrogram Feature Analysis (PEFA) Technique. *Heart Rhythm* 18, 723–731. doi: 10.1016/j.hrthm.2020.12.022
- Deng, D., Arevalo, H. J., Prakosa, A., Callans, D. J., and Trayanova, N. A. (2016). A Feasibility Study of Arrhythmia Risk Prediction in Patients with Myocardial Infarction and Preserved Ejection Fraction. *Europace* 18, iv60–iv66. doi: 10.1093/europace/euw351
- Deng, D., Arevalo, H., Pashakhanloo, F., Prakosa, A., Ashikaga, H., McVeigh, E., et al. (2015). Accuracy of Prediction of Infarct-Related Arrhythmic Circuits from Image-Based Models Reconstructed from Low and High Resolution MRI. *Front. Physiol.* 6:282. doi: 10.3389/fphys.2015.00282
- Deng, D., Prakosa, A., Shade, J., Nikolov, P., and Trayanova, N. A. (2019a). Characterizing Conduction Channels in Postinfarction Patients Using a Personalized Virtual Heart. *Biophys. J.* 117, 2287–2294. doi: 10.1016/j.bpj.2019.07.024
- Deng, D., Prakosa, A., Shade, J., Nikolov, P., and Trayanova, N. A. (2019b). Sensitivity of Ablation Targets Prediction to Electrophysiological Parameter Variability in Image-Based Computational Models of Ventricular Tachycardia in Post-infarction Patients. *Front. Physiol.* 10:628. doi: 10.3389/fphys.2019.00628
- Eggen, M. D., Swingen, C. M., and Laizzo, P. A. (2012). Ex vivo diffusion tensor MRI of human hearts: Relative effects of specimen decomposition. *Magnet. Reson. Med.* 67, 1703–1709. doi: 10.1002/mrm.23194
- Fernández-Armenta, J., Berrueto, A., Andreu, D., Camara, O., Silva, E., Serra, L., et al. (2013). Three-dimensional architecture of scar and conducting channels based on high resolution ce-CMR: insights for ventricular tachycardia ablation. *Circulat. Arrhythmia Electrophysiol.* 6, 528–537. doi: 10.1161/CIRCEP.113.000264
- Hennemuth, A., Friman, O., Huellebrand, M., and Peitgen, H.-O. (2013). "Mixture-Model-Based Segmentation of Myocardial Delayed Enhancement MRI," in *International Workshop on Statistical Atlases and Computational Models of the Heart*, (Lima: STACOM).
- Josephson, M. E., Almendral, J., and Callans, D. J. (2014). Resetting and entrainment of reentrant ventricular tachycardia associated with myocardial infarction. *Heart Rhythm* 11, 1239–1249. doi: 10.1016/j.hrthm.2014.03.046
- Katritsis, D. G., Zareba, W., and Camm, A. J. (2012). Nonsustained Ventricular Tachycardia. *J. Am. Coll. Cardiol.* 60, 1993–2004. doi: 10.1016/j.jacc.2011.12.063
- Klinke, V., Muzzarelli, S., Lauriers, N., Locca, D., Vincenti, G., Monney, P., et al. (2013). Quality Assessment of Cardiovascular Magnetic Resonance in the Setting of the European CMR Registry: Description and Validation of Standardized Criteria. *J. Cardiovasc. Magnetic Reson.* 15:55. doi: 10.1186/1532-429X-15-55

- Kramer, C. M., Barkhausen, J., Bucciarelli-Ducci, C., Flamm, S. D., Kim, R. J., and Nagel, E. (2020). Standardized Cardiovascular Magnetic Resonance Imaging (CMR) Protocols: 2020 Update. *J. Cardiovasc. Magnetic Resonan.* 22:17. doi: 10.1186/s12968-020-00607-1
- Kruihof, E., Amirrajab, S., Cluitmans, M. J. M., Lau, K. D., and Breeuwer, M. (2021). Influence of image artifacts on image-based computer simulations of the cardiac electrophysiology. *Comput. Biol. Med.* 137:104773. doi: 10.1016/j.combiomed.2021.104773
- Kusumoto, F. M., Bailey, K. R., Chaouki, A. S., Deshmukh, A. J., Gautam, S., Kim, R. J., et al. (2018). Systematic Review for the 2017AHA/ACC/HRS Guideline for Management of Patients With Ventricular Arrhythmias and the Prevention of Sudden Cardiac Death. *J. Am. Coll. Cardiol.* 72, 1653–1676. doi: 10.1016/j.jacc.2017.10.052
- Lawson, B. A. J., Oliveira, R. S., Berg, L. A., Silva, P. A. A., Burrage, K., and Dos Santos, R. W. (2020). Variability in electrophysiological properties and conducting obstacles controls re-entry risk in heterogeneous ischaemic tissue. *Philosop. Transact. R. Soc. Math. Phys. Eng. Sci.* 378:20190341. doi: 10.1098/rsta.2019.0341
- Lombaert, H., Peyrat, J. M., Croisille, P., Rapacchi, S., Fanton, L., Cheriet, F., et al. (2012). Human atlas of the cardiac fiber architecture: study on a healthy population. *IEEE Trans. Med. Imaging* 31, 1436–1447. doi: 10.1109/TMI.2012.2192743
- Lopez-Perez, A., Sebastian, R., Izquierdo, M., Ruiz, R., Bishop, M., and Ferrero, J. M. (2019). Personalized Cardiac Computational Models: From Clinical Data to Simulation of Infarct-Related Ventricular Tachycardia. *Front. Physiol.* 10:580. doi: 10.3389/fphys.2019.00580
- Martin, R., Maury, P., Bisceglia, C., Wong, T., Estner, H., Meyer, C., et al. (2018). Characteristics of Scar-Related Ventricular Tachycardia Circuits Using Ultra-High-Density Mapping. *Circulat. Arrhythmia Electrophysiol.* 11:e006569. doi: 10.1161/CIRCEP.118.006569
- Nishimura, T., Upadhyay, G. A., Aziz, Z. A., Beaser, A. D., Shatz, D. Y., Nayak, H. M., et al. (2020). Circuit Determinants of Ventricular Tachycardia Cycle Length: Characterization of Fast and Unstable Human VT. *Circulation* 143, 212–226. doi: 10.1161/CIRCULATIONAHA.120.050363
- Plank, G., Loewe, A., Neic, A., Augustin, C., Huang, Y. L., Gsell, M. A. F., et al. (2021). The openCARP Simulation Environment for Cardiac Electrophysiology. *Comp. Methods Prog. Biomed.* 208:106223. doi: 10.1016/j.cmpb.2021.106223
- Plank, G., Zhou, L., Greenstein, J. L., Cortassa, S., Winslow, R. L., O'Rourke, B., et al. (2008). From mitochondrial ion channels to arrhythmias in the heart: computational techniques to bridge the spatio-temporal scales. *Phil. Trans. A Math. Phys. Eng. Sci.* 366, 3381–3409. doi: 10.1098/rsta.2008.0112
- Pop, M., Ghugre, N. R., Ramanan, V., Morikawa, L., Stanisz, G., Dick, A. J., et al. (2013). Quantification of Fibrosis in Infarcted Swine Hearts by Ex Vivo Late Gadolinium-Enhancement and Diffusion-Weighted MRI Methods. *Physics Med. Biol.* 58, 5009–5028. doi: 10.1088/0031-9155/58/15/5009
- Prakosa, A., Arevalo, H. J., Deng, D., Boyle, P. M., Nikolov, P. P., Ashikaga, H., et al. (2018). Personalized Virtual-Heart Technology for Guiding the Ablation of Infarct-Related Ventricular Tachycardia. *Nat. Biomed. Eng.* 2, 732–740. doi: 10.1038/s41551-018-0282-2
- Soto-Iglesias, D., Penela, D., Jáuregui, B., Acosta, J., Fernández-Armenta, J., Linhart, M., et al. (2020). Cardiac Magnetic Resonance-Guided Ventricular Tachycardia Substrate Ablation. *JACC Clin. Electrophysiol.* 6, 436–447. doi: 10.1016/j.jacep.2019.11.004
- ten Tusscher, K. H., Noble, D., Noble, P. J., and Panfilov, A. V. (2004). A model for human ventricular tissue. *Am. J. Physiol. Heart Circ. Physiol.* 286, H1573–H1589. doi: 10.1152/ajpheart.00794.2003
- Toussaint, N., Mansi, T., Delingette, H., Ayache, N., and Sermesant, M. (2008). “An Integrated Platform for Dynamic Cardiac Simulation and Image Processing: Application to Personalised Tetralogy of Fallot Simulation,” in *Proceedings of the Eurographics Workshop on Visual Computing for Biomedicine*, (The Netherlands: VCBM).
- Ukwatta, E., Arevalo, H., Rajchl, M., White, J., Pashakhanloo, F., Prakosa, A., et al. (2015). Image-Based Reconstruction of Three-Dimensional Myocardial Infarct Geometry for Patient-Specific Modeling of Cardiac Electrophysiology. *Med. Phys.* 42, 4579–4590. doi: 10.1118/1.4926428
- Ukwatta, E., Nikolov, P., Zabihollahy, F., Trayanova, N. A., and Wright, G. A. (2018). Virtual electrophysiological study as a tool for evaluating efficacy of MRI techniques in predicting adverse arrhythmic events in ischemic patients. *Physics Med. Biol.* 63:225008. doi: 10.1088/1361-6560/aae8b2
- Woodard, P. K., Bluemke, D. A., Cascade, P. N., Finn, J. P., Stillman, A. E., Higgins, C. B., et al. (2007). ACR Practice Guideline for the Performance and Interpretation of Cardiac Magnetic Resonance Imaging (MRI). *Yearbook Diagnos. Radiol.* 3, 665–676. doi: 10.1016/j.jacr.2006.06.007
- Wu, K. C. (2017). Sudden Cardiac Death Substrate Imaged by Magnetic Resonance Imaging: From Investigational Tool to Clinical Applications. *Circ. Cardiovasc. Imaging* 10:e005461. doi: 10.1161/CIRCIMAGING.116.005461
- Wu, Z. H., Sun, L. P., Liu, Y. L., Dong, D. D., Tong, L., Deng, D. D., et al. (2021). Fully Automatic Scar Segmentation for Late Gadolinium Enhancement MRI Images in Left Ventricle with Myocardial Infarction. *Curr. Med. Sci.* 41, 398–404. doi: 10.1007/s11596-021-2360-z

**Conflict of Interest:** The authors declare that the research was conducted in the absence of any commercial or financial relationships that could be construed as a potential conflict of interest.

**Publisher's Note:** All claims expressed in this article are solely those of the authors and do not necessarily represent those of their affiliated organizations, or those of the publisher, the editors and the reviewers. Any product that may be evaluated in this article, or claim that may be made by its manufacturer, is not guaranteed or endorsed by the publisher.

Copyright © 2021 Tong, Zhao, Fu, Dong, Wu, Wang, Zhang, Wang, Cao, Sun, Zheng, Xia and Deng. This is an open-access article distributed under the terms of the Creative Commons Attribution License (CC BY). The use, distribution or reproduction in other forums is permitted, provided the original author(s) and the copyright owner(s) are credited and that the original publication in this journal is cited, in accordance with accepted academic practice. No use, distribution or reproduction is permitted which does not comply with these terms.



# Advantages of publishing in Frontiers



## OPEN ACCESS

Articles are free to read  
for greatest visibility  
and readership



## FAST PUBLICATION

Around 90 days  
from submission  
to decision



## HIGH QUALITY PEER-REVIEW

Rigorous, collaborative,  
and constructive  
peer-review



## TRANSPARENT PEER-REVIEW

Editors and reviewers  
acknowledged by name  
on published articles

## Frontiers

Avenue du Tribunal-Fédéral 34  
1005 Lausanne | Switzerland

Visit us: [www.frontiersin.org](http://www.frontiersin.org)

Contact us: [frontiersin.org/about/contact](http://frontiersin.org/about/contact)



## REPRODUCIBILITY OF RESEARCH

Support open data  
and methods to enhance  
research reproducibility



## DIGITAL PUBLISHING

Articles designed  
for optimal readership  
across devices



## FOLLOW US

@frontiersin



## IMPACT METRICS

Advanced article metrics  
track visibility across  
digital media



## EXTENSIVE PROMOTION

Marketing  
and promotion  
of impactful research



## LOOP RESEARCH NETWORK

Our network  
increases your  
article's readership